Airborne Strapdown Gravity Measurements for Geodesy and Geophysics

Jensen, Tim Enzlberger

Publication date:
2018

Document Version
Publisher's PDF, also known as Version of record

DTU Space
National Space Institute

Airborne Strapdown Gravity Measurements for Geodesy and Geophysics

Dissertation submitted for the degree of

Philosophiæ Doctor

to the PhD School of the National Space Institute,
Technical University of Denmark

on August 31st, 2018 by

Tim Enzlberger Jensen

Academic supervisors:

Rene Forsberg & Arne Vestergaard Olesen

Abstract

The determination of gravity from an airborne platform, commonly known as airborne gravimetry, has been recognised as an operational procedure since the 1990s, using spring-type gravimeters mounted on a stabilised platform. Although it has been demonstrated that inertial-grade sensors directly attached to the chassis of the aircraft, i.e. in a strapdown configuration, can have similar accuracy, stabilised-platform systems have remained the predominant method in airborne gravimetry. This is because the long wavelength information in the gravity estimates are contaminated by uncompensated sensor errors, leaking into the gravity estimates. The use of a strapdown gravimeter does however present some appealing practical advantages, since an off-the-shelf Inertial Measurement Unit (IMU), designed for navigation purposes, can be simply installed and used for gravimetry.

In collaboration with the Technical University of Darmstadt, the Danish National Space Institute has been operating a strapdown gravimeter on a number of airborne campaigns since 2013. Based on this experience, the strapdown system has gained recognition as an exceptional complement to the stabilised platform system, increasing the operational flexibility and resilience against dynamic flight conditions. Additionally, the use of off-line temperature calibration methods has been shown to significantly constrain the erroneous long wavelength information, promoting the use of strapdown gravimetry as a stand-alone system. The operational flexibility and compact size of the strapdown system makes it a feasible candidate for a number of future applications, such as the use in Unmanned Arial Vehicles (UAVs) and surveying marine-terminating glaciers in remote areas of the world.

This thesis is a contribution to the development of strapdown airborne gravimetry based on inertial technology. A newly purchased IMU has been flown on a number of airborne surveys, demonstrating the feasibility and flexibility of using a strapdown system. The different environment of each collected data set is an indication of the superior dynamic range of the IMU-based system, demonstrating the enormous potential for future applications.

Resume

Måling af Jordens tyngdekraft fra luften har været anerkendt som en operationel metode siden 1990erne. Den anvendte teknologi består af fjeder-baseret gravimetre, monteret på en stabiliseret platform. En alternativ teknologi består af inertielle accelerometre og gyroskoper, monteret direkte på flyets ramme. Denne alternative tilgang er derfor også kendt som "strapdown"-metoden. Selvom en lignende nøjagtighed er blevet demonstreret for denne alternative teknologi, består den platform-basererede teknologi som den foretrukne metode. Dette er fordi at ukompenserede fejl i måleinstrumenterne resulterer i fejlagtig estimering af den langbøljede information i tyngde-estimaterne. Strapdown-metoden tilbyder dog en række fordele, da denne er baseret på en såkaldt "Inertial Measurement Unit" (IMU), som er designet til navigation og kan anvendes til tyngde-estimering uden yderligere modifikationer.

I samarbejde med det Tekniske Universitet i Darmstadt, har Institut for Rumforskning og -teknologi ved Danmarks Tekniske Universitet medbragt et strapdown-gravimeter på flere luftbårne kampagner siden 2013. I løbet af disse kampagner har strapdown-teknologien vist sig bedre at kunne håndtere dynamiske forhold i form af manøvrer og turbulens, samt at tilbyde mere operationel fleksibilitet. I denne tid har det også vist sig at temperaturkalibrering af instrumentet er i stand til at forbedre målenøjagtigheden i det langbøljede spektrum, hvilket giver en forhåbning om at instrumentet i fremtiden kan erstatte det platformbaserede system i nogle applikationer. På grund af dets betydeligt mindre størrelse og evne til bedre at håndtere dynamiske forhold, er strapdown-systemet en oplagt kandidat applikationer som f.eks. droner og udforskning af gletsjere i ellers ufremkommelige egne.

Denne afhandling har til formål at bidrage til udviklingen af strapdown-metoden, baseret på inertiel teknologi. Med baggrund i en ny-indkøbt IMU, vil metodens anvendelighed og øgede fleksibilitet blive demonstreret under en række test-flyvninger. I forbindelse med disse test-flyvninger, vil systemet blive udsat for forskellige forhold der demonstrerer den forbedrede dynamiske rækkevidde og det enorme potentiale teknologien besidder i forhold til fremtidige applikationer.

Preface

This PhD dissertation has been written during my enrolment as a PhD student at the Department of Geodynamics at the National Space Institute (DTU Space) of the Technical University of Denmark. The project was supervised by *Rene Forsberg* and *Arne V. Olesen*.

The work done during this enrolment has also contributed to two peer-reviewed publications:

1. Rene Forsberg and Tim Jensen (2015), *New Geoid of Greenland: A Case Study of Terrain and Ice Effects, GOCE and Use of Local Sea Level Data*. In: Jin S., Barzaghi R. (eds) IGFS 2014. International Association of Geodesy Symposia, vol 144. Springer.
2. Tim E. Jensen, J. Emil Nielsen, Arne V. Olesen and Rene Forsberg (2017), *Strapdown Airborne Gravimetry Using a Combination of Commercial Software and Stable-Platform Gravity Estimates*. In: International Association of Geodesy Symposia. Springer, Berlin, Heidelberg

along with a manuscript titled:

3. Tim E. Jensen and Rene Forsberg, *Helicopter Test of a Strapdown Airborne Gravimetry System*

submitted to the peer-reviewed journal *sensors* on August 14th, 2018. The two publications along with the submitted manuscript are attached in Appendix F.

In this dissertation equations will be referenced using parenthesis () and citations will be referenced using square brackets []. To this end it should be noted that the dissertation contains a reference list after each of the four parts and an additional reference list after the appendices. The references listed in the introduction refers to the list after the first part. References to figures and tables will be written out explicitly. In order to provide some overview, a list of abbreviations, symbols, figures and tables are supplied at the end of the dissertation along with an index referencing key terms.

Acknowledgements

First of all, I want to thank my supervisors, *Rene Forsberg*, who has given me this opportunity and trusted in my abilities, and *Arne V. Olesen*, who has openly shared his many years of experience in airborne gravimetry.

Second, I want to express my gratitude towards my colleague, *David Becker*, at TU Darmstadt (now Curtin University), who has openly and continuously provided me insight into the subject of strapdown gravimetry, towards my (now former) colleague, *Emil Nielsen*, whose helpful attitude has made him my unofficial supervisor and towards my colleague, *Peter Schack*, at TU Munich for fruitful discussions and good company.

Although not directly involved in this PhD, I also want to thank my colleague, *Gabriel Strykowski*, who was my first entry-point into the field of geodesy and still remains supportive, and to my *remaining colleagues at DTU Space* who have provided me with all kinds of help and support.

During the course of my PhD, I have had considerable communication with iMAR Navigation. I therefore want to express my gratitude towards *Matthias Hoss* and *Alexander Dreyer* at iMAR Navigation for their support and collaboration.

I also want to thank, *Mikael B. Larsen* and *Martin J. Jørgensen*, at Sonardyne / DTU Compute for sharing knowledge and accepting my drop-by discussion sessions.

The airborne survey in the South China Sea was done as part of the Marine Geodetic Infrastructure in Malaysian Waters (MAGIC) project on behalf of Info-Geomatik Sdn. Bhd. and the Department of Survey and Mapping Malaysia (JUPEM). The Greenland helicopter test was part of work for maintaining the Greenland gravity network on behalf of the Danish Mapping Agency (SDFE). The Odenwald survey was carried out by iMAR Navgation, in order to test the development of their systems for gravimetry.

Finally, I want to express my sincere gratitude towards my wife and children, who have supported me throughout this endeavour. As these lines are the last ones written in this dissertation, I will not attempt to find words for my gratitude, but simply go home and spend some time with my family ...

Contents

Part II: Inertial Navigation and Sensors

Appendices

Glossary and Index

1 Introduction

A gravimeter is essentially an accelerometer, meaning that it measures a combination of gravitational and kinematic acceleration. When mounted on a moving vehicle, the gravimeter in itself is therefore not sufficient to estimate the gravitational attraction. In order to retrieve the gravitational component, an additional sensor monitoring the movement of the vehicle is required. Additionally, since accelerometers measure along a single sensitive axis, it is necessary to keep track of the sensor orientation during manoeuvres. These two fundamental problems in airborne gravimetry are sketched in Figure 1.1.

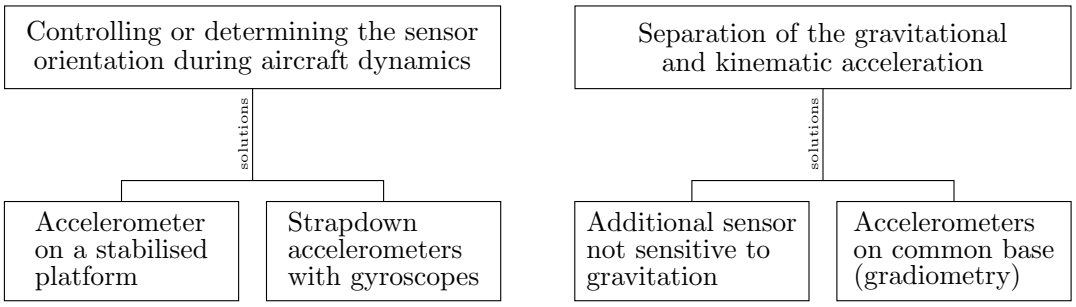

Figure 1.1: Airborne gravimetry has two fundamental problems, which are outlined in [43] along with common solutions

The first problem is usually handled in one of two ways. Either the accelerometers are mounted on a **stabilised platform** that is to some extent isolated from the movements of the vehicle and thus maintains a known direction in space. This is usually accomplished using accelerometers and gyroscopes in a mechanical feedback system, that can also take advantage of the Global Navigation Satellite System (GNSS). Otherwise a triad of accelerometers and gyroscopes can be mounted in a **strapdown configuration**, i.e. physically attaching the instrument to the aircraft. This allows for numerical determination of the sensor orientation and is generally accomplished using an Inertial Measurement Unit (IMU).

In order to obtain the gravity vector, the measured accelerations must be corrected for any effects originating from movement. This kinematic acceleration is usually derived from GNSS observations. Therefore, an airborne gravimetry system consists of two measurement systems:

1. An accelerometer on a stabilised platform or an IMU in strapdown configuration
2. A GNSS system consisting of receiver and antenna on board the aircraft and possibly a reference station on ground

This dissertation focuses on a strapdown IMU system, also known as Strapdown Airborne Gravimetry (SAG). Although the IMU in itself only represents half the measurement system, the GNSS system will not receive much attention here. The GNSS observations will be processed using the Waypoint commercial software suite from NovAtel, in order to yield estimates of velocity and/or position, which are then fed into the processing algorithm.

Gravity estimates are therefore essentially obtained by differencing the output from two measurement systems, meaning that it is well suited for spectral analysis. This is important because the spectral band of interest is dependent on the intended application. In Table 1.1 the applications are divided into three main categories and associated with requirements in terms of both spatial resolution and accuracy.

Area of Application	**Half-Wavelength Resolution**	**RMS Accuracy**
Geodesy (including marine geodesy)	10 - 500 km	1-3 mGal
	50 - 500 km	0.1 mGal
Geophysics (science)	5 - 100 km	1-2 mGal
Exploration	<5 km	<0.5 mGal

Table 1.1: Overview of main areas of application with associated requirements for spatial resolution and accuracy

The main application in **geodesy** is the determination of a reference surface corresponding to sea level. This surface is known as the Geoid and provides both a reference surface and direction for the vertical. In marine geodesy, the slope of the Geoid at sea is compared with the slope of the sea surface as measured by a radar or laser altimeter. This enables the determination of the gravity vector over the ocean [41]. Both these applications have very strict requirements regarding the accuracy of long wavelength information in the gravity estimates. At a half-wavelength resolution of 50-500 km, the accuracy should be better than 0.1 mGal [44]. The applications in **geophysics** are typically concerned with monitoring of the cryosphere or sub-surface geological structures. As gravity provides information regarding the sub-surface density distribution, it is often flown in conjunction with other measurement systems such as magnetometers and radar/laser altimeters. The combination of information is commonly used to interpret the current state and past evolution of the solid Earth or cryosphere and an often used method for this is mathematical inversion. In **exploration**, the aim is also detection of sub-surface geological structures. However, geophysics is concerned with local and regional structures such as sub-ice topography, tectonic evolution, fault lines and volcanoes, whereas exploration is concerned with geological structures of much smaller scale such as sediment basins, salt domes and mineral deposits. This poses much higher requirements for the accuracy and spatial resolution of the gravity estimates, but relaxes requirements on the accuracy of the long wavelength components of the signal.

Having already introduced requirements in the form of spatial resolution and Root-Mean-Square (RMS) accuracy, it is in order to mention that these concepts will be properly introduced in Section 4. The concept of spatial resolution is related to the decomposition of a signal into waveforms, such that spatial resolution can be described in terms of either the full- or half-wavelength of each waveform. The power spectrum of such a decomposition determines the influence of each waveform. The waveform with shortest wavelength and enough power to considerably influence the signal determines the resolution. Therefore, the terms spatial resolution and half-wavelength will be used synonymously throughout this dissertation. In order to ease discussion, it is useful to define the following regions of the wavelength spectrum [10]:

- High spatial resolution: Half-wavelength below 5 km (short wavelength)
- Medium spatial resolution: Half-wavelength of 5-150 km (medium wavelength)
- Low spatial resolution: Half-wavelength above 150 km (long wavelength)

which are concerned with various measurement techniques as illustrated in Figure 1.2. Airborne gravimetry is therefore concerned with all three resolution domains, but cannot resolve the entire spectrum simultaneously at the required accuracy. The combination of airborne gravimetry with other measurement techniques is therefore an important subject.

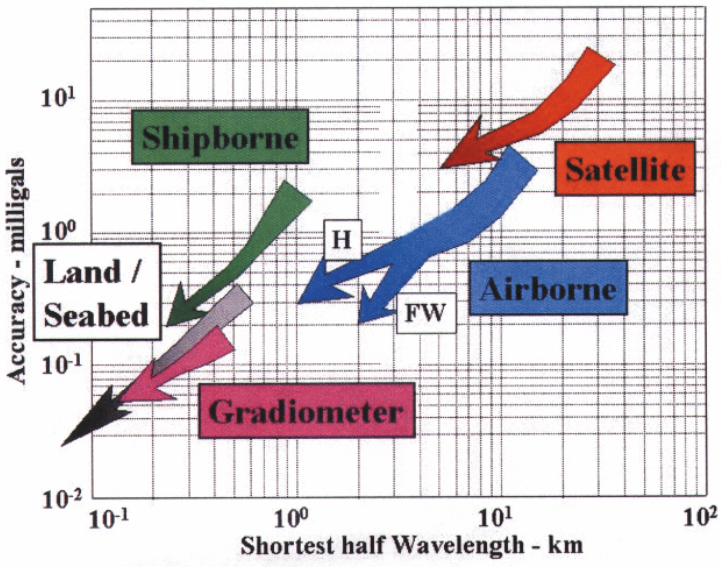

Figure 1.2: Overview of accuracy and resolution of different measurement systems (arrow points represent current claims). FW = fixed wing; H = helicopter. Image credit: [13]

Measurement methods in gravimetry involve terrestrial observations, which are point-wise and usually non-uniform in coverage and accuracy, and satellite observations which cover most of the Earth with a uniform accuracy, but is limited in resolution by the attenuation of gravity with altitude. Airborne measurements therefore cover an important intermediate area between terrestrial and satellite gravity methods in terms of both resolution and coverage. Moreover, airborne surveys are usually designed in order to obtain uniform accuracy over the surveyed area. For these reasons airborne gravity estimates are especially well suited to be combined with other sources of information.

Since the advent of the Global Positioning System (GPS) in the 1990s, airborne gravimetry has been an operational method using stabilised platform systems [16]. This dissertation focuses on the use of a strapdown IMU for airborne gravimetry. Although such a configuration poses more stringent requirements for the sensor performance, e.g. larger dynamic range, higher resolution and better scale factor stability, it does have several significant advantages over the platform system:

1. An off-the-shelf IMU, designed for navigation purposes, can be used
   - 1a The gravity system simultaneously provides a navigation solution
   - 1b As the market for navigation systems is much larger than for gravity systems, the price is usually lower
2. The mechanical platform can be omitted
   - 2a As processing methods evolve, a better orientation can be obtained
   - 2b No operation is required during flight
   - 2c Smaller size
   - 2d Less power consumption
   - 2e Lower fail rate
   - 2f Increased operational flexibility

The usefulness of the strapdown approach for medium-resolution gravity estimates has been repeatedly demonstrated [49, 18, 31] and a comparison test has shown that the accuracy is comparable to that of stabilised platform systems [19]. However, these results have also demonstrated that erroneous long wavelength information is leaking into the strapdown gravity estimates. For this reason, stable platform systems remain the preferred choice for geodetic airborne observations.

Several of these publications propose that this erroneous long wavelength information originates from uncompensated long-term drift in the accelerometers. It has been shown that the long term stability of the accelerometers can be improved by applying either precise temperature control [14] or using off-line calibration methods [4]. However, since precise temperature control introduces additional system complexity and advanced calibration methods require access to professional calibration facilities, both of these approaches challenge many of the advantages offered by the strapdown system.

1.1 A Brief Historical Overview

Airborne gravimetry has intrigued scientists for generations. The first proposals for measurement systems came in the late 1950s and early 1960s [46]. This led to the first airborne gravimetry test in 1958 using a LaCoste shipboard gravimeter on board an Air Force KC-135 fixed-wing aircraft [47]. This test yielded an accuracy of about 10 mGal when averaged over 5 minute intervals. As the instruments of the time were not accurate enough, the first tests were feasibility trials consisting of modified marine gravimeters along with photogrammetric cameras and/or doppler radar systems for positioning and unique hypsometers for measuring altitude variations [21]. In order to improve the results, the use of a helicopter platform was suggested, since it would be able to fly closer to the ground and move at a slower speed. The first successful helicopter test was performed in 1965, using an Air Force CH3E helicopter equipped with a LaCoste&Romberg marine gravimeter on a gimballed platform. The position was derived using radar tracking and the altitude was measured using a laser altimeter. This kind of approach was similarly attempted in the 1980s using fixed-wing aircrafts and demonstrated that a combination of stabilisation and improved vertical accelertion determination resulted in system improvement [32, 23, 9].

The navigational accuracy did however remain a concern until the advent of GPS in the 1990s, which revolutionised the entire field of geodesy [45, 8, 30]. This new technology not

only led to improvement in navigation and determination of the kinematic acceleration, but also led to improvements in instrument stabilisation, when combined with existing inertial technology. This basically made airborne gravimetry an operational method for wide-area airborne gravity surveys, which was pioneered by the US Naval Weapons Laboratory. A milestone along in the production-oriented use of airborne gravimetry was the survey of Greenland in coorporation with the Danish National Survey and Cadastre [7]. The Danish National Survey and Cadastre (now DTU space) has continued this effort, resulting in large-scale airborne gravity surveys on all seven continents.

The use of IMU technology for airborne gravimetry was first demonstrated in the 1980s [42, 15]. Although some studies were performed in order to investigate the requirements for strapdown airborne gravimetry [44, 27], it was not until 1995 that an actual flight test was carried out [49]. Since then, a number of studies have demonstrated the feasibility of using strapdown technology in order to derive gravity estimates in the medium-resolution domain [18, 31, 10]. Although these studies were based on high-grade (navigation-grade) IMUs, the use of low-cost IMUs for obtaining gravity estimates of 5-10 mGal accuracy in a limited 10-100 km half-wavelength band has been demonstrated [2]. In corporation with the University of Darmstadt (TU Darmstadt), DTU Space has brought a strapdown IMU on a number of airborne campaigns since 2013 [3]. These results have demonstrated that the strapdown system can produce reliable gravity estimates that nicely complements the platform estimates, resulting in increased spatial resolution and resistance against aircraft dynamics.

1.2 Motivation for Strapdown Airborne Gravimetry

Airborne gravimetry has long been recognized as a reliable method for obtaining useful gravity estimates in the medium and long wavelength bands. Since airborne gravimetry is superior to point-wise terrestrial methods in terms of economy and efficiency, there have been considerable efforts to make this an operational procedure. Marine gravimetry offers many of the same properties and can obtain a better spatial resolution, since it is closer to the source of gravitation. However, marine gravimetry has the obvious disadvantage of being restricted to ocean areas. This restriction also applies to gravity estimates obtained from satellite altimetry. Since terrestrial methods are restricted to land areas, airborne gravimetry also has the unique advantage of being able to survey coastal areas. As most of the worlds population live along the coast lines, it is especially important to have a precise Geoid in these areas. Additionally, airborne gravimetry has brought along the capability of surveying remote areas, not accessible by land.

As demonstrated by the joined efforts of TU Darmstadt and DTU Space the recent years, strapdown gravimetry is capable of providing high quality gravity estimates that complements the stabilised-platform system in terms of increased spatial resolution and resistance against turbulent conditions. Moreover, it has been demonstrated that off-line temperature calibrations are capable of reducing the erroneous long wavelength information otherwise known to corrupt the strapdown estimates [5]. For these reasons, DTU Space has purchased an iMAR iNAT navigation-grade IMU to be used as a strapdown gravimeter on airborne surveys. This dissertation presents the first results from this system and describes the development of a processing methodology for Strapdown Airborne Gravimetry (SAG).

1.3 Overview of this Dissertation

This dissertation is divided into four parts that will sequentially introduce theory, develop and test the processing algorithm and finally present results from four different surveys. The first part is devoted to the introduction of theoretical concepts that are fundamental to geodesy and airborne gravimetry. The second part will develop the framework used for IMU technology and its intended application for inertial navigation. The third part is concerned with the integration of IMU and GNSS observations using a Kalman filter framework in order to improve the navigation solution. Finally, in the fourth part, the processing methodology for airborne gravimetry will be developed and tested on both simulated data and real observations collected using the iMAR iNAT IMU unit. The dissertation is concluded with a discussion of the results and an outlook for future work.

Part I:

Prerequisites

2 Reference Systems and Frames

Central to the theory of navigation and airborne geodetic observations, is the definition of a number of reference systems and their realisations. Historically, at least more than today, these systems have been intrinsically connected with Earth's gravity field. The advent of the Global Positioning System (GPS) has revolutionised this subject, like many other subjects in the field of geodesy. As there are numerous local, regional and global reference systems, one important aspect is to relate these systems to one another as well as to some "absolute" frame, defined with respect to the celestial sphere. The International Earth Rotation Service (IERS) is responsible for defining and realizing such an "absolute" reference system, known as the International Celestial Reference System (ICRS).

Before venturing further into this subject, it is useful to understand the difference between a reference system and a reference frame. According to the IERS, the two concepts are defined as follows [28, Sect. 1.2]:

> A **reference system** is a set of prescriptions and conventions together with the modelling required to define at any time a triad of coordinate axes, and
>
> A **reference frame** realises the system by means of coordinates of definite points that are accessible either directly by occupation or by observation.

An example of a reference system is the International Terrestrial Reference System (ITRS) also defined by the IERS. The origin of this frame is geocentric, i.e. at the centre of mass of the Earth. The orientation of the three axes are aligned with Earth's spin axis, a prime vertical (Greenwich) meridian, and a third direction orthogonal to these two. The scale of the axes is defined by the speed of light in vacuum according to the Système International d'unités (SI). The corresponding example of a reference frame is the International Terrestrial Reference Frame (ITRF), which is realized by providing coordinates for a set of physical points, distributed around the surface of the Earth. The movement of these physical points are monitored using a variety of geodetic techniques and linked to a realisation of the ICRS, called the International Celestial Reference Frame (ICRF). Since the observation techniques continuously improve and the available data increases, the IRTF is constantly being updated, resulting in a number of realizations. Therefore, a frame cannot exist without a system and a system is of no practical value without a frame. These two complementary concepts in geodesy are closely related to the concept of a geodetic datum, which will be introduced in section 2.2.3.

This section is divided into two subsections. First, a number of reference frames relevant to inertial navigation are introduced. These reference frames are either used for navigation directly or are useful for expressing geodetic observations. In the second subsection, a brief introduction to geodetic coordinates is given. These are used to express coordinates in the vicinity of Earth's surface.

2.1 Coordinate Frames for Navigation

This subsection is devoted to the introduction of a number of relevant coordinate frames. Tables 2.1 and 2.2 provide an overview of the reference frames that are to be introduced.

Reference Frame	**Alternative Name**	**Notation**
Inertial Frame	ECI (Earth-Centred Inertial) frame	i
Terrestrial Frame	ECEF (Earth-Centred-Earth-Fixed) frame	e
Navigation Frame	Local-level or NED (North-East-Down) frame	n
Wander-Azimuth Frame		w
Body frame		b
Sensor frame		s

Table 2.1: Overview of the various reference frames and their notation.

Frame	**Origin**	**z-axis**	**x-axis**	**y-axis**
i	Earth centre of mass	Earth rotational axis	Equatorial plane, vernal equinox	Completes right-handed system
e	Earth centre of mass	Earth rotational axis	Equatorial plane, Greenwich meridian	Completes right-handed system
n	Instrument location	Down along ellipsoidal normal	North	East
w	Instrument location	Down along ellipsoidal normal	Initial north	Initial east
b	Instrument location	Through-the-floor (down)	Forward	Starboard (right)
s	Instrument location	Sensor Z-axis	Sensor X-axis	Sensor Y-axis

Table 2.2: Axis definition of the various reference frames

It should be noted that different coordinate frames are merely different tools to represent the same physical quantity. Such a quantity is therefore not restricted to one reference frame, but can in principle be represented in any of the reference frames. The need for all these frames are merely a matter of convenience and they are all, in theory, equally valid representations. The inertial reference frame for example is the most intuitive one in which to express the laws of motion. The terrestrial frame is most convenient for expressing gravity measurements, because we expect the main variability of those measurements to be spatially correlated with the surface of the Earth. Some frames are merely the natural frames at which the measurements are performed and others again are convenient from a practical, implementation perspective.

All of the reference frames introduced are three-dimensional, right-handed and orthogonal. Superscripts will be used to denote the frame of reference in which they are expressed. The notation used here, i.e. i, e, n, w, b and s, are in my experience the most common notation

in the literature, at least in more recent texts. However, I have also encountered different notations. The inertial and terrestrial frames are usually used to express coordinates, whereas the navigation and wander-azimuth frames provide more intuitive representations of velocity and attitude. Finally, the vehicle, platform and sensor frames are naturally related to the data acquisition.

2.1.1 The Inertial Reference Frame (i-frame)

The inertial reference frame, also denoted the Earth-Centred Inertial (ECI) frame, is the most fundamental of the reference frames, since it is the one where Newton's classical laws of motion apply. It is defined as:

- The origin is at the centre of mass of the Earth
- The z-axis coincides with the rotational axis of the Earth
- The x-axis is in the equatorial plane, pointing towards the vernal equinox (the direction of intersection of the equatorial plane of the Earth with the plane of the Earth's orbit around the Sun)
- The y-axis is defined to complete a right-handed system and will be in the equatorial plane

Since the origin coincides with the Earth centre of mass it is in free fall and since the orientation is constant with respect to fixed stars it is (almost) not rotating. Strictly speaking, this reference frame is not truly inertial. As will be argued later, this frame does not obey Newton's laws of motion, which must be modified. This frame is therefore sometimes referred to as a "quasi-inertial" frame, being "practically" inertial, meaning that its approximation will suffice for our purposes.

2.1.2 The Terrestrial Reference Frame (e-frame)

The terrestrial reference frame, or Earth-Centred Earth-Fixed (ECEF) frame, is fixed to the Earth and therefore rotating with respect to the i-frame. It is defined as:

- The origin is at the centre of mass of the Earth
- The z-axis coincides with the rotational axis of the Earth
- The x-axis is in the equatorial plane and coincides with the mean Greenwich meridian
- The y-axis is defined to complete a right-handed system and will be in the equatorial plane

The e-frame is coincident with the i-frame at some time $t = t_0$. The z-axes of the two frames are coincident at all times, such that the two frames are rotating with respect to one another at an angular rate ω_{ie}. An example of such a frame is the IRTF introduced earlier.

A terrestrial reference frame can also be realised through a geodetic reference system, whose components are the geodetic latitude, ϕ, geodetic longitude, λ and height, h, relative to a mathematically defined ellipsoid of revolution. These components are illustrated in Figure 2.3 and will be further explained in Section 2.2.

2.1.3 The Navigation Frame (n-frame)

The navigation frame is also called a local-level frame, since it is a local frame defined with respect to the local (normal) gravity vector. It is defined as:

- The origin is at the instrument location
- The z-axis points in the "down" direction, along the ellipsoidal normal
- The x-axis points north
- The y-axis points east

The reader should be aware that this definition is not consistent in the literature. One can find a range of definitions, such as "east, north, up", "north, west, up", etc., so caution is needed when "navigating" through the literature. The transformation between these reference frames are easily accomplished, as for example

$$x_{NED} = y_{ENU} \ , \quad y_{NED} = x_{ENU} \quad \text{and} \quad z_{NED} = -z_{ENU} \ . \tag{2.1}$$

One should notice that, the instrument location in this reference frame will always be $(x^n, y^n, z^n) = (0, 0, 0)$. This reference frame is therefore not used to specify position. For navigation purposes, the position is usually specified in terms of the e-frame, (x^e, y^e, z^e), while the velocity, (v_N, v_E, v_D), and acceleration, (a_N, a_E, a_D), are resolved about the axes of the n-frame.

2.1.4 The Wander-Azimuth Frame (w-frame)

The wander-azimuth frame is maybe more of a modification of the n-frame than a frame of its own. It is of practical interest when navigating in polar regions, because the n-frame possesses singularities at the geographic poles. In the n-frame, the x- and y-axis are north- and east-slaved, respectively. As the instrument moves over the surface of the Earth, the n-frame must rotate at a rate, $\boldsymbol{\omega}_{en}$, in order to keep its axes along the north, east and down directions. This rotational rate is known as the transport-rate and may be expressed as

$$\boldsymbol{\omega}^n_{en} = \begin{bmatrix} \omega^n_{en,N} \\ \omega^n_{en,E} \\ \omega^n_{en,D} \end{bmatrix} = \begin{bmatrix} v_E / (R+h) \\ -v_N / (R+h) \\ -v_E \tan\phi / (R+h) \end{bmatrix} , \tag{2.2}$$

where v_E and v_N are velocities along the east and north directions, respectively, R is the Earth radius, h the instrument height above the reference ellipsoid and ϕ is the latitude. When the instrument is navigating in polar regions, the term $\tan\phi$ becomes very large and eventually infinite directly at the pole. This leads to very large values of the rotational rate, $\omega^n_{en,D}$, and therefore also potential numerical instability.

The w-frame is then a variant of the n-frame that allows navigation in polar regions by setting $\omega^n_{en,D} = 0$, thus avoiding polar singularities. This means that the reference frame does not rotate about its vertical axis (other than by Earth's rotational rate) and therefore remains oriented in the same direction as it was initialised. The angle between the wander-azimuth axes and the north-east-axes of the n-frame is known as the wander angle and will be denoted ψ_{nw}. The wander angle will not be constant, but vary with the vehicle position.

2.1.5 Vehicle, Platform and Sensor Frames

In addition to the aforementioned general coordinate frames, it is also useful to define some reference frames that are associated with the host vehicle and the measurement system. These frames are:

- The body frame (b-frame) refers to the vehicle to be navigated, i.e. the body of the aircraft. The axes are conventionally defined along the forward, starboard and though-the-floor directions, also known as front, right, down. These axes are also denoted the roll-, pitch- and yaw axis respectively, since the rotation around these axes are denoted roll, pitch and yaw
- The sensor frame (s-frame) is related to the instrument. It serves as an analytical reference frame for the instrument, where instrument errors can be identified, modelled and possibly filtered. For strapdown systems, this frame will coincide with the b-frame, while for local-level gimballed systems it corresponds to the n-frame
- The instruments of an IMU are accelerometers and gyroscopes, which each have their own coordinate frame, namely an accelerometer frame (acc-frame) and gyro frame ($gyro$-frame). Both of these frames are assumed to be orthogonal, but might have some misalignment, which is handled through calibration procedures. The origin is the point of specific force computation for both of the frames
- The platform frame (p-frame) refers to the platform on which the sensors are mounted. This frame provides a common origin for the cluster of instruments.

The geometrical relationship between some of these frames are illustrated in Figure 2.1. Ultimately, all measurements must be transformed into the i-, e- or n-frame, whichever one has chosen to navigate with respect to. The transformation from one reference frame to the other is accomplished by rotation operators, which will be covered in Section 5.1 and Appendix A.

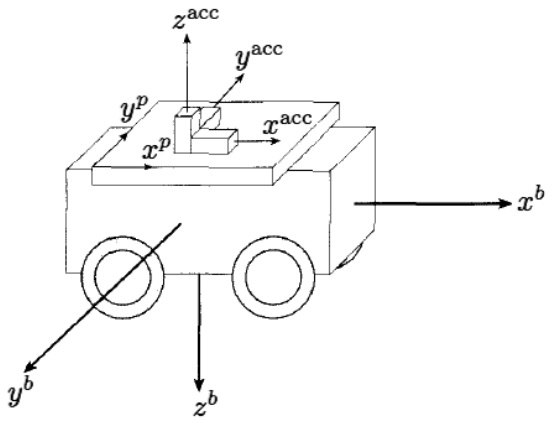

Figure 2.1: Illustration of the body (x^b, y^b, z^b), platform (x^p, y^p, z^p) and accelerometer $(x^{\text{acc}}, y^{\text{acc}}, z^{\text{acc}})$ components. Image credit: [29].

2.2 Coordinate Frames in Geodesy

In geodesy, coordinates have traditionally been adapted to Earth's shape, being some kind of spherical or ellipsoidal coordinates, for regional and global applications, while Cartesian coordinates have been preferred for local applications, where a planar approximation is valid. The reason for this is nicely illustrated in [34, Sect. 3.1.1]:

> Imagine giving your position coordinates in meters as $(x^e, y^e, z^e) = (1510885, -4463460, 4283905)$. One can tell that you are on the northern hemisphere ($z^e > 0$). Those who remember their sine/cosine tables and can do some quick computations in their heads, can tell that you are at mid-latitudes. It is hard to tell if you are on the Earth, or above or below it, and by how much. And, of course, all three coordinates would change in general as you climb up a pole, or move to an upstairs room.

A more intuitive approach is therefore the separation of horizontal and vertical coordinates by the introduction of curvilinear coordinates. The horizontal position is expressed as angular coordinates, i.e. latitude and longitude, while the height is expressed with respect to the surface of the Earth. The definition of such a set of coordinates is however not straightforward, since the shape of the Earth is irregular and changeable. The solution has been to approximate the Earth using a model, which needs to be simple, smooth and easy-to-use, and then characterise the actual shape of the Earth with respect to this model. An early model was the sphere, which led to the introduction of latitude and longitude. A refinement of this model came with Newton, whose study of gravity led him to believe that Earth was flattened slightly at the poles and bulged somewhat at the equator. His measurements indicated that the distance from the centre of the Earth to the pole was about 20 km shorter than the distance to the equator. The Earth could then be approximated as an ellipsoid of revolution, formed by rotating an ellipse about its minor axis. This form is also referred to as an oblate ellipsoid. The next best approximation after the ellipsoid is known as the geoid, which will be properly introduced in Section 3. While the mean Earth sphere deviates by up to 14 km from a mean Earth ellipsoid at the poles, the difference between the ellipsoid and the geoid is no more that 110 m [28, Sect. 1.3]. The ellipsoid is therefore an extremely good approximation of the figure of the Earth, at least over the oceans, which represents more than 70% of Earth's surface.

With the introduction of GPS, the Cartesian coordinates have also become important for global geospatial referencing. However, the curvilinear coordinates continue to have the largest appeal to terrestrial applications, i.e. surveying, near-surface navigation, positioning and mapping. In the following, geodetic coordinates will therefore be briefly introduced along with some related concepts, that are central to geodesy.

2.2.1 Spherical Coordinates

Realising that Earth is almost a sphere, it seems natural to use spherical coordinates to describe positions on the Earth. The geometry of these coordinates are shown in Figure 2.2 and they are related to the Cartesian coordinates as

$$\begin{aligned} x &= r\cos\phi'\cos\lambda \\ y &= r\cos\phi'\sin\lambda \\ z &= r\sin\phi' \end{aligned} \quad \Leftrightarrow \quad \begin{aligned} r &= \sqrt{x^2+y^2+z^2} \\ \phi' &= \sin^{-1}[z/r] \\ \lambda &= \tan^{-1}[y/x] \end{aligned} \quad , \tag{2.3}$$

where one must account for all quadrants of the inverse tangent function, i.e. use atan2 in MATLAB. The spherical latitude is here denoted ϕ' and referred to as the geocentric latitude. This is because ϕ is reserved for the geodetic latitude, which will be introduced in the following section. Often, the colatitude, θ, is used instead of the latitude, ϕ'. The colatitude is the angle from the pole instead of the angle from equator and the two are related as

$$\phi' = 90 - \theta \quad \Rightarrow \quad \sin\phi' = \cos\theta \, . \tag{2.4}$$

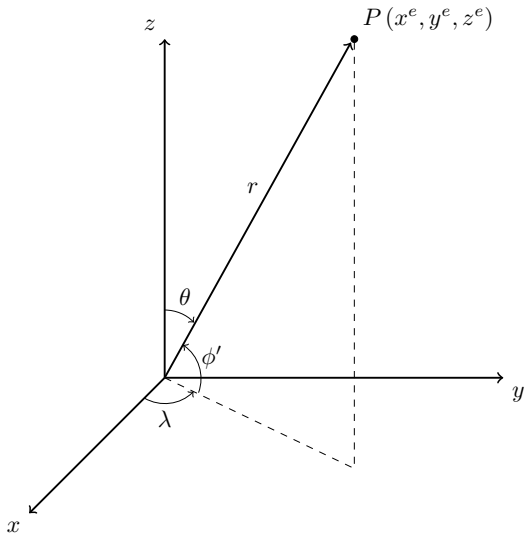

Figure 2.2: Sketch of the geometry relating the spherical coordinates, (r, ϕ', λ), to the Cartesian coordinates, (x^e, y^e, z^e), of a point, P, in space. Here, r is the radial distance, ϕ' is the geocentric latitude, λ is the longitude and θ is the colatitude.

For navigation purposes, it is fundamental to be able to transform curvilinear distances into linear distances. Incremental distances are related as

$$\begin{aligned} \mathrm{d}N &= R \, \mathrm{d}\phi \\ \mathrm{d}E &= R \cos\phi' \, \mathrm{d}\lambda \, , \end{aligned} \tag{2.5}$$

where R is the radius of the sphere and where N and E denote the north and east directions, respectively.

2.2.2 Ellipsoidal Coordinates

As with spherical coordinates, the oblate ellipsoid has both its origin (centre of mass) and orientation (Earth spin axis) in common with the ECEF Cartesian coordinate system. The geometry of the ellipsoid is defined as

$$\frac{x^2 + y^2}{a^2} + \frac{z^2}{b^2} = 1 \, , \tag{2.6}$$

with a and b being the semi-major and semi-minor axes respectively. Alternatively, the shape of the ellipsoid can be characterised by the geometrical **flattening**, f, the **linear eccentricity**, E, or the **first eccentricity**, e, defined as

$$f = \frac{a-b}{a}\,, \quad E = \sqrt{a^2 - b^2}\,, \quad e = \frac{\sqrt{a^2-b^2}}{a} \quad \text{and} \quad e^2 = 2f - f^2\,, \tag{2.7}$$

relating the flattening to the first eccentricity. It is customary to define the ellipsoid by a and f rather than a and b. Having defined a mathematical shape of the Earth, in the form of an ellipsoid, one can define the **geodetic coordinates** (also called **geographic** or **ellipsoidal** coordinates) of a point P as follows:

- **geodetic latitude** ϕ: the angle measured in the meridian plane through the point P between the equatorial plane of the ellipsoid and the line perpendicular to the surface of the ellipsoid at P,
- **geodetic longitude** λ: the angle measured in the equatorial plane between the reference meridian and the meridian plane passing through P,
- **geodetic height** h: measured along the normal to the ellipsoid through P.

These coordinates are sketched together with the Cartesian and spherical coordinates in Figure 2.3. Any point, Q, on the surface of the ellipsoid can be specified using the geodetic latitude, ϕ, and longitude, λ. For a point, P, outside the ellipsoid, the local vertical is defined by the surface normal, $\mathbf{n}$, at the point Q. The ellipsoidal height is the distance between P and Q along this normal.

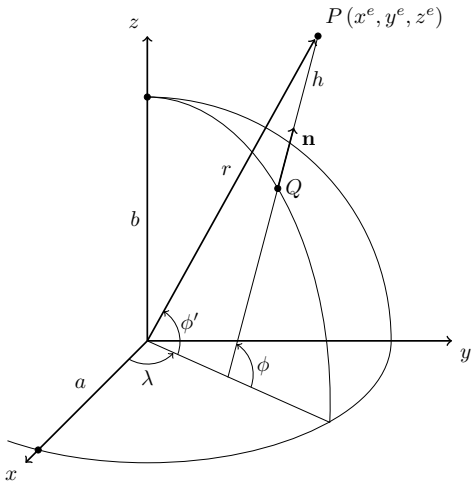

Figure 2.3: Sketch of the geometry relating geodetic coordinates, (ϕ, λ, h), to Cartesian coordinates, (x^e, y^e, z^e) and spherical coordinates, (r, ϕ', λ). The parameters a and b are the semi-major and semi-minor axes respectively, Q is a point on the ellipsoid and P is a point outside the ellipsoid. The distance QP is the height h. The vertical line connecting Q and P is defined by the ellipsoidal surface normal $\mathbf{n}$. The angle of intersection between this line and the equatorial plane is the geodetic latitude ϕ.

For an ellipsoid it is not as straightforward to transform curvilinear distances into linear distances, since the radius is not constant. Actually, the radius is different in the two directions and they are known as radii of curvature, since they are related to the curvature, κ, of a curve on the ellipsoid [38, Sect. 2]. The inverse of the curvature

$$\varrho = \frac{1}{\kappa} \,, \tag{2.8}$$

is known as the **radius of curvature** and denotes the distance along the principal normal to the curve. In the special case that the curvature is constant, i.e. for a circle, the radius is also constant. We may therefore think of the radius of curvature as being the radius of a circle tangent to the curve at this specific point and having the same curvature as the circle. In Figure 2.4, this tangent circle is sketched for a point, Q, on the ellipsoid. Since the curvature is different along the north and east directions, the radius of curvature will be different. The radius of curvature along the east direction, R_E, also known as the **radius of curvature of the prime vertical** is given by [48, Eq. 4.15]:

$$R_E = \frac{a}{\sqrt{1 - e^2 \sin^2 \phi}} \,. \tag{2.9}$$

and is most often denoted by N, since its direction is normal to the ellipsoidal surface. The radius of curvature along the north direction, R_N, also known as the **radius of curvature of the meridian** is given by [48, Eq. 4.13]:

$$R_N = \frac{a\left(1 - e^2\right)}{\left(1 - e^2 \sin^2 \phi\right)^{3/2}} = R_E \, \frac{1 - e^2}{1 - e^2 \sin^2 \phi} \,, \tag{2.10}$$

and is most often denoted by M for meridian. In this dissertation I will deviate from the traditional M and N notation, in order to confine with the notation used in [20] and because I find it more intuitive. For a proper derivation of the above expressions in terms of differential geometry, see [28, Sect. 2.1.3]. Using the two radii of curvature, one can transform curvilinear distance to linear distance similar to (2.5) as

$$\begin{aligned} \mathrm{d}N &= R_N \, \mathrm{d}\phi \\ \mathrm{d}E &= R_E \cos\phi \, \mathrm{d}\lambda \,. \end{aligned} \tag{2.11}$$

The interrelation of the Cartesian coordinates, (x, y, z), and the geodetic coordinates, (ϕ, λ, h), can be expressed as [48, Eq. 4.27-4.28]

$$\begin{aligned} x &= (R_E + h) \cos\phi \cos\lambda \\ y &= (R_E + h) \cos\phi \sin\lambda \\ z &= \left(R_E\left(1 - e^2\right) + h\right) \sin\phi \end{aligned} \quad \Leftrightarrow \quad \begin{aligned} \phi &= \tan^{-1}\left[\frac{z/\sqrt{x^2+y^2}}{1 - e^2 R_E/(R_E+h)}\right] \\ \lambda &= \tan^{-1}\left[y/x\right] \\ h &= \frac{\sqrt{x^2+y^2}}{\cos\phi} - R_E \end{aligned} \tag{2.12}$$

where the latter must be solved iteratively, due to their interdependence. Close to the Earth's surface ($h \ll R_E$) this process will converge quickly.

An alternative pair of ellipsoidal coordinates, (u, β, λ), also exists. These coordinates are related to ellipsoidal harmonic functions and are therefore also known as **ellipsoidal-harmonic coordinates**. Although Earth closely resembles an ellipsoid of revolution, ellipsoidal harmonics are only used in certain special cases. Due to their relative simplicity,

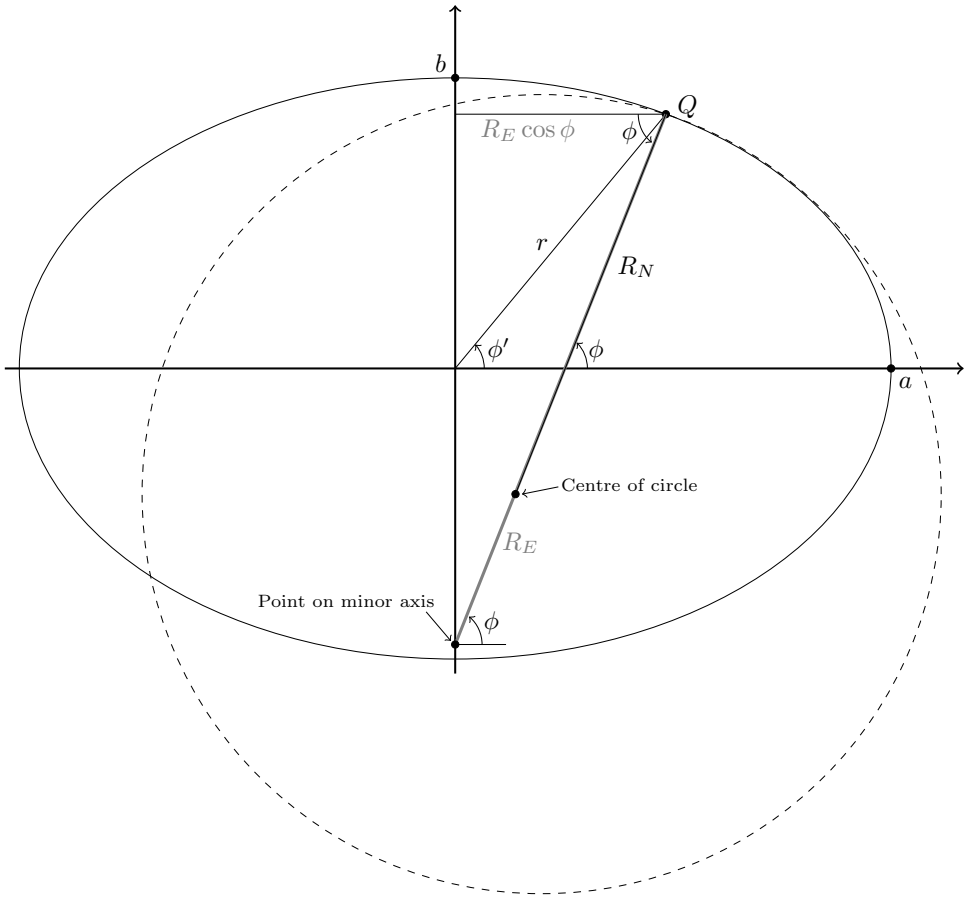

Figure 2.4: Sketch illustrating the geometry of the two important radii of curvature for the ellipsoid. The radius of curvature of the prime vertical, R_E, is illustrated in gray color in order to recognise it from the radius of curvature of the meridian, R_N. The length of R_E is from the point Q to the point on the minor axis, along the ellipsoidal normal. This radius is commonly used in conjunction with $\cos\phi$ in order to derive linear distances along the east-west direction. The length of R_N is from Q to the centre of a circle that is tangent to Q and has the same curvature as the ellipse along the meridian direction, at the point Q. This radius is commonly used to derive linear distance along the north-south direction.

spherical harmonic functions are most often used instead. Spherical harmonic functions will be introduced in Section 3, whereas ellipsoidal harmonic functions will not be introduced in this dissertation. The reader is instead referred to [25, Sect. 1.15-1.16].

Problems involving the computation of normal gravity, which will be introduced in Section 3.3, are such special cases where ellipsoidal harmonics are used. For this reason, ellipsoidal-harmonic coordinates will be briefly introduced. Consider an ellipsoid of revolution that passes through the point $P\left(x^e, y^e, z^e\right)$, whose centre is the origin of the Earth, whose rotation axis coincides with the z-axis and has a linear eccentricity E. This is sketched in Figure 2.5 along with a sphere having a radius, v, equal to the semi-major axis of the new ellipsoid.

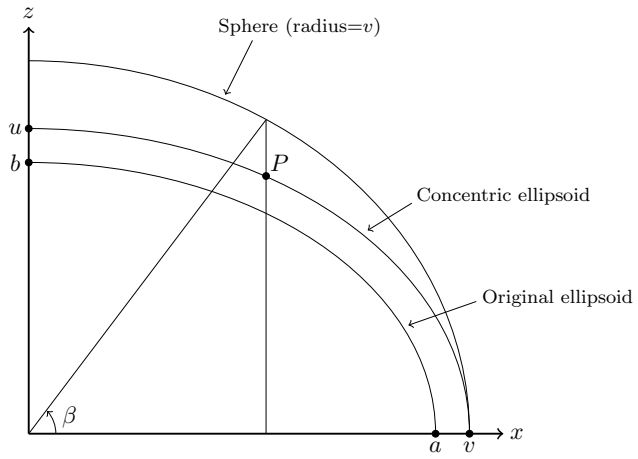

Figure 2.5: Sketch of the geometry related to ellipsoidal-harmonic coordinates. A concentric ellipsoid through P is defined with the same linear eccentricity, E, as the original ellipsoid. The reduced latitude, β, is then related to a sphere having radius, v, equal to the semi-major axis of this new ellipsoid.

The coordinate, u, is the semi-minor axis of this ellipsoid. The reduced latitude, β, is related to the additional sphere of radius v and the intersection of a vertical line passing through P as illustrated in the figure. It is related to the geodetic latitude as [39, Eq. 3.63]:

$$\beta = \tan^{-1}\left[\sqrt{1-e^2}\tan\phi\right] = \tan^{-1}\left[(1-f)\tan\phi\right] \ . \tag{2.13}$$

The ellipsoidal-harmonic coordinates are related to the Cartesian coordinates as [25, Eq. 1-151] and [35, Eqs. 4-8,4-9]:

$$\begin{array}{rclcrcl} x &=& v\cos\beta\cos\lambda & & u &=& \left[\frac{1}{2}\left(x^2+y^2+z^2-E^2\right)\left\{1+\sqrt{1+\frac{4E^2z^2}{\left(x^2+y^2+z^2-E^2\right)^2}}\right\}\right]^{\frac{1}{2}} \\ y &=& v\cos\beta\sin\lambda & \Leftrightarrow & & & \\ z &=& u\,\sin\beta & & \beta &=& \tan^{-1}\left[\frac{z\sqrt{u^2+E^2}}{u\sqrt{x^2+y^2}}\right] \\ & & & & \lambda &=& \tan^{-1}\left[y/x\right] \end{array} \tag{2.14}$$

noting that $v = \sqrt{u^2+E^2}$.

2.2.3 Geodetic Datums, Geodetic Reference Systems and Map Projections

In the literature, the **geodetic datum** is often defined with respect to a certain application, meaning that no consistent definition exists [28, Sect. 3]. The concept is also further complicated by the fact that a geodetic datum have traditionally been separated into a horizontal datum, making it possible to map points onto the ellipsoid, and a vertical datum, which is a one-dimensional height linked to the gravitational field. A more clear and basic definition is presented in [28, Sect. 3]:

> A **geodetic datum** is a set of parameters and constants that defines a coordinate system, including its origin and (where appropriate) its orientation and scale, in such a way as to make these accessible for geodetic applications

More practically, a geodetic datum usually defines the reference system *and* utilizes the reference frame in terms of a number of parameters, making it possible to compute the coordinates of a point in space. A global datum is normally realised in terms of a reference ellipsoid, which is specified as two ellipsoidal parameters, three origin point coordinates and three orientation parameters. However, if the reference ellipsoid is geocentric, the three origin parameters will be zero, and if the orientation is along the spin axis and Greenwich meridian, the orientation parameters will also be zero. Examples of such geocentric reference ellipsoids are the Geodetic Reference System 1980 (GRS80) and World Geodetic System 1984 (WGS84). The ITRF solutions are specified using Cartesian coordinates and do therefore not directly use an ellipsoid.

A **geodetic reference system** requires the definition of two additional physical parameters. By defining Earth's rotational rate, ω_{ie}, and Earth's gravitational constant, GM, together with a rotational ellipsoid, a reference field for gravity is also uniquely defined. This subject will be discussed further in Section 3. An overview of the geometric and physical parameters of WGS84 is presented in Table 2.3.

DEFINING PARAMETERS	Symbol	Value
Semi-major axis	a	6378137.0 m
Flattening	$1/f$	298.257223563
Angular velocity of Earth	ω_{ie}	$7292115.0 \cdot 10^{-11}$ rad/s
Earth's gravitational constant	GM	$3986004.418 \cdot 10^{8}$ m^3/s^2
DERIVED GEOMETRIC CONSTANTS		
Second-degree zonal harmonic	J_2	$-0.484166774985 \cdot 10^{-3}$
Semi-minor axis	b	6356752.3142 m
First eccentricity	e	$8.1819190842622 \cdot 10^{-2}$
Second eccentricity	e'	$8.2094437949696 \cdot 10^{-2}$
Linear eccentricity	E	$5.2185400842339 \cdot 10^{5}$
Axis ratio	b/a	0.996647189335
DERIVED PHYSICAL CONSTANTS		
Normal gravity potential of the ellipsoid	U_0	62636851.7146 m^2/s^2
Normal gravity at the equator	γ_e	9.7803253359 m/s^2
Normal gravity at the pole	γ_p	9.8321849378 m/s^2
Mean value of normal gravity	$\overline{\gamma}$	9.7976432222 m/s^2

Table 2.3: The defining parameters of WGS84 along with some derived geometric and physical constants [35]. WGS84 is based on the Earth Gravitational Model 96 (EGM96), meaning that it is obtained as a best fit to this geoid.

When mapping smaller regions, it is convenient to define an ellipsoid that best fits the region of interest. It is therefore not a requirement that the ellipsoid be geocentric or oriented along the axis of rotation (see Figure 2.6). Having defined an ellipsoid, one can project each point on the surface of the Earth onto the ellipsoid and associate it with latitude and longitude coordinates. The next step is then to represent these geographical coordinates as rectangular coordinates on a map.

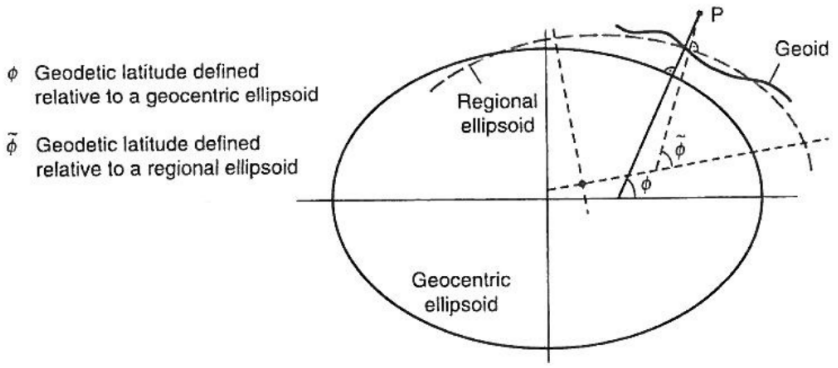

Figure 2.6: Illustration of global and regional datums. Illustration is from [34].

The mapping of curvilinear coordinates onto a flat surface in terms of rectangular coordinates is achieved in terms of a **map projection**. Hundreds of such map projections have been proposed over the years, but they will always contain some distortion. A nice analogy is to imagine the Earth as an orange. Then peel the orange and attempt to press the peel onto a table. In order to accomplish this, the peel must be distorted in some way. It is not the intention to venture further into the subject of map projections here. The aim is simply to provide an overview of some important concepts in geodesy and also make it clear that coordinates are defined with respect to a reference frame (or map projection). It is therefore important to always be clear about which reference frame is used.

3 Gravitation, Gravity and the Geodetic Earth Model

The figure of the Earth is closely related to the gravity field of the Earth. For this reason, the gravity field is of fundamental importance in geodesy and many geodetic observations are related to the gravity field. This section is divided into three subsections. In the first subsection, the idea of gravitation will be introduced, based on the theory of classical mechanics by Sir Isaac Newton. This is followed by an introduction to the useful mathematical concept of a potential field. In the second subsection, gravity will be introduced and some connections with the geometry of the Earth will be presented. Finally, all of these concepts are combined to form what will here be denoted a "Geodetic Earth Model", constituting a reference system for both geometric and gravimetric observations in the vicinity of Earth's surface.

3.1 Gravitation and the Gravitational Potential

The law of universal gravitation is one foundation of classical mechanics that we owe to Sir Isaac Newton. In the third volume of his *Principia*, Newton recognised that the force that makes an apple fall to the ground from a tree, is the same fundamental force that holds the Moon in orbit and governs the orbital motion of all the planets. Newton found that this force is proportional with the "quantities of solid matter that the object contains" (i.e. mass) and with the inverse of the squared distance. Mathematically, the gravitational force, $\mathbf{F}_g$, between two point masses, m and m', separated by the vector $\boldsymbol{\zeta}$ of length $\zeta = |\boldsymbol{\zeta}|$, is

$$\mathbf{F}_g(\boldsymbol{\zeta}) = G\frac{mm'}{\zeta^2}\hat{\boldsymbol{\zeta}}\ , \tag{3.1}$$

where G is the gravitational constant and $\hat{\boldsymbol{\zeta}}$ is a vector of unit length. The geometry of the situation is illustrated in Figure 3.1. The force exerted by a number of point masses, $m'_1, m'_2, ..., m'_N$, on the mass m, can be expressed using the principle of superposition

$$\begin{aligned}\mathbf{F}_g(\mathbf{r}) &= \mathbf{F}_1(\boldsymbol{\zeta}_1) + \mathbf{F}_2(\boldsymbol{\zeta}_2) + ... + \mathbf{F}_N(\boldsymbol{\zeta}_N) = G\left(\frac{mm'_1}{\zeta_1^2}\hat{\boldsymbol{\zeta}}_1 + \frac{mm'_2}{\zeta_2^2}\hat{\boldsymbol{\zeta}}_2 + ... + \frac{mm'_N}{\zeta_N^2}\hat{\boldsymbol{\zeta}}_N\right)\\ &= G\left(\frac{m'_1}{\zeta_1^2}\hat{\boldsymbol{\zeta}}_1 + \frac{m'_2}{\zeta_2^2}\hat{\boldsymbol{\zeta}}_2 + ... + \frac{m'_N}{\zeta_N^2}\hat{\boldsymbol{\zeta}}_N\right)m = m\,\bar{\mathbf{g}}(\mathbf{r})\ ,\end{aligned} \tag{3.2}$$

where

$$\bar{\mathbf{g}}(\mathbf{r}) \equiv G\sum_{i=1}^{N}\frac{m'_i}{\zeta_i^2}\hat{\boldsymbol{\zeta}}_i \overset{\text{Earth}}{=} G\iiint\frac{\rho(\mathbf{r}')}{\zeta^2}\hat{\boldsymbol{\zeta}}\,\mathrm{d}V' \tag{3.3}$$

is the **gravitational field**. The Earth can be seen as a continuous collection of such mass objects, that make up a volume, V'. In this case the summation becomes an integral over the density, $\rho(\mathbf{r}')$, as is indicated in the expression above. Notice that the gravitational field is not a force, but an acceleration.

3.1.1 Gravitational Potential

The gravitational field, $\bar{\mathbf{g}}(\mathbf{r})$, is a **conservative vector field**, meaning that it has certain properties associated with it. These properties allow us to express the vector field in terms

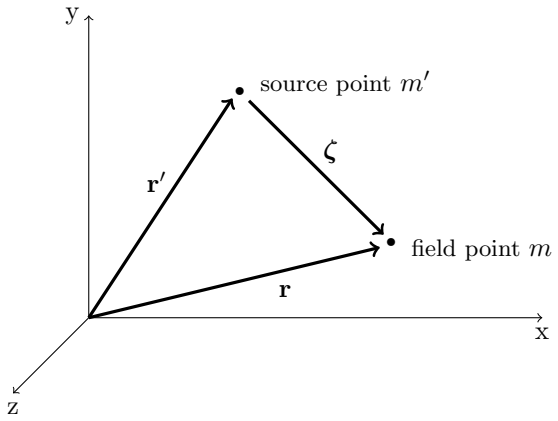

Figure 3.1: Sketch of the geometry describing the gravitational attraction between two point masses.

of the gradient of a **scalar potential field**, V, as

$$\bar{\mathbf{g}}\left(\mathbf{r}\right) \equiv -\nabla V\left(\mathbf{r}\right) \ . \tag{3.4}$$

In order to see why this is possible, we can consider the integral of the gravitational field, resulting from a single point mass located at the origin. The integral is performed from a point **a** to a point **b** in space

$$\begin{aligned} \int_{\mathbf{a}}^{\mathbf{b}} \bar{\mathbf{g}}\left(\mathbf{r}\right) \cdot \mathrm{d}\mathbf{l} &= G \int_{\mathbf{a}}^{\mathbf{b}} \frac{m}{r^2} \hat{\mathbf{r}} \cdot \mathrm{d}\mathbf{l} = G \int_{\mathbf{a}}^{\mathbf{b}} \frac{m}{r^2} \hat{\mathbf{r}} \cdot \left(\mathrm{d}r\, \hat{\mathbf{r}} + r \mathrm{d}\theta\, \mathrm{d}\hat{\boldsymbol{\theta}} + r \sin\theta \mathrm{d}\phi\, \mathrm{d}\hat{\boldsymbol{\phi}} \right) \\ &= G \int_{\mathbf{a}}^{\mathbf{b}} \frac{m}{r^2} \mathrm{d}r = G \left(\frac{m}{r_a} - \frac{m}{r_b} \right) \ , \end{aligned} \tag{3.5}$$

where $\mathrm{d}\mathbf{l}$ is the unit vector along the path of integration. Since the result only depends on the end points, r_a and r_b, the integral is independent on the path of integration chosen from point **a** to a point **b**. This property is characteristic of conservative fields. It can be exploited by choosing a reference point, $\mathcal{O}$, and defining the gravitational potential as

$$V\left(\mathbf{r}\right) \equiv -\int_{\mathcal{O}}^{\mathbf{r}} \bar{\mathbf{g}}\left(\mathbf{r}'\right) \cdot \mathrm{d}\mathbf{l}' \ , \tag{3.6}$$

which will be the same no matter which path of integration we choose from $\mathcal{O}$ to $\mathbf{r}$. The potential, $V\left(\mathbf{r}\right)$, is therefore a well-defined scalar quantity that contains the same amount of information as the gravitational field, $\bar{\mathbf{g}}\left(\mathbf{r}\right)$, which is a vector quantity. This information can be retrieved by using (3.4), i.e. the gradient of the potential. We can then compute the gravitational potential as

$$\begin{aligned} V\left(\mathbf{r}\right) &= -\int_{\mathcal{O}}^{\mathbf{r}} \left(G \sum_{i=1}^{N} \frac{m_i}{\zeta_i'^2} \hat{\boldsymbol{\zeta}}_i' \right) \cdot d\mathbf{l}' = -G \int_{\mathcal{O}}^{\zeta_i} \sum_{i=1}^{N} \frac{m_i}{\zeta_i'^2}\, d\zeta' \\ &= -G \sum_{i=1}^{N} \int_{\mathcal{O}}^{\zeta_i} \frac{m_i}{\zeta_i'^2}\, d\zeta' = G \sum_{i=1}^{N} \left(\frac{m_i}{\zeta_i} - \frac{m_i}{\mathcal{O}} \right) \ . \end{aligned} \tag{3.7}$$

For reasons of convenience, we choose the reference point, $\mathcal{O}$, to be located at infinity, because then $m_i/\mathcal{O} = 0$ and the above becomes

$$V(\mathbf{r}) = G\sum_{i=1}^{N}\frac{m_i}{\zeta_i} \overset{\text{Earth}}{=} G\iiint\frac{\rho(\mathbf{r}')}{\zeta}\,\mathrm{d}V' \,. \tag{3.8}$$

Having defined the gravitational potential, we can introduce the **equipotential surface**, which is a surface of constant potential. Since every point on this surface has the same potential value, no work is done in moving from one point to another on this surface. This also means that the force and acceleration vectors of the gravitational field are perpendicular to this surface.

3.1.2 Properties of the Gravitational Potential

Determining the gravitational field, $\bar{\mathbf{g}}(\mathbf{r})$, of the Earth using (3.3) is an impossible task, since we do not know the density distribution of the Earth. Determining the potential field, $V(\mathbf{r})$, from (3.8) has the same issue. The only thing we can actually measure is the total gravitational field or potential outside the attracting mass of the Earth. When concerned with the gravitational field of the Earth, it is therefore useful to express the problem in differential form using **Poisson's equation** as

$$\nabla^2 V(\mathbf{r}) = -4\pi G\rho(\mathbf{r}) \,, \tag{3.9}$$

where

$$\nabla^2 V(\mathbf{r}) = \nabla\cdot[\nabla V(\mathbf{r})] = \frac{\partial^2 V}{\partial x^2} + \frac{\partial^2 V}{\partial y^2} + \frac{\partial^2 V}{\partial z^2} \tag{3.10}$$

is the Laplace operator. Poisson's equation, combined with appropriate boundary conditions, is equivalent to (3.8). Outside the attracting mass of the Earth, we have that

$$\nabla^2 V(\mathbf{r}) = 0 \,, \tag{3.11}$$

because $\rho(\mathbf{r}) = 0$. This is known as **Laplace's equation**. From (3.3), (3.8) and (3.11) it is clear that the gravitational potential, along with its first and second derivatives, are continuous functions and that it satisfies Laplace's equation. It is therefore a **harmonic function** by definition [25, Sect. 1].

Inside the attracting mass of the Earth, the function and its first derivative will be discontinuous where the point of computation coincides with the point of integration, i.e. $\zeta = 0$. The second derivative will be discontinuous at points where the density distribution is discontinuous. The potential inside the attracting mass of the Earth is therefore not harmonic. It does not satisfy Laplace's equation, but only Poisson's equation.

3.1.3 The Potential in Terms of Spherical Harmonics

In geodesy it is customary to write the gravitational potential as a series expansion in terms of spherical harmonic functions as

$$V(\mathbf{r}) = \frac{GM}{r}\sum_{n=0}^{N}\left(\frac{a}{r}\right)^n\sum_{m=0}^{n}\bar{P}_{n,m}(\sin\phi')\left[C_{n,m}\cos m\lambda + S_{n,m}\sin m\lambda\right] \,, \tag{3.12}$$

where

$\mathbf{r} = (r, \phi', \lambda)$	is a point in space exterior to Earth (r is the radius, ϕ' is the geocentric latitude and λ the longitude)
G	is the gravitational constant
M	is the mass of the Earth
a	is the radius of the Earth
$C_{n,m}$ and $S_{n,m}$	are the (dimensionless) Stokes spherical harmonic coefficients
$\tilde{P}_{n,m}(\sin\phi')$	are the fully normalised associated Legendre polynomials
n	is the degree and
m	is the order.

In this expression, the first term, $(a/r)^n$, describes the attenuation of the gravitational signal as one moves away from the source, i.e. the Earth. The second term, $\tilde{P}_{n,m}(\sin\phi')$, is an oscillating function along the latitudinal direction and the third term, $C_{n,m}\cos(m\phi) + S_{n,m}\sin(n\phi)$, is an oscillating function along the longitudinal direction. The product of the second and third terms therefore constitute a series of two-dimensional waveforms, which are superimposed on one another in order to arrive at the resulting function. In this way, the spherical harmonics are a natural extension of the Fourier series into two dimensions on the sphere.

One should be aware that the fully normalised associated Legendre polynomials are normalised according to the customs of geodesy. Other fields, such as seismology, quantum mechanics and magnetics also use spherical harmonic functions, but have their own conventions on the normalisation. Another point that one should be aware of is that many authors use colatitude, θ, instead of latitude, ϕ'. In this case, we have that $\tilde{P}_{n,m}(\sin\phi') = \tilde{P}_{n,m}(\cos\theta)$. Finally, one should remark that these are **spherical** harmonic functions and that spherical coordinates (r, ϕ', λ) are used in the formulation. In Appendix E.2, a method for evaluating the above formula and its derivatives is outlined.

3.2 The Gravity Field of the Earth

The total force acting on a body at rest on the Earth's surface is the resultant of gravitational force, $m\,\bar{\mathbf{g}}$, and centrifugal force, $m\,\mathbf{f}_c$, due to the Earth's rotation. This resultant force is denoted **gravity** and can be expressed as

$$m\,\mathbf{g} = m\,\bar{\mathbf{g}} + m\,\mathbf{f}_c\ , \tag{3.13}$$

indicating that, in geodesy, we distinguish between the terms gravity, $\mathbf{g}$, and gravitation, $\bar{\mathbf{g}}$. Since the mass occurs on all terms above, it can be divided out from the equation in order to obtain the expression

$$\mathbf{g} = \bar{\mathbf{g}} + \mathbf{f}_c\ , \tag{3.14}$$

for the gravity vector. Since this is an acceleration, it has the SI unit of $\mathrm{m/s^{-2}}$. The value of $\mathbf{g}$ will depend both on local geology (mass), height (distance from mass) and latitude (centripetal force).

3.2.1 The Gravity Potential

The gravity field consists of components originating from the gravitational attraction and centrifugal force, as indicated by (3.14). Similarly, the gravity potential, $W(\mathbf{r})$, can be written as the sum of two components

$$W(\mathbf{r}) = V(\mathbf{r}) + \Phi(\mathbf{r}) \ , \tag{3.15}$$

where the gravitational potential, $V(\mathbf{r})$, have already been introduced and $\Phi(\mathbf{r})$ is an extra term that accounts for the centrifugal component. Assuming that the Earth is a solid body rotating with constant speed, ω_{ie}, about the z-axis, we can write the angular velocity, $\boldsymbol{\omega}_{ie}$, as

$$\boldsymbol{\omega}_{ie} = \begin{bmatrix} \omega_x \\ \omega_y \\ \omega_z \end{bmatrix} = \begin{bmatrix} 0 \\ 0 \\ \omega_{ie} \end{bmatrix} \ , \tag{3.16}$$

where ω_{ie} is in units of angle per time. The centrifugal acceleration is therefore

$$\mathbf{f}_c = \boldsymbol{\omega}_{ie} \times (\boldsymbol{\omega}_{ie} \times \mathbf{r}) = \begin{bmatrix} \omega_{ie}^2 x \\ \omega_{ie}^2 y \\ 0 \end{bmatrix} \ . \tag{3.17}$$

Since the acceleration, $\mathbf{f}_c$, is related to the potential, $\Phi(\mathbf{r})$, as

$$\mathbf{f}_c = \nabla\Phi = \begin{bmatrix} \frac{\partial\Phi}{\partial x} & \frac{\partial\Phi}{\partial y} & \frac{\partial\Phi}{\partial z} \end{bmatrix}^\top \ , \tag{3.18}$$

the potential can be expressed as

$$\Phi(\mathbf{r}) = \frac{1}{2}\,\omega_{ie}^2\,\left(x^2 + y^2\right) = \frac{1}{2}\,\omega_{ie}^2\,r^2\cos^2\phi' \ . \tag{3.19}$$

We therefore have the following expressions for the gravity potential:

$$W(\mathbf{r}) = V(\mathbf{r}) + \Phi(\mathbf{r}) = G\iiint \frac{\rho(\mathbf{r}')}{\zeta}\,\mathrm{d}V' + \frac{1}{2}\,\omega_{ie}^2\,r^2\cos^2\phi' \ , \tag{3.20}$$

and the generalised Poisson equation

$$\nabla^2 W(\mathbf{r}) = -4\pi G\rho(\mathbf{r}) + 2\,\omega_{ie}^2 \ . \tag{3.21}$$

These equations show that W and its first derivatives are everywhere single-valued, finite and continuous. The second derivate of W inherits the same discontinuities as $\nabla^2 V(\mathbf{r})$ at discontinuities of density, $\rho(\mathbf{r})$. For geodesy, the most important discontinuity is the physical surface of the Earth. When concerned with equipotential surfaces, $W(\mathbf{r}) =$ constant, one should be aware that such a surface might not always be outside the physical surface of the Earth.

3.2.2 Level Surfaces, Plumb Lines and the Geoid

The equipotential surfaces where $W(\mathbf{r}) = \text{constant}$ are also denoted **level surfaces** and receive large attention in geodesy because they are closely related to the intuitive concepts of horizontal and vertical. The surface normal, and therefore also the direction of the gravity vector, defines the vertical direction. The tangential plane, which is perpendicular to the gravity vector, defines the horizontal.

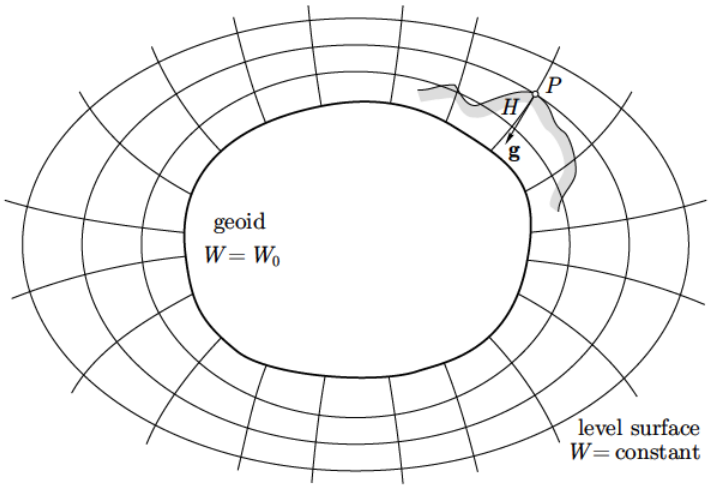

Figure 3.2: Illustration of level surfaces and plumb lines from [25].

The (idealised) surface of the oceans follow such an equipotential surface. This level surface was proposed by C.F. Gauss as the mathematical figure of the Earth and is still considered so in many aspects. It is defined as

$$W(\mathbf{r}) = W_0(\mathbf{r}) = \text{constant} \tag{3.22}$$

and is of fundamental importance in geodesy. It is commonly known as **the geoid**.

The lines that intersect all equipotential surfaces orthogonally are not exactly straight, but curved as illustrated in Figure 3.2. They are denoted as **plumb lines** and their directions are similar to the direction of the gravity vector and the vertical. The **orthometric height**, H, above sea level, is measured along the plumb line, starting from the geoid. The incremental distance, dH, along the plumb line, in the direction of increasing height, is

$$\mathrm{d}H = \left\| \begin{bmatrix} \mathrm{d}x \\ \mathrm{d}y \\ \mathrm{d}z \end{bmatrix} \right\| = \|\mathrm{d}\mathbf{x}\| \ , \tag{3.23}$$

from which we can obtain the expression

$$\mathbf{g} \cdot \mathrm{d}\mathbf{x} = -g\,\mathrm{d}H = \mathrm{d}W \ , \tag{3.24}$$

relating the height, H, to the potential, W. This expression is an example of how the geometry of the Earth is closely related to its gravity field. Traditionally, many geodetic mea-

surements such as theodolite measurements, levelling, satellite techniques, etc., are referred to the system of level surfaces and plumb lines. The geometric-gravimetric interdependence is therefore central to geodesy and the determination of the geoid (to be introduced shortly) remain an essential part of geodesy.

3.3 The Geodetic Earth Model

The term "Geodetic Earth Model" is here meant to encompass the various reference models for position and gravity that are used within the field of geodesy. These models have already been introduced and are closely related to the concepts of geodetic datums and reference systems introduced in Section 2. To be more specific, the components of a geodetic Earth model encompass the following reference models:

- The geoid
- The reference ellipsoid
- The normal gravity field

In geodesy, the shape of the geoid is considered to represent the figure of the Earth. Although this figure is not an exact ellipsoid, the ellipsoidal shape and the resulting gravity response, is much easier to handle mathematically, than the geoidal figure. Moreover, the deviations from the actual field are so small that they can be considered linear. For this reason, the level ellipsoid is used as an approximation to the geoid.

The reference ellipsoid is defined by two geometrical parameters, a and f, as introduced in Section 2.2.2. The definition of such a reference ellipsoid also allows the introduction of geodetic coordinates (ϕ, λ, h). In addition to these geometrical parameters, we can associate the ellipsoid with a total mass, M, and a rotational angular velocity, ω_{ie}, in order to uniquely define a gravity field, composed of gravitation and centrifugal acceleration. This gravity field is known as the **normal gravity field**. Instead of defining a total mass M, it is customary to define a standard gravitational parameter GM, where G is the gravitational constant. Together, these four parameters define a geodetic reference system, encompassing the geometry of the Earth along with the external gravity field.

DEFINING PARAMETERS OF A GEODETIC REFERENCE SYSTEM	
Semi-major axis	a
Flattening	f
Angular velocity of Earth	ω_{ie}
Earth's gravitational constant	GM

Table 3.1: Table listing the four defining parameters of a geodetic reference system. The first two parameters, a and f, are geometrical parameters defining the shape of the ellipsoid (theoretical Earth) and the remaining two, ω_{ie} and GM, are physical parameters defining the gravity field external to the ellipsoid.

The geoid on the other hand is more difficult to utilize. As a first approximation, it is a sphere. As a second approximation, one may consider the small degree of flattening due to the rotation of the Earth, and consider it as an ellipsoid of revolution. However, the actual

figure will be bumpy and irregular, reflecting the variable gravitational pull from density variations inside the Earth and variations in topography. The geoid is therefore only realised through extensive gravitational measurements and calculations.

3.3.1 The Geoid

Historically, the height of a point relative to another has been measured as the separation between their horizontal planes, defined using levelling instruments. When it came to absolute height, the natural choice of reference was the idealised mean sea level, i.e. the geoid. By definition, the level surface is perpendicular to the plumb line, meaning that the height was closely connected with the gravity field. The height with respect to the geoid is denoted **orthometric height**, H, and is related to the ellipsoidal height, h, as

$$h = H + N \,, \tag{3.25}$$

where N is known as the geoidal height (also called geoid undulation). It is the height of the geoid, with respect to the ellipsoid, measured along the line orthogonal to the ellipsoid, as illustrated in Figure 3.3. The above relation is an approximation. This is because the direction of the plumb line (called the **vertical**), which is orthogonal to the geoid, is generally not the same as the direction perpendicular to the ellipsoid (called the **normal**).

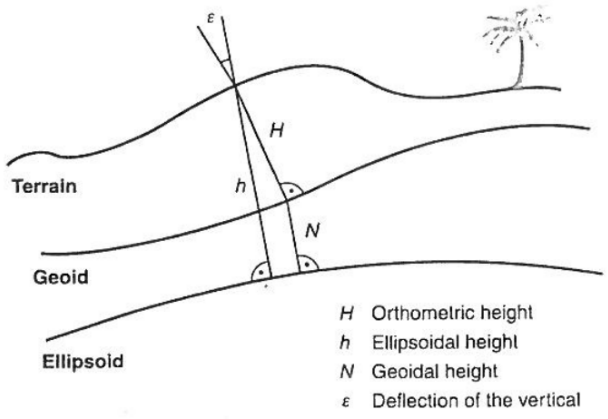

Figure 3.3: Illustration of the relationship between geodetic height h, orthometric height H and geoidal height N. Image credit: [34].

3.3.2 The Normal Gravity Field

By defining the physical parameters GM and ω_{ie}, in addition to the geometrical parameters of the reference ellipsoid, we can uniquely define a normal gravity field, exterior to the ellipsoid. This is according to the theorem of Stokes-Poincaré [48, p. 103]. The external gravity field will be composed of gravitational acceleration (attraction from mass) and centrifugal acceleration (due to Earth rotation).

The expression for the normal gravity potential, U, can be expressed in closed form and the derivation is carried out in detail in [25, sect. 2.7]:

$$U(u,\beta) = \frac{GM}{E}\tan^{-1}\left(\frac{E}{u}\right) + \frac{1}{2}\omega_{ie}^2 a^2 \frac{q}{q_0}\left(\sin^2\beta - \frac{1}{3}\right) + \frac{1}{2}\omega_{ie}^2\left(u^2+E^2\right)\cos^2\beta\ , \tag{3.26}$$

where E is the linear eccentricity, (β, λ, u) are the ellipsoidal-harmonic coordinates introduced in Section 2.2.2 and

$$\begin{aligned} q &= \frac{1}{2}\left[\left(1+3\frac{u^2}{E^2}\right)\tan^{-1}\left(\frac{E}{u}\right) - 3\frac{u}{E}\right]\ , \\ q_0 &= q\Big|_{u=b} = \frac{1}{2}\left[\left(1+3\frac{b^2}{E^2}\right)\tan^{-1}\left(\frac{E}{b}\right) - 3\frac{b}{E}\right]\ . \end{aligned} \tag{3.27}$$

Similar to the "true" gravity potential, W, in Section 3.2.1, we can write the normal gravity potential in terms of a gravitational potential and a centrifugal force component. If we express the gravitational potential in terms of a spherical harmonic expansion, we can exploit the symmetry of the normal gravity field in order to simplify the expression in (3.12). Symmetry about the rotational axis means that all tesseral terms are zero, i.e. everything that depends on the order, m, vanishes, and symmetry about the equatorial plane means that all odd zonal terms are zero, i.e. odd degree terms vanish. We can therefore express the normal gravity potential as the series expansion [48, Eq. 4.45]:

$$U(\mathbf{r}) = \frac{GM}{r}\left(1 - \sum_{n=1}^{\infty}\left(\frac{a}{r}\right)^{2n} J_{2n}\tilde{P}_{2n}(\sin\phi')\right) + \frac{1}{2}\omega_{ie}^2 r^2\cos^2\phi'\ , \tag{3.28}$$

where J_{2n} are geometric parameters related to the ellipsoidal shape, see Table 2.3. Notice that this is not an expression in closed form, since the summation is done to infinity.

Having defined the normal gravity potential, the normal gravity vector, $\boldsymbol{\gamma}$, can be derived as the gradient of the potential field as

$$\boldsymbol{\gamma} = \nabla U(\mathbf{r})\ , \tag{3.29}$$

which, when applied to (3.26), leads to a representation along the u-, β- and λ-axes [35, Eqs. 4-5,4-6]:

$$\begin{aligned} \gamma_u &= -\frac{1}{w}\left[\frac{GM}{v^2} + \frac{\omega_{ie}^2 a^2 E}{v^2}\frac{q'}{q_0}\left(\frac{1}{2}\sin^2\beta - \frac{1}{6}\right)\right] + \frac{1}{w}\omega_{ie}^2 u\cos^2\beta \\ \gamma_\beta &= \frac{1}{w}\frac{\omega_{ie}^2 a^2}{v}\frac{q}{q_0}\sin\beta\cos\beta - \frac{1}{w}\omega_{ie}^2 v\sin\beta\cos\beta \\ \gamma_\lambda &= 0 \end{aligned} \tag{3.30}$$

where

$$\begin{aligned} v^2 &= u^2 + E^2\ , \quad w = \sqrt{\frac{u^2+E^2\sin^2\beta}{v^2}} \quad \text{and} \\ q' &= 3\left[1+\frac{u^2}{E^2}\right]\left[1 - \frac{u}{E}\tan^{-1}\left(\frac{E}{u}\right)\right] - 1\ . \end{aligned} \tag{3.31}$$

This vector can be transformed into components of the rectangular system using [35, Eq. 4-18]:

$$\begin{bmatrix}\gamma_x\\ \gamma_y\\ \gamma_z\end{bmatrix} = \begin{bmatrix}\frac{u}{wv}\cos\beta\cos\lambda & -\frac{1}{w}\sin\beta\cos\lambda & -\sin\lambda\\ \frac{u}{wv}\cos\beta\sin\lambda & -\frac{1}{w}\sin\beta\sin\lambda & \cos\lambda\\ \frac{1}{w}\sin\beta & \frac{u}{wv}\cos\beta & 0\end{bmatrix}\begin{bmatrix}\gamma_u\\ \gamma_\beta\\ \gamma_\lambda\end{bmatrix}, \tag{3.32}$$

and further into the spherical system using [35, Eq. 4-19]:

$$\begin{bmatrix}\gamma_r\\ \gamma_{\phi'}\\ \gamma_\lambda\end{bmatrix} = \begin{bmatrix}\cos\phi'\cos\lambda & \cos\phi'\sin\lambda & \sin\phi'\\ -\sin\phi'\cos\lambda & -\sin\phi'\sin\lambda & \cos\phi'\\ -\sin\lambda & \cos\lambda & 0\end{bmatrix}\begin{bmatrix}\gamma_x\\ \gamma_y\\ \gamma_z\end{bmatrix}. \tag{3.33}$$

Finally, the vector can be transformed into components of the geodetic coordinate system using the angular difference $\alpha = \phi - \phi'$ between the geodetic and geocentric latitudes

$$\begin{bmatrix}\gamma_\phi\\ \gamma_\lambda\\ \gamma_h\end{bmatrix} = \begin{bmatrix}-\sin\alpha & \cos\alpha & 0\\ 0 & 0 & 1\\ -\cos\alpha & -\sin\alpha & 0\end{bmatrix}\begin{bmatrix}\gamma_r\\ \gamma_{\phi'}\\ \gamma_\lambda\end{bmatrix}. \tag{3.34}$$

In Appendix E.1 an implementation of the above formulas is described. The results from this implementation are compared with a much simpler Taylor expansion approach in order to evaluate the differences.

3.3.3 Gravity Disturbance and Gravity Anomaly

The normal gravity field constitutes a reference for gravity in the sense that the actual gravity vector, $\mathbf{g}_P$, can be split into a component of normal gravity vector, $\boldsymbol{\gamma}_P$, resulting from a theoretical ellipsoid, and component of **disturbing gravity vector**, $\delta\mathbf{g}_P$, accounting for all that remains:

$$\mathbf{g}_P = \boldsymbol{\gamma}_P + \delta\mathbf{g}_P \quad \Leftrightarrow \quad \delta\mathbf{g}_P = \mathbf{g}_P - \boldsymbol{\gamma}_P\,, \tag{3.35}$$

where the subscript P refers to the measurement point, meaning that all components are evaluated at P. The **gravity disturbance**, δg, as a scalar quantity is not the magnitude of the gravity disturbance vector. Instead, the gravity disturbance is defined as the difference in magnitudes [1, Eq. 27]:

$$\delta g = \|\mathbf{g}_P\| - \|\boldsymbol{\gamma}_P\| = g_P - \gamma_P\,. \tag{3.36}$$

The reason for this definition is the practical process. Since a gravimeter only measures the magnitude of gravity, g_P, and not the direction of the plumb line, this definition is more convenient.

The **gravity anomaly vector**, $\triangle\mathbf{g}$, related to the measurement point P, is specifically defined as

$$\triangle\mathbf{g} = \mathbf{g}_{W_0} - \boldsymbol{\gamma}_Q\,, \tag{3.37}$$

where $\mathbf{g}_{W_0}$ is the gravity vector at the geoid and $\boldsymbol{\gamma}_Q$ is the normal gravity vector on the reference ellipsoid, having the same *geocentric* latitude as the measurement point, P. Again, the scalar quantity of **gravity anomaly** is defined as the difference in magnitude:

$$\triangle g = \|\mathbf{g}_{W_0}\| - \left\|\boldsymbol{\gamma}_Q\right\| = g_{W_0} - \gamma_Q \ . \tag{3.38}$$

As gravity measurements are usually performed on the topography, ocean or in the air, they have to be reduced onto the surface of the geoid. This process is strictly an upward or downward continuation process, which requires knowledge of the local vertical gradient of gravity. In practice, this vertical gradient is very difficult to estimate accurately, especially since it is sometimes required below the surface of the Earth. Instead, the vertical gradient of normal gravity, commonly known as the **free-air correction**, is used. This approximation is however often a poor one [22].

The ellipsoidal height, h_P, is therefore required to compute the gravity disturbance, whereas the orthometric height, H_P, is required to compute the gravity anomaly. Before the advent of GPS, the ellipsoidal height was not available to the surveyor. Instead the orthometric height, H_P, was available at benchmarks established on the local vertical datum. For this reason, gravity anomalies have been the most widely adopted quantity in geodesy. Since the gravity anomaly is associated with some ambiguity related to the reduction process and the geodetic height is readily available by GPS, the gravity disturbance is used here. For a discussion on this subject, see [22, sect. 2.3].

3.3.4 Deflection of the Vertical

The difference in direction between the gravity vector, $\mathbf{g}$, and normal gravity vector, $\boldsymbol{\gamma}$, is known as the deflection of the vertical. It is usually decomposed into a north-south component, ξ, and an east-west component, η. As with the gravity anomaly, the deflection of the vertical is related to a reference point and direction. Common definitions are the Helmert, Pizetti and Molodensky definitions, none of which are naturally related to the gravity disturbance [26]. In practice, it is usually assumed that $|g_N| \ll |g_D|$ and $|g_E| \ll |g_D|$, validating the following approximation

$$\xi \approx -\frac{\delta g_N}{g} \qquad \text{and} \qquad \eta \approx -\frac{\delta g_E}{g} \ , \tag{3.39}$$

where the components of the gravity disturbance vector, $\delta\mathbf{g}^n = (\delta g_N, \delta g_E, \delta g_D)$, refer to the north, east and down directions of the navigation frame and g is the magnitude of the gravity vector, $\|\mathbf{g}\|$. Inversely, the gravity vector may be recovered from the magnitude and deflection angles as

$$\mathbf{g} \approx \begin{bmatrix} -\xi\, g & -\eta g & g \end{bmatrix}^\top \ . \tag{3.40}$$

4 Fundamental Concepts in Airborne Gravimetry

The fundamental concept of airborne gravimetry is based on Newton's laws of motion, presented in his famous work *Philosophiæ Naturalis Principa Mathematica*. They are commonly expressed in terms of three statements:

- ***The first law:*** *Unless acted upon by an unbalanced force, an object will maintain a constant velocity*
- ***The second law:*** *The change of motion* [momentum] *is proportional to the motive force impressed, and is made in the direction of the straight line in which that force is impressed*
- ***The third law:*** *All forces occur in pairs, and these two forces are equal in magnitude and opposite in direction*

Since the position of an object can only be described in reference to something, one must introduce the concept of reference frames in order to describe motion. Many such reference frames can be defined, but it turns out that Newton's laws of motion are only valid in an inertial reference frame, i.e. the *i*-frame. Such a frame of reference is said to describe time and space homogeneously, isotropically and in a time-independent manner. All inertial frames are in a state of constant, rectilinear motion with respect to another, such that an accelerometer moving with one of these will detect no acceleration. In practice it is difficult to define an inertial frame of reference. This is partly because any frame in the vicinity of the Earth is influenced by gravitational forces from other stars and planets, but also because the orientation is at best defined relative to fixed stars, which we know are not truly fixed. We will however not abandon everything at this point, but instead define a reference system which is "operationally inertial" as described in [6, Sect. 3.1] and introduces very little discrepancy. This frame was introduced, along with other coordinate frames, in Section 2.

The second law of motion, stating that the change in momentum, $m\dot{\mathbf{r}}$, is proportional to the applied force, $\mathbf{F}$, can be expressed mathematically as

$$\mathbf{F} = \frac{\mathrm{d}}{\mathrm{d}t}\left(m\dot{\mathbf{r}}\right) \approx m\ddot{\mathbf{r}} \,, \tag{4.1}$$

where the dot denotes the time derivative and the approximation follows from a constant mass assumption. Realising that our solar system does not represent an inertial frame of reference, since it is permeated by a gravitational field, we can modify the above equation by adding a term accounting for the gravitational field:

$$m_i\,\ddot{\mathbf{r}} = \mathbf{F} + \mathbf{F}_g = m\,\mathbf{f} + m_g\,\bar{\mathbf{g}} \,, \tag{4.2}$$

where $m_i\,\ddot{\mathbf{r}}$ represents the kinematic component, i.e. due to movement, and $\mathbf{F}_g = m_g\,\bar{\mathbf{g}}$ represents the gravitational component. Since the mass occurs on all terms above, it can be divided out from the equation. The reader should notice that the concept of mass is quite abstract and two different concepts of mass have already been introduced. One is the passive gravitational mass in Newton's law of gravitation (3.1), which measures the gravitational force experienced by an object in a gravitational field. The other is the inertial mass from Newton's law of motion, which measures an object's resistance to being accelerated. Although inertial and gravitational masses are conceptually distinct and the theory of classical mechanics offers no compelling reason that they should be the same, no experiment has ever

unambiguously demonstrated any distinction [24, Sect. 2.1]. In the theory of general relativity, the two concepts are treated distinctly, but according to the weak equivalence principle, no experiment will ever detect a difference between them. In any case, since we are not dealing with very high speeds for which we have to consider Einstein's theory of relativity, we will assume that inertial mass and gravitational mass are the same, in which case we can divide out the masses to obtain

$$\boxed{\ddot{\mathbf{r}}^i = \mathbf{f}^i + \bar{\mathbf{g}}^i \,,} \tag{4.3}$$

where the superscript, i, means that this expression is valid in an inertial reference frame and $\mathbf{f}$ is known as the **specific force**. This expression is the most basic equation, not only in airborne gravimetry, but in gravimetry in general.

4.1 Mechanisations and Measurement Systems

The fundamental expression (4.3) indicates that gravity is derived by differencing specific force observations, $\mathbf{f}^i$, measured using an accelerometer, and kinematic accelerations, $\ddot{\mathbf{r}}^i$, typically derived from GNSS observations. As already mentioned in the introduction, the separation of these two components are one of two fundamental problems in airborne gravimetry [43]. This separation is usually not an issue for terrestrial gravimetry, since the accelerometer is stationary and the kinematic component can easily be inferred from knowledge of Earth rotation. Since accelerometers measure along one sensitive axis, another fundamental problem in airborne gravimetry is the determination of sensor orientation. Again, this does not pose a huge difficulty for terrestrial gravimetry, since the accelerometer is easily aligned with the plumb line using a levelling device. However, the dynamic environment of a moving platform makes it difficult not only to keep the accelerometer levelled, but the movement-induced accelerations also makes it difficult to determine the direction of the plumb line. These two issues will be discussed in the following along with some common approaches to overcome these difficulties.

4.1.1 System Mechanisations

The issue of sensor orientation is usually approached either mechanically in an attempt to control the sensor orientation or computationally in order to determine the sensor orientation. The mechanical approach consists of placing the accelerometer on a stabilising platform, that to some extend isolates the movement of the aircraft from the movement of the accelerometer using one or two gimbals. The most common platform is the damped two-axes system often used in combination with the LaCoste&Romberg gravimeter. A conceptual overview of this system is shown in Figure 4.1. The set of two horizontal gyroscopes will measure any changes in the tilt of the aircraft, which are mechanically compensated using a feedback loop to the torque motors. An additional set of horizontal accelerometers help to define the direction of the plumb line by averaging horizontal accelerations over time. The time frame over which the horizontal accelerations should even out is determined by a damping period, which is manually tuned in order to balance aircraft dynamics, feedback loop accuracy and gravity sensor resolution. The damped two-axis platform is therefore sensitive to horizontal accelerations and typically requires operation during flight as aircraft manoeuvring would otherwise infer a false plumb line direction.

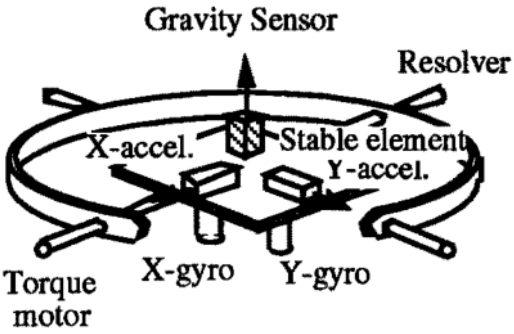

Figure 4.1: Conceptual illustration of a damped two-axes platform system. Image credit [43]

Another mechanical system is the three-axes inertially stabilised platform system used by Sander Geophysics Ltd. This platform uses three gyroscopes in a mechanical feedback loop to account for rotations about all three axes. As the platform does not attempt to compensate for horizontal accelerations and align the accelerometer with the plumb line, a triad of accelerometers are needed in order to derive gravity. This system has been shown to be less sensitive to aircraft dynamics and to operate during draped flying conditions, i.e. following the terrain [13].

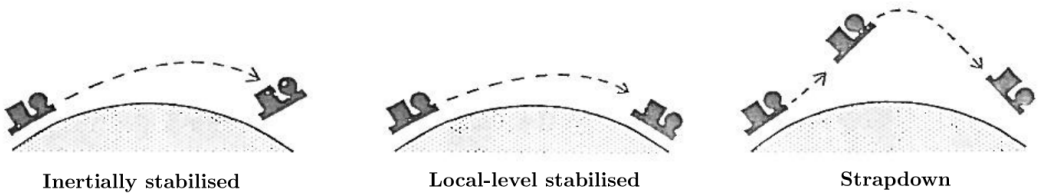

Figure 4.2: Conceptual overview of mechanisations

As an alternative to the mechanical platform system, a triad of accelerometers can be physically attached to the vehicle. This is known as a strapdown configuration and requires an additional triad of gyroscopes in order to monitor rotational motion. By storing angular rates measured by the gyroscopes, the orientation can be determined computationally during post-mission processing.

In practice, the mechanical and computational approaches may be combined. This can for example be done for the damped two-axes platform by using the horizontal accelerations and modelling the platform tilt error [36].

4.1.2 Deriving Gravity from Observations

In order to realise the challenge of deriving gravity from the difference between two observations systems, it can be insightful to have a look at the actual observations. Figure 4.3 illustrates the observed specific force and derived kinematic acceleration along an approximately 40 km flight line in eastern Greenland. The specific force is compensated for normal gravity and corrected for the Eötvös effect, which will be explained in Section 10.1. These

accelerations are collected using a stradown IMU with a 300 Hz sampling rate. The kinematic accelerations in the bottom figure are derived by fitting a spline function to 1 Hz GNSS position estimates and double-differencing the function. As can be seen from the bottom figure, kinematic accelerations are in the range of $\pm 1\,\mathrm{m/s^2}$.

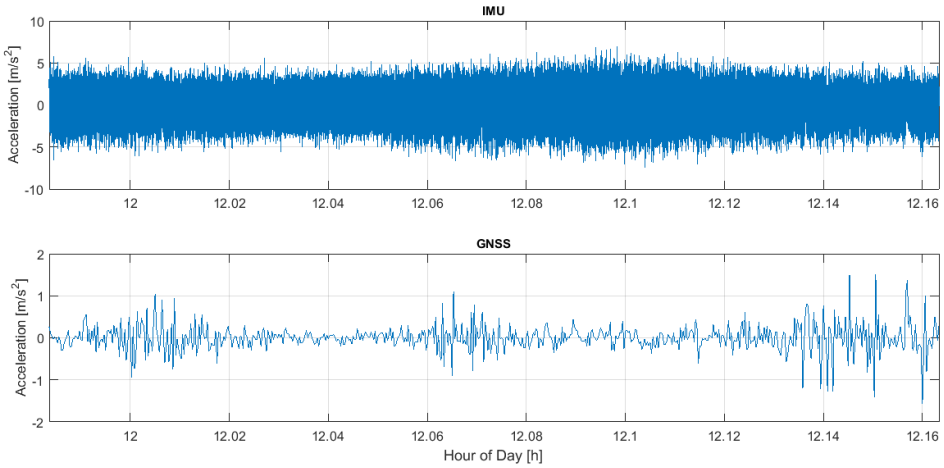

Figure 4.3: Accelerations observed by the gravimeter and GNSS measurement system for a single flight line. (Top:) Specific force observed by the accelerometers of an IMU compensated for normal gravity and the Eötvös effect; (Bottom:) Accelerations derived by fitting a spline function to the position estimates of a GNSS system

In geophysics, gravity is often expressed in units of Gal, with 1 Gal = $\mathrm{cm/s^2}$. The small changes in gravity due to geological structures are usually measured in milligal (mGal), meaning that the gravity signal is five orders of magnitude smaller than the observed signal. In Figure 4.4 the IMU and GNSS-derived accelerations are shown after being subject to a two-pass Butterworth filter of 120 s width.

	$\mathrm{m/s^2}$	g	Gal	mGal	μGal
1 $\mathrm{m/s^2}$	1	$1.01972 \cdot 10^{-1}$	10^2	10^5	10^8
1 g	9.80665 (≈ 10)	1	980.665 ($\approx 10^3$)	$9.80665 \cdot 10^5$ ($\approx 10^6$)	$9.80665 \cdot 10^8$ ($\approx 10^9$)
1 Gal	10^{-2}	$1.01972 \cdot 10^{-3}$	1	10^3	10^6
1 mGal	10^{-5}	$1.01972 \cdot 10^{-6}$	10^{-3}	1	10^3
1 μGal	10^{-8}	$1.01972 \cdot 10^{-9}$	10^{-6}	10^{-3}	1

Table 4.1: Conversion between common units of acceleration. The unit g refers to a standard gravity value of $g_0 = 9.80655\,\mathrm{m/s^{-2}}$, which is also commonly denoted by g_n

As indicated by Figure 4.4 the observed accelerations have a very similar profile and are on the order of several thousand milligal, indicating that the majority of the observed signal

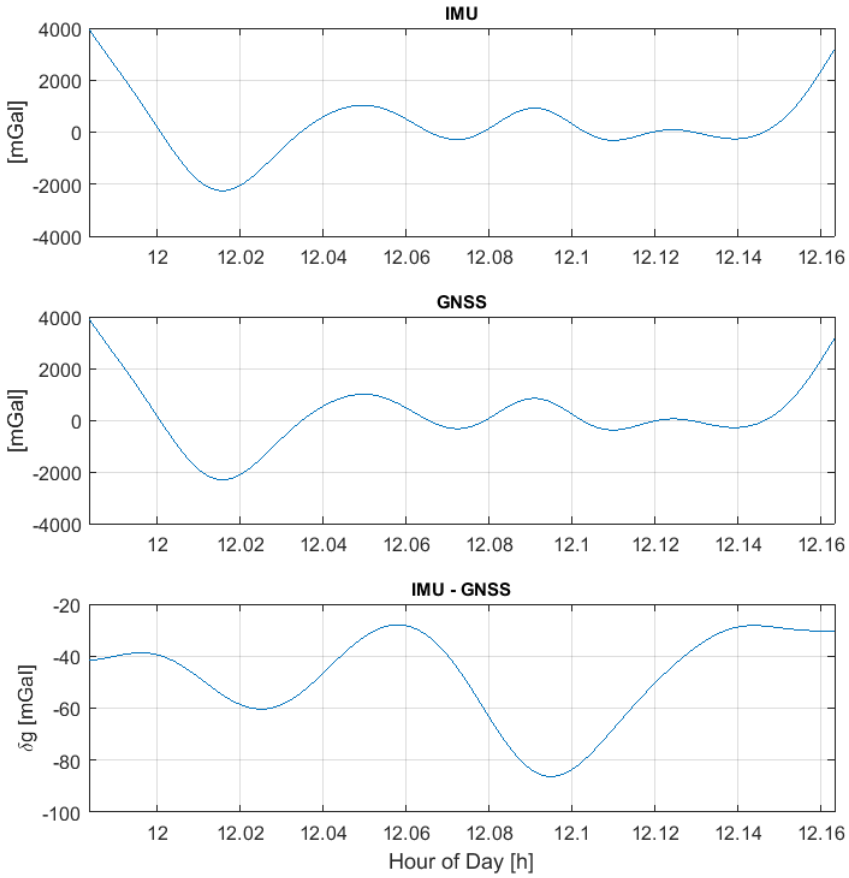

Figure 4.4: Filtered acceleration along with derived gravity signal. (Top): IMU accelerations subject to a two-pass Butterworth filter of 120 s width; (Middle): GNSS-derived accelerations subject to a two-pass Butterworth filter of 120 s width; (Bottom:) Difference between the upper two accelerations

originates from vehicle movement. The gravity variation extracted by differencing the two signals are two orders of magnitude smaller than the filtered signal. For this reason, spectral analysis and the topic of filtering are very important to airborne gravimetry and have been extensively studied. This also means that operational procedures can be developed in order to resolve some frequency range of interest.

4.1.3 Methods of Airborne Gravimetry

The gravity acceleration is by nature a vector quantity. However, estimation of the gravity vector requires information on both direction and magnitude. Currently, only systems based on inertial technology are capable of estimating all three components of the gravity vector. This includes inertially-stabilised platform systems and strapdown IMU systems. Since the vertical component of gravity is typically six orders of magnitude larger than the horizontal components, even small attitude errors can cause large errors to leak into the horizontal

estimates. For this reason, the horizontal components are usually estimated with poorer accuracy than the vertical component. Estimation of all three vector components is usually denoted as vector gravimetry. In general, airborne gravimetry can be divided into one of three overall groups, depending on the nature of the estimated quantity:

- Scalar gravimetry
- Vector gravimetry
- Gravity gradiometry

In scalar gravimetry, only the magnitude of the gravity vector is estimated. This approach is typically relevant for stabilised platform systems, where only a single accelerometer is responsible for measuring gravity. One approach to scalar gravimetry that uses a triad of accelerometers in order to eliminate the orientation requirement is known as Rotation Invariant Scalar Gravimetry (RISG). In this method, gravity is derived by differencing the magnitude between specific force and kinematic accelerations [49]. In gravity gradiometry, the along-track gravity gradients are derived by differencing observations from two carefully aligned triads of accelerometers on a common platform [12]. Of these three kinds of airborne gravimetry, the technology used in gravity gradiometry is capable of providing superior results in terms of both accuracy and resolution [11].

4.2 Resolution of Gravity Observations

Gravity estimates obtained from airborne observations are most commonly represented by a set of discrete spatial samples along the flight profile. Usually, the sampling rate is defined in the time domain, meaning that the spatial resolution is dependent on the along-track speed. Imagine for example that 1 Hz samples are obtained at a flight speed of 100 m/s, implying a spatial separation of 100 m between successive samples. According to the Nyquist sampling theorem, the highest obtainable resolution of the estimated gravity signal in terms of the wavelength is 200 m. This leads us directly to a waveform decomposition of the gravity signal in terms of spherical harmonic functions (3.12), repeated here:

$$V(\mathbf{r}) = \frac{GM}{R}\sum_{n=0}^{N}\left(\frac{R}{r}\right)^{n+1}\sum_{m=0}^{n}\bar{P}_{n,m}\left(\sin\phi'\right)\left[C_{n,m}\cos m\lambda + S_{n,m}\sin m\lambda\right] \ , \tag{4.4}$$

where n is the degree and m the order of the series expansion. These spherical harmonic functions are waveforms on the surface of a sphere with frequency increasing with degree and order. The relation between spherical harmonic functions and spatial resolution will be discussed in the following section. Before continuing, it should be pointed out that there is a difference between full-wavelength and half-wavelength resolution. Returning to the Nyquist sampling theorem, samples that are spatially separated by 100 m will have a maximum possible full-wavelength resolution of 200 m and half-wavelength resolution of 100 m.

4.2.1 Resolution and Wavelength

The gravity field is commonly presented in terms of a series of spherical harmonic functions (4.4), with the upper limit, n_{max}, defining the resolution of the representation. Since the harmonic functions represent oscillating functions on the sphere, these can be related to a spatial resolution in terms of the half- or full-wavelength of the highest-degree harmonic

function. A harmonic function of degree, n, will have n zero-points along the interval from 0 to 2π. A simple measure of the half-wavelength resolution is therefore the distance between two successive zero-points on the equator

$$\psi_{min}(n) \approx \frac{\pi R}{n} \tag{4.5}$$

where R is the Earth radius. However, as the resolution of spherical harmonics on the sphere is uniform, a better measure of the half-wavelength resolution is formed by dividing the surface of the sphere, $4\pi R^2$, into as many equal area components, A, as there are harmonic functions in the series representation

$$A(n) = \frac{4\pi R^2}{(n+1)^2} \, . \tag{4.6}$$

A measure of the half-wavelength resolution is the diameter of a spherical cap of this size [1, Eq. 114]:

$$\psi_{min}(n) = 4 \arcsin\left(\frac{1}{n+1}\right) \, , \tag{4.7}$$

which represents the size of the smallest bump on the sphere, produced by the $(n+1)^2$ parameters. Global gravity models such as GGM05G and GOCO05S are derived solely from satellite gravity observations and have maximum degrees of 240 and 280, respectively [40, 33]. As seen in Table 4.2, this corresponds to a half-wavelength spatial resolution of around 100 km. Combined models, such as EGM08 and EIGEN-6C4, use additional information from satellite altimetry along with airborne, shipborne and terrestrial gravity observations in order to reach a maximum degree of 2190 [37, 17]. This corresponds to a half-wavelength spatial resolution of around 12 km.

In Figure 4.5, the gravity disturbance is computed from the EGM08 global gravity model at different truncation degrees. The computation is done using the algorithm described in Appendix E.2 with ellipsoidal height, $h = 0$. The figure illustrates that the degree of truncation works similar to a low pass filter, with a low truncation degree corresponding to a smoother gravity signal.

4.2.2 Attenuation of the Gravity Signal

According to Newton's law of gravitation (3.1), the magnitude of the gravitational attraction decays as a function of distance from the attracting mass. This attenuation is inversely proportional to the squared distance and is represented in the spherical harmonic expansion (4.4) as

$$\text{attenuation} = \left(\frac{R}{r}\right)^{n+1} \approx \left(\frac{R}{R+h}\right)^{n+1} \, , \tag{4.8}$$

indicating that the attenuation is dependent on the degree, n, of the harmonic function. This means that high-resolution signatures of the gravity signal are more damped than low-resolution signatures at a similar distance from the source, i.e. the amplitude of high-resolution components decrease faster with increasing distance.

In Figure 4.6, the EGM08 global gravity model is evaluated at different altitudes in order to illustrate the attenuation. From the figure it can be seen how the "high"-resolution

Maximum degree	Half-wavelength spatial resolution	
2	8653.876 km	
5	4264.030 km	
10	2318.182 km	
50	499.342 km	low resolution
180	140.690 km	
240	105.743 km	
280	90.691 km	
360	70.540 km	
500	50.828 km	
1000	25.439 km	medium
2190	11.631 km	
5000	5.092 km	
10000	2.546 km	
20000	1.274 km	high
50000	0.510 km	

Table 4.2: Some examples of spatial resolution (in terms of diameter of smallest bump) derived from maximum spherical harmonic degree. The low, medium and high resolution domains as defined in this dissertation are also shown

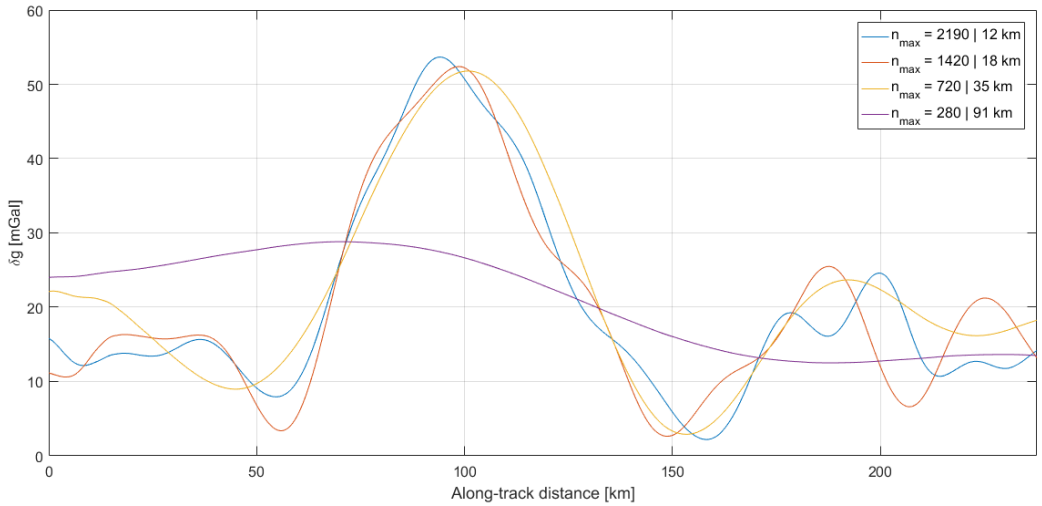

Figure 4.5: Gravity disturbance from EGM08 with various truncation degrees. The computation is done at zero ellipsoidal height along the Denmark flight profile presented in Section 11.1

signatures attenuates with altitude, while the magnitude of the "low"-resolution features are less affected.

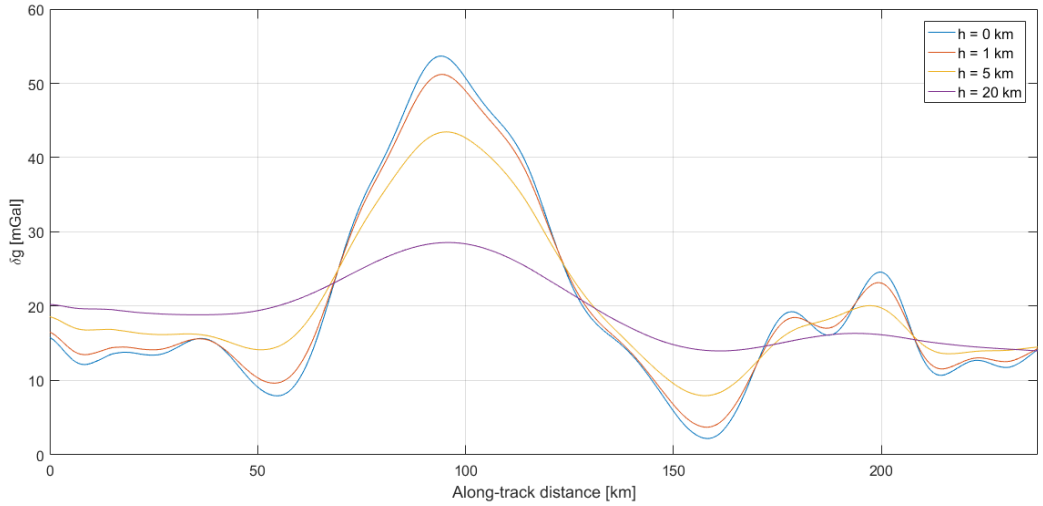

Figure 4.6: Gravity disturbance from EGM08 at various ellipsoidal heights. The computation is done at full resolution, i.e. $n_{max} = 2190$, along the Denmark flight profile presented in Section 11.1

This attenuation effect has direct implications on the airborne observations, since they are obtained at some flight altitude. The closer the aircraft can fly to the ground, the higher is the resolution of the *observed* gravity signal. However, neglecting factors such as air traffic regulations, topography, weather conditions, etc. that make it impossible to fly closer to the ground, the *estimated* gravity signal may not benefit from this due to increased aircraft dynamics and limited measurement precision. Moreover, with reference to the applications mentioned in the introduction, higher resolution may not be desired. A survey is often designed with respect to the intended application, since covering larger areas, saving time, budget limitations, etc. may be more important than obtaining high resolution estimates.

4.2.3 Along-Track Sampling

As already mentioned, the gravity estimates are usually represented by a set of discrete samples along the flight trajectory. Typical aircraft speed is in the range of 50 m/s to 200 m/s. With 1 Hz samples, this implies a half-wavelength spatial resolution of 50 to 200 m. However, the gravity estimates are corrupted by noise, which is handled by low-pass filtering the estimated gravity profile. Typical filter lengths are between 60 and 200 s, implying a maximum half-wavelength spatial resolution of 1.5 to 5 km at 50 m/s and 6 to 20 km at 200 m/s. It is therefore important to realise that the along-track sampling frequency does not represent the true resolution of the along-track gravity estimates.

As seen in Figure 4.7, airborne gravity surveys are usually designed in terms of parallel line segments. The across-track resolution is therefore limited by the line spacing. In order to interpolate airborne gravity estimates onto a grid of uniform spacing, this over-sampling effect need to be taken into account by first down-sampling the along track estimates.

4.3 Methods of Evaluation

This section presents some common methods for evaluating the quality of the gravity estimates in airborne gravimetry. The discussion is limited to internal evaluation methods and does not consider the evaluation with respect to external estimates. For both the cross-over differences and repeat track methods presented here, the quality is evaluated in terms of the difference between gravity disturbance estimates at the same point in terms of horizontal coordinates. The difference between two flight trajectories, A and B, can be expressed as

$$\boldsymbol{\epsilon}_{A,B} = \delta\hat{\mathbf{g}}_A - \delta\hat{\mathbf{g}}_B \ , \tag{4.9}$$

which can be used as a measure of agreement between the two line estimates. This expression is readily modified for the case of scalar gravimetry and the use of gravity anomalies. The horizontal components are often evaluated in terms of deflection angles using (3.39) and expressed in arc seconds rather than milligal.

Although the two estimates represent similar horizontal coordinates, they are in general expected to have some vertical offset with respect to one another. As the gravitational attraction is distance dependent, the gravity vector is not expected to be the same at two different altitudes. The vertical gravity gradient is commonly approximated using the free-air gravity gradient [48, Sec. 6.1.2]:

$$\frac{\delta\gamma}{\delta h} \approx -0.3086\,\text{mGal/m} \tag{4.10}$$

which is derived from the normal gravity field. By comparing gravity disturbances, this free-air gradient is therefore already accounted for. In general, the true gravity gradient will however not be the same as the normal gravity gradient, meaning that any residual gravity gradient may induce a height-dependent difference in the residuals. As the gravity gradient is generally not known and the residual gradient is assumed to be small, the height-dependent effect is typically neglected. One should however be careful when comparing line segments with a considerable separation in altitude.

4.3.1 Cross-Over Differences

Airborne gravity surveys are often designed in terms of parallel line segments in order to cover large areas without spending an excess of time and fuel. The spacing between these parallel line segments are designed in order to obtain some desired resolution, in combination with ground speed and altitude, as discussed in the previous section. In order to evaluate the accuracy of the derived gravity estimates, a few across-track lines are usually flown as seen in Figure 4.7.

If a considerable number of cross-over points can be identified, it is possible to derive some statistics of the differences in order to evaluate the results. Typical statistical measures are the mean, μ, and standard deviation, σ:

$$\mu = \frac{1}{N}\sum_{i=1}^{N}\epsilon_i \quad \text{and} \quad \sigma = \sqrt{\frac{1}{N-1}\sum_{n=1}^{N}\left(\epsilon_i - \mu\right)^2} \ , \tag{4.11}$$

along with the minimum and maximum differences:

$$\epsilon_{\min} = \min\left[\epsilon_i\right] \quad \text{and} \quad \epsilon_{\max} = \max\left[\epsilon_i\right] \ . \tag{4.12}$$

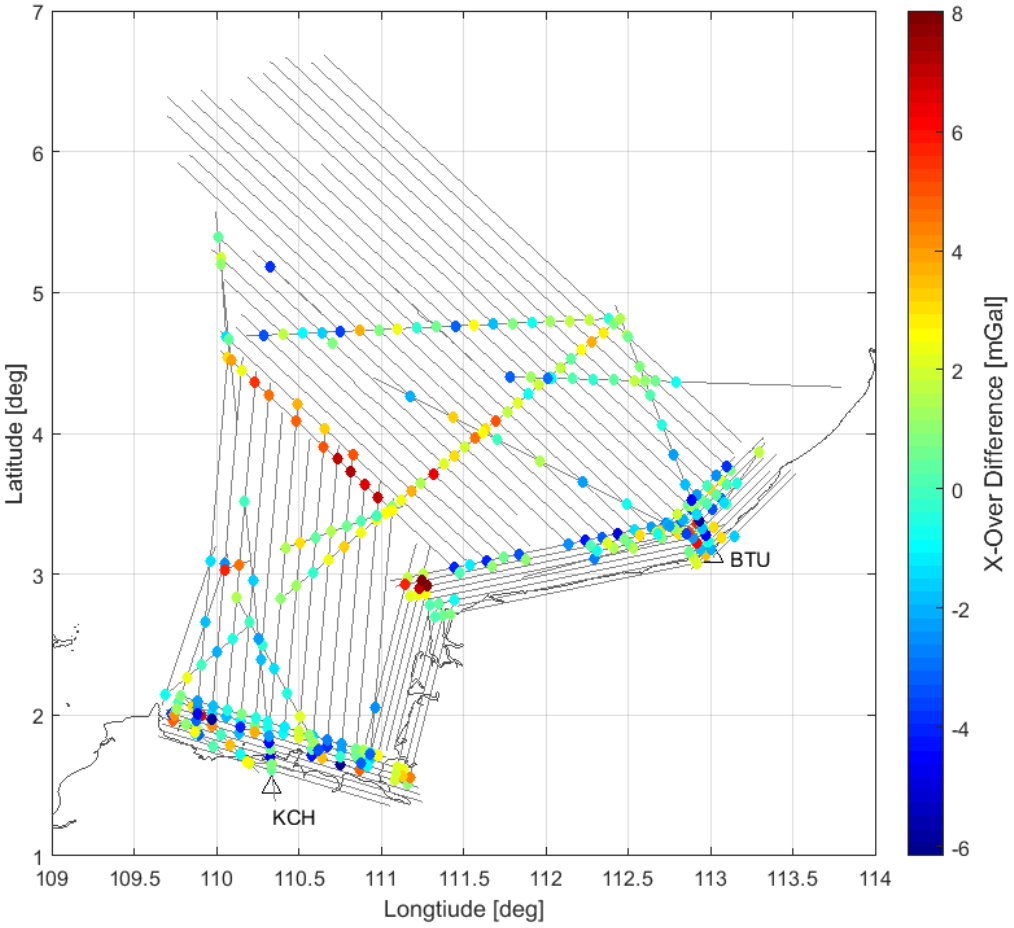

Figure 4.7: Overview of flight lines and cross-over differences for the Malaysia 2016 campaign, to be presented in Section 11

and the Root-Mean-Square deviation:

$$\mathrm{RMS} = \sqrt{\frac{1}{N}\sum_{n=1}^{N}\epsilon_i^2}\,. \tag{4.13}$$

In order to interpret these results, it is assumed that the estimates represent the outcome of a stochastic process. At the crossing point, we can imagine having two samples of a random variable. If the standard deviation of each sample is σ, the standard deviation about the sample mean is $\sigma/\sqrt{2}$. This factor of $1/\sqrt{2}$ is therefore often applied to the RMS-measure as

$$\mathrm{RMSE} = \mathrm{RMS}/\sqrt{2} \tag{4.14}$$

in order to obtain an estimate of the uncertainty on each individual estimate. This measure

is known as the Root-Mean-Square-Error (RMSE) and assumes that the uncertainty is distributed equally between the two estimates. The RMSE measure is the most commonly used measure of evaluation in airborne gravimetry.

4.3.2 Repeated Line Segments

Repeated line segments can be evaluated using the same tools as for the cross-over differences. In this case, the along-track differences are formed rather than a single cross-over difference. One should be aware of any horizontal separation between the two lines and altitude differences can be observed in terms of signal attenuation, which is similar to a low-pass filtering.

Repeated line segments can also be compared in terms of the along-track correlation in order to identify erroneous long wavelength information in the gravity estimates. As will be seen in Section 11, repeated line segments do therefore not only offer evaluation measures, but also some insight into the error characteristics of the gravity estimates.

4.3.3 Cross-Over Adjustment

If a significant number of cross-over residuals are available, the presence of erroneous long wavelength information can be dealt with using a cross-over adjustment. The cross-over adjustment consists of correcting the long wavelength information on a line-to-line typically in terms of a bias and linear trend. Each line segment is corrected for a bias and linear trend, in order to minimise the cross-over differences.

The cross-over adjustment basically makes the relative information more consistent on the cost of introducing erroneous long wavelength information since the relative observations are with respect to some arbitrary plane in space. This plane can be related to the absolute gravity field using known values for at least three locations in the area. Such cross-over adjustment is generally not used for geodetic applications, since a tilt in the resulting plane may induce a corresponding tilt in the estimated geoid. Cross-over adjustment will also not be used in this dissertation.

References

[1] Franz Barthelmes. *Definition of Functionals of the Geopotential and their calculation from spherical harmonic modeles*. Tech. rep. Helmholtz-Zentrum Potsdam, 2013. DOI: 10.2312/GFZ.b103-0902-26.

[2] L. Bastos et al. "Gravity anomalies from airborne measurements — experiments using a low cost IMU device". In: *Gravity, Geoid and Geodynamics 2000*. Ed. by Michael G. Sideris. Berlin, Heidelberg: Springer Berlin Heidelberg, 2002, pp. 253–258. ISBN: 978-3-662-04827-6. DOI: 10.1007/978-3-662-04827-6_42.

[3] D. Becker et al. "Latest results in strapdown airborne gravimetry using an iMAR RQH unit". In: *Proceedings of the 4th IAG Symposium on Terrestrial Gravimetry: Static and Mobile Measurements (TG-SMM 2016)*. State Research Center of the Russian Federation, 2016, pp. 19–25.

[4] David Becker. "Advanced Calibration Methods for Strapdown Airborne Gravimetry". PhD thesis. Darmstadt: Technische Universität Darmstadt, 2016. URL: http://tuprints.ulb.tu-darmstadt.de/5691/.

[5] David Becker et al. "Drift reduction in strapdown airborne gravimetry using a simple thermal correction". In: *Journal of Geodesy* 89.11 (2015), pp. 1133–1144. ISSN: 14321394. DOI: 10.1007/s00190-015-0839-8.

[6] Kenneth R. Britting. *Inertial Navigation Systems Analysis*. 1971, p. 267. ISBN: 978-1608070787.

[7] J. M. Brozena. "The Greenland Aerogeophysics Project: Airborne Gravity, Topographic and Magnetic Mapping of an Entire Continent". In: *From Mars to Greenland: Charting Gravity With Space and Airborne Instruments*. Ed. by Oscar L. Colombo. New York, NY: Springer New York, 1992, pp. 203–214. ISBN: 978-1-4613-9255-2. DOI: 10.1007/978-1-4613-9255-2_19.

[8] J M Brozena, G L Mader, and M F Peters. "Interferometric Global Positioning System: Three-dimensional positioning source for airborne gravimetry". In: *Journal of Geophysical Research* 94.B9 (1989), p. 12153. ISSN: 0148-0227. DOI: 10.1029/JB094iB09p12153. URL: http://doi.wiley.com/10.1029/JB094iB09p12153.

[9] John M Brozena. "A preliminary analysis of the NRL airborne gravimetry system". In: *GEOPHYSICS* 49.7 (1984), pp. 1060–1069. ISSN: 0016-8033. DOI: 10.1190/1.1441721. URL: http://library.seg.org/doi/10.1190/1.1441721.

[10] Alexander Mark Bruton. "Improving the Accuracy and Resolution of SINS / DGPS Airborne Gravimetry". PhD thesis. University of Calgary, 2000, p. 235. URL: https://www.ucalgary.ca/engo{_}webdocs/KPS/00.20145.AMBruton.pdf.

[11] Mark Dransfield. "Airborne Gravity Gradiometry in the Search for Mineral Deposits". In: *Proceedings of Exploration 07: Fifth Decennial International Conference on Mineral Exploration*. Ed. by B. Milkereit. 2007, pp. 341–354.

[12] Mark Dransfield and James B. Lee. "The FALCON airborne gravity gradiometer survey systems". In: *Airborne Gravity 2004: Abstracts from the ASEG-PESA Airborne Gravity 2004 Workshop*. Ed. by Richard Lane. Geoscience Australia, 2004, pp. 15–19.

[13] J. Derek Fairhead and Mark E. Odegard. "Advances in gravity survey resolution". In: *The Leading Edge* 21.1 (2002), pp. 36–37. ISSN: 1070-485X. DOI: 10.1190/1.1445845. URL: http://tle.geoscienceworld.org/cgi/content/extract/21/1/36http://library.seg.org/doi/10.1190/1.1445845.

[14] S. T. Ferguson and Y. Hammada. "Experiences with AIRGrav: Results from a New Airborne Gravimeter". In: *Gravity, Geoid and Geodynamics 2000*. Ed. by Michael G. Sideris. Berlin, Heidelberg: Springer Berlin Heidelberg, 2002, pp. 211–216. ISBN: 978-3-662-04827-6. DOI: 10.1007/978-3-662-04827-6_35.

[15] R. Forsberg et al. "Inertial gravimetryA comparison of Kalman filtering-smoothing and post-mission adjustment techniques". In: *Bulletin Géodésique* 60.2 (1986), pp. 129–142. ISSN: 0007-4632. DOI: 10.1007/BF02521013. URL: http://link.springer.com/10.1007/BF02521013.

[16] Rene Forsbger and Arne V. Olesen. "Airborne Gravity Field Determination". In: *Sciences of Geodesy - I: Advances and Future Directions*. Ed. by Guochang Xu. Berlin, Heidelberg: Springer Berlin Heidelberg, 2010, pp. 83–104. ISBN: 978-3-642-11741-1. DOI: 10.1007/978-3-642-11741-1_3.

[17] Christoph Förste et al. *EIGEN-6C4 The latest combined global gravity field model including GOCE data up to degree and order 2190 of GFZ Potsdam and GRGS Toulouse*. GFZ Data Services. 2014. URL: http://doi.org/10.5880/icgem.2015.1.

[18] C. Glennie and K. P. Schwarz. "A comparison and analysis of airborne gravimetry results from two strapdown inertial/DGPS systems". In: *Journal of Geodesy* 73.6 (1999), pp. 311–321. ISSN: 09497714. DOI: 10.1007/s001900050248.

[19] C. L. Glennie et al. "A comparison of stable platform and strapdown airborne gravity". In: *Journal of Geodesy* 74.5 (2000), pp. 383–389. ISSN: 09497714. DOI: 10.1007/s001900000082.

[20] Paul D. Groves. *Principles of GNSS, Inertial, and Multisensor Integrated Navigation Systems*. 2nd. Artech House Remote Sensing Library, 2013. ISBN: 978-1608070053.

[21] William R. Gumert. "An historical review of airborne gravity". In: *The Leading Edge* 17.1 (1998), pp. 113–116. DOI: 10.1190/1.1437808.

[22] R. I. Hackney and W. E. Featherstone. "Geodetic versus geophysical perspectives of the 'gravity anomaly'". In: *Geophysical Journal International* 154.1 (2003), pp. 35–43. ISSN: 0956540X. DOI: 10.1046/j.1365-246X.2003.01941.x.

[23] Sigmund Hammer. "Airborne gravity is here!" In: *GEOPHYSICS* 48.2 (1983), pp. 213–223. ISSN: 0016-8033. DOI: 10.1190/1.1441460. URL: http://library.seg.org/doi/10.1190/1.1441460.

[24] Bernhard Hofmann-Wellenhof and Helmut Moritz. *Physical geodesy*. 2005, pp. 1–405. ISBN: 3211235841. DOI: 10.1007/b139113. arXiv: arXiv:1011.1669v3.

[25] Bernhard Hofmann-Wellenhof and Helmut Moritz. *Physical Geodesy*. 2nd, corrected. SpringerWienNewYork, 2006. ISBN: 3-211-33544-7.

[26] C. Jekeli. "An analysis of vertical deflections derived from high-degree spherical harmonic models". In: *Journal of Geodesy* 73.1 (1999), pp. 10–22. ISSN: 0949-7714. DOI: 10.1007/s001900050213. URL: http://link.springer.com/10.1007/s001900050213.

[27] Christopher Jekeli. "Airborne vector gravimetry using precise, position-aided inertial measurement units". In: *Bulletin Géodésique* 69.1 (1994), pp. 1–11. ISSN: 00074632. DOI: 10.1007/BF00807986.

[28] Christopher Jekeli. *Geometric Reference Systems in Geodesy*. 2006.

[29] Christopher Jekeli. *Inertial Navigation Systems with Geodetic Applications*. 2001, pp. 51–54. ISBN: 3110159031. DOI: 10.1515/9783110800234.

[30] Alfred Kleusberg, Derrick Peyton, and David Wells. "Airborne gravimetry and the Global Positioning System". In: *IEEE Symposium on Position Location and Navigation. A Decade of Excellence in the Navigation Sciences*. IEEE, 1990, pp. 273–278. DOI: 10.1109/PLANS.1990.66188.

[31] J. H. Kwon and C. Jekeli. "A new approach for airborne vector gravimetry using GPS/INS". In: *Journal of Geodesy* 74.10 (2001), pp. 690–700. ISSN: 09497714. DOI: 10.1007/s001900000130.

[32] Lucien LaCoste et al. "Gravity measurements in an airplane using stateoftheart navigation and altimetry". In: *GEOPHYSICS* 47.5 (1982), pp. 832–838. ISSN: 0016-8033. DOI: 10.1190/1.1441351. URL: http://library.seg.org/doi/10.1190/1.1441351.

[33] Torsten Mayer-Gürr and GOCO consortium. *The combined satellite only model GOCO05s*. Presentation at EGU 2015, Vienna. 2015. URL: https://www.bgu.tum.de/iapg/forschung/schwerefeld/goco/.

[34] Pratap Misra and Per Enge. *Global Positioning System: Signals, Measurements, and Performance*. 2nd, revised. Ganga-Jamuna Press, 2006. ISBN: 978-0-970-95441-1.

[35] National Imagery and Mapping Agency. *World Geodetic System 1984: Its Definition and Relationships with Local Geodetic Systems*. Tech. rep. U.S. Department of Defence, 2000.

[36] Arne V. Olesen. "Improved airborne scalar gravimetry for regional gravity field mapping and geoid determination". PhD thesis. University of Copenhagen, 2002. URL: ftp://ftp.dsri.dk/pub/avo/AG/DOC/avo_techrep.pdf.

[37] Nikolaos K. Pavlis et al. "The development and evaluation of the Earth Gravitational Model 2008 (EGM2008)". In: *Journal of Geophysical Research: Solid Earth* 117.B4 (2012), n/a–n/a. ISSN: 01480227. DOI: 10.1029/2011JB008916. URL: http://doi.wiley.com/10.1029/2011JB008916.

[38] Andrew Presley. *Elementary Differential Geometry*. 2nd. Springer, 2010. ISBN: 978-1-84882-890-2.

[39] Richard Rapp. *Geometric geodesy: Part I*. 1991. URL: http://hdl.handle.net/1811/24333.

[40] J. Ries et al. *Development and Evaluation of the Global Gravity Model GGM05*. CSR-16-02, Center for Space Research, The University of Texas at Austin. 2016. URL: http://www2.csr.utexas.edu/grace/gravity/.

[41] David T. Sandwell and Walter H.F. Smith. "Marine gravity anomaly from Geosat and ERS 1 satellite altimetry". In: *Journal of Geophysical Research B: Solid Earth* 102.B5 (1997), pp. 10039–10054. ISSN: 21699356. DOI: 10.1029/96JB03223.

[42] K. P. Schwarz. "Inertial surveying and geodesy". In: *Reviews of Geophysics* 21.4 (1983), p. 878. ISSN: 8755-1209. DOI: 10.1029/RG021i004p00878. URL: http://doi.wiley.com/10.1029/RG021i004p00878.

[43] K. P. Schwarz and Zuofa Li. "An introduction to airborne gravimetry and its boundary value problems". In: *Geodetic Boundary Value Problems in View of the One Centimeter Geoid* (), pp. 312–358. DOI: 10.1007/BFb0011709. URL: http://www.springerlink.com/index/10.1007/BFb0011709.

[44] K P Schwarz et al. "Requirements for Airborne Vector Gravimetry". In: *From Mars to Greenland: Charting Gravity With Space and Airborne Instruments*. 1992, pp. 273–283. ISBN: 0387978577. DOI: 10.1007/978-1-4613-9255-2_25. URL: http://link.springer.com/10.1007/978-1-4613-9255-2{_}25.

[45] K.P. Schwarz, Elizabeth Cannon, and R.V.C. Wong. "A comparison of GPS kinematic models for the determination of position and velocity along a trajectory". In: 14 (Jan. 1989), pp. 345–353.

[46] Lloyd G. D. Thompson. "Airborne gravity meter test". In: *Journal of Geophysical Research* 64.4 (1959), pp. 488–488. ISSN: 01480227. DOI: 10.1029/JZ064i004p00488. URL: http://doi.wiley.com/10.1029/JZ064i004p00488.

[47] Lloyd G. D. Thompson and Lucien J. B. LaCoste. "Aerial gravity measurements". In: *Journal of Geophysical Research* 65.1 (1960), pp. 305–322. ISSN: 01480227. DOI: 10.1029/JZ065i001p00305. URL: http://doi.wiley.com/10.1029/JZ065i001p00305.

[48] Wolfgang Torge. *Geodesy*. Walter de Gruyter, 2001, p. 432. ISBN: 3-11-017072-8. DOI: 10.1515/9783110879957.

[49] M. Wei and K. P. Schwarz. “Flight test results from a strapdown airborne gravity system”. In: *Journal of Geodesy* 72.6 (1998), pp. 323–332. ISSN: 0949-7714. DOI: 10.1007/s001900050171.

Part II:

Inertial Navigation and Sensors

The IMU consists of inertial sensors and is intended for inertial navigation. In order to achieve a better understanding of the sensor, it is therefore important to understand these concepts. Although the intended application here is not navigation, most (if not all) of the framework developed here is directly applicable in airborne gravimetry. This part is therefore devoted to the introduction of inertial navigation and inertial sensors. It is divided into three sections. The first section will introduce the concepts of attitude and inertial navigation. Some effort is made to properly introduce attitude in terms of rotation operators, whereas the navigation equations are only briefly introduced. The derivation of the navigation equations and a discussion of their implementation is provided in Appendix C. The second section introduces sensor and navigation errors along with a set of error dynamics equations. Additionally, after briefly introducing the IMU used in this dissertation, the temperature calibration applied to the results in Section 11 will be described. The final section is devoted to data simulation and describes the development of a simulation algorithm used in this dissertation. The simulated observations are used to asses the performance of different implementations of the navigation equations described in Appendix C.

5 Attitude Representations and Inertial Navigation

Before diving into the subject of inertial navigation, it is important to understand the concept of attitude. The attitude of an aeroplane is commonly associated with three angles, namely the **roll, pitch and heading** angles, describing the orientation of the vehicle with respect to the local level and north directions, i.e. the b-frame relative to the n-frame. The attitude is however a more general term describing the relative orientation of two coordinate frames. This could be the orientation of the b-frame with respect to the n-frame, but in principle any set of rectangular coordinate frames are valid. By orientation is meant how to transform from one coordinate frame to another. Therefore, the terms attitude and coordinate transformation are equivalent. The most common attitude representations are:

- Direction Cosines Matrix (DCM),
- Triple of Euler angles and
- Quaternions.

These three representations are all common in inertial navigation and will be introduced in this section. The roll, pitch and heading angles should not be thought of as orientation in the sense of angles between the axes of the b- and n-frames. Instead, these angles refer to a sequence of rotations that must be applied sequentially in order to transform from one frame to another. As we will see, many sequences of rotations will lead to the same transformation, meaning that the Euler angles are not unique, but depend on the chosen sequence. Moreover, one must also specify the direction of the transformation ($b \to n$ or $n \to b$), in order to obtain a consistent definition of the sign on the angles. Therefore, merely specifying roll, pitch and heading angles does not fully describe the orientation of the vehicle. First we must agree upon some conventions, such that everyone knows what these angles refer to. Such conventions may be different, depending on the field of application.

5.1 Rotation Operators

In general, we have some physical quantity, $\mathbf{v}^t$, represented in a reference frame, t. For now, we assume this to be a vector quantity. We then want to rotate this vector into another reference frame, a. This can be done using a rotation operator, which we assume to be a matrix operator for now, as

$$\boxed{\mathbf{v}^a = \mathbf{C}_t^a \, \mathbf{v}^t \, ,} \tag{5.1}$$

where it is assumed that both t and a are right-handed, rectangular reference frames. The rotation operator may be interpreted from two points of view. Assuming that we are rotating by some angle, θ, about an axis, u, these two points of view are [11, Sec. 5.11]:

- **First Perspective**: The observer is fixed to the coordinate frame. To her it appears that the operator rotates the vector about the **u**-axis through an angle, θ. That is, in the *counter-clockwise* direction. From this perspective, we may think of the coordinate frame as being fixed, while the vector is rotated
- **Second Perspective**: The observer is fixed to the vector. To him it appears that the operator rotates the coordinate frame about the **u**-axis through an angle, $-\theta$. That is, in the *clockwise* direction. From this perspective, the vector is fixed, while the reference frame is being rotated.

Both these perspectives are equally valid. They represent rotations that are equal in magnitude, but opposite in direction, which is important to keep in mind in the following development. In our case, $\mathbf{v}$ will typically represent some physical quantity (e.g. force, velocity or acceleration) which we do not intend to change. Our point of perspective will therefore be the second, namely the transformation between reference frames, fundamentally meaning that we want to represent such a vector quantity along some other set of basis vectors.

As mentioned previously, the rotation operator can take other forms than a matrix. Using Euler angles, the operator takes the form of three successive rotations, whereas the quaternion approach takes the form of a hyper-complex number of rank four and a "Hamilton" product, which is the quaternion equivalent to the vector-dot-product. All three approaches therefore encompass different mathematical operations, but can be related to one another through closed formulas. In general, the matrix product notation in (5.1) will be used, since this is most well-known. In the more general sense, $\mathbf{C}_t^a$ should be thought of as an operator, which is not necessarily a matrix quantity, but whose nature is determined by the method used for coordinate transformations.

The expression in (5.1) is only relevant for vector quantities. If we instead want to transform the set of coordinates, $\mathbf{r}^t$, of a point in space, we need to also consider a translation between the origin of the two coordinate systems. Letting $\mathbf{r}_{a,0}$ and $\mathbf{r}_{t,0}$ denote the origin of the two coordinate frames, respectively, the transformation of a point in space is accomplished as

$$\begin{aligned} \mathbf{r}^a &= \mathbf{C}_t^a \left(\mathbf{r}^t - \mathbf{r}_{a,0}^t \right) = \mathbf{C}_t^a \, \mathbf{r}^t + \mathbf{r}_{t,0}^a \quad \text{and} \\ \mathbf{r}^t &= \mathbf{C}_a^t \left(\mathbf{r}^a - \mathbf{r}_{t,0}^a \right) = \mathbf{C}_a^t \, \mathbf{r}^a + \mathbf{r}_{a,0}^t \, , \end{aligned} \tag{5.2}$$

where the geometrical relations

$$\mathbf{r}_{t,0}^{a} = -\mathbf{C}_{t}^{a}\,\mathbf{r}_{a,0}^{t} \quad \text{and} \quad \mathbf{r}_{a,0}^{t} = -\mathbf{C}_{a}^{t}\,\mathbf{r}_{t,0}^{a} \tag{5.3}$$

were exploited. Also matrix quantities, $\mathbf{A}^{t}$, are defined with respect to some reference frame. The orthogonal transformation of such a 3×3 matrix, from the t-frame to the a-frame, can be derived as

$$\mathbf{y}^{t} = \mathbf{A}^{t}\,\mathbf{x}^{t} \quad \Rightarrow \quad \mathbf{C}_{a}^{t}\,\mathbf{y}^{a} = \mathbf{A}^{t}\,\mathbf{C}_{a}^{t}\,\mathbf{x}^{a} \quad \Rightarrow \quad \mathbf{y}^{a} = \mathbf{C}_{t}^{a}\,\mathbf{A}^{t}\,\mathbf{C}_{a}^{t}\,\mathbf{x}^{a}\;, \tag{5.4}$$

such that

$$\boxed{\mathbf{A}^{a} = \mathbf{C}_{t}^{a}\,\mathbf{A}^{t}\,\mathbf{C}_{a}^{t}\;,} \tag{5.5}$$

This of course means that even the transformation operator, $\mathbf{C}_{t}^{a}$, is defined with respect to some reference frame. The notation used here is that subscripts refer to the "from"-frame and superscripts to the "to"-frame. For example, $\mathbf{C}_{t}^{a}$ transforms from the t-frame to the a-frame. Moreover, the superscript also refers to the reference frame about which the components are resolved. Therefore, the components of $\mathbf{C}_{t}^{a}$ are resolved about the axes of the a-frame.

All of these factors mean that dealing with rotation operators can be a complicated matter. In the following, each of the three rotation operators mentioned earlier will be introduced. In doing so, we need to keep in mind that our perspective is that of rotating the frame, not the quantity itself. Moreover, it is customary to define a reference frame (e.g. the n-frame) and an object frame (e.g. the b-frame). The attitude is defined as the rotation from the reference frame to the object frame, meaning that the rotation is positive in this direction. In inertial navigation we usually transform quantities from the object frame to the reference frame, i.e. in the opposite direction of what defines the attitude.

5.1.1 Direction Cosines Matrix

We let a vector, $\mathbf{v}$, be represented in two arbitrary frames a and t as

$$\mathbf{v}^{a} = \begin{bmatrix} v_{x}^{a} \\ v_{y}^{a} \\ v_{z}^{a} \end{bmatrix} \quad \text{and} \quad \mathbf{v}^{t} = \begin{bmatrix} v_{x}^{t} \\ v_{y}^{t} \\ v_{z}^{t} \end{bmatrix}\;, \tag{5.6}$$

where the superscripts refer to the coordinate frame. The scalar quantities (v_x, v_y, v_z) represent factors that are to be multiplied with the respective unit vectors $\mathbf{e}_x$, $\mathbf{e}_y$ and $\mathbf{e}_z$ and can be interpreted as orthogonal projections of the vector, $\mathbf{v}$, onto the three basis vectors. These projections are accomplished through vector dot products as

$$v_{x}^{a} = \mathbf{v}^{a} \cdot \mathbf{e}_{x}^{a}\;, \quad v_{y}^{a} = \mathbf{v}^{a} \cdot \mathbf{e}_{y}^{a} \quad \text{and} \quad v_{z}^{a} = \mathbf{v}^{a} \cdot \mathbf{e}_{z}^{a}\;. \tag{5.7}$$

In the same manner, the unit vectors of one coordinate frame can be orthogonally projected onto the unit vectors of the other coordinate frame as

$$c_{j,k} = \mathbf{e}_{j}^{a} \cdot \mathbf{e}_{k}^{t} = \left|\mathbf{e}_{j}^{a}\right| \left|\mathbf{e}_{k}^{t}\right| \cos\theta_{j,k} = \cos\theta_{j,k}\;, \tag{5.8}$$

where $j = x, y, z$, $k = x, y, z$ and $\theta_{j,k}$ is the angle between the two vectors. We can therefore write one basis vector in terms of the other as

$$\begin{bmatrix} \mathbf{e}_x^a \\ \mathbf{e}_y^a \\ \mathbf{e}_z^a \end{bmatrix} = \begin{bmatrix} c_{x,x} & c_{x,y} & c_{x,z} \\ c_{y,x} & c_{y,y} & c_{y,z} \\ c_{z,x} & c_{z,y} & c_{z,z} \end{bmatrix} \begin{bmatrix} \mathbf{e}_x^t \\ \mathbf{e}_y^t \\ \mathbf{e}_z^t \end{bmatrix} = \mathbf{C}_t^a \begin{bmatrix} \mathbf{e}_x^t \\ \mathbf{e}_y^t \\ \mathbf{e}_z^t \end{bmatrix} , \tag{5.9}$$

where

$$\mathbf{C}_t^a = \begin{bmatrix} c_{x,x} & c_{x,y} & c_{x,z} \\ c_{y,x} & c_{y,y} & c_{y,z} \\ c_{z,x} & c_{z,y} & c_{z,z} \end{bmatrix} = \begin{bmatrix} \cos\theta_{x,x} & \cos\theta_{x,y} & \cos\theta_{x,z} \\ \cos\theta_{y,x} & \cos\theta_{y,y} & \cos\theta_{y,z} \\ \cos\theta_{z,x} & \cos\theta_{z,y} & \cos\theta_{z,z} \end{bmatrix} \tag{5.10}$$

is known as the **Direction Cosine Matrix** (DCM). The kth column of this matrix represents the unit vector $\mathbf{e}_k^t$ in the a-frame, while the jth row represents the unit vector $\mathbf{e}_j^a$ in the t-frame. This means that the columns and rows are orthogonal and that

$$\mathbf{C}_t^a \, \mathbf{C}_t^{a\top} = \mathbf{I} \quad \Rightarrow \quad \mathbf{C}_t^a = \mathbf{C}_a^{t\,-1} = \mathbf{C}_a^{t\,\top} \quad \Rightarrow \quad \mathbf{C}_t^a \, \mathbf{C}_a^t = \mathbf{I} \, . \tag{5.11}$$

The main result here is really that the transformation of a vector, $\mathbf{v}^t$, represented in the frame t, into a representation in another frame a, can be accomplished as

$$\mathbf{v}^a = \mathbf{C}_t^a \, \mathbf{v}^t \, , \tag{5.12}$$

where the transformation matrix is formed using (5.10). One should notice that the order of the subscripts on $\theta_{j,k}$ is important, meaning that $\theta_{x,y}$ is not the same angle as $\theta_{y,x}$. This also means that the DCM is not symmetric. In fact, as stated above, the inverse rotation is accomplished by the matrix transpose.

5.1.2 Euler Angles

Euler angles refer to a sequence of three successive rotations about an axis orthogonal to that of its predecessor and/or successor. The rotation of a vector, through the angle θ, about the x-, y- or z-axis is accomplished by applying one of the following rotation matrices:

$$\begin{aligned} \mathbf{R}_x(\theta) &= \begin{bmatrix} 1 & 0 & 0 \\ 0 & \cos\theta & \sin\theta \\ 0 & -\sin\theta & \cos\theta \end{bmatrix} , \quad \mathbf{R}_y(\theta) = \begin{bmatrix} \cos\theta & 0 & -\sin\theta \\ 0 & 1 & 0 \\ \sin\theta & 0 & \cos\theta \end{bmatrix} \\ \text{and} \quad \mathbf{R}_z(\theta) &= \begin{bmatrix} \cos\theta & \sin\theta & 0 \\ -\sin\theta & \cos\theta & 0 \\ 0 & 0 & 1 \end{bmatrix} , \end{aligned} \tag{5.13}$$

where $\mathbf{R}_x$ rotates about the x-axis, $\mathbf{R}_y$ about the y-axis and $\mathbf{R}_z$ about the z-axis. These matrices can be derived as DCMs and therefore share the properties

$$\mathbf{R}^{-1}(\theta) = \mathbf{R}^{\top}(\theta) \quad \text{and} \quad \mathbf{R}^{-1}(\theta) = \mathbf{R}(-\theta) \, . \tag{5.14}$$

It is important to notice that these matrices rotate the quantity itself by an angle, θ, about the corresponding axis. Therefore, from our perspective, the reference frame is rotated by the angle, $-\theta$, about the relevant axis. Defining a reference frame, a, and an object frame, t, we may express the rotation of the reference frame as

$$\mathbf{v}^a = \mathbf{R}_i(\theta)\ \mathbf{v}^t\ , \tag{5.15}$$

where $i = x, y, z$ and θ is positive in the direction from the reference frame to the object frame, i.e. $a \to t$. Expressing the rotation operator, $\mathbf{R}_i$, as $\mathbf{R}_t^a$, this notation corresponds to the one introduced previously for the attitude, i.e. the rotation is positive from the reference to the object frame and the superscript refers to the frame about which the components are resolved.

In general, the rotation from the object frame, a, to the reference frame, t, can always be accomplished by a sequence of three rotations as

$$\mathbf{v}^a = \mathbf{R}_i(\alpha_{at})\ \mathbf{R}_j(\beta_{at})\ \mathbf{R}_k(\gamma_{at})\ \mathbf{v}^t\ , \tag{5.16}$$

where α_{at}, β_{at} and γ_{at} are denoted the **Euler angles**, noticing again that these angles are positive in the direction $a \to t$, and i, j and k may refer to either x, y or z. This indicates that the transformation from one frame to another can be accomplished by a variety of sequences. There are in fact 12 possible sequences that are valid [4, Eq. 48]:

$$\begin{aligned}(i,j,k) \in \{&(x,y,x),(x,y,z),(x,z,x),(x,z,y)\\ &(y,x,y),(y,x,z),(y,z,x),(y,z,y)\\ &(z,x,y),(z,x,z),(z,y,x),(z,y,z)\}\ ,\end{aligned} \tag{5.17}$$

noticing that the rotations are applied from right to left. The chosen sequence naturally affects the Euler angles, which are therefore not unique, but related to the chosen sequence. It is thus important to specify both the sequence (i, j, k) and the Euler angles (α, β, γ).

In aeronautics, the sequence (x, y, z) is preferred and the corresponding Euler angles, α, β and γ, are denoted **roll, pitch and yaw**, respectively. Therefore, suppose we are given a vector, $\mathbf{v}^t$, represented in the object frame (t-frame) and want to transform it into a representation along the axes of the reference frame (a-frame). To accomplish this, we start by performing a rotation through the yaw angle γ_{at} about the z-axis as

$$\begin{aligned}\mathbf{v}^\gamma = \mathbf{R}_z(\gamma_{at})\,\mathbf{v}^t &= \begin{bmatrix}\cos(\gamma_{at}) & \sin(\gamma_{at}) & 0\\ -\sin(\gamma_{at}) & \cos(\gamma_{at}) & 0\\ 0 & 0 & 1\end{bmatrix}\begin{bmatrix}v_x^t\\ v_y^t\\ v_z^t\end{bmatrix}\\ \Rightarrow \quad \begin{bmatrix}v_x^\gamma\\ v_y^\gamma\\ v_z^\gamma\end{bmatrix} &= \begin{bmatrix}v_x^t\cos(\gamma_{at}) + v_y^t\sin(\gamma_{at})\\ -v_x^t\sin(\gamma_{at}) + v_y^t\cos(\gamma_{at})\\ v_z^t\end{bmatrix}\ ,\end{aligned} \tag{5.18}$$

in order to arrive at the first intermediate frame, denoted γ. This rotation changes the x and y components of the vector, but leaves the z component unchanged. Next, the pitch step changes the "new" x and z components, but leaves the y component unchanged, by rotating about the y-axis by the pitch angle β_{at}

$$\begin{aligned} \mathbf{v}^{\beta} = \mathbf{R}_y\left(\beta_{at}\right)\mathbf{v}^{\gamma} &= \begin{bmatrix} \cos\beta_{at} & 0 & -\sin\beta_{at} \\ 0 & 1 & 0 \\ \sin\beta_{at} & 0 & \cos\beta_{at} \end{bmatrix} \begin{bmatrix} v_x^{\gamma} \\ v_y^{\gamma} \\ v_z^{\gamma} \end{bmatrix} \\ \Rightarrow \quad \begin{bmatrix} v_x^{\beta} \\ v_y^{\beta} \\ v_z^{\beta} \end{bmatrix} &= \begin{bmatrix} v_x^{\gamma}\,\cos\beta_{at} - v_z^{\gamma}\,\sin\beta_{at} \\ v_y^{\gamma} \\ v_x^{\gamma}\,\sin\beta_{at} + v_z^{\gamma}\,\cos\beta_{at} \end{bmatrix} . \end{aligned} \tag{5.19}$$

This results in a representation in the second intermediate frame, which we denote β. Finally, the roll step will transform the y and z components, by performing a rotation about the "even newer" x-axis through the roll angle α_{at}. This produces a vector resolved about the axes of the a-frame, which was the overall goal:

$$\begin{aligned} \mathbf{v}^{a} = \mathbf{R}_x\left(\alpha_{at}\right)\mathbf{v}^{\beta} &= \begin{bmatrix} 1 & 0 & 0 \\ 0 & \cos\alpha_{at} & \sin\alpha_{at} \\ 0 & -\sin\alpha_{at} & \cos\alpha_{at} \end{bmatrix} \begin{bmatrix} v_x^{\beta} \\ v_y^{\beta} \\ v_z^{\beta} \end{bmatrix} \\ \Rightarrow \quad \begin{bmatrix} v_x^{a} \\ v_y^{a} \\ v_z^{a} \end{bmatrix} &= \begin{bmatrix} v_x^{\beta} \\ v_y^{\beta}\,\cos\alpha_{at} + v_z^{\beta}\,\sin\alpha_{at} \\ -v_y^{\beta}\,\sin\alpha_{at} + v_z^{\beta}\,\cos\alpha_{at} \end{bmatrix} . \end{aligned} \tag{5.20}$$

In summary, we have performed the sequence of rotations

$$\boxed{\mathbf{v}^{a} = \mathbf{R}_x\left(\alpha_{at}\right)\ \mathbf{R}_y\left(\beta_{at}\right)\ \mathbf{R}_z\left(\gamma_{at}\right)\ \mathbf{v}^{t}\ ,} \tag{5.21}$$

transforming a vector $\mathbf{v}^t$, from a representation in the t-frame, to a representation in the a-frame. In order to reverse the transformation, one needs to reverse the sequence and change the sign of the Euler angles. This follows from both geometrical considerations, but also from the fact that each individual rotation is orthogonal, such that

$$\begin{aligned} \left(\mathbf{R}_x\left(\alpha_{at}\right)\ \mathbf{R}_y\left(\beta_{at}\right)\ \mathbf{R}_z\left(\gamma_{at}\right)\right)^{-1} &= \left(\mathbf{R}_x\left(\alpha_{at}\right)\ \mathbf{R}_y\left(\beta_{at}\right)\ \mathbf{R}_z\left(\gamma_{at}\right)\right)^{\top} \\ &= \mathbf{R}_z\left(\gamma_{at}\right)^{\top}\ \mathbf{R}_y\left(\beta_{at}\right)^{\top}\ \mathbf{R}_x\left(\alpha_{at}\right)^{\top} \\ &= \mathbf{R}_z\left(-\gamma_{at}\right)\ \mathbf{R}_y\left(-\beta_{at}\right)\ \mathbf{R}_x\left(-\alpha_{at}\right) \\ &= \mathbf{R}_z\left(\gamma_{ta}\right)\ \mathbf{R}_y\left(\beta_{ta}\right)\ \mathbf{R}_x\left(\alpha_{ta}\right)\ . \end{aligned} \tag{5.22}$$

On top of the specific sequence (x, y, z) and the direction in which the angles are positive, there is one final convention that we need to agree upon. Since the Euler rotation $(\alpha_{at} + \pi, \pi - \beta_{at}, \gamma_{at} + \pi)$ results in the same transformation as the Euler rotation $(\alpha_{at}, \beta_{at}, \gamma_{at})$, the pitch rotation is limited to the range $-\pi/2 \leq \beta \leq \pi/2$ $(-90° \leq \beta \leq 90°)$ in order to avoid duplicate sets of Euler angles representing the same attitude [5, Sec. 2.2.1].

This convention leads to a very intuitive interpretation of the attitude, describing the transformation **from the n-frame to the b-frame** of the vehicle. First, the yaw angle, γ_{nb}, represents a rotation about the local vertical. In the aeronautics field, this angle is also referred to as the **heading** or **azimuth** of the vehicle. The second rotation is about the right-pointing axis of the first intermediate frame. This axis will always lie in the horizontal plane, meaning that the pitch angle, β_{nb}, represents the deviation from the horizontal plane and is denoted **elevation**. After the first two rotations, the original north-pointing axis

is now aligned with the nose-direction of the vehicle. The final rotation by the roll angle, α_{nb}, will therefore be about this forward-pointing axis and is denoted the **bank** angle in aeronautics. The bank and elevation are also collectively known as **tilts** [5, Sec. 2.2.1].

To summarize on the notation. When the specific sequence (x, y, z) is used, the Euler angles are referred to as roll, pitch and yaw, respectively. If we are concerned with the attitude describing the relative orientation of the b- and n-frame, with the transformation from the n-frame to the b-frame denoting the positive direction, the roll, pitch and yaw angles may be referred to as bank, elevation and heading of the vehicle. In my experience this convention seems to be well adopted in the field of aeronautics. Even in the commercial software that I have used, i.e. NovAtel's Inertial Explorer, the attitude is presented in this format although a different definition is used for the internal algorithm [9].

5.1.3 Quaternions Introduced

Before discussing how quaternions can be used to rotate vectors in three dimensions, this section is devoted to introducing the concept and some of the properties of quaternions. Quaternions are, in a sense, a number system that extends the complex numbers. It therefore makes sense to briefly recapitulate on complex numbers before introducing quaternions. A complex number, z, is the sum of real and imaginary parts

$$z = x + iy \,, \tag{5.23}$$

where x and y are real numbers and $i^2 = -1$ represents the imaginary unit. Such a complex number has two components and can therefore be written in vector-form as

$$\mathbf{z} = \begin{bmatrix} x \\ y \end{bmatrix} \,, \tag{5.24}$$

where the first entry represents the real component and the second entry the imaginary component of the complex number. This representation naturally leads to the association with a two-dimensional coordinate system, where x represents the projection onto an axis of real numbers and y represents the projection onto an axis of imaginary numbers. An equivalent form of the complex number is

$$z = \rho e^{i\theta} \,, \tag{5.25}$$

where ρ may be interpreted as the magnitude of the vector and θ as the angle that the vector makes with the real axis. The decomposition into its real and imaginary components is easily accomplished using Euler's equation

$$z = \rho e^{i\theta} = \rho \left(\cos\theta + i \sin\theta\right) = \rho\cos\theta + i\rho\sin\theta \quad \Rightarrow \quad \mathbf{z} = \begin{bmatrix} x \\ y \end{bmatrix} = \begin{bmatrix} \rho\cos\theta \\ \rho\sin\theta \end{bmatrix} \,. \tag{5.26}$$

The rotation of such a "complex vector" about the origin can be accomplished through the multiplication with a complex number, $e^{i\phi}$, as

$$w = e^{i\phi} z = e^{i\phi}\rho e^{i\theta} = \rho e^{i(\theta+\phi)} \quad \Rightarrow \quad \mathbf{w} = \begin{bmatrix} \rho\cos\left(\theta+\phi\right) \\ \rho\sin\left(\theta+\phi\right) \end{bmatrix} \,, \tag{5.27}$$

so that the angle with the real axis is now $\theta + \phi$.

Quaternions are complex numbers with two additional "imaginary units", j and k. The quaternion, q, is given by the sum

$$q = a + ib + jc + kd \,, \tag{5.28}$$

where a, b, c and d are real numbers. For quaternions, the imaginary units are subject to the constraints [11, Sec. 5.4]:

$$\begin{array}{lllllllll} i^2 & = & -1 & ij & = & k & ik & = & -j \\ ji & = & -k & j^2 & = & -1 & jk & = & i \\ ki & = & j & kj & = & -i & k^2 & = & -1 \end{array} \tag{5.29}$$

indicating that unlike units are non-commutative. The quaternion has four components and can be written on vector-form as

$$\mathbf{q} = \begin{bmatrix} a \\ b \\ c \\ d \end{bmatrix} \,, \tag{5.30}$$

where the entries represent the components along the real, i, j and k axes, respectively. As with complex numbers, we define a conjugate of q by reversing the sign of all the imaginary units

$$q^* = a - ib - jc - kd \,, \tag{5.31}$$

such that the squared magnitude of q becomes

$$qq^* = q^*q = a^2 + b^2 + c^2 + d^2 \,, \tag{5.32}$$

analogous to complex numbers. In general, the sum and product of two quaternions are again quaternions. However, since the imaginary units are non-commutative, the product of two quaternions are also non-commutative, i.e.

$$q_1 q_2 \neq q_2 q_1 \,. \tag{5.33}$$

The product of two quaternions is known as the **Hamilton product** and can be derived from their properties (5.29). On vector-form, the product may be expressed as

$$\begin{aligned} \mathbf{q}_1 \circ \mathbf{q}_2 &= \begin{bmatrix} a_1 \\ b_1 \\ c_1 \\ d_1 \end{bmatrix} \circ \begin{bmatrix} a_2 \\ b_2 \\ c_2 \\ d_2 \end{bmatrix} = \begin{bmatrix} a_1a_2 - b_1b_2 - c_1c_2 - d_1d_2 \\ a_1b_2 + b_1a_2 + c_1d_2 - d_1c_2 \\ a_1c_2 - b_1d_2 + c_1a_2 + d_1b_2 \\ a_1d_2 + b_1c_2 - c_1b_2 + d_1a_2 \end{bmatrix} \\ &= \begin{bmatrix} a_1 & -b_1 & -c_1 & -d_1 \\ b_1 & a_1 & -d_1 & c_1 \\ c_1 & d_1 & a_1 & -b_1 \\ d_1 & -c_1 & b_1 & a_1 \end{bmatrix} \begin{bmatrix} a_2 \\ b_2 \\ c_2 \\ d_2 \end{bmatrix} \,, \end{aligned} \tag{5.34}$$

which is clearly not similar to the ordinary vector dot-product.

5.1.4 Quaternion Rotations

In three-dimensional space, according to **Euler's rotation theorem**, any sequence of rotations of a rigid body (or reference frame) about a fixed point is equivalent to a single rotation by a given angle, θ, about a fixed axis, called the Euler axis, that runs through the fixed point. This Euler axis is typically represented by a unit vector, $\mathbf{u}$. Therefore, any coordinate transformation in three dimensions can be represented as a combination of a vector, $\mathbf{u}$, and a scalar, θ. This axis-angle representation is what quaternions are particularly good at encoding in terms of four numbers. The corresponding rotation of a vector, $\mathbf{v}$, can be carried out by forming the Hamilton product of the associated quaternions.

Suppose we have an arbitrary vector, $\mathbf{v}^t$, represented in the t-frame, by the set of basis vectors $\left(\mathbf{e}_x^t, \mathbf{e}_y^t, \mathbf{e}_z^t\right)$. We can then represent this vector as a quaternion with no component along the real axis as

$$\mathbf{v}^t = \begin{bmatrix} v_x^t \\ v_y^t \\ v_z^t \end{bmatrix} \quad \mapsto \quad \mathbf{q}^t = \begin{bmatrix} 0 \\ v_x^t \\ v_y^t \\ v_z^t \end{bmatrix} , \tag{5.35}$$

where the quaternion "vector" is denoted by $\mathbf{q}$. The basis vectors are then associated with the imaginary parts of the quaternion as

$$i \mapsto \mathbf{e}_x^t , \quad j \mapsto \mathbf{e}_y^t \quad \text{and} \quad k \mapsto \mathbf{e}_z^t . \tag{5.36}$$

Suppose we want to rotate the quaternion, $\mathbf{q}^t$, about the Euler axis, $\mathbf{u}^t = \left(u_x^t, u_y^t, u_z^t\right)$, by an amount, θ, in the counter-clockwise direction. We start by defining a **rotation quaternion** as

$$\begin{aligned} q_\theta = e^{\frac{\theta}{2}\left(u_x^t i + u_y^t j + u_z^t k\right)} &= \cos\left(\frac{\theta}{2}\right) + \left(u_x^t i + u_y^t j + u_z^t k\right)\sin\left(\frac{\theta}{2}\right) \\ \Rightarrow \quad \mathbf{q}_\theta &= \begin{bmatrix} \cos\left(\theta/2\right) \\ \sin\left(\theta/2\right) u_x^t \\ \sin\left(\theta/2\right) u_y^t \\ \sin\left(\theta/2\right) u_z^t \end{bmatrix} , \end{aligned} \tag{5.37}$$

which will rotate the quaternion $\mathbf{q}^t$, through the angle θ, about the Euler axis as [11, Eq. 5.5]:

$$\mathbf{q}_{\text{rotated}}^t = \mathbf{q}_\theta^* \circ \mathbf{q}^t \circ \mathbf{q}_\theta , \tag{5.38}$$

where $\mathbf{q}_{\text{rotated}}$ denotes the rotated vector, the circle, $\circ$, denotes the Hamilton product and the asterisk, $*$, denotes the complex conjugate, formed as

$$\mathbf{q}_\theta^* = \begin{bmatrix} \cos\left(-\theta/2\right) \\ \sin\left(-\theta/2\right) u_x^t \\ \sin\left(-\theta/2\right) u_y^t \\ \sin\left(-\theta/2\right) u_z^t \end{bmatrix} = \begin{bmatrix} \cos\left(\theta/2\right) \\ -\sin\left(\theta/2\right) u_x^t \\ -\sin\left(\theta/2\right) u_y^t \\ -\sin\left(\theta/2\right) u_z^t \end{bmatrix} . \tag{5.39}$$

Again, our purpose is not to rotate the vector, but to decompose the quantity, $\mathbf{q}^t$, along the axes of another reference frame, a. In order to accomplish this, we need to rotate the

reference frame, rather than $\mathbf{q}^t$ itself. This is essentially accomplished using the reverse rotation [11, Sec. 5.15]:

$$\mathbf{q}^a = \mathbf{q}_\theta \circ \mathbf{q}^t \circ \mathbf{q}_\theta^* \,. \tag{5.40}$$

In order to agree with the conventions mentioned earlier regarding attitude, the rotation angle needs to be positive from the reference frame, a, to the object frame, t. We therefore define the quaternion attitude as

$$\mathbf{q}_t^a = \begin{bmatrix} \cos\left(\alpha_{at}/2\right) \\ \sin\left(\alpha_{at}/2\right) u_x^a \\ \sin\left(\alpha_{at}/2\right) u_y^a \\ \sin\left(\alpha_{at}/2\right) u_z^a \end{bmatrix} \,, \tag{5.41}$$

where, α_{at}, is the rotation angle, positive from the reference frame, a, to the object frame, t. The reference frame transformation is then accomplished as

$$\boxed{\mathbf{q}^a = \mathbf{q}_t^a \circ \mathbf{q}^t \circ \mathbf{q}_a^t \,,} \tag{5.42}$$

where $\mathbf{q}_t^a = \mathbf{q}_a^{t\,*}$ is the complex conjugate. Notice that the vector quantity is represented by the three imaginary parts of the quaternion, while real part will be zero.

When performing successive rotations, we have that

$$\begin{aligned} \mathbf{q}^a &= \mathbf{q}_h^a \circ \mathbf{q}_t^h \circ \mathbf{q}^t \circ \mathbf{q}_t^{h*} \circ \mathbf{q}_h^{a*} \\ &= \left(\mathbf{q}_h^a \circ \mathbf{q}_t^h\right) \circ \mathbf{q}^t \circ \left(\mathbf{q}_h^a \circ \mathbf{q}_t^h\right)^* \\ &= \mathbf{q}_t^a \circ \mathbf{q}^t \circ \mathbf{q}_t^{a*} = \mathbf{q}_t^a \circ \mathbf{q}^t \circ \mathbf{q}_a^t \,, \end{aligned} \tag{5.43}$$

indicating that successive rotations can be combined into a single rotation as

$$\mathbf{q}_t^a = \mathbf{q}_h^a \circ \mathbf{q}_t^h \,, \tag{5.44}$$

noting that the order is critical, since rotations themselves do not commute.

5.1.5 Relations Between Attitude Representations

We have now introduced three attitude representations, which describe the relative orientation of two right-handed orthogonal reference frames. These attitudes are of course only tools capable of describing the same thing in different ways. Eventually, it is up to oneself to determine which representation is most suitable for the application at hand. In this section, the formulas for transforming between the attitude representations will be listed.

Direction Cosines and Euler Angles

The direction cosines matrix, $\mathbf{C}_a^t$, is obtained from the roll, pitch and yaw angles, $(\alpha_{at}, \beta_{at}, \gamma_{at})$, by forming the triple matrix product in (5.21) as

$$
\begin{aligned}
\mathbf{C}_a^t &= \mathbf{R}_x\left(\alpha_{at}\right)\mathbf{R}_y\left(\beta_{at}\right)\mathbf{R}_z\left(\gamma_{at}\right) \\
&= \begin{bmatrix} 1 & 0 & 0 \\ 0 & \cos\alpha_{at} & \sin\alpha_{at} \\ 0 & -\sin\alpha_{at} & \cos\alpha_{at} \end{bmatrix} \begin{bmatrix} \cos\beta_{at} & 0 & -\sin\beta_{at} \\ 0 & 1 & 0 \\ \sin\beta_{at} & 0 & \cos\beta_{at} \end{bmatrix} \begin{bmatrix} \cos\gamma_{at} & \sin\gamma_{at} & 0 \\ -\sin\gamma_{at} & \cos\gamma_{at} & 0 \\ 0 & 0 & 1 \end{bmatrix} \\
&= \begin{bmatrix} \cos\beta_{at}\cos\gamma_{at} & \cos\beta_{at}\sin\gamma_{at} & -\sin\beta_{at} \\ \begin{matrix}-\cos\alpha_{at}\sin\gamma_{at} \\ +\sin\alpha_{at}\sin\beta\cos\gamma_{at}\end{matrix} & \begin{matrix}\cos\alpha_{at}\cos\gamma_{at} \\ +\sin\alpha_{at}\sin\beta_{at}\sin\gamma_{at}\end{matrix} & \sin\alpha_{at}\cos\beta_{at} \\ \begin{matrix}\sin\alpha_{at}\sin\gamma_{at} \\ +\cos\alpha_{at}\sin\beta_{at}\cos\gamma_{at}\end{matrix} & \begin{matrix}-\sin\alpha_{at}\cos\gamma_{at} \\ +\cos\alpha_{at}\sin\beta_{at}\sin\gamma_{at}\end{matrix} & \cos\alpha_{at}\cos\beta_{at} \end{bmatrix}
\end{aligned}
\tag{5.45}
$$

noticing that roll, pitch and yaw is defined as positive from the reference frame, a, to the object frame, t. The reverse conversion is obtained from [5, Eq. 2.23]:

$$
\begin{aligned}
\alpha_{at} &= \arctan_2\left(\mathbf{C}_{a2,3}^t, \mathbf{C}_{a3,3}^t\right) \\
\beta_{at} &= -\arcsin\left(\mathbf{C}_{a1,3}^t\right) \\
\gamma_{at} &= \arctan_2\left(\mathbf{C}_{a1,2}^t, \mathbf{C}_{a1,1}^t\right) \ ,
\end{aligned}
\tag{5.46}
$$

noticing that four-quadrant arctangent functions must be used for the roll and yaw angles. Most often, however, we are performing transformations from the object frame, t, to the reference frame, a. This transformation is easily obtained from the matrix transpose as

$$
\mathbf{C}_t^a = \left(\mathbf{C}_a^t\right)^\top = \begin{bmatrix} \cos\beta_{at}\cos\gamma_{at} & \begin{matrix}-\cos\alpha_{at}\sin\gamma_{at} \\ +\sin\alpha_{at}\sin\beta_{at}\cos\gamma_{at}\end{matrix} & \begin{matrix}\sin\alpha_{at}\sin\gamma_{at} \\ +\cos\alpha_{at}\sin\beta_{at}\cos\gamma_{at}\end{matrix} \\ \cos\beta_{at}\sin\gamma_{at} & \begin{matrix}\cos\alpha_{at}\cos\gamma_{at} \\ +\sin\alpha_{at}\sin\beta_{at}\sin\gamma_{at}\end{matrix} & \begin{matrix}-\sin\alpha_{at}\cos\gamma_{at} \\ +\cos\alpha_{at}\sin\beta_{at}\sin\gamma_{at}\end{matrix} \\ -\sin\beta_{at} & \sin\alpha_{at}\cos\beta_{at} & \cos\alpha_{at}\cos\beta_{at} \end{bmatrix} \ . \tag{5.47}
$$

However, since the roll, pitch and yaw angles are still positive in the direction from the reference frame to the object frame, we have that

$$
\begin{aligned}
\alpha_{at} &= \arctan_2\left(\mathbf{C}_{t3,2}^a, \mathbf{C}_{t3,3}^a\right) \\
\beta_{at} &= -\arcsin\left(\mathbf{C}_{t3,1}^a\right) \\
\gamma_{at} &= \arctan_2\left(\mathbf{C}_{t2,1}^a, \mathbf{C}_{t1,1}^a\right) \ .
\end{aligned}
\tag{5.48}
$$

In situations where the pitch angle, β, approaches 90°, or similarly $\pi/2$ radians, the equations for α and γ become indeterminate, because the numerator and denominator approaches zero simultaneously. This phenomenon is commonly known as gimbal lock and occurs because the x- and z-axis become parallel and a degree of freedom is lost. In this case, the roll and yaw angles can be derived based on alternative elements of the transformation matrix $\mathbf{C}_t^a$ as

$$
\begin{aligned}
\gamma_{at} - \alpha_{at} &= \arctan_2\left(\mathbf{C}_{t2,3}^a - \mathbf{C}_{t1,2}^a, \mathbf{C}_{t1,3}^a + \mathbf{C}_{t2,2}^a\right) \quad \text{for} \quad \beta_{at} \approx \tfrac{\pi}{2} \\
\gamma_{at} + \alpha_{at} &= \arctan_2\left(\mathbf{C}_{t2,3}^a + \mathbf{C}_{t1,2}^a, \mathbf{C}_{t1,3}^a - \mathbf{C}_{t2,2}^a\right) \quad \text{for} \quad \beta_{at} \approx -\tfrac{\pi}{2} \ .
\end{aligned}
\tag{5.49}
$$

Separate solutions for α and γ cannot be obtained under these circumstances, since they represent rotations about the same axis. One practical approach would be to 'freeze' one of

the two angles at its current value, when β approaches the $\pi/2$ region. During iterations the angle that is frozen can be alternated in order to avoid 'jumps' in the values of α and γ [13, Sec. 3.6.5.3].

Direction Cosines and Quaternions

If we carry out the computations in (5.42), we have that

$$\begin{aligned}
\mathbf{q}^a = \mathbf{q}_t^a \circ \mathbf{q}^t \circ \mathbf{q}_a^t &= \begin{bmatrix} a \\ b \\ c \\ d \end{bmatrix} \circ \begin{bmatrix} 0 \\ v_x^t \\ v_y^t \\ v_z^t \end{bmatrix} \circ \begin{bmatrix} a \\ -b \\ -c \\ -d \end{bmatrix} \\
&= \begin{bmatrix} 0 \\ \left(a^2+b^2-c^2-d^2\right) v_x^t + 2\left(bc-ad\right) v_y^t + 2\left(bd+ac\right) v_z^t \\ 2\left(bc+ad\right) v_x^t + \left(a^2-b^2+c^2-d^2\right) v_y^t + 2\left(cd-ab\right) v_z^t \\ 2\left(bd-ac\right) v_x^t + 2\left(cd+ab\right) v_y^t + \left(a^2-b^2-c^2+d^2\right) v_z^t \end{bmatrix} \\
&= \begin{bmatrix} 0 & 0 & 0 & 0 \\ 0 & \left(a^2+b^2-c^2-d^2\right) & 2\left(bc-ad\right) & 2\left(bd+ac\right) \\ 0 & 2\left(bc+ad\right) & \left(a^2-b^2+c^2-d^2\right) & 2\left(cd-ab\right) \\ 0 & 2\left(bd-ac\right) & 2\left(cd+ab\right) & \left(a^2-b^2-c^2+d^2\right) \end{bmatrix} \begin{bmatrix} 0 \\ v_x^t \\ v_y^t \\ v_z^t \end{bmatrix} \\
&= \begin{bmatrix} 0 & \mathbf{0}_{1\times 3} \\ \mathbf{0}_{3\times 1} & \mathbf{C}_t^a \end{bmatrix} \begin{bmatrix} 0 \\ \mathbf{v}^t \end{bmatrix},
\end{aligned} \tag{5.50}$$

indicating that the direction cosine matrix, $\mathbf{C}_a^t$, is obtained from the quaternion components, (a, b, c, d) as

$$\mathbf{C}_a^t = \begin{bmatrix} \left(a^2+b^2-c^2-d^2\right) & 2\left(bc+ad\right) & 2\left(bd-ac\right) \\ 2\left(bc-ad\right) & \left(a^2-b^2+c^2-d^2\right) & 2\left(cd+ab\right) \\ 2\left(bd+ac\right) & 2\left(cd-ab\right) & \left(a^2-b^2-c^2+d^2\right) \end{bmatrix}, \tag{5.51}$$

where a is again the reference frame and t the object frame. The components of the quaternion is obtained using the following relation from [5, Eq. 2.35]:

$$\begin{aligned}
a &= \tfrac{1}{2}\sqrt{1+\mathbf{C}_{a1,1}^t+\mathbf{C}_{a2,2}^t+\mathbf{C}_{a3,3}^t} &&= \tfrac{1}{2}\sqrt{1+\mathbf{C}_{t1,1}^a+\mathbf{C}_{t2,2}^a+\mathbf{C}_{t3,3}^a} \\
b &= \frac{\mathbf{C}_{a2,3}^t-\mathbf{C}_{a3,2}^t}{4a} &&= \frac{\mathbf{C}_{t3,2}^a-\mathbf{C}_{t2,3}^a}{4a} \\
c &= \frac{\mathbf{C}_{a3,1}^t-\mathbf{C}_{a1,3}^t}{4a} &&= \frac{\mathbf{C}_{t1,3}^a-\mathbf{C}_{t3,1}^a}{4a} \\
d &= \frac{\mathbf{C}_{a1,2}^t-\mathbf{C}_{a2,1}^t}{4a} &&= \frac{\mathbf{C}_{t2,1}^a-\mathbf{C}_{t1,2}^a}{4a},
\end{aligned} \tag{5.52}$$

noticing that t is the object frame, while a is the reference frame. Alternatively, where the first quaternion component $a \approx 0$, the components can be computed as

$$\begin{aligned}
a &= \tfrac{1}{2}\sqrt{1+\mathbf{C}^t_{a1,1}-\mathbf{C}^t_{a2,2}-\mathbf{C}^t_{a3,3}} &&= \tfrac{1}{2}\sqrt{1+\mathbf{C}^a_{t1,1}-\mathbf{C}^a_{t2,2}-\mathbf{C}^a_{t3,3}} \\
b &= \frac{\mathbf{C}^t_{a2,3}-\mathbf{C}^t_{a3,2}}{4b} &&= \frac{\mathbf{C}^a_{t3,2}-\mathbf{C}^a_{t2,3}}{4b} \\
c &= \frac{\mathbf{C}^t_{a2,1}-\mathbf{C}^t_{a1,2}}{4b} &&= \frac{\mathbf{C}^a_{t1,2}-\mathbf{C}^a_{t2,1}}{4b} \\
d &= \frac{\mathbf{C}^t_{a3,1}-\mathbf{C}^t_{a1,3}}{4b} &&= \frac{\mathbf{C}^a_{t1,3}-\mathbf{C}^a_{t3,1}}{4b} \ .
\end{aligned} \tag{5.53}$$

Euler Angles and Quaternions

The transformation between quaternions and Euler angles is [5, Eq. 2.37]:

$$\begin{aligned}
\alpha_{at} &= \arctan_2\left\{2\left(ab+cd\right), \left(1-2b^2-2c^2\right)\right\} \\
\beta_{at} &= \arcsin\left\{2\left(ac-bd\right)\right\} \\
\gamma_{at} &= \arctan_2\left\{2\left(ad+bc\right), \left(1-2c^2-2d^2\right)\right\} \ ,
\end{aligned} \tag{5.54}$$

where four-quadrant arctangent functions must be used and [5, Eq. 2.38]:

$$\begin{aligned}
a &= \cos\left(\frac{\alpha_{at}}{2}\right)\cos\left(\frac{\beta_{at}}{2}\right)\cos\left(\frac{\gamma_{at}}{2}\right)+\sin\left(\frac{\alpha_{at}}{2}\right)\sin\left(\frac{\beta_{at}}{2}\right)\sin\left(\frac{\gamma_{at}}{2}\right) \\
b &= \sin\left(\frac{\alpha_{at}}{2}\right)\cos\left(\frac{\beta_{at}}{2}\right)\cos\left(\frac{\gamma_{at}}{2}\right)-\cos\left(\frac{\alpha_{at}}{2}\right)\sin\left(\frac{\beta_{at}}{2}\right)\sin\left(\frac{\gamma_{at}}{2}\right) \\
c &= \cos\left(\frac{\alpha_{at}}{2}\right)\sin\left(\frac{\beta_{at}}{2}\right)\cos\left(\frac{\gamma_{at}}{2}\right)+\sin\left(\frac{\alpha_{at}}{2}\right)\cos\left(\frac{\beta_{at}}{2}\right)\sin\left(\frac{\gamma_{at}}{2}\right) \\
d &= \cos\left(\frac{\alpha_{at}}{2}\right)\cos\left(\frac{\beta_{at}}{2}\right)\sin\left(\frac{\gamma_{at}}{2}\right)-\sin\left(\frac{\alpha_{at}}{2}\right)\sin\left(\frac{\beta_{at}}{2}\right)\cos\left(\frac{\gamma_{at}}{2}\right) \ .
\end{aligned} \tag{5.55}$$

5.2 Inertial Navigation

An inertial navigation system (INS) contains a triad of orthogonal accelerometers measuring the specific force, $\mathbf{f}^s_{is}$, of the sensor (s-frame) with respect to inertial space (i-frame). In relation to (4.3), these observations are corrected for gravity and double-integrated in order to yield position. The INS also contains an orthogonal triad of three gyroscopes, measuring angular rates, $\boldsymbol{\omega}^i_{is}$, which are integrated once in order to yield the orientation of the sensed specific force vector. The INS therefore measures the following two quantities:

Accelerometers:	$\mathbf{f}^s \equiv \mathbf{f}^s_{is}$	(specific force)
Gyroscopes:	$\boldsymbol{\omega}^s_{is}$	(angular rates)

both decomposed in terms of the internal sensor frame (s-frame). It should be stressed out that the **observations are made with respect to inertial space**, which is also why the sensors are called inertial sensors and the cluster forms an Inertial Measurement Unit (IMU). The basic concept behind the INS is that:

- Gyroscopes sense the rotational motion, making it possible to determine the orientation of the vehicle, and

- Accelerometers sense the translational motion, making it possible to determine the velocity and position of the vehicle.

Inertial navigation is therefore an example of a **dead reckoning** system, meaning that initial values of attitude, velocity and position are required to initialise the system and that incremental values are added as observations become available. In practice, the observations form some components in a system of coupled differential equations. For each available observation this set of equations is formed and solved for attitude, velocity and position. These equations are derived in Appendix C.1 and will be briefly presented here.

5.2.1 The Inertial Reference Frame

In Appendix C.1, it is shown how the second order differential equation (4.3) can be split into two first order differential equations and a third equation is added governing the attitude. This leads to the set of first order differential equations that are needed in order to perform inertial navigation in the **inertial reference frame** (C.10):

$$\boxed{\begin{aligned} \dot{\mathbf{r}}^i &= \mathbf{v}^i \\ \dot{\mathbf{v}}^i &= \mathbf{C}_s^i \, \mathbf{f}^s + \bar{\mathbf{g}}^i \\ \dot{\mathbf{C}}_s^i &= \mathbf{C}_s^i \, \mathbf{\Omega}_{is}^s \ , \end{aligned}} \tag{5.56}$$

where $\mathbf{f}^s$ are the specific force observations and $\mathbf{\Omega}_{is}^s$ is a skew-symmetric matrix (A.8):

$$\mathbf{\Omega}_{is}^s = [\boldsymbol{\omega}_{is}^s \times] = \begin{bmatrix} 0 & -\omega_z & \omega_y \\ \omega_z & 0 & -\omega_x \\ -\omega_y & \omega_x & 0 \end{bmatrix} \ , \tag{5.57}$$

formed using the observed angular rates, $\boldsymbol{\omega}_{is}^s = (\omega_x, \omega_y, \omega_z)$. It should be noted that $\mathbf{r}^i$ and $\mathbf{v}^i$ are vectors, while $\mathbf{C}_s^i$ is a matrix, meaning that the above system actually represents 15 first order differential equations. It should also be clear that the equations are coupled and therefore not independent of one another.

5.2.2 The Terrestrial Reference Frame

The equivalent set of coupled first order differential equations in the **terrestrial reference frame** is (C.11):

$$\boxed{\begin{aligned} \dot{\mathbf{r}}^e &= \mathbf{v}^e \\ \dot{\mathbf{v}}^e &= \mathbf{C}_s^e \, \mathbf{f}^s - 2\mathbf{\Omega}_{ie}^e \, \mathbf{v}^e + \mathbf{g}^e \\ \dot{\mathbf{C}}_s^e &= \mathbf{C}_s^e \, \mathbf{\Omega}_{es}^s \ , \end{aligned}} \tag{5.58}$$

where $\mathbf{g}^e$ is now the gravity vector (in contrast to gravitation). These equations take into account that our reference frame, i.e. the e-frame, is rotating with respect to the i-frame. If we imagine standing at a fixed position on the surface of the Earth, our position in the e-frame, $\mathbf{r}^e$, will remain constant. However, since the sensors measure with respect to inertial space, they will measure the effect of the Earth rotating. Basically, in order to make the observations "become zero", we need to compensate for this effect by adding fictitious forces

to the equations. The angular rates, $\boldsymbol{\omega}_{is}^{s}$, are therefore corrected for the component of Earth rotation as

$$\boldsymbol{\omega}_{es}^{s} = \boldsymbol{\omega}_{is}^{s} - \mathbf{C}_{e}^{s}\,\boldsymbol{\omega}_{ie}^{e}\ , \tag{5.59}$$

and the specific force, $\mathbf{f}^{e}$, is corrected for a centrifugal force, $\boldsymbol{\Omega}_{ie}^{e}\ \boldsymbol{\Omega}_{ie}^{e}\ \mathbf{r}^{e}$, (which has been consumed by the gravity term) and a Coriolis force, $2\boldsymbol{\Omega}_{ie}^{e}\,\mathbf{v}^{e}$, which is velocity dependent.

5.2.3 The Navigation Frame

In the **navigation frame**, the origin of the reference frame is fixed to the moving vehicle, meaning that the position remains constant. Instead, the Earth-referenced position, $\mathbf{r}^{e}$, is used and the velocity, $\mathbf{v}^{e}$, is simply resolved about the axes of the n-frame as

$$\mathbf{v}^{n} \equiv \mathbf{C}_{e}^{n}\,\mathbf{v}^{e}\ . \tag{5.60}$$

This leads to the coupled set of first order differential equations from (C.18):

$$\boxed{\begin{aligned}\dot{\mathbf{r}}^{e} &= \mathbf{C}_{n}^{e}\mathbf{v}^{n}\\ \dot{\mathbf{v}}^{n} &= \mathbf{C}_{s}^{n}\,\mathbf{f}^{s} - (2\boldsymbol{\Omega}_{ie}^{n} + \boldsymbol{\Omega}_{en}^{n})\,\mathbf{v}^{n} + \mathbf{g}^{n}\\ \dot{\mathbf{C}}_{s}^{n} &= \mathbf{C}_{s}^{n}\,\boldsymbol{\Omega}_{ns}^{s}\ ,\end{aligned}} \tag{5.61}$$

where an additional fictitious term, $\boldsymbol{\Omega}_{en}^{n}\,\mathbf{v}^{n}$, known as the **transport-rate term**, has appeared. This term originates from the rotational motion that is required to keep the axes of the vehicle aligned with the north, east and down axes of the n-frame as one moves across the surface of the Earth. This rotation also needs to be compensated for in the angular rates as

$$\boldsymbol{\omega}_{ns}^{s} = \boldsymbol{\omega}_{ne}^{s} + \boldsymbol{\omega}_{ei}^{s} + \boldsymbol{\omega}_{is}^{s} = \boldsymbol{\omega}_{is}^{s} - \mathbf{C}_{n}^{s}\,(\boldsymbol{\omega}_{en}^{n} + \mathbf{C}_{e}^{n}\,\boldsymbol{\omega}_{ie}^{e})\ . \tag{5.62}$$

Alternatively, one might want to express the position in terms of geodetic coordinates

$$\mathbf{p} = \begin{bmatrix}\phi & \lambda & h\end{bmatrix}^{\top}\ , \tag{5.63}$$

which is accomplished by replacing, $\dot{\mathbf{r}}^{e} = \mathbf{C}_{n}^{e}\mathbf{v}^{n}$, in (5.61) by (C.26):

$$\dot{\mathbf{p}} = \begin{bmatrix}\dot{\phi}\\ \dot{\lambda}\\ \dot{h}\end{bmatrix} = \begin{bmatrix} v_N/\,(R_N + h)\\ v_E/\,(R_E + h)\cos\phi\\ -v_D\end{bmatrix}\ . \tag{5.64}$$

5.2.4 Navigation Frame and Strapdown Configuration

The mechanisation will naturally affect how the navigation equations should be implemented. This dissertation will only consider a **strapdown mechanisation**, meaning that inertial observations are obtained directly in the body frame of the vehicle or are simply transformed to this frame. The navigation equations have been implemented in the **navigation frame**. Therefore, setting $s = b$ in (5.61), we obtain the system

$$\dot{\phi} = v_N / (R_N + h) \tag{5.65a}$$
$$\dot{\lambda} = v_E / (R_E + h) \cos\phi \tag{5.65b}$$
$$\dot{h} = -v_D \tag{5.65c}$$
$$\dot{\mathbf{v}}^n = \mathbf{C}_b^n \, \mathbf{f}^b - (2\boldsymbol{\Omega}_{ie}^n + \boldsymbol{\Omega}_{en}^n) \, \mathbf{v}^n + \mathbf{g}^n \tag{5.65d}$$
$$\dot{\mathbf{C}}_b^n = \mathbf{C}_b^n \, \boldsymbol{\Omega}_{nb}^b \, , \tag{5.65e}$$

where the geodetic coordinates are utilized and

$$\boldsymbol{\omega}_{nb}^b = \boldsymbol{\omega}_{ne}^b + \boldsymbol{\omega}_{ei}^b + \boldsymbol{\omega}_{ib}^b = \boldsymbol{\omega}_{ib}^b - \mathbf{C}_n^b \, (\boldsymbol{\omega}_{en}^n + \mathbf{C}_e^n \, \boldsymbol{\omega}_{ie}^e) = \begin{bmatrix} \omega_x \\ \omega_y \\ \omega_z \end{bmatrix} \, . \tag{5.66}$$

The practical implementation of these equations can be done more or less accurately depending on the desired complexity, precision and computational power. Different solution strategies and some examples are given in Appendix C.2.

5.2.5 Choosing an Attitude Representation

The above navigation equations use a DCM attitude representation, but as discussed in Section 5.1, quaternion attitude or Euler angles can also be used. The differential equation governing the DCM is (5.65e). The corresponding differential equation governing the quaternion attitude is (C.44):

$$\dot{\mathbf{q}}_b^n = \tfrac{1}{2} \, \mathbf{A}^b \, \mathbf{q}_b^n \quad \text{with} \quad \mathbf{A}^b = \begin{bmatrix} 0 & -\omega_{nb,x}^b & -\omega_{nb,y}^b & -\omega_{nb,z}^b \\ \omega_{nb,x}^b & 0 & \omega_{nb,z}^b & -\omega_{nb,y}^b \\ \omega_{nb,y}^b & -\omega_{nb,z}^b & 0 & \omega_{nb,x}^b \\ \omega_{nb,z}^b & \omega_{nb,y}^b & -\omega_{nb,x}^b & 0 \end{bmatrix} \, , \tag{5.67}$$

and for the triplet of Euler angles (A.33):

$$\begin{bmatrix} \dot{\alpha} \\ \dot{\beta} \\ \dot{\gamma} \end{bmatrix} = \begin{bmatrix} 1 & \sin\alpha \tan\beta & \cos\alpha \tan\beta \\ 0 & \cos\alpha & -\sin\alpha \\ 0 & \sin\alpha \sec\beta & \cos\alpha \sec\beta \end{bmatrix} \boldsymbol{\omega}_{nb}^b \, , \tag{5.68}$$

where α, β and γ represent the bank, elevation and heading angles, respectively. One issue with the Euler approach is that a singularity occurs as the elevation angle approaches $\pm 90°$. The singularity is represented by the components

$$\tan\beta = \frac{\sin\beta}{\cos\beta} \quad \text{and} \quad \sec\beta = \frac{1}{\cos\beta} \, , \tag{5.69}$$

that are undefined when the denominator becomes zero. This phenomenon is known as **gimbal lock** and more intuitively reflects that, when the vehicle is pointing straight up (or down), the heading and bank correspond to the same motion and a degree of freedom is lost. More importantly, however, the Euler angles cannot be used directly as a transformation operator. First, a transformation operator must be formed, which introduces additional computational load. For these reasons, the Euler attitude is usually not used in the implementation.

As outlined in Appendix C.2, the attitude is involved in two processes. One is that the attitude must be updated at each iteration, which can be expressed as

$$\begin{aligned} \mathbf{C}(+) &= \mathbf{C}(-)\,\mathbf{C}(+,-) && \text{for direction cosines, and} \\ \mathbf{q}(+) &= \mathbf{q}(-) \circ \mathbf{q}(+,-) && \text{for quaternions,} \end{aligned}$$

where $\mathbf{C}(+,-)$ and $\mathbf{q}(+,-)$ are "transition operators". The other process is the transformation of the specific force into the n-frame. This is accomplished as

$$\begin{aligned} \mathbf{f}^n &= \mathbf{C}_b^n\,\mathbf{f}^b && \text{for direction cosines, and} \\ \mathbf{q}^n &= \mathbf{q}_b^n \circ \mathbf{q}^b \circ \mathbf{q}_n^b && \text{for quaternions,} \end{aligned}$$

where one is a simple matrix-vector product, while the other is a double Hamilton product. In Table 5.1 these two operations are broken down into numbers of multiplications and additions/subtractions, in order to compare the performance of the two methods.

STORAGE	**DCM**	vs	**Quaternion**
Number of parameters	9		4
ATTITUDE UPDATE	$\mathbf{C}\,\mathbf{C}$	vs	$\mathbf{q} \circ \mathbf{q}$
Scalar multiplications	27		16
Additions/subtractions	24		12
Total number of operations	**51**		**28**
FRAME TRANSFORMATION	$\mathbf{C}\,\mathbf{v}$	vs	$\mathbf{q}^* \circ \mathbf{v} \circ \mathbf{q}$
Scalar multiplications	9		24*
Additions/subtractions	6		17*
Total number of operations	**15**		**41**

Table 5.1: Performance comparison of rotation vector and pure quaternion methods. *In general (5.42) encompasses 32 multiplications and 24 additions/subtractions. This reduces to 24 multiplications and 17 additions/subtractions, if we take into account that some elements are destined to be zero.

Although [5] recommends the use of direction cosine matrices, there seems to be a general tendency that quaternions is the preferred tool. Basically, both methods can be applied in order to arrive at the same level of accuracy. The transformation matrix is more intuitive to use, while the quaternion representation is more compact, since it contains only four components, compared to the nine components of the matrix representation. From the table, it is not straightforward to determine which method is computationally most efficient. The quaternion approach seems to be most effective in terms of storage and attitude update, while the direction cosines approach is most effective in the reference frame transformation.

6 The Inertial Measurement Unit and Related Errors

The output from inertial sensors will be subject to errors. Fundamentally, sensor errors consist of both systematic and random components. The random component will have no correlation with previous observations and can therefore not be accounted for by calibration. The systematic component can be accounted for, at least theoretically, through laboratory calibration and/or integration with other sensors. Since errors will eventually propagate onto the navigation solution and gravity estimates, it is important to understand the error sources and their effects, in order to improve the results.

This section is divided into three subsections. The first subsection is concerned with sensor errors and will introduce the various components along with their effect on the sensor output. The second subsection will introduce the IMU unit used for this dissertation and describe the calibration that has been applied. The third subsection will define the navigation and gravity errors and present a set of error dynamics equations. This set of equations can be used to study the propagation of errors in order to achieve an understanding of their effects and evolution. The error dynamics equations will moreover be of fundamental importance in developing an integrated INS/GNSS navigation system in Section 9.

6.1 Sensor Error Characteristics

The output from accelerometers and gyroscopes are typically corrupted by errors in the form of bias, scale factor, cross-coupling errors and some random noise. Letting $\mathbf{f}^s$ and $\boldsymbol{\omega}_{is}^s$ denote the "true" specific force or angular rate, which is input to the sensor, the error is

$$\delta\mathbf{f}^s = \tilde{\mathbf{f}}^s - \mathbf{f}^s \qquad \text{and} \qquad \delta\boldsymbol{\omega}_{is}^s = \tilde{\boldsymbol{\omega}}_{is}^s - \boldsymbol{\omega}_{is}^s \,, \tag{6.1}$$

where $\tilde{\mathbf{f}}^s$ and $\tilde{\boldsymbol{\omega}}_{is}^s$ denote the output. The quality of an inertial sensor can be categorised based on bias errors as shown in Table 6.1. It should be noted that no universally-agreed-upon definition exists.

IMU GRADE	ACCELEROMETER BIAS		GYRO BIAS	
	mg	m/s^2	$^\circ$/h	rad/s
Consumer	>3	>0.03	>100	$> 5 \cdot 10^{-4}$
Tactical	1-10	0.01-0.1	1-100	$5 \cdot 10^{-6} - 5 \cdot 10^{-4}$
Intermediate	0.1-1	$10^{-3} - 10^{-2}$	0.1	$5 \cdot 10^{-7}$
Navigation (Aviation)	0.03-0.1	$3 \cdot 10^{-4} - 10^{-3}$	0.01	$5 \cdot 10^{-8}$
Marine	0.01	10^{-4}	0.001	$5 \cdot 10^{-9}$

Table 6.1: Typical accelerometer and gyro bias for different grades of IMU from [5, Table 4.1]

It is important to distinguish between systematic and random errors. The systematic error sources can be divided into four categories [5, Sec. 4.4]:

- A **fixed contribution**, which is always present when the unit is turned on. This contribution is always the same and is usually accounted for by laboratory calibrations.

- A **temperature dependent variation**, which is seen as a variation with temperature. This is typically also handled through laboratory calibrations and will have the strongest effect while the sensors are warming up. However, the temperature of each individual sensor does not necessarily correspond to the temperature measured by the IMU temperature sensor. Moreover, temperature variations might inflect distortions to the physical configuration itself, making it complicated to fully account for this effect.
- A **run-to-run variation**, which is different each time the sensor is turned on, but remains constant until powered off. This contribution cannot be accounted for by laboratory calibrations, but must be handled through alignment and/or integration with other sensors.
- An **in-run variation**, which varies with time when the unit is turned on. This contribution can not be accounted for by laboratory calibrations and also not by alignment. In theory, it can be accounted for by integration with other sensors, but this may be difficult in practice.

Systematic errors can therefore, at least theoretically, be accounted for either through laboratory calibrations or through integration with other sensors. Random errors on the other hand are not correlated with previous observations and must instead be accounted for using stochastic tools. In the following, each of the four kinds of errors will be briefly introduced and its input-output relation will be defined mathematically.

Bias

The bias is independent of the true specific force or angular rate input to the sensor. The accelerometer and gyro biases can be denoted as vectors

$$\mathbf{b}_a = \begin{bmatrix} b_{a,x} & b_{a,y} & b_{a,z} \end{bmatrix}^\top \qquad \text{and} \qquad \mathbf{b}_g = \begin{bmatrix} b_{g,x} & b_{g,y} & b_{g,z} \end{bmatrix}^\top , \tag{6.2}$$

such that the sensor output, $\tilde{\mathbf{f}}^s$ or $\tilde{\boldsymbol{\omega}}_{is}^s$, is related to the sensor input, $\mathbf{f}^s$ or $\boldsymbol{\omega}_{is}^s$, as

$$\tilde{\mathbf{f}}^s = \mathbf{b}_a + \mathbf{f}^s \qquad \text{and} \qquad \tilde{\boldsymbol{\omega}}_{is}^s = \mathbf{b}_g + \boldsymbol{\omega}_{is}^s \, . \tag{6.3}$$

The bias is often divided into static and dynamic components. The static components represent the run-to-run variation along with any residual fixed contributions and is constant during the operating time. The dynamic component represents the in-run variation along with any residual temperature dependent variation. Typically, sensor biases represent the dominant term in the overall error budget.

Scale Factor

The scale factor is proportional to the sensor input, such that

$$\tilde{\mathbf{f}}^s = \mathbf{b}_a + \mathbf{M}_a \, \mathbf{f}^{s\top} \qquad \text{and} \qquad \tilde{\boldsymbol{\omega}}_{is}^s = \mathbf{b}_g + \mathbf{M}_g \, \boldsymbol{\omega}_{is}^{s\top} , \tag{6.4}$$

where

$$\mathbf{M}_a = \begin{bmatrix} s_{a,x} & 0 & 0 \\ 0 & s_{a,y} & 0 \\ 0 & 0 & s_{a,z} \end{bmatrix} \qquad \text{and} \qquad \mathbf{M}_g = \begin{bmatrix} s_{g,x} & 0 & 0 \\ 0 & s_{g,y} & 0 \\ 0 & 0 & s_{g,z} \end{bmatrix} , \tag{6.5}$$

are vectors representing the scale factor for each inertial sensor.

Cross-Coupling

The main reason for cross-coupling errors are misalignment of the sensitive axes of the sensors with respect to being orthogonal. For this reason, cross-coupling errors are sometimes referred to as misalignment errors. It is practically impossible to achieve perfect orthogonality of the sensors. Although such misalignment may be handled through laboratory calibrations, physical forces or temperature variations may cause distortion of the physical configuration. Typically, cross-coupling errors are expressed together with scale factor errors as

$$\mathbf{M}_a = \begin{bmatrix} s_{a,x} & m_{a,xy} & m_{a,xz} \\ m_{a,yx} & s_{a,y} & m_{a,yz} \\ m_{a,zx} & m_{a,zy} & s_{a,z} \end{bmatrix} \qquad \text{and} \qquad \mathbf{M}_g = \begin{bmatrix} s_{g,x} & m_{g,xy} & m_{g,xz} \\ m_{g,yx} & s_{g,y} & m_{g,yz} \\ m_{g,zx} & m_{g,zy} & s_{g,z} \end{bmatrix} , \tag{6.6}$$

where for example $m_{a,xy}$ denotes the cross-coupling of the y-axis sensed by the x-axis accelerometer. This means that these matrices are not symmetric. Both scale factor and cross-coupling errors are unitless and typically expressed in parts per million (ppm).

Random Noise

Random noise originates from a number of sources such as electronics and quantisation of measurements. Due to its random nature, there is no correlation between past and future values, making it impossible to compensate for these errors through calibrations. The random noise on each sensor sample can be denoted by a vector

$$\mathbf{w}_a = \begin{bmatrix} w_{a,x} & w_{a,y} & w_{a,z} \end{bmatrix}^\top \qquad \text{and} \qquad \mathbf{w}_g = \begin{bmatrix} w_{g,x} & w_{g,y} & w_{g,z} \end{bmatrix}^\top , \tag{6.7}$$

such that the sensor output is related to the input as

$$\tilde{\mathbf{f}}^s = \mathbf{b}_a + \mathbf{M}_a \, \mathbf{f}^s + \mathbf{w}_a \qquad \text{and} \qquad \tilde{\boldsymbol{\omega}}^s_{is} = \mathbf{b}_g + \mathbf{M}_g \, \boldsymbol{\omega}^s_{is} + \mathbf{w}_g \, . \tag{6.8}$$

The spectrum of accelerometer and gyro noise for frequencies below 1 Hz is approximately white and the sensor noise is typically quoted in terms of root power spectral density [5, Sec. 4.4.3]. Accelerometer random noise is therefore in units of $\mu g/\sqrt{\text{Hz}}$ and gyro random noise is in units of $^\circ/\sqrt{\text{hr}}$. For a more comprehensive description of random processes, see Appendix D.

6.1.1 The Inertial Measurement Unit

DTU Space owns an iMAR iNAT-RQH-0001 IMU (iNAT), see Figure 6.1, containing Honeywell QA-2000 accelerometers [8] and GG1320AN ring laser gyroscopes [7]. An excerpt of the manufacturer specifications is presented in Table 6.2. A comparison of bias drift with Table 6.1 indicates that the iNAT is a navigation-grade unit.

Figure 6.1: The iMAR iNAT-RQH-0001 IMU

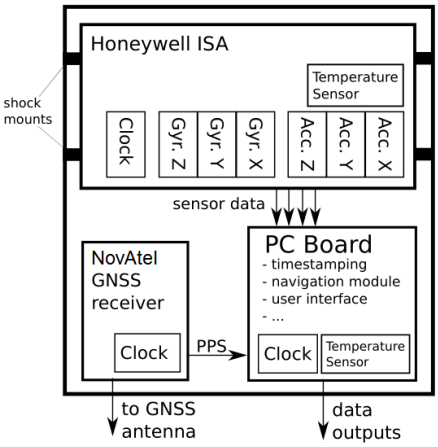

Figure 6.2: iMAR iNAT-RQH-0001 system design. Modified from [1, Fig. 6.2]

SPECIFICATIONS		
Data output rate	$\leq$ 300 Hz (1800 Hz internal)	
Data latency	$<$ 3 ms	
Operating temperatures	-40°C to 71°C	
Weight	$\approx$ 8 kg	
Size	$\approx$ 187 x 128 x 296 mm (310 mm with cables)	
Position accuracy	$<$ 0.2 nmi/hr (0.4 km/hr)	
PERFORMANCE CHARACTERISTICS	Gyroscopes	Accelerometers
Range	$\pm$ 800 °/s	$\pm$ 20 g
Drift (unaided) / offset	$<$ 0.003 °/hr	$<$ 25 μg
Bias instability (const. temp.)	$<$ 0.002 °/hr	$<$ 10 μg
Random walk	$<$ 0.0011 °/$\sqrt{\text{hr}}$	$<$ 8 $\mu g/\sqrt{\text{Hz}}$
Resolution	$<$ 0.001 °/s	$<$ 5 μg
Scale error	$<$ 5 ppm	$<$ 100 ppm
Linearity error	$<$ 5 ppm	$<$ 20 $\mu g/g^2$

Table 6.2: Excerpt of iMAR iNAT-RQH-0001 manufacturer specifications

The basic components of the iNAT unit is an Inertial Sensor Assembly (ISA) manufactured by Honeywell International, a NovAtel GNSS receiver and a PC board. The ISA contains the core elements of the IMU, i.e. the three accelerometers and gyroscopes. The GNSS receiver provides a NMEA data stream and a Pulse-Per-Second (PPS) signal, making it possible to time stamp the observations. The PC board combines the information from the ISA and GNSS receiver, providing time-stamped inertial observations along with temperature. The PC board also includes an internal navigation algorithm making it possible to obtain real-time navigation solutions and an internal memory making it possible to store the

observations and/or navigation solution. Additional sensor calibrations added by iMAR is also applied by the PC board. For a more detailed description of the iNAT unit, the reader is referred to [1, Sec. 6], which is a description of the similar iMAR-RQH-1003 unit (RQH), owned by TU Darmstadt.

6.1.2 Thermal Dependence of Sensor Output

Figure 6.3 shows the time increments between 300 successive IMU observations. From the figure, it is clear that the time stamps have some degree of truncation with a mean value corresponding roughly to the 300 Hz sampling rate of the IMU.

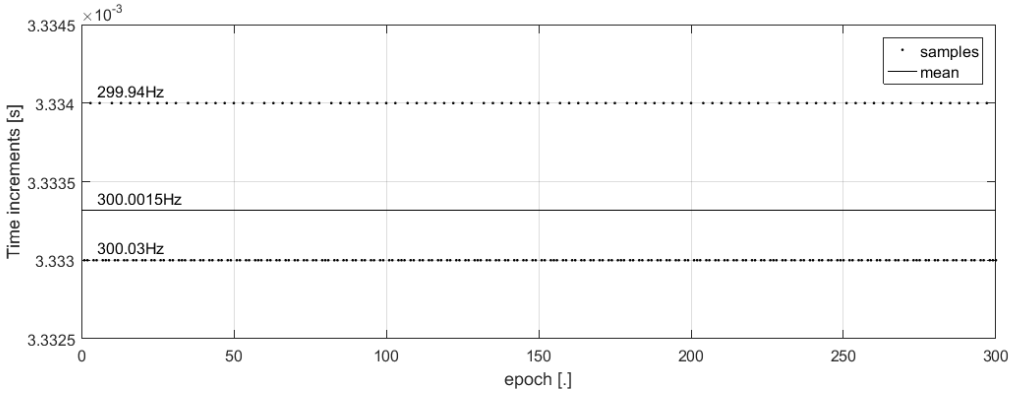

Figure 6.3: Time increments between 300 successive observations

In Figure 6.4, the sampling rate, i.e. inverse of time increments, is shown for an approximately six hour period where the device was sitting statically on a concrete floor. Also shown is the IMU temperature log for the same period, indicating that the internal clock is sensitive to temperature variations. It should be noted that the variation in sampling rate is within the quantisation bounds indicated in Figure 6.3. The time increments were therefore averaged over eight second intervals, before converted to sampling rates.

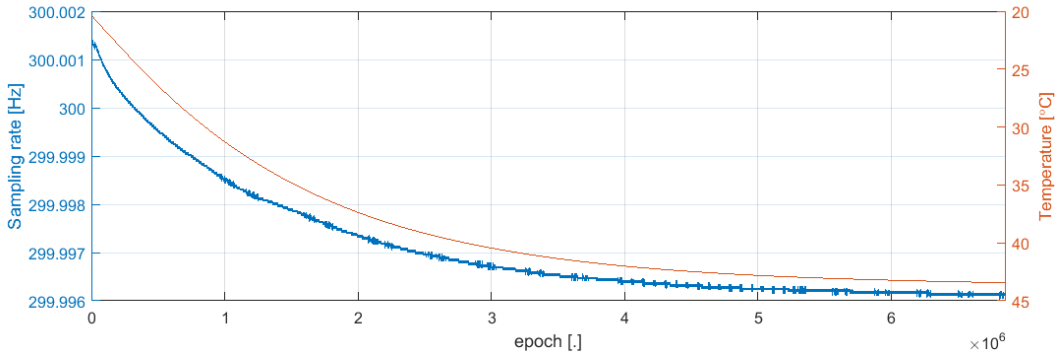

Figure 6.4: IMU sampling rate (averaged over eight seconds) and temperature log

The Honeywell ISA contained within the iNAT unit outputs velocity increments, $\mathbf{f}^s\,\delta t$, and angle increments, $\boldsymbol{\omega}_{is}^s\,\delta t$. These increments are converted to specific force and angular rate by the internal PC board. This conversion is done using a constant value corresponding to 300 Hz and therefore indirectly introduces a temperature dependent scale factor. The clock-induced scale factor can be reversed by dividing accelerations and angular rates by 300 Hz, essentially converting back to velocity and angle increments, and then multiplying by the (smoothed) sampling rate inferred from Figure 6.4.

The accelerometer and gyro observations for the six hour interval are shown in Figure 6.5, both with and without the thermal clock correction. From the figure it is evident that these corrections are small (not visible) for all but the vertical accelerometer. There also seems to be a temperature dependence on all three accelerometers, but the gyroscopes do not show any sign of drift during the logging session.

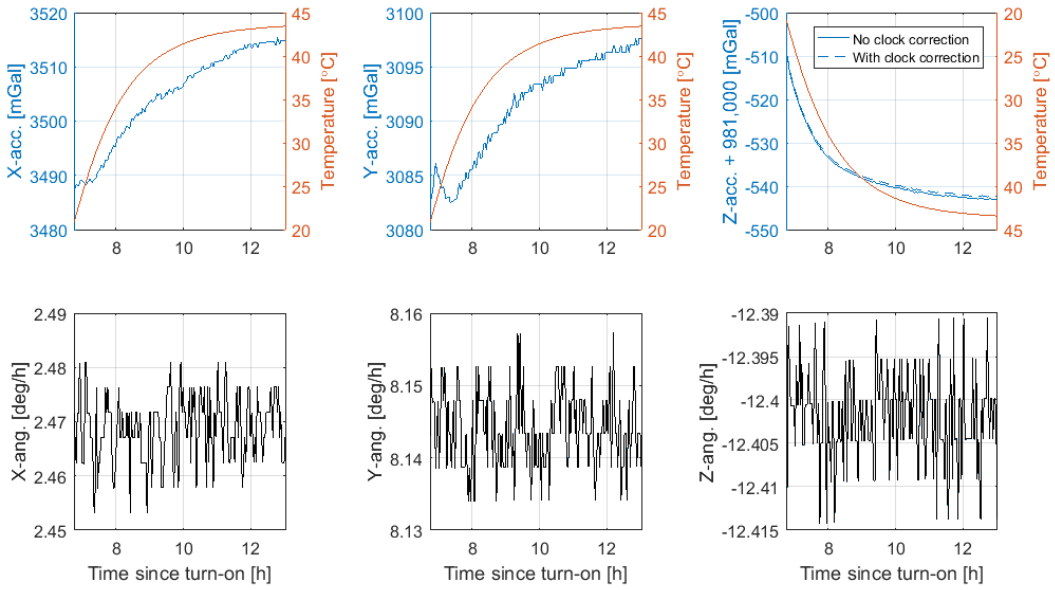

Figure 6.5: IMU observations (averaged over four minutes) and temperature log. Observations are shown both with and without thermal clock correction (only visible for Z-axis accelerations)

In an attempt to compensate for the observed accelerometer drift, a simple thermal calibration will be outlined in the following section. As no drift was observed for the gyroscopes, further calibration was not attempted. It should be noted that some temperature calibration is already applied internally by the manufacturer. The majority of the thermal effects are therefore already accounted for. What is seen in Figure 6.5 are the remaining uncompensated thermal effects.

6.1.3 Thermal Calibration of the Accelerometers

The results presented later in this dissertation, will be subject to the warm-up temperature calibration method presented in [2]. This calibration only affects the accelerometers. The

method assumes that the majority of the observed drift is temperature dependent and purely originates from bias variation. Figure 6.5 indicates that the first assumption may have some validity, whereas the second assumption is less likely. However, this kind of calibration can be performed without access to advanced calibration facilities and is shown to significantly reduce the drift of the gravity estimates. The practical calibration process is outlined here:

1. Place the IMU on a firm platform such as a concrete floor
2. Turn on the device and let it log accelerations and temperature as the internal sensors generate heat and increase the internal temperature
3. Let it log for some time, e.g. over the course of a day, until the temperature saturates. The unit should not be disturbed during this period
4. Turn off the device and let it cool down, e.g. over night
5. Repeat. Do not move the device in between sessions

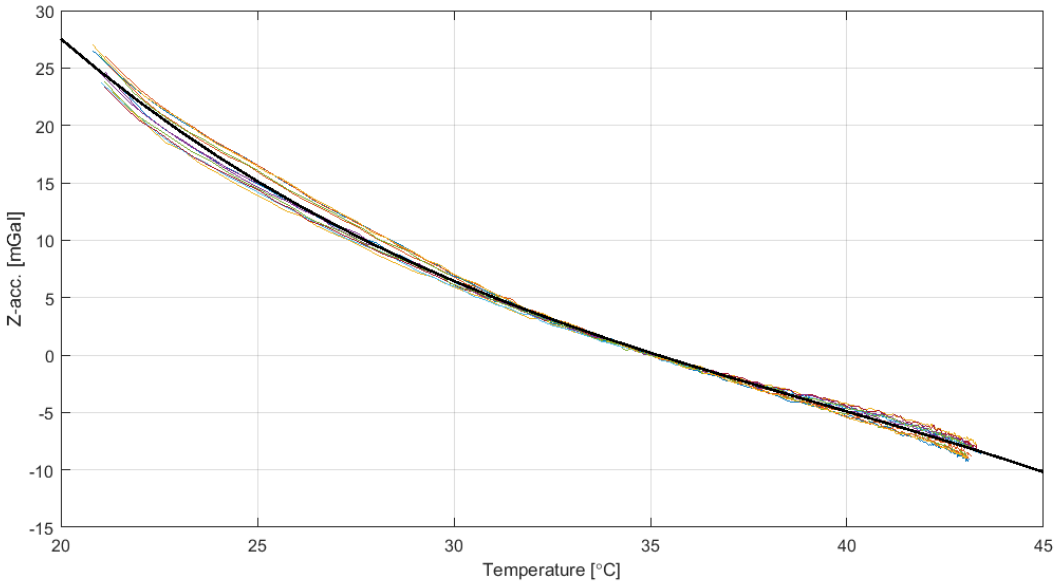

Figure 6.6: Z-axis accelerations (averaged over four minutes) shifted to zero at 35°C and temperature log for the 12 sessions in 2018. Black curve is the best fitting (in a least squares sense) 3rd order polynomial

This calibration process was repeated twice: In 2016, the process consisted of nine sessions, with the unfortunate mistake of moving the device in between some sessions. This meant that some readings did not correlate with the majority and was discarded. Moreover, no clear correlation was found for the horizontal accelerometers. In 2018, the process was repeated with 12 sessions. Figure 6.6 shows the Z-axis accelerometer readings for these 12 sessions, subject to a four-minute averaging window and shifted to zero at 35°C. The repeatability of the 12 curves motivates a calibration curve, which is formed by fitting a third

order polynomial to the twelve curves. For the calibration process, this polynomial is evaluated using the temperature log and used to correct the observed Z-axis acceleration for a temperature-dependent bias using (6.3).

Figure 6.7 illustrates the X- and Y-axis accelerations for the 12 sessions, also showing a repeatable temperature-dependent variation. Similar to the Z-axis, calibrations curves are constructed for the X- and Y-axis using third order polynomials, which are used to correct observations for temperature-dependent bias.

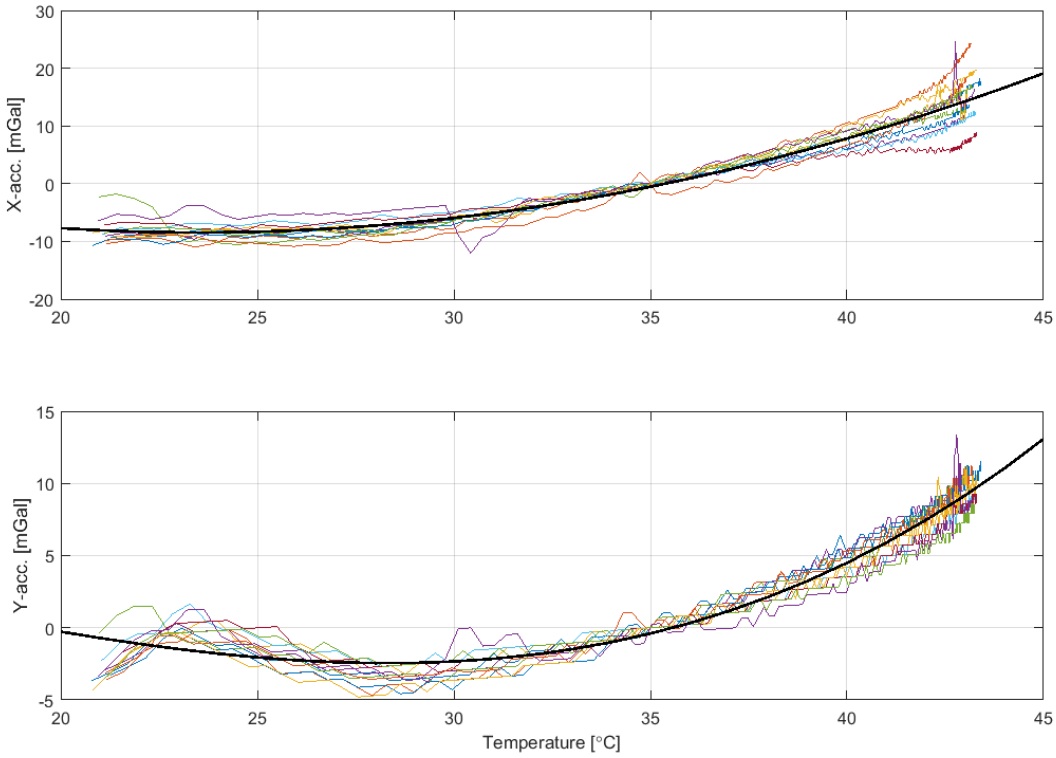

Figure 6.7: X- and Y-axis accelerations (averaged over four minutes) shifted to zero at 35°C and temperature log for the 12 sessions in 2018. Black curve is the best fitting (in a least squares sense) 3rd order polynomial

The effects of these calibration curves will be shown in Section 11. It should be noted that the iNAT unit underwent several hardware replacements and calibrations at the manufacturer during 2017. The 2016 and 2018 calibrations are therefore restricted to data collected before and after 2017, respectively. The 2016 calibration resulted in a calibration curve for the Z-axis accelerometer only, whereas the 2018 calibration resulted in calibration curves for all three accelerometer axes.

6.2 Error Propagation Analysis

When performing inertial navigation as discussed in Appendix C, sensor errors will propagate onto the navigation solution in terms of attitude, velocity and position errors. Additionally, initialisation errors and errors related to the computational procedure will also lead to errors in the navigation solution. The performance of an inertial navigation system is often characterised by its drift in position error with time. In Table 6.3, the definitions from [10] and [5] are listed, noticing again that no universally-agreed-upon definition exists.

[10, Sec. 4.1]	[5, Sec. 4]	Drift rate	Applications
Low Accuracy	Consumer Grade		Pedometers, phones, airbags (not navigation)
	Tactical Grade		Guided weapons, Unmanned Air Vehicles (UAVs)
	Intermediate Grade	10-40 km/hr 5-20 nmi/hr	Small aircraft, helicopters
Medium Accuracy	Navigation Grade (Aviation grade)	1-4 km/hr 0.5-2 nmi/hr	Commercial airliners, military aircraft
High Accuracy	Marine Grade	<1.8 km/day <1 nmi/day	Military ships, submarines, intercontinental missiles, spacecraft

Table 6.3: Overview of INS performance categories from [10] and [5] (nmi=nautical miles)

The evolution and interrelation of errors can be described in terms of a set of error dynamics equations, which are derived in Appendix C.3 and will be introduced later in this section. INS error propagation is also dependent on the dynamics of the host vehicle, since these influence the sensor input. A full account of INS error propagation is therefore very complex and is usually studied using simulation software that mimics the environment and dynamics of the intended application. This section only aims to introduce some basic tools and concepts that are needed later in this dissertation. For a more thorough treatment of the issue, the reader is referred to [3], [12], [10] or [13].

6.2.1 Definition of Error Terms

The error in position and velocity are defined as

$$\begin{aligned} \delta\mathbf{r}^a &= \hat{\mathbf{r}}^a - \mathbf{r}^a \\ \delta\mathbf{v}^a &= \hat{\mathbf{v}}^a - \mathbf{v}^a \\ \delta\phi &= \hat{\phi} - \phi \\ \delta\lambda &= \hat{\lambda} - \lambda \\ \delta h &= \hat{h} - h \ , \end{aligned} \tag{6.9}$$

where $\mathbf{r}^a$, $\mathbf{v}^a$, ϕ, λ and h denote the true values of these parameters and the hat denotes estimates thereof. The superscript, a, denotes an arbitrary frame of reference. For the attitude, the estimated rotation operator, $\hat{\mathbf{C}}_s^a$, is related to the true operator, $\mathbf{C}_s^a$, as

$$\hat{\mathbf{C}}_s^a = \mathbf{B}_a^{\tilde{a}}\,\mathbf{C}_s^a \ , \tag{6.10}$$

where $\mathbf{B}_a^{\hat{a}}$ represents a transformation from the true reference frame to the estimated reference frame. For small angle misalignments, the transformation matrix (5.47) may be approximated using the small-angle approximation[1] as

$$\begin{aligned}\mathbf{B}_a^{\hat{a}} &= \begin{bmatrix} \cos(\delta\beta_{as}^a)\cos(\delta\gamma_{as}^a) & \begin{matrix}-\cos(\delta\alpha_{as}^a)\sin(\delta\gamma_{as}^a)\\ +\sin(\delta\alpha_{as}^a)\sin(\delta\beta_{as}^a)\cos(\delta\gamma_{as}^a)\end{matrix} & \begin{matrix}\sin(\delta\alpha_{as}^a)\sin(\delta\gamma_{as}^a)\\ +\cos(\delta\alpha_{as}^a)\sin(\delta\beta_{as}^a)\cos(\delta\gamma_{as}^a)\end{matrix} \\ \cos(\delta\beta_{as}^a)\sin(\delta\gamma_{as}^a) & \begin{matrix}\cos(\delta\alpha_{as}^a)\cos(\delta\gamma_{as}^a)\\ +\sin(\delta\alpha_{as}^a)\sin(\delta\beta_{as}^a)\sin(\delta\gamma_{as}^a)\end{matrix} & \begin{matrix}-\sin(\delta\alpha_{as}^a)\cos(\delta\gamma_{as}^a)\\ +\cos(\delta\alpha_{as}^a)\sin(\delta\beta_{as}^a)\sin(\delta\gamma_{as}^a)\end{matrix} \\ -\sin(\delta\beta_{as}^a) & \sin(\delta\alpha_{as}^a)\cos(\delta\beta_{as}^a) & \cos(\delta\alpha_{as}^a)\cos(\delta\beta_{as}^a) \end{bmatrix} \\ &\approx \begin{bmatrix} 1 & -\delta\gamma_{as}^a & \delta\beta_{as}^a \\ \delta\gamma_{as}^a & 1 & -\delta\alpha_{as}^a \\ -\delta\beta_{as}^a & \delta\alpha_{as}^a & 1 \end{bmatrix} = \mathbf{I}_3 + [\delta\boldsymbol{\psi}_{as}^a\times] \ , \end{aligned} \tag{6.11}$$

with the skew-symmetric form of the misalignment vector $\delta\boldsymbol{\psi}_{as}^a$

$$[\delta\boldsymbol{\psi}_{as}^a\times] = \begin{bmatrix} 0 & -\delta\gamma_{as}^a & \delta\beta_{as}^a \\ \delta\gamma_{as}^a & 0 & -\delta\alpha_{as}^a \\ -\delta\beta_{as}^a & \delta\alpha_{as}^a & 0 \end{bmatrix} \quad \text{and} \quad \delta\boldsymbol{\psi}_{as}^a = \begin{bmatrix} \delta\alpha_{as}^a \\ \delta\beta_{as}^a \\ \delta\gamma_{as}^a \end{bmatrix} \ . \tag{6.12}$$

The delta (error) angles, $\delta\alpha_{as}^a$, $\delta\beta_{as}^a$ and $\delta\gamma_{as}^a$, are the roll, pitch and yaw angles, respectively, meaning that they are positive from the reference frame, a, to the object frame, s. The error in the attitude representation may then be expressed as

$$\begin{aligned}\delta\mathbf{C}_s^a = \hat{\mathbf{C}}_s^a - \mathbf{C}_s^a &\approx (\mathbf{I}_3 + [\delta\boldsymbol{\psi}_{as}^a\times])\,\mathbf{C}_s^a - \mathbf{C}_s^a \\ &= [\delta\boldsymbol{\psi}_{as}^a\times]\ \mathbf{C}_s^a \ , \end{aligned} \tag{6.13}$$

where it should be noticed that a small error approximation has been applied in order to arrive at this expression.

Additionally, since we are ultimately interested in estimating gravity, it is also useful to define the error in the gravity model as

$$\delta\mathbf{g} = \boldsymbol{\gamma}^a - \mathbf{g}^a \ , \tag{6.14}$$

where $\boldsymbol{\gamma}^a$ refers to the gravity vector derived from the model and $\mathbf{g}^a$ is true gravity. The quantity, $\delta\mathbf{g}$, is also used for the gravity disturbance vector. Although, the two are not generally the same, normal gravity, $\boldsymbol{\gamma}$, is often used for the gravity model in which case they are the same.

6.2.2 Error Dynamics Equations

In order to study the propagation and evolution of errors in the navigation equations, a set of error dynamics equations can be derived. These are derived by applying a small perturbation

[1] The trigonometric approximations $\sin\theta \approx \theta$ and $\cos\theta \approx 1$. Then neglect second-order and higher-order products.

to all terms in the navigation equations and then neglecting all higher-order terms, such that the equations become linear with respect to the error terms

$$(\delta\boldsymbol{\psi}^a_{as}\,,\,\delta\mathbf{v}^a\,,\,\delta\mathbf{r}^a\,,\,\delta\boldsymbol{\omega}^s_{is}\,,\,\delta\mathbf{f}^s\,,\,\delta\mathbf{g}^a)\ ,$$

introduced earlier in this section. The underlying assumption is therefore that all errors are small, such that the linear model is a reasonable approximation. In this way, the "smallness" of the errors reflects the validity and accuracy of the error dynamics model. The error dynamics equations for each set of navigation equations are derived in Appendix C.3. The error dynamics equations for the n-frame are from (C.134):

$$\delta\dot{\mathbf{x}}^n = \mathbf{F}^n\,\delta\mathbf{x}^n\ , \tag{6.15}$$

where the error state vector, $\delta\mathbf{x}^n$, represents the error terms

$$\delta\mathbf{x}^n = \begin{bmatrix}\delta\boldsymbol{\psi}^n_{ns} & \delta\mathbf{v}^n & \delta\mathbf{p} & \delta\mathbf{f}^s & \delta\boldsymbol{\omega}^s_{is} & \delta\mathbf{g}^n\end{bmatrix}^\top \tag{6.16}$$

and

$$\mathbf{F}^n = \left[\begin{array}{ccc|ccc} -\boldsymbol{\Omega}^n_{in} & \mathbf{F}^n_{12} & \mathbf{F}^n_{13} & \mathbf{0}_3 & \mathbf{C}^n_s & \mathbf{0}_3 \\ -[\mathbf{f}^n\times] & \mathbf{F}^n_{22} & \mathbf{F}^n_{23} & \mathbf{C}^n_s & \mathbf{0}_3 & \mathbf{I}_3 \\ \mathbf{0}_3 & \mathbf{F}^n_{32} & \mathbf{F}^n_{33} & \mathbf{0}_3 & \mathbf{0}_3 & \mathbf{0}_3 \\ \hline \mathbf{0}_3 & \mathbf{0}_3 & \mathbf{0}_3 & \mathbf{0}_3 & \mathbf{0}_3 & \mathbf{0}_3 \\ \mathbf{0}_3 & \mathbf{0}_3 & \mathbf{0}_3 & \mathbf{0}_3 & \mathbf{0}_3 & \mathbf{0}_3 \\ \mathbf{0}_3 & \mathbf{0}_3 & \mathbf{0}_3 & \mathbf{0}_3 & \mathbf{0}_3 & \mathbf{0}_3 \end{array}\right]\ , \tag{6.17}$$

is the system matrix. Notice again that linearity with respect to the error terms originate from approximations. The components of the matrix can be found in (C.135) through (C.140).

6.2.3 A Simple Example

As an example of how the error dynamics equations can be used to study the propagation and evolution of errors, the example from [13, Sec. 12.3.2.1] will be briefly presented here. This example nicely illustrates some fundamental concepts of the error dynamics equations and gives some insight into their nature. However, the vertical channel is said to be unstable [10, Sec. 5], meaning that errors in the vertical components of velocity and position grows exponentially with time. In the following analysis, the vertical channel is therefore omitted, such that the state vector becomes

$$\delta\mathbf{x}^n = \begin{bmatrix}\delta\boldsymbol{\psi}^n_{ns} & \delta v_N & \delta v_E & \delta\phi & \delta\lambda & \delta f^s_x & \delta f^s_y & \delta\boldsymbol{\omega}^s_{is}\end{bmatrix}^\top\ , \tag{6.18}$$

and the corresponding 12×12 system matrix is

$$\mathbf{F}^n_{\text{no-vertical}} = \left[\begin{array}{ccc|cc} -\boldsymbol{\Omega}^n_{in} & (\mathbf{F}^n_{12})_{1:3,1:2} & (\mathbf{F}^n_{13})_{1:3,1:2} & \mathbf{0}_{3\times 2} & \mathbf{C}^n_s \\ -([\mathbf{f}^n\times])_{1:2,1:3} & (\mathbf{F}^n_{22})_{1:2,1:2} & (\mathbf{F}^n_{23})_{1:2,1:2} & (\mathbf{C}^n_s)_{1:2,1:2} & \mathbf{0}_{2\times 3} \\ \mathbf{0}_{2\times 3} & (\mathbf{F}^n_{32})_{1:2,1:2} & (\mathbf{F}^n_{33})_{1:2,1:2} & \mathbf{0}_{2\times 2} & \mathbf{0}_{2\times 3} \\ \hline \mathbf{0}_{2\times 3} & \mathbf{0}_{2\times 2} & \mathbf{0}_{2\times 2} & \mathbf{0}_{2\times 2} & \mathbf{0}_{2\times 3} \\ \mathbf{0}_3 & \mathbf{0}_{3\times 2} & \mathbf{0}_{3\times 2} & \mathbf{0}_{3\times 2} & \mathbf{0}_3 \end{array}\right]\ , \tag{6.19}$$

where everything related to the vertical channel is removed.

In the example, we imagine an IMU that is stationary on the surface of the Earth, meaning that the attitude and position is constant. We define them to be

$$\mathbf{C}_b^n = \mathbf{I}_3 \,, \quad \phi = 45°\mathrm{N} \,, \quad \lambda = 12°\mathrm{E} \quad \text{and} \quad h = 0 \,.$$

This enables us to form the constant system matrix in (6.19) and the corresponding transition matrix, $\mathbf{\Phi}^n(t, t_0)$, that allows us to transition the state vector and covariance matrix forward in time. This concept is introduced in Appendix D.4.

The accelerometer and gyro observations are assumed to be free of random noise, but subject to bias values:

Gyroscope bias:	$\delta b_g = 0.01\,°/\mathrm{h}$
Accelerometer bias:	$\delta b_a = 0.1\,mg$

while the initial navigation solution is assumed to be corrupted by the following initialisation errors:

Initial roll error:	$\delta\alpha_0 = 0.1\,\mathrm{mrad}$
Initial pitch error:	$\delta\beta_0 = 0.1\,\mathrm{mrad}$
Initial heading error:	$\delta\gamma_0 = 1.0\,\mathrm{mrad}$

The error covariance matrix, $\mathbf{P}$, therefore becomes

$$\mathbf{P}(t_0) = \left[\begin{array}{ccccccccccccc}
\delta\alpha_0^2 & 0 & 0 & & & & & & & & & & \\
0 & \delta\beta_0^2 & 0 & & & & & & & & & & \\
0 & 0 & \delta\gamma_0^2 & & & & & & & & & & \\
 & & & 0 & 0 & & & & & & & & \\
 & & & 0 & 0 & & & & & & & & \\
 & & & & & 0 & 0 & & & & & & \\
 & & & & & 0 & 0 & & & & & & \\
\hline
 & & & & & & & \delta b_a^2 & 0 & & & & \\
 & & & & & & & 0 & \delta b_a^2 & & & & \\
 & & & & & & & & & \delta b_g^2 & 0 & 0 & \\
 & & & & & & & & & 0 & \delta b_g^2 & 0 & \\
 & & & & & & & & & 0 & 0 & \delta b_g^2 &
\end{array}\right] , \tag{6.20}$$

with all the left-out-components being zero. This error covariance matrix can be transitioned forward in time using the transition matrix as

$$\mathbf{P}(t) = \mathbf{\Phi}^n(t, t_0)\, \mathbf{P}(t_0)\, \mathbf{\Phi}^n(t, t_0)^\top \,. \tag{6.21}$$

The results for a 36 hour period are illustrated in Figure 6.8. Assuming that the errors are Gaussian, we can interpret these errors as the 1σ confidence interval.

Figure 6.8 clearly shows some periodical behaviour that reflects three distinct frequencies characterising the error propagation in inertial navigation. The roll and pitch errors are subject to an oscillation known as the **Schuler oscillation** with frequency

$$\omega_s = \sqrt{g/R_E} \,, \tag{6.22}$$

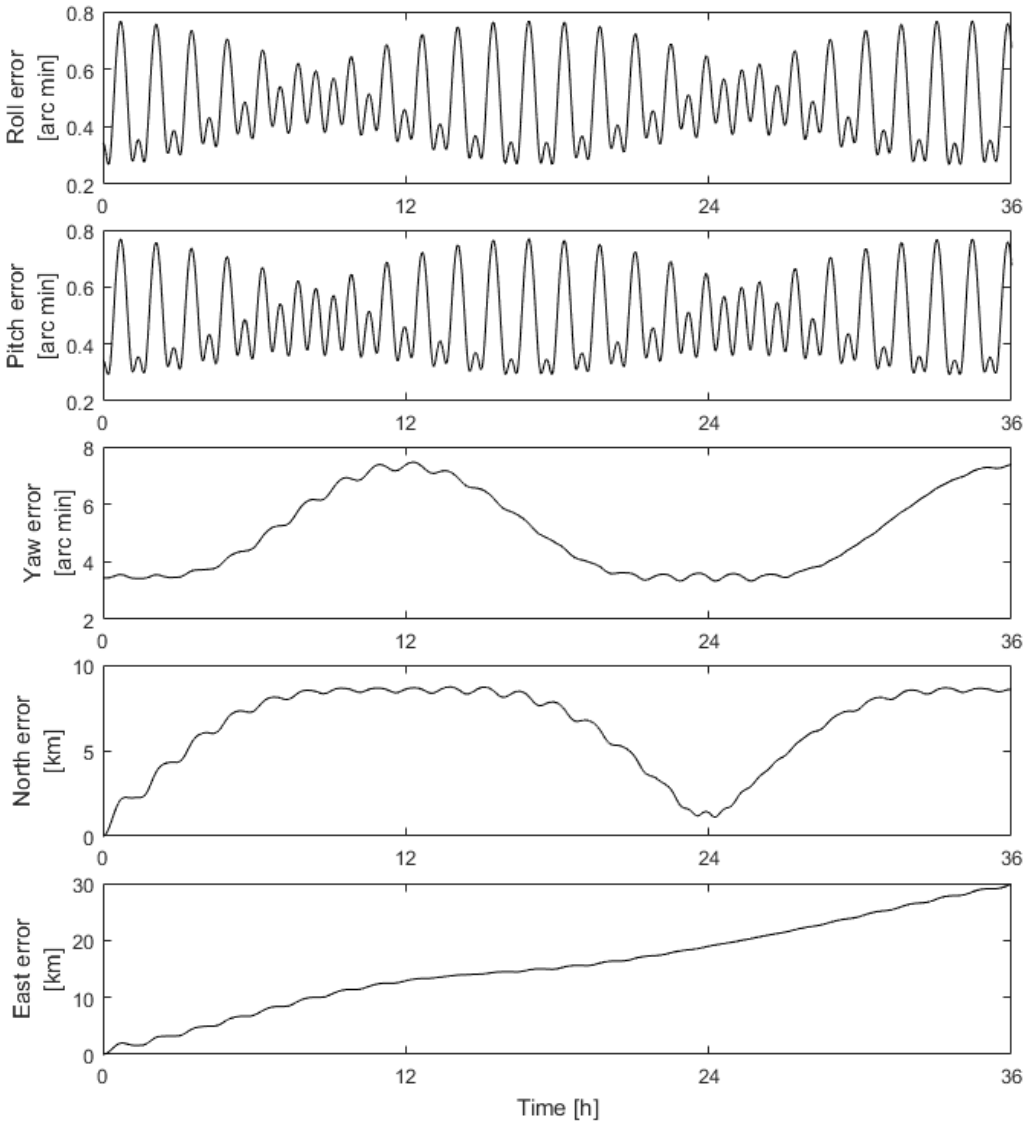

Figure 6.8: Navigation errors for a 36 hour period

where g is the gravity acceleration and R_E is the Earth radius. The period of the Schuler oscillation is therefore $2\pi/\omega_s \approx 84.4$ minutes. The Schuler oscillation is modulated by the **Foucault oscillation**, having a frequency that is latitude dependent [13, Sec. 12.3.2]:

$$\omega_f = \omega_{ie} \sin\phi \,, \tag{6.23}$$

such that the period becomes $2\pi/\omega_f \approx 34$ h. Finally, the heading and position errors are subject to a **24 h oscillation**, directly related to the rotation of the Earth.

In gravity dedicated airborne surveys, the aircraft is usually only airborne for 4-8 hours at a time, such that the Foucault and 24 hour oscillations may be disregarded. Figure 6.9 shows the error evolution for a 4 hour period, illustrating that the Schuler oscillation is the dominant frequency during time intervals of this length.

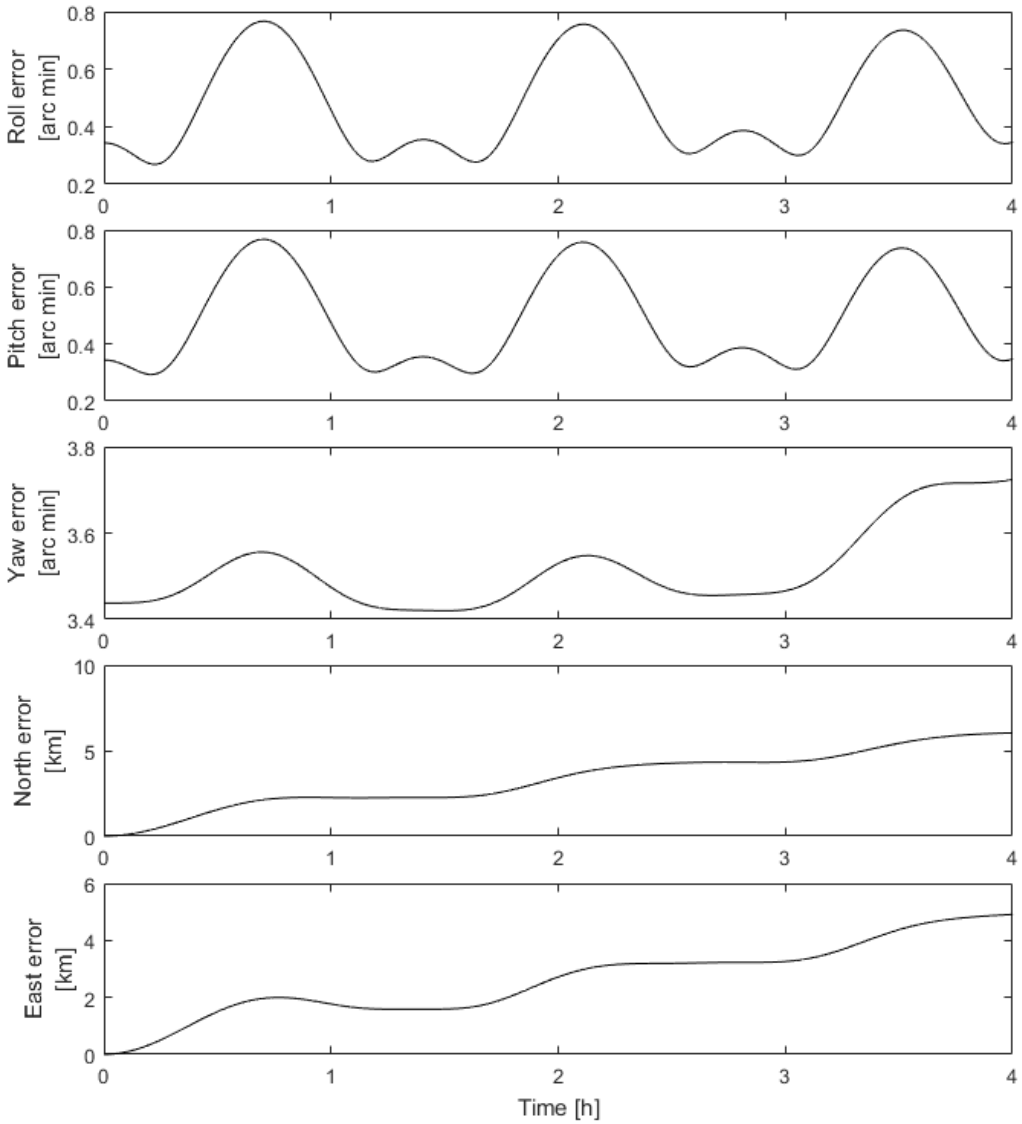

Figure 6.9: Navigation errors for a 4 hour period

From the two figures it should be clear that errors in inertial navigation is not just something that grows in time without bounds (except for the vertical channel). The different error components are interrelated and shows some oscillatory behaviour that evolves with time. Before we leave this section, it should be stressed out that this is a very simplified example. For a more comprehensive study on the evolution of errors, one typically resolves to simulations that closely mimics the dynamics of the intended application.

7 Simulating Inertial Measurements

As argued in the previous section, error propagation can be studied in more detail using simulated observations. Moreover, simulation allows for testing and performance prediction of both software and hardware. In order to obtain reliable results, the simulation should represent realistic input that mimics the environment and dynamics of the intended application. This section is devoted to the development of a simulation algorithm that uses input profiles of attitude and velocity in order to generate IMU observations. By using profiles from actual flights as input, the generated output will naturally mimic the environment of the intended application.

This section is divided into four subsections. The first subsection presents the flight profile that will be used as input to the algorithm. The second subsection will describe the simulation algorithm. The third subsection represents an application of inertial navigation to the generated, error-free, observations, in order to compare the performance of different implementations. The fourth subsection describes how random errors can be generated and added to the observations.

7.1 The Sample Profile

In an attempt to mimic the flight environment encountered in airborne surveys, data from an actual flight in Malaysia during summer 2016 was used to simulate data, see Figure 7.1. The long straight lines are typical for airborne gravity campaigns, where the flight dynamics are kept to a minimum. Typically, data is only used from the straight line segments and some perpendicular lines are flown in order to validate the results.

The approximately 4 hour long flight started from Kuching Airport, where a reference GNSS station was deployed. On board the airplane was the iMAR iNAT IMU along with a GNSS receiver and antenna. Using the NovAtel Inertial Explorer software, a differential GNSS solution was produced and combined with IMU observations using a loosely coupled Kalman filter framework. After processing, 1 Hz profiles for attitude, velocity and position were created and is used as input for the simulation software.

7.2 The Simulation Software

This section describes how simulated IMU observations are generated from velocity and attitude profiles. The observations are derived using the navigation equations from (5.65):

$$\dot{\phi} = v_N / (R_N + h) \tag{7.1a}$$

$$\dot{\lambda} = v_E / (R_E + h) \cos\phi \tag{7.1b}$$

$$\dot{h} = -v_D \tag{7.1c}$$

$$\dot{\mathbf{v}}^n = \mathbf{C}_b^n \, \mathbf{f}^b - (2\boldsymbol{\Omega}_{ie}^n + \boldsymbol{\Omega}_{en}^n) \, \mathbf{v}^n + \mathbf{g}^n \tag{7.1d}$$

$$\dot{\mathbf{C}}_b^n = \mathbf{C}_b^n \, \boldsymbol{\Omega}_{nb}^b \, , \tag{7.1e}$$

with

$$\boldsymbol{\omega}_{nb}^b = \boldsymbol{\omega}_{ib}^b - \mathbf{C}_n^b \, (\boldsymbol{\omega}_{en}^n + \boldsymbol{\omega}_{ie}^n) \ . \tag{7.2}$$

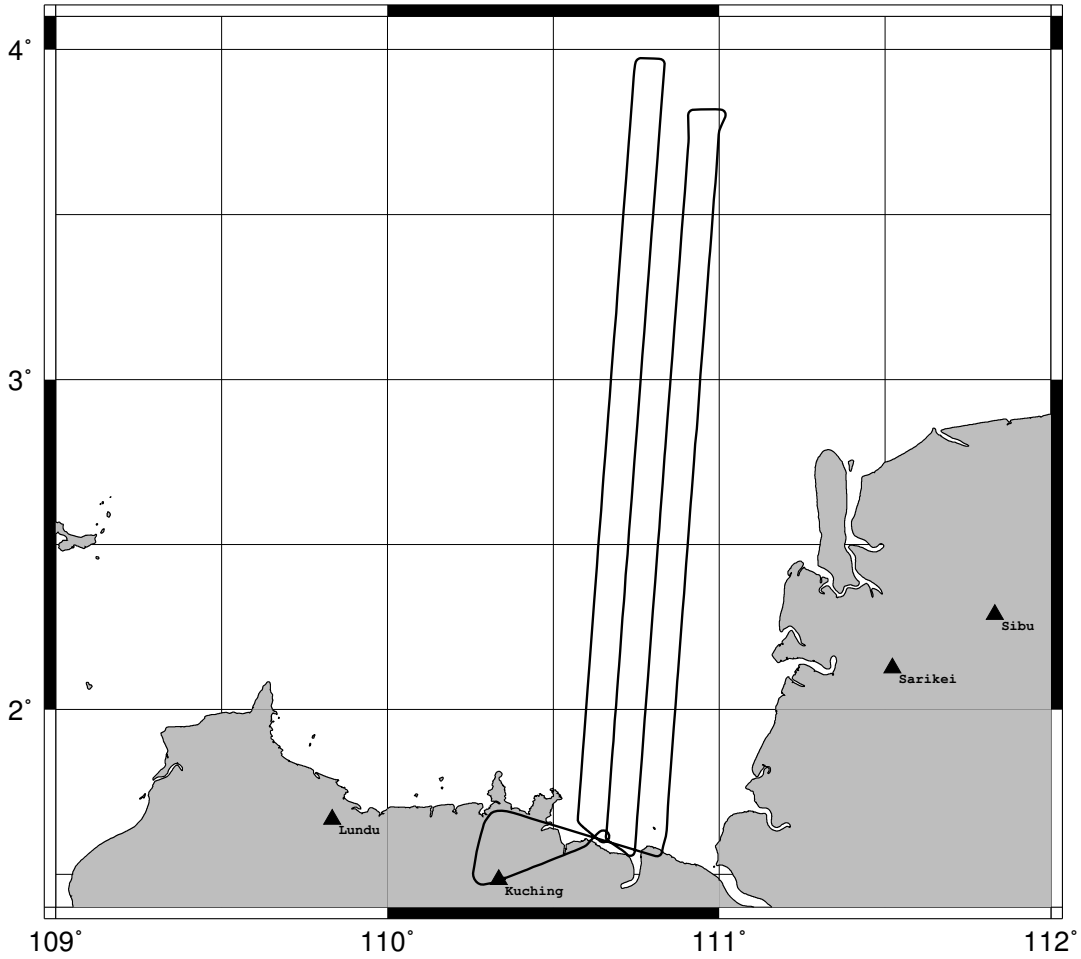

Figure 7.1: Flight trajectory from a flight in Malaysia 2016. Total flight time is approximately four hours, with approximately one hour on ground before the flight and half-an-hour after the flight, i.e. data corresponding to 6.5 hours.

The implementation of a recursive solution to these equations is discussed in Appendix C.2. Some of these principles will also be used to simulate observations using velocity and attitude as the input parameters. The strategy will be to:

Part 1: Generate Position Profile that is Consistent with Simulated Data

1. Integrate velocity, $\mathbf{v}^n$, for position, (ϕ, λ, h)

Part 2: Derive Gyroscope Observations from Attitude Profile

2. Differentiate attitude, $\mathbf{C}_b^n$, for angular rates, $\boldsymbol{\omega}_{nb}^b$,
3. Correct angular rates for fictitious forces in order to obtain gyro observations, $\boldsymbol{\omega}_{ib}^b$.

Part 2: Derive Accelerometer Observations from Velocity Profile

4. Differentiate velocity, $\mathbf{v}^n$, for acceleration, $\dot{\mathbf{v}}^n$,

5. Correct acceleration for fictitious forces in order to obtain specific force, $\mathbf{f}^n$, and

6. Transform specific force, $\mathbf{f}^n$, into body frame in order to obtain accelerometer observations, $\mathbf{f}^b$

The angular rate and specific force are generated at a very high rate, e.g. 2400 Hz, in order to minimize approximation errors originating from position and velocity dependent terms in the navigation equations. The assumption for this is that position, velocity and their dependent terms do not vary significantly during $1/2400$ Hz ≈ 417 ns. This is of course dependent on aircraft dynamics. The algorithm developed for generating these observations are presented in Section 7.2.2.

The gravitational acceleration can be added from any source available or simply set to zero. In appendix E.2, a method for the evaluation of a gravitational model in terms of spherical harmonic coefficients is outlined. This can be exploited to derive the gravity vector from a global model such as EGM2008.

7.2.1 Creating a Continuous Input Profile

In order to construct continuous profiles of velocity and attitude, a piecewise cubic hermite interpolating polynomial was fitted to each component of the two profiles. These polynomials can be evaluated at any point in time and preserve the sample values at the input sample times. The first derivative of the function can also be evaluated and will be continuous. The second derivative will not be continuous in general. This interpolating function was chosen because it is shape preserving and easily utilized in MATLAB.

One should be especially careful when interpolating the heading values, since these may contain discontinuities due to the limited 2π interval. As indicated in Figure 7.3, these discontinuities may be corrected for by allowing the attitude to freely grow and decrease without bounds. This causes no issues in the algorithm since the transformation from Euler angles to DCM attitude is accomplished through sine and cosine functions.

In order to create a position profile that is consistent with the simulated observations, the positions are generated as part of the algorithm presented in Section 7.2.2. In order to accomplish this, some initial position is required as input to the algorithm. This initial position need not be at the beginning of the time series, as the algorithm needs no modifications to iterate backwards in time.

Finally, these attitude, velocity and position profiles can be used to form additional observations that can be fed into the Kalman filter framework. The velocity and position profiles can for example be used to form GNSS observations.

7.2.2 Deriving Angular Rates and Accelerations

In theory, the first derivatives of the interpolating polynomials could be evaluated in order to compute exact derivatives of attitude and velocity. However, since gyroscopes and accelerometers do also not measure at exact instances in time, this was not exploited in the simulation software. Instead, the acceleration, $\mathbf{f}^n$, was evaluated from the velocity profile as

$$\mathbf{f}^n = \frac{\mathbf{v}^n(+) - \mathbf{v}^n(-)}{\delta t} + [2\boldsymbol{\Omega}^n_{ie} + \boldsymbol{\Omega}^n_{en}] \, \frac{\mathbf{v}^n(-) + \mathbf{v}^n(+)}{2} - \frac{\mathbf{g}^n(-) + \mathbf{g}^n(+)}{2} \,, \tag{7.3}$$

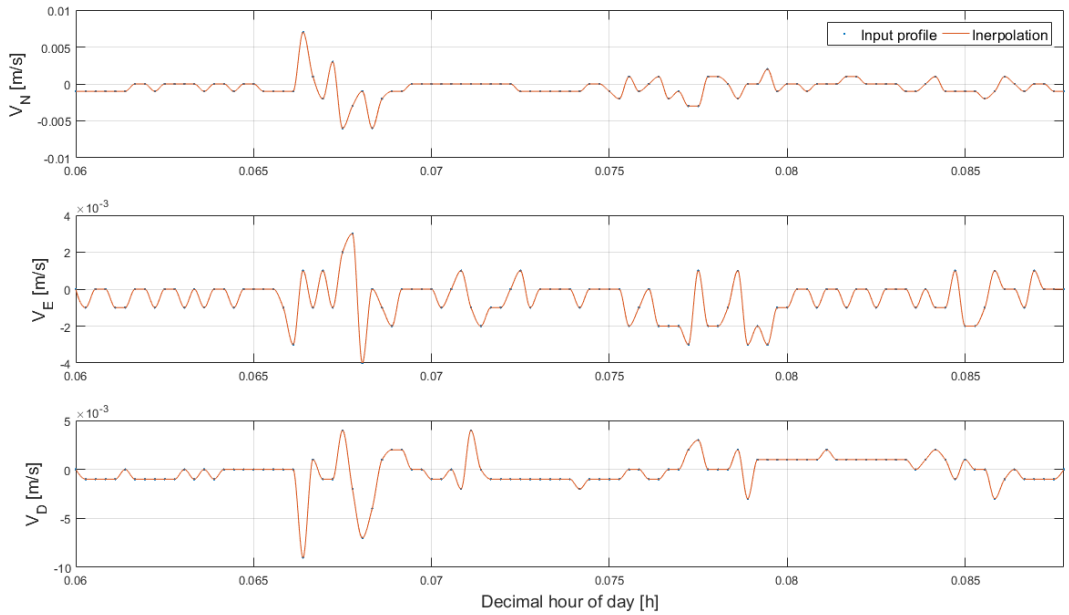

Figure 7.2: Illustration of interpolation using piecewise cubic hermite interpolating polynomial (red) between one second points of velocity profile (blue dots). This piece of the profile represents an interval where the vehicle is standing still at the airport

where $(-)$ and $(+)$ denotes the values before and after the update interval, respectively. For the angular rates, we have that

$$\mathbf{C}_b^n(+) = \mathbf{C}_b^n(-)\, e^{\left[\boldsymbol{\alpha}_{nb}^b \times\right]} \qquad \Rightarrow \qquad \mathbf{R} = e^{\left[\boldsymbol{\alpha}_{nb}^b \times\right]} = \left(\mathbf{C}_b^n(-)\right)^\top \mathbf{C}_b^n(+)\,, \tag{7.4}$$

where $\mathbf{C}_b^n(-)$ and $\mathbf{C}_b^n(+)$ can be evaluated from the interpolating polynomials and $\mathbf{R}$ is the updating rotation operator. If we therefore evaluate the matrix logarithm

$$\left[\boldsymbol{\alpha}_{nb}^b \times\right] = \ln\left(\mathbf{R}\right)\,, \tag{7.5}$$

the angular rates can be derived as

$$\boldsymbol{\omega}_{nb}^b = \frac{\boldsymbol{\alpha}_{nb}^b}{\delta t} = \frac{1}{\delta t}\begin{bmatrix} \left[\boldsymbol{\alpha}_{nb}^b \times\right]_{3,2} \\ \left[\boldsymbol{\alpha}_{nb}^b \times\right]_{1,3} \\ \left[\boldsymbol{\alpha}_{nb}^b \times\right]_{2,1} \end{bmatrix}\,. \tag{7.6}$$

The matrix logarithm can be computed using (B.75):

$$\left[\boldsymbol{\alpha}_{nb}^b \times\right] = \frac{\left|\boldsymbol{\alpha}_{nb}^b\right|}{\sin\left|\boldsymbol{\alpha}_{nb}^b\right|}\frac{\mathbf{R} - \mathbf{R}^\top}{2}\,, \tag{7.7}$$

where

$$\left|\boldsymbol{\alpha}_{nb}^b\right| = \cos^{-1}\left[\frac{\mathrm{Tr}\left[\mathbf{R}\right] - 1}{2}\right]\,. \tag{7.8}$$

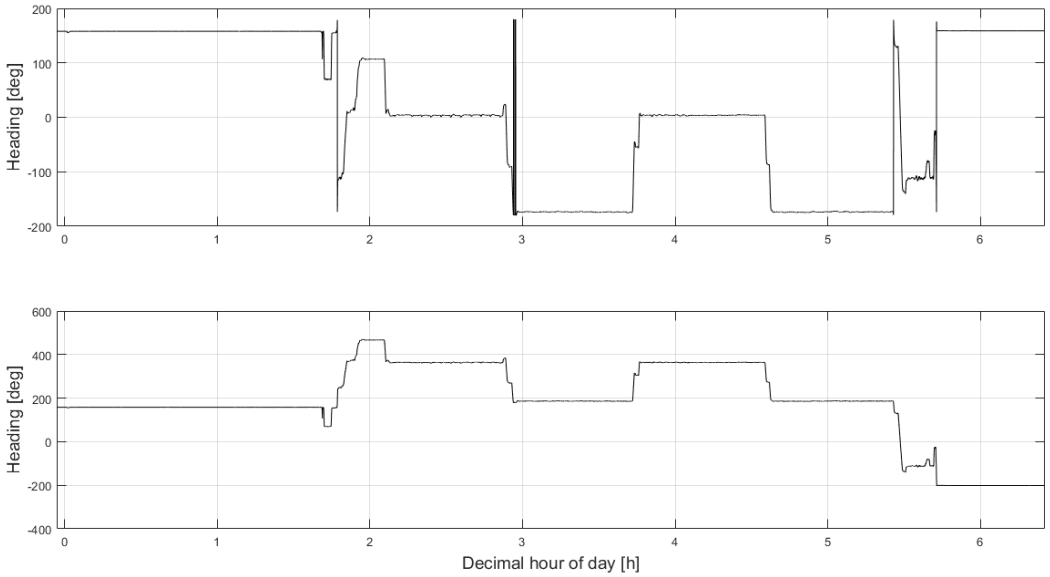

Figure 7.3: Illustration of interpolation of the heading angle. (Top): The initial profile has discontinuities, which will produce inconsistent values and large angular rates when interpolated. (Bottom): In order to achieve a smooth interpolation, the discontinuities must be corrected for. Since the Euler angles are converted to DCM attitudes using sine and cosine functions, this will not influence the simulation algorithm

However, in order to avoid numerical instability when dividing by very small numbers, a truncated power series expansion from (B.58)

$$\frac{\sin\left|\boldsymbol{\alpha}_{nb}^{b}\right|}{\left|\boldsymbol{\alpha}_{nb}^{b}\right|}=\sum_{k=0}^{\infty}(-1)^{k}\frac{\left|\boldsymbol{\alpha}_{nb}^{b}\right|^{2k}}{(2k+1)!}\approx 1-\frac{\left|\boldsymbol{\alpha}_{nb}^{b}\right|^{2}}{3!}+\frac{\left|\boldsymbol{\alpha}_{nb}^{b}\right|^{4}}{5!}-\cdots, \tag{7.9}$$

should be used whenever $\left|\boldsymbol{\alpha}_{nb}^{b}\right|$ is either very small or close to π. Notice that the above power series represent the inverse of the coefficient. In the following is an outline of how this algorithm is built.

Example Algorithm: Deriving Angular Rates and Specific Force from Attitude and Velocity Profiles

---

1. Derive the update interval, δt, and extract values of velocity, attitude and gravity before and after the interval, i.e.

$$\begin{array}{ccccc}\mathbf{v}^{n}(-) & \alpha_{nb}(-) & \beta_{nb}(-) & \gamma_{nb}(-) & \mathbf{g}^{n}(-)\\ \mathbf{v}^{n}(+) & \alpha_{nb}(+) & \beta_{nb}(+) & \gamma_{nb}(+) & \mathbf{g}^{n}(+)\end{array}$$

2. Compute radii of curvature using (2.9) and (2.10):

$$R_E(-) = \frac{a}{\sqrt{1 - e^2 \sin^2 \phi(-)}} \quad \text{and} \quad R_N(-) = R_E(-) \frac{1 - e^2}{1 - e^2 \sin^2 \phi(-)} \, .$$

Step 1: Position Update

3. Update height and latitude using (C.77) and (C.78):

$$\begin{aligned} h(+) &= h(-) - \frac{\delta t}{2} \left(v_D^n(-) + v_D^n(+) \right) \, , \\ \phi(+) &= \phi(-) + \frac{\delta t}{2} \left(\frac{v_N^n(-)}{R_N(-) + h(-)} + \frac{v_N^n(+)}{R_N(-) + h(+)} \right) \, . \end{aligned}$$

4. Compute radii of curvature using (2.9) and (2.10):

$$R_E(+) = \frac{a}{\sqrt{1 - e^2 \sin^2 \phi(+)}} \quad \text{and} \quad R_N(+) = R_E(+) \frac{1 - e^2}{1 - e^2 \sin^2 \phi(+)} \, .$$

5. Update longitude using (C.79):

$$\lambda(+) = \lambda(-) + \frac{\delta t}{2} \left(\frac{v_E^n(-)}{[R_E(-) + h(-)] \cos \phi(-)} + \frac{v_E^n(+)}{[R_E(+) + h(+)] \cos \phi(+)} \right) \, .$$

Step 2: Derive Angular Increments

6. Form transformation matrices using (5.47)

$$\mathbf{C}_b^n(-) = \begin{bmatrix} \cos\beta_{nb}(-)\cos\gamma_{nb}(-) & \begin{array}{c} -\cos\alpha_{nb}(-)\sin\gamma_{nb}(-) \\ +\sin\alpha_{nb}(-)\sin\beta_{nb}(-)\cos\gamma_{nb}(-) \end{array} & \begin{array}{c} \sin\alpha_{nb}(-)\sin\gamma_{nb}(-) \\ +\cos\alpha_{nb}(-)\sin\beta_{nb}(-)\cos\gamma_{nb}(-) \end{array} \\ \cos\beta_{nb}(-)\sin\gamma_{nb}(-) & \begin{array}{c} \cos\alpha_{nb}(-)\cos\gamma_{nb}(-) \\ +\sin\alpha_{nb}(-)\sin\beta_{nb}(-)\sin\gamma_{nb}(-) \end{array} & \begin{array}{c} -\sin\alpha_{nb}(-)\cos\gamma_{nb}(-) \\ +\cos\alpha_{nb}(-)\sin\beta_{nb}(-)\sin\gamma_{nb}(-) \end{array} \\ -\sin\beta_{nb}(-) & \sin\alpha_{nb}(-)\cos\beta_{nb}(-) & \cos\alpha_{nb}(-)\cos\beta_{nb}(-) \end{bmatrix} .$$

$$\mathbf{C}_b^n(+) = \begin{bmatrix} \cos\beta_{nb}(+)\cos\gamma_{nb}(+) & \begin{array}{c} -\cos\alpha_{nb}(+)\sin\gamma_{nb}(+) \\ +\sin\alpha_{nb}(+)\sin\beta_{nb}(+)\cos\gamma_{nb}(+) \end{array} & \begin{array}{c} \sin\alpha_{nb}(+)\sin\gamma_{nb}(+) \\ +\cos\alpha_{nb}(+)\sin\beta_{nb}(+)\cos\gamma_{nb}(+) \end{array} \\ \cos\beta_{nb}(+)\sin\gamma_{nb}(+) & \begin{array}{c} \cos\alpha_{nb}(+)\cos\gamma_{nb}(+) \\ +\sin\alpha_{nb}(+)\sin\beta_{nb}(+)\sin\gamma_{nb}(+) \end{array} & \begin{array}{c} -\sin\alpha_{nb}(+)\cos\gamma_{nb}(+) \\ +\cos\alpha_{nb}(+)\sin\beta_{nb}(+)\sin\gamma_{nb}(+) \end{array} \\ -\sin\beta_{nb}(+) & \sin\alpha_{nb}(+)\cos\beta_{nb}(+) & \cos\alpha_{nb}(+)\cos\beta_{nb}(+) \end{bmatrix} .$$

7. Form rotation operator using (7.4)

$$\mathbf{R} = \mathbf{C}_b^n(-)^\top \mathbf{C}_b^n(+) \, ,$$

8. Compute magnitude of rotation from (7.8)

$$\left| \boldsymbol{\alpha}_{nb}^b \right| = \cos^{-1} \left[\frac{\mathrm{Tr}\left[\mathbf{R}\right] - 1}{2} \right] \, .$$

9. Derive skew-symmetric form of $\boldsymbol{\alpha}_{nb}^{b}$ using (7.7) or (7.9):
   if $\left|\boldsymbol{\alpha}_{nb}^{b}\right| > 10^{-8}$

$$\left[\boldsymbol{\alpha}_{nb}^{b}\times\right] = \frac{\left|\boldsymbol{\alpha}_{nb}^{b}\right|}{\sin\left|\boldsymbol{\alpha}_{nb}^{b}\right|}\frac{\mathbf{R}-\mathbf{R}^{\top}}{2}$$

   else

$$\left[\boldsymbol{\alpha}_{nb}^{b}\times\right] = \frac{5040}{5040-840\left|\boldsymbol{\alpha}_{nb}^{b}\right|^{2}+42\left|\boldsymbol{\alpha}_{nb}^{b}\right|^{4}-\left|\boldsymbol{\alpha}_{nb}^{b}\right|^{6}}\frac{\mathbf{R}-\mathbf{R}^{\top}}{2}$$

   end

10. Extract increments

$$\boldsymbol{\alpha}_{nb}^{b} = \begin{bmatrix}\left[\boldsymbol{\alpha}_{nb}^{b}\times\right]_{3,2}\\ \left[\boldsymbol{\alpha}_{nb}^{b}\times\right]_{1,3}\\ \left[\boldsymbol{\alpha}_{nb}^{b}\times\right]_{2,1}\end{bmatrix}$$

Step 3: Form Average Transformation Matrix

11. Form average transformation matrix using (C.69) or (C.71)
    if $\left|\boldsymbol{\alpha}_{nb}^{b}\right| > 10^{-8}$

$$\overline{\mathbf{C}}_{b}^{n} = \mathbf{C}_{b}^{n}(-)\left[\mathbf{I}+\frac{1-\cos\left|\boldsymbol{\alpha}_{nb}^{b}\right|}{\left|\boldsymbol{\alpha}_{nb}^{b}\right|^{2}}\left[\boldsymbol{\alpha}_{nb}^{b}\times\right]+\frac{1}{\left|\boldsymbol{\alpha}_{nb}^{b}\right|^{2}}\left(1-\frac{\sin\left|\boldsymbol{\alpha}_{nb}^{b}\right|}{\left|\boldsymbol{\alpha}_{nb}^{b}\right|}\right)\left[\boldsymbol{\alpha}_{nb}^{b}\times\right]^{2}\right]$$

    else

$$\overline{\mathbf{C}}_{b}^{n} = \mathbf{C}_{b}^{n}(-)\left[\mathbf{I}+\left(\frac{1}{2}-\frac{\left|\boldsymbol{\alpha}_{nb}^{b}\right|^{2}}{24}+\frac{\left|\boldsymbol{\alpha}_{nb}^{b}\right|^{4}}{720}\right)\left[\boldsymbol{\alpha}_{nb}^{b}\times\right]+\left(\frac{1}{6}-\frac{\left|\boldsymbol{\alpha}_{nb}^{b}\right|^{2}}{120}+\frac{\left|\boldsymbol{\alpha}_{nb}^{b}\right|^{4}}{5040}\right)\left[\boldsymbol{\alpha}_{nb}^{b}\times\right]^{2}\right]$$

    end

Step 4: Derive Observations

12. Compute Earth rotational rate in n-frame using (A.23)

$$\boldsymbol{\omega}_{ie}^{n} = \boldsymbol{\omega}_{ie}\begin{bmatrix}\frac{1}{2}\left(\cos\phi(-)+\cos\phi(+)\right)\\ 0\\ -\frac{1}{2}\left(\sin\phi(-)+\sin\phi(+)\right)\end{bmatrix}$$

13. Compute transport-rate using (C.43)

$$\boldsymbol{\omega}_{en}^{n} = \begin{bmatrix}\frac{1}{2}\left(\frac{v_E(-)}{R_E(-)+h(-)}+\frac{v_E(+)}{R_E(+)+h(+)}\right)\\ -\frac{1}{2}\left(\frac{v_N(-)}{R_N(-)+h(-)}+\frac{v_N(+)}{R_N(+)+h(+)}\right)\\ -\frac{1}{2}\left(\frac{v_E(-)\tan\phi(-)}{R_E(-)+h(-)}+\frac{v_E(+)\tan\phi(+)}{R_E(+)+h(+)}\right)\end{bmatrix}.$$

14. Derive angular rate and add rotation effects

$$\boldsymbol{\omega}_{ib}^{b} = \frac{\boldsymbol{\alpha}_{nb}^{b}}{\delta t} + \overline{\mathbf{C}}_{b}^{n\top} \left(\boldsymbol{\omega}_{ie}^{n} + \boldsymbol{\omega}_{en}^{n}\right)$$

15. Derive n-frame acceleration and correct for rotation effects and gravity using (C.75)

$$\mathbf{f}^{n} = \frac{\mathbf{v}^{n}(+) - \mathbf{v}^{n}(-)}{\delta t} + \left[2\boldsymbol{\Omega}_{ie}^{n} + \boldsymbol{\Omega}_{en}^{n}\right] \frac{\mathbf{v}^{n}(-) + \mathbf{v}^{n}(+)}{2} - \frac{\mathbf{g}^{n}(-) + \mathbf{g}^{n}(+)}{2}$$

16. Transform specific force into body frame

$$\mathbf{f}^{b} = \overline{\mathbf{C}}_{b}^{n\top}\, \mathbf{f}^{n}$$

End of example

7.2.3 Generating IMU Observations

In an attempt to imitate the data output of the IMU, the angular rates and accelerations are generated at a fundamental frequency of 2400 Hz and then subsequently averaged to an IMU output frequency of 300 Hz. The simulated data therefore consists of angular rate, $\boldsymbol{\omega}_{ib}^{b}$, and specific force, $\mathbf{f}^{b}$, with an associated time stamp. The observations represent average values from the previous to the current time stamp. This is illustrated in Figure 7.4.

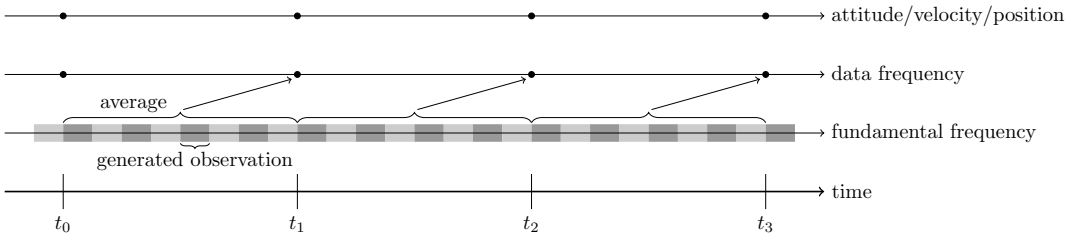

Figure 7.4: Illustration of how data are generated from simulated observations. Observations are generated at 2400 Hz and subsequently averaged to 300 Hz, representing the IMU data output. The associated time stamp refer to the end of the averaging interval. Also shown are the navigation parameters, i.e. attitude, velocity and position, which represent the corresponding variables at instants in time

7.3 Testing the Navigation Equations

The implementation of the navigation equations in (7.1) is discussed in Appendix C.2. In Appendix C.2.7, two example algorithms are presented that differs in implementation complexity and precision. The most fundamental difference is that the first-order algorithm uses a truncated series expansion for the attitude update, i.e. the transition matrix, whereas the precise algorithm uses Rodrigues' formula to exactly evaluate this operator in terms of sine and cosine functions (Rodrigues' formula is derived in Appendix B.3).

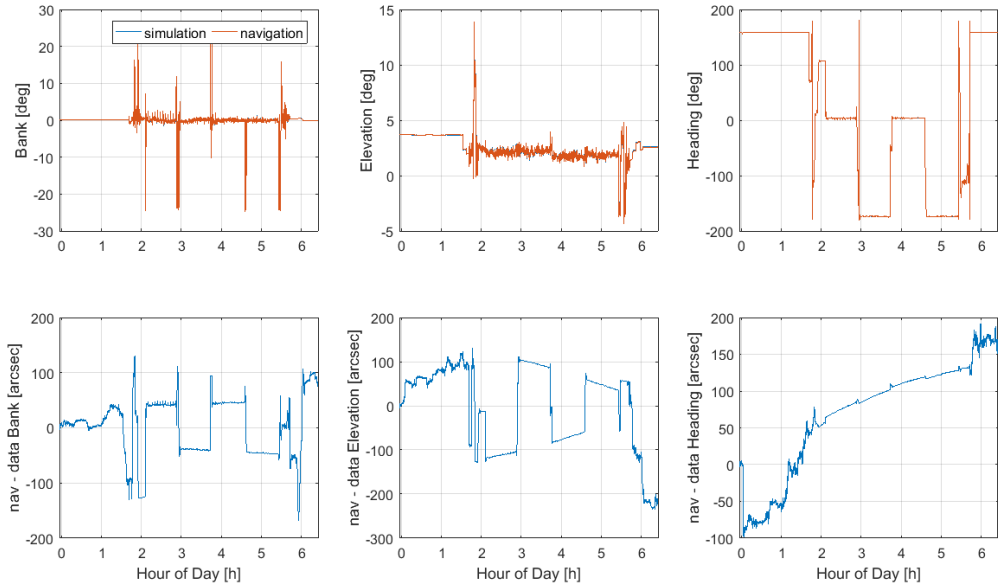

Figure 7.5: Attitude results from the precise navigation algorithm presented in Appendix C.2.7 applied to the simulated IMU observations. The bottom row shows the difference between the navigation results and the attitude profile input to the simulation algorithm

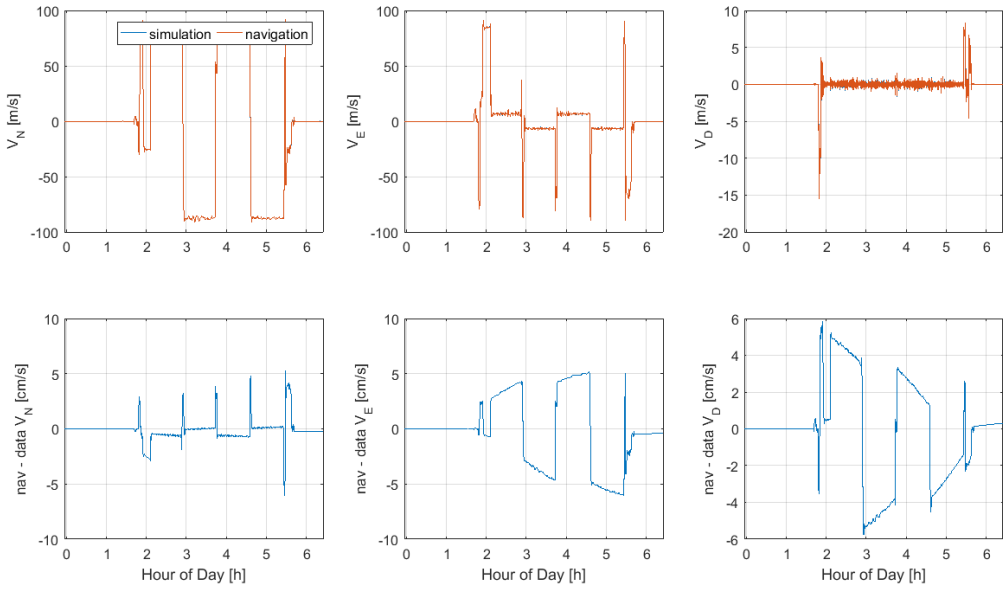

Figure 7.6: Velocity results from the precise navigation algorithm presented in Appendix C.2.7 applied to the simulated IMU observations. The bottom row shows the difference between the navigation results and the velocity profile input to the simulation algorithm

Figures 7.5 through 7.7 illustrate the results from applying the precise algorithm to the simulated data at the 2400 Hz rate, i.e. with no averaging to 300 Hz. The results from the navigation algorithm are compared with the attitude and velocity profiles, input to the simulation algorithm, and with the position profile generated by the simulation algorithm. As indicated by the figures, the errors are in the range of ±100 arc seconds for attitude, ±6 cm/s for the velocity and ±150 meters for the position.

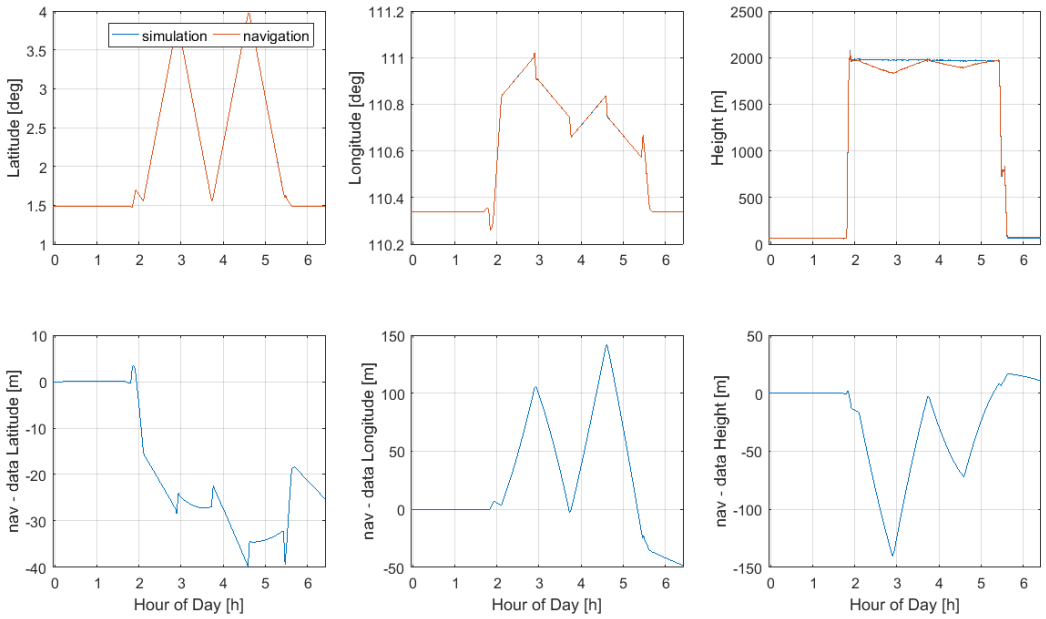

Figure 7.7: Position results from the precise navigation algorithm presented in Appendix C.2.7 applied to the simulated IMU observations. The bottom row shows the difference between the navigation results and the position profile generated by the simulation algorithm

When the simulated observations are averaged to 300 Hz and the navigation algorithm is applied again, the same results occur. Changing the attitude representation from DCM to quaternion does also not affect the results. Additionally, maybe a bit surprisingly, applying the first-order algorithm does also not seem to affect the results. This may be due to the fact that aircraft manoeuvring is kept to a minimum for airborne gravimetry.

The results from the different navigation algorithms are summarized in Table 7.1, indicating that only the processing time varies. The processing time for all algorithms is around 3 seconds when applied to approximately 6.5 hours of data at 300 Hz rate. Difference in accuracy and runtime of any algorithm tested here is therefore not sufficient to prefer one algorithm over the other.

Attitude	Algorithm	Proc. Time	Attitude Errors	Velocity Errors
DCM	First Order	2.67 s	±100”	±6 cm/s
DCM	Precise	3.62 s	±100”	±6 cm/s
Quaternion	Precise	3.18 s	±100”	±6 cm/s

Table 7.1: Algorithm processing time and accuracy for different attitude representation and implementation strategy (algorithm). The implementation strategy refer to the example algorithms presented in Appendix C.2.7. The navigation equations were implemented as a MATLAB C MEX file

7.4 Adding Errors to the Data

Real observations are expected to be corrupted by errors such as random noise, bias, scale factors and cross-coupling errors. In order to yield more realistic observations and to study the effects of various error components, errors can be generated and added to the simulated observations using the relations in Eqs. (6.2) through (6.8). This section will discuss only the generation of random errors. For other error sources such as systematic errors, bandlimiting and quantisation effects, the reader is referred to [5, Appendix J].

7.4.1 Random Sequences

A random sequence representing any of the stochastic processes presented in Appendix D, can be generated from a normally distributed, zero-mean, white noise sequence. The MATLAB function `randn` is able to generate numbers from a standard normal distribution, i.e. a normal distribution having zero mean and unit variance. Such a random number generator will be denoted by $\mathcal{N}(0,1)$ in the following.

White Noise
The standard deviation, σ_w, of a discrete white noise sequence is related to the amplitude, S_{wn}, of the Power Spectral Density function (PSD) as (D.22)

$$\sigma_w = \sqrt{S_{\text{wn}}/\triangle t}\,, \tag{7.10}$$

where $\triangle t$ is the sampling interval. A white noise sequence of variance, σ_w^2, is generated as

$$x_k = \sigma_w \mathcal{N}(0,1)\,, \tag{7.11}$$

where $\mathcal{N}(0,1)$ is a random number generator as for example MATLABs `randn` function.

Random Constant
A random constant can be generated as with white noise. In this case, however, only a single value needs to be generated, since the value is constant during the entire run.

Random Walk
A random walk sequence can be generated iteratively as

$$x_k = x_{k-1} + \sigma_w \mathcal{N}(0,1)\,, \tag{7.12}$$

where the PSD amplitude of the associated white noise process is again related to the standard deviation as (7.10).

Gauss-Markov Process

An exponentially correlated first-order Gauss-Markov sequence with constant variance can be generated as [5, Eq. J.12]:

$$x_k = e^{-\beta \triangle t}\, x_{k-1} + \sqrt{1 - e^{-2\beta \triangle t}}\, \sigma_{gm}\, \mathcal{N}(0,1)\ , \tag{7.13}$$

where $T = 1/\beta$ is the correlation time and σ_{gm}^2 is the variance of the process. The PSD amplitude of the associated white noise process is (D.83):

$$S_m athrmwn = 2\sigma_{gm}^2 \beta\ . \tag{7.14}$$

7.4.2 Correlated Errors

One approach for generating correlated errors is presented in [5, Appendix J.4.3]. This is particularly relevant when simulating GNSS position and velocity errors, which are naturally correlated. Suppose we have a vector, $\mathbf{x}$, of length n, containing correlated error sources, this could for example be the position. The confidence and correlation among the individual components is described by a covariance matrix, $\mathbf{C}_x$.

The covariance matrix may be decomposed into a diagonal matrix, $\mathbf{C}_y$, and a unit lower triangular matrix, $\mathbf{L}$, using Cholesky factorization [6, Sec. 2.5.1] such that

$$\mathbf{C}_x = \mathbf{L}\, \mathbf{C}_y\, \mathbf{L}^\top\ . \tag{7.15}$$

Based on the diagonal covariance matrix, $\mathbf{C}_y$, it is possible to generate a vector, $\mathbf{y}$, of n independent random variables using (7.11), i.e. use the square-root of the diagonal entries as the standard deviation. These n components are then made correlated according to $\mathbf{C}_x$ by applying the lower triangular matrix as

$$\mathbf{x} = \mathbf{L}\, \mathbf{y}\ . \tag{7.16}$$

7.4.3 Examples

As an example accelerometer errors will be generated based on the manufacturer specifications for the iNAT unit, see Table 6.2. The accelerometer noise is specified in terms of the root-PSD of the associated random walk process on the velocity. Using (7.10) the root-PSD value of 8 $\mu g/\sqrt{\text{Hz}} \approx 8\,\text{mGal}/\sqrt{\text{Hz}}$ can be converted to a standard deviation as

$$\sigma_w = 8\, \frac{\text{mGal}}{\sqrt{\text{Hz}}}\ \cdot\ \sqrt{300\,\text{Hz}} = 138.56\,\text{mGal}\ , \tag{7.17}$$

where 300 Hz is the IMU sampling rate. Using this standard deviation, white noise can be generated using (7.11) along with the `randn` function in MATLAB. In Figure 7.8, an example of such a white noise process is shown together with a static bias component generated using a standard deviation of 25 mGal and a dynamic bias component generated using a first-order Gauss-Markov process. The Gauss-Markov sequence was generated using a standard deviation of 10 mGal and a correlation parameter of $\beta = 1/12\,\text{min}$ using (7.13). Such errors could then be added to the simulated IMU observations in order to generate more realistic data.

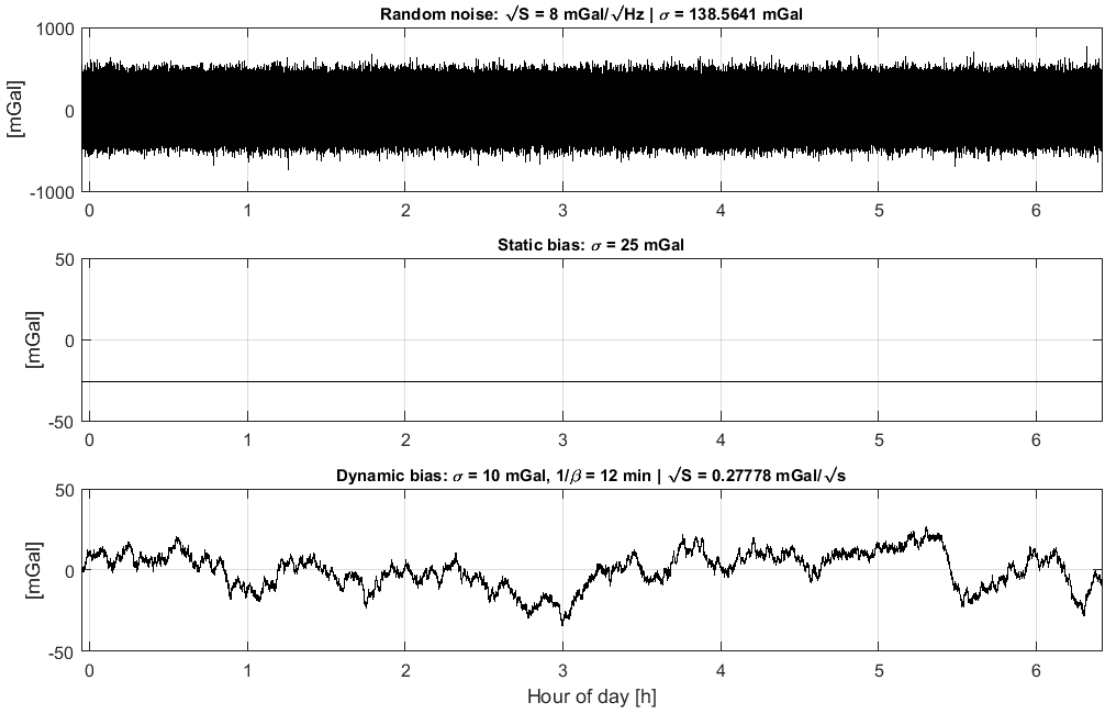

Figure 7.8: Example of accelerometer errors generated using values from iNAT manufacturer specifications in Table 6.2. The random noise is generated using a white noise stochastic model, the static bias uses a random constant stochastic model and the dynamic bias uses a first-order Gauss-Markov stochastic model

As an example of correlated errors, we can consider errors on the GNSS position estimates. A representative error covariance matrix for the estimated GNSS position along the flight profile in Figure 7.1 is

$$\mathbf{C}_x = \begin{bmatrix} 5.00 \cdot 10^{-4} & 5.00 \cdot 10^{-5} & 5.00 \cdot 10^{-5} \\ 5.00 \cdot 10^{-5} & 5.00 \cdot 10^{-4} & -5.00 \cdot 10^{-5} \\ 5.00 \cdot 10^{-5} & -5.00 \cdot 10^{-5} & 5.00 \cdot 10^{-3} \end{bmatrix}, \tag{7.18}$$

where the components are the north, east and down direction, respectively, and units are in meters. This corresponds to a standard deviation of approximately 2 cm on the horizontal and 7 cm on the vertical direction. Correlated errors using this covariance matrix can be generated using Cholesky factorisation as outlined in the previous section.

However, since the GNSS software applies a Kalman filter and smoother in the processing, the flight trajectory is more smooth than a white noise process would imply. Therefore, a more realistic set of observations is formed by generating a white noise signal at 0.01 Hz sampling rate, i.e. each 100 s, and then interpolating between these 0.01 Hz samples. An example of such errors is illustrated in Figure 7.9.

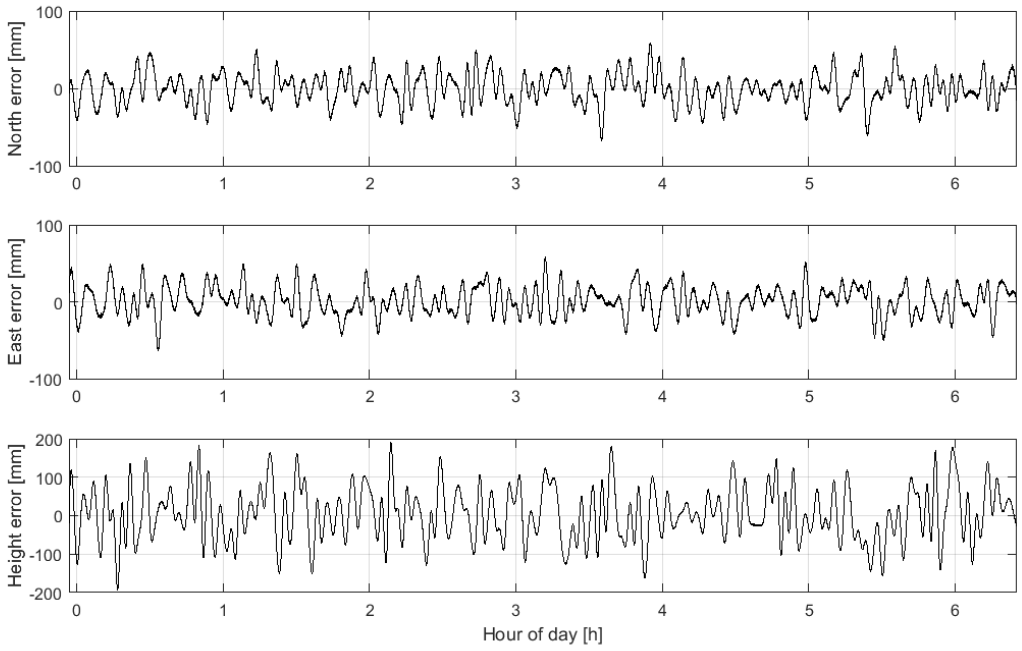

Figure 7.9: Example of correlated position errors generated using the covariance matrix in (7.18) and a 100 s time window

References

[1] David Becker. "Advanced Calibration Methods for Strapdown Airborne Gravimetry". PhD thesis. Darmstadt: Technische Universität Darmstadt, 2016. URL: http://tuprints.ulb.tu-darmstadt.de/5691/.

[2] David Becker et al. "Drift reduction in strapdown airborne gravimetry using a simple thermal correction". In: *Journal of Geodesy* 89.11 (2015), pp. 1133–1144. ISSN: 14321394. DOI: 10.1007/s00190-015-0839-8.

[3] Kenneth R. Britting. *Inertial Navigation Systems Analysis*. 1971, p. 267. ISBN: 978-1608070787.

[4] James Diebel. *Representing attitude: Euler angles, unit quaternions, and rotation vectors*. 2006. DOI: 10.1.1.110.5134. URL: http://citeseerx.ist.psu.edu/viewdoc/summary?doi=10.1.1.110.5134.

[5] Paul D. Groves. *Principles of GNSS, Inertial, and Multisensor Integrated Navigation Systems*. 2nd. Artech House Remote Sensing Library, 2013. ISBN: 978-1608070053.

[6] Michael T. Heath. *Scientific Computing: An Introductory Survey*. 2nd. McGraw-Hill Higher Education, 2002. ISBN: 978-0-07-239910-3.

[7] Honeywell International Inc. *GG1320AN Digital Laser Gyro*. URL: https://aerospace.honeywell.com/en/products/navigation-and-sensors/gg1320an-digital-ring-laser-gyroscope.

[8] Honeywell International Inc. *Q-Flex QA-2000 Accelerometer*. 2005. URL: https://aerospace.honeywell.com/en/products/navigation-and-sensors/accelerometers.

[9] *Inertial Explorer User Guide*. Inertial Explorer software version 8.60. NovAtel. Nov. 2014.

[10] Christopher Jekeli. *Inertial Navigation Systems with Geodetic Applications*. 2001, pp. 51–54. ISBN: 3110159031. DOI: 10.1515/9783110800234.

[11] Jack B. Kuipers. *Quaternions and Rotation Sequences: A Primer with Applications to Orbits, Aerospace and Virtual Reality*. Princeton University Press, 2002. ISBN: 0-691-10298-8.

[12] Paul Savage. *Strapdown Analytics*. Strapdown Associates, Inc., 2000.

[13] David Titterton and John L. Weston. "Strapdown Inertial Navigation Technology, 2nd Edition". In: (2004).

Part III:

Kalman Filtering and Integrated INS/GNSS Navigation Systems

Whereas the previous part was concerned with the IMU and its use for navigation, this part is concerned with the integration of IMU and GNSS observations. The combination of these systems will not only lead to an improved navigation solution, but the GNSS observations will prevent the INS solution from drifting off by continuously calibrating the IMU sensor errors. The framework used here for the integration is the Kalman filter, which will be introduced in Section 8, along with some associated tools. This section focuses on the working principle of the Kalman filter, but will also introduce the extended Kalman filter along with some associated derivations. The Kalman filter framework is based on the theory of linear dynamic systems driven by stochastic processes, which is introduced more elaborately in Appendix D. Section 9 is devoted to the development of an integrated INS/GNSS navigation algorithm using the Kalman filter framework. After describing the algorithm used in this dissertation, it will be applied to the simulated data from Section 7 and the results will be discussed.

8 Kalman Filtering

The Kalman filter constitutes a practical framework for combining all available information regarding a dynamic system and deriving "optimal" estimates of the variables of interest. The framework is based on a **linear dynamic system model**, driven by stochastic input:

$$\dot{\mathbf{x}}(t) = \mathbf{F}(t)\,\mathbf{x}(t) + \mathbf{G}(t)\,\mathbf{w}_s(t)\ , \tag{8.1}$$

where

- $\mathbf{x}(t)$ is an n-dimensional state vector containing the set of n variables that are used to describe the system, i.e. position, velocity, attitude, sensor biases and scale factors and possibly gravity
- $\mathbf{F}(t)$ is an $n \times n$ system matrix describing the dynamics of the system. Here it will be formed using the navigation equations (or error dynamics equations)
- $\mathbf{w}_s(t)$ is a k-dimensional vector representing stochastic input to the system. In the Kalman filter, these noise terms are restricted to zero-mean Gaussian white noise
- $\mathbf{G}(t)$ is an $n \times k$ system noise distribution matrix relating white noise to the state variables of the system

This means that the dynamic system is described in a stochastic sense using probability density functions (PDF). A more elaborate introduction to stochastic modelling is given in Appendix D. One underlying assumption in the Kalman filter is that the PDFs are Gaussian, such that they are completely defined in terms of the first and second order moments.

Practically, we define a state vector, $\mathbf{x}$, that contains some variables describing the state of the system. For our purposes, these variables are composed of position, velocity, attitude and sensor errors (e.g. bias, scale factor, etc.). In this probabilistic framework, the state of the system is described in terms of the mean and covariance of these variables and the dynamic system model governs the temporal evolution of these.

In addition to being Gaussian, the driving noise terms in $\mathbf{w}_s(t)$ are assumed to be zero-mean white noise processes. As argued in Appendix D.2, such a process is not physically realisable. However, it can be argued that any physical system has a certain frequency bandpass, meaning that input above this frequency has no useful effect. Within this system bandpass region, the system noise will typically have almost constant amplitude, making it very similar to the fictitious white noise [7, Sec. 1.4]. Regarding the assumption of Gaussianity, such an assumption is tractable, since it severely simplifies the mathematics involved. Additionally, as described in Appendix D.4.3, the dynamic system can be augmented using a shaping filter, in order to "shape" white noise into other stochastic processes.

The stochastic component, $\mathbf{G}(t)\,\mathbf{w}_s(t)$, is used to model the influence of sensor errors such as noise, scale factor and bias in terms of stochastic processes. However, since the deterministic component, $\mathbf{F}(t)\,\mathbf{x}(t)$, is often incomplete, meaning that things like aircraft vibrations, bending, wind busts, etc. are not included in the model, the stochastic component must additionally take these effects into account. Additionally, some mathematical and numerical approximations must also be accounted for.

In order to introduce new observations into the system, we can define a **measurement model**, relating some observations, $\mathbf{z}$, to the state variables, $\mathbf{x}$, as

$$\mathbf{z}(t_k) = \mathbf{H}(t_k)\,\mathbf{x}(t_k) + \mathbf{w}_m(t_k)\ , \tag{8.2}$$

where

$\mathbf{z}(t_k)$	is an m-dimensional measurement vector
$\mathbf{H}(t_k)$	is an $m \times n$ measurement matrix relating the state variables to the system output or observables
$\mathbf{w}_m(t_k)$	is an m-dimensional measurement noise vector

The observations are therefore assumed to be a linear combination of state variables, corrupted by noise. Again, the observations are assumed to be completely described in terms of mean and covariance. Notice that observations are typically introduced at discrete points in time.

In its basic form, the Kalman filter is based on linear system and measurement models, which may not be the case in practice. In our case, for example, the system model is formed using the navigation equations, which are not linear with respect to the state variables. This is handled by linearisation about some estimated trajectory, leading to an error model implementation. This is the basic idea behind the Extended Kalman Filter, which will be introduced later. Some cases, where the linear model prove inadequate, require special attention, but the linear model is in general desirable, since the mathematical theory and tools are much more complete and easily applicable.

8.1 An Overview of The Kalman Filter

The Kalman filter is denoted in [7] as an *optimal recursive data processing algorithm*. The framework is claimed to be optimal because it is able to incorporate all information available

in terms of system dynamics, sensor behaviour, system noise, measurement noise, uncertainties in the mathematical model and initial conditions. Rather than ignoring any information, the Kalman filter is able to incorporate it, regardless of its precision.

The numerical solution of (8.1) only exists in general when the system matrix, $\mathbf{F}$, is constant. Since this matrix is generally not constant, the forward propagation of the state vector, $\mathbf{x}$, is broken into pieces and updated recursively over short propagation intervals. The Kalman filter is therefore a recursive algorithm by nature. Additionally, it is important to realise that the Kalman filter basically consists of two phases:

1. **System-propagation phase**: The current mean and covariance is projected forward in time using the system model, which incorporates both system dynamics and stochastic driving terms

2. **Measurement-update phase**: As new measurement information becomes available, these are incorporated into the system based on some probabilistic measure of optimality. Since the stochastic driving terms will result in constantly increasing uncertainty on the state variables, this is necessary to maintain reliable estimates

The Kalman filter therefore has a "projection-correction" structure, which is often depicted cyclic as in Figure 8.6, alternating between forward propagation and measurement updates. This also means that measurement information is introduced recursively and need not be stored and re-processed every time new information is available. This is a very convenient feature for real-time applications, since only new data is processed on each iteration and old data is simply discarded.

In general, one cannot directly measure all of the variables describing the system, i.e. position, velocity, attitude, sensor errors and gravity. Estimates of these quantities therefore need to be inferred indirectly from the available data. Since a variety of sources will introduce noise into the system, we need to filter the noisy data. The Kalman filter accomplishes this by combining prior knowledge with new observations in order to minimize the error in a statistical sense. The Kalman framework is therefore a filter in the sense that it filters all the available information in order to derive statistically optimal estimates of the state variables.

8.1.1 The Kalman Filter Principle: An Example

In [7, Sec. 1.5], a simple example is used to demonstrate the working principle of the Kalman filter. Here, a similar example will be used to illustrate this using a one-dimensional example of navigation. Consider therefore the objective of determining the position of a train, moving along a railway track on a perfectly flat plane. The situation is depicted in Figure 8.1.

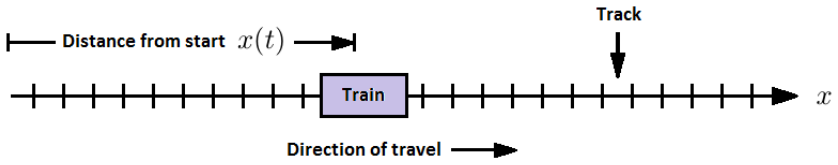

Figure 8.1: Illustration of one-dimensional navigation example.

Suppose that the initial position, $x_0 \equiv x\,(t_0)$, is known with some associated uncertainty, σ_{x_0}. Under the assumption that the underlying probability density function is Gaussian,

these two parameters completely define the probability density function, $f_{x_0}(x)$, illustrated in Figure 8.2.

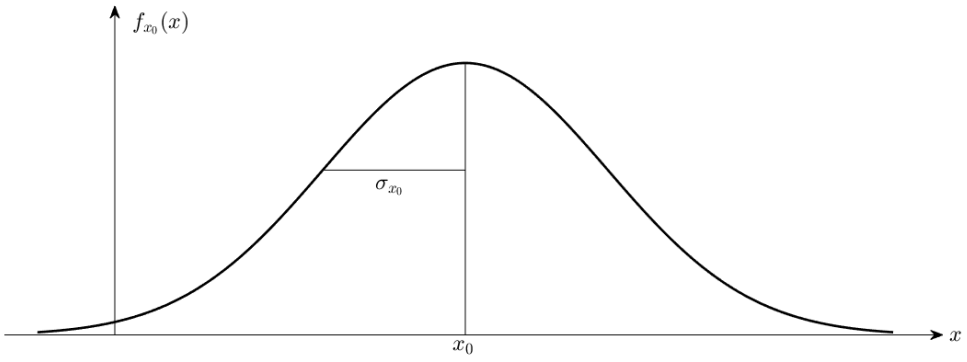

Figure 8.2: Initial probability density function governing the position, $x(t)$, at time $t = t_0$

Besides our initial estimate, x_0, on the position, we have some instrument capable of measuring the position, $z_0 \equiv z(t_0)$, with some associated uncertainty, σ_{z_0}, as illustrated in Figure 8.3. This could for example be a GNSS positioning device.

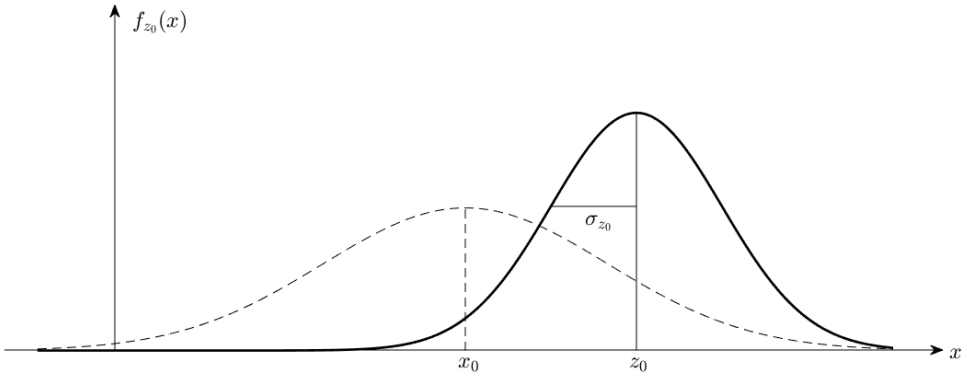

Figure 8.3: Probability density function governing the measurement, z_0, made at time $t = t_0$

In order to derive an optimal estimate, we want to combine the information from the measurement with the information of the initial estimate. Since the two density distributions are Gaussian, we can combine these in order to arrive at a new Gaussian density distribution with mean, μ, and standard deviation, σ, as

$$\mu = \frac{\sigma_{z_0}^2\, x_0 + \sigma_{x_0}^2\, z_0}{\sigma_{x_0}^2 + \sigma_{z_0}^2} \qquad \text{and} \qquad \sigma^2 = \left(\frac{1}{\sigma_{x_0}^2} + \frac{1}{\sigma_{z_0}^2} \right)^{-1}, \tag{8.3}$$

where σ is necessarily less than σ_{x_0} and/or σ_{z_0}, meaning that our confidence in the estimate has increased. This is illustrated in Figure 8.4. Because the probability densities are

Gaussian, the combined estimate

$$\hat{x}\left(t_0\right) = \mu \ , \tag{8.4}$$

represents both the mean, mode and median of the distribution. It corresponds to both the weighted least squares estimate and the maximum likelihood estimate. This indicates that it is optimal with respect to all of the common measures of optimality. The "updated" estimate, $\hat{x}\left(t_0\right)$, can be seen as a linear combination of the initial estimate, x_0, and the measurement, z_0. In a Kalman filtering setting, this is usually written as

$$\hat{x}\left(t_0\right) = \frac{\sigma_{z_0}^2 \, x_0 + \sigma_{x_0}^2 \, z_0}{\sigma_{x_0}^2 + \sigma_{z_0}^2} = x_0 + \frac{\sigma_{x_0}^2}{\sigma_{x_0}^2 + \sigma_{z_0}^2} \left(z_0 - x_0\right) = x_0 + K\left(t_0\right)\left(z_0 - x_0\right) \tag{8.5}$$

where

$$K\left(t_0\right) = \frac{\sigma_{x_0}^2}{\sigma_{x_0}^2 + \sigma_{z_0}^2} \ , \tag{8.6}$$

is the Kalman gain factor, determining the weight of the new measurement information. Similarly, we may write the "uncertainty update" as

$$\sigma_x^2\left(t_0\right) = \sigma_{x_0}^2 - K\left(t_0\right)\sigma_{x_0}^2 \ . \tag{8.7}$$

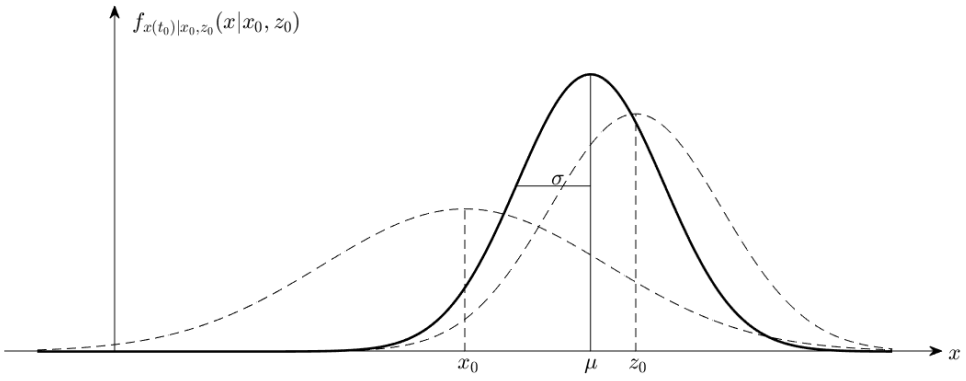

Figure 8.4: Probability density function after combining initial estimate with observation

This outlines the basic principle of the measurement update phase. In the system propagation phase, we need to propagate this estimate and associated uncertainty forward in time. This is usually done using a differential equation, governing the dynamics of the system. Assuming that the train is moving with constant velocity, a simple model of the train movement would be

$$\frac{\mathrm{d}}{\mathrm{dt}} x\left(t\right) = v + w \ , \tag{8.8}$$

where v is the train speed and w is a system noise term representing the uncertainty in our knowledge of the speed. This uncertainty term will account for effects of velocity disturbances,

physics not accounted for in the simple model and the like. The noise term is modelled as a zero-mean white Gaussian process with variance σ_w^2. From this model, we can derive the expressions

$$\hat{x}^- (t) = \hat{x} (t_0) + v (t - t_0) \qquad \text{and} \qquad \sigma_{x-}^2 (t) = \sigma_x^2 (t_0) + \sigma_w^2 (t - t_0) \ , \tag{8.9}$$

governing the temporal evolution of the mean and variance. This evolution is illustrated in Figure 8.5. As time progresses, the estimated position evolves according to the dynamic model and the probability density spreads out as a result of a decreasing confidence in the estimated position. The minus on the above values indicate that new measurement information has not yet been included into the model.

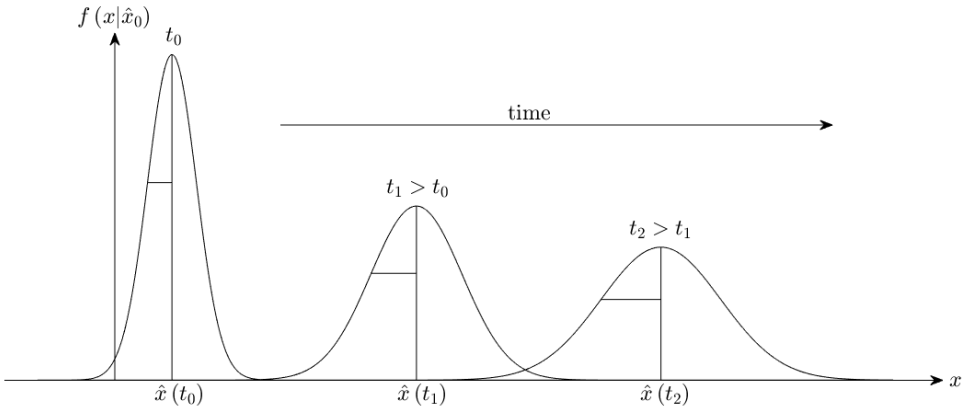

Figure 8.5: Propagation of the probability density function with time.

At some time, $t_1 > t_0$, we may again obtain some measurement of position, z_1, with associated uncertainty, σ_1. We can include this additional information into the system using (8.5) and (8.7) as

$$\begin{aligned} \hat{x} (t_1) &= x_0 + K (t_1) \left[z_1 - \hat{x}^- (t_1) \right] \quad \text{and} \\ \sigma_x^2 (t_1) &= \sigma_{x-}^2 (t_1) - K (t_1) \, \sigma_{x-}^2 (t_1) \ , \end{aligned} \tag{8.10}$$

with

$$K (t_1) = \frac{\sigma_{x-}^2 (t_1)}{\sigma_{x-}^2 (t_1) + \sigma_{z_1}^2} \ . \tag{8.11}$$

These mean and variance values may then be propagated forward in time until the next measurement update and so will the Kalman filter iterate until it runs out of data. For more intuitive interpretations of the Kalman filter, the reader is referred to [3, Sec. 5].

8.1.2 An Outline of the Kalman Filter Algorithm

As previously mentioned, the Kalman filter has a recursive nature, alternating between forward propagation of the state estimates and measurement updates. This is often depicted as in Figure 8.6. The Kalman filter framework revolves around a state vector, $\mathbf{x}$, comprising a set of state variables that adequately describes the system under consideration. The

dynamic system model (8.1) governs the temporal evolution of these states and the measurement model (8.2) relates the states to the observations. This is more elaborately described in Appendix D.4, where the corresponding discrete-time model is derived (D.60):

$$\mathbf{x}_{k+1} = \mathbf{\Phi}_k \, \mathbf{x}_k + \mathbf{\Gamma}_k \, \mathbf{w}_{s,k} \ , \tag{8.12a}$$

$$\mathbf{z}_k = \mathbf{H}_k \, \mathbf{x}_k + \mathbf{w}_{m,k} \ . \tag{8.12b}$$

The components are discretised as $\mathbf{x}_k \equiv \mathbf{x}(t_k)$ and $\mathbf{\Phi}_k$ is the transition matrix over the propagation interval, $\delta t = t_{k+1} - t_k$. The transition matrix is defined as

$$\mathbf{\Phi}_k \equiv \mathbf{\Phi}\left(t_{k+1}, t_k\right) = e^{\mathbf{F}_k \delta t} = \mathbf{I} + \sum_{n=1}^{\infty} \frac{(\mathbf{F}_k \delta t)^n}{n!} \ , \tag{8.13}$$

where the system matrix, $\mathbf{F}(t)$, is assumed constant over the propagation interval. The stochastic component, $\mathbf{\Gamma}_k \, \mathbf{w}_{s,k}$, is related to both the transition matrix and to the power spectral densities of the associated stochastic models as in (D.63). Both the transition matrix and stochastic component will here be derived using the method of Van Loan as described in Appendix D.4.2.

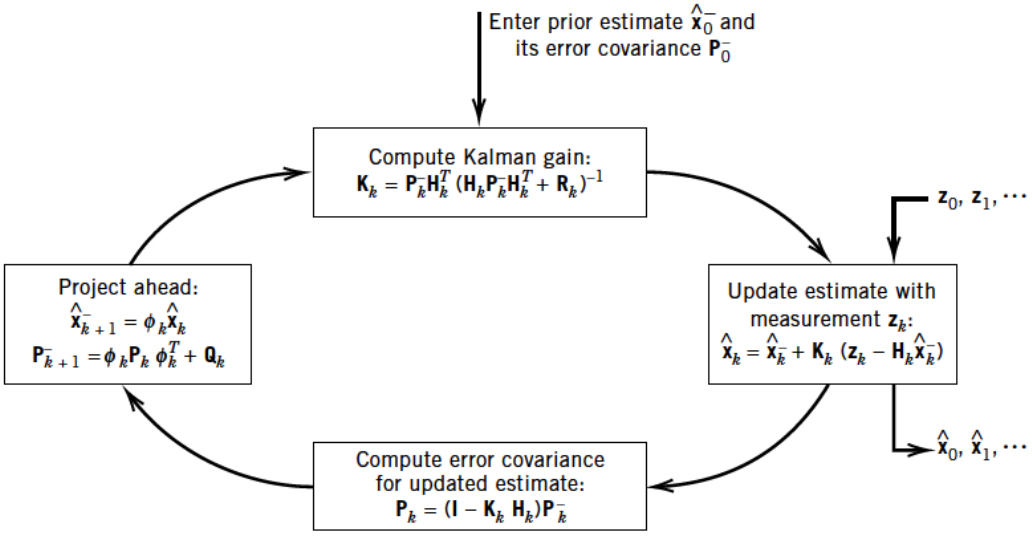

Figure 8.6: Illustration of a Kalman filter loop. Illustration is from [2].

Since the Kalman filter is a stochastic framework, the state variables are characterised in terms of both estimates, $\hat{\mathbf{x}}$, and covariance, $\mathbf{P}$, which both evolve as time progresses and updates when measurement information is included. The error covariance matrix does not only represent the uncertainties on the state variables, but also the degree of correlation between the errors on those estimates. This is important for three reasons [6, Sec. 3.1.1]:

1. It enables the error distribution, and therefore the associated confidence interval, to be fully represented,

2. The measurements do not always contain enough information to estimate all of the state elements independently. The available correlation information may enable some states to be estimated as linear combinations of other states, and

3. Correlations between errors can build up over the time intervals between measurements. Modelling this can enable one state to be determined from another (e.g. velocity from a series of positions).

In the following, the Kalman filter algorithm will be outlined in terms of step-by-step procedure, divided into a forward-propagation phase and a measurement update phase. It should be noted that the Kalman filter does not strictly have to be implemented in this order.

Forward-Propagation Phase

1. Form the system matrix, $\mathbf{F}_k$, for the current propagation interval. This matrix is generally a function of both time and other parameters that vary over time, such as position, velocity and even IMU observations themselves. It must therefore be formed at each iteration of the Kalman filter

2. Form spectral density matrix, $\mathbf{W}_{s,k}$, which is a diagonal matrix describing the power spectral amplitude of the associated stochastic model

3. Compute the transition matrix, $\mathbf{\Phi}_k$ and system noise covariance, $\mathbf{\Gamma}_k \, \mathbf{Q}_k \, \mathbf{\Gamma}_k^\top$, using the method of Van Loan described in Appendix D.4.2. These are formed using the system matrix, $\mathbf{F}_k$ and spectral density matrix, $\mathbf{W}_{s,k}$

4. Propagate the state estimates, $\hat{\mathbf{x}}_k$, and covariance matrix, $\mathbf{P}_k$, forward in time using (D.61):

$$\begin{aligned} \hat{\mathbf{x}}_{k+1}^- &= \mathbf{\Phi}_k \, \hat{\mathbf{x}}_k \\ \mathbf{P}_{k+1}^- &= \mathbf{\Phi}_k \, \mathbf{P}_k \, \mathbf{\Phi}_k^\top + \mathbf{\Gamma}_k \, \mathbf{Q}_k \, \mathbf{\Gamma}_k^\top \end{aligned} \tag{8.14}$$

It should be noted that the state vector and error covariance matrix need not be propagated forward at the same rate. Depending on the system model and the dynamics encountered, it may be advantageous to propagate these at different rates.

Measurement-Update Phase

5. Form the measurement matrix, $\mathbf{H}_k$, for the current measurement. This matrix generally varies depending on the type of measurement, but also with time and time varying parameters such as position and attitude

6. Form measurement innovation as

$$\delta \mathbf{z}_k^- = \mathbf{z}_k - \mathbf{H}_k \, \hat{\mathbf{x}}_k^- \, , \tag{8.15}$$

where $\mathbf{z}_k$ is the measurement and $\hat{\mathbf{x}}_k^-$ is the current state vector estimate

7. Form Kalman gain matrix using the error covariance matrix, $\mathbf{P}_k^-$, and measurement noise covariance matrix, $\mathbf{R}_k$, as (D.107):

$$\mathbf{K}_k = \mathbf{P}_k^- \, \mathbf{H}_k^\top \left(\mathbf{H}_k \, \mathbf{P}_k^- \, \mathbf{H}_k^\top + \mathbf{R}_k \right)^{-1} \ . \tag{8.16}$$

8. Update the state vector estimate using (D.98) as

$$\hat{\mathbf{x}}_k = \hat{\mathbf{x}}_k^- + \mathbf{K}_k \, \delta \mathbf{z}_k^- \tag{8.17}$$

9. Update the error covariance matrix using (D.102) as

$$\begin{aligned} \mathbf{P}_k &= \left(\mathbf{I} - \mathbf{K}_k \mathbf{H}_k \right) \mathbf{P}_k^- \left(\mathbf{I} - \mathbf{K}_k \mathbf{H}_k \right)^\top + \mathbf{K}_k \mathbf{R}_k \mathbf{K}_k^\top \\ &= \left(\mathbf{I} - \mathbf{K}_k \, \mathbf{H}_k \right) \mathbf{P}_k^- \\ &= \mathbf{P}_k^- - \mathbf{K}_k \left(\mathbf{H}_k \, \mathbf{P}_k^- \right) \end{aligned} \tag{8.18}$$

8.1.3 The Extended Kalman Filter

In many applications, including INS/GNSS integrated navigation systems, the state variables will not evolve in a linear manner, indicating that simple linear system models will not be adequate. Additionally, observations may not be linearly related to the state variables. In this case the system model (8.1) and measurement model (8.2), may be written as

$$\dot{\mathbf{x}}(t) = \mathbf{f} \left(\mathbf{x}(t), t \right) + \mathbf{G}(t) \, \mathbf{w}_s(t) \quad \text{and} \tag{8.19a}$$

$$\mathbf{z}(t_k) = \mathbf{h} \left(\mathbf{x}(t_k), t_k \right) + \mathbf{w}_m(t_k) \ , \tag{8.19b}$$

where $\mathbf{f}$ and $\mathbf{h}$ denote nonlinear functions of the state variables $\mathbf{x}$. One approach to handle the non-linearity is to simply linearise the equations about some reference trajectory. This approach is tractable since it allows us to use all the tools of the basic linear Kalman filter. Additionally, the linearisation approach has proven itself worthy in a wide range of applications. Let us therefore start by defining a reference trajectory, $\bar{\mathbf{x}}$, that satisfies the following relations

$$\dot{\bar{\mathbf{x}}}(t) = \mathbf{f} \left(\bar{\mathbf{x}}(t), t \right) \quad \text{and} \quad \bar{\mathbf{z}}(t_k) = \mathbf{h} \left(\bar{\mathbf{x}}(t_k), t_k \right) \ . \tag{8.20}$$

The objective is to linearise the equations about this trajectory such that the linearisation error, $\| \delta \mathbf{x}(t) \|$, with

$$\delta \mathbf{x}(t) \equiv \mathbf{x}(t) - \bar{\mathbf{x}}(t) \ , \tag{8.21}$$

is small within the range of interest and the linearisation is thus a valid approximation.

The System Model

Linearisation of the system model is accomplished by expanding the function, $\mathbf{f} \left(\mathbf{x}(t), t \right)$, in a Taylor series about the reference trajectory, $\bar{\mathbf{x}}(t)$, and truncating at first order as

$$\begin{aligned} \mathbf{f} \left(\mathbf{x}(t), t \right) &= \mathbf{f} \left(\bar{\mathbf{x}}(t), t \right) + \nabla \mathbf{f} \left(\bar{\mathbf{x}}(t), t \right) \, \delta \mathbf{x} + \nabla^2 \mathbf{f} \left(\bar{\mathbf{x}}(t), t \right) \, \delta \mathbf{x}^2 + \cdots \\ &\approx \mathbf{f} \left(\bar{\mathbf{x}}(t), t \right) + \nabla \mathbf{f} \left(\bar{\mathbf{x}}(t), t \right) \, \delta \mathbf{x} \ , \end{aligned} \tag{8.22}$$

with

$$\{\nabla \mathbf{f}\left(\bar{\mathbf{x}}(t), t\right)\}_{i,j} \equiv \left.\frac{\partial \mathbf{f}_i\left(\mathbf{x}(t), t\right)}{\partial x_j}\right|_{\mathbf{x}=\bar{\mathbf{x}}(t)} . \tag{8.23}$$

Inserting this into the system model, we obtain the expression

$$\begin{aligned} \dot{\mathbf{x}}(t) = \dot{\bar{\mathbf{x}}}(t) + \delta\dot{\mathbf{x}}(t) &\approx \mathbf{f}\left(\bar{\mathbf{x}}(t), t\right) + \nabla \mathbf{f}\left(\bar{\mathbf{x}}(t), t\right)\, \delta\mathbf{x} + \mathbf{G}(t)\, \mathbf{w}_s(t) \\ \Rightarrow \qquad \delta\dot{\mathbf{x}}(t) &= \nabla \mathbf{f}\left(\bar{\mathbf{x}}(t), t\right)\, \delta\mathbf{x} + \mathbf{G}(t)\, \mathbf{w}_s(t) , \end{aligned} \tag{8.24}$$

being a first-order (linear) approximation of how the error, $\delta\dot{\mathbf{x}}(t)$, between the true and reference trajectories, evolve with time. Assuming that the Jacobian, $\nabla \mathbf{f}\left(\bar{\mathbf{x}}(t), t\right) = \nabla \mathbf{f}$, is constant over the propagation interval, the error state vector, $\delta\mathbf{x}$, and associated covariance matrix, $\mathbf{P}$, can be updated over the propagation interval, $\delta t = t_k - t_{k-1}$, as

$$\delta\mathbf{x}_k = \mathbf{\Phi}_{k-1}\, \delta\mathbf{x}_{k-1} \tag{8.25a}$$

$$\mathbf{P}_k = \mathbf{\Phi}_{k-1}\, \mathbf{P}_{k-1}\, \mathbf{\Phi}_{k-1}^\top + \mathbf{\Gamma}_{k-1}\, \mathbf{Q}_{k-1}\, \mathbf{\Gamma}_{k-1}^\top , \tag{8.25b}$$

where $\delta\mathbf{x}_k \equiv \delta\mathbf{x}(t_k)$ and $\mathbf{P}_k \equiv \mathbf{P}(t_k)$. The transition matrix, $\mathbf{\Phi}_{k-1}$ is formed as

$$\mathbf{\Phi}_{k-1} = e^{\nabla \mathbf{f}\, \delta t} , \tag{8.26}$$

and $\mathbf{\Gamma}_{k-1}\, \mathbf{Q}_{k-1}\, \mathbf{\Gamma}_{k-1}^\top$ is the noise component. Having propagated the error state, $\delta\mathbf{x}$, forward in time, the total state vector, $\mathbf{x}$, can be retrieved as

$$\mathbf{x}_k = \bar{\mathbf{x}}_k + \delta\mathbf{x}_k , \tag{8.27}$$

whereas the error covariance matrix, $\mathbf{P}$, is valid for both the error state and total state.

Practically, the reference trajectory is generated using IMU observations along with some initial values. The differential equations (8.20) are therefore the navigation equations introduced in Section 5.2. The IMU observations are integrated outside the Kalman filter framework and not introduced as observations in the system.

The Measurement Model

In the case that the measurement model is nonlinear, a similar linearisation approach can be used where

$$\mathbf{h}\left(\mathbf{x}(t_k), t_k\right) \approx \mathbf{h}\left(\bar{\mathbf{x}}(t_k), t_k\right) + \nabla \mathbf{h}\left(\bar{\mathbf{x}}(t_k), t_k\right)\, \delta\mathbf{x} , \tag{8.28}$$

such that the measurement innovation becomes

$$\delta\mathbf{z}(t_k) = \mathbf{z}(t_k) - \bar{\mathbf{z}}(t_k) = \nabla \mathbf{h}\left(\bar{\mathbf{x}}(t_k), t_k\right)\, \delta\mathbf{x} + \mathbf{w}_m(t_k) . \tag{8.29}$$

To this end, it should be noticed that the measurement innovation can be evaluated without the use of linearisation as

$$\delta\mathbf{z}(t_k) = \mathbf{z}(t_k) - \mathbf{h}\left(\bar{\mathbf{x}}(t_k), t_k\right) , \tag{8.30}$$

where $\mathbf{z}(t_k)$ is the actual observation and $\mathbf{h}\left(\bar{\mathbf{x}}(t_k), t_k\right)$ is the measurement model evaluated using $\bar{\mathbf{x}}(t_k)$. The linearisation is however exploited to form the Kalman gain from (D.107) as

$$\mathbf{K}_k = \mathbf{P}_k^- \, \mathbf{H}_k^\top \left(\mathbf{H}_k \, \mathbf{P}_k^- \, \mathbf{H}_k^\top + \mathbf{R}_k \right)^{-1} \ , \tag{8.31}$$

where $\mathbf{P}_k^-$ is the state covariance before the measurement update, $\mathbf{R}_k$ is the measurement covariance matrix and

$$\mathbf{H}_k \equiv \nabla \mathbf{h} \left(\bar{\mathbf{x}}(t_k), t_k \right) \ . \tag{8.32}$$

The error or total state vector are updated using (D.98) as

$$\hat{\mathbf{x}}_k = \hat{\mathbf{x}}_k^- + \mathbf{K}_k \, \delta \mathbf{z}_k \quad \text{or} \quad \delta \hat{\mathbf{x}}_k = \mathbf{K}_k \, \delta \mathbf{z}_k \ , \tag{8.33}$$

and the error covariance matrix is updated using (D.102) as

$$\mathbf{P}_k = \mathbf{P}_k^- - \mathbf{K}_k \left(\mathbf{H}_k \, \mathbf{P}_k^- \right) \ . \tag{8.34}$$

As already mentioned, IMU observations are not fed to the Kalman filter as observations, but instead used to derive the reference trajectory. Since IMU measurements are usually output at a very high rate, the formulation of the Kalman gain for each IMU observations would be computationally expensive. Instead, GNSS observations are fed to the Kalman filter as measurement updates, since GNSS observations are usually made at a much lower rate.

The Extended Kalman Filter

In the Extended Kalman Filter (EKF), the reference trajectory is defined to be equal to the estimated trajectory [4, Sec. 5.10.5.2]:

$$\bar{\mathbf{x}}(t) = \hat{\mathbf{x}}(t) \ , \tag{8.35}$$

which is accomplished by replacing $\bar{\mathbf{x}}(t)$ by $\hat{\mathbf{x}}(t)$ in all of the equations above. The computation of the Kalman gain, $\mathbf{K}_k$, therefore becomes a function of the state estimate, $\hat{\mathbf{x}}(t)$, which is essentially a stochastic process. As a result, $\mathbf{K}_k$, also becomes a stochastic process, introducing another instability factor in the approximation. On the other hand, the Kalman filter estimates are usually closer to the "true" state than any other predefined trajectory. In this case, the EKF will have a superior performance since the linearisation will be a more accurate approximation.

In general, the validity of the linearisation is dependent upon the smallness of errors. This can cause potential instability problems and resulting divergence of the result. An EKF implementation therefore requires careful tuning of the individual terms in the Kalman filter and is especially sensitive to the initialisation of the covariance matrix.

One approach to improving the linear approximation is to use an **error state implementation** rather than a total state implementation. Assuming that the estimated trajectory closely resembles the true trajectory, it can be argued that the error on the state variables, i.e. position, velocity, attitude and sensor errors, evolve more slowly with time than the actual variables themselves, leading to a better linear approximation. The EKF framework developed in this section is already capable of handling such an error state implementation. Propagation of the error state and covariance is accomplished using (8.25). However, in the error state implementation it is not the navigation equations that need to be linearised, but rather the error dynamics equations that was introduced in Section 6.2 and derived in Appendix C.3.

8.2 Additional Tools of the Kalman Filter

With the basic principles of the Kalman filter outlined, this section will introduce some additional useful tools that are of practical interest. Most importantly, the Kalman smoother will be introduced, which will be applied to all datasets in order to improve the results. The Kalman smoother also removes the need for applying any additional filtering to gravity estimates.

8.2.1 Forward-Backward Processing and Kalman Smoothing

With careful implementation, the Kalman filter need no modifications in order to iterate backwards in time. This is sometimes useful in practice if the observations are not complete over an entire survey or broken into pieces. It also allows for an evaluation of the results, since the forward and backward solution can be compared.

Since the forward Kalman filter state estimate, $\hat{\mathbf{x}}_k$, is based on all the information on the interval $0 \leq t \leq t_k$, and the backward Kalman filter estimate, $\hat{\mathbf{x}}_{b,k}$, is based on all the information on the interval $t_k \leq t \leq T$, the two estimates have uncorrelated errors. They may therefore be combined in order to yield an optimal estimate

$$\hat{\mathbf{x}}_{k|T} = \mathbf{A}\,\hat{\mathbf{x}}_k + \mathbf{A}'\,\hat{\mathbf{x}}_{b,k}\ , \tag{8.36}$$

where $\mathbf{A}$ and $\mathbf{A}'$ are weighting matrices. This is known as **optimal linear smoothing** and is customary within the Kalman filtering framework.

In [5, Sec. 5.1] the weighting matrices are derived based on minimizing the diagonal elements of the error covariance matrix, i.e. least squares approach. This leads to the expressions

$$\hat{\mathbf{x}}_{k|T} = \mathbf{P}_{k|T}\left(\mathbf{P}_k^{-1}\,\hat{\mathbf{x}}_k + \mathbf{P}_{b,k}^{-1}\,\hat{\mathbf{x}}_{b,k}\right) \tag{8.37a}$$

$$\mathbf{P}_{k|T} = \left(\mathbf{P}_k^{-1} + \mathbf{P}_{b,k}^{-1}\right)^{-1}\ , \tag{8.37b}$$

for the state vector and error covariance, respectively. This approach is known as the **forward-backward filter** and it should be noticed that the two solutions are treated independent, meaning that the backward filter cannot be initialised using estimates from the forward filter.

8.2.2 The Rauch-Tung-Striebel Smoother

The Rauch-Tung-Striebel (RTS) smoother is another form of the forward-backward filter. When smoothed estimates are required at every point, the RTS smoother is more computer efficient, since it avoids performing the backward filtering directly. For the RTS smoother, a forward run of the Kalman filter is required. During this run, the state vector estimates, $\hat{\mathbf{x}}_k^-$ and $\hat{\mathbf{x}}_k^+$, before and after each measurement update are stored. Additionally, the error covariance estimates, $\mathbf{P}_k^-$ and $\mathbf{P}_k^+$, are stored along with the transition matrix, $\mathbf{\Phi}_k$, from epoch k to $k+1$. After the forward run is complete, the RTS smoother is initialised using the final forward estimates as

$$\hat{\mathbf{x}}_{N|T} = \hat{\mathbf{x}}_N^+ \tag{8.38a}$$

$$\mathbf{P}_{N|T} = \mathbf{P}_N^+\ , \tag{8.38b}$$

and the smoothed estimates are generated by iterating backwards in time as

$$\hat{\mathbf{x}}_{k|T} = \hat{\mathbf{x}}_k^+ + \mathbf{A}_k \left(\hat{\mathbf{x}}_{k+1|T} - \hat{\mathbf{x}}_{k+1}^- \right) \tag{8.39a}$$

$$\mathbf{P}_{k|T} = \mathbf{P}_k^+ + \mathbf{A}_k \left(\mathbf{P}_{k+1|T} - \mathbf{P}_{k+1}^- \right) \mathbf{A}_k^\top \tag{8.39b}$$

$$\mathbf{A}_k = \mathbf{P}_k^+ \, \mathbf{\Phi}_k^\top \, \left(\mathbf{P}_{k+1}^- \right)^{-1} \ . \tag{8.39c}$$

This procedure is less requiring than running the backward filter directly, although additional storage space is required for the forward run. Due to large differences in the order of magnitude of the state variables and their error covariance, numerical instability might destabilise the smoother. In this case, the estimates can be re-scaled using a scaling matrix, $\mathbf{S}$. This scaling matrix is applied to all the components as

$$\begin{array}{rclcrcl} \hat{\mathbf{x}}_k^+ & = & \mathbf{S}\,\hat{\mathbf{x}}_k^+ & \text{and} & \hat{\mathbf{x}}_k^- & = & \mathbf{S}\,\hat{\mathbf{x}}_k^- \\ \hat{\mathbf{P}}_k^+ & = & \mathbf{S}\,\hat{\mathbf{P}}_k^+\,\mathbf{S} & \text{and} & \hat{\mathbf{P}}_k^- & = & \mathbf{S}\,\hat{\mathbf{P}}_k^-\,\mathbf{S} \\ \mathbf{\Phi}_k & = & \mathbf{S}\,\mathbf{\Phi}_k\,\mathbf{S}^{-1} & , & & & \end{array} \tag{8.40}$$

before the smoothing is performed. The scaling then needs to be reversed after smoothing as

$$\hat{\mathbf{x}}_{k|T} = \mathbf{S}^{-1}\,\hat{\mathbf{x}}_{k|T} \quad \text{and} \quad \hat{\mathbf{P}}_{k|T} = \mathbf{S}^{-1}\,\hat{\mathbf{P}}_{k|T}\,\mathbf{S}^{-1} \ . \tag{8.41}$$

8.2.3 The Mahalanobis Distance

As we have seen, the Kalman gain is a weighting factor determining the relative influence of state estimates and new measurement information. From (8.16), the Kalman gain is computed as

$$\mathbf{H}_k\,\mathbf{K}_k = \frac{\mathbf{H}_k\,\mathbf{P}_k^-\,\mathbf{H}_k^\top}{\mathbf{H}_k\,\mathbf{P}_k^-\,\mathbf{H}_k^\top + \mathbf{R}_k} \ , \tag{8.42}$$

where $\mathbf{P}_k^-$ represents the confidence in the state estimates and $\mathbf{R}_k$ the confidence in the observations. With respect to (8.16), an additional factor, $\mathbf{H}_k$, appears on both sides of the above equation. The measurement matrix, $\mathbf{H}_k$, relates the state vector to the observations and essentially has the effect of transforming between state and measurement space. In the above equation, the Kalman gain is therefore expressed in the measurement space. Multiplication of $\mathbf{H}_k^\top$ would have the effect of transforming into state space.

In the above equation, $\mathbf{H}_k\,\mathbf{P}_k^-\,\mathbf{H}_k^\top$, is the covariance of the state estimates, expressed in the measurement space. The Kalman gain is therefore the ratio between the confidence in the state estimates (numerator) and the combined confidence in the state estimates and observations (denominator). Since the stochastic models applied within the Kalman filter will influence the error covariance matrix, $\mathbf{P}_k^-$, these will indirectly influence the relative weighting between state estimates and observations.

As the stochastic models are dictated by the user, careful tuning is required in order to achieve a proper weighting of the observations. It can therefore be useful to test whether the measurement innovations (8.15)

$$\delta\mathbf{z}_k^- = \mathbf{z}_k - \mathbf{H}_k\,\hat{\mathbf{x}}_k^- \ , \tag{8.43}$$

are within the confidence bounds defined by the confidence region, $\mathbf{H}_k \mathbf{P}_k^- \mathbf{H}_k^\top + \mathbf{R}_k$. Theoretically, the distribution of measurement innovations should match the confidence region. To this end it is useful to track the Mahalanobis distance

$$d_M = \sqrt{\left(\delta \mathbf{z}_k^-\right)^\top \left(\mathbf{H}_k \mathbf{P}_k^- \mathbf{H}_k^\top + \mathbf{R}_k\right)^{-1} \delta \mathbf{z}_k^-} \,, \tag{8.44}$$

which is a measure of the distance between a point and a distribution. The distance is zero, if the point is at the mean of the distribution, one if the point is one standard deviation away and so forth. This measure is therefore an indication of whether the relative weighting between state estimates and observations is reasonable and can also be used to identify possible bad observations.

9 Integrated INS/GNSS Navigation Algorithm

In Section 5 the concept of inertial navigation was introduced. The combined system of IMU and an inertial navigation processor will here be denoted an Inertial Navigation System (INS). This section will describe how the INS can be combined with GNSS observations within the Kalman filter framework. The GNSS observations can be processed independently to yield position and velocity, whereas the INS yields independent estimates of attitude, velocity and position. Since the two systems have complementary properties it is desirable to combine the observations:

- The GNSS system is characterised by a long-term stability, but the accuracy is poor with respect to an INS, at least at short time intervals. Additionally, the output rate of a GNSS system is usually much lower than the IMU. Finally, the GNSS system is dependent on communication with satellites, which makes it sensitive to signal disturbances

- The IMU has a poor long-term stability, since the errors are integrated as time progresses. On the other hand, the short-term accuracy is superior to GNSS, provided the observations and processing algorithm are precise. Once initialised, the INS requires no external information, making it invulnerable to signal disturbances

An integrated INS/GNSS navigation solution therefore produces a more continuous, high-resolution, complete navigation solution with superior long- and short-term accuracy. The GNSS observations prevent the INS solution from drifting off and continually calibrates the inertial sensors, while the IMU observations smooth the GNSS solution and bridges signal outages [6, Sec. 14].

9.1 Integration Architecture

Let us begin this section with outlining the basic set-up. We have two measurement systems, which are basically capable of performing navigation themselves. The IMU and GNSS observations can be combined on several levels. Most commonly, an inertial navigation solution is produced outside the integration algorithm, i.e. outside the Kalman filter. The GNSS observations are introduced as measurement updates in the integration algorithm and can be introduced on several levels:

1. **Loosely coupled integration** uses the GNSS velocity and/or position solution as input to the Kalman filter. This is a cascaded architecture where the GNSS observations have already been pre-processed.

2. **Tightly coupled integration** uses the GNSS pseudo-range and pseudo-range-rate measurements as input to the Kalman filter.

3. **Deeply coupled integration** introduces GNSS at its most basic level by including GNSS signal tracking into the Kalman filter.

This dissertation uses the loosely coupled approach, meaning that GNSS observations are processed into velocity and position estimates using some other processing software. For this, the NovAtel Waypoint software suite was used. For other integration architectures, the

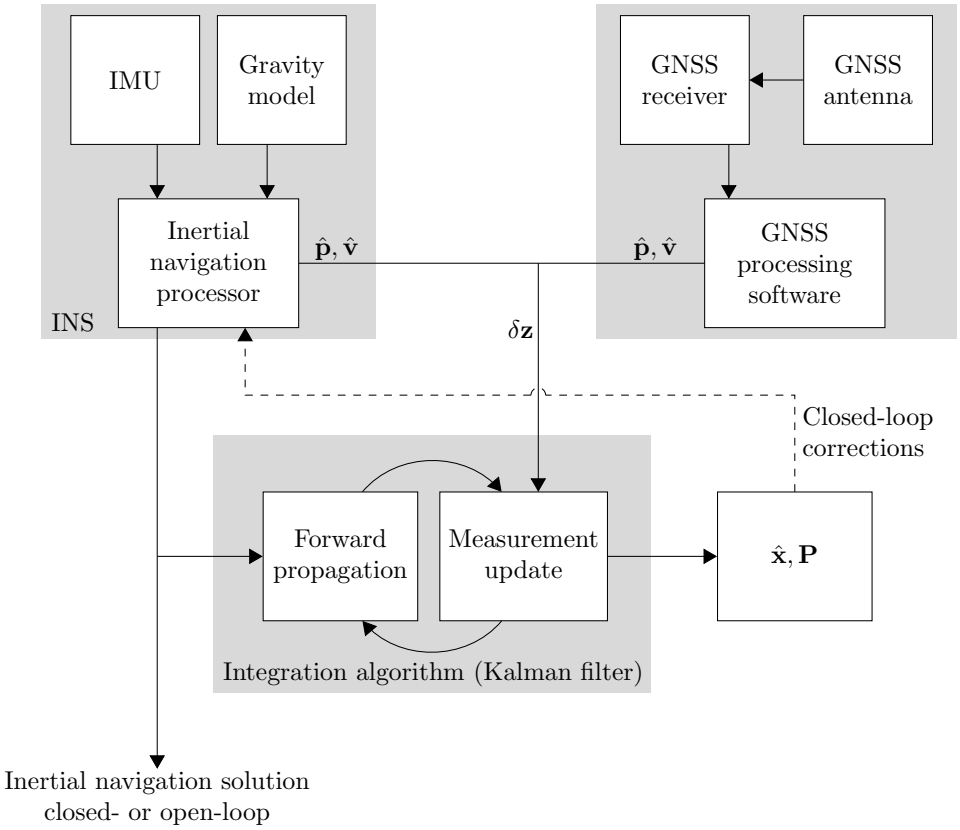

Figure 9.1: Integration architecture of the loosely coupled INS/GNSS processing scheme

reader is referred to [6, Sec. 14]. A schematic overview of the loosely coupled INS/GNSS architecture is illustrated in Figure 9.1.

Basically, the IMU and GNSS observations are processed separately and produce two independent navigation solutions. These two solutions are combined within the Kalman filter framework, in order to derive statistically optimal navigation estimates. In the integration algorithm an error-state implementation of the EKF introduced in Section 8.1.3 is used. In the n-frame implementation of a strapdown system, the basic state vector will be

$$\delta\mathbf{x} = [\ \delta\boldsymbol{\psi}^n_{nb}\ ,\ \delta\mathbf{v}^n\ ,\ \delta\mathbf{p}\ ,\ \delta\mathbf{b}_a\ ,\ \delta\mathbf{b}_g\ ]^\top\ , \tag{9.1}$$

where $\delta\boldsymbol{\psi}^n_{nb}$ is the attitude error in terms of Euler angles, i.e. the bank, elevation and heading angle, $\delta\mathbf{v}^n$ is the velocity error with respect to the ECEF reference frame, but resolved about the north, east and down axes of the n-frame, $\delta\mathbf{p} = (\delta\phi, \delta\lambda, \delta h)$ are errors on the geodetic coordinates and $\delta\mathbf{b}_a$ and $\delta\mathbf{b}_g$ are errors the accelerometer and gyroscope biases, respectively.

The Kalman filter will therefore derive estimates of the errors on the navigation solution and sensor biases, i.e. the components of the above vector. These estimates can be fed back to the inertial navigation processor in order to correct the observations and the navigation solution. This is known as **closed-loop implementation** and increases the stability of the EKF by minimizing the navigation errors and thus assuring that the linear approximation is

valid. On the other hand, an open-loop implementation may sometimes be useful to maintain a pure INS solution for integrity monitoring, for example when a high-quality INS is used with a low-quality integration algorithm. Here, a closed-loop implementation will be pursued. Depending on the implementation, the attitude can be corrected using either [6, Eq. 14.7] or [6, Eq. E.45]:

$$\hat{\mathbf{C}}_b^n(+) = \left(\mathbf{I}_3 - \left[\delta\hat{\boldsymbol{\psi}}_{nb}^n\times\right]\right)\hat{\mathbf{C}}_b^n(-) \quad \text{or} \tag{9.2a}$$

$$\hat{\mathbf{q}}_b^n(+) = \begin{pmatrix} 1 \\ -\frac{1}{2}\delta\hat{\boldsymbol{\psi}}_{nb}^n \end{pmatrix} \circ \hat{\mathbf{q}}_b^n(-)\ , \tag{9.2b}$$

where the suffixes $(-)$ and $(+)$ denote before and after the correction, respectively. The velocity and position estimates are corrected as

$$\hat{\mathbf{v}}^n(+) = \hat{\mathbf{v}}^n(-) - \delta\hat{\mathbf{v}}^n \tag{9.3}$$

and

$$\hat{\mathbf{p}}(+) = \hat{\mathbf{p}}(-) - \delta\hat{\mathbf{p}}\ , \tag{9.4}$$

while the sensor bias estimates are corrected as

$$\hat{\mathbf{b}}_a(+) = \hat{\mathbf{b}}_a(-) + \delta\hat{\mathbf{b}}_a \quad \text{and} \quad \hat{\mathbf{b}}_g(+) = \hat{\mathbf{b}}_g(-) + \delta\hat{\mathbf{b}}_g \tag{9.5}$$

and applied to the accelerometer and gyroscope observations as

$$\mathbf{f}^b(+) = \mathbf{f}^b(-) - \hat{\mathbf{b}}_a(+) \quad \text{and} \quad \boldsymbol{\omega}_{ib}^b(+) = \boldsymbol{\omega}_{ib}^b(-) - \hat{\mathbf{b}}_g(+)\ . \tag{9.6}$$

These corrections are applied after each measurement update, in order to keep the inertial navigation errors at a minimum. In this way, the GNSS observations continuously re-calibrate the IMU observations and re-initialises the navigation solution. Notice that the navigation solution is only updated at the measurement time, t_k, while the bias estimates are used to correct the IMU observations from the current epoch until the next measurement update. After correction, the error state vector, $\delta\hat{\mathbf{x}}$, should be zeroed, since the estimated errors are now all zero.

9.1.1 The System Model

Using an error-state implementation with the state vector (9.1), the continuous-time system model from (8.1) becomes

$$\begin{array}{rcccccc} \delta\dot{\mathbf{x}}^n(t) & = & & \mathbf{F}^n(t) & & \delta\mathbf{x}^n(t) & + \quad \mathbf{G}(t) \quad \mathbf{w}_s(t) \end{array}$$

$$\frac{\mathrm{d}}{\mathrm{d}t}\left[\begin{array}{c} \delta\boldsymbol{\psi}_{nb}^n \\ \delta\mathbf{v}^n \\ \hline \delta\mathbf{p} \\ \hline \delta\mathbf{b}_a \\ \delta\mathbf{b}_g \end{array}\right] = \left[\begin{array}{ccc|cc} -\boldsymbol{\Omega}_{in}^n & \mathbf{F}_{12}^n & \mathbf{F}_{13}^n & \mathbf{0}_3 & \mathbf{C}_b^n \\ -[\mathbf{f}^n\times] & \mathbf{F}_{22}^n & \mathbf{F}_{23}^n & \mathbf{C}_b^n & \mathbf{0}_3 \\ \mathbf{0}_3 & \mathbf{F}_{32}^n & \mathbf{F}_{33}^n & \mathbf{0}_3 & \mathbf{0}_3 \\ \hline \mathbf{0}_3 & \mathbf{0}_3 & \mathbf{0}_3 & \mathbf{0}_3 & \mathbf{0}_3 \\ \mathbf{0}_3 & \mathbf{0}_3 & \mathbf{0}_3 & \mathbf{0}_3 & \mathbf{0}_3 \end{array}\right]\left[\begin{array}{c} \delta\boldsymbol{\psi}_{nb}^n \\ \delta\mathbf{v}^n \\ \hline \delta\mathbf{p} \\ \hline \delta\mathbf{b}_a \\ \delta\mathbf{b}_g \end{array}\right] + \left[\begin{array}{cc} \mathbf{I}_3 & \mathbf{0}_3 \\ \mathbf{0}_3 & \mathbf{I}_3 \\ \mathbf{0}_3 & \mathbf{0}_3 \\ \hline \mathbf{0}_3 & \mathbf{0}_3 \\ \mathbf{0}_3 & \mathbf{0}_3 \end{array}\right]\left[\begin{array}{c} \mathbf{w}_{\text{att}} \\ \mathbf{w}_{\text{vel}} \end{array}\right] \tag{9.7}$$

where the system matrix, $\mathbf{F}^n(t)$, is composed of the error dynamics equations from Section 6.2.2, Eq. (6.17). The components of this matrix are dependent on attitude, velocity, position

and IMU observations. It is therefore formed using output from both IMU and the inertial navigation processor, as indicated in Figure 9.1.

The system noise components represented by the noise vector, $\mathbf{w}_s$, generates white noise that propagates onto the state variables through the system noise distribution matrix, $\mathbf{G}$. In the above equation, stochastic driving noise only affects the attitude and velocity components. Effectively this means that the white noise on the gyro and accelerometer observations are modelled as random walk processes on the attitude and velocity, while the bias components, $\delta\mathbf{b}_a$ and $\delta\mathbf{b}_g$, are modelled as random constants. By adding system noise to the bias components, the bias variation will also be modelled as random walk processes.

Since the system noise vector, $\mathbf{w}_s$, only contains white noise processes, the basic set-up only allows for modelling random constant and random walk processes. Modelling bias variation as a Gauss-Markov process requires the introduction of a "shaping filter", that shapes white noise into a Gauss-Markov process. The shaping filter usually requires the introduction of additional state variables, i.e. state augmentation as introduced in Appendix D.4.3. As an example, consider the separation of accelerometer bias into static and dynamic components, $\mathbf{b}_{a,s}$ and $\mathbf{b}_{a,d}$, such that the state vector becomes

$$\delta\mathbf{x} = [\ \delta\boldsymbol{\psi}^n_{nb}\ ,\ \delta\mathbf{v}^n\ ,\ \delta\mathbf{p}\ ,\ \delta\mathbf{b}_{a,s}\ ,\ \delta\mathbf{b}_{a,d}\ ,\ \delta\mathbf{b}_g\ ]^\top\ . \tag{9.8}$$

We can then model the static component as a random constant and the dynamic component as a first-order Gauss-Markov model by forming the system matrix

$$\mathbf{F}^n = \left[\begin{array}{ccc|ccc} -\boldsymbol{\Omega}^n_{in} & \mathbf{F}^n_{12} & \mathbf{F}^n_{13} & \mathbf{0}_3 & \mathbf{0_3} & \mathbf{C}^n_b \\ -[\mathbf{f}^n\times] & \mathbf{F}^n_{22} & \mathbf{F}^n_{23} & \mathbf{C}^n_b & \mathbf{C}^n_b & \mathbf{0}_3 \\ \mathbf{0}_3 & \mathbf{F}^n_{32} & \mathbf{F}^n_{33} & \mathbf{0}_3 & \mathbf{0}_3 & \mathbf{0}_3 \\ \hline \mathbf{0}_3 & \mathbf{0}_3 & \mathbf{0}_3 & \mathbf{0}_3 & \mathbf{0}_3 & \mathbf{0}_3 \\ \mathbf{0}_3 & \mathbf{0}_3 & \mathbf{0}_3 & \mathbf{0}_3 & \mathbf{0}_3 & -\boldsymbol{\beta} \\ \mathbf{0}_3 & \mathbf{0}_3 & \mathbf{0}_3 & \mathbf{0}_3 & \mathbf{0}_3 & \mathbf{0}_3 \end{array}\right]\ , \tag{9.9}$$

where $\boldsymbol{\beta}$ is a diagonal matrix containing the correlation parameters (inverse of correlation time) for each of the three bias components. The system noise distribution matrix and system noise vector then becomes

$$\mathbf{G} = \begin{bmatrix} \mathbf{I}_3 & \mathbf{0}_3 & \mathbf{0}_3 \\ \mathbf{0}_3 & \mathbf{I}_3 & \mathbf{0}_3 \\ \mathbf{0}_3 & \mathbf{0}_3 & \mathbf{0}_3 \\ \mathbf{0}_3 & \mathbf{0}_3 & \mathbf{0}_3 \\ \mathbf{0}_3 & \mathbf{0}_3 & \mathbf{I}_3 \\ \mathbf{0}_3 & \mathbf{0}_3 & \mathbf{0}_3 \end{bmatrix} \qquad \text{and} \qquad \mathbf{w}_s = \begin{bmatrix} \mathbf{w}_{\text{att}} \\ \mathbf{w}_{\text{vel}} \\ \mathbf{w}_{a,d} \end{bmatrix}\ , \tag{9.10}$$

where $\mathbf{w}_{a,d}$ is the white noise process, driving the Gauss-Markov process.

In order to proceed, the continuous-time system model is sampled at discrete points in time in order to arrive at the corresponding discrete-time model (D.60a)

$$\delta\mathbf{x}_{k+1} = \boldsymbol{\Phi}_k\,\delta\mathbf{x}_k + \boldsymbol{\Gamma}_k\,\mathbf{w}_{s,k}\ , \tag{9.11}$$

where the transition matrix, $\boldsymbol{\Phi}_k$, is defined as

$$\boldsymbol{\Phi}_k \equiv \boldsymbol{\Phi}\left(t_{k+1}, t_k\right) = e^{\mathbf{F}_k \delta t} = \mathbf{I} + \sum_{n=1}^{\infty} \frac{\left(\mathbf{F}_k \delta t\right)^n}{n!} \,, \tag{9.12}$$

and the discrete-time noise component is related to the continuous-time model as (D.63)

$$\boldsymbol{\Gamma}_k \, \mathbf{Q}_k \, \boldsymbol{\Gamma}_k^\top \equiv \int_{t_k}^{t_{k+1}} e^{\mathbf{F}_k \left(t_{k+1} - t'\right)} \, \mathbf{G}_k \, \mathbf{W}_{s,k} \, \mathbf{G}_k^\top e^{\mathbf{F}_k^\top \left(t_{k+1} - t'\right)} \, \mathrm{d}t' \,. \tag{9.13}$$

In both cases, the system matrix, $\mathbf{F}$, and system noise distribution matrix, $\mathbf{G}$, is assumed constant over the update interval, $\delta t = t_{k+1} - t_k$. The matrix, $\mathbf{W}$, is known as the spectral density matrix and is a diagonal matrix containing the spectral amplitude of the associated white noise processes, see Appendix D. In practice, the system noise is therefore defined in terms of a spectral density matrix

$$\mathbf{W} = \begin{bmatrix} \mathbf{S}_{wn,\mathrm{att}} & \mathbf{0}_3 & \mathbf{0}_3 \\ \mathbf{0}_3 & \mathbf{S}_{wn,\mathrm{vel}} & \mathbf{0}_3 \\ \mathbf{0}_3 & \mathbf{0}_3 & 2\,\boldsymbol{\sigma}^2\,\boldsymbol{\beta} \end{bmatrix} \,, \tag{9.14}$$

where $\boldsymbol{\sigma}$ and $\boldsymbol{\beta}$ are diagonal matrices containing the parameters of the first-order Gauss-Markov model. In Appendix D, it is seen that the power spectral density (PSD) is generally not constant for different stochastic models and that some processes are not even stationary, meaning that no associated PSD exists. However, the PSD in the above matrix refers to the underlying white noise process that drives the system. The PSD for a white noise process has a constant amplitude and is therefore unambiguously defined. In this respect the following should be noted:

- A random constant has no associated driving noise
- The random walk process is simply integrated white noise. Thus, modelling velocity and attitude error as a random walk corresponds to modelling white noise on the gyro and accelerometer observations
- The PSD of a Gauss-Markov process is not constant and should not be used as driving noise in the Kalman filter. Instead, the amplitude of the associated white noise PSD should be derived using the equations in Appendix D and used as driving noise in the Kalman filter

Finally, it should be noted that the PSD is usually specified in terms of its square root. These root-PSDs should therefore be squared when used in the spectral density matrix. Therefore, in practice, the components $\mathbf{F}_k$ and $\mathbf{G}_k \, \mathbf{W}_{s,k} \, \mathbf{G}_k^\top$ are first formed. The transition matrix, $\boldsymbol{\Phi}_k$, and system noise matrix, $\boldsymbol{\Gamma}_k \, \mathbf{Q}_k \, \boldsymbol{\Gamma}_k^\top$, are then derived using the method of Van Loan described in Appendix D.4.2. This method will also be outlined in Section 9.1.4. Having formed these components, the error state vector and error covariance matrix can be propagated forward in time as (8.25):

$$\delta \mathbf{x}_{k+1} = \boldsymbol{\Phi}_k \, \delta \mathbf{x}_k \tag{9.15a}$$

$$\mathbf{P}_{k+1} = \boldsymbol{\Phi}_k \, \mathbf{P}_k \, \boldsymbol{\Phi}_k^\top + \boldsymbol{\Gamma}_k \, \mathbf{Q}_k \, \boldsymbol{\Gamma}_k^\top \,. \tag{9.15b}$$

However, due to the closed-loop implementation, the error state vector, $\delta \mathbf{x}_k$, will always be zeroed after measurement updates and is not performed in practice.

9.1.2 The Measurement Model

As indicated in Figure 9.1, velocity and position estimates from the GNSS system will be introduced into the Kalman filter as measurement updates. In general, the GNSS navigation solution refers to the position and velocity of the GNSS antenna, whereas the INS solution refers to the IMU observation point. The position of the GNSS antenna with respect to the IMU is known as the **lever arm**, denoted here as $\mathbf{l}$. In a strapdown configuration, both the IMU and GNSS antenna are rigidly attached to the moving vehicle and the lever arm, $\mathbf{l}^b$, is assumed constant when resolved about the b-frame axes. In practice this might not be completely true due to aircraft vibration and deformation. The antenna coordinates with respect to the IMU are therefore

$$\mathbf{p}_{\text{GNSS}} = \mathbf{p}_{\text{IMU}} + \mathbf{T}_r^p \, \mathbf{C}_b^n \, \mathbf{l}^b \,, \tag{9.16}$$

where

$$\mathbf{T}_r^p = \begin{bmatrix} \frac{1}{R_N+h} & 0 & 0 \\ 0 & \frac{1}{(R_E+h)\cos\phi} & 0 \\ 0 & 0 & -1 \end{bmatrix} \tag{9.17}$$

is the Cartesian-to-curvilinear position transformation matrix. When the vehicle is rotating, the lever arm will also introduce a velocity component as

$$\begin{aligned} \mathbf{v}_{\text{GNSS}}^n &= \mathbf{v}_{\text{IMU}}^n + \mathbf{C}_b^n \, \left(\boldsymbol{\omega}_{eb}^b \times \mathbf{l}^b\right) \\ &= \mathbf{v}_{\text{IMU}}^n + \mathbf{C}_b^n \, \left(\boldsymbol{\omega}_{ib}^b \times \mathbf{l}^b\right) - \mathbf{C}_b^n \, \left(\boldsymbol{\omega}_{ie}^b \times \mathbf{l}^b\right) \\ &= \mathbf{v}_{\text{IMU}}^n + \mathbf{C}_b^n \, \left(\boldsymbol{\omega}_{ib}^b \times \mathbf{l}^b\right) - \boldsymbol{\Omega}_{ie}^n \, \mathbf{C}_b^n \, \mathbf{l}^b \,. \end{aligned} \tag{9.18}$$

In this way, the GNSS velocity and position is coupled with the attitude through $\mathbf{C}_b^n$, although this coupling is weak [6, Sec. 14.3.1]. The GNSS velocity is additionally (weakly) coupled with the gyroscope sensor errors, i.e. the gyro bias. Using these relations, the measurement innovation is formed as

$$\delta\mathbf{z}^n = \begin{bmatrix} \hat{\mathbf{p}}_{\text{GNSS}} - \hat{\mathbf{p}}_{\text{IMU}} - \hat{\mathbf{T}}_r^p \, \hat{\mathbf{C}}_b^n \, \mathbf{l}^b \\ \hat{\mathbf{v}}_{\text{GNSS}}^n - \hat{\mathbf{v}}_{\text{IMU}}^n - \hat{\mathbf{C}}_b^n \, \left(\hat{\boldsymbol{\omega}}_{ib}^b \times \mathbf{l}^b\right) + \hat{\boldsymbol{\Omega}}_{ie}^n \, \hat{\mathbf{C}}_b^n \, \mathbf{l}^b \end{bmatrix} \,. \tag{9.19}$$

In order to perform the measurement update, we need to form the linear error-state measurement model

$$\delta\mathbf{z}_k = \mathbf{H}_k \, \delta\mathbf{x}_k + \mathbf{w}_{m,k} \,, \tag{9.20}$$

which means that we need to linearise the above relations with respect to the error state variables. Using the small-angle approximation (6.11), the estimated attitude, $\hat{\mathbf{C}}_b^n$, is related to the true attitude, $\mathbf{C}_b^n$, as

$$\hat{\mathbf{C}}_b^n = \left(\mathbf{I}_3 + [\delta\boldsymbol{\psi}_{nb}^n\times]\right) \, \mathbf{C}_b^n \,, \tag{9.21}$$

which can be inserted into the above such that

$$\hat{\mathbf{C}}_b^n \, \mathbf{l}^b \approx \mathbf{C}_b^n \, \mathbf{l}^b + [\delta\boldsymbol{\psi}_{nb}^n\times] \, \mathbf{C}_b^n \, \mathbf{l}^b = \mathbf{C}_b^n \, \mathbf{l}^b - \left[\mathbf{C}_b^n \, \mathbf{l}^b\times\right] \, \delta\boldsymbol{\psi}_{nb}^n \tag{9.22}$$

and

$$
\begin{aligned}
\hat{\mathbf{C}}_b^n \left(\hat{\boldsymbol{\omega}}_{ib}^b \times \mathbf{l}^b\right) &\approx \left(\mathbf{I}_3 + [\delta\boldsymbol{\psi}_{nb}^n\times]\right) \mathbf{C}_b^n \left(\hat{\boldsymbol{\omega}}_{ib}^b \times \mathbf{l}^b\right) \\
&= \mathbf{C}_b^n \left(\hat{\boldsymbol{\omega}}_{ib}^b \times \mathbf{l}^b\right) + [\delta\boldsymbol{\psi}_{nb}^n\times] \mathbf{C}_b^n \left(\hat{\boldsymbol{\omega}}_{ib}^b \times \mathbf{l}^b\right) \\
&= \mathbf{C}_b^n \left(\hat{\boldsymbol{\omega}}_{ib}^b \times \mathbf{l}^b\right) - \left[\mathbf{C}_b^n \left(\hat{\boldsymbol{\omega}}_{ib}^b \times \mathbf{l}^b\right)\times\right] \delta\boldsymbol{\psi}_{nb}^n \\
&\approx \mathbf{C}_b^n \left(\boldsymbol{\omega}_{ib}^b \times \mathbf{l}^b\right) + \mathbf{C}_b^n \left(\delta\mathbf{b}_g \times \mathbf{l}^b\right) - \left[\mathbf{C}_b^n \left(\hat{\boldsymbol{\omega}}_{ib}^b \times \mathbf{l}^b\right)\times\right] \delta\boldsymbol{\psi}_{nb}^n \\
&= \mathbf{C}_b^n \left(\boldsymbol{\omega}_{ib}^b \times \mathbf{l}^b\right) - \mathbf{C}_b^n \left[\mathbf{l}^b\times\right] \delta\mathbf{b}_g - \left[\mathbf{C}_b^n \left(\hat{\boldsymbol{\omega}}_{ib}^b \times \mathbf{l}^b\right)\times\right] \delta\boldsymbol{\psi}_{nb}^n \,.
\end{aligned} \tag{9.23}
$$

Using these relations, we can arrive at the linear measurement model from [6, Eq. 14.114]

$$
\mathbf{H}_k^n = \begin{bmatrix} \mathbf{H}_{p1}^n & \mathbf{0}_3 & -\mathbf{I}_3 & \mathbf{0}_3 & \mathbf{0}_3 \\ \mathbf{H}_{v1}^n & -\mathbf{I}_3 & \mathbf{0}_3 & \mathbf{0}_3 & \mathbf{H}_{v5}^n \end{bmatrix} \,, \tag{9.24}
$$

with

$$
\mathbf{H}_{p1}^n = \hat{\mathbf{T}}_r^p \left[\mathbf{C}_b^n \, \mathbf{l}^b\times\right] \tag{9.25a}
$$

$$
\mathbf{H}_{v1}^n = \left[\left\{\mathbf{C}_b^n \left(\hat{\boldsymbol{\omega}}_{ib}^b \times \mathbf{l}^b\right) - \hat{\boldsymbol{\Omega}}_{ie}^n \, \mathbf{C}_b^n \, \mathbf{l}^b\right\}\times\right] \tag{9.25b}
$$

$$
\mathbf{H}_{v5}^n = \mathbf{C}_b^n \left[\mathbf{l}^b\times\right] \,. \tag{9.25c}
$$

Having formed the measurement innovation using (9.19) and the measurement matrix using (9.24), the measurement update can be performed using (8.31), (8.33) and (8.34):

$$
\mathbf{K}_k = \mathbf{P}_k^- \, \mathbf{H}_k^\top \left(\mathbf{H}_k \, \mathbf{P}_k^- \, \mathbf{H}_k^\top + \mathbf{R}_k\right)^{-1} \tag{9.26a}
$$

$$
\delta\hat{\mathbf{x}}_k = \delta\hat{\mathbf{x}}_k^- + \mathbf{K}_k \, \delta\mathbf{z}_k \tag{9.26b}
$$

$$
\mathbf{P}_k = \mathbf{P}_k^- - \mathbf{K}_k \left(\mathbf{H}_k \, \mathbf{P}_k^-\right) \,, \tag{9.26c}
$$

noticing that $\delta\hat{\mathbf{x}}_k^-$ will be zero after the forward-propagation phase. This term will however not be zero if sequential measurement updates are performed.

9.1.3 Choosing Units to Increase Numerical Stability

Since the state and measurement vectors are concerned with errors on parameters such as position, angles, velocity, angular rates and accelerations, the magnitude of these errors may span a large range of values, leading to numerical instability in the related processes. It is therefore recommended to diverge from SI units in order to improve numerical stability. The choice of units should reflect the magnitude of errors and measurement innovations, such that the range of values is limited. The units chosen in this dissertation are listed in Table 9.1. It should be noted that changing the units on the error state variables will also affect the system matrix and the measurement matrix.

Error Component	Unit	Conversion
attitude	arc seconds	$[''] = 60 \cdot 60 \cdot \frac{180}{\pi} \cdot [\text{rad}]$
velocity	meters per second	[m/s]
position	meters	$[\text{m}] = (R_N + h) \cdot [\text{rad}]$ $[\text{m}] = (R_E + h) \cdot \cos\phi \cdot [\text{rad}]$
accelerometer	milli-Gal	$[\text{mGal}] = 10^5 \cdot [\text{m/s}^2]$
gyroscope	degrees per hour	$[^\circ/\text{h}] = 60 \cdot 60 \cdot \frac{180}{\pi} \cdot [\text{rad/s}]$
gravity	milli-Gal	$[\text{mGal}] = 10^5 \cdot [\text{m/s}^2]$

Table 9.1: Overview of the units used for the error state variables along with their conversion from SI units.

9.1.4 Outline of Algorithm

This subsection presents an outline of how the integration algorithm can be structured. It is assumed that initial estimates of all variables are available, i.e. $\hat{\boldsymbol{\psi}}^n_{nb}$, $\hat{\mathbf{v}}^n$, $\hat{\mathbf{p}}$, $\hat{\mathbf{b}}_a$ and $\hat{\mathbf{b}}_g$, along with an associated error covariance matrix, $\mathbf{P}_k$. The algorithm represents an iteration from some current time, t_k, until the time, t_{k+1}, where the next GNSS position and velocity measurement is available. The propagation interval is denoted $\delta t = t_{k+1} - t_k$.

Example Algorithm: INS/GNSS Integration Algorithm

1. Extract IMU observations for the interval $t_k < t \leq t_{k+1}$ and correct for bias estimates, $\hat{\mathbf{b}}_a$ and $\hat{\mathbf{b}}_g$
2. Perform inertial navigation to obtain navigation estimates, $\hat{\boldsymbol{\psi}}^n_{nb}$, $\hat{\mathbf{v}}^n$, $\hat{\mathbf{p}}$, $\hat{\mathbf{b}}_a$ and $\hat{\mathbf{b}}_g$ at next measurement epoch (see Appendix C.2)

Forward Propagation Phase

3. Form system matrix, $\mathbf{F}_k$, using error dynamics equations (6.17) and spectral density matrix, $\mathbf{W}_k$
4. Use the method of Van Loan to form the transition matrix, $\boldsymbol{\Phi}_k$, and system noise covariance matrix, $\boldsymbol{\Gamma}_k \, \mathbf{Q}_k \, \boldsymbol{\Gamma}_k^\top$. This is done by first forming the $2n \times 2n$ matrix

$$\mathbf{A}_k = \left[\begin{array}{c|c} -\mathbf{F}_k & \mathbf{G}_k \, \mathbf{W}_{s,k} \, \mathbf{G}_k^\top \\ \hline \mathbf{0} & \mathbf{F}^\top \end{array}\right] \delta t \, ,$$

where n is the dimension of $\mathbf{x}$ and δt is the propagation interval. Then compute the matrix exponential (can be done using MATLAB or other software)

$$\mathbf{B}_k = \text{expm}\,(\mathbf{A}_k) = \left[\begin{array}{c|c} e^{-\mathbf{F}_k \delta t} & e^{-\mathbf{F}_k \delta t} \boldsymbol{\Gamma}_k \, \mathbf{Q}_k \, \boldsymbol{\Gamma}_k^\top \\ \hline \mathbf{0} & e^{\mathbf{F}_k^\top \delta t} \end{array}\right] = \left[\begin{array}{c|c} \boldsymbol{\Phi}_k^{-1} & \boldsymbol{\Phi}_k^{-1} \boldsymbol{\Gamma}_k \, \mathbf{Q}_k \, \boldsymbol{\Gamma}_k^\top \\ \hline \mathbf{0} & \boldsymbol{\Phi}_k^\top \end{array}\right] .$$

The transition matrix is then obtained by transposing the lower-right partition of $\mathbf{B}_k$ and the system noise covariance matrix is obtained by applying the transition matrix, $\mathbf{\Phi}_k$, to the upper-right partition of $\mathbf{B}_k$

5. Propagate the error covariance matrix forward in time using (9.15b)

$$\mathbf{P}_{k+1} = \mathbf{\Phi}_k \, \mathbf{P}_k \, \mathbf{\Phi}_k^\top + \mathbf{\Gamma}_k \, \mathbf{Q}_k \, \mathbf{\Gamma}_k^\top$$

Measurement Update Phase

6. Form measurement innovation using (9.19)

$$\delta \mathbf{z}_{k+1}^n = \begin{bmatrix} \hat{\mathbf{p}}_{\text{GNSS}} - \hat{\mathbf{p}}_{\text{IMU}} - \hat{\mathbf{T}}_r^p \, \hat{\mathbf{C}}_b^n \, \mathbf{l}^b \\ \hat{\mathbf{v}}_{\text{GNSS}}^n - \hat{\mathbf{v}}_{\text{IMU}}^n - \hat{\mathbf{C}}_b^n \left(\hat{\boldsymbol{\omega}}_{ib}^b \times \mathbf{l}^b \right) + \hat{\mathbf{\Omega}}_{ie}^n \, \hat{\mathbf{C}}_b^n \, \mathbf{l}^b \end{bmatrix} .$$

7. Form measurement matrix using (9.24)

$$\mathbf{H}_k^n = \begin{bmatrix} \mathbf{H}_{p1}^n & \mathbf{0}_3 & -\mathbf{I}_3 & \mathbf{0}_3 & \mathbf{0}_3 \\ \mathbf{H}_{v1}^n & -\mathbf{I}_3 & \mathbf{0}_3 & \mathbf{0}_3 & \mathbf{H}_{v5}^n \end{bmatrix} ,$$

8. Compute Kalman gain and update Kalman filter estimates using (9.26)

$$\mathbf{K}_{k+1} = \mathbf{P}_{k+1}^- \, \mathbf{H}_{k+1}^\top \left(\mathbf{H}_{k+1} \, \mathbf{P}_{k+1}^- \, \mathbf{H}_k^\top + \mathbf{R}_{k+1} \right)^{-1} \tag{9.27a}$$

$$\delta \hat{\mathbf{x}}_{k+1} = \mathbf{K}_{k+1} \, \delta \mathbf{z}_{k+1} \tag{9.27b}$$

$$\mathbf{P}_{k+1} = \mathbf{P}_{k+1}^- - \mathbf{K}_{k+1} \left(\mathbf{H}_{k+1} \, \mathbf{P}_{k+1}^- \right) , \tag{9.27c}$$

9. Update navigation estimates and sensor bias estimates using Eqs. (9.2) through (9.5)

$$\hat{\mathbf{q}}_b^n(+) = \begin{pmatrix} 1 \\ -\frac{1}{2} \delta \hat{\boldsymbol{\psi}}_{nb}^n \end{pmatrix} \circ \hat{\mathbf{q}}_b^n(-) ,$$

$$\hat{\mathbf{v}}^n(+) = \hat{\mathbf{v}}^n(-) - \delta \hat{\mathbf{v}}^n ,$$

$$\hat{\mathbf{p}}(+) = \hat{\mathbf{p}}(-) - \delta \hat{\mathbf{p}} ,$$

$$\hat{\mathbf{b}}_a(+) = \hat{\mathbf{b}}_a(-) + \delta \hat{\mathbf{b}}_a \quad \text{and}$$

$$\hat{\mathbf{b}}_g(+) = \hat{\mathbf{b}}_g(-) + \delta \hat{\mathbf{b}}_g$$

End of example

9.1.5 Smoothing

After the Kalman filter has successfully run through all the data, the RTS smoother presented in Section 8.2.2 is applied to the estimates. In the closed-loop, error-state implementation, the smoothed estimates are generated in a backwards iteration as

$$\delta\hat{\mathbf{x}}_{k|T} = \delta\hat{\mathbf{x}}_k^+ + \mathbf{A}_k \left(\delta\hat{\mathbf{x}}_{k+1|T} - \delta\hat{\mathbf{x}}_{k+1}^-\right) \tag{9.28a}$$

$$\mathbf{P}_{k|T} = \mathbf{P}_k^+ + \mathbf{A}_k \left(\mathbf{P}_{k+1|T} - \mathbf{P}_{k+1}^-\right) \mathbf{A}_k^\top \tag{9.28b}$$

$$\mathbf{A}_k = \mathbf{P}_k^+ \, \mathbf{\Phi}_k^\top \, \left(\mathbf{P}_{k+1}^-\right)^{-1} \ , \tag{9.28c}$$

where it should be noted that the estimated errors, $\delta\hat{\mathbf{x}}_k^+$, from the forward run, have already been applied as a correction to the navigation solution. In order not to apply the same correction twice, the residual correction

$$\triangle\delta\hat{\mathbf{x}}_k = \delta\hat{\mathbf{x}}_{k|T} - \delta\hat{\mathbf{x}}_k^+ \ , \tag{9.29}$$

is formed and applied to the navigation solution as outlined previously in this section.

9.1.6 Initialisation

In order to perform inertial navigation, the navigation solution must be initialised. That is, initial estimates of position, velocity and attitude must be provided. This is usually accomplished during an initialisation period where the vehicle is stationary. The position and velocity must be inferred from external sources, since the IMU cannot initialise these parameters itself. In our case, a GNSS system will be available for initialising the position and velocity. The physical separation between the IMU and GNSS antenna, i.e. the lever arm, should be taken into account using some estimate of attitude.

The attitude can be initialised from an external source, but also by the IMU observations themselves. The attitude initialisation process is also known as **alignment**, referring to the platform initialisation process of aligning the instrument axes with the navigation frame axes. The IMU self-alignment process consists of two components: (1) a levelling process for estimating the bank and elevation angles, and (2) a gyrocompassing process for estimating the heading angle. These will be briefly presented in the following.

Levelling

The levelling procedure exploits that the IMU is stationary and therefore only senses the reaction to gravity in the upward direction. The specific force, $\mathbf{f}^b$, sensed by the accelerometers is therefore

$$\mathbf{f}^b = \begin{bmatrix} f_x^b \\ f_y^b \\ f_z^b \end{bmatrix} = -\mathbf{C}_n^b \, \mathbf{g}^n \approx -\mathbf{C}_n^b \begin{bmatrix} 0 \\ 0 \\ g_D^n \end{bmatrix} = \begin{bmatrix} \sin\beta_{nb} \\ -\sin\alpha_{nb}\cos\beta_{nb} \\ -\cos\alpha_{nb}\cos\beta_{nb} \end{bmatrix} g_D^n \ , \tag{9.30}$$

representing a set of three equations with two unknowns. This set of equations may be solved for the bank and elevation angles as [6, Eq. 5.101]:

$$\beta_{nb} = \arctan\left(\frac{f_x^b}{\sqrt{{f_y^b}^2 + {f_z^b}^2}}\right) \quad \text{and} \quad \alpha_{nb} = \arctan_2\left(-f_y^b, -f_z^b\right) \ , \tag{9.31}$$

noticing that a four-quadrant arctangent function must be used for the bank angle. It should also be noted that an aircraft parked at the airport is usually not completely stationary due to wind bursts, fuelling, people entering or exiting, etc. Assuming that these motions average out over time, the accelerometer readings may be averaged over the initialisation period.

Gyrocompassing

The gyrocompassing procedure also exploits that the IMU is stationary and therefore only senses the rotation of the Earth. This rotation is about the Z-axis of the ECEF frame, meaning that the angular rate, $\boldsymbol{\omega}_{ib}^{b}$, sensed by the gyroscopes is related to the attitude as

$$\boldsymbol{\omega}_{ib}^{b} = \begin{bmatrix} \omega_{ib,x}^{b} \\ \omega_{ib,y}^{b} \\ \omega_{ib,z}^{b} \end{bmatrix} = \mathbf{C}_{n}^{b}\, \mathbf{C}_{e}^{n} \begin{bmatrix} 0 \\ 0 \\ \omega_{ie} \end{bmatrix} = \mathbf{C}_{n}^{b} \begin{bmatrix} \cos\phi \\ 0 \\ -\sin\phi \end{bmatrix} \omega_{ie} \,. \tag{9.32}$$

Having already obtained estimates of bank and elevation from the levelling procedure, this set of equations may be solved for the heading angle as [6, Eq. 5.105]:

$$\begin{aligned} \gamma_{nb} &= \arctan_2\left(\sin\gamma_{nb}, \cos\gamma_{nb}\right) \\ \sin\gamma_{nb} &= -\omega_{ib,y}^{b}\, \cos\alpha_{nb} + \omega_{ib,z}^{b}\, \sin\alpha_{nb} \\ \cos\gamma_{nb} &= \omega_{ib,x}^{b}\, \cos\beta_{nb} + \omega_{ib,y}^{b}\, \sin\alpha_{nb}\, \sin\beta_{nb} + \omega_{ib,z}^{b}\, \cos\alpha_{nb}\, \sin\beta_{nb} \,, \end{aligned} \tag{9.33}$$

where a four-quadrant arctangent function must again be used. When the vehicle is not completely stationary, it may again be necessary to average the gyro observations over some initialisation period. At the poles, the rotation axis coincides with the direction of gravity, meaning that gyrocompassing is not useful in polar regions. This may be handled using iterative processing [1, Sec. 8.4.1].

The levelling and gyrocompassing procedures are sometimes collectively denoted as **coarse alignment**. The initialisation errors can be derived from the data [6, Sec. 5.6.2] or manually pre-defined in terms of the standard deviation. For this dissertation, the manual approach was preferred with default values listed in Table 9.2. These values will be highly dependent on equipment and initialisation environment. The velocity, accelerometer bias and gyro bias are initialised as zeroes.

Parameter	**Standard deviation**
roll, pitch	1°
heading	5°
velocity	0.5 m/s
latitude, longitude	1 m
height	5 m
accelerometer bias	30 mGal
gyroscope bias	0.001 °/h

Table 9.2: Default values of confidence in the initial estimates from coarse alignment

Fine Alignment

The coarse alignment is usually followed by a period of fine alignment, where the attitude estimates are calibrated. There are three main different fine alignment techniques [6, Sec. 5.6.3]:

1. Quasi-stationary alignment assuming that the IMU is stationary and using zero-velocity updates or integrals thereof
2. GNSS alignment using position and velocity updates derived from GNSS
3. Transfer alignment using position, velocity and/or attitude updates from another INS or INS/GNSS navigation system

Here, GNSS alignment is used, meaning that the INS and GNSS navigation estimates are combined in the EKF framework. This is done exactly as described in the previous sections, meaning that no explicit fine alignment process is performed but occurs implicitly in the integration algorithm. If GNSS observations are not available for a significant amount of time, the alignment period may be expanded using the quasi-stationary alignment technique as described in [6, Sec. 15.2.2].

9.2 Application to Simulated Data

In order to test the algorithm developed in this section, it will be applied to simulated data generated with the algorithm presented in Section 7. The simulated data is again based on the trajectory in Figure 7.1 with a constant gravity vector of

$$\mathbf{g}^n = [0, 0, 9.81]^\top \ , \tag{9.34}$$

added to the acceleration (units of $\mathrm{m/s^2}$). The effect of gravity is fully compensated in the processing using an exact gravity model. The main reason for adding this vector is because the initialisation procedure requires a dominant gravity component along the vertical direction. Using the error generation tools presented in Section 7.4, errors were added to the IMU observations as described in Table 9.3.

Error component	Model	Standard deviation	System Noise
Gyroscope noise	White noise	$1.14\,^\circ/\mathrm{h}$	$0.0011\,^\circ/\sqrt{\mathrm{h}}$
Gyroscope bias	Random constant	$0.03\,^\circ/\mathrm{h}$	$0\,^\circ/\mathrm{h}/\sqrt{s}$
Accelerometer noise	White noise	$138.56\,\mathrm{mGal}$	$8\,\mathrm{mGal}/\sqrt{\mathrm{Hz}}$
Accelerometer bias	Random constant	$25\,\mathrm{mGal}$	$0\,\mathrm{mGal}/\sqrt{s}$

Table 9.3: Stochastic models used for generating IMU sensor errors in terms of standard deviation and system noise (root PSD of the associated white noise process). These error models are based on the manufacturer specifications for the iNAT unit, see Table 6.2

The position profile generated from the simulation algorithm was used to form a series of GNSS position observations at 1 Hz rate. As these locations represent the IMU position, a lever arm of

$$\mathbf{l}^b = [-1.5, -0.5, -1.5]^\top \ , \tag{9.35}$$

was added to the positions (units of meters) using the simulated attitude profile together with (9.19). Finally, errors were added to the GNSS position estimates as described in Section 7.4.3, using the constant error covariance matrix

$$\mathbf{C}_x = \begin{bmatrix} 5.00 \cdot 10^{-4} & 5.00 \cdot 10^{-5} & 5.00 \cdot 10^{-5} \\ 5.00 \cdot 10^{-5} & 5.00 \cdot 10^{-4} & -5.00 \cdot 10^{-5} \\ 5.00 \cdot 10^{-5} & -5.00 \cdot 10^{-5} & 5.00 \cdot 10^{-3} \end{bmatrix}, \tag{9.36}$$

in units of meters and a 100 second time window with error interpolated using a cubic spline function.

The simulated IMU observations were used to feed the inertial navigation processor. Using the INS/GNSS integration algorithm developed in this section, the GNSS position observations were introduced as measurement updates in a Kalman filter with error state variables and associated stochastic models listed in Table 9.4. The results from this processing is shown in Figures 9.2 and 9.3.

Error State	**Model**	**Initial uncertainty**	**System Noise**
Attitude	Random walk	$[1, 1, 5]$ °	$0.0660\,''/\sqrt{\text{s}}$
Velocity	Random walk	.5 m/s	$8 \cdot 10^{-5}$ m/s$\sqrt{\text{s}}$
Position	None	$[1, 1, 5]$ m	$0\,\text{m}/\sqrt{\text{s}}$
Accelerometer bias	Random constant	25 mGal	$0\,\text{mGal}/\sqrt{s}$
Gyroscope bias	Random constant	0.003 °/h	$0\,°/\text{h}/\sqrt{s}$

Table 9.4: Stochastic models used for modelling IMU sensor errors and the system noise (root PSD of the associated white noise process). The system noise corresponds exactly to the errors added in Table 9.3. Initial errors are in terms of standard deviation

The errors in Figure 9.2 are with respect to the simulated profiles and are in the range of ±5 cm for the horizontal positions and ±10 cm for the vertical position, with errors increasing up to 20 cm during turns. The errors on velocity are in the range of ±0.1 cm/s for the horizontal and ±0.2 cm/s for the vertical, with errors up to 1 cm/s during turns. The bank and elevation errors appear to have bias components that varies between flight lines, i.e. heading dependent. The magnitude of these biases are up to 10 arc seconds with a superimposed on-line variation of less than 1 arc second. During turns the errors can reach 10 arc seconds. Although the straight flight lines are also evident in the heading error, this error component has some associated drift. The error does not seem to increase during turns, but rather the drift characteristic changes and reaches 30 arc seconds during one flight line (≈45 minutes). It should be noted that the navigation errors are related to the initialisation process and the observability of the state variables, including the sensor errors [1, 6, 7].

The estimated sensor errors are shown together with simulated errors in Figure 9.3. From this figure it appears that only the gyroscope X- and Y-bias, along with the accelerometer Z-axis bias, converges towards the true/simulated error. This corresponds well with the observed attitude errors, since an erroneous gyro Z-axis bias estimate would induce a drift in the heading, while the accelerometer X- and Y-biases are coupled with the bank and elevation angles introducing heading-dependent biases [6, Sec. 5.6.2].

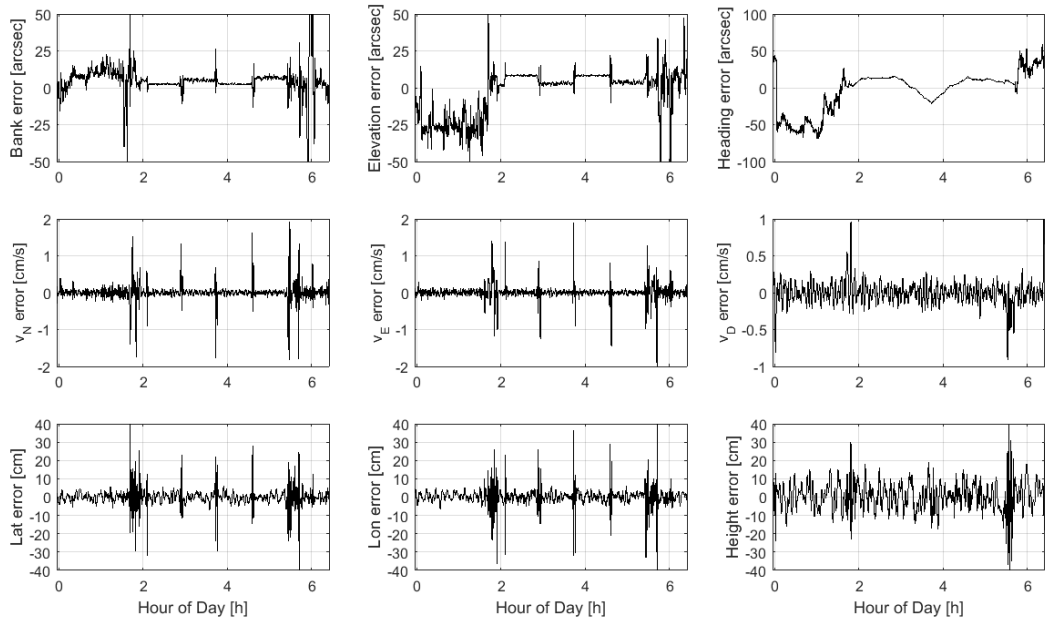

Figure 9.2: Errors on the navigation solution using stochastic models exactly as they are used to generate errors

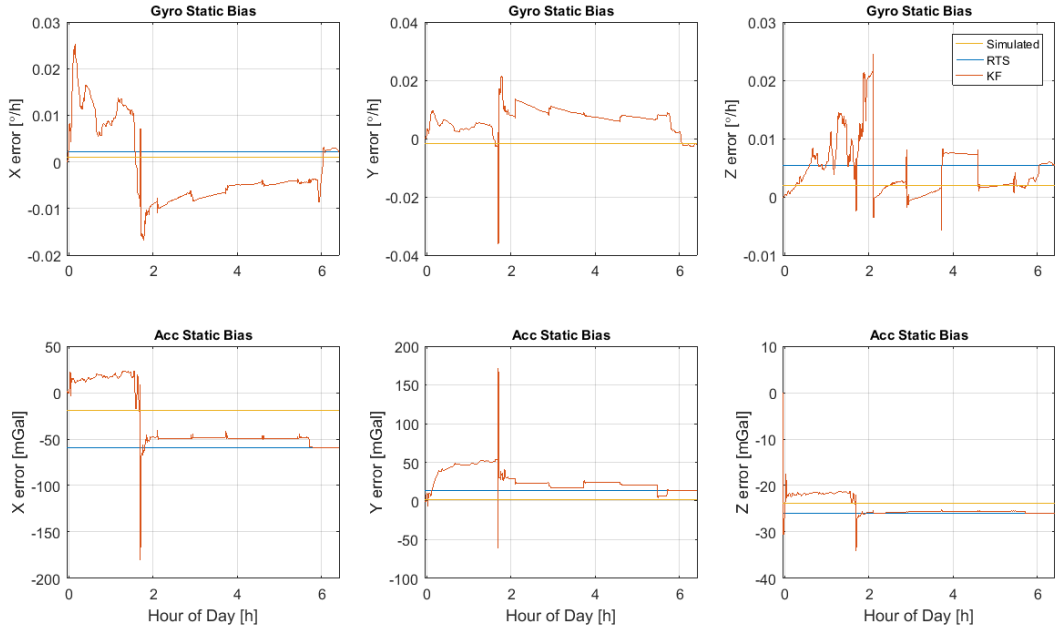

Figure 9.3: Errors on the sensor error estimates using stochastic models exactly as they are used to generate errors

In Figure 9.4 the Mahalanobis distance for each GNSS position update along the flight is shown. Recall that this distance is the distance between the GNSS estimate and the current Kalman filter estimate in terms of number of standard deviations of their combined probability distribution. According to a Gaussian distribution, 68% of observations should be within one standard deviation, 95% within two standard deviations, 99.7% within three standard deviation, etc. This is illustrated by the theoretical curve in the bottom figure.

On the straight line segments, the agreement between Kalman filter and GNSS observations is very good, i.e. within one standard deviation, while the disagreement during take-off, turns and landing can be up to 15 standard deviations. While stationary, the agreement is generally below 2 standard deviations. This creates a distribution where 67% of observations are below one standard deviation and 20% is above two standard deviations, indicating that the distribution is not Gaussian and is dependent on flight dynamics. The Mahalanobis distance has been proposed as a method of fault detecting and identifies questionable observations [8, 9], but in this dissertation it will only be used as an indicator of whether or not the stochastic models are reasonable.

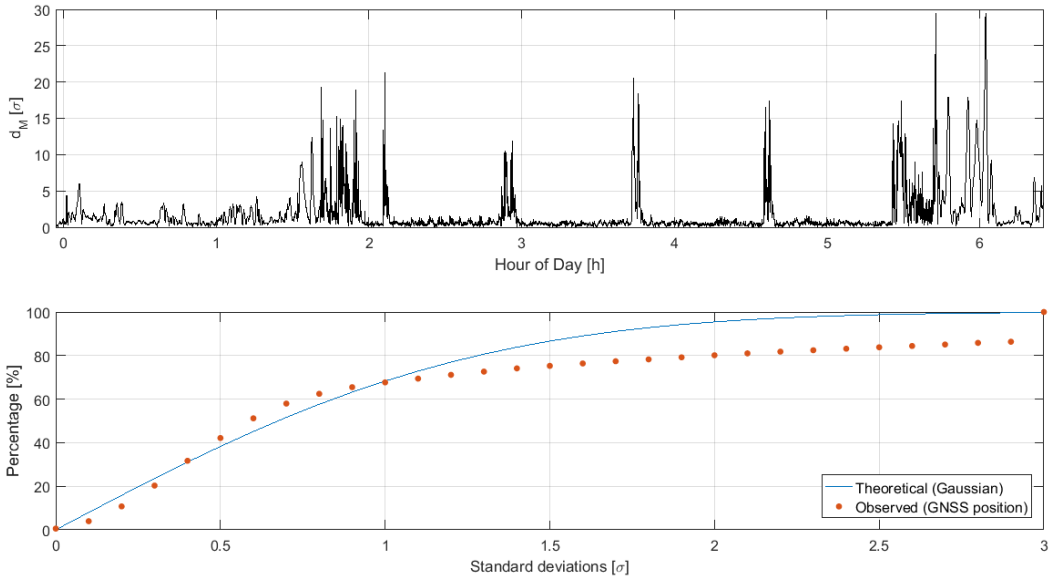

Figure 9.4: Mahalanobis distance computed during processing. (Top:) Mahalanobis distance for each GNSS position update along the flight; (Bottom:) Distribution of Mahalanobis distance in percent along with theoretical Gaussian distribution

References

[1] David Becker. "Advanced Calibration Methods for Strapdown Airborne Gravimetry". PhD thesis. Darmstadt: Technische Universität Darmstadt, 2016. URL: `http://tuprints.ulb.tu-darmstadt.de/5691/`.

[2] Robert Grover Brown and Patric Y. C. Hwang. *Random Signals and Applied Kalman Filtering*. John Wiley & Sons, Inc., 2012. ISBN: 978-0-470-60969-9.

[3] Hugh Durrant-Whyte. *Introduction to estimation and the Kalman filter*. 2001. URL: http://www.isip40.it/resources/Dispense/DataFusionSIIT/Estimation{_}KF.pdf.

[4] Jay A. Farrell. *Aided Navigation: GPS with High Rate Sensors*. 1st. Vol. 1542. McGraw-Hill Education, 2008. ISBN: 978-0071493291. arXiv: arXiv:1011.1669v3.

[5] Arthur Gelb et al. *Applied optimal estimation*. Ed. by Arthur Gelb. The M.I.T Press, 1974. ISBN: 0262200279.

[6] Paul D. Groves. *Principles of GNSS, Inertial, and Multisensor Integrated Navigation Systems*. 2nd. Artech House Remote Sensing Library, 2013. ISBN: 978-1608070053.

[7] P S Maybeck. *Stochastic models, estimation, and control*. Vol. 1. 1. 1979. ISBN: 0124807011. URL: http://www.cs.unc.edu/{~}welch/media/pdf/maybeck{_}ch1.pdf.

[8] Robert Piché. "Online tests of Kalman filter consistency". In: *International Journal of Adaptive Control and Signal Processing* 30.1 (2016), pp. 115–124. DOI: 10.1002/acs. URL: http://onlinelibrary.wiley.com/doi/10.1002/acs.967/abstract.

[9] R. R. Pinho, J. M.R.S. Tavares, and M. V. Correia. "Efficient approximation of the mahalanobis distance for tracking with the Kalman filter". In: *International Journal of Simulation Modelling* 6.2 (2007), pp. 84–92. ISSN: 17264529. DOI: 10.2507/IJSIMM06(2)S.03.

Part IV:

Strapdown Airborne Gravimetry

10 Principles of Strapdown Airborne Gravimetry

The most basic equation, not only for airborne gravimetry, but for gravimetry in general is the modified version of Newton's second law from (4.3):

$$\boxed{\bar{\mathbf{g}}^i = \ddot{\mathbf{r}}^i - \mathbf{f}^i \ ,} \tag{10.1}$$

where $\ddot{\mathbf{r}}^i$ is the acceleration originating from vehicle movement and $\mathbf{f}^i$ is the specific force sensed by an accelerometer, i.e. the combined effect of movement and gravitation. The equation indicates that gravity is the difference between position observations, $\mathbf{r}^i$, and acceleration observations, $\mathbf{f}^i$. In order to derive the gravity signal, one can therefore choose either of the following approaches [14]:

1. The **direct approach** by differentiating observations of position and/or velocity and differencing the two signals

2. The **indirect approach** by integrating specific force observations and deriving gravity through compensation of the observed accelerations

These two approaches are completely general and although some combinations remain uncommon or even untested, they can be applied to any combination of physical configuration and processing strategy. It should also be noted that an interesting variant of the direct approach is to directly differentiate GNSS carrier phase observations [12, 16, 15].

Since both components in the above equation are expected to have some associated errors, one important tool that has been intensively studied for airborne gravimetry is signal filtering [5, 22]. Filtering of the signal can also be inferred indirectly using both deterministic and stochastic models, both of which are readily included in a Kalman filter framework [17]. Even if the Kalman filter is not used for the direct estimation of gravity, it is often used during some part of the processing, as Kalman filtering is a standard tool in GNSS and INS/GNSS navigation algorithms. It should be noted that both filtering and modelling essentially introduces a priori knowledge on the gravity signal and that gravity estimates can be derived from a Kalman filter without actually modelling it directly as a state variable [17].

The purpose here is not to give a full overview of the different processing strategies (I do not even posses such an overview), but merely to present some examples and to stress out that the various strategies are not confined to certain approaches or physical configurations. As the work in this dissertation is concerned with an IMU in a strapdown configuration, the following subsection will be limited to the topic of Strapdown Airborne Gravimetry (SAG). First, some basic concepts will be introduced and some common, successful processing strategies will be presented. Second, the processing strategy used in this dissertation will be outlined. Finally, this processing strategy will be applied to simulated data in order to validate the approach.

10.1 An Overview of Approaches

In this dissertation, a navigation-frame implementation is pursued. This means that all observations are initially referenced to an ECEF frame and decomposed along the north, east and down directions. It should be stressed out that SAG is not confined to the n-frame, but is the most common choice of reference frame. In this representation, the expression (10.1) becomes (C.18):

$$\mathbf{g}^n = \dot{\mathbf{v}}^n - \mathbf{C}_b^n \, \mathbf{f}^b + (2\boldsymbol{\Omega}_{ie}^n + \boldsymbol{\Omega}_{en}^n) \, \mathbf{v}^n \ , \tag{10.2}$$

where the specific force, $\mathbf{f}^b$, is resolved about the vehicle body frame. The fictitious forces, represented by the third term on the RHS, are introduced since the specific force is sensed with respect to inertial space. The above equation consists of three terms:

1. The **dynamic** term, $\dot{\mathbf{v}}^n$, which is most commonly derived from GNSS observations. Before the advent of GPS, other sensors such as cameras, Doppler radar, barometers and laser altimeters have been used for estimating the dynamic term

2. The **acceleration** term, $\mathbf{C}_b^n \, \mathbf{f}^b$, which is derived from IMU observations. The IMU contains a triad of accelerometers providing specific force observations, $\mathbf{f}^b$, and a triad of gyroscopes providing angular rate observations from which the attitude matrix, $\mathbf{C}_b^n$, can be estimated

3. The **Eötvös** term, representing the compensation for the fictitious Coriolis, $2\boldsymbol{\Omega}_{ie}^n \, \mathbf{v}^n$, and transport-rate, $\boldsymbol{\Omega}_{en}^n \, \mathbf{v}^n$, forces. The combined effect of the vertical components of these two terms, i.e.

$$E = 2\omega_{ie} \cos\phi \, v_E + \frac{v_N^2}{R_N + h} + \frac{v_E^2}{R_E + h} \ , \tag{10.3}$$

   is denoted in airborne gravimetry as the Eötvös correction [10]. The Coriolis component originates from the well-known Coriolis effect, while the transport-rate component represents the rotation required to keep the axes aligned with the north, east and down directions. Both forces are velocity dependent

Most commonly, the attitude matrix, $\mathbf{C}_b^n$, is derived by integrating IMU and GNSS observations in a Kalman filter framework as described in Section 9. From here, the most common approaches diverge into two general strategies:

- **Centralised approach**: The gravity vector (or some anomalous gravity vector) is estimated wihtin the Kalman filter framework by including its components as state variables [21, 6, 3, 1]. The estimates are subsequently smoothed using the RTS smoother

- **Cascaded approach**: The accelerometer specific force is decomposed about the n-frame axes using the attitude matrix. The dynamic component is derived from GNSS observations by differencing position/velocity estimates or GNSS carrier phase observations [5, 7]. Gravity is then derived by differencing the two signals and applying some kind of low-pass filter [8, 9, 4, 11]. The Eötvös correction is typically derived from GNSS observations, but can also be derived from the integrated IMU/GNSS solution

Both approaches therefore commonly exploit the Kalman filter framework. Whereas the cascaded approach only uses the integrated solution for determining the attitude and splits the processes into several steps, the aim of the centralised approach is to include all information in a single processing framework. The cascaded strategy is typically concerned with the direct approach introduced earlier, whereas the centralised strategy is typically concerned with the indirect approach, although the direct approach has been applied with success [12].

10.1.1 The Indirect Centralised Kalman Filter Approach

In this dissertation, a traditional indirect approach will be pursued based on the combination of all available information within a Kalman filtering framework and modelling the variation of the gravity disturbance vector as a stochastic process. This approach is denoted here as the Indirect Centralised Kalman Filter (ICKF) approach. Although the name implies so, all information will actually not be processed in a single iteration, since the GNSS observations will be pre-processed and included in the Kalman filter using a loosely coupled architecture.

To this end, a normal gravity model will be used to compensate the specific force for inertial navigation. This means that the remaining component of gravity, namely the gravity disturbance vector, $\delta\mathbf{g}$, is unaccounted for and will be modelled as an exponentially correlated stochastic process using a third-order Gauss-Markov model. Using an error state implementation, the state vector becomes

$$\delta\mathbf{x} = [\ \delta\boldsymbol{\psi}^n_{nb}\ ,\ \delta\mathbf{v}^n\ ,\ \delta\mathbf{p}\ ,\ \delta\mathbf{b}_a\ ,\ \delta\mathbf{b}_g\ ,\ \delta\delta\mathbf{g}\ ,\ \delta\delta\dot{\mathbf{g}}\ ,\ \delta\delta\ddot{\mathbf{g}}\ ]^\top\ , \tag{10.4}$$

where $\delta\delta\mathbf{g}$ is the error on the gravity disturbance vector and dots denote time derivatives thereof. By system augmentation (see Appendix D.4.3), the system matrix becomes

$$\mathbf{F}^n = \left[\begin{array}{ccc|cc|ccc} -\boldsymbol{\Omega}^n_{in} & \mathbf{F}^n_{12} & \mathbf{F}^n_{13} & \mathbf{0}_3 & \mathbf{C}^n_b & \mathbf{0}_3 & \mathbf{0}_3 & \mathbf{0}_3 \\ -[\mathbf{f}^n\times] & \mathbf{F}^n_{22} & \mathbf{F}^n_{23} & \mathbf{C}^n_b & \mathbf{0}_3 & \mathbf{C}^n_b & \mathbf{0}_3 & \mathbf{0}_3 \\ \mathbf{0}_3 & \mathbf{F}^n_{32} & \mathbf{F}^n_{33} & \mathbf{0}_3 & \mathbf{0}_3 & \mathbf{0}_3 & \mathbf{0}_3 & \mathbf{0}_3 \\ \hline \mathbf{0}_3 & \mathbf{0}_3 & \mathbf{0}_3 & \mathbf{0}_3 & \mathbf{0}_3 & \mathbf{0}_3 & \mathbf{0}_3 & \mathbf{0}_3 \\ \mathbf{0}_3 & \mathbf{0}_3 & \mathbf{0}_3 & \mathbf{0}_3 & \mathbf{0}_3 & \mathbf{0}_3 & \mathbf{0}_3 & \mathbf{0}_3 \\ \hline \mathbf{0}_3 & \mathbf{0}_3 & \mathbf{0}_3 & \mathbf{0}_3 & \mathbf{0}_3 & \mathbf{0}_3 & \mathbf{I}_3 & \mathbf{0}_3 \\ \mathbf{0}_3 & \mathbf{0}_3 & \mathbf{0}_3 & \mathbf{0}_3 & \mathbf{0}_3 & \mathbf{0}_3 & \mathbf{0}_3 & \mathbf{I}_3 \\ \mathbf{0}_3 & \mathbf{0}_3 & \mathbf{0}_3 & \mathbf{0}_3 & \mathbf{0}_3 & -\boldsymbol{\beta}^3_3 & -3\boldsymbol{\beta}^2_3 & -3\boldsymbol{\beta}_3 \end{array}\right]\ , \tag{10.5}$$

where $\boldsymbol{\beta}_3$ are diagonal matrices, containing the correlation parameter of the Gauss-Markov model. Since the variation of gravity disturbance is correlated with space rather than time, the correlation parameter is typically specified in terms of distance. The correlation is then converted to time during processing as

$$\begin{bmatrix} \beta_{3,N} & 0 & 0 \\ 0 & \beta_{3,E} & 0 \\ 0 & 0 & \beta_{3,D} \end{bmatrix} = |v_{\mathrm{hor}}| \begin{bmatrix} \beta'_{3,N} & 0 & 0 \\ 0 & \beta'_{3,E} & 0 \\ 0 & 0 & \beta'_{3,D} \end{bmatrix}\ , \tag{10.6}$$

where β' denotes the correlation in terms of distance, i.e. units of $1/\mathrm{m}$, and $|v_{\mathrm{hor}}|^2 = v_N^2 + v_E^2$ is the ground speed, derived from the navigation algorithm. The corresponding spectral density matrix is

$$\mathbf{G}\,\mathbf{W}\,\mathbf{G}^\top = \left[\begin{array}{ccc|cc|ccc} \mathbf{S}_{\text{att}} & \mathbf{0}_3 & \mathbf{0}_3 & \mathbf{0}_3 & \mathbf{0}_3 & \mathbf{0}_3 & \mathbf{0}_3 & \mathbf{0}_3 \\ \mathbf{0}_3 & \mathbf{S}_{\text{vel}} & \mathbf{0}_3 & \mathbf{0}_3 & \mathbf{0}_3 & \mathbf{0}_3 & \mathbf{0}_3 & \mathbf{0}_3 \\ \mathbf{0}_3 & \mathbf{0}_3 & \mathbf{0}_3 & \mathbf{0}_3 & \mathbf{0}_3 & \mathbf{0}_3 & \mathbf{0}_3 & \mathbf{0}_3 \\ \hline \mathbf{0}_3 & \mathbf{0}_3 & \mathbf{0}_3 & \mathbf{S}_{\text{acc-bias}} & \mathbf{0}_3 & \mathbf{0}_3 & \mathbf{0}_3 & \mathbf{0}_3 \\ \mathbf{0}_3 & \mathbf{0}_3 & \mathbf{0}_3 & \mathbf{0}_3 & \mathbf{S}_{\text{gyro-bias}} & \mathbf{0}_3 & \mathbf{0}_3 & \mathbf{0}_3 \\ \hline \mathbf{0}_3 & \mathbf{0}_3 & \mathbf{0}_3 & \mathbf{0}_3 & \mathbf{0}_3 & \mathbf{0}_3 & \mathbf{0}_3 & \mathbf{0}_3 \\ \mathbf{0}_3 & \mathbf{0}_3 & \mathbf{0}_3 & \mathbf{0}_3 & \mathbf{0}_3 & \mathbf{0}_3 & \mathbf{0}_3 & \mathbf{0}_3 \\ \mathbf{0}_3 & \mathbf{0}_3 & \mathbf{0}_3 & \mathbf{0}_3 & \mathbf{0}_3 & \mathbf{0}_3 & \mathbf{0}_3 & \frac{16}{3}\boldsymbol{\beta}_3^5\sigma^2 \end{array}\right], \tag{10.7}$$

where σ is the standard deviation associated with the third-order Gauss-Markov model. This means that the attitude and velocity errors, along with the accelerometer and gyroscope bias variation, are modelled as random walk processes.

Estimates of velocity and position will be introduced as measurement updates by first computing the measurement innovation using (9.19), then forming the measurement model using an extended form of (9.24)

$$\mathbf{H}^n_{k,\text{GNSS}} = \left[\begin{array}{ccc|cc|ccc} \mathbf{H}^n_{p1} & \mathbf{0}_3 & -\mathbf{I}_3 & \mathbf{0}_3 & \mathbf{0}_3 & \mathbf{0}_3 & \mathbf{0}_3 & \mathbf{0}_3 \\ \mathbf{H}^n_{v1} & -\mathbf{I}_3 & \mathbf{0}_3 & \mathbf{0}_3 & \mathbf{H}^n_{v5} & \mathbf{0}_3 & \mathbf{0}_3 & \mathbf{0}_3 \end{array}\right], \tag{10.8}$$

and finally performing the measurement update as in (9.26).

External gravity observations can also be introduced into the Kalman filter as measurement updates. This is done by first forming the measurement innovation

$$\delta\mathbf{z}^n_{\delta g} = \delta\mathbf{g}_{\text{obs}} - \delta\mathbf{g}_{\text{KF}}\,, \tag{10.9}$$

where $\delta\mathbf{g}_{\text{obs}}$ denotes the measurement of gravity disturbance and $\delta\mathbf{g}_{\text{KF}}$ the Kalman filter estimates thereof. The measurement matrix is then formed as

$$\mathbf{H}^n_{k,\delta g} = \left[\begin{array}{ccc|cc|ccc} \mathbf{0}_3 & \mathbf{0}_3 & \mathbf{0}_3 & \mathbf{0}_3 & \mathbf{0}_3 & \mathbf{I}_3 & \mathbf{0}_3 & \mathbf{0}_3 \end{array}\right], \tag{10.10}$$

and a measurement update is performed as in (9.26). Since the SAG system will only estimate variations in the gravity signal, introducing external gravity observations at each end of the survey will relate the estimates to absolute values of the gravity field. Such observations are known as tie values and are typically available either by direct observation, using an absolute gravimeter, or by transferring a nearby point of known gravity to the airport using a relative gravimeter. However, terrestrial methods usually provide estimates of the gravity disturbance in terms of a scalar quantity, δg, which is not simply related to the corresponding vector quantity, $\delta\mathbf{g}$, see Section 3.3.3. This inconsistency will here be handled through the approximation

$$\delta\mathbf{g}_{\text{obs}} \approx \begin{bmatrix} 0 & 0 & \delta g \end{bmatrix}^\top, \tag{10.11}$$

and introduced as a 3D gravity vector observation with a standard deviation of 0.03 mGal on each component. This means that the horizontal components still represent relative estimates, whereas the vertical component may have some small associated bias, assumed here to be negligible (the total vertical component is approximately six orders of magnitude

larger than the horizontal components). If the vehicle is not parked at the exact same position in the exact same direction at each end of the survey, this may also introduce some linear drift in the horizontal estimates. The introduction of horizontal observations was however found to generate superior gravity estimates for all three components.

10.1.2 Validation of Algorithm

In order to test if the algorithm developed in this dissertation is capable of producing consistent gravity estimates, it will be applied to simulated data. The simulated data is again generated using the profile in Figure 7.1 and the algorithm developed in Section 7. Gravity values were computed from EGM08 along the profile and input to the simulation algorithm. Sensor errors were added to the IMU observations using the error models from Table 9.3, meaning that white noise were added to the gyroscope and accelerometer observations along with a constant bias.

The position observations generated in Section 9.2 are again introduced as measurement updates along with gravity tie values at each end of the survey. The gravity tie values were generated by taking the mean value of gravity disturbance computed from EGM08 during the alignment period at each end of the survey.

In order to model the gravity disturbance as a stochastic process, the autocorrelation function was derived from input gravity signal, i.e. EGM08 gravity disturbance, in terms of the along-track distance. The parameters of both first-, second-, third- and fourth-order Gauss-Markov models were derived by least squares fitting of the correspond autocorrelation function to each component of the gravity vector as illustrated in Figure 10.1. These autocorrelation functions are listed in Table D.1 and the parameters obtained are listed in Table 10.1.

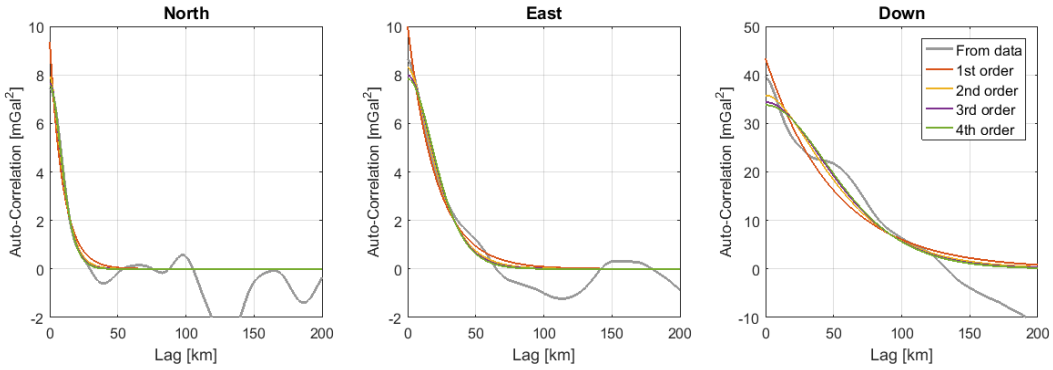

Figure 10.1: Autocorrelation function derived from EGM08 gravity disturbance along the flight profile. The autocorrelation function of a first-, second-, third- and fourth-order Gauss-Markov process is fitted (in a least squares sense) to the estimated autocorrelation of the profile

	North			East			Down		
GM	σ	$1/\beta$	Corr.L.	σ	$1/\beta$	Corr.L.	σ	$1/\beta$	Corr.L.
Order	mGal	km	km	mGal	km	km	mGal	km	km
1	3.1	9.8	9.8	3.1	21.1	21.1	6.6	50.8	50.8
2	2.8	5.6	12.0	2.9	12.4	26.6	6.0	30.5	65.5
3	2.8	4.3	12.5	2.8	9.6	27.9	5.9	23.7	68.8
4	2.8	3.6	12.6	2.8	8.1	28.5	5.8	20.1	70.6

Table 10.1: Parameters of the best fitting (least squares) Gauss-Markov models to EGM08 gravity disturbance along the flight profile. Also shown is the implied correlation lengths, see e.g. [19]

The attitude, velocity, position and bias error states are modelled as in Table 9.4, whereas the gravity error state is modelled as either a first-, second-, third- or fourth-order Gauss-Markov process using the parameters listed in Table 10.1. The vertical component of gravity disturbance estimated using each of the four models is shown in Figure 10.2 along with the EGM08 values for the entire data span.

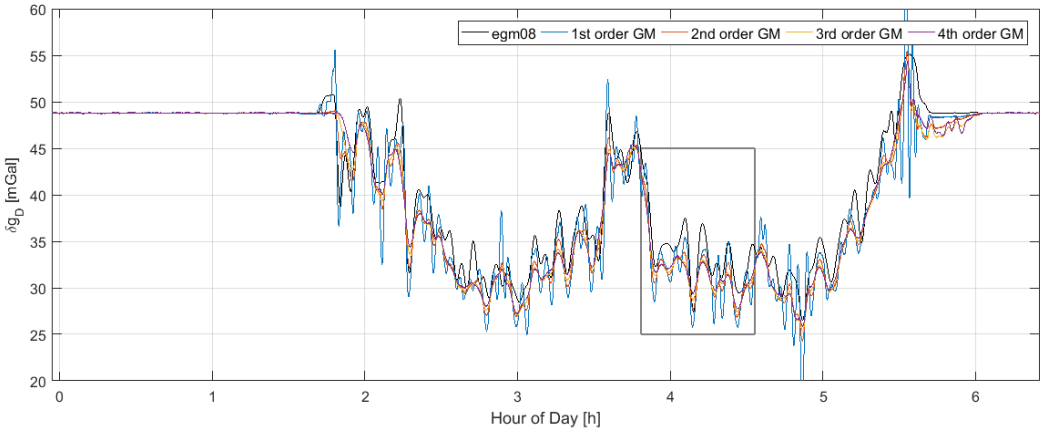

Figure 10.2: Vertical component of EGM08 gravity disturbance across the entire flight along with estimates using the 1st, 2nd, 3rd and 4th order Gauss-Markov models. The contents of the box is shown in Figure 10.3

From the figure it is apparent that the different models imply varying degrees of smoothing. This becomes even more evident if we zoom in to the single straight line segment shown in Figure 10.3. Although the stochastic models used are derived from the input data, the second-, third- and fourth-order models appear to severely smooth the estimated gravity signal. However, as is especially apparent from the first order model, some features of the estimated signal are not present in the actual gravity signal, meaning that the degree of smoothing is a compromise between amplifying errors and allowing gravity to vary with its full amplitude. By increasing the standard deviation used for the stochastic model, the amplitude of the estimated gravity signal can be varied. This is shown for the third-order model

in Figure 10.4, where the standard deviation for the vertical component is increased to 20 mGal. As seen in the figure, the amplitude of the gravity signal increases along with the amplitude of the erroneous features, meaning that the accuracy does not improve in terms of neither standard deviation nor Root-Mean-Square (RMS) of the difference between estimates and input.

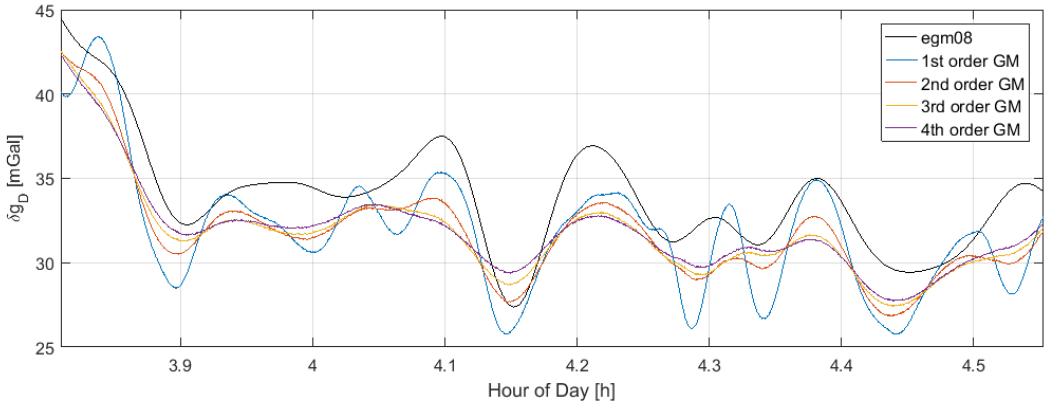

Figure 10.3: Vertical component of EGM08 gravity disturbance across a single flight line (straight line segment) along with estimates using the 1st, 2nd, 3rd and 4th order Gauss-Markov models

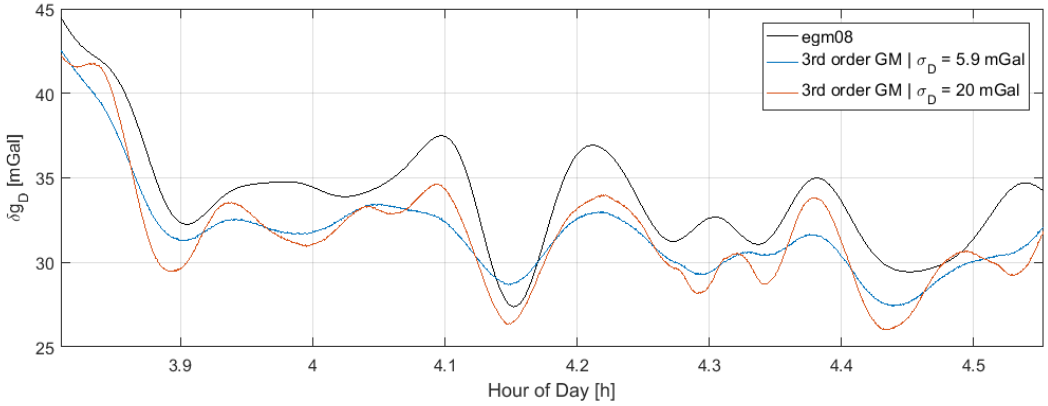

Figure 10.4: Vertical component of EGM08 gravity disturbance across a single flight line (straight line segment) along with estimates using a 3rd order Gauss-Markov model with two different standard deviation parameters

As can be seen from the above figures, the gravity estimates also appear to be biased with respect to the input signal. This is despite the introduction of tie values, that effectively removes the bias at the end points as illustrated in Figure 10.2. This is quite interesting, since bias variation is thought to be the main factor affecting the long wavelength components of the estimated gravity signal. Since the gyroscope and accelerometer biases are constant in this simulation, there is indication that even such static components can affect the long wavelengths. Probably in combination with attitude errors.

Some statistics in terms of difference between EGM08 and the estimated gravity disturbance is computed along the four straight line segments and shown in Table 10.2. This means that the two signals being compared do not have the same resolution. For the vertical component, the third- and fourth-order models are seen to produce similar statistics, while the second-order model performs slightly better and the first-order model worse. However, all four models are seen to produce consistent gravity estimates, although some additional smoothing should be applied to the first-order model.

GM order	Mean	STD	Min.	Max.	RMS	RMSE	
NORTH COMPONENT							
1	-25.6	17.6	-68.1	16.2	31.1	22.0	mGal
2	-16.3	13.0	-51.6	15.1	20.8	14.7	mGal
3	-15.2	11.5	-48.4	14.4	19.0	13.5	mGal
4	-15.2	11.5	-48.4	14.4	19.0	13.5	mGal
EAST COMPONENT							
1	-7.5	10.1	-29.0	10.0	12.6	8.9	mGal
2	-1.1	6.1	-12.5	9.7	6.2	4.4	mGal
3	-1.8	5.1	-12.1	7.6	5.5	3.9	mGal
4	-1.8	5.1	-12.1	7.6	5.5	3.9	mGal
DOWN COMPONENT							
1	-1.8	2.0	-8.4	4.3	2.7	1.9	mGal
2	-2.0	1.2	-5.6	1.4	2.3	1.6	mGal
3	-2.0	1.4	-7.2	2.3	2.4	1.7	mGal
4	-2.0	1.4	-7.2	2.3	2.4	1.7	mGal

Table 10.2: Statistics of the difference between EGM08 gravity disturbance input to the simulation algorithm and gravity disturbance estimated by the integration algorithm on the four straight line segments

For the horizontal components, the statistics are again similar for the third- and fourth-order models, which perform better than the first- and second-order models. The horizontal gravity estimates are shown for each of the four straight line segments in Figures 10.5 and 10.6. For the east component, the first-order model does not seem to have much resemblance with the input signal. Otherwise, the gravity estimates appear to be smoothed with respect to EGM08 and contain erroneous long wavelength information.

Based on this analysis, it is seen that the processing framework developed here produce consistent gravity estimates that are smoothed to some degree in order to attenuate erroneous features in the estimated gravity signal. The statistics in Table 10.2 are therefore not representable for the processing accuracy, since the comparison is based on a model with higher spatial resolution. It is also seen that the third- and fourth-order Gauss-Markov models produce similar results. Therefore, a third-order Gauss-Markov model will be used in the following development in order to limit processing complexity.

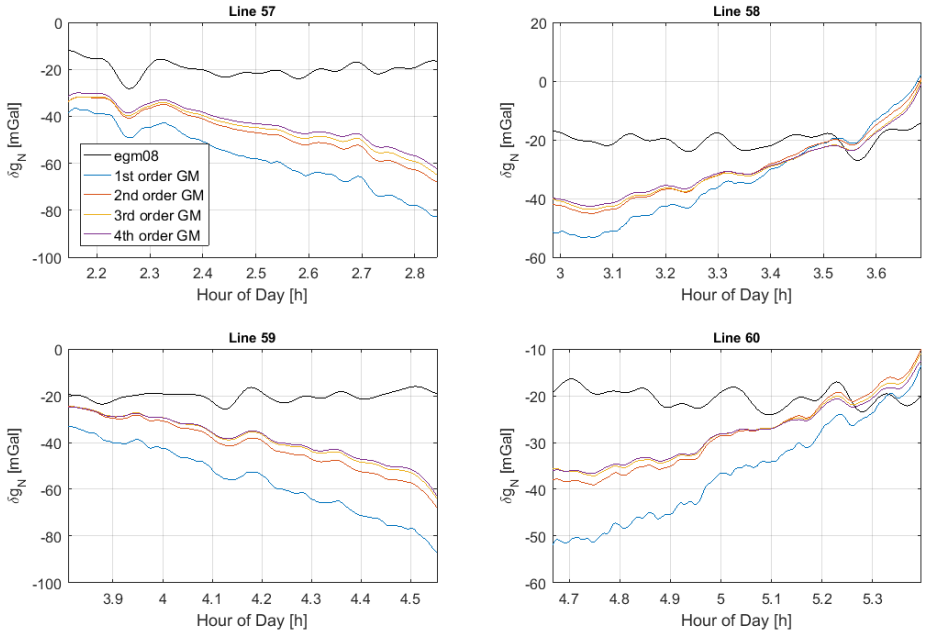

Figure 10.5: North component of EGM08 gravity disturbance across the four straight line segments along with estimates using the 1st, 2nd, 3rd and 4th order Gauss-Markov models

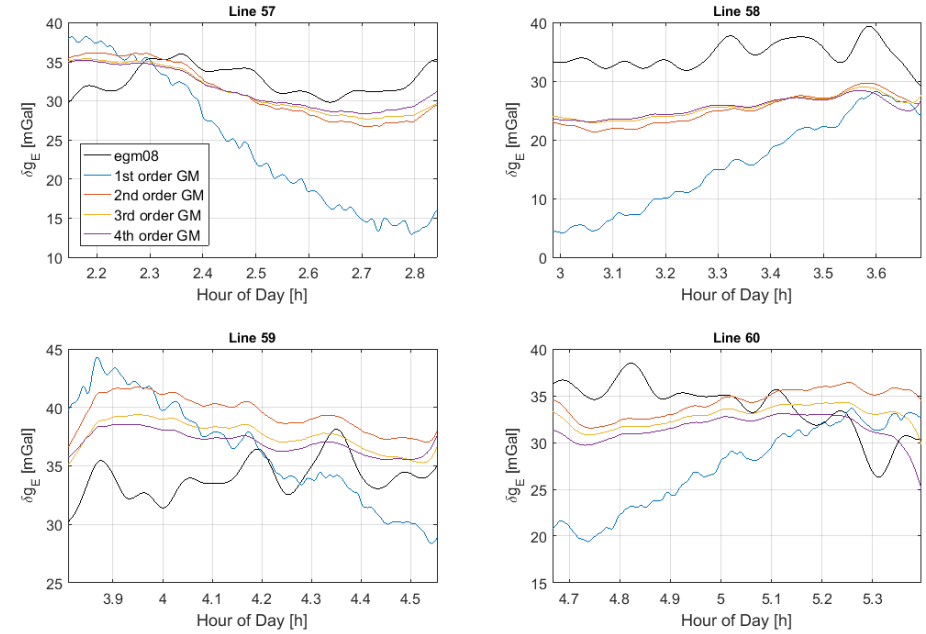

Figure 10.6: East component of EGM08 gravity disturbance across the four straight line segments along with estimates using the 1st, 2nd, 3rd and 4th order Gauss-Markov models

10.2 Outline of the Processing Methodology

In the next section, the airborne surveys used in this dissertation will be presented along with the gravity results. Before continuing, this subsection will outline the processing methodology used to obtain the gravity estimates. All the tools used in the processing have already been presented, such that only a brief overview will be given here.

IMU Observations
The accelerometer observations are corrected using the temperature calibration curve from Section 6.1.3. For surveys performed in 2016, such a calibration curve is only available for the vertical accelerometer, while calibration curves are available for all three components for surveys carried out in 2018.

GNSS Observations
The GNSS observations are processed using the Waypoint commercial software suite by NovAtel in order to arrive at velocity and position estimates with associated error covariance matrices. The results in Section 11 are all based on a Precise Point Positioning (PPP) solution using the final satellite ephemerides data product from the Inernational GNSS Service (IGS). These products are available after 12-18 days for the GPS network and 11-17 days for the GLONASS network[2].

The Gravity Model
The observed IMU accelerations are compensated using a model of normal gravity. In Appendix E.1 is a discussion on the computation of the normal gravity vector. This computation is not performed on-line, but computed using the GNSS trajectory and interpolated onto the IMU time stamps. At the end of processing, the gravity model is again added to the gravity estimates, making this an example of the Remove-Compute-Restore approach. Having derived the final gravity estimates, these are converted to gravity disturbance using position estimates from the integrated navigation solution.

Gravity Tie Values
External gravity observations are used to form observations of the gravity disturbance vector as outlined in Section 10.1.1. These estimates are used to form gravity observations at a 1 Hz rate during the stationary alignment period in both ends of the flight.

The Integration Algorithm
The IMU and GNSS observations are combined within the Kalman filter framework as described in Section 10.1.1. To this end, the error on the gravity disturbance is modelled along with other navigation parameters as stochastic processes shown in Table 10.3.

The IMU observations are processed within this framework using an implementation of the n-frame inertial navigation equations, while GNSS position and velocity estimates are introduced as measurement updates in a loosely coupled fashion. The gravity tie values are also introduced as measurement updates during the stationary alignment period at both ends of the flight. The parameters in Table 10.3 used for modelling the gravity disturbance represent initial or default values that are used in a first processing iteration.

[2] see `www.igs.org/products`

Error State	Model	Initial uncertainty	System Noise
Attitude	Random walk	$[1, 1, 5]$ °	$0.2''/\sqrt{\text{s}}$
Velocity	Random walk	.5 m/s	$5 \cdot 10^{-5}$ m/s$\sqrt{\text{s}}$
Position	None	$[1, 1, 5]$ m	$0\,\text{m}/\sqrt{\text{s}}$
Accelerometer bias	Random constant	30 mGal	$0.01\,\text{mGal}/\sqrt{s}$
Gyroscope bias	Random constant	$0.001\,°/\text{h}$	$0\,°/\text{h}/\sqrt{s}$
Gravity disturbance	3rd order Gauss-Markov model	0.03 mGal	$\sigma = 100\,\text{mGal}$ $\beta = 1/\,(20\,\text{km})$

Table 10.3: Overview of stochastic models used in the processing along with initial uncertainty and system noise in terms of root-PSD of the associated white noise process. Initial errors are in terms of standard deviation. For the Gauss-Markov process, the defining parameters are listed instead of the system noise. The system noise can be derived from Table D.1 (keeping the difference between root-PSD and PSD in mind)

Extracting Straight Line Segments

The estimated gravity disturbance is manually extracted for the straight line segments, representing the flight lines of the airborne gravity survey. As some erroneous features may occur during turns, these will propagate into both ends of the straight line segment. The definition of straight line segments is therefore a subjective matter and often involves comparison with any other available information.

Deriving Stochastic Model Parameters

Having extracted gravity estimates from each straight line segment, the along-track distance is derived. For each line segment, the autocorrelation function is then computed as a function of distance, d. A third-order Gauss-Markov model of the form

$$R(d) = \sigma^2 e^{-\beta_3|d|}\left(1 + \beta_3|d| + \tfrac{1}{3}\beta_3^2|d|^2\right) , \tag{10.12}$$

is then fitted to the estimated autocorrelation functions in a least squares manner. It should be noted that a mean value is subtracted from each line segment before computing the autocorrelation function. If this is not done, the least squares fitting approach may not converge or give meaningless results.

Finally, the parameters obtained from the least squares fitting are used in a second processing iteration of the entire survey. The gravity estimates derived from this second iteration represents the final gravity estimates.

11 Results

The previous section presented the processing approach and algorithm developed here to derive estimates of the gravity vector from a SAG system. The SAG system owned by DTU Space consists of the iNAT unit in a strapdown configuration, along with a GNSS receiver and antenna set. This section will present results from the following four data sets:

1. A first test flight of the iNAT unit through a section of Denmark known to have significant gravity variation
2. A large scale gravity-dedicated airborne campaign over the South China Sea, north of the Island of Borneo
3. A helicopter test flight over the Jakobshavn glacier in Greenland
4. A test flight surveying a small grid over the Odenwald mountain range in Germany

All of the above have been acquired using the iNAT unit in a strapdown configuration. The results from each of these data sets will be evaluated internally in terms of cross-over differences and repeated line segments. An overview of the data sets and results is presented in Table 11.1.

The iNAT unit has been along on a number of additional geophysical surveys focusing on radar and laser altimetry. As these surveys do not present any means of internal evaluation, they will not be presented here.

	Denmark Test Flight	Malaysia Gravity Campaign	Greenland Helicopter Test	Germany Test Flight
Time period	April 2016	June/July 2016	August 2016	March 2018
Carrier	182T Skylane Cessna	Super King Air 200 Beechcraft	AS350 Ecureuil Eurocopter	TU206 Stationair Cessna
Autopilot	yes	yes	no	yes
Survey Overview				
Number of flights	1	30	1	1
Number of lines	2	108	8	54
Airborne duration	3h 36min	125h 22min	2h 48min	7h 18min
Airborne distance	746 km	30,493 km	404 km	1,375 km
Distance on lines	549 km	22,147 km	288 km	875 km
Flight Characteristics for Straight Line Segments (mean/STD/min./max.)				
Ground speed [m/s]	67/2/61/72	88/2/73/119	52/6/41/64	55/2/49/62
Flight altitude [m]	605/4/594/626	1956/129/816/3604	768/224/295/1221	948/11/914/988
Terrain altitude [m]	20/30/-32/109	3/27/0/928	-	218/75/85/437
Terrain clearance [m]	585/30/493/632	1953/136/739/3603	-	730/77/517/881
Evaluation using Repeated Line Segments (North/East/Down)				
No. of lines	1	0	1	1
Times repeated	2	-	3	2
Mean [mGal]	-4.4/2.1/0.2	-	17.4/-12.8/1.5	21.8/-38.4/4.9
STD [mGal]	4.1/0.8/0.8	-	15.6/8.8/3.5	1.6/3.9/0.6
Minimum [mGal]	-12.2/1.0/-1.8	-	-10.5/-23.4/-8.7	19.7/-44.5/3.7
Maximum [mGal]	6.4/4.9/3.0	-	39.9/4.1/9.0	23.9/-31.1/5.9
RMS [mGal]	6.1/2.8/0.8	-	23.4/15.5/3.8	21.8/38.6/4.9
RMSE [mGal]	4.3/1.6/0.6	-	16.5/11.0/2.7	15.4/27.3/3.5
Evaluation using Cross-Over Points (Down)				
No. of points	0	351	3	522
Mean [mGal]	-	0.5	-	-4.2
STD [mGal]	-	2.6	-	2.6
Minimum [mGal]	-	-6.1	-	-10.2
Maximum [mGal]	-	8.0	-	5.3
RMS [mGal]	-	2.7	-	5.0
RMSE [mGal]	-	1.9	-	3.5
Parameters used in 3rd order Gauss-Markov Model (North/East/Down)				
σ [mGal]	11.7/5.0/13.6	11.0/9.0/10.2	23.9/11.8/23.7	5.8/6.7/14.9
$1/\beta_3$ [km]	5.8/9.5/7.2	11.0/10.5/7.8	2.1/2.0/1.3	2.0/1.5/1.2
Corr. length [km]	16.8/27.5/20.9	32.0/30.6/22.6	6.1/5.8/3.8	5.8/4.2/3.4

Table 11.1: Overview of data sets used in this dissertation along with evaluation statistics from repeated line segments and cross-over points. Heights are with respect to WGS84 and terrain altitude is inferred from SRTM30.

11.1 Denmark (2016) - Test Flight

Immediately after acquiring the iNAT unit from iMAR in April 2016, a simple flight test was performed on April 25th. The IMU was installed on the back seat of a Cessna 182T Skylane aircraft and the GNSS antenna was attached to the rear windscreen as shown in Figure 11.1. The purpose of this survey was to test the device in a simple way. Most of the equipment was packed in a box, which was placed on the back seat and fixed by simply pushing back the front seat as much as possible. The IMU was therefore not rigidly attached to the aircraft and may have moved during the flight.

Figure 11.1: Pictures from the installation of the test flight. (Top:) The Cessna 182T aircraft; (Bottom left:) The box containing IMU, GNSS receiver and some batteries; (Bottom right:) The GNSS antenna taped to the rear windscreen.

The survey was based from Roskilde Airport (RKE) in Denmark and consists of only a single flight line which was flown twice, see Figure 11.2. The line was arranged such that the profile crosses over the Silkeborg gravity high and through the Danish Salt Dome Province in northwestern Jutland [20, 18]. The average ground speed during the two straight line segments was 67 m/s and the average altitude above terrain was 585 m.

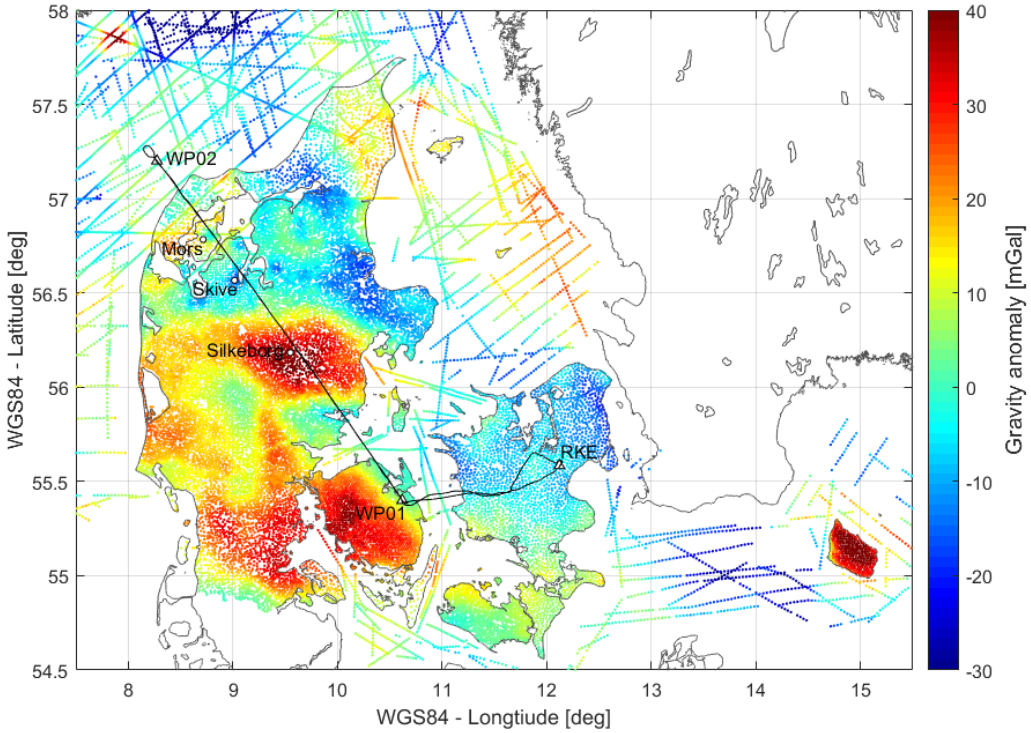

Figure 11.2: Ground track of the survey (black line) along with gravity anomalies measured across Denmark (ground and ship). Also shown are Roskilde Airport (RKE), the two waypoints defining the flight line and some important locations along the profile.

After the first processing iteration, the autocorrelation function was computed from the two straight line segments. The results from least squares fitting of a third-order Gauss-Markov autocorrelation function are shown in Table 11.2. These parameters were used in a second processing iteration, resulting in the estimated vertical component shown in Figure 11.3.

Component	σ	$1/\beta_3$	Corr.L.
North	11.66 mGal	5.79 km	16.8 km
East	5.05 mGal	9.47 km	27.5 km
Down	13.62 mGal	7.21 km	20.9 km

Table 11.2: Parameters of the third-order Gauss-Markov model obtained by fitting model to autocorrelation function computed from the two straight line segments, along with the implied correlation length

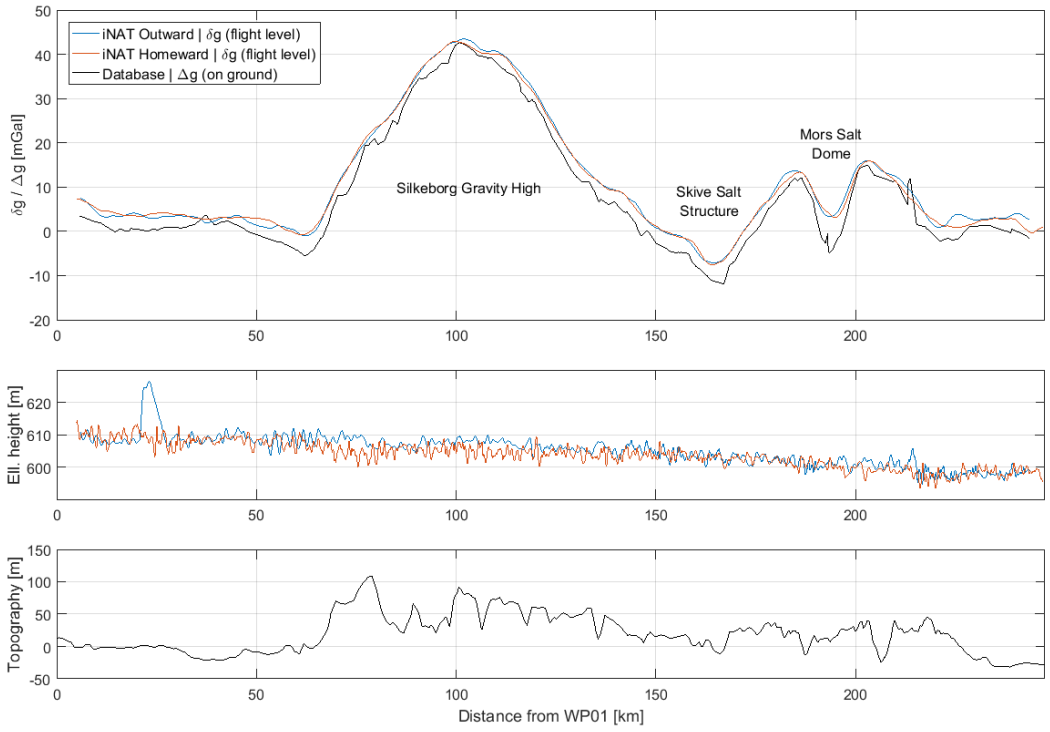

Figure 11.3: Estimated gravity disturbance profile. (Top:) Estimated gravity disturbance in both directions along with gravity anomalies interpolated from the ground measurements (the two spikes around 200 km are probably artefacts of the interpolation); (Middle:) Flight altitude in both directions; (Bottom:) Topography/bathymetry along the profile from SRTM30+ with respect to WGS84.

In the figure it is seen that the outward and homeward profiles correlate well with each other and with the ground observations. The estimated profiles are naturally more smooth due to the upward continuation of the gravity field. The gravity high around Silkeborg and the two salt structures are all visible in the gravity profiles. Some relevant statistics from the difference between the outward and homeward gravity profiles are shown in Table 11.3 for both the vertical and horizontal components.

	Mean	**STD**	**Min.**	**Max.**	**RMS**	**RMSE**	
North	-4.4	4.1	-12.2	6.4	6.1	4.3	mGal
East	2.1	0.8	1.0	4.9	2.8	1.6	mGal
Down	0.2	0.8	-1.8	3.0	0.8	0.6	mGal

Table 11.3: Statistics of the difference in gravity disturbance between the two profiles.

Table 11.3 indicates that the accuracy of the horizontal components are about an order of magnitude worse than the vertical component. Since no temperature calibration was applied to the horizontal accelerometers, the long wavelength components were expected to drift more than the vertical component. Estimates for the two horizontal components are shown in Figure 11.4.

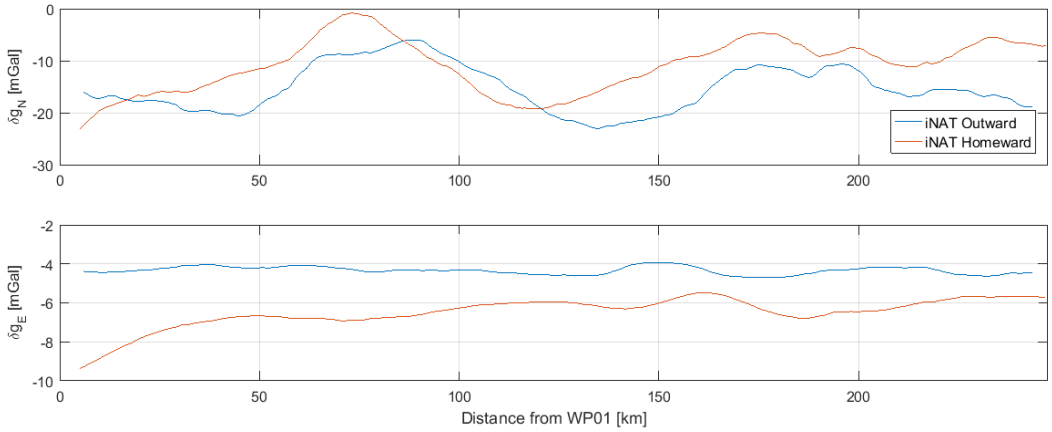

Figure 11.4: Gravity disturbance estimates for the horizontal components: (Top:) North component; (Bottom:) East component.

By removing a linear trend from each line, the statistics improves as shown in Table 11.4. The agreement improves dramatically for the horizontal components, indicating that the major error resides in the long wavelength spectrum for these components. For the vertical component, the statistics only improves slightly.

	Mean	**STD**	**Min.**	**Max.**	**RMS**	**RMSE**	
North	0	3.7	-6.0	8.5	3.7	2.6	mGal
East	0	0.5	-0.8	1.7	0.5	0.4	mGal
Down	0	0.7	-2.0	2.2	0.7	0.5	mGal

Table 11.4: Statistics of the difference in gravity disturbance after removing a linear model from each profile.

11.2 Malaysia (2016) - Airborne Campaign

After a successful test flight, the iNAT unit was brought along on a large gravity-dedicated airborne campaign in Malaysia during summer 2016. The aircraft used for this campaign was the Beechcraft Super King Air 200 shown in Figure 11.5. As shown in Figure 11.6, the iNAT unit was installed alongside the LaCoste&Romberg platform-stabilised gravimeter that is routinely operated by DTU Space.

Figure 11.5: Picture of the Beechcraft Super King Air BE-200 used for the gravity campaign in Malaysia 2016

Figure 11.6: Picture of the installation inside the aircraft. The IMU is attached to the floor of the aircraft next to the LaCoste&Romberg platform. This picture is actually from 2015 with the iMAR RQH unit owned by the University of Darmstadt installed in the aircraft. Unfortunately, no picture was available from the installation in 2016, but the IMU was placed at the exact same spot.

The entire campaign consisted of more than 125 flight hours distributed on 30 flights. These flights were broken into 108 straight line segments with an average ground speed of 88 m/s and an average altitude of approximately 2 km. An overview of the entire survey is shown in Figure 11.7, illustrating that most of the survey was carried out over open water.

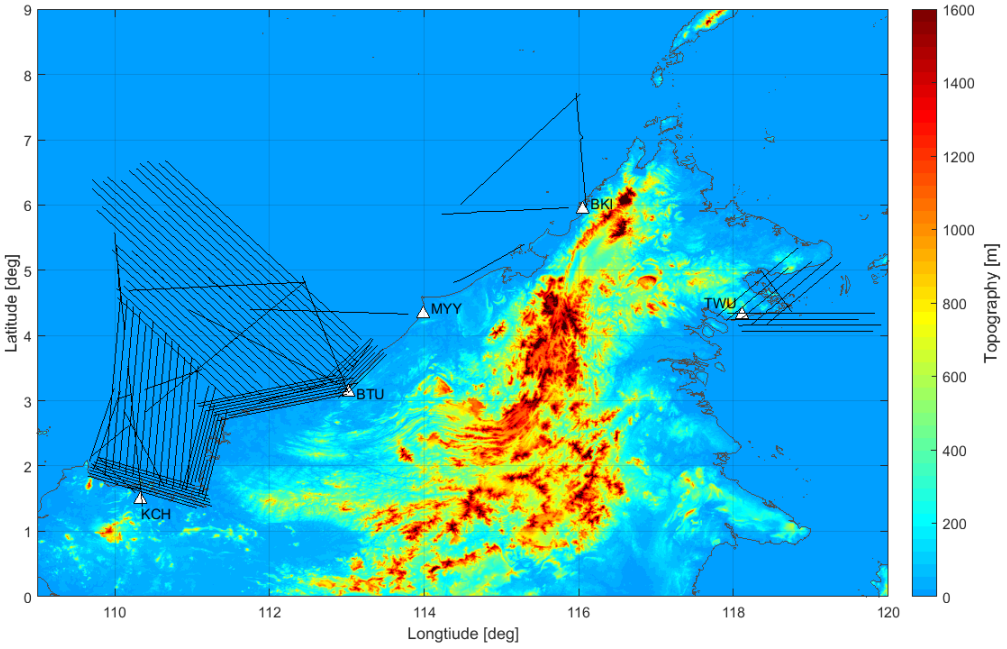

Figure 11.7: Straight line segments from the campaign (black lines) along with topography from SRTM30. Also shown are the airports used for the campaign: Kuching (KCH), Bintulu (BTU), Miri (MYY), Kota Kinabalu (BKI) and Tawau (TWU)

The parameters obtained by fitting a third-order Gauss-Markov model to the autocorrelation functions computed from the 108 straight line segments are shown in Table 11.5. In Figure 11.8, the vertical gravity estimates are shown for the 94 lines representing the main area of the survey. From the total 108 line segments, 351 crossing points were identified. Some statistics from the difference between gravity estimates at these crossing points is shown in Table 11.6. As seen from the table, there is an enormous discrepancy among the horizontal estimates. This will be further commented on in the discussion.

Component	σ	$1/\beta_3$	Corr.L.
North	11.04 mGal	11.02 km	32.0 km
East	8.96 mGal	10.54 km	30.6 km
Down	10.23 mGal	7.80 km	22.6 km

Table 11.5: Parameters of the third-order Gauss-Markov model obtained by fitting model to autocorrelation function computed from the 108 straight line segments, along with the implied correlation length

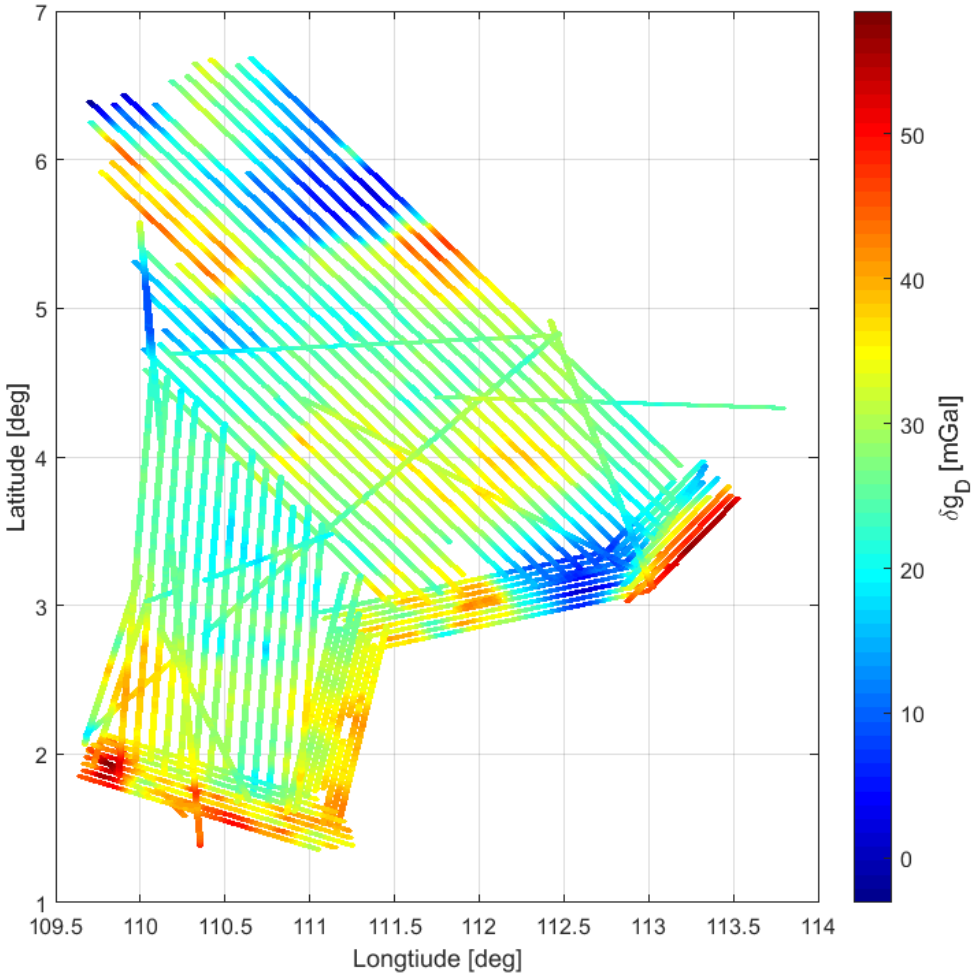

Figure 11.8: Vertical component of the estimated gravity disturbance along the straight line segments of the main part of the campaign (94 line segments)

	Mean	**STD**	**Min.**	**Max.**	**RMS**	**RMSE**	
North	$7.6 \cdot 10^4$	$1.9 \cdot 10^5$	$-1.5 \cdot 10^5$	$8.6 \cdot 10^5$	$2.0 \cdot 10^5$	$1.5 \cdot 10^5$	mGal
East	$3.6 \cdot 10^5$	$1.2 \cdot 10^5$	$1.7 \cdot 10^5$	$8.5 \cdot 10^5$	$3.7 \cdot 10^5$	$2.6 \cdot 10^5$	mGal
Down	0.5	2.6	-6.1	8.0	2.7	1.9	mGal

Table 11.6: Statistics of the difference between the 351 crossing points of the Malaysia gravity campaign

11.3 Illulisat Glacier, Greenland (2016) - Helicopter Test

In August 2016, an opportunity arose to test the iNAT unit in a helicopter environment. The original purpose of going to Greenland was to measure absolute gravity values at a number of reference points around Ilulissat (Jakobshavn) and Qeqertarsuaq (Godhavn) near the Jakobshavn glacier. Since a helicopter was required to reach the Kangia North GPS site (KAGA), the iNAT unit was installed in the helicopter and flown across the glacier while the absolute gravimeter was measuring. The installation was done very quickly by attaching the iNAT unit to the floor and front seat using straps and two GNSS receivers to the inside of the upper-front windscreen using tape. The installation is shown in Figure 11.9.

Figure 11.9: Pictures from the installation of the helicopter test flight in Greenland. (Top:) The Eurocopter AS350 helicopter at KAGA; (Bottom left:) Installation of the iNAT unit behind the front seat using straps and tape; (Bottom right:) Two GNSS antennas taped to inside of the upper-front windscreen

The entire survey was based from Ilulissat Airport (JAV) and consists of the six flight lines shown in Figure 11.10. The line between JAV and KAGA was repeated three times, resulting in eight straight line segments. The entire survey lasted approximately four hours with an average ground speed of 52 m/s and altitude of 768 m on the straight line segments. It was not possible to get a consistent terrain height over the glacier, so the height over terrain is currently unknown. The helicopter first dropped off the absolute gravimeter at KAGA

and returned to the airport to pick up additional passengers. The helicopter then headed for the P1 waypoint, resulting in an unintended profile between JAV and P1. The profiles between P1-P2, P3-P4 and P5-P6 crossed over the glacier and have previously been flown under Operation IceBridge[3] (OIB) using the AIRGrav gravimeter from Sander Geophysics. The gravity estimates from OIB are made available by NASA and exist for the years 2010, 2011 and 2012, resulting in nine total profiles. The OIB flights were carried out using a fixed-wing aircraft with an average ground speed of 134 m/s. These profiles are therefore not expected to represent the true resolution of the gravity field across the glacier, which is more than 1 km thick. The iNAT gravity estimates using a slower-moving platform, could therefore supply additional information across the glacier. Finally, having surveyed the three profiles, the helicopter returned to the KAGA site to pick up the absolute gravimeter. This resulted in a cross-over line between P7 and KAGA. After picking up the instrument, the helicopter headed back to JAV, resulting in a third profile along the JAV-KAGA line.

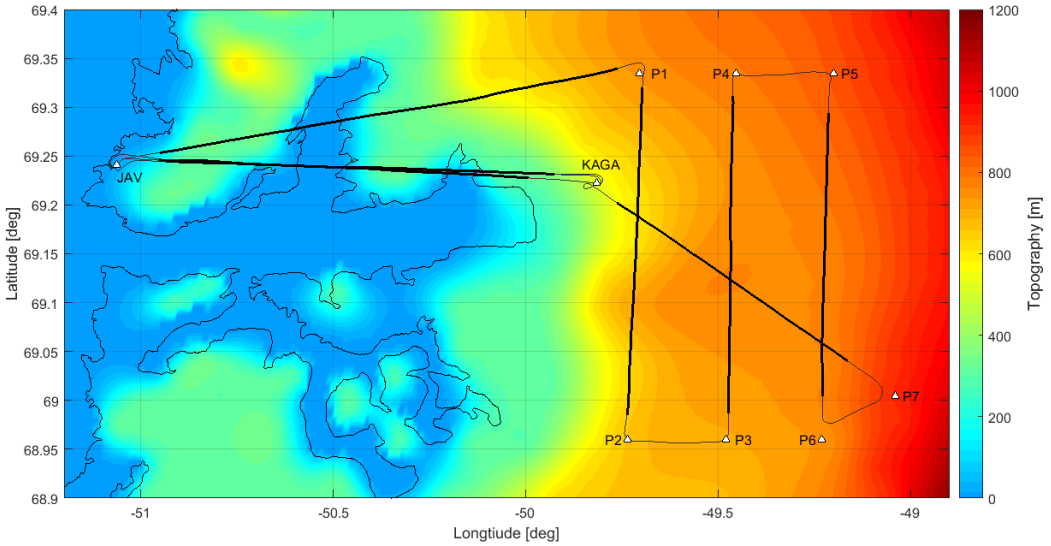

Figure 11.10: Overview of the Greenland helicopter survey with ground track (gray line) and straight line segments (black lines). The three lines between P1-P2, P3-P4 and P5-P6 correspond to lines flown previously within Operation IceBridge. Also shown are Ilulissat Airport (JAV) and Kangia North GPS station (KAGA)

The parameters obtained from fitting a third-order Gauss-Markov model to the initial estimates are listed in Table 11.7. The estimated gravity disturbance from the second processing iteration is shown for the three glacier profiles in Figure 11.11, along with the OIB estimates. Except for a small bias, the iNAT estimates are very similar to the OIB estimates in terms of long wavelength information. The increased resolution of the iNAT estimates is also apparent at the lowest part of the profile, representing the deepest part of the glacier.

[3] icebridge.gsfc.nasa.gov/

Component	σ	$1/\beta_3$	Corr.L.
North	23.87 mGal	2.11 km	6.1 km
East	11.79 mGal	1.98 km	5.8 km
Down	23.72 mGal	1.32 km	3.8 km

Table 11.7: Parameters of the third-order Gauss-Markov model obtained by fitting model to autocorrelation function computed from the 8 straight line segments, along with the implied correlation length

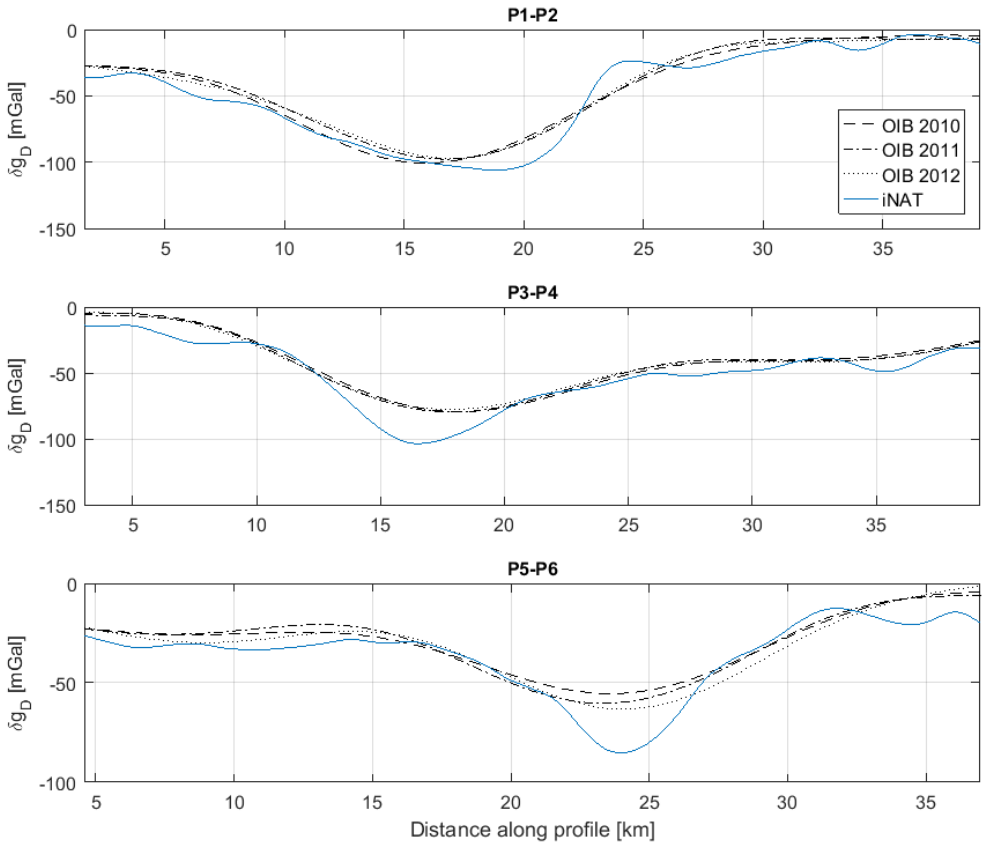

Figure 11.11: Vertical component of estimated gravity disturbance along with estimates from OIB along the three profiles P1-P2, P3-P4 and P5-P6

Figure 11.12 illustrates the vertical estimates along the profile between P7 and KAGA, along with values inferred from the three crossing profiles. The overall profile corresponds well with the crossing points and the increased resolution at the center of the glacier (around 20 km) becomes apparent with respect to the OIB estimates.

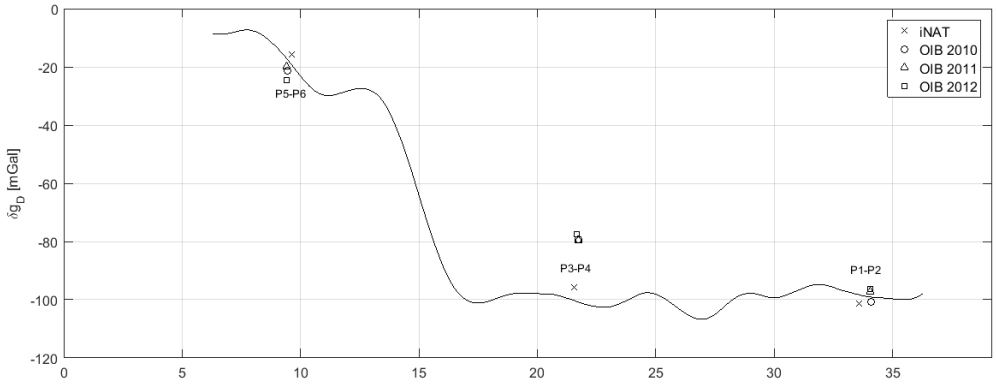

Figure 11.12: Vertical component of estimated gravity disturbance along the profile from P7 to KAGA alogn with values inferred from crossing profiles. Cross over differences are from left to right: 3.5, 4.6 and 3.0 mGal (internal to survey)

In Figures 11.13 and 11.14 the vertical and horizontal estimates are shown for the repeated line segment between JAV and KAGA. The overall profile between the three line segments shows reasonable agreement, with significant biases for the horizontal components. It can be noticed that the second and third profiles are less biased. Since the first profile was flown in opposite direction than the other two, there is indication that the bias can be direction dependent and related to attitude errors. Table 11.8 lists some statistics from individual differences between these repeated profiles.

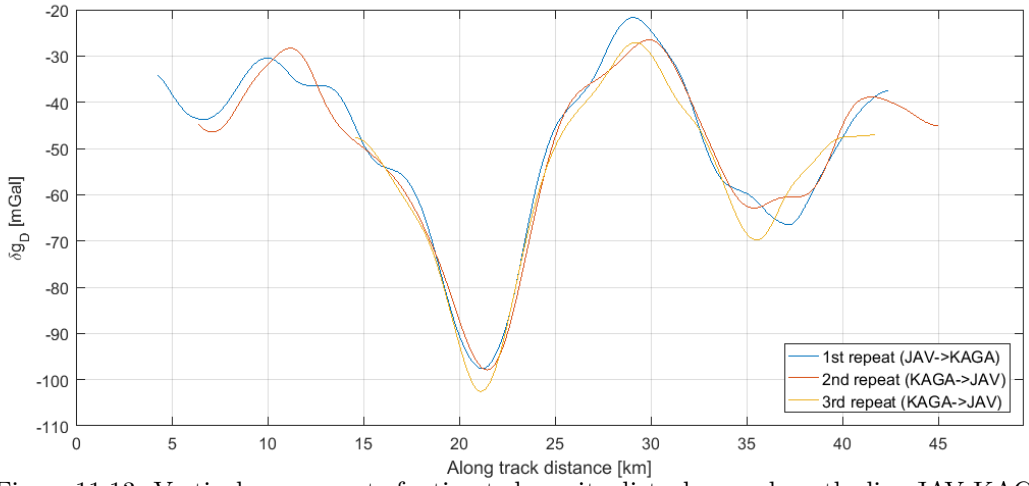

Figure 11.13: Vertical component of estimated gravity disturbance along the line JAV-KAGA, which was repeated three times

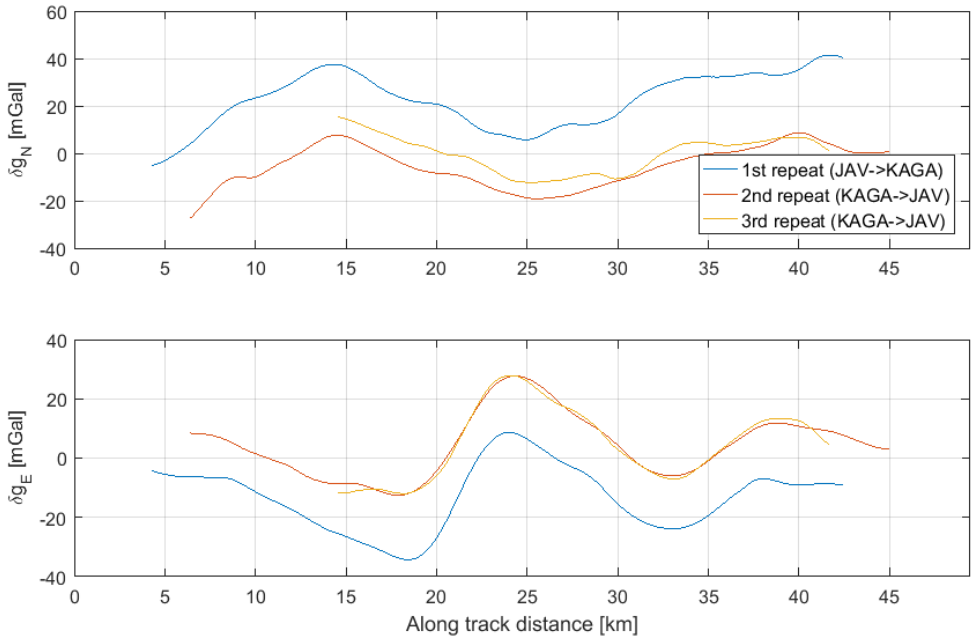

Figure 11.14: Horizontal components of estimated gravity disturbance along the line JAV-KAGA, which was repeated three times

	Mean	**STD**	**Min.**	**Max.**	**RMS**	**RMSE**	
NORTH							
Line 1-2	29.7	3.3	22.8	38.7	29.9	21.1	mGal
Line 1-3	23.7	5.6	14.4	39.9	24.4	17.2	mGal
Line 2-3	-5.2	3.4	-10.5	2.8	6.3	4.4	mGal
EAST							
Line 1-2	-17.9	2.6	-23.4	-12.2	18.1	12.8	mGal
Line 1-3	-19.0	1.8	-22.8	-13.6	19.1	13.5	mGal
Line 2-3	0.2	1.3	-1.9	4.1	1.3	0.9	mGal
DOWN							
Line 1-2	0.7	3.2	-6.7	7.6	3.3	2.3	mGal
Line 1-3	2.2	3.8	-8.7	9.0	4.4	3.1	mGal
Line 2-3	1.7	3.3	-5.8	8.2	3.8	2.7	mGal

Table 11.8: Statistics of the individual differences between the three estimated profiles along the repeated line segment. For example, line 1-2 denoted estimates from first pass minus estimates from second pass

11.4 Odenwald, Germany (2018) - Test Flight

After having exchanged some electronics inside the iNAT unit, iMAR arranged a comparison flight between three of their systems: The iNAT unit owned by DTU Space, the similar (but older) RQH system owned by TU Darmstadt and the more advanced system, also based on a similar iNAT unit, owned by the national mapping agency of Turkey (HGK). All three units were installed in a Cessna 206 Stationair aircraft as shown in Figures 11.15 and 11.16.

Figure 11.15: Picture of the Cessna TU206G T Stationair 2 aircraft used for the Odenwald test flight

Figure 11.16: Picture of the installation inside the aircraft. The iNAT unit is placed on the rack in the back end of the aircraft, together with the iMAR RQH unit owned by the University of Darmstadt. The front rack represents the airborne gravimetry system owned by national mapping agency of Turkey (HGK), also developed by iMAR

The survey was based from Mainz-Finthen airport (QMZ) in Germany and surveys a small area of approximately 25x10 km in the Odenwald mountain range as illustrated in Figure 11.17. The survey consists of 15 East-West oriented lines and 37 North-South oriented lines. An additional straight line segment was added on the approach and repeated in the homewards direction as seen in the figure. The average along-track speed was 55 m/s and the average flight altitude was 948 m. The flight altitude on the lines is shown in Figure 11.18 along with the terrain height derived from the SRTM30 data product.

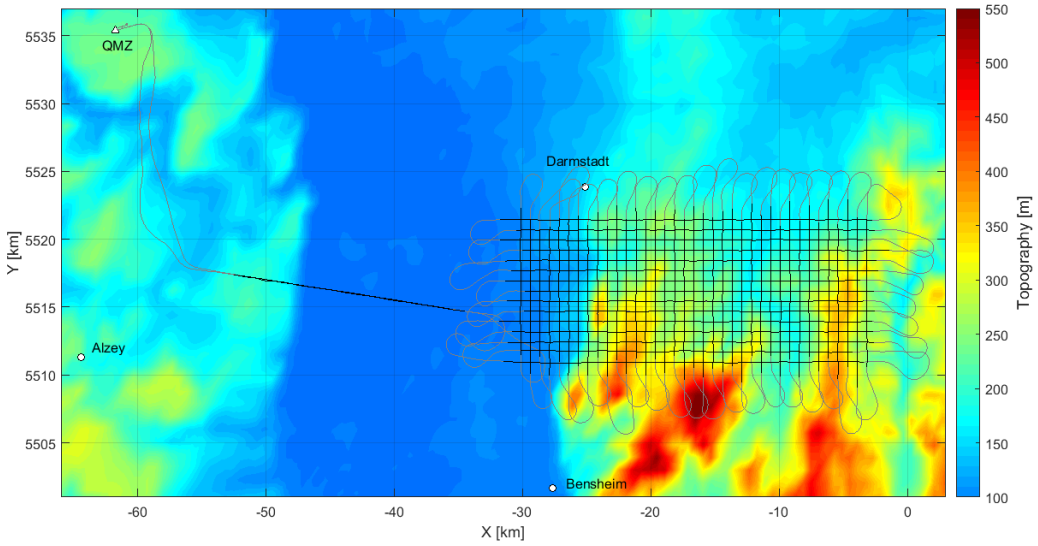

Figure 11.17: Survey overview along with topography from SRTM30. The survey was based from Mainz-Finthen airport (QMZ) and mainly represents a grid in the Odenwald mountain range. Coordinates are with respect to UTM zone 32

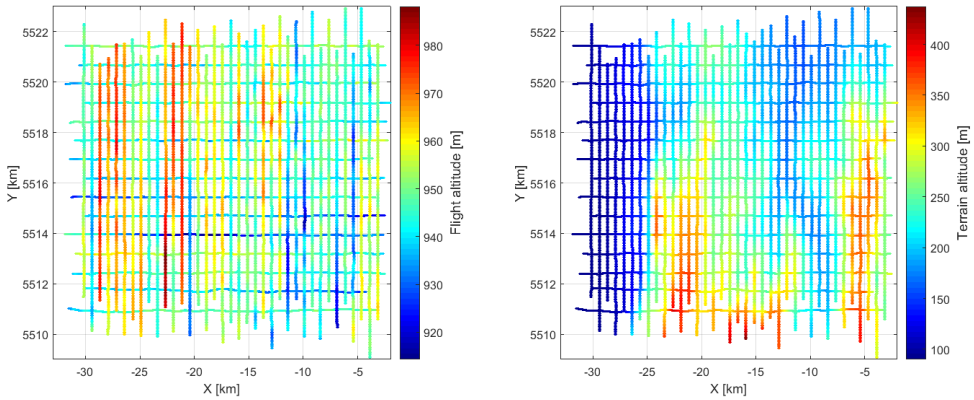

Figure 11.18: Altitude along the straight line segments of the Odenwald grid. (Left:) Flight altitude; (Right:) Terrain altitude. Both heights are with respect to WGS84 and coordinates are with respect to UTM zone 32

Autocorrelation functions derived for the vertical component of the estimated gravity disturbance from the first processing iteration are shown in Figure 11.19. A clear distinction is seen between the East-West oriented lines, the North-South oriented lines and the two repeat-line segments. As the North-South oriented lines are very short (≈10 km), the least-squares fitting of the Gauss-Markov model is based solely on the East-West oriented lines as seen in the figure. The resulting parameters are listed in Table 11.9.

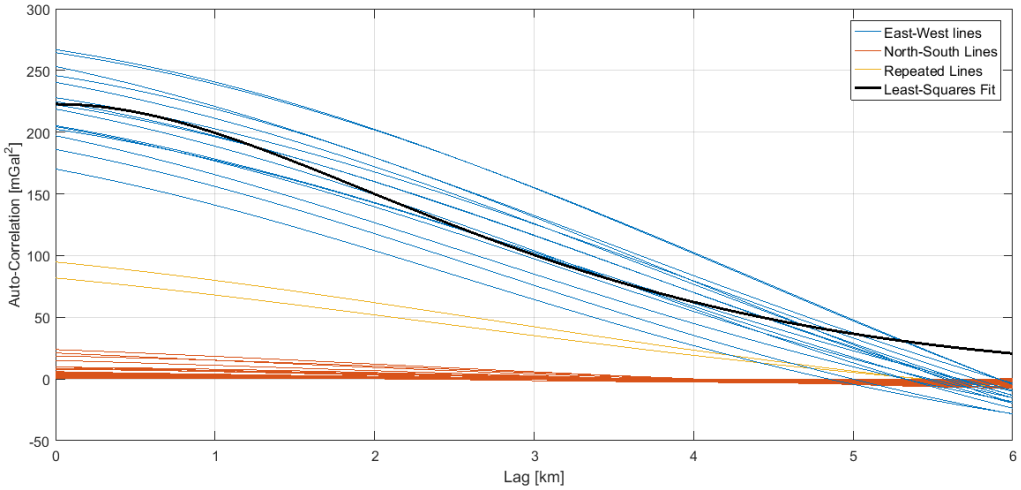

Figure 11.19: Autocorrelation functions derived from the vertical component of estimated gravity disturbance from the first processing iteration

Component	σ	$1/\beta_3$	Corr.L.
North	5.76 mGal	2.01 km	5.8 km
East	6.74 mGal	1.45 km	4.2 km
Down	14.92 mGal	1.19 km	3.4 km

Table 11.9: Parameters of the third-order Gauss-Markov model obtained by fitting model to autocorrelation function computed from the 15 East-West oriented line segments, along with the implied correlation length

	Mean	**STD**	**Min.**	**Max.**	**RMS**	**RMSE**	
North	$-1.7 \cdot 10^4$	$7.9 \cdot 10^3$	$-3.0 \cdot 10^4$	$-3.1 \cdot 10^4$	$1.8 \cdot 10^4$	$1.3 \cdot 10^4$	mGal
East	$5.5 \cdot 10^6$	$3.1 \cdot 10^3$	$5.5 \cdot 10^6$	$5.5 \cdot 10^6$	$5.5 \cdot 10^6$	$3.9 \cdot 10^6$	mGal
Down	-4.3	2.6	-10.2	5.3	5.0	3.5	mGal

Table 11.10: Statistics of the cross-over differences for the Odenwald grid

The vertical component of the estimated gravity disturbance using the model parameters listed in Table 11.9 is shown in Figure 11.20. Table 11.10 lists some statistics from the cross-over differences. Again, the cross-over statistics from the horizontal components show a large discrepancy.

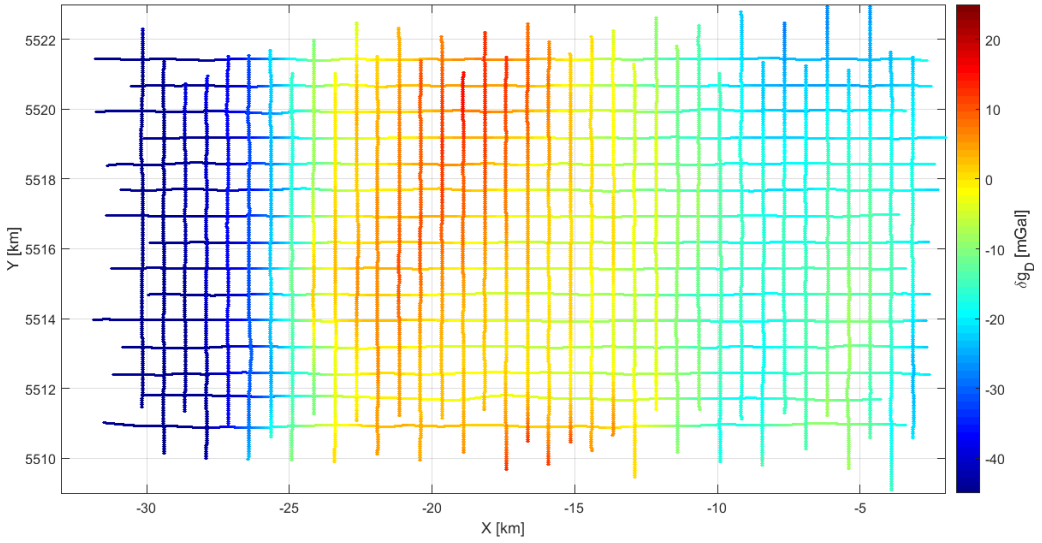

Figure 11.20: Vertical component of estimated gravity disturbance over the Odenwald grid

Figure 11.21 illustrates the gravity estimates along the repeated line segment. As this line is flown at each end of the survey, there is indication that a bias variation of approximately 5 mGal occurs during the survey for the vertical component. Some statistics for the difference between these two line estimates are shown in Table 11.11. For the vertical component, the RMSE is similar to the one computed from cross-over differences. As the standard deviation is only 0.6 mGal, this could indicate that a long-term bias variation is the limiting factor for the vertical component.

	Mean	**STD**	**Min.**	**Max.**	**RMS**	**RMSE**	
North	21.8	1.6	19.7	23.9	21.8	15.4	mGal
East	-38.4	3.9	-44.5	-31.1	38.6	27.3	mGal
Down	4.9	0.6	3.7	5.9	4.9	3.5	mGal

Table 11.11: Statistics if the difference between the two profiles along the repeated line segment of the Odenwald survey

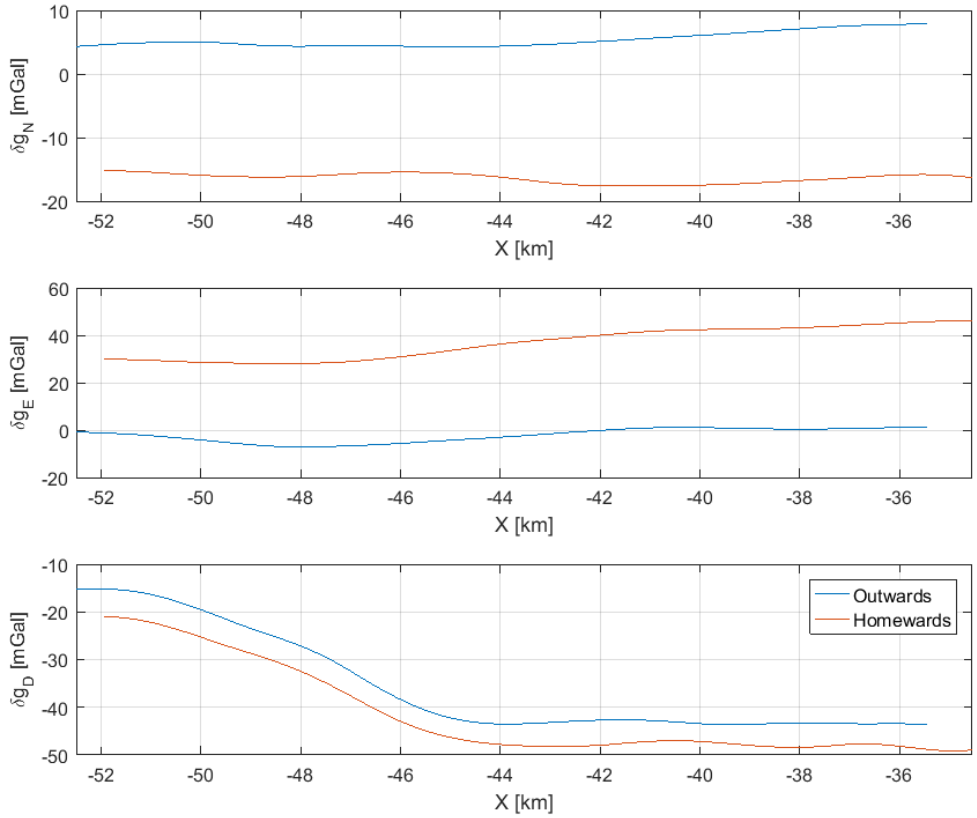

Figure 11.21: Estimated gravity disturbance along the repeated line segment

12 Discussion

The results presented in the previous section were evaluated both in terms of repeated line segments and cross-over differences. The statistics derived from the cross-over differences yielded an accuracy of 1.9 and 3.5 mGal for the vertical component, in terms of RMSE. For the horizontal components, these statistics yielded large inconsistencies. The repeated line segments offered some insight into the dominant errors, which appears to be in the long wavelength spectrum of the estimates. The corruption of long wavelength information will therefore be discussed first, in the following subsection. This is followed by a short section illustrating some effects of the RTS smoother on the horizontal gravity estimates. In the third subsection, the topic of spatial resolution will be briefly discussed. Finally, in the fourth subsection, some indications of the dynamic range of the SAG system will be presented.

12.1 The Corruption of Long Wavelength Information

The comparison of repeated line segments indicated that long term bias variation continues to corrupt the estimates, despite the simple temperature calibration applied in this dissertation. Whether this erroneous long term variation is temperature independent or originates from calibration insufficiency is currently unknown. As the simulation in Section 10.1.2 indicated, these long term effects may not even originate from sensor errors, but from the processing algorithm developed here. The erroneous long term information in the gravity estimates could be the main factor influencing the statistics computed from cross-over differences.

The iNAT and LaCoste&Romberg estimates from the Malaysia 2016 campaign were combined in the paper attached in Appendix F.2, in an attempt to retrieve the long term variation from the LaCoste&Romberg gravity estimates. Inferring a simple linear model from the LaCoste&Romberg estimates showed significant improvement, again indicating that large errors exist in the long wavelength information. Retrieval of long wavelength information from other sources, both ground-, air-, ship- and space-borne methods, is an interesting subject that should receive attention in the future.

Comparison of the horizontal components along the straight line segments showed large biases. The variation along profiles did however seem to agree quite well as seen in Figures 11.4, 11.14 and 11.21. As the measure of standard deviation is very similar to the Root-Mean-Square measure, only with the mean value removed, the general reduction in magnitude from RMS to STD in Table 11.1 is an indication of the improvement due to bias removal. The long term variation on the horizontal components were seen to be much larger than for the vertical direction. In the case where temperature calibration was applied to the horizontal accelerometers, differences of up to 30 mGal were observed over the course of a flight, see Figure 11.21. However, evaluation of the horizontal components in terms of cross-over differences resulted in a discrepancy of several m/s^2!

In Figure 11.14 there was some indication that the horizontal bias was direction-dependent rather than time-dependent. If the estimated tilt angles (bank and elevation) are wrong, the presence of an uncompensated accelerometer bias could propagate into the horizontal gravity estimates as a direction-dependent bias. Again, if long wavelength information can be inferred from other sources and included in the processing as for example measurement updates, this could constrain the long wavelength variation of the gravity estimates and possibly even lead to improved attitude and sensor bias estimates.

12.2 Effects Originating from the RTS Smoother

In Figure 12.1, the north component of estimated gravity is shown, both before and after smoothing, for a single flight in Malaysia. The flight represents two parallel line segments, flown sequentially in opposite directions, approximately 10 km apart. The gravity profile for the two lines should therefore be similar (but opposite in direction), which seems to be the case for the non-smoothed Kalman filter estimates. The RTS smoother eliminates most of the signal structure and adds an additional bias to the estimates. As the RTS smoother is essentially a linear combination of the forward and backward Kalman filter estimates, there seems to be a discrepancy among the two. This effect has not been investigated further in this dissertation, but does require further investigation.

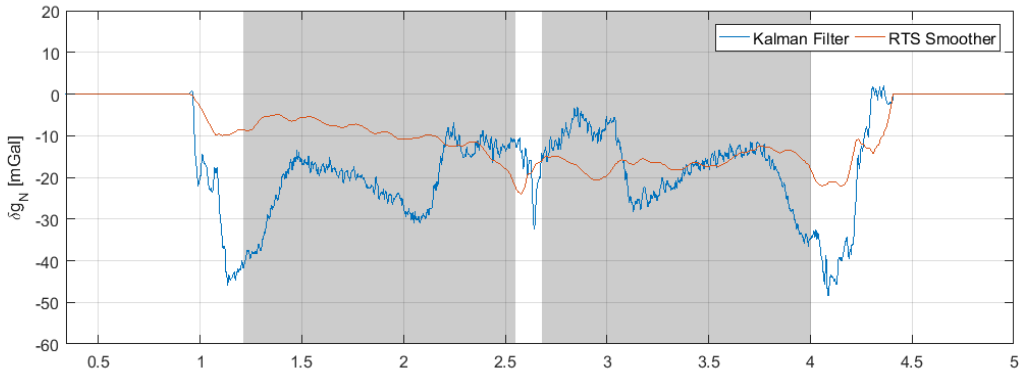

Figure 12.1: Estimates of north component during an entire flight, representing two parallel line segments. Shown are estimates both before smoothing (Kalman filter) and after smoothing (RTS smoother). Gray areas mark straight line segments

12.3 Resolution of Gravity Estimates

As the gravity estimates are smoothed using the RTS smoother, they essentially represent a linear combination of forward and backward Kalman filter estimates. As there is no filter width associated with this kind of smoothing, the spatial resolution is not easily inferred as when using a regular filter.

As the gravity disturbance is modelled as a stochastic process, the resolution is related to the parameters used for the Gauss-Markov model. However, as was seen by simulation in Section 10.1.2, the gravity estimates may be additionally smoothed in order to attenuate erroneous features in the estimates. Therefore, if a connection between resolution and stochastic parameters should be established, these parameters should probably be inferred from the estimated signal, instead of the parameters used for processing.

The relative weighting between forward and backward solutions is determined by the associated confidence bounds, represented by the error covariance matrix. The error covariance matrix is also estimated within the Kalman filter framework and will be dependent on factors such as aircraft dynamics, confidence in measurements, stochastic modelling etc. For this reason, the associated resolution may not even be uniform.

In the paper attached in Appendix F.3, a method for inferring the spatial resolution of the gravity estimates was attempted. This method represents a comparison between the centralized and cascaded approaches defined in Section 10.1. First, gravity estimates were derived using the ICKF algorithm developed in this dissertation. Using the navigation solution from the integration algorithm, the IMU accelerations were resolved about the n-frame axes and corrected for the Eötvös effect. Kinematic accelerations were derived by double differencing GNSS position estimates (derivation from splines yielded similar results, single difference of velocity estimates yielded poorer results) and subtracted from the rotated accelerations. A two-pass Butterworth filter of varying width was then applied to these differences and compared with the ICKF estimates. The filter width that leads to the best agreement, indicates the spatial resolution. However, this approach did not lead to consistent results, since the implied spatial resolution was different for each line. This need however not be an indication that the approach is not useful, but could also mean that line-to-line resolution is actually not the same.

Spatial resolution is an important concept in airborne gravimetry. It is essential for evaluating the results and in order to combine information with other sources. The spatial resolution of gravity estimates using a Kalman filter is therefore an important topic that requires further attention.

12.4 Dynamic Range of the Strapdown System

Traditional platform stabilised systems are usually confined to gravity estimates along straight line segments, in order to assure that the sensitive axis of the gravimeter is aligned with the plumb line. Any aircraft dynamics or even changes in altitude can corrupt the resulting gravity estimates. Since a strapdown gravimeter contains three accelerometers, it does not need to be levelled in order to provide useful gravity estimates, but rely on sensor precision and computation accuracy.

Although not shown in this dissertation, some lines flown in the Greenland helicopter test was not flown at constant altitude. This is described in the associated paper, attached in Appendix F.3. The three profiles crossing the Jakobshavn glacier were flown in draped mode, i.e. following the terrain. As seen in Figure 11.11, the estimates are consistent with external estimates, indicating that the SAG system is capable of providing useful gravity estimates while drape-flying.

Figure 12.2 illustrates gravity estimates for part of the Denmark test flight, before and after the straight line segment, together with ground observations. The trajectory for this flight is shown in Figure 11.2, indicating the degree of dynamics along the track. Although some erroneous features exist, the gravity estimates do have a large degree of similarity with the ground observations.

There is therefore indication that the SAG system is more resilient to manoeuvring and dynamic conditions than the traditional stabilised-platform systems. An interesting topic of further investigation is therefore how aircraft dynamics influence gravity estimates of the SAG system. It is of great practical importance to know when dynamics leads to degradation of the gravity estimates and to which degree the estimates are degraded.

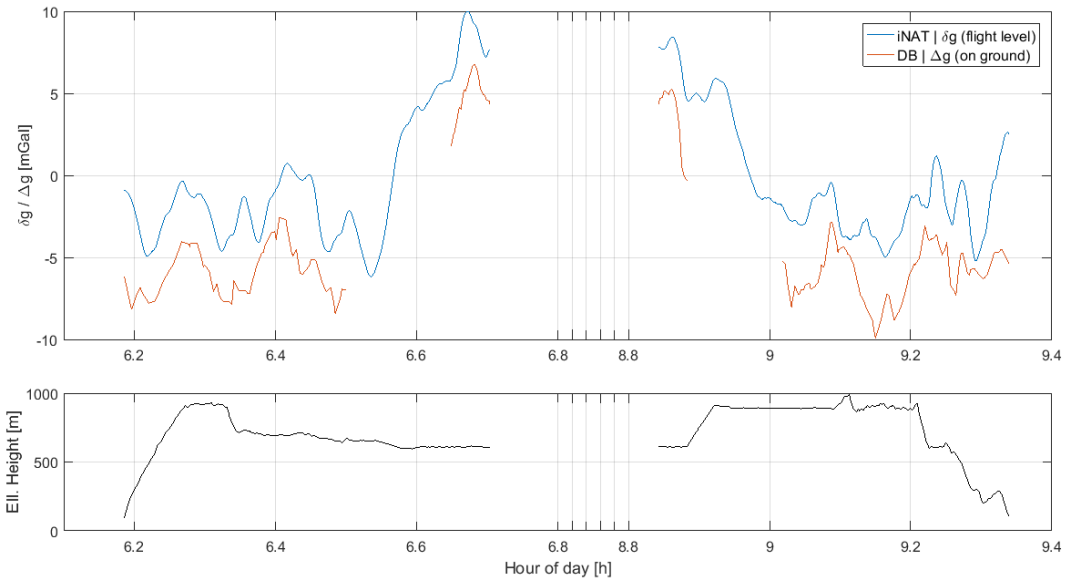

Figure 12.2: Gravity estimates from the Roskilde test survey for the segments not on the flight lines. The trajectory is illustrated in Figure 11.2. (Top:) Vertical component of estimated gravity disturbance along with gravity anomalies interpolated from the database. (Bottom:) Flight altitude for the two segments with respect to WGS84.

13 Conclusion

The results presented in the previous section have shown that the processing algorithm developed here is capable of producing consistent gravity estimates using the iMAR iNAT unit in a strapdown configuration, combined with GNSS observations processed using NovAtel's Waypoint software suite.

For the vertical component, the evaluation in terms of both repeated line segments and cross-over differences yielded an accuracy between 0.6 and 3.5 mGal. Comparison between repeated line segments showed that the dominant error source resides in the long wavelength part of the spectrum. The use of a simple temperature calibration was therefore not found to fully compensate for long term drift in the gravity estimates. As indicated by simulation, such erroneous long wavelength information may however not only originate from variation in the sensor errors, but also from uncompensated static effects.

For the horizontal components, the cross-over differences yielded great inconsistency. Comparison of the repeated line segments did however show reasonable agreement between along-track profiles, but indicated that the long wavelength information may be corrupted by both time- and direction-dependent bias variation. It was also seen that the RTS smoother may have the effect of smearing out variation and introducing erroneous long term variation.

The ability to provide useful gravity estimates under dynamic conditions was also observed. The Greenland test flight demonstrated that the SAG system can operate in a helicopter environment, flying in draped mode, with no autopilot, without any obvious performance degradation. Similarly, inspection of gravity estimates from the Denmark test flight, indicated that useful gravity estimates are not confined to the straight line segments of the flight.

The surveys presented here demonstrate the attractiveness of using a SAG system. Such a system can be purchased off the shelf and derive useful gravity estimates without any modification. The iNAT unit requires no operation during flight, but is simply installed and turned on. The ease of installation was demonstrated in the Denmark test flight, where the unit was simply put on the back seat of the aircraft, and in the Greenland helicopter test, where the unit was attached to the floor using straps and tape. In both cases, the GNSS receiver was also simply attached to the inside of the windscreen using tape. Such installations can be done within a very short time frame.

14 Outlook

Erroneous information in the long wavelength spectrum of the gravity estimates continues to be a limiting factor for SAG. Although off-line temperature calibrations have been shown to significantly improve the long wavelength information obtained using a similar SAG system [2], the simple temperature calibration used in this dissertation was not found to fully constrain the long wavelength information. Using more advanced temperature calibration methods, taking into account scale factors and cross-coupling effects may lead to improved results. However, the use of advanced off-line calibration methods is conditioned by the access to professional calibration facilities. It is also unknown, whether the erroneous long term variation originates from residual temperature-dependent effects, other sensor errors or from the processing method.

The manufacturer of the iNAT unit (iMAR), have now developed a temperature stabilising chamber, that will be tested in the future. In theory, this should eliminate any temperature-dependent variation, as the temperature will remain constant. The practical implications of using such a device is however of concern, since it challenges some of the advantages of using an off-the-shelf strapdown system. Namely, smaller size, lower price, less power consumption and no operation. In practice, there may not be time to wait for temperature stabilisation due to changing weather conditions and burning off fuel at the airport. Moreover, using an off-the-shelf IMU may be interesting for the use in geophysical surveys, where gravity is not a first priority. In this case, the extra cost required to purchase a navigation-grade IMU may be more tractable if it results in both improved attitude estimation and useful gravity estimates.

It would therefore be interesting to investigate other methods of estimating the long wavelength information. To this end, [2] attempted to use a satellite-only gravity model to compensate the IMU accelerations and model the anomalous gravity field with respect to such a model. Although this did not lead to any significant improvement, further investigations could be interesting. For example, the satellite-only gravity estimates could be introduced as measurements in the Kalman filter or the stochastic model could be modified to represent a gravity field with no long wavelength information as in [13].

In order to both evaluate results and further use of the gravity estimates, it is important to have some information on the spatial resolution of the estimates. To the best of my knowledge, there is currently no reliable method for inferring the spatial resolution of gravity estimates filtered using the RTS smoother. As previously argued, the resolution resulting from the RTS smoother may not even be uniform.

The spatial resolution is obviously related to the parameters of the stochastic model used in the processing. It is however questionable if any direct relation between the two can be established. In the processing applied here, the stochastic parameters were kept constant during entire flight and surveys. As the characteristics of the gravity field varies with position, one could image using stochastic parameters that are flight dependent, line dependent or even established some kind of spatially correlated model.

It has yet to be demonstrated if an implementation of a tightly coupled integration architecture will lead to improved gravity estimates. The GNSS solution obtained during straight line flight segments is generally expected to be of high quality, leading to high accuracy in the estimated position and/or velocity. The derived accelerations should therefore be well constrained. However, the use of carrier-phase observations for acceleration determination has

been shown to better accommodate changes in satellite constellation and be more resilient to turbulent flying conditions and high atmospheric activity [16, 15]. Since the gravity field varies slowly with position, the precision of the position solution is not important to airborne gravimetry as long as the gravity is precisely estimated.

The smaller size and lower power consumption of the SAG system, enables it to be used on a smaller platform, such as an Unmanned Arial Vehicle (UAV). As such platforms offer great operational flexibility and lower fuel consumption, these may play an important role in the future. Such system are currently attractive for surveying remote areas, where fuel is not easily supplied. This is especially relevant for studying marine terminating glaciers, since other geophysical techniques are limited by the presence of both ice and water. However, the small platform offered by a UAV will represent a more dynamic environment due to increased sensitivity to turbulence and weather conditions. This means that the ability of deriving useful gravity estimates from a UAV has yet to be demonstrated.

References

[1] Diogo Ayres-Sampaio et al. "A Comparison Between Three IMUs for Strapdown Airborne Gravimetry". In: *Surveys in Geophysics* 36.4 (2015), pp. 571–586. ISSN: 0169-3298. DOI: 10.1007/s10712-015-9323-5. URL: http://link.springer.com/10.1007/s10712-015-9323-5.

[2] David Becker. "Advanced Calibration Methods for Strapdown Airborne Gravimetry". PhD thesis. Darmstadt: Technische Universität Darmstadt, 2016. URL: http://tuprints.ulb.tu-darmstadt.de/5691/.

[3] David Becker et al. "Drift reduction in strapdown airborne gravimetry using a simple thermal correction". In: *Journal of Geodesy* 89.11 (2015), pp. 1133–1144. ISSN: 14321394. DOI: 10.1007/s00190-015-0839-8.

[4] A M Bruton et al. "Deriving Acceleration from DGPS: Toward Higher Resolution Applications of Airborne Gravimetry". In: *GPS Solutions* 5.3 (2002), pp. 1–14. ISSN: 1080-5370. DOI: 10.1007/PL00012894. URL: http://www.springerlink.com/content/7h6dlempv7bprxclhttp://link.springer.com/10.1007/PL00012894.

[5] Alexander Mark Bruton. "Improving the Accuracy and Resolution of SINS / DGPS Airborne Gravimetry". PhD thesis. University of Calgary, 2000, p. 235. URL: https://www.ucalgary.ca/engo{_}webdocs/KPS/00.20145.AMBruton.pdf.

[6] R A Deurloo. "Development of a Kalman Filter Integrating System and Measurement Models for a Low-cost Strapdown Airborne Gravimetry System". PhD dissertation. University of Porto, 2011.

[7] C. Glennie and K. P. Schwarz. "A comparison and analysis of airborne gravimetry results from two strapdown inertial/DGPS systems". In: *Journal of Geodesy* 73.6 (1999), pp. 311–321. ISSN: 0949-7714. DOI: 10.1007/s001900050248. URL: https://www.ucalgary.ca/engo{_}webdocs/KPS/02.20160.SKennedy.pdfhttp://link.springer.com/10.1007/s001900050248.

[8] C. Glennie and K. P. Schwarz. "A comparison and analysis of airborne gravimetry results from two strapdown inertial/DGPS systems". In: *Journal of Geodesy* 73.6 (1999), pp. 311–321. ISSN: 09497714. DOI: 10.1007/s001900050248.

[9] C. L. Glennie et al. "A comparison of stable platform and strapdown airborne gravity". In: *Journal of Geodesy* 74.5 (2000), pp. 383–389. ISSN: 09497714. DOI: 10.1007/s001900000082.

[10] Raymond B Harlan. "Eotvos corrections for airborne gravimetry". In: *Journal of Geophysical Research* 73.14 (1968), pp. 4675–4679. ISSN: 01480227. DOI: 10.1029/JB073i014p04675. URL: http://doi.wiley.com/10.1029/JB073i014p04675.

[11] Yangming Huang et al. "SGA-WZ: A New Strapdown Airborne Gravimeter". In: *Sensors* 12.7 (2012), pp. 9336–9348. ISSN: 1424-8220. DOI: 10.3390/s120709336. URL: http://www.mdpi.com/1424-8220/12/7/9336.

[12] C. Jekeli and R. Garcia. "GPS phase accelerations for moving-base vector gravimetry". In: *Journal of Geodesy* 71.10 (1997), pp. 630–639. ISSN: 09497714. DOI: 10.1007/s001900050130.

[13] Christopher Jekeli. "Airborne vector gravimetry using precise, position-aided inertial measurement units". In: *Bulletin Géodésique* 69.1 (1994), pp. 1–11. ISSN: 00074632. DOI: 10.1007/BF00807986.

[14] Christopher Jekeli. *Theoretical Fundamentals of Inertial Gravimetry*. Presentation at 2016 Airborne Gravimetry for Geodesy Summer School. 2016. URL: https://www.ngs.noaa.gov/GRAV-D/2016SummerSchool/presentations/day-4/1aJekeli_Part_V_InertialAirborneGrav.pdf.

[15] S. L. Kennedy. "Precise Acceleration Determination from Carrier-Phase Measurements". In: *Navigation* 50.1 (2003), pp. 9–19. ISSN: 00281522. DOI: 10.1002/j.2161-4296.2003.tb00314.x. URL: http://doi.wiley.com/10.1002/j.2161-4296.2003.tb00314.x.

[16] S L Kennedy, A M Bruton, and K P Schwarz. "Improving DGPS Accelerations for Airborne Gravimetry: GPS Carrier Phase Accelerations Revisited". In: *Vistas for Geodesy in the New Millennium*. Ed. by K. P. Schwarz and J. Ádám. Vol. 125. International Association of Geodesy Symposia, 2002, pp. 211–216. DOI: 10.1007/978-3-662-04709-5_35. URL: http://link.springer.com/10.1007/978-3-662-04709-5{_}35.

[17] J. H. Kwon and C. Jekeli. "A new approach for airborne vector gravimetry using GPS/INS". In: *Journal of Geodesy* 74.10 (2001), pp. 690–700. ISSN: 09497714. DOI: 10.1007/s001900000130.

[18] Ivan Madirazza, Bo Holm Jacobsen, and Niels Abrahamsen. "Late Triassic tectonic evolution in northwest Jutland , Denmark". In: *Bulletin of the Geological Society of Denmark* (1990), pp. 77–84.

[19] Sameh Nassar and Naser El-sheimy. "Accuracy Improvement of Stochastic Modeling of". In: *Zeitschrift für Geodäsie, Geoinformation und Land- management (ZfV)* 130.3 (2005), pp. 146–155.

[20] Ivar B. Ramberg and Gustaf Lind. "Gravity Measurements on the Paarup Salt Dome". In: (1968).

[21] K P Schwarz and M Wei. "A framework for modeling kinematic measurements in gravity field applications". In: *J. Geodesy* 64.4 (1990), pp. 331–346.

[22] Yuanxi Yang. *Adaptively robust kalman filters with applications in navigation*. 2010, pp. 49–82. ISBN: 9783642117404. DOI: 10.1007/978-3-642-11741-1_2.

Appendices

A Reference Frame Kinematics

The various reference frames introduced in Section 2 represent a variety of different frames, relative to which any physical quantity can be described. Each reference frame is uniquely defined and has its own properties that may or may not be advantageous depending on the application. For example, Newton's laws of motion, which are the basic principles on which inertial navigation is built, are only valid in an inertial frame of reference. In any other coordinate frame, some fictitious forces, such as the centrifugal or Coriolis forces, will be introduced, increasing the complexity of the equations. Another example is the representation of gravity, which is conveniently described in the navigation frame. In order to further explore some of these differences, the first part of this appendix is concerned with some properties of rotating coordinate frames.

A.1 Rotating Coordinate Frames

Rotation operators, able to transform coordinates, vectors and matrices from one reference frame to another, are introduced in Section 5.1. Here, we will assume that such an operator is represented by a matrix, $\mathbf{C}_t^a$. The vector quantity, $\mathbf{v}^t$, is thus rotated into the a-frame as

$$\mathbf{v}^a = \mathbf{C}_t^a \, \mathbf{v}^t \, , \tag{A.1}$$

such that the components of this vector are now resolved about the a-frame axes. The a and t frames are arbitrary frames of reference.

Due to the nature of inertial measurements, we are bound to handle information regarding angles and angular rates. It is therefore convenient to define an axial vector, $\boldsymbol{\psi}$, as the ordered triple of Eulerian angles

$$\boldsymbol{\psi} = \begin{bmatrix} \alpha \\ \beta \\ \gamma \end{bmatrix} \, , \tag{A.2}$$

where α, β and γ are angles. However, such a vector will not in general have the same properties as a "true" vector. Only in the case that the angles are small, can we assume that the axial vector will have all the properties of a normal vector. In this case all second- and higher- order terms will be small [15, Sec. 1.3.4]. This especially means that $\boldsymbol{\psi}$ will transform according to (A.1).

A.1.1 Small Angle Approximation of the Transformation Matrix

In the case that the three Eulerian angles, α, β and γ, are the bank, elevation and heading angles, respectively, the coordinate transformation matrix can be written in terms of three rotations as

$$\begin{aligned}\mathbf{C}_t^a &= \mathbf{R}_x(\alpha)\ \mathbf{R}_y(\beta)\ \mathbf{R}_z(\gamma) \\ &= \begin{bmatrix}1 & 0 & 0\\ 0 & \cos\alpha & \sin\alpha\\ 0 & -\sin\alpha & \cos\alpha\end{bmatrix}\begin{bmatrix}\cos\beta & 0 & -\sin\beta\\ 0 & 1 & 0\\ \sin\beta & 0 & \cos\beta\end{bmatrix}\begin{bmatrix}\cos\gamma & \sin\gamma & 0\\ -\sin\gamma & \cos\gamma & 0\\ 0 & 0 & 1\end{bmatrix} \\ &= \begin{bmatrix}\cos\beta\cos\gamma & \cos\beta\sin\gamma & -\sin\beta\\ -\cos\alpha\sin\gamma+\sin\alpha\sin\beta\cos\gamma & \cos\alpha\cos\gamma+\sin\alpha\sin\beta\sin\gamma & \sin\alpha\cos\beta\\ \sin\alpha\sin\gamma+\cos\alpha\sin\beta\cos\gamma & -\sin\alpha\cos\gamma+\cos\alpha\sin\beta\sin\gamma & \cos\alpha\cos\beta\end{bmatrix}.\end{aligned} \tag{A.3}$$

Then, assuming that the angles are small, we may approximate the terms as $\cos\alpha \approx 1$, $\sin\alpha \approx \alpha$, etc., such that the above expression becomes

$$\begin{aligned}\mathbf{C}_t^a &\approx \begin{bmatrix}1 & \gamma & -\beta\\ -\gamma+\alpha\beta & 1+\alpha\beta\gamma & \alpha\\ \alpha\gamma+\beta & -\alpha+\beta\gamma & 1\end{bmatrix} \approx \begin{bmatrix}1 & \gamma & -\beta\\ -\gamma & 1 & \alpha\\ \beta & -\alpha & 1\end{bmatrix} \\ &= \begin{bmatrix}1 & 0 & 0\\ 0 & 1 & 0\\ 0 & 0 & 1\end{bmatrix} - \begin{bmatrix}0 & -\gamma & \beta\\ \gamma & 0 & -\alpha\\ -\beta & \alpha & 0\end{bmatrix} \\ &= \mathbf{I}_3 - \boldsymbol{\Psi}\ ,\end{aligned} \tag{A.4}$$

where only the first order terms have been retained. The matrix, $\boldsymbol{\Psi}$, is the skew-symmetric form of the axial vector, $\boldsymbol{\psi}$, such that

$$\begin{aligned}\mathbf{v}^a &= \mathbf{C}_t^a\,\mathbf{v}^t = (\mathbf{I}_3 - \boldsymbol{\Psi})\,\mathbf{v}^t = \mathbf{v}^t - \boldsymbol{\Psi}\,\mathbf{v}^t \\ &= \mathbf{v}^t - \boldsymbol{\psi}\times\mathbf{v}^t\ ,\end{aligned} \tag{A.5}$$

which is only valid for small angles.

A.1.2 Angular Rates

Angular rates of rotation are concerned with the rotation rate of one coordinate frame, t, with respect to another coordinate frame, a. This is specified in terms of subscripts on the angular rate, i.e. as $\boldsymbol{\omega}_{at}$. The rate of rotation may be expressed in either of the frames, which are related through a coordinate transformation as

$$\boldsymbol{\omega}_{at}^a = \mathbf{C}_t^a\,\boldsymbol{\omega}_{at}^t\ . \tag{A.6}$$

One should notice that the order of the subscripts is important. For example, $\boldsymbol{\omega}_{at}^a$ denotes the angular rate of the t-frame with respect to the a-frame. This means that exchanging the order of the subscripts we have

$$\boldsymbol{\omega}_{ta}^a = -\boldsymbol{\omega}_{at}^a\ , \tag{A.7}$$

since we are now referring to the angular rate of the a-frame with respect to the t-frame. From an observers point of view, the rotation will be equal in magnitude, but opposite in direction.

The angular velocity is mostly expressed in skew symmetric matrix form, containing the same components as the vector quantity

$$\boldsymbol{\omega}_{at}^{a} = \begin{bmatrix} \omega_x \\ \omega_y \\ \omega_z \end{bmatrix} \quad \mapsto \quad [\boldsymbol{\omega}_{at}^{a}\times] = \boldsymbol{\Omega}_{at}^{a} = \begin{bmatrix} 0 & -\omega_z & \omega_y \\ \omega_z & 0 & -\omega_x \\ -\omega_y & \omega_x & 0 \end{bmatrix}, \tag{A.8}$$

such that

$$\boldsymbol{\omega}_{at}^{a} \times \mathbf{r}^{a} = \boldsymbol{\Omega}_{at}^{a}\, \mathbf{r}^{a}. \tag{A.9}$$

The skew symmetric matrix transforms according to (5.5), like any other matrix.

A.1.3 The Time Derivative of the Transformation Matrix

Since the rotational motion of a reference frame is always given with respect to another reference frame, it can be thought of as a relative motion, involving two reference frames. A position in one reference frame, $\mathbf{r}^{t}$, can be transformed to a position, $\mathbf{r}^{a}$, in another reference frame using the transformation matrix, $\mathbf{C}_{t}^{a}$. If the two frames are rotating with respect to one another, the transformation matrix will not be constant. The time derivative of the transformation matrix can be defined as

$$\dot{\mathbf{C}}_{t}^{a} = \lim_{\triangle\tau\to 0} \frac{\triangle \mathbf{C}_{t}^{a}}{\triangle\tau} = \lim_{\triangle\tau\to 0} \frac{\mathbf{C}_{t}^{a}\left(\tau+\triangle\tau\right) - \mathbf{C}_{t}^{a}\left(\tau\right)}{\triangle\tau}, \tag{A.10}$$

where τ denotes the time and $\triangle\tau$ a time interval. For small time intervals, the transformation matrix, $\mathbf{C}_{t}^{a}\left(\tau+\triangle\tau\right)$, can be written as a perturbation of the former matrix, $\mathbf{C}_{t}^{a}\left(\tau\right)$, as

$$\mathbf{C}_{t}^{a}\left(\tau+\triangle\tau\right) = \mathbf{C}_{t}^{a}\left(\tau\right)\left(\mathbf{I}_3 + \triangle\boldsymbol{\Theta}^{t}\right), \tag{A.11}$$

where $\mathbf{I}_3 + \triangle\boldsymbol{\Theta}^{t}$ is the matrix relating the t-frame at time τ to the rotated t-frame at time $\tau+\triangle\tau$. In the limit that $\triangle\tau$ goes to zero, we can assume that we are dealing with small angles and an approximation similar to the one in section A.1.1 can be applied as

$$\triangle\boldsymbol{\Theta}^{t} = \begin{bmatrix} 0 & -\triangle\theta_Z & \triangle\theta_Y \\ \triangle\theta_Z & 0 & -\triangle\theta_X \\ -\triangle\theta_Y & \triangle\theta_X & 0 \end{bmatrix}. \tag{A.12}$$

Now, substitution of (A.11) into (A.10) leads to the expression

$$\dot{\mathbf{C}}_{t}^{a} = \mathbf{C}_{t}^{a}\left(\tau\right) \lim_{\triangle\tau\to 0} \frac{\triangle\boldsymbol{\Theta}^{t}}{\triangle\tau}, \tag{A.13}$$

but in the limit that $\triangle\tau \to 0$, the rotational rate will correspond to the angular velocity, such that

$$\lim_{\triangle\tau\to 0} \frac{\triangle\boldsymbol{\Theta}^{t}}{\triangle\tau} = \boldsymbol{\Omega}_{at}^{t} = \begin{bmatrix} 0 & -\omega_Z & \omega_Y \\ \omega_Z & 0 & -\omega_X \\ -\omega_Y & \omega_X & 0 \end{bmatrix}. \tag{A.14}$$

The derivative of the transformation matrix is therefore related to the angular velocity as

$$\boxed{\dot{\mathbf{C}}_{t}^{a} = \mathbf{C}_{t}^{a}\, \boldsymbol{\Omega}_{at}^{t}\,.} \tag{A.15}$$

A.1.4 Derivatives of the Position Vector

Consider the transformation of the components of the position vector from some arbitrary frame, t, into some arbitrary frame, a, as

$$\mathbf{r}^a = \mathbf{C}_t^a \, \mathbf{r}^t \, . \tag{A.16}$$

Since the a-frame will generally be rotating with respect to the t-frame (for example the e-frame with respect to the i-frame), some fictitious forces will appear when differentiating the above equation with respect to time. The first derivative is

$$\dot{\mathbf{r}}^a = \frac{\partial}{\partial t} \left(\mathbf{C}_t^a \, \mathbf{r}^t \right) = \mathbf{C}_t^a \, \dot{\mathbf{r}}^t + \dot{\mathbf{C}}_t^a \, \mathbf{r}^t \, , \tag{A.17}$$

in which we can insert relation (A.15) to obtain

$$\boxed{\dot{\mathbf{r}}^a = \mathbf{C}_t^a \left(\dot{\mathbf{r}}^t + \boldsymbol{\Omega}_{at}^t \, \mathbf{r}^t \right) \, ,} \tag{A.18}$$

which is the **law of Coriolis**. The second term inside the brackets on the RHS is the Coriolis term. A second time derivation of the above leads to the expression

$$\boxed{\ddot{\mathbf{r}}^a = \mathbf{C}_t^a \left(\ddot{\mathbf{r}}^t + \boldsymbol{\Omega}_{at}^t \, \boldsymbol{\Omega}_{at}^t \, \mathbf{r}^t + 2\boldsymbol{\Omega}_{at}^t \, \dot{\mathbf{r}}^t + \dot{\boldsymbol{\Omega}}_{at}^t \, \mathbf{r}^t \right) \, ,} \tag{A.19}$$

where the fictitious centrifugal, Coriolis and Euler forces have appeared as the second, third and fourth terms in the brackets, respectively. The combined effect of the vertical components of the Coriolis and Euler forces (third and fourth term) is sometimes referred to as the Eötvös effect.

A.2 Specific Transformations

In the following, expressions of some specific transformation matrices will be presented.

A.2.1 From Inertial to Terrestrial Frame

Since the i-frame and e-frame have the same z-axis and origin, they are related only through a rotation about the z-axis as [4, Eq. 3-12]

$$\mathbf{C}_i^e = \begin{bmatrix} \cos \omega_{ie} t & \sin \omega_{ie} t & 0 \\ -\sin \omega_{ie} t & \cos \omega_{ie} t & 0 \\ 0 & 0 & 1 \end{bmatrix} \, , \tag{A.20}$$

where t denotes the time and

$$\boldsymbol{\omega}_{ie}^i = \boldsymbol{\omega}_{ie}^e = \begin{bmatrix} 0 & 0 & \omega_{ie} \end{bmatrix}^\top \, , \tag{A.21}$$

is the rate of rotation. It is here assumed that the effects of polar motion, along with precession and nutation of the Earth's spin axis, are negligible. It is also assumed that the rotation rate ω_{ie} is constant.

A.2.2 From Navigational to Terrestrial Frame

The transformation from the n-frame to the e-frame is accomplished first through a rotation about the local east-axis by the angle $(\pi/2 + \phi)$ and then about the new z-axis by the angle $-\lambda$, such that

$$\mathbf{C}_n^e = \mathbf{R}_z\left(-\lambda\right)\mathbf{R}_y\left(\pi/2 + \phi\right) \ , \tag{A.22}$$

where ϕ and λ are the geodetic latitude and longitude respectively. The resulting transformation matrix is [15, Eq. 1.87]:

$$\mathbf{C}_n^e = \begin{bmatrix} -\sin\phi\cos\lambda & -\sin\lambda & -\cos\phi\cos\lambda \\ -\sin\phi\sin\lambda & \cos\lambda & -\cos\phi\sin\lambda \\ \cos\phi & 0 & -\sin\phi \end{bmatrix} . \tag{A.23}$$

The angular rate is [15, Eq. 1.88]:

$$\begin{aligned} \boldsymbol{\omega}_{en}^n &= \left[\dot{\lambda}\cos\phi, -\dot{\phi}, -\dot{\lambda}\sin\phi\right]^\top \quad \text{and} \\ \boldsymbol{\Omega}_{en}^n &= \begin{bmatrix} 0 & \dot{\lambda}\sin\phi & -\dot{\phi} \\ -\dot{\lambda}\sin\phi & 0 & -\dot{\lambda}\cos\phi \\ \dot{\phi} & \dot{\lambda}\cos\phi & 0 \end{bmatrix} , \end{aligned} \tag{A.24}$$

where $\dot{\phi}$ and $\dot{\lambda}$ are the changes in latitude and longitude of a vehicle travelling parallel to the ellipsoidal surface.

A.2.3 From Navigational to Inertial Frame

The transformation between the i-frame and n-frame is similar to the e-frame-n-frame transformation. The only difference is that geodetic longitude, λ, is substituted by the angular difference $(\lambda + \omega_{ie}t)$ and is given in [4, Eq. 3-10] as

$$\mathbf{C}_n^i = \begin{bmatrix} -\sin\phi\cos\left(\lambda + \omega_{ie}t\right) & -\sin\left(\lambda + \omega_{ie}t\right) & -\cos\phi\cos\left(\lambda + \omega_{ie}t\right) \\ -\sin\phi\sin\left(\lambda + \omega_{ie}t\right) & \cos\left(\lambda + \omega_{ie}t\right) & -\cos\phi\sin\left(\lambda + \omega_{ie}t\right) \\ \cos\phi & 0 & -\sin\phi \end{bmatrix} , \tag{A.25}$$

with the angular velocity [4, Eq. 3-8]

$$\begin{aligned} \boldsymbol{\omega}_{in}^n &= \left[\left(\dot{\lambda} + \omega_{ie}\right)\cos\phi, -\dot{\phi}, -\left(\dot{\lambda} + \omega_{ie}\right)\sin\phi\right]^\top \quad \text{and} \\ \boldsymbol{\Omega}_{in}^n &= \begin{bmatrix} 0 & \left(\dot{\lambda} + \omega_{ie}\right)\sin\phi & -\dot{\phi} \\ -\left(\dot{\lambda} + \omega_{ie}\right)\sin\phi & 0 & -\left(\dot{\lambda} + \omega_{ie}\right)\cos\phi \\ \dot{\phi} & \left(\dot{\lambda} + \omega_{ie}\right)\cos\phi & 0 \end{bmatrix} . \end{aligned} \tag{A.26}$$

A.2.4 From Body to Navigational Frame

The transformation from the b-frame to the n-frame is particularly relevant in navigation, since it relates the forward, starboard and down axes of the b-frame to the north, east and down axes of the n-frame, thereby defining the orientation of the vehicle as described in Section 5.1. Since the vehicle can have any orientation, there is no fixed form of the transformation matrix. Instead, a differential equation governing the transformation operator will here be derived. This differential equation is formed using the measurements of angular rate, i.e. gyroscope observations. For this the rotational rates, $\boldsymbol{\omega}_{nb}^{b}$, are needed. These rates can be derived from the observed angular rates, $\boldsymbol{\omega}_{is}^{s}$, as

$$\boldsymbol{\omega}_{nb}^{b} = \boldsymbol{\omega}_{ne}^{b} + \boldsymbol{\omega}_{ei}^{b} + \boldsymbol{\omega}_{is}^{b} + \boldsymbol{\omega}_{sb}^{b} = \mathbf{C}_{s}^{b}\left(\boldsymbol{\omega}_{is}^{s} + \boldsymbol{\omega}_{sb}^{s}\right) - \mathbf{C}_{n}^{b}\left(\boldsymbol{\omega}_{en}^{n} + \mathbf{C}_{e}^{n}\boldsymbol{\omega}_{ie}^{e}\right) \ , \tag{A.27}$$

where $\boldsymbol{\omega}_{en}^{n}$ is computed from (A.24) based on position and velocity, $\boldsymbol{\omega}_{ie}^{e}$ is Earth's rotation rate (A.21) and $\boldsymbol{\omega}_{sb}^{s}$ is the angular velocity of the sensor with respect to the body of the vehicle. In strapdown mode, this term will vanish, but it is here included for generality in case the sensor is mounted on a moving platform. The transformation matrix, $\mathbf{C}_{n}^{b}$, is the variable that we intend to solve for (making it a *coupled* differential equation) and $\mathbf{C}_{s}^{b}$ is the transformation from the measurement or sensor frame to the body frame. For a strapdown system, this matrix will be constant (measured by the operator) and equal the identity matrix if the axes of the sensor frame are aligned with the axes of the body frame.

As described in Section 5.1, the transformation operator from the n-frame to the b-frame defines the orientation of the vehicle with respect to the north, east and vertical axes of the n-frame. This operator is therefore defines the attitude of the vehicle and may be expressed either as a transformation matrix (direction cosines), three Euler angles or a quaternion. In the following, differential equations are therefore formed for each of these representations.

Direction Cosines

The differential equation governing the temporal evolution of $\mathbf{C}_{b}^{n}$ have already been introduced in (A.15) as

$$\dot{\mathbf{C}}_{b}^{n} = \mathbf{C}_{b}^{n}\,\boldsymbol{\Omega}_{nb}^{b} \ , \tag{A.28}$$

where $\boldsymbol{\Omega}_{nb}^{b}$ is formed using the observed angular rates. In practice some initial value, $\mathbf{C}_{b}^{n}(t)$, will be known and the above equation is used to solve for, $\mathbf{C}_{b}^{n}\left(t+\triangle t\right)$, at some later time. How this can be done is discussed in Appendix C.2, but there is of course more than one way to do this.

Euler Angles

The derivation of a differential equation governing the three Euler angles is done in [15, Sec. 1.5]. When using Euler angles, the transformation from the b-frame to the n-frame is accomplished by the sequence of rotations in (5.21) as

$$\mathbf{C}_{b}^{n} = \mathbf{R}_{z}\left(-\gamma\right)\mathbf{R}_{y}\left(-\beta\right)\mathbf{R}_{x}\left(-\alpha\right) = \mathbf{C}_{b_2}^{n}\,\mathbf{C}_{b_1}^{b_2}\,\mathbf{C}_{b}^{b_1} \ , \tag{A.29}$$

where the bank, elevation and heading angles, α, β and γ, are introduced in Section 5.1. This sequence of rotations can also be interpreted as three subsequent transformations, into two intermediate reference frames, b_1 and b_2, as indicated above. Since all of these frames are rotating with respect to one another, we can write the angular rate, $\boldsymbol{\omega}_{nb}^{b}$, as

$$\begin{aligned}\boldsymbol{\omega}_{nb}^{b} &= \boldsymbol{\omega}_{nb_2}^{b} + \boldsymbol{\omega}_{b_2b_1}^{b} + \boldsymbol{\omega}_{b_1b}^{b} \\ &= \mathbf{C}_{b_1}^{b}\, \mathbf{C}_{b_2}^{b_1}\, \boldsymbol{\omega}_{nb_2}^{b_2} + \mathbf{C}_{b_1}^{b}\, \boldsymbol{\omega}_{b_2b_1}^{b_1} + \boldsymbol{\omega}_{b_1b}^{b}\ .\end{aligned} \tag{A.30}$$

Although the angular rates sensed by the gyroscopes are the components of $\boldsymbol{\omega}_{nb}^{b}$, the decomposition into the three terms $\boldsymbol{\omega}_{nb_2}^{b_2}$, $\boldsymbol{\omega}_{b_2b_1}^{b_1}$ and $\boldsymbol{\omega}_{b_1b}^{b}$ is useful because these are directly related to the Euler angles involved in the transformation as

$$\boldsymbol{\omega}_{nb_2}^{b_2} = \begin{bmatrix}0\\0\\\dot{\gamma}\end{bmatrix}\ , \quad \boldsymbol{\omega}_{b_2b_1}^{b_1} = \begin{bmatrix}0\\\dot{\beta}\\0\end{bmatrix} \quad \text{and} \quad \boldsymbol{\omega}_{b_1b}^{b} = \begin{bmatrix}\dot{\alpha}\\0\\0\end{bmatrix}\ . \tag{A.31}$$

This is due to that fact that subsequent rotations also rotate the initial axes, such that only the first rotation is directly related to the measured angular rate. Therefore, the measured angular rates, $\boldsymbol{\omega}_{nb}^{b}$, must be transformed into the appropriate intermediate coordinate systems in order to determine the Euler angles. Combining the above two expressions and using (A.29), we obtain

$$\begin{aligned}\boldsymbol{\omega}_{nb}^{b} &= \mathbf{R}_x(\alpha)\, \mathbf{R}_y(\beta) \begin{bmatrix}0\\0\\\dot{\gamma}\end{bmatrix} + \mathbf{R}_x(\alpha) \begin{bmatrix}0\\\dot{\beta}\\0\end{bmatrix} + \begin{bmatrix}\dot{\alpha}\\0\\0\end{bmatrix} \\ &= \begin{bmatrix}1 & 0 & -\sin\beta \\ 0 & \cos\alpha & \cos\beta\sin\alpha \\ 0 & -\sin\alpha & \cos\beta\cos\alpha\end{bmatrix} \begin{bmatrix}\dot{\alpha}\\\dot{\beta}\\\dot{\gamma}\end{bmatrix}\ ,\end{aligned} \tag{A.32}$$

relating the sensed angular rates, $\boldsymbol{\omega}_{nb}^{b}$, to the Euler angles α, β and γ of the transformation. Since, we actually want to determine the Euler angles from the measurement, we rewrite the above as [15, Eq. 1.95]:

$$\begin{bmatrix}\dot{\alpha}\\\dot{\beta}\\\dot{\gamma}\end{bmatrix} = \begin{bmatrix}1 & \sin\alpha\tan\beta & \cos\alpha\tan\beta \\ 0 & \cos\alpha & -\sin\alpha \\ 0 & \sin\alpha\sec\beta & \cos\alpha\sec\beta\end{bmatrix} \boldsymbol{\omega}_{nb}^{b}\ , \tag{A.33}$$

which is the system of coupled differential equations, that may be integrated in order to obtain the attitude angles of the vehicle as a function of time. One should notice that these equations become singular for elevation angles $\beta = \pm 90^\circ$ due to the $\tan\beta$ and $\sec\beta$ terms.

This singularity issue is one reason why Euler angles are usually not solved for directly in practice. Another, more compelling argument, is that the Euler angles are not used directly in the implementing of the navigation equations and must therefore first be transformed into a direction cosines matrix or a quaternion, introducing additional computational load.

Quaternion

Alternatively, one might express the attitude in terms of a quaternion and therefore desire a differential equation governing the quaternion attitude. From (5.44), we have that sequential rotations are carried out as

$$\mathbf{q}_b^n(+) = \delta\mathbf{q}^n \circ \mathbf{q}_b^n(-) = \mathbf{q}_b^n(-) \circ \delta\mathbf{q}^b\ , \tag{A.34}$$

where the initial quaternion attitude, $(-)$, is rotated by a small amount, $\delta\alpha_{nb} = \omega_{nb}\,\delta t$, about the normalised axis, $\mathbf{u} = (u_x, u_y, u_z)$, to arrive at the new attitude, $(+)$. The rotation quaternion is formed using (5.41) as

$$\delta\mathbf{q}^n = \begin{bmatrix} \cos(\delta\alpha/2) \\ \sin(\delta\alpha/2)\, u_x^n \\ \sin(\delta\alpha/2)\, u_y^n \\ \sin(\delta\alpha/2)\, u_z^n \end{bmatrix} \quad \text{or} \quad \delta\mathbf{q}^b = \begin{bmatrix} \cos(\delta\alpha/2) \\ \sin(\delta\alpha/2)\, u_x^b \\ \sin(\delta\alpha/2)\, u_y^b \\ \sin(\delta\alpha/2)\, u_z^b \end{bmatrix} . \tag{A.35}$$

As we let $\delta t \to 0$ we have that $\delta\alpha_{nb} \to \omega_{nb}$, such that the above expression becomes a differential equation:

$$\dot{\mathbf{q}}_b^n = \frac{1}{2} \begin{bmatrix} 0 \\ \omega_{nb,x}^n \\ \omega_{nb,y}^n \\ \omega_{nb,z}^n \end{bmatrix} \circ \mathbf{q}_b^n = \frac{1}{2}\, \mathbf{q}_b^n \circ \begin{bmatrix} 0 \\ \omega_{nb,x}^b \\ \omega_{nb,y}^b \\ \omega_{nb,z}^b \end{bmatrix} , \tag{A.36}$$

where the small angle approximations, $\cos\alpha \approx 1$ and $\sin\alpha \approx \alpha$, have been exploited. This can also be expressed in matrix form using (5.34) to arrive at

$$\dot{\mathbf{q}}_b^n = \frac{1}{2}\, \mathbf{A}^n\, \mathbf{q}_b^n = \frac{1}{2}\, \mathbf{A}^b\, \mathbf{q}_b^n , \tag{A.37}$$

with

$$\mathbf{A}^n = \begin{bmatrix} 0 & -\omega_{nb,x}^n & -\omega_{nb,y}^n & -\omega_{nb,z}^n \\ \omega_{nb,x}^n & 0 & -\omega_{nb,z}^n & \omega_{nb,y}^n \\ \omega_{nb,y}^n & \omega_{nb,z}^n & 0 & -\omega_{nb,x}^n \\ \omega_{nb,z}^n & -\omega_{nb,y}^n & \omega_{nb,x}^n & 0 \end{bmatrix} \quad \text{and} \quad \mathbf{A}^b = \begin{bmatrix} 0 & -\omega_{nb,x}^b & -\omega_{nb,y}^b & -\omega_{nb,z}^b \\ \omega_{nb,x}^b & 0 & \omega_{nb,z}^b & -\omega_{nb,y}^b \\ \omega_{nb,y}^b & -\omega_{nb,z}^b & 0 & \omega_{nb,x}^b \\ \omega_{nb,z}^b & \omega_{nb,y}^b & -\omega_{nb,x}^b & 0 \end{bmatrix} . \tag{A.38}$$

B Ordinary Differential Equations and their Solution

In order to perform inertial navigation, we need to solve a set of coupled differential equations for each available observation. This appendix is included to introduce the tools we need to solve these equations. It is not the intent to fully develop the theory for differential equations and their solutions. In the following, the concept of of Ordinary Differential Equations (ODEs) will be introduced, after which the topic will be constrained to linear differential equations and Initial Value Problems (IVPs). The concept of a state space formulation of a linear differential equation will also be introduced, since this is central to the Kalman filtering technique that is introduced in Section REF!!. Having introduced these basic concepts, the two subsequent sections are devoted to the analytical and numerical solution of linear ODEs, respectively.

B.1 Ordinary Differential Equations

Suppose that the state of a system at any given time t is described by some vector function $\mathbf{x}(t)$. For example, the components of $\mathbf{x}(t)$ might represent the spatial coordinates of a projectile. This vector $\mathbf{x}(t)$ is known as the **state vector**, since it describes the state of the system at a given time t. A differential equation prescribes a relationship between this unknown state function $\mathbf{x}(t)$ and one or more of its derivatives with respect to t, that must hold at any given time. In solving a differential equation the objective is to determine a differentiable function, $\mathbf{x}(t)$, that satisfies the prescribed relationship. Finding such a solution of the differential equation is important because it will enable us to predict the future evolution of the system over time.

When there is only one independent variable, such as time, then all derivatives are with respect to that independent variable and we have an ODE. If more than one independent variable exists, the derivatives are partial derivatives and we have a partial differential equation (PDE). In the following, we will restrict ourselves to ODEs and denote the derivative with respect to that independent variable, which we will assume to be time, by a dot. The implicit form of such a kth order ODE may be written as

$$\mathbf{f}\left(t, \mathbf{x}, \dot{\mathbf{x}}, \ddot{\mathbf{x}}, ..., \mathbf{x}^{(k)}\right) = \mathbf{0} \,, \tag{B.1}$$

where $\mathbf{f}$ is a known function and $\mathbf{x}(t)$ is a k times differentiable function, that is to be determined. A kth order ODE is said to be explicit if it can be written on the form

$$\mathbf{x}^{(k)} = \mathbf{f}\left(t, \mathbf{x}, \dot{\mathbf{x}}, \ddot{\mathbf{x}}, ..., \mathbf{x}^{(k-1)}\right) \,. \tag{B.2}$$

In order to obtain an expression on this form, some manipulation is usually required (this is not always possible). From hereon, we will consider only explicit ODEs. A further restriction that we will make is to only consider first order ODEs. This is however not a real restriction, since we can define k new unknowns as

$$\mathbf{u}_1(t) = \mathbf{x}(t) \,, \quad \mathbf{u}_2(t) = \dot{\mathbf{x}}(t) \,, \; ... \,, \quad \mathbf{u}_k(t) = \mathbf{x}^{(k-1)}(t) \,,$$

and transform the kth order ODE into a system of coupled first order differential equations as

$$\dot{\mathbf{u}} = \begin{bmatrix} \dot{\mathbf{u}}_1 \\ \dot{\mathbf{u}}_2 \\ \vdots \\ \dot{\mathbf{u}}_k \end{bmatrix} = \begin{bmatrix} \mathbf{u}_2 \\ \mathbf{u}_3 \\ \vdots \\ \mathbf{f}\left(t, \mathbf{u}_1, \mathbf{u}_2, ..., \mathbf{u}_k\right) \end{bmatrix} = \mathbf{g}\left(t, \mathbf{u}\right) \ , \tag{B.3}$$

where a matrix notation is naturally introduced. Since a dynamic system may be described by more than one differential equation and exploiting that higher order differential equations can be written as a set of coupled first order differential equations, we will in general be able to describe the system through a set of n coupled first order differential equations as

$$\dot{\mathbf{x}} = \dot{\mathbf{x}}(t) = \begin{bmatrix} \dot{x}_1(t) \\ \dot{x}_2(t) \\ \vdots \\ \dot{x}_n(t) \end{bmatrix} = \begin{bmatrix} f_1\left(t, \mathbf{x}\right) \\ f_2\left(t, \mathbf{x}\right) \\ \vdots \\ f_n\left(t, \mathbf{x}\right) \end{bmatrix} = \mathbf{f}\left(t, \mathbf{x}(t)\right) = \mathbf{f}\left(t, \mathbf{x}\right) \ . \tag{B.4}$$

This system of n coupled differential equations is said to have a solution on the interval $\alpha < t < \beta$ if there exists a set of n functions

$$x_1 = \phi_1(t) \ , \quad x_2 = \phi_2(t) \ , \ ... \ , \quad x_n = \phi_n(t) \ , \tag{B.5}$$

that are differentiable at all points in the interval $\alpha < t < \beta$ and that satisfy the system of equations (B.4) at all points in this interval. However, although the solution exists, such a system of ODEs does not by itself determine a unique solution, because only the derivatives are known. Therefore, an infinite family of functions usually satisfy the ODE and in order to single out a particular solution, the value of the solution function $\mathbf{x}_0 \equiv \mathbf{x}_0\left(t_0\right)$, at a particular time t_0, must be specified. This requirement is called an initial condition and an ODE together with an initial condition is called an **Initial Value Problem** (IVP). Starting from its initial state, $\mathbf{x}_0$, at time, t_0, the ODEs govern the dynamic evolution of the system for $t \geq 0$, and we seek a function, $\mathbf{x}(t)$, that satisfies the initial condition and describes the state of the system as a function of time.

A linear system of differential equations is one where the functional, $\mathbf{f}\left(t, \mathbf{x}\right)$, is linear with respect to the function, $\mathbf{x}(t)$, and all its derivatives. Such a system can therefore be expressed on the form

$$\dot{\mathbf{x}}(t) = \mathbf{f}\left(t, \mathbf{x}\right) = \mathbf{A}(t)\,\mathbf{x}(t) + \mathbf{b}(t) \ , \tag{B.6}$$

where $\mathbf{A}(t)$ is an $n \times n$ matrix, $\mathbf{b}(t)$ is a vector of length n and both are functions of t. If the matrix $\mathbf{A}$ does not depend on t, then the ODE is said to have **constant coefficients**, and if $\mathbf{b}(t) = \mathbf{0}$, then the ODE is said to be **homogeneous**.

B.2 Solving Linear Systems of Ordinary Differential Equations

In order to obtain a solution, $\mathbf{x}(t)$, to the linear system of ODEs (B.6), we could, in theory, perform an integration which, together with the initial conditions, leads to the integral equation

$$\mathbf{x}(t) = \mathbf{x}_0 + \int_{t_0}^{t} \left\{\mathbf{A}(t')\,\mathbf{x}(t') + \mathbf{b}(t')\right\} \, \mathrm{d}t' \ , \tag{B.7}$$

that must be satisfied by the solution, $\mathbf{x}(t)$, of the IVP. However, since the integral depends on the solution itself, this is usually no easier than solving the original IVP [11, p. ??]. Instead we resolve to other analytical or numerical means of determining the solution.

The usual approach is to separate the solution, $\mathbf{x}(t)$, into two components

$$\mathbf{x}(t) = \mathbf{x}_H(t) + \mathbf{x}_P(t) \,, \tag{B.8}$$

where $\mathbf{x}_H(t)$ is denoted the complementary or **homogeneous solution**, satisfying the homogeneous equation, formed by setting $\mathbf{b}(t) = \mathbf{0}$ in (B.6) to obtain

$$\dot{\mathbf{x}}(t) = \mathbf{A}(t)\,\mathbf{x}(t) \,. \tag{B.9}$$

The other component, $\mathbf{x}_P(t)$, is denoted the **particular solution**, which can be any function that satisfies (B.6), provided it is linearly independent of $\mathbf{x}_H(t)$. It should be emphasised that *any* form of $\mathbf{x}_P(t)$ is valid, no matter how simple or complicated this expression is. Inserting (B.8) into (B.6), we have that

$$\begin{aligned} \frac{\mathrm{d}}{\mathrm{d}t}\left[\mathbf{x}_H(t) + \mathbf{x}_P(t)\right] &= \mathbf{A}(t)\left[\mathbf{x}_H(t) + \mathbf{x}_P(t)\right] + \mathbf{b}(t) \\ \dot{\mathbf{x}}_H(t) + \dot{\mathbf{x}}_P(t) &= \left[\mathbf{A}(t)\,\mathbf{x}_H(t)\right] + \left[\mathbf{A}(t)\,\mathbf{x}_P(t) + \mathbf{b}(t)\right] \\ \dot{\mathbf{x}}_H(t) + \dot{\mathbf{x}}_P(t) &= \dot{\mathbf{x}}_H(t) + \dot{\mathbf{x}}_P(t) \,, \end{aligned} \tag{B.10}$$

showing that the sum of the homogeneous and particular solutions satisfies the differential equation (B.6).

It is important to notice that this method for finding the general solution to an ODE by superposition of a homogeneous and particular solution is based on the assumption that the ODE is linear. For non-linear equations this method cannot be used and it is often impossible to find closed-form solutions to such equations [18, Sec. 15].

B.2.1 The Homogeneous Solution

The general form of the solution to the homogeneous equation (B.9) is a combination of n linearly independent functions that satisfy it [3, Sec. 7.4]. This can be expressed as

$$\mathbf{x}_H(t) = c_1\,\mathbf{x}_{H,1}(t) + c_2\,\mathbf{x}_{H,2}(t) + \cdots + c_n\,\mathbf{x}_{H,n}(t) \,, \tag{B.11}$$

where $c_1, ..., c_n$ are arbitrary constants, which may be determined if n boundary conditions or initial values are provided, i.e. $\mathbf{x}_0$ is provided. In order to write the solution as a linear combination, the individual solutions must be linearly independent. In other words, the independence of all the individual solutions assures that the solution exists, while an initial condition is necessary for the solution to be unique.

The above set $\mathbf{x}_{H,1}(t), ..., \mathbf{x}_{H,n}(t)$ is known as a **fundamental set of solutions** and can be expressed more compactly as

$$\mathbf{x}_H(t) = \sum_{j=1}^{n} c_j\,\mathbf{x}_{H,j} = \mathbf{\Psi}(t)\,\mathbf{c} \,, \tag{B.12}$$

where $\mathbf{\Psi}(t) = [\mathbf{x}_{H,1}, \cdots, \mathbf{x}_{H,n}]$ is denoted the **fundamental matrix** and $\mathbf{c} = [c_1, c_2, ..., c_n]^\top$ is a vector of constants. Since the columns of $\mathbf{\Psi}(t)$ are linearly independent, the matrix is non-singular and the inverse exists. Using the initial conditions, we have that

$$\mathbf{c} = \mathbf{\Psi}^{-1}(t_0)\,\mathbf{x}_0\ , \tag{B.13}$$

which leads to the solution

$$\boxed{\mathbf{x}_H(t) = \mathbf{\Psi}(t)\mathbf{\Psi}^{-1}(t_0)\,\mathbf{x}_0 = \mathbf{\Phi}(t,t_0)\,\mathbf{x}_0\ ,} \tag{B.14}$$

where

$$\mathbf{\Phi}(t,t_0) = \mathbf{\Psi}(t)\mathbf{\Psi}^{-1}(t_0) \tag{B.15}$$

is known as the **transition matrix**, because it transitions the state vector from its initial state, $\mathbf{x}_0$, to its current state, $\mathbf{x}(t)$. Although the transition matrix, $\mathbf{\Phi}(t,t_0)$, is more complicated than the fundamental matrix, $\mathbf{\Psi}(t)$, it is especially helpful if the same system of differential equations is to be solved repeatedly, subject to different initial conditions.

Substituting (B.14) into the homogeneous equation (B.9), we have that

$$\left[\frac{\mathrm{d}}{\mathrm{d}t}\mathbf{\Phi}(t,t_0) + \mathbf{A}(t)\mathbf{\Phi}(t,t_0)\right]\mathbf{x}_0 = \mathbf{0}\ , \tag{B.16}$$

indicating that

$$\frac{\mathrm{d}}{\mathrm{d}t}\mathbf{\Phi}(t,t_0) + \mathbf{A}(t)\mathbf{\Phi}(t,t_0) = \mathbf{0}\ , \tag{B.17}$$

with initial condition $\mathbf{\Phi}(t_0,t_0) = \mathbf{I}$. This is the differential equation governing the transition matrix. However, no standard techniques apply for obtaining its solution [15, Sec. 2.3.1].

B.2.2 Homogeneous Linear Systems with Constant Coefficients

Assuming that we have only a single differential equation $n = 1$, with constant coefficient a, the system reduces to the scalar initial value problem

$$\dot{x}(t) = a\,x(t) \quad \text{with} \quad x(t_0) = x_0\ , \tag{B.18}$$

with a solution of the form

$$x(t) = x_0 e^{a(t-t_0)}\ . \tag{B.19}$$

Now, if we consider the corresponding initial value problem for an $n \times n$ system with constant coefficients

$$\dot{\mathbf{x}}(t) = \mathbf{A}\,\mathbf{x}(t) \quad \text{with} \quad \mathbf{x}(t_0) = \mathbf{x}_0\ , \tag{B.20}$$

we have a solution on the form

$$\mathbf{x}_H(t) = \mathbf{\Phi}(t,t_0)\,\mathbf{x}_0\ , \quad \mathbf{\Phi}(t_0,t_0) = \mathbf{I}\ . \tag{B.21}$$

If we compare the two solutions, it would suggest that the matrix $\mathbf{\Phi}(t,t_0)$ might have an exponential character. The scalar exponential function can be represented as a power series

$$e^{a(t-t_0)} = 1 + \sum_{n=1}^{\infty} \frac{a^n\,(t-t_0)^n}{n!}\ , \tag{B.22}$$

which converges for all t. If we replace the scalar, a, by the constant matrix, $\mathbf{A}$, we can consider the corresponding series

$$\mathbf{I} + \sum_{n=1}^{\infty} \frac{\mathbf{A}^n (t-t_0)^n}{n!} = \mathbf{I} + \mathbf{A}(t-t_0) + \frac{\mathbf{A}^2 (t-t_0)^2}{2!} + \cdots + \frac{\mathbf{A}^n (t-t_0)^n}{n!} + \cdots , \quad \text{(B.23)}$$

where each term in the series is an $n \times n$ matrix. Each element of the resulting matrix sum will converge for all t as $n \to \infty$ [3, Sec. 7.7]. Therefore, the sum of the series defines a new matrix, which we will denote as

$$e^{\mathbf{A}(t-t_0)} = \mathbf{I} + \sum_{n=1}^{\infty} \frac{\mathbf{A}^n (t-t_0)^n}{n!} , \quad \text{(B.24)}$$

analogous to the expansion of the scalar function. By differentiating each term in the series, we obtain

$$\begin{aligned} \frac{\mathrm{d}}{\mathrm{d}t}\left(e^{\mathbf{A}(t-t_0)}\right) &= \sum_{n=1}^{\infty} \frac{\mathbf{A}^n (t-t_0)^{n-1}}{(n-1)!} = \mathbf{A}\left[\mathbf{I} + \sum_{n=1}^{\infty} \frac{\mathbf{A}^n (t-t_0)^n}{n!}\right] \\ &= \mathbf{A} e^{\mathbf{A}(t-t_0)} . \end{aligned} \quad \text{(B.25)}$$

This indicates that $e^{\mathbf{A}(t-t_0)}$ satisfies the same differential equation (B.17) as $\mathbf{\Phi}$. Moreover, they also share the same initial condition

$$e^{\mathbf{A}(t-t_0)}\Big|_{t=t_0} = \mathbf{I} , \quad \text{(B.26)}$$

which leads us to conclude that, when $\mathbf{A}$ is constant, the two matrices are are the same [15, Eq. 2.58]

$$\boxed{\mathbf{\Phi}(t, t_0) = e^{\mathbf{A}(t-t_0)} .} \quad \text{(B.27)}$$

This expression appears simple and compact and will be of great use to us later. However, in general it cannot be computed directly since the exponent of a matrix is not the matrix of its exponent. Instead, we resolve to using the expansion (B.23) and truncating the power series depending on the required accuracy.

B.2.3 The Particular Solution

Having obtained a solution, $\mathbf{x}_H(t)$, to the homogeneous differential equation (B.9), we can obtain the particular solution, $\mathbf{x}_P(t)$, using the method of **variation of parameters** [3, Sec. 7.9]. We therefore return to the non-homogeneous equation (B.6), repeated here with initial conditions

$$\dot{\mathbf{x}}(t) = \mathbf{A}(t)\,\mathbf{x}(t) + \mathbf{b}(t) , \quad \text{(B.28)}$$

$$\mathbf{x}(t_0) = \mathbf{x}_0 . \quad \text{(B.29)}$$

This method seeks a solution that can be expressed as a linear combination

$$\mathbf{x}(t) = \sum_{j=1}^{n} u_j(t)\,\mathbf{x}_{H,j} = \mathbf{\Psi}(t)\,\mathbf{u}(t) , \quad \text{(B.30)}$$

with time-varying coefficients, $\mathbf{u}(t)$, rather than the constant coefficients of (B.12). Again, $\mathbf{\Psi}(t)$ is a fundamental matrix, meaning that it satisfies the condition $\dot{\mathbf{\Psi}}(t) = \mathbf{A}(t)\,\mathbf{\Psi}(t)$. Inserting the above expression into (B.28), we obtain

$$\begin{aligned} \dot{\mathbf{\Psi}}(t)\,\mathbf{u}(t) + \mathbf{\Psi}(t)\,\dot{\mathbf{u}}(t) &= \mathbf{A}(t)\,\mathbf{\Psi}(t)\,\mathbf{u}(t) + \mathbf{b}(t) \\ \mathbf{A}(t)\,\mathbf{\Psi}(t)\,\mathbf{u}(t) + \mathbf{\Psi}(t)\,\dot{\mathbf{u}}(t) &= \mathbf{A}(t)\,\mathbf{\Psi}(t)\,\mathbf{u}(t) + \mathbf{b}(t) \\ \mathbf{\Psi}(t)\,\dot{\mathbf{u}}(t) &= \mathbf{b}(t)\ . \end{aligned} \tag{B.31}$$

Since $\mathbf{\Psi}(t)$ is non-singular, the inverse exists, and we can isolate $\mathbf{u}(t)$ by integration as

$$\mathbf{u}(t) = \int_{t_0}^{t} \mathbf{\Psi}^{-1}(t')\,\mathbf{b}(t')\,\mathrm{d}t' + \mathbf{c}\ , \tag{B.32}$$

where $\mathbf{c}$ is a constant vector. Inserting this into (B.30) we arrive at an expression for the general form of $\mathbf{x}(t)$:

$$\mathbf{x}(t) = \mathbf{\Psi}(t)\,\mathbf{c} + \mathbf{\Psi}(t) \int_{t_0}^{t} \mathbf{\Psi}^{-1}(t')\,\mathbf{b}(t')\,\mathrm{d}t'\ . \tag{B.33}$$

Now, we want to use the initial condition in order to determine $\mathbf{c}$. For $t = t_0$, the integral part of the expression is zero, so the initial condition leads to the coefficients

$$\mathbf{x}_0 = \mathbf{\Psi}\left(t_0\right)\,\mathbf{c} \quad \Leftrightarrow \quad \mathbf{c} = \mathbf{\Psi}^{-1}\left(t_0\right)\,\mathbf{x}_0\ . \tag{B.34}$$

Substituting this back into (B.33), we have that

$$\mathbf{x}(t) = \mathbf{\Psi}(t)\,\mathbf{\Psi}^{-1}\left(t_0\right)\,\mathbf{x}_0 + \mathbf{\Psi}(t) \int_{t_0}^{t} \mathbf{\Psi}^{-1}(t')\,\mathbf{b}(t')\,\mathrm{d}t' \tag{B.35}$$

$$= \mathbf{\Phi}\left(t, t_0\right)\,\mathbf{x}_0 + \int_{t_0}^{t} \mathbf{\Phi}\left(t, t'\right)\,\mathbf{b}(t')\,\mathrm{d}t'\ , \tag{B.36}$$

where $\mathbf{\Phi}\left(t, t_0\right)$ is the transition matrix, satisfying $\mathbf{\Phi}\left(t_0, t_0\right) = \mathbf{I}$. Notice that the first term on the RHS is the solution to the homogeneous equation, $\mathbf{x}_H(t)$. This indicates that the second term corresponds to the particular solution, $\mathbf{x}_P(t)$.

B.2.4 Generalisation to Matrix Differential Equations

We can generalise the results derived in this section such that they concern linear differential equations of matrix functions. Such systems are on the form

$$\dot{\mathbf{X}}(t) = \mathbf{A}(t)\,\mathbf{X}(t) + \mathbf{B}(t)\ , \tag{B.37}$$

where $\mathbf{X}(t)$ and $\mathbf{B}(t)$ are $n \times p$ matrices and $\mathbf{A}(t)$ remains an $n \times n$ matrix. The initial condition is

$$\mathbf{X}\left(t_0\right) = \mathbf{X}_0\ . \tag{B.38}$$

Since we may think of $\mathbf{X}(t)$ as a collection of column vectors

$$\mathbf{X}(t) = \left[\mathbf{x}_1(t), \cdots \mathbf{x}_p(t)\right]\ , \tag{B.39}$$

the homogeneous solution to each of the individual vectors $\mathbf{x}_1(t), ..., \mathbf{x}_p(t)$ have the same form, but the coefficients of the linear combination are different, due to the different columns of the initial condition $\mathbf{X}_0$. The general solution to the homogeneous equation can therefore be expressed according to (B.14) as

$$\mathbf{X}_H(t) = \mathbf{\Phi}(t, t_0)\, \mathbf{X}_0 = e^{\mathbf{A}(t-t_0)}\, \mathbf{X}_0 \,, \tag{B.40}$$

where the last equality only holds for constant $\mathbf{A}$. A similar straightforward extension holds for the particular solution (B.35), where the vector of time-varying components $\mathbf{b}(t)$ is simply substituted by the matrix $\mathbf{B}(t)$ as

$$\begin{aligned} \mathbf{X}(t) &= \mathbf{\Phi}(t, t_0)\, \mathbf{X}_0 + \mathbf{\Phi}(t, t_0) \int_{t_0}^{t} \mathbf{\Phi}^{-1}(t', t_0)\, \mathbf{B}(t')\, \mathrm{d}t' \\ &= \mathbf{\Phi}(t, t_0)\, \mathbf{X}_0 + \int_{t_0}^{t} \mathbf{\Phi}^{-1}(t, t')\, \mathbf{B}(t')\, \mathrm{d}t' \,. \end{aligned} \tag{B.41}$$

B.3 Skew-Symmetric Matrices and Power Relations

The skew symmetric form of a vector was discretely introduced in Appendix A. Basically, the skew-symmetric form of a vector, $\boldsymbol{\psi}$, is the matrix, $\mathbf{\Psi}$:

$$[\boldsymbol{\psi}\times] = \left[\begin{bmatrix}\alpha\\ \beta\\ \gamma\end{bmatrix}\times\right] = \begin{bmatrix} 0 & -\gamma & \beta \\ \gamma & 0 & -\alpha \\ -\beta & \alpha & 0 \end{bmatrix} = \mathbf{\Psi} \,. \tag{B.42}$$

such that the cross-product can be expressed as a matrix-vector dot product. The skew-symmetric form is often used for axial vectors, which is a triplet containing angles and therefore not a "true" vector. The term "skew symmetric" comes from the property that $\mathbf{\Psi}^\top = -\mathbf{\Psi}$. Notice that the matrix consists only of the components of the vector.

In inertial navigation, the skew-symmetric matrix enters the navigation equations when angular rates are integrated for attitude. They are therefore components of the differential equations that are to be solved. Typically, the attitude is updated iteratively using a transition matrix as in (B.27), which can be expressed as a power series

$$e^{\mathbf{A}} = \mathbf{I}_3 + \sum_{k=1}^{\infty} \frac{\mathbf{A}^k}{k!} = \mathbf{I}_3 + \mathbf{A} + \frac{\mathbf{A}^2}{2!} + \frac{\mathbf{A}^3}{3!} + \cdots \,, \tag{B.43}$$

where $\mathbf{A}$ will be a skew-symmetric matrix. This section will illustrate how the properties of skew-symmetric matrices can be exploited to arrive exact expressions for the power series. This exact expression is known as Rodrigues' formula.

B.3.1 Power Relations

We let $[\boldsymbol{\alpha}\times]$ be the skew-symmetric form of the vector $\boldsymbol{\alpha} = [\alpha_x, \alpha_y, \alpha_z]^\top$. This vector is characterised by a magnitude, α, and a direction in the form of a unit vector, $\mathbf{e}_\alpha$, as

$$\alpha = |\boldsymbol{\alpha}| = \sqrt{\alpha_x^2 + \alpha_y^2 + \alpha_z^2} \quad \text{and} \quad \mathbf{e}_\alpha = \frac{\boldsymbol{\alpha}}{\alpha} = \begin{bmatrix} \mathbf{e}_{\alpha,1} \\ \mathbf{e}_{\alpha,2} \\ \mathbf{e}_{\alpha,3} \end{bmatrix} \,, \tag{B.44}$$

which allows us to write the skew-symmetric matrix as

$$[\boldsymbol{\alpha}\times] = \alpha\,[\mathbf{e}_\alpha\times] \quad \text{with} \quad [\mathbf{e}_\alpha\times] = \begin{bmatrix} 0 & -\mathbf{e}_{\alpha,3} & \mathbf{e}_{\alpha,2} \\ \mathbf{e}_{\alpha,3} & 0 & -\mathbf{e}_{\alpha,1} \\ -\mathbf{e}_{\alpha,2} & \mathbf{e}_{\alpha,1} & 0 \end{bmatrix} . \tag{B.45}$$

The outer product of this basis vector with itself is

$$\begin{aligned} \mathbf{e}_\alpha\mathbf{e}_\alpha^\top &= \begin{bmatrix} \mathbf{e}_{\alpha,1} \\ \mathbf{e}_{\alpha,2} \\ \mathbf{e}_{\alpha,3} \end{bmatrix} \begin{bmatrix} \mathbf{e}_{\alpha,1} & \mathbf{e}_{\alpha,2} & \mathbf{e}_{\alpha,3} \end{bmatrix} = \begin{bmatrix} \mathbf{e}_{\alpha,1}^2 & \mathbf{e}_{\alpha,1}\mathbf{e}_{\alpha,2} & \mathbf{e}_{\alpha,1}\mathbf{e}_{\alpha,3} \\ \mathbf{e}_{\alpha,2}\mathbf{e}_{\alpha,1} & \mathbf{e}_{\alpha,2}^2 & \mathbf{e}_{\alpha,2}\mathbf{e}_{\alpha,3} \\ \mathbf{e}_{\alpha,3}\mathbf{e}_{\alpha,1} & \mathbf{e}_{\alpha,3}\mathbf{e}_{\alpha,2} & \mathbf{e}_{\alpha,3}^2 \end{bmatrix} \\ &= \begin{bmatrix} 1 & 0 & 0 \\ 0 & 1 & 0 \\ 0 & 0 & 1 \end{bmatrix} + \begin{bmatrix} -\mathbf{e}_{\alpha,2}^2 - \mathbf{e}_{\alpha,3}^2 & \mathbf{e}_{\alpha,1}\mathbf{e}_{\alpha,2} & \mathbf{e}_{\alpha,1}\mathbf{e}_{\alpha,3} \\ \mathbf{e}_{\alpha,2}\mathbf{e}_{\alpha,1} & -\mathbf{e}_{\alpha,1}^2 - \mathbf{e}_{\alpha,3}^2 & \mathbf{e}_{\alpha,2}\mathbf{e}_{\alpha,3} \\ \mathbf{e}_{\alpha,3}\mathbf{e}_{\alpha,1} & \mathbf{e}_{\alpha,3}\mathbf{e}_{\alpha,2} & -\mathbf{e}_{\alpha,1}^2 - \mathbf{e}_{\alpha,2}^2 \end{bmatrix} \\ &= \mathbf{I}_3 + [\mathbf{e}_\alpha\times]^2 \ , \end{aligned} \tag{B.46}$$

where the relation $\mathbf{e}_{\alpha,1}^2 + \mathbf{e}_{\alpha,2}^2 + \mathbf{e}_{\alpha,3}^2 = 1$ was exploited. This can be re-arranged to obtain

$$[\mathbf{e}_\alpha\times]^2 = \mathbf{e}_\alpha\mathbf{e}_\alpha^\top - \mathbf{I}_3 \ , \tag{B.47}$$

which can be used to form an expression for the third power of $[\mathbf{e}_\alpha\times]$ as

$$\begin{aligned} [\mathbf{e}_\alpha\times]^3 &= \left([\mathbf{e}_\alpha\times]^2\right)^\top [\mathbf{e}_\alpha\times] = \left(\mathbf{e}_\alpha\mathbf{e}_\alpha^\top - \mathbf{I}\right)^\top [\mathbf{e}_\alpha\times] \\ &= \left(\left(\mathbf{e}_\alpha\mathbf{e}_\alpha^\top\right)^\top - \mathbf{I}\right)[\mathbf{e}_\alpha\times] = \mathbf{e}_\alpha\mathbf{e}_\alpha^\top\,[\mathbf{e}_\alpha\times] - [\mathbf{e}_\alpha\times] \\ &= \begin{bmatrix} \mathbf{e}_{\alpha,1}^2 & \mathbf{e}_{\alpha,1}\mathbf{e}_{\alpha,2} & \mathbf{e}_{\alpha,1}\mathbf{e}_{\alpha,3} \\ \mathbf{e}_{\alpha,2}\mathbf{e}_{\alpha,1} & \mathbf{e}_{\alpha,2}^2 & \mathbf{e}_{\alpha,2}\mathbf{e}_{\alpha,3} \\ \mathbf{e}_{\alpha,3}\mathbf{e}_{\alpha,1} & \mathbf{e}_{\alpha,3}\mathbf{e}_{\alpha,2} & \mathbf{e}_{\alpha,3}^2 \end{bmatrix} \begin{bmatrix} 0 & -\mathbf{e}_{\alpha,3} & \mathbf{e}_{\alpha,2} \\ \mathbf{e}_{\alpha,3} & 0 & -\mathbf{e}_{\alpha,1} \\ -\mathbf{e}_{\alpha,2} & \mathbf{e}_{\alpha,1} & 0 \end{bmatrix} - [\mathbf{e}_\alpha\times] \\ &= \mathbf{0} - [\mathbf{e}_\alpha\times] = -\,[\mathbf{e}_\alpha\times] \ . \end{aligned} \tag{B.48}$$

From heron, one can derive the expressions for higher powers of $[\mathbf{e}_\alpha\times]$ as

$$\begin{aligned} [\mathbf{e}_\alpha\times]^4 &= -\,[\mathbf{e}_\alpha\times]^2 \\ [\mathbf{e}_\alpha\times]^5 &= -\,[\mathbf{e}_\alpha\times]^3 = [\mathbf{e}_\alpha\times] \\ [\mathbf{e}_\alpha\times]^6 &= -\,[\mathbf{e}_\alpha\times]^4 = [\mathbf{e}_\alpha\times]^2 \quad \text{etc} \ , \end{aligned} \tag{B.49}$$

from which we can arrive at the more general relations:

$$\begin{aligned} [\mathbf{e}_\alpha\times]^{2k} &= (-1)^{k-1}\,[\mathbf{e}_\alpha\times]^2 \quad \text{for} \quad k \geq 2 \\ [\mathbf{e}_\alpha\times]^{2k+1} &= (-1)^k\,[\mathbf{e}_\alpha\times] \quad \text{for} \quad k \geq 1 \ . \end{aligned} \tag{B.50}$$

If we also include the magnitude of the vector, we have that for powers larger than two:

$$\begin{aligned} [\boldsymbol{\alpha}\times]^{2k} &= (-1)^{k-1}\,\alpha^{2k}\,[\mathbf{e}_\alpha\times]^2 \\ &= (-1)^{k-1}\left(\alpha_x^2 + \alpha_y^2 + \alpha_z^2\right)^k [\mathbf{e}_\alpha\times]^2 \quad \text{for} \quad k \geq 2 \end{aligned} \tag{B.51}$$

and

$$\begin{aligned}[\boldsymbol{\alpha}\times]^{2k+1} &= (-1)^k\,\alpha^{2k+1}\,[\mathbf{e}_\alpha\times] \\ &= (-1)^k\left(\alpha_x^2+\alpha_y^2+\alpha_z^2\right)^{k+1}[\mathbf{e}_\alpha\times] \quad \text{for} \quad k\geq 1\,.\end{aligned} \tag{B.52}$$

B.3.2 Rodrigues' Formula

The objective here is to write the power series

$$e^{[\boldsymbol{\alpha}\times]} = \mathbf{I}_3 + \sum_{k=1}^{\infty}\frac{[\boldsymbol{\alpha}\times]^k}{k!} = \mathbf{I}_3 + [\boldsymbol{\alpha}\times] + \frac{[\boldsymbol{\alpha}\times]^2}{2!} + \frac{[\boldsymbol{\alpha}\times]^3}{3!} + \cdots\,, \tag{B.53}$$

in terms of sines and cosines, since these have very similar power series and are, of course, related to the exponential through Euler's formula

$$e^{ix} = \cos x + i\,\sin x\,. \tag{B.54}$$

We start by introducing the power series

$$\begin{aligned}\cos x &= 1 - \frac{x^2}{2!} + \frac{x^4}{4!} - \frac{x^6}{6!} + \cdots = \sum_{k=0}^{\infty}(-1)^k\,\frac{x^{2k}}{(2k)!} \\ \sin x &= x - \frac{x^3}{3!} + \frac{x^5}{5!} - \frac{x^7}{7!} + \cdots = \sum_{k=0}^{\infty}(-1)^k\,\frac{x^{2k+1}}{(2k+1)!}\,,\end{aligned} \tag{B.55}$$

for the sine and cosine functions. We then make a power series expansion of the exponential e^{ix} to obtain the expression

$$e^{ix} = 1 + i\,x + \frac{(ix)^2}{2!} + \frac{(ix)^3}{3!} + \frac{(ix)^4}{4!} + \frac{(ix)^5}{5!} + \frac{(ix)^6}{6!}\,\cdots\,, \tag{B.56}$$

in which we can exponentiate the i as $i^2=-1$, $i^3=-i$, $i^4=1$ and $i^5=i$ in order to obtain the relation

$$\begin{aligned}e^{ix} &= 1 + i\,x - \frac{x^2}{2!} - \frac{x^3}{3!} + \frac{x^4}{4!} + \frac{x^5}{5!} - \frac{x^6}{6!}\,\cdots \\ &= \left(1 - \frac{x^2}{2!} + \frac{x^4}{4!} - \frac{x^6}{6!} + \cdots\right) + i\left(x - \frac{x^3}{3!} + \frac{x^5}{5!} - \frac{x^7}{7!} + \cdots\right) \\ &= \cos x + i\,\sin x\,.\end{aligned} \tag{B.57}$$

Now, having introduced Euler's formula and the power series expansion of the sine and cosine functions, we return to the expression (B.53), which we can reformulate in terms of the basis functions introduced in the previous section and apply the power properties of (B.50) to obtain

$$
\begin{aligned}
e^{[\boldsymbol{\alpha}\times]} &= \mathbf{I}_3 + \alpha\,[\mathbf{e}_\alpha\times] + \frac{\alpha^2\,[\mathbf{e}_\alpha\times]^2}{2!} + \frac{\alpha^3\,[\mathbf{e}_\alpha\times]^3}{3!} + \frac{\alpha^4\,[\mathbf{e}_\alpha\times]^4}{4!} + \frac{\alpha^5\,[\mathbf{e}_\alpha\times]^5}{5!} + \cdots \\
&= \mathbf{I}_3 + \alpha\,[\mathbf{e}_\alpha\times] + \frac{\alpha^2\,[\mathbf{e}_\alpha\times]^2}{2!} - \frac{\alpha^3\,[\mathbf{e}_\alpha\times]}{3!} - \frac{\alpha^4\,[\mathbf{e}_\alpha\times]^2}{4!} + \frac{\alpha^5\,[\mathbf{e}_\alpha\times]}{5!} + \cdots \\
&= \mathbf{I}_3 + \left(\alpha - \frac{\alpha^3}{3!} + \frac{\alpha^5}{5!} - \cdots\right)[\mathbf{e}_\alpha\times] + \left(\frac{\alpha^2}{2!} - \frac{\alpha^4}{4!} + \frac{\alpha^6}{6!} - \cdots\right)[\mathbf{e}_\alpha\times]^2 \ .
\end{aligned}
\tag{B.58}
$$

From this expression we see how the terms inside the brackets are very similar to the power series expansions of the sine and cosine functions. Using (B.55) we can write the above as [6]:

$$
\boxed{
\begin{aligned}
e^{[\boldsymbol{\alpha}\times]} &= \mathbf{I}_3 + \sin\alpha\,[\mathbf{e}_\alpha\times] + (1-\cos\alpha)\,[\mathbf{e}_\alpha\times]^2 \\
&= \mathbf{I}_3 + \frac{\sin\alpha}{\alpha}\,[\boldsymbol{\alpha}\times] + \frac{1-\cos\alpha}{\alpha^2}\,[\boldsymbol{\alpha}\times]^2 \ ,
\end{aligned}
}
\tag{B.59}
$$

which is known as **Rodrigues' rotation formula**.

B.3.3 Rodrigues' Formula for Quaternions

Quaternions are used to represent the attitude of a vehicle and are introduced in Section 5.1. In contrast to vectors, quaternions have four components and the related "skew-symmetric" matrix is a 4×4 matrix

$$
[\boldsymbol{\sigma}\wedge] = \begin{bmatrix} 0 & -\sigma_x & -\sigma_y & -\sigma_z \\ \sigma_x & 0 & \sigma_z & -\sigma_y \\ \sigma_y & -\sigma_z & 0 & \sigma_x \\ \sigma_z & \sigma_y & -\sigma_x & 0 \end{bmatrix} \ , \tag{B.60}
$$

where $\boldsymbol{\sigma} = [\sigma_x, \sigma_y, \sigma_z]^\top$ is a vector with magnitude and direction

$$
\sigma = |\boldsymbol{\sigma}| = \sqrt{\sigma_x^2 + \sigma_y^2 + \sigma_z^2} \quad \text{and} \quad \mathbf{e}_\sigma = \frac{\boldsymbol{\sigma}}{\sigma} = \begin{bmatrix} \mathbf{e}_{\sigma,1} \\ \mathbf{e}_{\sigma,2} \\ \mathbf{e}_{\sigma,3} \end{bmatrix} \ , \tag{B.61}
$$

such that the above matrix can be written as

$$
[\boldsymbol{\sigma}\wedge] = \sigma\,[\mathbf{e}_\sigma\wedge] \quad \text{with} \quad [\mathbf{e}_\alpha\wedge] = \begin{bmatrix} 0 & -\mathbf{e}_{\sigma,1} & -\mathbf{e}_{\sigma,2} & -\mathbf{e}_{\sigma,3} \\ \mathbf{e}_{\sigma,1} & 0 & \mathbf{e}_{\sigma,3} & -\mathbf{e}_{\sigma,2} \\ \mathbf{e}_{\sigma,2} & -\mathbf{e}_{\sigma,3} & 0 & \mathbf{e}_{\sigma,1} \\ \mathbf{e}_{\sigma,3} & \mathbf{e}_{\sigma,2} & -\mathbf{e}_{\sigma,1} & 0 \end{bmatrix} \ . \tag{B.62}
$$

By exploiting that $\mathbf{e}_{\sigma,1}^2 + \mathbf{e}_{\sigma,2}^2 + \mathbf{e}_{\sigma,3}^2 = 1$, it can be verified that

$$
\begin{aligned}
[\mathbf{e}_\alpha\wedge]^2 &= -\mathbf{I}_4 \\
[\mathbf{e}_\alpha\wedge]^3 &= [\mathbf{e}_\alpha\wedge]^2\,[\mathbf{e}_\alpha\wedge] = -[\mathbf{e}_\alpha\wedge] \\
[\mathbf{e}_\alpha\wedge]^4 &= [\mathbf{e}_\alpha\wedge]^2\,[\mathbf{e}_\alpha\wedge]^2 = \mathbf{I}_4 \\
[\mathbf{e}_\alpha\wedge]^5 &= [\mathbf{e}_\alpha\wedge]^2\,[\mathbf{e}_\alpha\wedge]^2\,[\mathbf{e}_\alpha\wedge] = [\mathbf{e}_\alpha\wedge] \\
[\mathbf{e}_\alpha\wedge]^6 &= [\mathbf{e}_\alpha\wedge]^2\,[\mathbf{e}_\alpha\wedge]^2\,[\mathbf{e}_\alpha\wedge]^2 = -\mathbf{I}_4 \quad \text{etc.}
\end{aligned}
\tag{B.63}
$$

which can be expressed in more general form as

$$
\begin{aligned}
[\mathbf{e}_\alpha\wedge]^{2k} &= (-1)^k\,\mathbf{I}_4 \quad \text{for} \quad k \geq 1 \\
[\mathbf{e}_\alpha\wedge]^{2k+1} &= (-1)^k\,[\mathbf{e}_\sigma\wedge] \quad \text{for} \quad k \geq 1\,,
\end{aligned}
\tag{B.64}
$$

or with the magnitude included as

$$
\begin{aligned}
[\boldsymbol{\sigma}\wedge]^{2k} &= (-1)^k\,\sigma^{2k}\,\mathbf{I}_4 \quad \text{for} \quad k \geq 1 \\
[\boldsymbol{\sigma}\wedge]^{2k+1} &= (-1)^k\,\sigma^{2k+1}\,[\mathbf{e}_\sigma\wedge] \quad \text{for} \quad k \geq 1\,.
\end{aligned}
\tag{B.65}
$$

Now, following a development similar to that in the previous section, we have the power series

$$
\begin{aligned}
e^{[\boldsymbol{\sigma}\wedge]} &= \mathbf{I}_4 + \sum_{k=1}^{\infty} \frac{[\boldsymbol{\sigma}\wedge]^k}{k!} \\
&= \mathbf{I}_4 + [\boldsymbol{\sigma}\wedge] + \frac{[\boldsymbol{\sigma}\wedge]^2}{2!} + \frac{[\boldsymbol{\sigma}\wedge]^3}{3!} + \frac{[\boldsymbol{\sigma}\wedge]^4}{4!} + \frac{[\boldsymbol{\sigma}\wedge]^5}{5!} \cdots\,, \\
&= \mathbf{I}_4 + \sigma\,[\mathbf{e}_\sigma\wedge] - \sigma^2\frac{\mathbf{I}_4}{2!} - \sigma^3\frac{[\mathbf{e}_\sigma\wedge]}{3!} + \sigma^4\frac{\mathbf{I}_4}{4!} + \sigma^5\frac{[\mathbf{e}_\sigma\wedge]}{5!} \cdots\,, \\
&= \left(1 - \frac{\sigma^2}{2!} + \frac{\sigma^4}{4!} - \cdots\right)\mathbf{I}_4 + \left(\sigma - \frac{\sigma^3}{3!} + \frac{\sigma^5}{5!} - \cdots\right)[\mathbf{e}_\sigma\wedge]\,.
\end{aligned}
\tag{B.66}
$$

Again, we can see the similarity with the power series for the sine and cosine functions (B.55), such that the above can be written as [10, Eq. E.38]:

$$
\boxed{
\begin{aligned}
e^{[\boldsymbol{\sigma}\wedge]} &= \cos\sigma\,\mathbf{I}_4 + \sin\sigma\,[\mathbf{e}_\sigma\wedge] \\
&= \cos\sigma\,\mathbf{I}_4 + \frac{\sin\sigma}{\sigma}\,[\boldsymbol{\sigma}\wedge]\,,
\end{aligned}
}
\tag{B.67}
$$

B.3.4 Logarithm of Rotation Matrix

The previous sections were concerned with expressions for the exponential of skew-symmetric matrices. This section is devoted to the inverse, namely finding the logarithm of a rotation matrix. Our starting point is therefore the rotation matrix

$$
\mathbf{R} = e^{[\boldsymbol{\alpha}\times]} = e^{\alpha\,[\mathbf{e}_\alpha\times]}\,,
\tag{B.68}
$$

that rotates about the axis $\mathbf{e}_\alpha$ by an angle $\alpha = |\boldsymbol{\alpha}|$, and our objective is to form an expression for $[\boldsymbol{\alpha}\times]$. Repeating Rodrigues' formula from (B.59), we have that

$$\mathbf{R} = \mathbf{I}_3 + \sin\alpha\,[\mathbf{e}_\alpha\times] + (1-\cos\alpha)\,[\mathbf{e}_\alpha\times]^2 \ , \tag{B.69}$$

from which we have that

$$\mathrm{Tr}\,[\mathbf{R}] = 3 + (1-\cos\alpha)\ \mathrm{Tr}\left[[\mathbf{e}_\alpha\times]^2\right] \ , \tag{B.70}$$

noticing that the trace of a skew-symmetric matrix is zero. From (B.46) we have that

$$\mathrm{Tr}\left[[\mathbf{e}_\alpha\times]^2\right] = -\mathbf{e}_{\alpha,2}^2 - \mathbf{e}_{\alpha,3}^2 - \mathbf{e}_{\alpha,1}^2 - \mathbf{e}_{\alpha,3}^2 - \mathbf{e}_{\alpha,1}^2 - \mathbf{e}_{\alpha,2}^2 = -2 \ , \tag{B.71}$$

such that the above can be written as

$$\mathrm{Tr}\,[\mathbf{R}] = 1 + 2\cos\alpha \qquad \Leftrightarrow \qquad \alpha = \cos^{-1}\left[\frac{\mathrm{Tr}\,[\mathbf{R}]-1}{2}\right] \ . \tag{B.72}$$

Returning again to Rodrigues' formula, we can exploit that $\mathbf{I}$ and $[\mathbf{e}_\alpha\times]^2$ are symmetric in order to form the expression

$$\mathbf{R}^\top = \mathbf{I}_3 + \sin\alpha\,[\mathbf{e}_\alpha\times]^\top + (1-\cos\alpha)\,[\mathbf{e}_\alpha\times]^2 \ , \tag{B.73}$$

which can be subtracted to yield

$$\mathbf{R} - \mathbf{R}^\top = \sin\alpha\left([\mathbf{e}_\alpha\times] - [\mathbf{e}_\alpha\times]^\top\right) \ . \tag{B.74}$$

By inspection of (B.42) it can be confirmed that $[\mathbf{e}_\alpha\times] - [\mathbf{e}_\alpha\times]^\top = 2\,[\mathbf{e}_\alpha\times]$, such that we can arrive at the desired expression [7]:

$$\boxed{\begin{aligned}[\mathbf{e}_\alpha\times] &= \frac{1}{\sin\alpha}\frac{\mathbf{R}-\mathbf{R}^\top}{2} \\ [\boldsymbol{\alpha}\times] &= \frac{\alpha}{\sin\alpha}\frac{\mathbf{R}-\mathbf{R}^\top}{2} \ .\end{aligned}} \tag{B.75}$$

In the case that $\alpha = 0$ or $\alpha = \pi$, we are dividing by zero since $\sin\alpha = 0$. In the first case we have that

$$\mathbf{R} = \mathbf{I} \quad \text{and} \quad [\boldsymbol{\alpha}\times] = \mathbf{0} \ . \tag{B.76}$$

In the second case, we can exploit that $\sin\alpha = 0$ and $\cos\alpha = -1$ in Rodrigues' formula, to arrive at

$$[\boldsymbol{\alpha}\times] = \alpha\frac{\mathbf{R}-\mathbf{I}}{2} \ . \tag{B.77}$$

C Navigation Equations and Error Dynamics Equations

C.1 Navigation Equations

Navigation using an inertial navigation system is fundamentally based on the integration of inertially sensed acceleration with respect to time. Mathematically, this means solving the second-order differential equation presented in (4.3):

$$\ddot{\mathbf{r}}^i = \mathbf{f}^i + \bar{\mathbf{g}}^i \ , \tag{C.1}$$

for the position, $\mathbf{r}^i$. Here $\mathbf{f}^i$ is the specific force sensed by the accelerometers and $\bar{\mathbf{g}}^i$ the acceleration due to gravitational attraction. This set of second order differential equations can be transformed into a set of coupled first order differential equations as

$$\begin{aligned} \dot{\mathbf{r}}^i &= \mathbf{v}^i \\ \dot{\mathbf{v}}^i &= \mathbf{f}^i + \bar{\mathbf{g}}^i \ , \end{aligned} \tag{C.2}$$

noticing that both $\mathbf{r}$ and $\mathbf{v}$ are vectors, meaning that they each have three components. In these equations, the components are specified with respect to an inertial reference frame. In general however, ignoring modelling or numerical errors, any choice of representation is essentially equivalent, since they are based on the same dynamic laws of motion. One simply has to take into account that any other reference frame may be rotating with respect to inertial space. It is therefore desirable to have similar analytical expressions in other relevant coordinate frames. Independent of the choice of reference frame, these equations are known as **the navigation equations**.

The above expression can be transformed into any arbitrary reference frame, a, by applying a coordinate transformation, $\mathbf{C}_i^a$, as

$$\mathbf{C}_i^a \, \ddot{\mathbf{r}}^i = \mathbf{C}_i^a \, \mathbf{f}^i + \mathbf{C}_i^a \, \bar{\mathbf{g}}^i = \mathbf{f}^a + \bar{\mathbf{g}}^a \ . \tag{C.3}$$

where a will, in general, be rotating with respect to the inertial frame. Such rotational effects will introduce fictitious forces in the navigation equations, depending on the choice of reference frame. Using (A.19), the above expression becomes

$$\ddot{\mathbf{r}}^a = -2\boldsymbol{\Omega}_{ia}^a \, \dot{\mathbf{r}}^a - \left(\dot{\boldsymbol{\Omega}}_{ia}^a + \boldsymbol{\Omega}_{ia}^a \, \boldsymbol{\Omega}_{ia}^a \right) \mathbf{r}^a + \mathbf{f}^a + \bar{\mathbf{g}}^a \ . \tag{C.4}$$

Although the choice of reference frame is generally a matter of convenience, the three components of specific force are always observed in the sensor frame (s-frame), which may be the body frame for a strapdown mechanisation or navigation frame for local-level gimballed systems. In the above, we therefore have that

$$\mathbf{f}^a = \mathbf{C}_s^a \, \mathbf{f}^s \ , \tag{C.5}$$

where $\mathbf{C}_s^a$ is the transformation from the s-frame to the a-frame. The transformation matrix is obtained through the integration of the angular rates $\boldsymbol{\omega}_{as}^a$. The angular rates observed by the gyroscopes, $\boldsymbol{\omega}_{is}^s$, are again bound to the sensor frame and will always be with respect to inertial space. The observations are thus related to the desired quantity as

$$\boldsymbol{\omega}_{as}^s = \boldsymbol{\omega}_{ai}^s + \boldsymbol{\omega}_{is}^s = \boldsymbol{\omega}_{is}^s - \boldsymbol{\omega}_{ia}^s = \boldsymbol{\omega}_{is}^s - \mathbf{C}_a^s \, \boldsymbol{\omega}_{ia}^a \ , \tag{C.6}$$

and can be expressed in differential form, using eq. (A.15), as

$$\dot{\mathbf{C}}_s^a = \mathbf{C}_s^a \, \mathbf{\Omega}_{as}^s \quad \text{with} \quad \mathbf{\Omega}_{as}^s = [\boldsymbol{\omega}_{as}^s \times] \ . \tag{C.7}$$

To summarize, we therefore have the general set of coupled first-order differential equations:

$$\boxed{\begin{aligned} \dot{\mathbf{r}}^a &= \mathbf{v}^a \\ \dot{\mathbf{v}}^a &= \mathbf{C}_s^a \, \mathbf{f}^s - 2\mathbf{\Omega}_{ia}^a \, \mathbf{v}^a - \left(\dot{\mathbf{\Omega}}_{ia}^a + \mathbf{\Omega}_{ia}^a \, \mathbf{\Omega}_{ia}^a\right) \mathbf{r}^a + \bar{\mathbf{g}}^a \\ \dot{\mathbf{C}}_s^a &= \mathbf{C}_s^a \, \mathbf{\Omega}_{as}^s \ , \end{aligned}} \tag{C.8}$$

where $\mathbf{f}^s$ is the observed specific force. The terms $2\mathbf{\Omega}_{ia}^a \, \mathbf{v}^a$ and $\left(\dot{\mathbf{\Omega}}_{ia}^a + \mathbf{\Omega}_{ia}^a \, \mathbf{\Omega}_{ia}^a\right) \mathbf{r}^a$ are fictitious forces that are functions of the vehicles position, velocity and rotation rate of the Earth. The gravitation term, $\bar{\mathbf{g}}^a$, is usually computed from a gravity model as described in appendix E.1 and the skew symmetric matrix, $\mathbf{\Omega}_{as}^s$, is formed from the observed angular rates using (C.6).

Most often, a *gravity model* is used instead of a *gravitational model*. The difference is that the gravity model includes the fictitious centripetal force, which is present in rotating reference frames. The two quantities are related as

$$\mathbf{g} \equiv \bar{\mathbf{g}} - \mathbf{\Omega}_{ie} \, \mathbf{\Omega}_{ie} \, \mathbf{r} \ , \tag{C.9}$$

where $\mathbf{g}$ is the gravity vector, $\bar{\mathbf{g}}$ the gravitational vector and $\mathbf{\Omega}_{ie}$ is the skew symmetric form of the inertially referenced angular velocity of the Earth. From (C.8) it is clear that this term appears in the general form of the navigation equations. This term will therefore often be consumed by the gravity term, as will become apparent shortly.

C.1.1 The Inertial Reference Frame

In order to obtain an expression for the navigation equations with respect to the i-frame, we set $a = i$ in (C.8). By doing this, all the fictitious force terms will vanish and we are left with the equations

$$\boxed{\begin{aligned} \dot{\mathbf{r}}^i &= \mathbf{v}^i \\ \dot{\mathbf{v}}^i &= \mathbf{C}_s^i \, \mathbf{f}^s + \bar{\mathbf{g}}^i \\ \dot{\mathbf{C}}_s^i &= \mathbf{C}_s^i \, \mathbf{\Omega}_{is}^s \ , \end{aligned}} \tag{C.10}$$

where the skew-symmetric matrix, $\mathbf{\Omega}_{is}^s$, is formed directly from the observed angular rates. This is the simplest form of the navigation equations, but is not commonly used for applications close to the surface of the Earth. If one uses a gravity model in order to account for the gravity field, one must first correct this model for the centripetal acceleration using (C.9).

C.1.2 The Terrestrial Reference Frame

In order to obtain the navigation equations in the terrestrial reference frame, we set $e = a$ in (C.8) to obtain the expression

$$\boxed{\begin{aligned}\dot{\mathbf{r}}^e &= \mathbf{v}^e \\ \dot{\mathbf{v}}^e &= \mathbf{C}_s^e\,\mathbf{f}^s - 2\boldsymbol{\Omega}_{ie}^e\,\mathbf{v}^e + \mathbf{g}^e \\ \dot{\mathbf{C}}_s^e &= \mathbf{C}_s^e\,\boldsymbol{\Omega}_{es}^s\ ,\end{aligned}} \tag{C.11}$$

where we have assumed that the rotational motion of the Earth is constant, i.e. $\dot{\boldsymbol{\Omega}}_{ie}^e = 0$, and made the substitution

$$\mathbf{g}^e = \bar{\mathbf{g}}^e - \boldsymbol{\Omega}_{ie}^e\,\boldsymbol{\Omega}_{ie}^e\,\mathbf{r}^e\ , \tag{C.12}$$

for the gravity vector. In this case we must consider the fact that our reference frame is rotating. This rotation is observed by the inertial sensors, but in order to navigate with respect to the rotating frame, we must correct our observations for the rotational effects of the reference frame. In terms of acceleration, the Earth rotation results in a centrifugal force, which is consumed by the gravity model, and a Coriolis term, $2\boldsymbol{\Omega}_{ie}^e\,\mathbf{v}^e$, which is velocity dependent. In terms of angular rate, the gyroscopes will directly observe the Earth rotation, $\boldsymbol{\omega}_{ie}^e$, which can be corrected for as

$$\boldsymbol{\omega}_{es}^s = \boldsymbol{\omega}_{is}^s - \mathbf{C}_e^s\,\boldsymbol{\omega}_{ie}^e\ . \tag{C.13}$$

C.1.3 The Navigation Frame

When dealing with the navigation frame, we define a velocity $\mathbf{v}^n$ relative to the surface of the Earth. Such a velocity is therefore referenced to the e-frame as

$$\mathbf{v}^n \equiv \mathbf{C}_e^n\,\mathbf{v}^e\ , \tag{C.14}$$

where $\mathbf{v}^n = (v_N, v_E, v_D)$. Note that from this definition $\mathbf{v}^n \neq \dot{\mathbf{r}}^n$. Since the n-frame is fixed to the moving vehicle, the vehicle does not move in the n-frame. The desired velocity is therefore referenced to the e-frame, but decomposed in terms of the n-frame axes. We therefore need to transform the differential equation for velocity from the previous section, using the above relation. For the LHS we apply the transformation $\mathbf{C}_e^n$ and use the expressions $\mathbf{v}^e = \mathbf{C}_n^e\mathbf{v}^n$ from (C.14) and $\dot{\mathbf{C}}_n^e = \mathbf{C}_n^e\boldsymbol{\Omega}_{en}^n$ from (A.15), such that

$$\begin{aligned}\mathbf{C}_e^n\,\dot{\mathbf{v}}^e &= \mathbf{C}_e^n\,\frac{\mathrm{d}}{\mathrm{d}t}\left(\mathbf{C}_n^e\mathbf{v}^n\right) = \mathbf{C}_e^n\left(\dot{\mathbf{C}}_n^e\mathbf{v}^n + \mathbf{C}_n^e\dot{\mathbf{v}}^n\right) \\ &= \mathbf{C}_e^n\left(\mathbf{C}_n^e\,\boldsymbol{\Omega}_{en}^n\mathbf{v}^n + \mathbf{C}_n^e\dot{\mathbf{v}}^n\right) = \mathbf{C}_e^n\,\mathbf{C}_n^e\left(\boldsymbol{\Omega}_{en}^n\mathbf{v}^n + \dot{\mathbf{v}}^n\right) \\ &= \boldsymbol{\Omega}_{en}^n\mathbf{v}^n + \dot{\mathbf{v}}^n\ .\end{aligned} \tag{C.15}$$

Similarly, applying the transformation, $\mathbf{C}_e^n$, and using again the relation $\mathbf{v}^e = \mathbf{C}_n^e\mathbf{v}^n$ together with $\boldsymbol{\Omega}_{ie}^e = \mathbf{C}_n^e\boldsymbol{\Omega}_{ie}^n\mathbf{C}_e^n$ from (5.5), we have that

$$\begin{aligned}\mathbf{C}_e^n\,\mathbf{C}_s^e\,\mathbf{f}^s + 2\mathbf{C}_e^n\,\boldsymbol{\Omega}_{ie}^e\,\mathbf{v}^e + \mathbf{C}_e^n\mathbf{g}^e &= \mathbf{C}_s^n\,\mathbf{f}^s + 2\mathbf{C}_e^n\,\boldsymbol{\Omega}_{ie}^e\,\mathbf{C}_n^e\,\mathbf{v}^n + \mathbf{g}^n \\ &= \mathbf{C}_s^n\,\mathbf{f}^s + 2\mathbf{C}_e^n\left(\mathbf{C}_n^e\,\boldsymbol{\Omega}_{ie}^n\,\mathbf{C}_e^n\right)\mathbf{C}_n^e\,\mathbf{v}^n + \mathbf{g}^n \\ &= \mathbf{C}_s^n\,\mathbf{f}^s + 2\boldsymbol{\Omega}_{ie}^n\,\mathbf{v}^n + \mathbf{g}^n\ .\end{aligned} \tag{C.16}$$

Equating the two expressions and rearranging, we obtain

$$\dot{\mathbf{v}}^n = \mathbf{C}_s^n\,\mathbf{f}^s - \left(2\boldsymbol{\Omega}_{ie}^n + \boldsymbol{\Omega}_{en}^n\right)\mathbf{v}^n + \mathbf{g}^n\ , \tag{C.17}$$

from which we can form the coupled system of differential equations:

$$\boxed{\begin{aligned}\dot{\mathbf{r}}^e &= \mathbf{C}_n^e \mathbf{v}^n \\ \dot{\mathbf{v}}^n &= \mathbf{C}_s^n \mathbf{f}^s - (2\boldsymbol{\Omega}_{ie}^n + \boldsymbol{\Omega}_{en}^n)\,\mathbf{v}^n + \mathbf{g}^n \\ \dot{\mathbf{C}}_s^n &= \mathbf{C}_s^n \boldsymbol{\Omega}_{ns}^s \ ,\end{aligned}} \tag{C.18}$$

governing the dynamics of our system. Again, the fictitious terms due to Earth rotation appears. However, in this frame we must also account for the fact that the reference frame must be rotated as we move across the surface of the Earth, in order to keep the axes aligned along the north, east and down directions. This results in the term $\boldsymbol{\Omega}_{en}^n \mathbf{v}^n$, known as the **transport-rate term**. Also the angular rates must be corrected for Earth rotation and transport rate as

$$\boldsymbol{\omega}_{ns}^s = \boldsymbol{\omega}_{ne}^s + \boldsymbol{\omega}_{ei}^s + \boldsymbol{\omega}_{is}^s = \boldsymbol{\omega}_{is}^s - \mathbf{C}_n^s \left(\boldsymbol{\omega}_{en}^n + \mathbf{C}_e^n \boldsymbol{\omega}_{ie}^e\right) \ . \tag{C.19}$$

Most often, the position is expressed in terms of geodetic coordinates

$$\mathbf{p} = \begin{bmatrix} \phi \\ \lambda \\ h \end{bmatrix} \ , \tag{C.20}$$

where ϕ is latitude, λ is longitude and h is the ellipsoidal height. Using the multivariable chain rule, we have that

$$\begin{aligned}\dot{\mathbf{r}} = \frac{d\mathbf{r}}{dt} &= \frac{d\mathbf{r}}{d\phi}\frac{d\phi}{dt} + \frac{d\mathbf{r}}{d\lambda}\frac{d\lambda}{dt} + \frac{d\mathbf{r}}{dh}\frac{dh}{dt} \\ &= \dot{\phi}\frac{d\mathbf{r}}{d\phi} + \dot{\lambda}\frac{d\mathbf{r}}{d\lambda} + \dot{h}\frac{d\mathbf{r}}{dh} \ ,\end{aligned} \tag{C.21}$$

where from (2.12):

$$\mathbf{r}^e = \begin{bmatrix} (R_E + h)\cos\phi\cos\lambda \\ (R_E + h)\cos\phi\sin\lambda \\ \left(R_E\left(1 - e^2\right) + h\right)\sin\phi \end{bmatrix} \ , \tag{C.22}$$

such that

$$\dot{\mathbf{r}} = \begin{bmatrix} -\dot{\phi}\,(R_N + h)\sin\phi\cos\lambda - \dot{\lambda}\,(R_E + h)\cos\phi\sin\lambda + \dot{h}\cos\phi\cos\lambda \\ -\dot{\phi}\,(R_N + h)\sin\phi\sin\lambda + \dot{\lambda}\,(R_E + h)\cos\phi\cos\lambda + \dot{h}\cos\phi\sin\lambda \\ \dot{\phi}\,(R_N + h)\cos\phi + \dot{h}\sin\phi \end{bmatrix} \ . \tag{C.23}$$

Here, the expressions (2.9) and (2.10) were exploited to arrive at

$$\begin{aligned}&\frac{d}{d\phi}\left((R_E + h)\cos\phi\right) = -\left(R_N + h\right)\sin\phi \quad \text{and} \\ &\frac{d}{d\phi}\left(\left(R_E\left(1 - e^2\right) + h\right)\sin\phi\right) = \left(R_N + h\right)\cos\phi \ .\end{aligned} \tag{C.24}$$

Using the expression for $\mathbf{v}^e$ in (C.23) and the transformation matrix in (A.23) we have that

$$\mathbf{v}^n = \mathbf{C}_e^n \, \mathbf{v}^e = \begin{bmatrix} v_N \\ v_E \\ v_D \end{bmatrix} = \begin{bmatrix} \dot{\phi} \, (R_N + h) \\ \dot{\lambda} \, (R_E + h) \cos \phi \\ -\dot{h} \end{bmatrix} , \tag{C.25}$$

where v_N, v_E and v_D are the north, east and down components of velocity, representing the components of the n-frame. Here, R_N is the radius of curvature of the meridian (north direction) and R_E is the radius of curvature of the prime vertical (east direction), see Section 2.2.2. Rearranging the above, we have that

$$\dot{\mathbf{p}} = \begin{bmatrix} \dot{\phi} \\ \dot{\lambda} \\ \dot{h} \end{bmatrix} = \begin{bmatrix} v_N / \left(R_N + h \right) \\ v_E / \left(R_E + h \right) \cos \phi \\ -v_D \end{bmatrix} , \tag{C.26}$$

which replaces $\dot{\mathbf{r}}^e = \mathbf{C}_n^e \mathbf{v}^n$ in (C.18).

C.1.4 The Wander-Azimuth Frame

The wander-azimuth reference frame is closely related to the navigation frame. The z-axes are coincidental, while the x- and y-axes are rotated about the z-axis by a wander angle, ψ_{nw}, that varies with position. In general, the wander angle is initialised at zero, at the start of navigation. The wander angle is the azimuthal or heading angle from the n-frame to the wander-azimuth frame, such that

$$\mathbf{C}_n^w = \begin{bmatrix} \cos \psi_{nw} & \sin \psi_{nw} & 0 \\ -\sin \psi_{nw} & \cos \psi_{nw} & 0 \\ 0 & 0 & 1 \end{bmatrix} \quad \text{and}$$

$$\mathbf{C}_e^w = \mathbf{C}_n^w \, \mathbf{C}_e^n = \begin{bmatrix} -\sin \phi \cos \lambda \cos \psi_{nw} & -\sin \phi \sin \lambda \cos \psi_{nw} & \cos \phi \cos \psi_{nw} \\ -\sin \lambda \sin \psi_{nw} & +\cos \lambda \sin \psi_{nw} & \\ \sin \phi \cos \lambda \sin \psi_{nw} & \sin \phi \sin \lambda \sin \psi_{nw} & -\cos \phi \sin \psi_{nw} \\ -\sin \lambda \cos \psi_{nw} & +\cos \lambda \cos \psi_{nw} & \\ -\cos \phi \cos \lambda & -\cos \phi \sin \lambda & -\sin \phi \end{bmatrix} , \tag{C.27}$$

where (A.23) was introduced. The navigation equations for the w-frame are therefore similar to those of the n-frame. From (C.18) we have that

$$\begin{aligned} \dot{\mathbf{r}}^e &= \mathbf{C}_w^e \mathbf{v}^w \\ \dot{\mathbf{v}}^w &= \mathbf{C}_s^w \, \mathbf{f}^s - (2\mathbf{C}_e^w \, \boldsymbol{\Omega}_{ie}^e \, \mathbf{C}_w^e + \boldsymbol{\Omega}_{ew}^w) \, \mathbf{v}^w + \mathbf{g}^w \\ \dot{\mathbf{C}}_s^w &= \mathbf{C}_s^w \, \boldsymbol{\Omega}_{ws}^s \, , \end{aligned} \tag{C.28}$$

indicating that we have to form two transformation operators, $\mathbf{C}_s^w$ and $\mathbf{C}_e^w$. The latter is governed by the differential equation

$$\dot{\mathbf{C}}_e^w = \mathbf{C}_e^w \, \boldsymbol{\Omega}_{ew}^w \, , \tag{C.29}$$

where the rotational rate, $\boldsymbol{\omega}_{ew}^w$, is related to the wander angle, ψ_{nw}, as

$$\begin{aligned}\boldsymbol{\omega}_{ew}^{w} &= \mathbf{C}_{n}^{w}\,\boldsymbol{\omega}_{ew}^{n} = \mathbf{C}_{n}^{w}\left(\boldsymbol{\omega}_{en}^{n} + \boldsymbol{\omega}_{ew}^{n}\right) \\ &= \mathbf{C}_{n}^{w}\left(\begin{bmatrix} v_e/\left(R_E+h\right) \\ -v_N/\left(R_N+h\right) \\ -v_e\tan\phi/\left(R_E+h\right)\end{bmatrix} + \begin{bmatrix} 0 \\ 0 \\ \dot{\psi}_{nw}\end{bmatrix}\right) .\end{aligned} \tag{C.30}$$

The term $\boldsymbol{\omega}_{en}^{n}$ is the transport-rate and represents the amount we need to rotate the frame, in order to keep the axes along its north, east and down directions, as we move across the surface of the Earth. As we see above, the term

$$\omega_{en,D}^{n} = -v_e\tan\phi/\left(R_E+h\right) \ , \tag{C.31}$$

becomes very large and eventually infinite as we approach the pole, i.e. when $\phi \approx \pm 90^{\circ}$. The purpose of the wander-azimuth mechanisation is to avoid these singularities, by forcing the turn rate about the vertical axis to be zero as

$$\boldsymbol{\omega}_{ew}^{w} = \mathbf{C}_{n}^{w}\begin{bmatrix}\omega_{ew,N}^{n} \\ \omega_{ew,E}^{n} \\ 0\end{bmatrix} \ , \tag{C.32}$$

which is obtained when

$$\dot{\psi}_{nw} = \frac{v_e}{R_E+h}\tan\phi \ . \tag{C.33}$$

However, we are not interested in solving this equation for the wander angle. Instead, we intent to solve the differential equation for the transformation operator, $\mathbf{C}_{e}^{w}$, directly. Therefore, we must form the skew-symmetric matrix $\boldsymbol{\Omega}_{ew}^{w} = [\boldsymbol{\omega}_{ew}^{w}\times]$. In order to do this, we must compute the rotational rate, $\boldsymbol{\omega}_{ew}^{w}$, which can be written in terms of the wander-referenced velocity, $\mathbf{v}^{w}$, as

$$
\begin{aligned}
\boldsymbol{\omega}_{ew}^{w} &= \mathbf{C}_{n}^{w} \begin{bmatrix} \omega_{ew,N}^{n} \\ \omega_{ew,E}^{n} \\ 0 \end{bmatrix} = \mathbf{C}_{n}^{w} \begin{bmatrix} v_e / \left(R_E + h\right) \\ -v_N / \left(R_N + h\right) \\ 0 \end{bmatrix} \\
&= \mathbf{C}_{n}^{w} \begin{bmatrix} 0 & 1/\left(R_E + h\right) & 0 \\ -1/\left(R_N + h\right) & 0 & 0 \\ 0 & 0 & 0 \end{bmatrix} \mathbf{v}^{n} \\
&= \mathbf{C}_{n}^{w} \begin{bmatrix} 0 & 1/\left(R_E + h\right) & 0 \\ -1/\left(R_N + h\right) & 0 & 0 \\ 0 & 0 & 0 \end{bmatrix} \mathbf{C}_{w}^{n} \mathbf{v}^{w} \\
&= \begin{bmatrix} \frac{\cos\psi_{nw}\sin\psi_{nw}}{R_E+h} - \frac{\cos\psi_{nw}\sin\psi_{nw}}{R_N+h} & \frac{\cos^2\psi_{nw}}{R_E+h} + \frac{\sin^2\psi_{nw}}{R_N+h} & 0 \\ -\frac{\cos^2\psi_{nw}}{R_N+h} - \frac{\sin^2\psi_{nw}}{R_E+h} & \frac{\cos\psi_{nw}\sin\psi_{nw}}{R_N+h} - \frac{\cos\psi_{nw}\sin\psi_{nw}}{R_E+h} & 0 \\ 0 & 0 & 0 \end{bmatrix} \mathbf{v}^{w} \\
&= \frac{1}{\left(R_N + h\right)\left(R_E + h\right)} \begin{bmatrix} e'^2\, R_N\, \mathbf{C}_{e1,2}^{w}\, \mathbf{C}_{e2,3}^{w} & R_N \left\{1 + \left(e'\, \mathbf{C}_{e2,3}^{w}\right)^2\right\} + h & 0 \\ -R_N \left\{1 + \left(e'\, \mathbf{C}_{e1,3}^{w}\right)^2\right\} + h & -e'^2\, R_N\, \mathbf{C}_{e1,2}^{w}\, \mathbf{C}_{e2,3}^{w} & 0 \\ 0 & 0 & 0 \end{bmatrix} \mathbf{v}^{w} \, .
\end{aligned}
\tag{C.34}
$$

The radii of curvature, R_N and R_E, in this expression can be formed directly from the elements of the matrix, $\mathbf{C}_{e}^{w}$, according to (2.9) and (2.10) as

$$
R_N = \frac{a\left(1 - e^2\right)}{\left\{1 - \left(e\, \mathbf{C}_{e3,3}^{w}\right)^2\right\}^{3/2}} \quad \text{and} \quad R_E = \frac{a}{\sqrt{1 - \left(e\, \mathbf{C}_{e3,3}^{w}\right)^2}} \, , \tag{C.35}
$$

where a is the semi-major axis of the ellipsoid and e is the first eccentricity. The parameter $e' = 1/\left(1 - e^2\right)$ is the second eccentricity of the ellipsoid. When we are close to the poles, we have that $R_N = R_E = a/\sqrt{1 - e^2}$, such that the above may be approximated as

$$
\boldsymbol{\omega}_{ew}^{w} \approx \left(\frac{a}{\sqrt{1 - e^2}} + h\right)^{-1} \begin{bmatrix} 0 & 1 & 0 \\ -1 & 0 & 0 \\ 0 & 0 & 0 \end{bmatrix} \mathbf{v}^{w} \, . \tag{C.36}
$$

Now, the latitude, longitude and wander angle, can be derived from the transformation matrix, $\mathbf{C}_{e}^{w}$, as

$$
\begin{aligned}
\phi &= -\arcsin\left(\mathbf{C}_{e3,3}^{w}\right) \\
\lambda &= \arctan_2\left(-\mathbf{C}_{e3,2}^{w}, -\mathbf{C}_{e3,1}^{w}\right) \\
\psi_{nw} &= \arctan_2\left(-\mathbf{C}_{e2,3}^{w}, \mathbf{C}_{e1,3}^{w}\right) \, ,
\end{aligned}
\tag{C.37}
$$

noting that the longitude and wander angle become undefined at the poles and may therefore become subject to significant computational rounding errors in these areas [10, Sec. 5.4.5]. Therefore, we do not need to solve explicitly for the latitude and longitude in the navigation equations, which then reduces to

$$\boxed{\begin{aligned} \dot{h} &= -v_D^w \\ \dot{\mathbf{v}}^w &= \mathbf{C}_s^w\,\mathbf{f}^s - (2\mathbf{C}_e^w\,\boldsymbol{\Omega}_{ie}^e\,\mathbf{C}_w^e + \boldsymbol{\Omega}_{ew}^w)\,\mathbf{v}^w + \mathbf{g}^w \\ \dot{\mathbf{C}}_s^w &= \mathbf{C}_s^w\,\boldsymbol{\Omega}_{ws}^s \\ \dot{\mathbf{C}}_e^w &= \mathbf{C}_e^w\,\boldsymbol{\Omega}_{ew}^w\ . \end{aligned}} \tag{C.38}$$

In order to solve for the transformation matrix, $\mathbf{C}_s^w$, we need to form the angular rate vector, $\boldsymbol{\omega}_{ws}^s$, as

$$\begin{aligned} \boldsymbol{\omega}_{ws}^s &= \boldsymbol{\omega}_{we}^s + \boldsymbol{\omega}_{ei}^s + \boldsymbol{\omega}_{is}^s = \boldsymbol{\omega}_{is}^s - \boldsymbol{\omega}_{ew}^s - \boldsymbol{\omega}_{ie}^s \\ &= \boldsymbol{\omega}_{is}^s - \mathbf{C}_w^s\,(\boldsymbol{\omega}_{ew}^w + \boldsymbol{\omega}_{ie}^w) \\ &= \boldsymbol{\omega}_{is}^s - \mathbf{C}_w^s\,(\boldsymbol{\omega}_{ew}^w + \mathbf{C}_e^w\,\boldsymbol{\omega}_{ie}^e)\ , \end{aligned} \tag{C.39}$$

where $\boldsymbol{\omega}_{ew}^w$ is formed using (C.34).

C.2 Implementation of the Navigation Equations

In this section, it will be discussed how the navigation equations can be implemented. It should be noted that there is no unique way of doing this and as will become apparent, such an implementation also depends on the desired complexity, precision and computational power. Only an implementation in the **navigation frame**, i.e. an implementation of the system in (5.61), will be considered here. For other implementations, the reader is referred to [10, Sec. 5]. Additionally, only the **strapdown configuration** is considered, meaning that observations are obtained directly in the b-frame of the vehicle, i.e. $s = b$. In this case, the system of equations become:

$$\dot{\phi} = v_N/\,(R_N + h) \tag{C.40a}$$

$$\dot{\lambda} = v_E/\,(R_E + h)\cos\phi \tag{C.40b}$$

$$\dot{h} = -v_D \tag{C.40c}$$

$$\dot{\mathbf{v}}^n = \mathbf{C}_b^n\,\mathbf{f}^b - (2\boldsymbol{\Omega}_{ie}^n + \boldsymbol{\Omega}_{en}^n)\,\mathbf{v}^n + \mathbf{g}^n \tag{C.40d}$$

$$\dot{\mathbf{C}}_b^n = \mathbf{C}_b^n\,\boldsymbol{\Omega}_{nb}^b\ , \tag{C.40e}$$

where the geodetic coordinates are utilized and

$$\boldsymbol{\omega}_{nb}^b = \boldsymbol{\omega}_{ne}^b + \boldsymbol{\omega}_{ei}^b + \boldsymbol{\omega}_{ib}^b = \boldsymbol{\omega}_{ib}^b - \mathbf{C}_n^b\,(\boldsymbol{\omega}_{en}^n + \mathbf{C}_e^n\,\boldsymbol{\omega}_{ie}^e)\ . \tag{C.41}$$

Here $\mathbf{C}_e^n$ may be computed from the position using (A.23) and $\boldsymbol{\omega}_{ie}^e = (0, 0, \omega_{ie})$ such that

$$\boldsymbol{\omega}_{ie}^n = \omega_{ie} \begin{bmatrix} \cos\phi \\ 0 \\ -\sin\phi \end{bmatrix}\ . \tag{C.42}$$

The transport rate, $\boldsymbol{\omega}_{en}^n$, may be computed from a combination of (A.24) and (5.64) as

$$\boldsymbol{\omega}_{en}^n = \begin{bmatrix} v_E/\,(R_E + h) \\ -v_N/\,(R_N + h) \\ -v_E \tan\phi/\,(R_E + h) \end{bmatrix}\ . \tag{C.43}$$

The skew-symmetric form of the angular rate is formed using (A.8) and the gravity component is computed from a (normal) gravity model as described in Appendix E.1. If one desires to express the attitude in terms of a quaternion (C.40e) may be replaced by (A.37):

$$\dot{\mathbf{q}}_b^n = \tfrac{1}{2}\,\mathbf{A}^b\,\mathbf{q}_b^n \quad \text{with} \quad \mathbf{A}^b = \begin{bmatrix} 0 & -\omega_{nb,x}^b & -\omega_{nb,y}^b & -\omega_{nb,z}^b \\ \omega_{nb,x}^b & 0 & \omega_{nb,z}^b & -\omega_{nb,y}^b \\ \omega_{nb,y}^b & -\omega_{nb,z}^b & 0 & \omega_{nb,x}^b \\ \omega_{nb,z}^b & \omega_{nb,y}^b & -\omega_{nb,x}^b & 0 \end{bmatrix} . \tag{C.44}$$

In the implementation, the set of differential equations are solved iteratively at the end of each sampling or measurement interval. At each iteration step, the differential equations are usually solved sequentially as

1. **Step 1: Attitude Update**
   Compute the transformation matrix, $\mathbf{C}_b^n$, or rotation quaternion, $\mathbf{q}_b^n$, using the measured angular rates, $\boldsymbol{\omega}_{ib}^b$,

2. **Step 2: Specific Force Transformation**
   Transform the observed specific force, $\mathbf{f}^b$, into an n-frame representation, $\mathbf{f}^n$,

3. **Step 3: Velocity Update**
   Correct the specific force, $\mathbf{f}^n$, for the Coriolis and transport-rate terms, $(2\boldsymbol{\Omega}_{ie}^n + \boldsymbol{\Omega}_{en}^n)\,\mathbf{v}^n$, along with the gravity acceleration, $\mathbf{g}^n$, in order to obtain the vehicle acceleration, $\dot{\mathbf{a}}^n$. Integrate the vehicle acceleration, $\dot{\mathbf{v}}^n$, over the sampling interval, in order to obtain the velocity, $\mathbf{v}^n$, and

4. **Step 4: Position Update**
   Integrate the velocity, $\mathbf{v}^n$, over the sampling interval in order to obtain the position, $\mathbf{p}$.

Each of these steps can be performed more or less accurate depending on approximations and the degree of truncations, along with the solution strategy or integration method. Since the equations are coupled, increased precision may also be obtained through several iterations. In the following, each of these four steps will be discussed and different solution strategies will be presented. This is followed by a discussion concerning precision and computational cost, which should both be considered when choosing an implementation strategy.

The observations, $\mathbf{f}^b$ and $\boldsymbol{\omega}_{ib}^b$, at some epoch, k, are associated with a time stamp, t_k. It will be assumed that t_k refers to the end of the measurement interval, such that the observations represent average values over the interval $\delta t = t_k - t_{k-1}$, from the previous to the current time stamp. The interval, δt, represents the interval over which we want to update our navigation solution. In order to distinguish between quantities at the beginning and the end of the update interval, values at the beginning of the interval, i.e. t_{k-1}, will be denoted by $(-)$ and values at the end of the interval, i.e. t_k, will be denoted by $(+)$. The values

$$\mathbf{p}(-)\,, \quad \mathbf{v}^n(-)\,, \quad \mathbf{C}_b^n(-) \quad \text{or} \quad \mathbf{q}_b^n(-)$$

therefore represent the position, velocity and attitude from the previous iteration (or initial values). These are also the variables that need to be updated for each iteration.

C.2.1 Step 1: Attitude Update

In order to determine the transformation operator (and therefore the attitude), we first need to correct the gyro measurements, $\boldsymbol{\omega}_{ib}^{b}$, for the Earth's rotation, $\boldsymbol{\omega}_{ie}^{b}$, and the transport rate, $\boldsymbol{\omega}_{en}^{b}$. However, this expression unfortunately involves the transformation, $\mathbf{C}_{n}^{b} = (\mathbf{C}_{b}^{n})^{\top}$, that is to be determined. As a first approximation, we can assume that all terms are constant over the update interval:

$$\boldsymbol{\omega}_{nb}^{b} \approx \boldsymbol{\omega}_{ib}^{b} - \mathbf{C}_{b}^{n}(-)^{\top} \left(\boldsymbol{\omega}_{ie}^{n}(-) + \boldsymbol{\omega}_{en}^{n}(-)\right) \ , \tag{C.45}$$

where we have used the transformation matrix $\mathbf{C}_{n}^{b}$ from the previous epoch and computed the terms $\boldsymbol{\omega}_{ie}^{n}$ and $\boldsymbol{\omega}_{en}^{n}$ using the position and velocity from the previous epoch. In high-precision, high-dynamic applications, the variation of the transport-rate term over the update interval may be significant. In such situations, it may be necessary to perform a two-step recursive method in order to properly account for the variation in the transport rate during the update interval as

$$\boldsymbol{\omega}_{nb}^{b} \approx \boldsymbol{\omega}_{ib}^{b} - \overline{\mathbf{C}}_{b}^{n\,\top} \left[\boldsymbol{\omega}_{ie}^{n}(-) + \tfrac{1}{2}\,\boldsymbol{\omega}_{en}^{n}(-) + \tfrac{1}{2}\,\boldsymbol{\omega}_{en}^{n}(+)\right] \ , \tag{C.46}$$

where $\overline{\mathbf{C}}_{b}^{n}$ is an average transformation operator, which will be further discussed in the next section. Having corrected the measured angular rates, we can solve the differential equation governing the attitude in terms of either (C.40e) or (C.44). Both of these differential equations are homogeneous, indicating that their solution can be expressed in terms of a transition matrix, $\boldsymbol{\Phi}\,(t, t_0)$, using (B.14) as

$$\mathbf{x}(+) = \boldsymbol{\Phi}\,(+,-)\,\mathbf{x}(-) \ , \tag{C.47}$$

where $\mathbf{x}$ corresponds to the terms $\mathbf{C}_{b}^{n}$ or $\mathbf{q}_{b}^{n}$. If we assume that the rotational rate, $\boldsymbol{\omega}_{nb}^{b}$, is constant over the update interval, δt, it can be written on the form (B.27). The solution to the differential equations (C.40e) and (C.44) then becomes

$$\mathbf{C}_{b}^{n}(+) = \mathbf{C}_{b}^{n}(-)\, e^{\boldsymbol{\Omega}_{nb}^{n}\delta t} \quad \text{and} \tag{C.48a}$$

$$\mathbf{q}_{b}^{n}(+) = e^{\mathbf{A}^{b}\delta t/2}\,\mathbf{q}_{b}^{n}(-) \ . \tag{C.48b}$$

These equations allow us to update the attitude from the beginning of the measurement interval, t_{k-1}, to the end of the measurement interval, t_k, under the assumption that $\boldsymbol{\omega}_{nb}^{b}$ is constant during this interval.

Solving for the Direction Cosine Matrix

As previously mentioned, we start by correcting the measured angular rates for Earth rotation and transport rate, forming the skew-symmetric matrix

$$\begin{aligned} \boldsymbol{\Omega}_{nb}^{b} &= \left[\boldsymbol{\omega}_{nb}^{b}\times\right] = \left[\left\{\boldsymbol{\omega}_{ib}^{b} - \mathbf{C}_{n}^{b}(-)\left(\boldsymbol{\omega}_{ie}^{n}(-) + \boldsymbol{\omega}_{en}^{n}(-)\right)\right\}\times\right] \\ &= \boldsymbol{\Omega}_{ib}^{b} - \mathbf{C}_{n}^{b}(-)\left[\boldsymbol{\Omega}_{ie}^{n}(-) + \boldsymbol{\Omega}_{en}^{n}(-)\right]\mathbf{C}_{b}^{n}(-) \ , \end{aligned} \tag{C.49}$$

where $\mathbf{C}_{n}^{b}(-)$ is the attitude at the previous epoch and $\boldsymbol{\Omega}_{ie}^{n}(-)$ and $\boldsymbol{\Omega}_{en}^{n}(-)$ are computed using the position and velocity at the previous epoch. Then, assuming that the rotational rate is constant during the update interval, we can compute the **angle increment**, $\boldsymbol{\alpha}_{nb}^{b}$, as

$$\boldsymbol{\alpha}_{nb}^{b} = \boldsymbol{\omega}_{nb}^{b}\,\delta t \quad \text{with} \quad \left[\boldsymbol{\alpha}_{nb}^{b}\times\right] = \boldsymbol{\Omega}_{nb}^{b}\,\delta t\,, \tag{C.50}$$

from which we want to form the transition matrix according to (C.48a) as

$$\boldsymbol{\Phi}\left(+,-\right) = e^{\left[\boldsymbol{\alpha}_{nb}^{b}\times\right]}\,, \tag{C.51}$$

that allows us to transition from the previous attitude, $\mathbf{C}_{n}^{b}(-)$, to the current attitude, $\mathbf{C}_{n}^{b}(+)$. In forming the transition matrix, we can use the power series expansion from (B.23):

$$e^{\left[\boldsymbol{\alpha}_{nb}^{b}\times\right]} = \mathbf{I} + \sum_{k=1}^{\infty}\frac{\left[\boldsymbol{\alpha}_{nb}^{b}\times\right]^{k}}{k!} = \mathbf{I} + \left[\boldsymbol{\alpha}_{nb}^{b}\times\right] + \frac{\left[\boldsymbol{\alpha}_{nb}^{b}\times\right]^{2}}{2!} + \frac{\left[\boldsymbol{\alpha}_{nb}^{b}\times\right]^{3}}{3!} + \cdots\,, \tag{C.52}$$

and then truncate the series at some order, depending on the desired precision. By truncating the series after the first two terms, we obtain the **first-order scheme**

$$\mathbf{C}_{b}^{n}(+) = \mathbf{C}_{b}^{n}(-)\,\left(\mathbf{I} + \left[\boldsymbol{\alpha}_{nb}^{b}\times\right]\right) = \mathbf{C}_{b}^{n}(-)\,\left(\mathbf{I} + \boldsymbol{\Omega}_{nb}^{b}\,\delta t\right)\,. \tag{C.53}$$

As shown in Appendix B.3.2, the transition matrix can also be expressed on a closed form known as **Rodrigues' formula** from (B.59):

$$\boxed{e^{\left[\boldsymbol{\alpha}_{nb}^{b}\times\right]} = \mathbf{I} + a_{s}\,\left[\boldsymbol{\alpha}_{nb}^{b}\times\right] + a_{c}\left[\boldsymbol{\alpha}_{nb}^{b}\times\right]^{2}\,,} \tag{C.54}$$

where the coefficients, a_s and a_c, can be computed using trigonometric functions as

$$a_{s} = \frac{\sin\left|\boldsymbol{\alpha}_{nb}^{b}\right|}{\left|\boldsymbol{\alpha}_{nb}^{b}\right|} \quad \text{and} \quad a_{c} = \frac{1-\cos\left|\boldsymbol{\alpha}_{nb}^{b}\right|}{\left|\boldsymbol{\alpha}_{nb}^{b}\right|^{2}}\,, \tag{C.55}$$

which may be computationally expensive. Moreover, in order to avoid division by zero, this formula should be replaced by an approximate version whenever $\left|\boldsymbol{\alpha}_{nb}^{b}\right|$ is very small. A series expansion of the coefficients is given in (B.58), which could for example be truncated at fourth order to yield

$$a_{s} = 1 - \frac{\left|\boldsymbol{\alpha}_{nb}^{b}\right|^{2}}{6} \quad \text{and} \quad a_{c} = \frac{1}{2} - \frac{\left|\boldsymbol{\alpha}_{nb}^{b}\right|^{2}}{24}\,. \tag{C.56}$$

As we iterate through the observations, the transformation matrix might drift away from being orthonormal. It is therefore necessary to re-orthonormalise the transformation matrix at regular intervals. This procedure is described in Section C.2.6.

Solving for the Quaternion Attitude

The approach for updating the quaternion attitude is almost identical to the approach when using a direction cosine attitude. First the angle increment, $\boldsymbol{\alpha}_{nb}^{b}$, is formed using (C.49) and (C.50), which is then used to form the transition matrix from (C.48b) as

$$\boldsymbol{\Phi}\left(+,-\right) \approx e^{\frac{1}{2}\mathbf{A}^{b}\delta t}\,, \tag{C.57}$$

under the assumption that $\boldsymbol{\omega}_{nb}^{b}$ is constant during the update interval. The exponent matrix is as

$$\left[\boldsymbol{\alpha}_{nb}^{b}\wedge\right] = \mathbf{A}^{b}\,\delta t = \begin{bmatrix} 0 & -\alpha_{nb,x}^{b} & -\alpha_{nb,y}^{b} & -\alpha_{nb,z}^{b} \\ \alpha_{nb,x}^{b} & 0 & \alpha_{nb,z}^{b} & -\alpha_{nb,y}^{b} \\ \alpha_{nb,y}^{b} & -\alpha_{nb,z}^{b} & 0 & \alpha_{nb,x}^{b} \\ \alpha_{nb,z}^{b} & \alpha_{nb,y}^{b} & -\alpha_{nb,x}^{b} & 0 \end{bmatrix} , \tag{C.58}$$

where $\boldsymbol{\alpha}_{nb}^{b}$ is again the angle increment. The transition matrix can be formed using a series expansion from (B.66):

$$\boxed{e^{\frac{1}{2}\left[\boldsymbol{\alpha}_{nb}^{b}\wedge\right]} = a_c\,\mathbf{I}_4 + a_s\,\left[\boldsymbol{\alpha}_{nb}^{b}\wedge\right]\ ,} \tag{C.59}$$

where the coefficients can be computed exactly using Rodrigues' formula from (B.67):

$$a_c = \cos\left(\left|\boldsymbol{\alpha}_{nb}^{b}\right|/2\right) \quad \text{and} \quad a_s = \frac{\sin\left(\left|\boldsymbol{\alpha}_{nb}^{b}\right|/2\right)}{\left|\boldsymbol{\alpha}_{nb}^{b}\right|}\ , \tag{C.60}$$

or using a series expansion from (B.66) to e.g. fourth order:

$$a_c \approx 1 - \frac{\left|\boldsymbol{\alpha}_{nb}^{b}\right|^2}{8} + \frac{\left|\boldsymbol{\alpha}_{nb}^{b}\right|^4}{384} \quad \text{and} \quad a_s \approx \frac{1}{2} - \frac{\left|\boldsymbol{\alpha}_{nb}^{b}\right|^2}{48}\ , \tag{C.61}$$

which is particularly relevant for the sine term, a_s, since we want to avoid division by very small values of $\left|\boldsymbol{\alpha}_{nb}^{b}\right|$. Again, it will be necessary to re-orthonormalise the quaternion attitude at regular intervals. This procedure is described in Section C.2.6.

Finally, it is possible to write the transition (C.48b) in terms of a Hamilton product as was also shown in Appendix A.2.4:

$$\begin{aligned} \mathbf{q}_b^n(+) &= \left(a_c\,\mathbf{I}_4 + a_s\,\left[\boldsymbol{\alpha}_{nb}^{b}\wedge\right]\right)\mathbf{q}_b^n(-) \\ &= \begin{bmatrix} a_c & -a_s\alpha_{nb,x}^{b} & -a_s\alpha_{nb,y}^{b} & -a_s\alpha_{nb,z}^{b} \\ a_s\alpha_{nb,x}^{b} & a_c & a_s\alpha_{nb,z}^{b} & -a_s\alpha_{nb,y}^{b} \\ a_s\alpha_{nb,y}^{b} & -a_s\alpha_{nb,z}^{b} & a_c & a_s\alpha_{nb,x}^{b} \\ a_s\alpha_{nb,z}^{b} & a_s\alpha_{nb,y}^{b} & -a_s\alpha_{nb,x}^{b} & a_c \end{bmatrix} \begin{bmatrix} a \\ b \\ c \\ d \end{bmatrix} = \begin{bmatrix} a\,a_c - b\,a_s\alpha_{nb,x}^{b} - c\,a_s\alpha_{nb,y}^{b} - d\,a_s\alpha_{nb,z}^{b} \\ a\,a_s\alpha_{nb,x}^{b} + b\,a_c + c\,a_s\alpha_{nb,z}^{b} - d\,a_s\alpha_{nb,y}^{b} \\ a\,a_s\alpha_{nb,y}^{b} - b\,a_s\alpha_{nb,z}^{b} + c\,a_c + d\,a_s\alpha_{nb,x}^{b} \\ a\,a_s\alpha_{nb,z}^{b} + b\,a_s\alpha_{nb,y}^{b} - c\,a_s\alpha_{nb,x}^{b} + d\,a_c \end{bmatrix} \\ &= \begin{bmatrix} a & -b & -c & -d \\ b & a & -d & c \\ c & d & a & -b \\ d & -c & b & a \end{bmatrix} \begin{bmatrix} a_c \\ a_s\,\alpha_{nb,x}^{b} \\ a_s\,\alpha_{nb,y}^{b} \\ a_s\,\alpha_{nb,z}^{b} \end{bmatrix} = \mathbf{q}_b^n(-) \circ \begin{bmatrix} a_c \\ a_s\,\alpha_{nb,x}^{b} \\ a_s\,\alpha_{nb,y}^{b} \\ a_s\,\alpha_{nb,z}^{b} \end{bmatrix} . \end{aligned} \tag{C.62}$$

C.2.2 Step 2: Specific Force Transformation

Having determined the direction cosine matrix, $\mathbf{C}_b^n$, or similarly the quaternion attitude, $\mathbf{q}_b^n$, we can perform the transformation of the sensed specific force, $\mathbf{f}^b$, into a representation in the n-frame. However, as mentioned previously, the observations represent average values over a measurement time interval, δt. In order to transform the observations from the b-frame to the n-frame, we need to similarly construct a transformation operator that reflects the "average" direction during the measurement interval.

For this step, only the formation of an average operator in the form of a direction cosine matrix, $\overline{\mathbf{C}}_b^n$, will be considered. If a quaternion attitude implementation is used, it may

therefore be necessary to form the corresponding direction cosine attitude matrix using the transpose of (5.51) as

$$\mathbf{C}_b^n\left(-\right) = \begin{bmatrix} \left(a^2+b^2-c^2-d^2\right) & 2\left(bc-ad\right) & 2\left(bd+ac\right) \\ 2\left(bc+ad\right) & \left(a^2-b^2+c^2-d^2\right) & 2\left(cd-ab\right) \\ 2\left(bd-ac\right) & 2\left(cd+ab\right) & \left(a^2-b^2-c^2+d^2\right) \end{bmatrix}, \tag{C.63}$$

with $\mathbf{q}_b^n\left(-\right) = \left[a, b, c, d\right]^\top$.

Assuming that we could form a transformation matrix, $\overline{\mathbf{C}}_b^n$, representing the "average" orientation during the update interval, δt, the specific force transformation would be accomplished as

$$\boxed{\mathbf{f}^n = \overline{\mathbf{C}}_b^n\, \mathbf{f}^b\ .} \tag{C.64}$$

A simple approximation of this average operator is

$$\overline{\mathbf{C}}_b^n = \frac{\mathbf{C}_b^n(-) + \mathbf{C}_b^n(+)}{2}\ , \tag{C.65}$$

which assumes that the angular rate is constant. This is however not always satisfactory, since the mean of two transformation matrices does not precisely produce the mean of the two attitudes [10, Sec. 5.2.2]. For a more precise estimate, we can resolve to the integral

$$\overline{\mathbf{C}}_b^n = \frac{1}{\delta t}\int_t^{t+\delta t} \mathbf{C}_b^n\left(t'\right)\,\mathrm{d}t'\ . \tag{C.66}$$

Assuming still that the angular velocity is constant, the variation of the transition matrix over the update interval will be linear. This can be expressed as

$$\mathbf{C}_b^n\left(t'\right) = \mathbf{C}_b^n(-)\,\left[\left\{\boldsymbol{\alpha}_{nb}^b\left(\frac{t'}{\delta t}\right)\right\}\times\right] = \mathbf{C}_b^n(-)\,\left[\mathbf{I} + \sum_{k=1}^{\infty}\frac{\left[\boldsymbol{\alpha}_{nb}^b\times\right]^k}{k!}\left(\frac{t'}{\delta t}\right)^k\right]\ , \tag{C.67}$$

with $0 \le t' \le \delta t$. Inserting this into the above integral, we obtain the expression

$$\begin{aligned} \overline{\mathbf{C}}_b^n &= \frac{\mathbf{C}_b^n(-)}{\delta t}\int_0^{\delta t}\left[\mathbf{I} + \sum_{k=1}^{\infty}\frac{\left[\boldsymbol{\alpha}_{nb}^b\times\right]^k}{k!}\left(\frac{t'}{\delta t}\right)^k\right]\,\mathrm{d}t' \\ &= \frac{\mathbf{C}_b^n(-)}{\delta t}\left[\int_0^{\delta t}\mathbf{I}\,\mathrm{d}t + \sum_{k=1}^{\infty}\frac{\left[\boldsymbol{\alpha}_{nb}^b\times\right]^k}{k!}\frac{1}{\delta t^k}\int_0^{\delta t}t'^k\,\mathrm{d}t'\right] \\ &= \frac{\mathbf{C}_b^n(-)}{\delta t}\left[\delta t + \sum_{k=1}^{\infty}\frac{\left[\boldsymbol{\alpha}_{nb}^b\times\right]^k}{k!}\frac{1}{\delta t^k}\frac{\delta t^{k+1}}{k+1}\right] \\ &= \mathbf{C}_b^n(-)\,\left[\mathbf{I} + \sum_{k=1}^{\infty}\frac{\left[\boldsymbol{\alpha}_{nb}^b\times\right]^k}{(k+1)!}\right]\ , \end{aligned} \tag{C.68}$$

onto which we can apply Rodrigues' formula (B.59) to obtain

$$\boxed{\overline{\mathbf{C}}_b^n = \mathbf{C}_b^n(-)\left(\mathbf{I} + a_c\left[\boldsymbol{\alpha}_{nb}^b\times\right] + a_s\left[\boldsymbol{\alpha}_{nb}^b\times\right]^2\right)\,,} \tag{C.69}$$

with

$$a_c = \frac{1-\cos\left|\boldsymbol{\alpha}_{nb}^b\right|}{\left|\boldsymbol{\alpha}_{nb}^b\right|^2} \quad \text{and} \quad a_s = \frac{1}{\left|\boldsymbol{\alpha}_{nb}^b\right|^2}\left(1 - \frac{\sin\left|\boldsymbol{\alpha}_{nb}^b\right|}{\left|\boldsymbol{\alpha}_{nb}^b\right|}\right)\,. \tag{C.70}$$

This expression allows us to compute the "average" transformation matrix, under the assumption that the angular rate is constant during the measurement interval. Again, in order to avoid division by zero, this expression should be replaced by an approximate version whenever $\left|\boldsymbol{\alpha}_{nb}^b\right|$ is very small. A fourth order approximation according to (B.58) is obtained with the coefficients

$$a_c = \frac{1}{2} - \frac{\left|\boldsymbol{\alpha}_{nb}^b\right|^2}{24} \quad \text{and} \quad a_s = \frac{1}{6} - \frac{\left|\boldsymbol{\alpha}_{nb}^b\right|^2}{120}\,. \tag{C.71}$$

C.2.3 Step 3: Velocity Update

Having resolved the specific force measurements about the n-frame axes, i.e. $\mathbf{f}^n = [f_N, f_E, f_D]^\top$, we can obtain the vehicle velocity by integrating the coupled set of differential equations

$$\dot{\mathbf{v}}^n = \mathbf{f}^n - (2\boldsymbol{\Omega}_{ie}^n + \boldsymbol{\Omega}_{en}^n)\,\mathbf{v}^n + \mathbf{g}^n\,. \tag{C.72}$$

However, once again, we have the issue that the variable we are trying to solve for depends on itself. Again, we can handle this issue through an approximation. The Coriolis term, $\boldsymbol{\Omega}_{ie}^n$, and the transport-rate term, $\boldsymbol{\Omega}_{en}^n$, will be smaller than both the specific force, $\mathbf{f}^n$, and gravity, $\mathbf{g}^n$. In most applications, it is therefore a reasonable approximation to neglect their variation over the integration interval [10, Sec. 5.4.3]. That is,

$$(2\boldsymbol{\Omega}_{ie}^n + \boldsymbol{\Omega}_{en}^n)\,\mathbf{v}^n \approx (2\boldsymbol{\Omega}_{ie}^n(-) + \boldsymbol{\Omega}_{en}^n(-))\,\mathbf{v}^n(-)\,. \tag{C.73}$$

Moreover, the gravity term, $\mathbf{g}^n$, is computed using a gravity model and therefore depends on the position. The gravity field however, varies only slowly with position. It is therefore also generally sufficient to use the previous position $\mathbf{p}(-)$, in order to compute the gravity term. To summarize, the vehicle acceleration can be approximated as

$$\dot{\mathbf{v}}^n \approx \mathbf{f}^n - (2\boldsymbol{\Omega}_{ie}^n(-) + \boldsymbol{\Omega}_{en}^n(-))\,\mathbf{v}^n(-) + \mathbf{g}^n(-)\,, \tag{C.74}$$

using the Coriolis, transport-rate and gravity terms as computed using the velocity and position at the previous epoch. The velocity of the vehicle is then obtained by integrating this equation with respect to time as

$$\boxed{\mathbf{v}^n(+) \approx \mathbf{v}^n(-) + [\mathbf{f}^n - (2\boldsymbol{\Omega}_{ie}^n(-) + \boldsymbol{\Omega}_{en}^n(-))\,\mathbf{v}^n(-) + \mathbf{g}^n(-)]\,\delta t\,.} \tag{C.75}$$

If greater precision is desired, this can again be accomplished using a two-step recursive update, by first "predicting" the velocity using (C.75) and completing all the steps to obtain an estimate of the position, $\mathbf{p}(+)$. Using this position, the transport rate, $\boldsymbol{\Omega}_{en}^n(+)$, and Earth

rotation rate, $\mathbf{\Omega}_{ie}^{n}(+)$, at the end of the update interval can be formed and a second iteration is performed. In the second iteration, the velocity update is then performed as

$$\begin{aligned}\mathbf{v}^{n}(+) \approx\ \mathbf{v}^{n}(-)\ + \Big\{ \mathbf{f}^{n} - \tfrac{1}{2}\left[2\mathbf{\Omega}_{ie}^{n}(-) + \mathbf{\Omega}_{en}^{n}(-)\right]\mathbf{v}^{n}(-) \\ - \tfrac{1}{2}\left[2\mathbf{\Omega}_{ie}^{n}(+) + \mathbf{\Omega}_{en}^{n}(+)\right]\mathbf{v}^{n\prime} + \mathbf{g}^{n}(-)\Big\}\,\delta t\ .\end{aligned} \tag{C.76}$$

C.2.4 Step 4: Position Update

The position is governed by the differential equations (C.40a), (C.40b) and (C.40c). This coupled set of differential equations are, again, dependent on themselves and each other, such that we must, once again, resolve to approximations. Since the variation of R_N with latitude is weak, it is acceptable to neglect its variation with latitude over the integration interval [10, Sec. 5.4.4]. Therefore, assuming that the velocity varies as a linear function of time over the integration interval, the above equations can be integrated sequentially as

$$h(+) = h(-) - \frac{\delta t}{2}\left(v_D^n(-) + v_D^n(+)\right)\ , \tag{C.77}$$

$$\phi(+) = \phi(-) + \frac{\delta t}{2}\left(\frac{v_N^n(-)}{R_N(-)+h(-)} + \frac{v_N^n(+)}{R_N(-)+h(+)}\right)\ , \tag{C.78}$$

after which the radius of curvature $R_E(+)$ can be computed using $h(+)$ and $\phi(+)$. This allows us to integrate for the longitude as

$$\lambda(+) = \lambda(-) + \frac{\delta t}{2}\left(\frac{v_E^n(-)}{[R_E(-)+h(-)]\cos\phi(-)} + \frac{v_E^n(+)}{[R_E(+)+h(+)]\cos\phi(+)}\right)\ . \tag{C.79}$$

C.2.5 Deriving Euler Angles

The Euler attitude representation in terms of the bank, α_{nb}, elevation, β_{nb}, and heading, γ_{nb}, angles are usually not used to perform inertial navigation. However, they do have a much more intuitive nature than the direction cosines matrix and quaternion attitude. They can be derived from the direction cosines matrix using (5.48):

$$\begin{aligned}\alpha_{nb} &= \arctan_2\left(\mathbf{C}_{b3,2}^{n}, \mathbf{C}_{b3,3}^{n}\right) \\ \beta_{nb} &= -\arcsin\left(\mathbf{C}_{b3,1}^{n}\right) \\ \gamma_{nb} &= \arctan_2\left(\mathbf{C}_{b2,1}^{n}, \mathbf{C}_{b1,1}^{n}\right)\ .\end{aligned} \tag{C.80}$$

or from the quaternion attitude using (5.54):

$$\begin{aligned}\alpha_{nb} &= \arctan_2\left\{2\left(ab+cd\right), \left(1-2b^2-2c^2\right)\right\} \\ \beta_{nb} &= \arcsin\left\{2\left(ac-bd\right)\right\} \\ \gamma_{nb} &= \arctan_2\left\{2\left(ad+bc\right), \left(1-2c^2-2d^2\right)\right\}\ ,\end{aligned} \tag{C.81}$$

The Euler angles can therefore easily be extracted at the end of an implementation algorithm, after the navigation equations have been solved. Notice, however, that four-quadrant arctangent functions are needed.

C.2.6 Orthonormalisation of the Transformation Operator

In order for a rotation operator to represent a pure rotation, the transformation matrix must be orthonormal and the quaternion must have unit length. These requirements can be expressed as

$$\mathbf{C}\,\mathbf{C}^\top = \mathbf{I} \quad \text{and} \quad |\mathbf{q}| = \sqrt{\mathbf{q}^\top\,\mathbf{q}} = 1\ . \tag{C.82}$$

These conditions should theoretically be maintained through exact solutions to the differential equations. However, due to numerical round-off errors and the use of approximations, the sequential computation of the transformation operators might cause them to deviate from these requirements. Therefore, in order to obtain a stable and precise algorithm, we should re-orthonormalise the operators at regular intervals. This is most easily done for the quaternion as

$$\mathbf{q}' = \frac{1}{\sqrt{\mathbf{q}^\top\,\mathbf{q}}}\,\mathbf{q}\ , \tag{C.83}$$

while it is somewhat more cumbersome for a matrix in terms of Gram-Schmidt orthonormalisation. However, in practical applications, other factors will contribute to the uncertainty and precision of the computed orientation, meaning that precise methods are not needed. Instead we can resolve to approximate methods that are simpler and more efficient. [10, Sec. 5.1.1] suggests the following method, which breaks the matrix down into three rows as

$$\mathbf{C} = \begin{bmatrix} \mathbf{c}_1^\top \\ \mathbf{c}_2^\top \\ \mathbf{c}_3^\top \end{bmatrix}\ . \tag{C.84}$$

Then if we compute the product for each pair of rows as

$$\triangle_{ij} = \mathbf{c}_i^\top\,\mathbf{c}_j\ , \tag{C.85}$$

the matrix can be orthogonalised by applying a correction to each row as

$$\begin{aligned} \mathbf{c}_1' &= \mathbf{c}_1 - \tfrac{1}{2}\,\triangle_{12}\,\mathbf{c}_2 - \tfrac{1}{2}\,\triangle_{13}\,\mathbf{c}_3 \\ \mathbf{c}_2' &= \mathbf{c}_2 - \tfrac{1}{2}\,\triangle_{12}\,\mathbf{c}_1 - \tfrac{1}{2}\,\triangle_{23}\,\mathbf{c}_3 \\ \mathbf{c}_3' &= \mathbf{c}_3 - \tfrac{1}{2}\,\triangle_{13}\,\mathbf{c}_1 - \tfrac{1}{2}\,\triangle_{23}\,\mathbf{c}_2\ , \end{aligned} \tag{C.86}$$

and, subsequently, normalised as

$$\mathbf{c}_i'' = \frac{1}{\sqrt{\mathbf{c}_i'^\top\,\mathbf{c}_i'}}\,\mathbf{c}_i' \approx \frac{2}{1 + \mathbf{c}_i'^\top\,\mathbf{c}_i'}\,\mathbf{c}_i'\ . \tag{C.87}$$

This approach can also be used by breaking the matrix down into three columns and following the same procedure. Notice that these corrections work best when the departure from orthonormality is small.

C.2.7 Implementation Examples

In this section, two example implementations of the navigation equations are presented. These two implementations differ in complexity, computational load and precision. These algorithms represent single iterations of the navigation equations and assumes that the initial attitude, $\mathbf{C}_b^n(-)$ or $\mathbf{q}_b^n(-)$, velocity, $\mathbf{v}^n(-)$ and position, $(\phi(-), \lambda(-), h(-))$, is known from the previous iteration or initialisation strategy. The gravity component, $\mathbf{g}^n(-)$, is moreover assumed to be computed using some gravitational model.

The first example algorithm uses a direction cosines attitude matrix and a first-order approximation of the rotation operator in order to avoid the computationally requiring tasks of evaluating sine and cosine functions.

Example Algorithm: First-Order Implementation, b-frame to n-frame

---

1. Extract time interval δt, gyroscope observation $\boldsymbol{\omega}_{ib}^b$ and accelerometer observation $\mathbf{f}^b$ from data representing the current epoch.

Step 1: Correct Gyro Observations

2. Compute Earth rotational rate in n-frame using (A.23)

$$\boldsymbol{\omega}_{ie}^n(-) = \begin{bmatrix} \boldsymbol{\omega}_{ie} \cos\phi(-) \\ 0 \\ -\boldsymbol{\omega}_{ie} \sin\phi(-) \end{bmatrix}$$

3. Compute radii of curvature using (2.9) and (2.10):

$$R_E(-) = \frac{a}{\sqrt{1 - e^2 \sin^2\phi(-)}} \quad \text{and} \quad R_N(-) = R_E(-) \frac{1 - e^2}{1 - e^2 \sin^2\phi(-)} \,.$$

4. Compute transport-rate using (C.43)

$$\boldsymbol{\omega}_{en}^n(-) = \begin{bmatrix} v_E(-) / \left[R_E(-) + h(-)\right] \\ -v_N(-) / \left[R_N(-) + h(-)\right] \\ -v_E(-) \tan\phi(-) / \left[R_E(-) + h(-)\right] \end{bmatrix} .$$

5. Correct gyro measurements for rotation effects

$$\boldsymbol{\omega}_{nb}^b = \boldsymbol{\omega}_{ib}^b - \mathbf{C}_b^{n\top}(-) \left[\boldsymbol{\omega}_{en}^n(-) + \boldsymbol{\omega}_{ie}^n(-)\right]$$

Step 2: Specific Force Transformation

6. Compute angle increment and form skew-symmetric matrix

$$\boldsymbol{\alpha}_{nb}^{b} = \boldsymbol{\omega}_{nb}^{b}\,\delta t\;, \quad \left|\boldsymbol{\alpha}_{nb}^{b}\right| = \sqrt{{\boldsymbol{\alpha}_{nb}^{b}}^{\top}\,\boldsymbol{\alpha}_{nb}^{b}} \quad \text{and}$$
$$\left[\boldsymbol{\alpha}_{nb}^{b}\times\right] = \begin{bmatrix} 0 & -\alpha_{nb,3}^{b} & \alpha_{nb,2}^{b} \\ \alpha_{nb,3}^{b} & 0 & -\alpha_{nb,1}^{b} \\ -\alpha_{nb,2}^{b} & \alpha_{nb,1}^{b} & 0 \end{bmatrix}$$

7. Form average transformation matrix using (C.71)

$$\overline{\mathbf{C}}_{b}^{n} = \mathbf{C}_{b}^{n}(-)\left[\mathbf{I} + \left(\frac{1}{2} - \frac{\left|\boldsymbol{\alpha}_{nb}^{b}\right|^{2}}{24}\right)\left[\boldsymbol{\alpha}_{nb}^{b}\times\right] + \left(\frac{1}{6} - \frac{\left|\boldsymbol{\alpha}_{nb}^{b}\right|^{2}}{120}\right)\left[\boldsymbol{\alpha}_{nb}^{b}\times\right]^{2}\right]$$

8. Apply transformation

$$\mathbf{f}^{n} = \overline{\mathbf{C}}_{b}^{n}\,\mathbf{f}^{b}$$

Step 3: Velocity Update

9. Correct and integrate specific force using (C.75)

$$\mathbf{v}^{n}(+) = \mathbf{v}^{n}(-) + \left[\mathbf{f}^{n} - \left(2\boldsymbol{\Omega}_{ie}^{n}(-) + \boldsymbol{\Omega}_{en}^{n}(-)\right)\mathbf{v}^{n}(-) + \mathbf{g}^{n}(-)\right]\delta t\;.$$

Step 4: Position Update

10. Update height and latitude using (C.77) and (C.78):

$$h(+) = h(-) - \frac{\delta t}{2}\left(v_{D}^{n}(-) + v_{D}^{n}(+)\right)\;,$$
$$\phi(+) = \phi(-) + \frac{\delta t}{2}\left(\frac{v_{N}^{n}(-)}{R_{N}(-) + h(-)} + \frac{v_{N}^{n}(+)}{R_{N}(-) + h(+)}\right)\;.$$

11. Compute radii of curvature using (2.9) and (2.10):

$$R_{E}(+) = \frac{a}{\sqrt{1 - e^{2}\sin^{2}\phi(+)}} \quad \text{and} \quad R_{N}(+) = R_{E}(+)\,\frac{1 - e^{2}}{1 - e^{2}\sin^{2}\phi(+)}\;.$$

12. Update longitude using (C.79):

$$\lambda(+) = \lambda(-) + \frac{\delta t}{2}\left(\frac{v_{E}^{n}(-)}{\left[R_{E}(-) + h(-)\right]\cos\phi(-)} + \frac{v_{E}^{n}(+)}{\left[R_{E}(+) + h(+)\right]\cos\phi(+)}\right)\;.$$

Step 5: Attitude Update

13. Update DCM attitude using (C.53):

$$\mathbf{C}_b^n(+) = \mathbf{C}_b^n(-)\,\left(\mathbf{I} + \left[\boldsymbol{\alpha}_{nb}^b\times\right]\right)$$

14. Ortho-normalise the DCM by forming the product of each pair of rows as

$$\begin{array}{lll} \triangle_{12} = \mathbf{c}_1^\top\,\mathbf{c}_2 & & \mathbf{c}_1 = \mathbf{C}_{1,:}^\top \\ \triangle_{13} = \mathbf{c}_1^\top\,\mathbf{c}_3 & \text{with} & \mathbf{c}_2 = \mathbf{C}_{2,:}^\top \\ \triangle_{23} = \mathbf{c}_2^\top\,\mathbf{c}_3 & & \mathbf{c}_3 = \mathbf{C}_{3,:}^\top \end{array} \tag{C.88}$$

First, the matrix is orthogonalised by applying a correction to each row as

$$\begin{aligned} \mathbf{c}_1' &= \mathbf{c}_1 - \tfrac{1}{2}\triangle_{12}\,\mathbf{c}_2 - \tfrac{1}{2}\triangle_{13}\,\mathbf{c}_3 \\ \mathbf{c}_2' &= \mathbf{c}_2 - \tfrac{1}{2}\triangle_{12}\,\mathbf{c}_1 - \tfrac{1}{2}\triangle_{23}\,\mathbf{c}_3 \\ \mathbf{c}_3' &= \mathbf{c}_3 - \tfrac{1}{2}\triangle_{13}\,\mathbf{c}_1 - \tfrac{1}{2}\triangle_{23}\,\mathbf{c}_2\ , \end{aligned}$$

and, subsequently, normalised as

$$\mathbf{c}_i'' = \frac{1}{\sqrt{\mathbf{c}_i'^\top\,\mathbf{c}_i'}}\,\mathbf{c}_i'\ .$$

End of example

The second implementation example uses a quaternion attitude. In order to yield more accurate representations of the transformation matrix and quaternion attitude, Rodrigues' formula is used in forming these components. Additionally, a semi-iterative approach is applied by forming average values of the rotational rates using the updated position at the end of the algorithm.

Example Algorithm: Precise Implementation, b-frame to n-frame

1. Extract time interval δt, gyroscope observation $\boldsymbol{\omega}_{ib}^b$ and accelerometer observation $\mathbf{f}^b$ from data representing the current epoch.

2. Form direction cosines matrix from quaternion $\mathbf{q}_n^n(-) = (a, b, c, d)$ using (5.51):

$$\mathbf{C}_b^n\,(-) = \begin{bmatrix} \left(a^2+b^2-c^2-d^2\right) & 2\,(bc-ad) & 2\,(bd+ac) \\ 2\,(bc+ad) & \left(a^2-b^2+c^2-d^2\right) & 2\,(cd-ab) \\ 2\,(bd-ac) & 2\,(cd+ab) & \left(a^2-b^2-c^2+d^2\right) \end{bmatrix}\ ,$$

Step 1: Correct Gyro Observations

3. Compute Earth rotational rate in n-frame using (A.23)

$$\boldsymbol{\omega}_{ie}^{n}(-) = \begin{bmatrix} \boldsymbol{\omega}_{ie}\cos\phi(-) \\ 0 \\ -\boldsymbol{\omega}_{ie}\sin\phi(-) \end{bmatrix}$$

4. Compute radii of curvature using (2.9) and (2.10):

$$R_E(-) = \frac{a}{\sqrt{1-e^2\sin^2\phi(-)}} \quad \text{and} \quad R_N(-) = R_E(-)\,\frac{1-e^2}{1-e^2\sin^2\phi(-)}\,.$$

5. Compute transport-rate using (C.43)

$$\boldsymbol{\omega}_{en}^{n}(-) = \begin{bmatrix} v_E(-)/\left[R_E(-)+h(-)\right] \\ -v_N(-)/\left[R_N(-)+h(-)\right] \\ -v_E(-)\tan\phi(-)/\left[R_E(-)+h(-)\right] \end{bmatrix}\,.$$

6. Correct gyro measurements for rotation effects

$$\boldsymbol{\omega}_{nb}^{b} = \boldsymbol{\omega}_{ib}^{b} - \mathbf{C}_{b}^{n\top}(-)\left[\boldsymbol{\omega}_{en}^{n}(-) + \boldsymbol{\omega}_{ie}^{n}(-)\right]$$

Step 2: Specific Force Transformation

7. Compute angle increment and form skew-symmetric matrix

$$\boldsymbol{\alpha}_{nb}^{b} = \boldsymbol{\omega}_{nb}^{b}\,\delta t\,, \quad \left|\boldsymbol{\alpha}_{nb}^{b}\right| = \sqrt{\boldsymbol{\alpha}_{nb}^{b\top}\,\boldsymbol{\alpha}_{nb}^{b}} \quad \text{and}$$

$$\left[\boldsymbol{\alpha}_{nb}^{b}\times\right] = \begin{bmatrix} 0 & -\alpha_{nb,3}^{b} & \alpha_{nb,2}^{b} \\ \alpha_{nb,3}^{b} & 0 & -\alpha_{nb,1}^{b} \\ -\alpha_{nb,2}^{b} & \alpha_{nb,1}^{b} & 0 \end{bmatrix}$$

8. Form average transformation matrix using (C.69) or (C.71)

if $\left|\boldsymbol{\alpha}_{nb}^{b}\right| > 10^{-8}$

$$\overline{\mathbf{C}}_{b}^{n} = \mathbf{C}_{b}^{n}(-)\left[\mathbf{I} + \frac{1-\cos\left|\boldsymbol{\alpha}_{nb}^{b}\right|}{\left|\boldsymbol{\alpha}_{nb}^{b}\right|^{2}}\left[\boldsymbol{\alpha}_{nb}^{b}\times\right] + \frac{1}{\left|\boldsymbol{\alpha}_{nb}^{b}\right|^{2}}\left(1-\frac{\sin\left|\boldsymbol{\alpha}_{nb}^{b}\right|}{\left|\boldsymbol{\alpha}_{nb}^{b}\right|}\right)\left[\boldsymbol{\alpha}_{nb}^{b}\times\right]^{2}\right]$$

else

$$\overline{\mathbf{C}}_{b}^{n} = \mathbf{C}_{b}^{n}(-)\left[\mathbf{I} + \left(\frac{1}{2} - \frac{\left|\boldsymbol{\alpha}_{nb}^{b}\right|^{2}}{24}\right)\left[\boldsymbol{\alpha}_{nb}^{b}\times\right] + \left(\frac{1}{6} - \frac{\left|\boldsymbol{\alpha}_{nb}^{b}\right|^{2}}{120}\right)\left[\boldsymbol{\alpha}_{nb}^{b}\times\right]^{2}\right]$$

end

9. Apply transformation

$$\mathbf{f}^n = \overline{\mathbf{C}}_b^n \, \mathbf{f}^b$$

Step 3: Velocity Update

10. Correct and integrate specific force using (C.75)

$$\mathbf{v}^n(+) = \mathbf{v}^n(-) + \left[\mathbf{f}^n - (2\boldsymbol{\Omega}_{ie}^n(-) + \boldsymbol{\Omega}_{en}^n(-))\,\mathbf{v}^n(-) + \mathbf{g}^n(-)\right]\delta t \; .$$

Step 4: Position Update

11. Update height and latitude using (C.77) and (C.78):

$$\begin{aligned} h(+) &= h(-) - \frac{\delta t}{2}\left(v_D^n(-) + v_D^n(+)\right) \; , \\ \phi(+) &= \phi(-) + \frac{\delta t}{2}\left(\frac{v_N^n(-)}{R_N(-)+h(-)} + \frac{v_N^n(+)}{R_N(-)+h(+)}\right) \; . \end{aligned}$$

12. Compute radii of curvature using (2.9) and (2.10):

$$R_E(+) = \frac{a}{\sqrt{1 - e^2 \sin^2 \phi(+)}} \quad \text{and} \quad R_N(+) = R_E(+)\,\frac{1-e^2}{1 - e^2 \sin^2 \phi(+)} \; .$$

13. Update longitude using (C.79):

$$\lambda(+) = \lambda(-) + \frac{\delta t}{2}\left(\frac{v_E^n(-)}{[R_E(-)+h(-)]\cos\phi(-)} + \frac{v_E^n(+)}{[R_E(+)+h(+)]\cos\phi(+)}\right) \; .$$

Step 5: Attitude Update

14. Compute Earth rotational rate in n-frame using (A.23)

$$\boldsymbol{\omega}_{ie}^n(+) = \begin{bmatrix} \boldsymbol{\omega}_{ie}\cos\phi(+) \\ 0 \\ -\boldsymbol{\omega}_{ie}\sin\phi(+) \end{bmatrix}$$

15. Compute transport-rate using (C.43)

$$\boldsymbol{\omega}_{en}^n(+) = \begin{bmatrix} v_E(+)/\left[R_E(+)+h(+)\right] \\ -v_N(+)/\left[R_N(+)+h(+)\right] \\ -v_E(+)\tan\phi(+)/\left[R_E(+)+h(+)\right] \end{bmatrix} \; .$$

16. Correct gyro measurements for rotation effects using (C.46):

$$\boldsymbol{\omega}_{nb}^b = \boldsymbol{\omega}_{ib}^b - \tfrac{1}{2}\,\overline{\mathbf{C}}_n^b\left[\boldsymbol{\omega}_{ie}^n(-) + \boldsymbol{\omega}_{ie}^n(+) + \boldsymbol{\omega}_{en}^n(-) + \boldsymbol{\omega}_{en}^n(+)\right] \; .$$

17. Compute angle increment and form skew-symmetric matrix

$$\boldsymbol{\alpha}_{nb}^{b} = \boldsymbol{\omega}_{nb}^{b}\,\delta t\;, \quad \left|\boldsymbol{\alpha}_{nb}^{b}\right| = \sqrt{{\boldsymbol{\alpha}_{nb}^{b}}^{\top}\,\boldsymbol{\alpha}_{nb}^{b}} \quad \text{and}$$
$$\left[\boldsymbol{\alpha}_{nb}^{b}\times\right] = \begin{bmatrix} 0 & -\alpha_{nb,3}^{b} & \alpha_{nb,2}^{b} \\ \alpha_{nb,3}^{b} & 0 & -\alpha_{nb,1}^{b} \\ -\alpha_{nb,2}^{b} & \alpha_{nb,1}^{b} & 0 \end{bmatrix}$$

18. Update quaternion attitude using (C.59) and (C.62):
if $\left|\boldsymbol{\alpha}_{nb}^{b}\right| > 10^{-8}$

$$a_c = \cos\left(\left|\boldsymbol{\alpha}_{nb}^{b}\right|/2\right) \text{ and } a_s = \frac{\sin\left(\left|\boldsymbol{\alpha}_{nb}^{b}\right|/2\right)}{\left|\boldsymbol{\alpha}_{nb}^{b}\right|}$$

else

$$a_c = \cos\left(\left|\boldsymbol{\alpha}_{nb}^{b}\right|/2\right) \text{ and } a_s = \tfrac{1}{2} - \frac{\left|\boldsymbol{\alpha}_{nb}^{b}\right|^2}{48}$$

end

$$\mathbf{q}_b^n(+) = \mathbf{q}_b^n(-) \circ \begin{bmatrix} a_c \\ a_s\,\alpha_{nb,x}^{b} \\ a_s\,\alpha_{nb,y}^{b} \\ a_s\,\alpha_{nb,z}^{b} \end{bmatrix} \;.$$

19. Normalise quaternion using (C.83)

$$\mathbf{q}_b^n(+) = \frac{1}{\sqrt{\mathbf{q}_b^n(+)^{\top}\,\mathbf{q}_b^n(+)}}\,\mathbf{q}_b^n(+)\;,$$

End of example

C.3 Error Dynamics Equations

In this section a set of equations governing the propagation and evolution of errors in the navigation equations are developed. First, we are interested in how measurement errors, $\delta\boldsymbol{\omega}_{is}^{s}$ and $\delta\mathbf{f}^{s}$, propagate onto the navigation solution in terms of attitude, velocity and position. These sensor errors can be decomposed into components of noise, bias, scale factor, etc. as described in Section 6. Second, we want to investigate how errors in attitude, $\delta\boldsymbol{\psi}_{as}^{a}$, velocity, $\delta\mathbf{v}^{a}$, and position, $\delta\mathbf{r}^{a}$, evolve with time and propagate onto one another as time progresses and inertial navigation is performed. Here, a refers to an arbitrary reference frame, i.e. i-, e- or n-frame. Third, since we are especially interested in the gravity component, we want to figure out how errors in the gravity component, $\delta\mathbf{g}^{a}$, are related to all of the components above. In airborne gravimetry, the objective is to estimate the error in the gravity model and thereby gravity itself. The ability to do so depends on the interrelation between gravity and other components in the navigation equations.

To summarize, we are interested in errors in attitude, velocity, position, observed angular rates, observed specific force and the gravity model:

$$(\delta\boldsymbol{\psi}^a_{as}\,,\,\delta\mathbf{v}^a\,,\,\delta\mathbf{r}^a\,,\,\delta\boldsymbol{\omega}^s_{is}\,,\,\delta\mathbf{f}^s\,,\,\delta\mathbf{g}^a)\;, \tag{C.89}$$

where each term can be decomposed and expanded to represent several components, but also in relation to stochastic models. As described in Section 6, the actual sensor errors are naturally unknown to us. However, we are able to describe these errors in a probabilistic sense using stochastic models, which sometimes requires a decomposition of the sensor errors. It should noted that the attitude errors are here in terms of three Euler angles, which are assumed to be small, meaning that a small angle approximation can be applied. The attitude, velocity and position errors therefore together constitute nine terms, whereas the gyroscope and accelerometer errors constitute six terms and the errors in the gravity model constitutes three terms. In a Kalman filter setting, these 18 terms comprise a state-vector, whose elements we intend to estimate.

The following development will follow an approach similar to that in [15, Sec. 5], by first developing a general framework. The starting point is therefore the general form of the navigation equations (C.8), repeated here as

$$\begin{aligned}
\dot{\mathbf{r}}^a &= \mathbf{v}^a \\
\dot{\mathbf{v}}^a &= \mathbf{C}^a_s\,\mathbf{f}^s - 2\boldsymbol{\Omega}^a_{ia}\,\mathbf{v}^a - \left(\dot{\boldsymbol{\Omega}}^a_{ia} + \boldsymbol{\Omega}^a_{ia}\,\boldsymbol{\Omega}^a_{ia}\right)\mathbf{r}^a + \bar{\mathbf{g}}^a \\
\dot{\mathbf{C}}^a_s &= \mathbf{C}^a_s\,\boldsymbol{\Omega}^s_{as}\;,
\end{aligned} \tag{C.90}$$

referenced to the arbitrary a-frame. The error equations are then obtained by perturbing the system by a small amount. We will refer to this perturbation as applying a differential or perturbation operator, δ, and assume that it commutes with the time differential operator, $\mathrm{d}/\mathrm{d}t$, i.e. the dot. We will assume that all errors are small and that a linear approximation is sufficient in order to describe the errors. We therefore neglect all higher order terms and obtain:

$$\frac{\mathrm{d}}{\mathrm{d}t}\delta\mathbf{C}^a_s = \delta\mathbf{C}^a_s\,\boldsymbol{\Omega}^s_{as} + \mathbf{C}^a_s\,\delta\boldsymbol{\Omega}^s_{as} \tag{C.91a}$$

$$\begin{aligned}
\frac{\mathrm{d}}{\mathrm{d}t}\delta\mathbf{v}^a = {}& \delta\mathbf{C}^a_s\,\mathbf{f}^s + \mathbf{C}^a_s\,\delta\mathbf{f}^s - 2\,\delta\boldsymbol{\Omega}^a_{ia}\,\mathbf{v}^a - 2\boldsymbol{\Omega}^a_{ia}\,\delta\mathbf{v}^a \\
& - \left(\delta\dot{\boldsymbol{\Omega}}^a_{ia} + \delta\boldsymbol{\Omega}^a_{ia}\,\boldsymbol{\Omega}^a_{ia} + \boldsymbol{\Omega}^a_{ia}\,\delta\boldsymbol{\Omega}^a_{ia}\right)\mathbf{r}^a \\
& - \left(\dot{\boldsymbol{\Omega}}^a_{ia} + \boldsymbol{\Omega}^a_{ia}\,\boldsymbol{\Omega}^a_{ia}\right)\delta\mathbf{r}^a + \delta\bar{\mathbf{g}}\,(\mathbf{r}^a)
\end{aligned} \tag{C.91b}$$

$$\frac{\mathrm{d}}{\mathrm{d}t}\delta\mathbf{r}^a = \delta\mathbf{v}^a\;. \tag{C.91c}$$

We then want to reformulate the above equations in terms of the error components in (C.89). This means that terms such as $\delta\boldsymbol{\Omega}^s_{as}$ should be decomposed into components of these errors. Eventually, we want to arrive at an expression that is linear with respect to these 18 terms. This will be done in the remainder of this section. First, since the attitude error in (C.91a) is in terms of a direction cosine matrix, we want to reformulate this in terms of errors in the Euler angles.

Attitude

The relationship between the attitude error, $\delta\mathbf{C}_s^a$, and the (small) errors in the Euler angles, $\delta\boldsymbol{\psi}_{as}^a$, is given by (6.13) as

$$\delta\mathbf{C}_s^a = [\delta\boldsymbol{\psi}_{as}^a\times]\ \mathbf{C}_s^a\ , \tag{C.92}$$

which we can differentiate with respect to time, in order to obtain the expression

$$\begin{aligned}\frac{\mathrm{d}}{\mathrm{d}t}\delta\mathbf{C}_s^a &= \tfrac{\mathrm{d}}{\mathrm{d}t}\,[\boldsymbol{\psi}_{as}^a\times]\ \mathbf{C}_s^a + [\boldsymbol{\psi}_{as}^a\times]\ \dot{\mathbf{C}}_s^a = \tfrac{\mathrm{d}}{\mathrm{d}t}\,[\boldsymbol{\psi}_{as}^a\times]\ \mathbf{C}_s^a + [\boldsymbol{\psi}_{as}^a\times]\ \mathbf{C}_s^a\,\boldsymbol{\Omega}_{as}^s \\ &= \tfrac{\mathrm{d}}{\mathrm{d}t}\,[\boldsymbol{\psi}_{as}^a\times]\ \mathbf{C}_s^a + \delta\mathbf{C}_s^a\,\boldsymbol{\Omega}_{as}^s\ .\end{aligned} \tag{C.93}$$

Replacing the LHS of (C.91a), we have that

$$\tfrac{\mathrm{d}}{\mathrm{d}t}\,[\boldsymbol{\psi}_{as}^a\times]\ \mathbf{C}_s^a + \delta\mathbf{C}_s^a\,\boldsymbol{\Omega}_{as}^s = \delta\mathbf{C}_s^a\ \boldsymbol{\Omega}_{as}^s + \mathbf{C}_s^a\,\delta\boldsymbol{\Omega}_{as}^s \quad \Leftrightarrow \tag{C.94}$$

$$\tfrac{\mathrm{d}}{\mathrm{d}t}\,[\boldsymbol{\psi}_{as}^a\times]\ \mathbf{C}_s^a = \mathbf{C}_s^a\,\delta\boldsymbol{\Omega}_{as}^s \quad \Leftrightarrow \tag{C.95}$$

$$\tfrac{\mathrm{d}}{\mathrm{d}t}\,[\boldsymbol{\psi}_{as}^a\times] = \mathbf{C}_s^a\,\delta\boldsymbol{\Omega}_{as}^s\,\mathbf{C}_a^s \quad , \tag{C.96}$$

which, in terms of vectors, is equivalent to

$$\delta\dot{\boldsymbol{\psi}}_{as}^a = \mathbf{C}_s^a\,\delta\boldsymbol{\omega}_{as}^s\ , \tag{C.97}$$

where $\delta\boldsymbol{\omega}_{as}^s$ is the error in the rotation rate of the s-frame with respect to the a-frame.

This expression can then be further separated into explicit components of gyro errors and orientation errors. The gyros sense the rotation rates, $\boldsymbol{\omega}_{is}^s$, with respect to inertial space, which can be written as the sum

$$\boldsymbol{\omega}_{is}^s = \boldsymbol{\omega}_{ia}^s + \boldsymbol{\omega}_{as}^s = \mathbf{C}_a^s\,\boldsymbol{\omega}_{ia}^a + \boldsymbol{\omega}_{as}^s\ . \tag{C.98}$$

Noting that the transpose of (C.92) is

$$\begin{aligned}\delta\mathbf{C}_a^s &= (\delta\mathbf{C}_s^a)^\top = ([\delta\boldsymbol{\psi}_{as}^a\times]\ \mathbf{C}_s^a)^\top \\ &= \mathbf{C}_s^{a\top}\ [\delta\boldsymbol{\psi}_{as}^a\times]^\top = -\mathbf{C}_a^s\ [\delta\boldsymbol{\psi}_{as}^a\times]\ ,\end{aligned} \tag{C.99}$$

we can perturb the expression above by applying the perturbation operator, δ, to obtain

$$\begin{aligned}\delta\boldsymbol{\omega}_{is}^s &= \delta\mathbf{C}_a^s\,\boldsymbol{\omega}_{ia}^a + \mathbf{C}_a^s\,\delta\boldsymbol{\omega}_{ia}^a + \delta\boldsymbol{\omega}_{as}^s \\ &= -\mathbf{C}_a^s\ [\delta\boldsymbol{\psi}_{as}^a\times]\ \boldsymbol{\omega}_{ia}^a + \mathbf{C}_a^s\,\delta\boldsymbol{\omega}_{ia}^a + \delta\boldsymbol{\omega}_{as}^s\ ,\end{aligned} \tag{C.100}$$

which can be inserted into (C.97) to yield

$$\begin{aligned}\delta\dot{\boldsymbol{\psi}}_{as}^a &= \mathbf{C}_s^a\,(\delta\boldsymbol{\omega}_{is}^s + \mathbf{C}_a^s\ [\delta\boldsymbol{\psi}_{as}^a\times]\ \boldsymbol{\omega}_{ia}^a - \mathbf{C}_a^s\,\delta\boldsymbol{\omega}_{ia}^a) \\ &= \mathbf{C}_s^a\,\delta\boldsymbol{\omega}_{is}^s + [\delta\boldsymbol{\psi}_{as}^a\times]\ \boldsymbol{\omega}_{ia}^a - \delta\boldsymbol{\omega}_{ia}^a \\ &= \mathbf{C}_s^a\,\delta\boldsymbol{\omega}_{is}^s - [\boldsymbol{\omega}_{ia}^a\times]\,\delta\boldsymbol{\psi}_{as}^a - \delta\boldsymbol{\omega}_{ia}^a\ .\end{aligned} \tag{C.101}$$

This is the differential equation governing the dynamic behaviour of $\delta\boldsymbol{\psi}_{as}^a$, representing the error angles between the true and estimated frames. The term $\delta\boldsymbol{\omega}_{is}^s$ represents the error in the sensed angular rates, while the term $\delta\boldsymbol{\psi}_{as}^a$ represents the attitude error. The last term, $\delta\boldsymbol{\omega}_{ia}^a$, represents the error in sensing the orientation of the a-frame with respect to the i-frame. It is of little value to investigate this term further until an explicit reference frame is specified.

Velocity

The differential equation governing the velocity error (C.91b) contains a number of components that needs further clarification. However, as before, it is of little value to explore the term $\delta\boldsymbol{\omega}_{ia}^{a}$ and its derivative further until an explicit reference frame is specified. The remaining terms are the attitude-sensor error, $\delta\mathbf{C}_{s}^{a}\,\mathbf{f}^{s}$, and the error in the gravitational model, $\delta\bar{\mathbf{g}}\left(\mathbf{r}^{a}\right)$. If we start by considering the attitude error, we have from (C.92) that

$$\begin{aligned}\delta\mathbf{C}_{s}^{a}\,\mathbf{f}^{s} &= \left[\delta\boldsymbol{\psi}_{as}^{a}\times\right]\,\mathbf{C}_{s}^{a}\,\mathbf{f}^{s} = \delta\boldsymbol{\psi}_{as}^{a}\times\mathbf{f}^{a} \\ &= -\mathbf{f}^{a}\times\delta\boldsymbol{\psi}_{as}^{a} = -\left[\mathbf{f}^{a}\times\right]\,\delta\boldsymbol{\psi}_{as}^{a}\;,\end{aligned} \tag{C.102}$$

where the term $\mathbf{f}^{a}$ is now written on skew-symmetric form, such that we obtain a linear relation with the attitude errors $\delta\boldsymbol{\psi}_{as}^{a}$.

For the gravity component, we need to consider two sources of error. One is an error in the gravity model itself. The other is that if the position is wrong, we will be computing the gravity value at a wrong location. These two terms appear, when the perturbation operator is applied to the gravity term as

$$\delta\bar{\mathbf{g}}\left(\mathbf{r}^{a}\right) = \delta\bar{\mathbf{g}}^{a} + \frac{\partial\bar{\mathbf{g}}^{a}}{\partial\mathbf{r}^{a}}\,\delta\mathbf{r}^{a} = \delta\bar{\mathbf{g}}^{a} + \bar{\boldsymbol{\Gamma}}^{a}\,\delta\mathbf{r}^{a}\;, \tag{C.103}$$

where the matrix $\bar{\boldsymbol{\Gamma}}^{a}$ is the Jacobian tensor composed of gravitational gradients in the a-frame.

Position

The differential equation governing position (C.91c), is already linearly related to the velocity. However, if one wishes to use geodetic coordinates, we need to apply the perturbation operator to (C.26) as

$$\frac{\mathrm{d}}{\mathrm{d}t}\delta\mathbf{p} = \frac{\mathrm{d}}{\mathrm{d}t}\begin{bmatrix}\delta\phi\\ \delta\lambda\\ \delta h\end{bmatrix} \approx \begin{bmatrix}\frac{\delta v_N}{R_N+h} - \frac{v_N}{(R_N+h)^2}\delta h\\ \frac{\delta v_E}{(R_E+h)\cos\phi} + \frac{v_E\sin\phi}{(R_E+h)\cos^2\phi}\delta\phi - \frac{v_E}{(R_E+h)^2\cos\phi}\delta h\\ -\delta v_D\;,\end{bmatrix}\;, \tag{C.104}$$

where the terms involving δR_N and δR_E have been neglected. We can write this in matrix-form as

$$\frac{\mathrm{d}}{\mathrm{d}t}\,\delta\mathbf{p} = \begin{bmatrix}\frac{1}{R_N+h} & 0 & 0\\ 0 & \frac{1}{(R_E+h)\cos\phi} & 0\\ 0 & 0 & -1\end{bmatrix}\begin{bmatrix}\delta v_N\\ \delta v_E\\ \delta v_D\end{bmatrix} + \begin{bmatrix}0 & 0 & \frac{-v_N}{(R_N+h)^2}\\ \frac{v_E\sin\phi}{(R_E+h)\cos^2\phi} & 0 & \frac{-v_E}{(R_E+h)^2\cos\phi}\\ 0 & 0 & 0\end{bmatrix}\begin{bmatrix}\delta\phi\\ \delta\lambda\\ \delta h\end{bmatrix}\;, \tag{C.105}$$

which constitutes a linear set of equations, with respect to the relevant error terms. As is apparent from the above expression, this relation is mostly relevant for the navigation frame implementation, where the velocity is coordinates along the local north, east and down directions.

Finally, combining the above expressions, we arrive at the general form of the linearised error dynamics equations:

$$\boxed{\begin{aligned}
\delta\dot{\boldsymbol{\psi}}^a_{as} &= \mathbf{C}^a_s\,\delta\boldsymbol{\omega}^s_{is} - [\boldsymbol{\omega}^a_{ia}\times]\,\delta\boldsymbol{\psi}^a_{as} - \delta\boldsymbol{\omega}^a_{ia} \\
\frac{\mathrm{d}}{\mathrm{d}t}\delta\mathbf{v}^a &= -[\mathbf{f}^a\times]\,\delta\boldsymbol{\psi}^a_{as} + \mathbf{C}^a_s\,\delta\mathbf{f}^s - 2\,\delta\boldsymbol{\Omega}^a_{ia}\,\mathbf{v}^a - 2\boldsymbol{\Omega}^a_{ia}\,\delta\mathbf{v}^a \\
&\quad - \left(\delta\dot{\boldsymbol{\Omega}}^a_{ia} + \delta\boldsymbol{\Omega}^a_{ia}\,\boldsymbol{\Omega}^a_{ia} + \boldsymbol{\Omega}^a_{ia}\,\delta\boldsymbol{\Omega}^a_{ia}\right)\mathbf{r}^a \\
&\quad - \left(\dot{\boldsymbol{\Omega}}^a_{ia} + \boldsymbol{\Omega}^a_{ia}\,\boldsymbol{\Omega}^a_{ia}\right)\delta\mathbf{r}^a + \delta\bar{\mathbf{g}}^a + \bar{\boldsymbol{\Gamma}}^a\,\delta\mathbf{r}^a \\
\frac{\mathrm{d}}{\mathrm{d}t}\delta\mathbf{r}^a &= \delta\mathbf{v}^a\ ,
\end{aligned}} \tag{C.106}$$

which, being referenced to the arbitrary a-frame, form the basic setting for deriving the error dynamics equations in any desired reference frame. In the following, the error dynamics equations will be derived for the inertial, terrestrial, navigation and wander-azimuth frames. These equations will be expressed in a linear state-space formulation, which is fundamental to the Kalman filtering approach.

C.3.1 Inertial Frame Equations

In order to arrive at the error dynamics equations in the i-frame, we set $a = i$ in (C.106). Exploiting that $\boldsymbol{\Omega}^i_{ii} = \delta\boldsymbol{\Omega}^i_{ii} = 0$, we obtain the equations

$$\boxed{\begin{aligned}
\frac{\mathrm{d}}{\mathrm{d}t}\delta\boldsymbol{\psi}^i_{is} &= \mathbf{C}^i_s\,\delta\boldsymbol{\omega}^s_{is} \\
\frac{\mathrm{d}}{\mathrm{d}t}\delta\mathbf{v}^i &= \mathbf{C}^i_s\,\delta\mathbf{f}^s - \left[\mathbf{f}^i\times\right]\delta\boldsymbol{\psi}^i_{is} + \delta\bar{\mathbf{g}}^i + \bar{\boldsymbol{\Gamma}}^i\delta\mathbf{r}^i \\
\frac{\mathrm{d}}{\mathrm{d}t}\delta\mathbf{r}^i &= \delta\mathbf{v}^i\ ,
\end{aligned}} \tag{C.107}$$

governing the error dynamics in the i-frame. These are non-homogenous, linear differential equations for the orientation, velocity and position errors, formulated in the i-frame. These may be expressed in state-space form as

$$\dot{\mathbf{x}}^i = \mathbf{F}^i\,\mathbf{x}^i\ , \tag{C.108}$$

with

$$\mathbf{x}^i = \begin{bmatrix}\delta\boldsymbol{\psi}^i_{is} & \delta\mathbf{v}^i & \delta\mathbf{r}^i & \delta\mathbf{f}^s & \delta\boldsymbol{\omega}^s_{is} & \delta\bar{\mathbf{g}}^i\end{bmatrix}^\top \tag{C.109}$$

and

$$\mathbf{F}^i = \left[\begin{array}{ccc|ccc}
\mathbf{0}_3 & \mathbf{0}_3 & \mathbf{0}_3 & \mathbf{0}_3 & \mathbf{C}^i_s & \mathbf{0}_3 \\
\left[-\mathbf{f}^i\times\right] & \mathbf{0}_3 & \bar{\boldsymbol{\Gamma}}^i & \mathbf{C}^i_s & \mathbf{0}_3 & \mathbf{I}_3 \\
\mathbf{0}_3 & \mathbf{I}_3 & \mathbf{0}_3 & \mathbf{0}_3 & \mathbf{0}_3 & \mathbf{0}_3 \\
\hline
\mathbf{0}_3 & \mathbf{0}_3 & \mathbf{0}_3 & \mathbf{0}_3 & \mathbf{0}_3 & \mathbf{0}_3 \\
\mathbf{0}_3 & \mathbf{0}_3 & \mathbf{0}_3 & \mathbf{0}_3 & \mathbf{0}_3 & \mathbf{0}_3 \\
\mathbf{0}_3 & \mathbf{0}_3 & \mathbf{0}_3 & \mathbf{0}_3 & \mathbf{0}_3 & \mathbf{0}_3
\end{array}\right]\ , \tag{C.110}$$

where $\mathbf{0}_3$ denotes a 3×3 matrix of zeros, $\mathbf{I}_3$ is the 3×3 identity matrix and $\left[-\mathbf{f}^i\times\right]$ is the skew symmetric form of $-\mathbf{f}^i$:

$$\left[-\mathbf{f}^i\times\right] = \begin{bmatrix} 0 & f_z^i & -f_y^i \\ -f_z^i & 0 & f_x^i \\ f_y^i & -f_x^i & 0 \end{bmatrix} . \tag{C.111}$$

C.3.2 Terrestrial Frame Equations

For the terrestrial frame we set $a = e$ in (C.106). Then assuming that the Earth rotational rate is constant and known very accurately, we can set $\delta\boldsymbol{\Omega}_{ie}^e = \dot{\boldsymbol{\Omega}}_{ie}^e = \delta\dot{\boldsymbol{\Omega}}_{ie}^e = 0$, to obtain

$$\boxed{\begin{aligned} \frac{\mathrm{d}}{\mathrm{d}t}\,\delta\boldsymbol{\psi}_{es}^e &= \mathbf{C}_s^e\,\delta\boldsymbol{\omega}_{is}^s - \boldsymbol{\Omega}_{ie}^e\,\delta\boldsymbol{\psi}_{es}^e \\ \frac{\mathrm{d}}{\mathrm{d}t}\,\delta\mathbf{v}^e &= -2\,\boldsymbol{\Omega}_{ie}^e\,\delta\mathbf{v}^e - \left(\boldsymbol{\Omega}_{ie}^e\,\boldsymbol{\Omega}_{ie}^e - \bar{\boldsymbol{\Gamma}}^e\right)\delta\mathbf{r}^e + \mathbf{C}_s^e\,\delta\mathbf{f}^e - \left[\mathbf{f}^e\times\right]\delta\boldsymbol{\psi}_{es}^e + \delta\bar{\mathbf{g}}^e \\ \frac{\mathrm{d}}{\mathrm{d}t}\,\delta\mathbf{r}^e &= \delta\mathbf{v}^e\ , \end{aligned}} \tag{C.112}$$

governing the error dynamics in the e-frame. This may, again, be expressed in state-space form as

$$\dot{\mathbf{x}}^e = \mathbf{F}^e\,\mathbf{x}^e\ , \tag{C.113}$$

with

$$\mathbf{x}^e = \begin{bmatrix} \delta\boldsymbol{\psi}_{es}^e & \delta\mathbf{v}^e & \delta\mathbf{r}^e & \delta\mathbf{f}^s & \delta\boldsymbol{\omega}_{is}^s & \delta\mathbf{g}^e \end{bmatrix}^\top \tag{C.114}$$

and

$$\mathbf{F}^e = \left[\begin{array}{ccc|ccc} -\boldsymbol{\Omega}_{ie}^e & \mathbf{0}_3 & \mathbf{0}_3 & \mathbf{0}_3 & \mathbf{C}_s^e & \mathbf{0_3} \\ \left[-\mathbf{f}^e\times\right] & -2\,\boldsymbol{\Omega}_{ie}^e & -\left(\boldsymbol{\Omega}_{ie}^e\boldsymbol{\Omega}_{ie}^e - \bar{\boldsymbol{\Gamma}}^e\right) & \mathbf{C}_s^e & \mathbf{0}_3 & \mathbf{I}_3 \\ \mathbf{0}_3 & \mathbf{I}_3 & \mathbf{0}_3 & \mathbf{0}_3 & \mathbf{0}_3 & \mathbf{0}_3 \\ \hline \mathbf{0}_3 & \mathbf{0}_3 & \mathbf{0}_3 & \mathbf{0}_3 & \mathbf{0}_3 & \mathbf{0}_3 \\ \mathbf{0}_3 & \mathbf{0}_3 & \mathbf{0}_3 & \mathbf{0}_3 & \mathbf{0}_3 & \mathbf{0}_3 \\ \mathbf{0}_3 & \mathbf{0}_3 & \mathbf{0}_3 & \mathbf{0}_3 & \mathbf{0}_3 & \mathbf{0}_3 \end{array}\right] , \tag{C.115}$$

where $\mathbf{0}_3$ denotes a 3×3 matrix of zeros, $\mathbf{I}_3$ is the 3×3 identity matrix and $[-\mathbf{f}^e\times]$ is the skew symmetric form of $-\mathbf{f}^e$.

C.3.3 Navigation Frame Equations

Since the velocity, $\mathbf{v}^n$, in the n-frame is defined with respect to the e-frame, we cannot simply set $a = n$ in (C.106) in order to arrive at the desired expression. Instead, we must apply the perturbation operator δ directly to (C.17) to obtain

$$\begin{aligned}\frac{\mathrm{d}}{\mathrm{d}t}\delta\mathbf{v}^n &= -\delta\left(2\boldsymbol{\Omega}_{ie}^n + \boldsymbol{\Omega}_{en}^n\right)\mathbf{v}^n - \left(2\boldsymbol{\Omega}_{ie}^n + \boldsymbol{\Omega}_{en}^n\right)\delta\mathbf{v}^n + \delta\mathbf{f}^n + \delta\mathbf{g}\left(\mathbf{r}^n\right) \\ &= -\delta\left(2\boldsymbol{\Omega}_{ie}^n + \boldsymbol{\Omega}_{en}^n\right)\mathbf{v}^n - \left(2\boldsymbol{\Omega}_{ie}^n + \boldsymbol{\Omega}_{en}^n\right)\delta\mathbf{v}^n \\ &\quad + \mathbf{C}_s^n\,\delta\mathbf{f}^s - \left[\mathbf{f}^n\times\right]\delta\boldsymbol{\psi}_{ns}^n + \delta\mathbf{g}^n + \boldsymbol{\Gamma}^n\delta\mathbf{p}^n\,,\end{aligned} \tag{C.116}$$

where the special notation $\delta\mathbf{p}^n$ was introduced to denote the position differentials along the latitudinal, longitudinal and vertical axes:

$$\delta\mathbf{p}^n = \begin{bmatrix}\delta\phi & \delta\lambda & \delta h\end{bmatrix}^\top\,. \tag{C.117}$$

Velocity Errors

The first two terms in (C.116) involve the rotational rates $\boldsymbol{\Omega}_{en}^n$ and $\boldsymbol{\Omega}_{ie}^n$, which can be expressed as

$$\boldsymbol{\Omega}_{en}^n = \begin{bmatrix} 0 & \frac{v_E\tan\phi}{R_E+h} & \frac{-v_N}{R_N+h} \\ \frac{-v_E\tan\phi}{R_E+h} & 0 & \frac{-v_E}{R_E+h} \\ \frac{v_N}{R_N+h} & \frac{v_E}{R_E+h} & 0 \end{bmatrix} \quad\text{and}\quad \boldsymbol{\Omega}_{ie}^n = \begin{bmatrix} 0 & \omega_{ie}\sin\phi & 0 \\ -\omega_{ie}\sin\phi & 0 & -\omega_{ie}\cos\phi \\ 0 & \omega_{ie}\cos\phi & 0 \end{bmatrix}. \tag{C.118}$$

These can be combined to yield

$$\boldsymbol{\Omega}_{in}^n = \begin{bmatrix} 0 & \frac{v_E\tan\phi}{R_E+h} + \omega_{ie}\sin\phi & \frac{-v_N}{R_N+h} \\ \frac{-v_E\tan\phi}{R_E+h} - \omega_{ie}\sin\phi & 0 & \frac{-v_E}{R_E+h} - \omega_{ie}\cos\phi \\ \frac{v_N}{R_N+h} & \frac{v_E}{R_E+h} + \omega_{ie}\cos\phi & 0 \end{bmatrix} \tag{C.119}$$

and

$$\left(\boldsymbol{\Omega}_{en}^n + 2\boldsymbol{\Omega}_{ie}^n\right) = \begin{bmatrix} 0 & \frac{v_E\tan\phi}{R_E+h} + 2\omega_{ie}\sin\phi & \frac{-v_N}{R_N+h} \\ \frac{-v_E\tan\phi}{R_E+h} - 2\omega_{ie}\sin\phi & 0 & \frac{-v_E}{R_E+h} - 2\omega_{ie}\cos\phi \\ \frac{v_N}{R_N+h} & \frac{v_E}{R_E+h} + 2\omega_{ie}\cos\phi & 0 \end{bmatrix}. \tag{C.120}$$

In order to derive an expression for the term $\delta\left(2\boldsymbol{\Omega}_{ie}^n + \boldsymbol{\Omega}_{en}^n\right)\mathbf{v}^n$, we apply the perturbation operator to the above expression one term at a time, assuming that $\delta R_N = \delta R_E = \delta\omega_{ie} = 0$. Doing this we have that

$$\begin{aligned}\delta\left(\boldsymbol{\Omega}_{en}^n + 2\boldsymbol{\Omega}_{ie}^n\right)_{12} &= \frac{\delta v_E\,\tan\phi + v_E\,\delta\phi\,\sec^2\phi}{R_E+h} - \frac{v_E\,\tan\phi}{\left(R_E+h\right)^2}\delta h + 2\omega_{ie}\,\delta\phi\,\cos\phi \\ \delta\left(\boldsymbol{\Omega}_{en}^n + 2\boldsymbol{\Omega}_{ie}^n\right)_{13} &= -\frac{\delta v_N}{R_N+h} + \frac{v_N}{\left(R_N+h\right)^2}\delta h \\ \delta\left(\boldsymbol{\Omega}_{en}^n + 2\boldsymbol{\Omega}_{ie}^n\right)_{23} &= -\frac{\delta v_E}{R_E+h} + \frac{v_E}{\left(R_E+h\right)^2}\delta h + 2\omega_{ie}\,\delta\phi\,\sin\phi\,.\end{aligned} \tag{C.121}$$

The remaining terms are simply zero or equals one of the above with reverse sign. Inserting them into the matrix, we have that

$$\delta\left(\boldsymbol{\Omega}_{en}^{n}+2\boldsymbol{\Omega}_{ie}^{n}\right)=$$
$$\begin{bmatrix} 0 & \frac{\tan\phi}{R_E+h}\delta v_E+\Big(\frac{v_E\sec^2\phi}{R_E+h}+2\,\omega_{ie}\cos\phi\Big)\delta\phi-\frac{v_E\tan\phi}{(R_E+h)^2}\delta h & -\frac{1}{R_N+h}\delta v_N+\frac{v_N}{(R_N+h)^2}\delta h \\ -\frac{\tan\phi}{R_E+h}\delta v_E-\Big(\frac{v_E\sec^2\phi}{R_E+h}+2\,\omega_{ie}\cos\phi\Big)\delta\phi+\frac{v_E\tan\phi}{(R_E+h)^2}\delta h & 0 & \frac{-1}{R_E+h}\delta v_E+2\,\omega_{ie}\sin\phi\,\delta\phi+\frac{v_E}{(R_E+h)^2}\delta h \\ \frac{1}{R_N+h}\delta v_N-\frac{v_N}{(R_N+h)^2}\delta h & \frac{1}{R_E+h}\delta v_E-2\,\omega_{ie}\sin\phi\,\delta\phi-\frac{v_E}{(R_E+h)^2}\delta h & 0 \end{bmatrix}. \tag{C.122}$$

Then forming the product with $\mathbf{v}^n$, we have that

$$\delta\left(\boldsymbol{\Omega}_{en}^{n}+2\boldsymbol{\Omega}_{ie}^{n}\right)\mathbf{v}^n$$
$$=\begin{bmatrix} \frac{v_E\tan\phi}{R_E+h}\delta v_E+\Big(\frac{v_E^2\sec^2\phi}{R_E+h}+2\,v_E\,\omega_{ie}\cos\phi\Big)\delta\phi-\frac{v_E^2\tan\phi}{(R_E+h)^2}\delta h-\frac{v_D}{R_N+h}\delta v_N+\frac{v_D\,v_N}{(R_N+h)^2}\delta h \\ -\frac{v_N\tan\phi}{R_E+h}\delta v_E-\Big(\frac{v_N\,v_E\sec^2\phi}{R_E+h}+2\,v_N\,\omega_{ie}\cos\phi\Big)\delta\phi+\frac{v_N\,v_E\tan\phi}{(R_E+h)^2}\delta h-\frac{v_D}{R_E+h}\delta v_E \\ +2\,v_D\,\omega_{ie}\sin\phi\,\delta\phi+\frac{v_D\,v_E}{(R_E+h)^2}\delta h \\ \frac{v_N}{R_N+h}\delta v_N-\frac{v_N^2}{(R_N+h)^2}\delta h+\frac{v_E}{R_E+h}\delta v_E-2\,v_E\,\omega_{ie}\sin\phi\,\delta\phi-\frac{v_E^2}{(R_E+h)^2}\delta h \end{bmatrix}$$

$$=\begin{bmatrix} -\frac{v_D}{R_N+h} & \frac{v_E\tan\phi}{R_E+h} & 0 \\ 0 & -\frac{v_N\tan\phi}{R_E+h}-\frac{v_D}{R_E+h} & 0 \\ \frac{v_N}{R_N+h} & \frac{v_E}{R_E+h} & 0 \end{bmatrix}\begin{bmatrix}\delta v_N\\ \delta v_E\\ \delta v_D\end{bmatrix} \tag{C.123}$$

$$+\begin{bmatrix} \frac{v_E^2\sec^2\phi}{R_E+h}+2\,v_E\,\omega_{ie}\cos\phi & 0 & \frac{v_D\,v_N}{(R_N+h)^2}-\frac{v_E^2\tan\phi}{(R_E+h)^2} \\ -\frac{v_N\,v_E\sec^2\phi}{R_E+h}-2\,v_N\,\omega_{ie}\cos\phi+2\,v_D\,\omega_{ie}\sin\phi & 0 & \frac{v_N\,v_E\tan\phi+v_D\,v_E}{(R_E+h)^2} \\ -2\,v_E\,\omega_{ie}\sin\phi & 0 & -\frac{v_N^2}{(R_N+h)^2}-\frac{v_E^2}{(R_E+h)^2} \end{bmatrix}\begin{bmatrix}\delta\phi\\ \delta\lambda\\ \delta h\end{bmatrix}.$$

Combining this expression with (C.120) we have that

$$
\begin{aligned}
&- \delta\left(2\boldsymbol{\Omega}_{ie}^{n} + \boldsymbol{\Omega}_{en}^{n}\right)\mathbf{v}^{n} - \left(2\boldsymbol{\Omega}_{ie}^{n} + \boldsymbol{\Omega}_{en}^{n}\right)\delta\mathbf{v}^{n} + \boldsymbol{\Gamma}^{n}\delta\mathbf{p}^{n} \\
&= \begin{bmatrix} \frac{v_D}{R_N+h} & \frac{-2v_E\,\tan\phi}{R_E+h} - \omega_{ie}\sin\phi & \frac{v_N}{R_N+h} \\ \frac{v_E\,\tan\phi}{R_E+h} + 2\omega_{ie}\sin\phi & \frac{v_N\,\tan\phi}{R_E+h} + \frac{v_D}{R_E+h} & \frac{v_E}{R_E+h} + 2\omega_{ie}\cos\phi \\ \frac{-2v_N}{R_N+h} & \frac{-2v_E}{R_E+h} - 2\omega ie\cos\phi & 0 \end{bmatrix} \begin{bmatrix} \delta v_N \\ \delta v_E \\ \delta v_D \end{bmatrix} \\
&\quad + \begin{bmatrix} \Gamma_{11}^{n} + \frac{-v_E^2\,\sec^2\phi}{R_E+h} - 2\,v_E\,\omega_{ie}\cos\phi & \Gamma_{12}^{n} & \Gamma_{13}^{n} + \frac{v_E^2\,\tan\phi}{(R_E+h)^2} - \frac{v_D\,v_N}{(R_N+h)^2} \\ \Gamma_{21}^{n} + \frac{v_N\,v_E\,\sec^2\phi}{R_E+h} + 2\,v_N\,\omega_{ie}\cos\phi - 2\,v_D\,\omega_{ie}\,\sin\phi & \Gamma_{22}^{n} & \Gamma_{23}^{n} + \frac{-v_N\,v_E\,\tan\phi - v_D\,v_E}{(R_E+h)^2} \\ \Gamma_{31}^{n} + 2\,v_E\,\omega_{ie}\,\sin\phi & \Gamma_{32}^{n} & \Gamma_{33}^{n} + \frac{v_N^2}{(R_N+h)^2} + \frac{v_E^2}{(R_E+h)^2} \end{bmatrix} \begin{bmatrix} \delta\phi \\ \delta\lambda \\ \delta h \end{bmatrix} \\
&= \mathbf{F}_{22}^{n}\,\delta\mathbf{v}^{n} + \mathbf{F}_{23}^{n}\,\delta\mathbf{p}^{n}\,.
\end{aligned}
\tag{C.124}
$$

Finally, we therefore have that

$$
\frac{\mathrm{d}}{\mathrm{d}t}\delta\mathbf{v}^{n} = -\left[\mathbf{f}^{n}\times\right]\delta\boldsymbol{\psi}_{ns}^{n} + \mathbf{F}_{22}^{n}\,\delta\mathbf{v}^{n} + \mathbf{F}_{23}^{n}\,\delta\mathbf{p}^{n} + \delta\mathbf{g}^{n} \tag{C.125}
$$

Position Errors

The position components, ϕ, λ and h, are the components that we want to use as our position in the n-frame implementation. Moreover, the velocity component, $\mathbf{v}^n$, is Earth-referenced, but resolved about the axes of the n-frame. This issue therefore requires extra consideration. From (C.26) we have that

$$\begin{aligned} \dot{\phi} &= \frac{v_N}{R_N + h} \\ \dot{\lambda} &= \frac{v_E}{(R_E + h)\cos\phi} \\ \dot{h} &= -v_D \ , \end{aligned} \tag{C.126}$$

to which we can apply the perturbation operator in order to arrive at

$$\begin{aligned} \delta\dot{\phi} &\approx \frac{\delta v_N}{R_N + h} - \frac{v_N}{(R_N + h)^2}\delta h \\ \delta\dot{\lambda} &\approx \frac{\delta v_E}{(R_E + h)\cos\phi} + \frac{v_E \sin\phi}{(R_E + h)\cos^2\phi}\delta\phi - \frac{v_E}{(R_E + h)^2\cos\phi}\delta h \\ \delta\dot{h} &\approx -\delta v_D \ , \end{aligned} \tag{C.127}$$

where the terms involving δR_N and δR_E have been neglected. We can write this in matrix-form as

$$\begin{aligned} \frac{\mathrm{d}}{\mathrm{d}t}\delta\mathbf{p} &= \begin{bmatrix} \frac{1}{R_N+h} & 0 & 0 \\ 0 & \frac{1}{(R_E+h)\cos\phi} & 0 \\ 0 & 0 & -1 \end{bmatrix} \begin{bmatrix} \delta v_N \\ \delta v_E \\ \delta v_D \end{bmatrix} + \begin{bmatrix} 0 & 0 & \frac{-v_N}{(R_N+h)^2} \\ \frac{v_E \sin\phi}{(R_E+h)\cos^2\phi} & 0 & \frac{-v_E}{(R_E+h)^2\cos\phi} \\ 0 & 0 & 0 \end{bmatrix} \begin{bmatrix} \delta\phi \\ \delta\lambda \\ \delta h \end{bmatrix} \\ &= \mathbf{F}_{32}^n\,\delta\mathbf{v}^n + \mathbf{F}_{33}^n\,\delta\mathbf{p}^n \ . \end{aligned} \tag{C.128}$$

Attitude Errors

For the attitude errors, we set $a = n$ in (C.101) in order to arrive at

$$\delta\dot{\boldsymbol{\psi}}_{ns}^n = \mathbf{C}_s^n\,\delta\boldsymbol{\omega}_{is}^s - \boldsymbol{\Omega}_{in}^n\,\delta\boldsymbol{\psi}_{ns}^n - \delta\boldsymbol{\omega}_{in}^n \ , \tag{C.129}$$

in which we have to derive an expression for $\delta\boldsymbol{\omega}_{in}^n$. An expression for the rotational rate $\boldsymbol{\omega}_{in}^n$ can be formed using (A.23) and (A.24). Applying the perturbation operator to this expression, we arrive at

$$
\begin{aligned}
-\delta\boldsymbol{\omega}_{in}^{n} = -\delta\boldsymbol{\omega}_{ie}^{n} - \delta\boldsymbol{\omega}_{en}^{n} &= \begin{bmatrix} \omega_{ie}\,\sin\phi\,\delta\phi \\ 0 \\ \omega_{ie}\,\cos\phi\,\delta\phi \end{bmatrix} - \begin{bmatrix} \frac{1}{R_E+h}\delta v_E - \frac{v_E}{(R_E+h)^2}\delta h \\ -\frac{1}{R_N+h}\delta v_N + \frac{v_N}{(R_N+h)^2}\delta h \\ -\frac{\tan\phi}{R_E+h}\delta v_E - \frac{v_E\,\sec^2\phi}{R_E+h}\delta\phi + \frac{v_E\,\tan\phi}{(R_E+h)^2}\delta h \end{bmatrix} \\
&= \begin{bmatrix} -\frac{1}{R_E+h}\delta v_E + \frac{v_E}{(R_E+h)^2}\delta h + \omega_{ie}\,\sin\phi\,\delta\phi \\ \\ \frac{1}{R_N+h}\delta v_N - \frac{v_N}{(R_N+h)^2}\delta h \\ \\ \frac{\tan\phi}{R_E+h}\delta v_E + \frac{v_E\,\sec^2\phi}{R_E+h}\delta\phi - \frac{v_E\,\tan\phi}{(R_E+h)^2}\delta h + \omega_{ie}\,\cos\phi\,\delta\phi \end{bmatrix} \\
&= \begin{bmatrix} 0 & \frac{-1}{R_E+h} & 0 \\ \frac{1}{R_N+h} & 0 & 0 \\ 0 & \frac{\tan\phi}{R_E+h} & 0 \end{bmatrix} \begin{bmatrix} \delta v_N \\ \delta v_E \\ \delta v_D \end{bmatrix} + \begin{bmatrix} \omega_{ie}\,\sin\phi & 0 & \frac{v_E}{(R_E+h)^2} \\ 0 & 0 & \frac{-v_N}{(R_N+h)^2} \\ \frac{v_E\,\sec^2\phi}{R_E+h} + \omega_{ie}\,\cos\phi & 0 & \frac{-v_E\,\tan\phi}{(R_E+h)^2} \end{bmatrix} \begin{bmatrix} \delta\phi \\ \delta\lambda \\ \delta h \end{bmatrix} \\
&= \mathbf{F}_{12}^{n}\,\delta\mathbf{v}^{n} + \mathbf{F}_{13}^{n}\,\delta\mathbf{p}^{n}\;,
\end{aligned}
\tag{C.130}
$$

which is then inserted into the previous expression to obtain

$$
\delta\dot{\boldsymbol{\psi}}_{ns}^{n} = \mathbf{C}_{s}^{n}\,\delta\boldsymbol{\omega}_{is}^{s} - \boldsymbol{\Omega}_{in}^{n}\,\delta\boldsymbol{\psi}_{ns}^{n} + \mathbf{F}_{12}^{n}\,\delta\mathbf{v}^{n} + \mathbf{F}_{13}^{n}\,\delta\mathbf{p}^{n}\;. \tag{C.131}
$$

State-Space Formulation

Finally, putting everything together we have that

$$
\dot{\mathbf{x}}^{n} = \mathbf{F}^{n}\,\mathbf{x}^{n}\;, \tag{C.132}
$$

with

$$
\mathbf{x}^{n} = \begin{bmatrix} \delta\boldsymbol{\psi}_{ns}^{n} & \delta\mathbf{v}^{n} & \delta\mathbf{p} & \delta\mathbf{f}^{s} & \delta\boldsymbol{\omega}_{is}^{s} & \delta\mathbf{g}^{n} \end{bmatrix}^{\top} \tag{C.133}
$$

and

$$
\mathbf{F}^{n} = \left[\begin{array}{ccc|ccc} -\boldsymbol{\Omega}_{in}^{n} & \mathbf{F}_{12}^{n} & \mathbf{F}_{13}^{n} & \mathbf{0}_3 & \mathbf{C}_{s}^{n} & \mathbf{0}_3 \\ -[\mathbf{f}^{n}\times] & \mathbf{F}_{22}^{n} & \mathbf{F}_{23}^{n} & \mathbf{C}_{s}^{n} & \mathbf{0}_3 & \mathbf{I}_3 \\ \mathbf{0}_3 & \mathbf{F}_{32}^{n} & \mathbf{F}_{33}^{n} & \mathbf{0}_3 & \mathbf{0}_3 & \mathbf{0}_3 \\ \hline \mathbf{0}_3 & \mathbf{0}_3 & \mathbf{0}_3 & \mathbf{0}_3 & \mathbf{0}_3 & \mathbf{0}_3 \\ \mathbf{0}_3 & \mathbf{0}_3 & \mathbf{0}_3 & \mathbf{0}_3 & \mathbf{0}_3 & \mathbf{0}_3 \\ \mathbf{0}_3 & \mathbf{0}_3 & \mathbf{0}_3 & \mathbf{0}_3 & \mathbf{0}_3 & \mathbf{0}_3 \end{array}\right]\;, \tag{C.134}
$$

noticing again that

$$\mathbf{F}_{12}^{n} = \begin{bmatrix} 0 & \frac{-1}{R_E+h} & 0 \\ \frac{1}{R_N+h} & 0 & 0 \\ 0 & \frac{\tan\phi}{R_E+h} & 0 \end{bmatrix}, \tag{C.135}$$

$$\mathbf{F}_{13}^{n} = \begin{bmatrix} \omega_{ie}\,\sin\phi & 0 & \frac{v_E}{(R_E+h)^2} \\ 0 & 0 & \frac{-v_N}{(R_N+h)^2} \\ \frac{v_E\,\sec^2\phi}{R_E+h} + \omega_{ie}\,\cos\phi & 0 & \frac{-v_E\,\tan\phi}{(R_E+h)^2} \end{bmatrix}, \tag{C.136}$$

$$\mathbf{F}_{22}^{n} = \begin{bmatrix} \frac{v_D}{R_N+h} & \frac{-2v_E\,\tan\phi}{R_E+h} - \omega_{ie}\sin\phi & \frac{v_N}{R_N+h} \\ \frac{v_E\,\tan\phi}{R_E+h} + 2\omega_{ie}\sin\phi & \frac{v_N\,\tan\phi}{R_E+h} + \frac{v_D}{R_E+h} & \frac{v_E}{R_E+h} + 2\omega_{ie}\cos\phi \\ \frac{-2v_N}{R_N+h} & \frac{-2v_E}{R_E+h} - 2\omega ie\cos\phi & 0 \end{bmatrix}, \tag{C.137}$$

$$\mathbf{F}_{23}^{n} = \begin{bmatrix} \Gamma_{11}^{n} + \frac{-v_E^2\,\sec^2\phi}{R_E+h} - 2\,v_E\,\omega_{ie}\cos\phi & \Gamma_{12}^{n} & \Gamma_{13}^{n} + \frac{v_E^2\,\tan\phi}{(R_E+h)^2} - \frac{v_D\,v_N}{(R_N+h)^2} \\ \Gamma_{21}^{n} + \frac{v_N\,v_E\,\sec^2\phi}{R_E+h} + 2\,v_N\,\omega_{ie}\cos\phi - 2\,v_D\,\omega_{ie}\,\sin\phi & \Gamma_{22}^{n} & \Gamma_{23}^{n} + \frac{-v_N\,v_E\,\tan\phi - v_D\,v_E}{(R_E+h)^2} \\ \Gamma_{31}^{n} + 2\,v_E\,\omega_{ie}\,\sin\phi & \Gamma_{32}^{n} & \Gamma_{33}^{n} + \frac{v_N^2}{(R_N+h)^2} + \frac{v_E^2}{(R_E+h)^2} \end{bmatrix}, \tag{C.138}$$

$$\mathbf{F}_{32}^{n} = \begin{bmatrix} \frac{1}{R_N+h} & 0 & 0 \\ 0 & \frac{1}{(R_E+h)\cos\phi} & 0 \\ 0 & 0 & -1 \end{bmatrix} \tag{C.139}$$

and

$$\mathbf{F}_{33}^{n} = \begin{bmatrix} 0 & 0 & \frac{-v_N}{(R_N+h)^2} \\ \frac{v_E\,\sin\phi}{(R_E+h)\cos^2\phi} & 0 & \frac{-v_E}{(R_E+h)^2\cos\phi} \\ 0 & 0 & 0 \end{bmatrix}. \tag{C.140}$$

If the n-frame coordinate axes were always perfectly aligned with the tangent to the local plumb line and the level surface, then all horizontal components of the gravity vector and its gradients would vanish. Therefore all components of $\mathbf{\Gamma}^n$, except for Γ_{33}^n, are expected to be small or at least of less consequence when compared to the velocity products in the corresponding matrix elements. These components are therefore usually omitted. The actual n-frame is however defined with respect to the ellipsoidal normal and the difference between this direction and the plumb line is known as the deflection of the vertical. The components of $\mathbf{\Gamma}^n$ are only expected to be of significance in rough terrain, in which they are also extremely localised and random in character, meaning that they would not significantly affect the dynamics of the navigation errors. The Γ_{33}^n term is however very important, since it represents a long-term systematic effect and is responsible for the rapid error growth in the vertical channel of the INS [15, p. 156-157]

C.3.4 Wander-Azimuth Frame Equations

The wander-azimuth frame is different from the other frames, since the navigation equations (C.38) involve a transformation matrix, $\mathbf{C}_e^w$, rather than the horizontal coordinates ϕ and λ (and ψ_{nw}). The state vector therefore looks like

$$\mathbf{x}^w = \begin{bmatrix} \delta\boldsymbol{\psi}^w_{ws} & \delta\mathbf{v}^w & \delta\boldsymbol{\psi}^w_{ew} & \delta h & \delta\mathbf{f}^s & \delta\boldsymbol{\omega}^s_{is} & \delta\mathbf{g}^n \end{bmatrix}^\top , \tag{C.141}$$

where $\delta\boldsymbol{\psi}^w_{ew}$ are errors on the Euler angles of the $\mathbf{C}^w_e$ matrix.

Attitude Errors

Turning first our attention to the attitude errors, we have from (C.101) that

$$\begin{aligned} \delta\dot{\boldsymbol{\psi}}^w_{ws} &= \mathbf{C}^w_s\, \delta\boldsymbol{\omega}^s_{is} - \boldsymbol{\Omega}^w_{iw}\, \delta\boldsymbol{\psi}^w_{ws} - \delta\boldsymbol{\omega}^w_{iw} \\ &= \mathbf{C}^w_s\, \delta\boldsymbol{\omega}^s_{is} - \boldsymbol{\Omega}^w_{iw}\, \delta\boldsymbol{\psi}^w_{ws} - \delta\boldsymbol{\omega}^w_{ie} - \delta\boldsymbol{\omega}^w_{ew} , \end{aligned} \tag{C.142}$$

where we need to express $\delta\boldsymbol{\omega}^w_{ie}$ and $\delta\boldsymbol{\omega}^w_{ew}$ in terms of our error states. For the first term we have that

$$\begin{aligned} \delta\boldsymbol{\omega}^w_{ie} &= \delta\left(\mathbf{C}^w_e\, \boldsymbol{\omega}^e_{ie}\right) = \delta\mathbf{C}^w_e\, \boldsymbol{\omega}^e_{ie} + \mathbf{C}^w_e\, \delta\boldsymbol{\omega}^e_{ie} \\ &= \left[\delta\boldsymbol{\psi}^w_{we}\times\right] \mathbf{C}^w_e \begin{bmatrix} 0 \\ 0 \\ \omega_{ie} \end{bmatrix} = -\left[\delta\boldsymbol{\psi}^w_{ew}\times\right] \mathbf{C}^w_e \begin{bmatrix} 0 \\ 0 \\ \omega_{ie} \end{bmatrix} \\ &= \left(\mathbf{C}^w_e \begin{bmatrix} 0 \\ 0 \\ \omega_{ie} \end{bmatrix} \times \right) \delta\boldsymbol{\psi}^w_{ew} = \omega_{ie} \left[\mathbf{C}^w_{e:,3}\times\right] \delta\boldsymbol{\psi}^w_{ew} , \end{aligned} \tag{C.143}$$

where (6.13) was used to introduce (small angle) attitude errors. For the second term, we apply the perturbation operator to (C.34) in order to obtain

$$\delta\boldsymbol{\omega}^w_{ew} = \delta\mathbf{W}\, \mathbf{v}^w + \mathbf{W}\, \delta\mathbf{v}^w , \tag{C.144}$$

where

$$\mathbf{W} = \begin{bmatrix} \frac{\cos\psi_{nw}\sin\psi_{nw}}{R_E+h} - \frac{\cos\psi_{nw}\sin\psi_{nw}}{R_N+h} & \frac{\cos^2\psi_{nw}}{R_E+h} + \frac{\sin^2\psi_{nw}}{R_N+h} & 0 \\ -\frac{\cos^2\psi_{nw}}{R_N+h} - \frac{\sin^2\psi_{nw}}{R_E+h} & \frac{\cos\psi_{nw}\sin\psi_{nw}}{R_N+h} - \frac{\cos\psi_{nw}\sin\psi_{nw}}{R_E+h} & 0 \\ 0 & 0 & 0 \end{bmatrix} . \tag{C.145}$$

Applying the perturbation operator to the $\mathbf{W}$ matrix, neglecting higher-order error products and variation in the radii of curvature parameters, we have that

$$
\delta\mathbf{W} \approx \begin{bmatrix}
\frac{-\sin^2\psi_{nw}+\cos^2\psi_{nw}}{R_E+h}\delta\psi_{nw} - \frac{\cos\psi_{nw}\sin\psi_{nw}}{(R_E+h)^2}\delta h & \frac{-2\sin\psi_{nw}\cos\psi_{nw}}{R_E+h}\delta\psi_{nw} - \frac{\cos^2\psi_{nw}}{(R_E+h)^2}\delta h & 0 \\
+\frac{\sin^2\psi_{nw}-\cos^2\psi_{nw}}{R_N+h}\delta\psi_{nw} + \frac{\cos\psi_{nw}\sin\psi_{nw}}{(R_N+h)^2}\delta h & +\frac{2\sin\psi_{nw}\cos\psi_{nw}}{R_N+h}\delta\psi_{nw} - \frac{\sin^2\psi_{nw}}{(R_N+h)^2}\delta h & \\
\frac{2\sin\psi_{nw}\cos\psi_{nw}}{R_N+h}\delta\psi_{nw} + \frac{\cos^2\psi_{nw}}{(R_N+h)^2}\delta h & \frac{-\sin^2\psi_{nw}+\cos^2\psi_{nw}}{R_N+h}\delta\psi_{nw} - \frac{\cos\psi_{nw}\sin\psi_{nw}}{(R_N+h)^2}\delta h & 0 \\
-\frac{2\sin\psi_{nw}\cos\psi_{nw}}{R_E+h}\delta\psi_{nw} + \frac{\sin^2\psi_{nw}}{(R_E+h)^2}\delta h & +\frac{\sin^2\psi_{nw}-\cos^2\psi_{nw}}{R_E+h}\delta\psi_{nw} + \frac{\cos\psi_{nw}\sin\psi_{nw}}{(R_E+h)^2}\delta h & \\
0 & 0 & 0
\end{bmatrix}
$$

$$
= \begin{bmatrix}
\frac{\cos 2\psi_{nw}}{R_E+h}\delta\psi_{nw} - \frac{\cos\psi_{nw}\sin\psi_{nw}}{(R_E+h)^2}\delta h & \frac{-\sin 2\psi_{nw}}{R_E+h}\delta\psi_{nw} - \frac{\cos^2\psi_{nw}}{(R_E+h)^2}\delta h & 0 \\
-\frac{\cos 2\psi_{nw}}{R_N+h}\delta\psi_{nw} + \frac{\cos\psi_{nw}\sin\psi_{nw}}{(R_N+h)^2}\delta h & +\frac{\sin 2\psi_{nw}}{R_N+h}\delta\psi_{nw} - \frac{\sin^2\psi_{nw}}{(R_N+h)^2}\delta h & \\
\frac{\sin 2\psi_{nw}}{R_N+h}\delta\psi_{nw} + \frac{\cos^2\psi_{nw}}{(R_N+h)^2}\delta h & \frac{\cos 2\psi_{nw}}{R_N+h}\delta\psi_{nw} - \frac{\cos\psi_{nw}\sin\psi_{nw}}{(R_N+h)^2}\delta h & 0 \\
-\frac{\sin 2\psi_{nw}}{R_E+h}\delta\psi_{nw} + \frac{\sin^2\psi_{nw}}{(R_E+h)^2}\delta h & -\frac{\cos 2\psi_{nw}}{R_E+h}\delta\psi_{nw} + \frac{\cos\psi_{nw}\sin\psi_{nw}}{(R_E+h)^2}\delta h & \\
0 & 0 & 0
\end{bmatrix}
$$

$$
= \begin{bmatrix}
\frac{\cos 2\psi_{nw}}{R_E+h} - \frac{\cos 2\psi_{nw}}{R_N+h} & \frac{-\sin 2\psi_{nw}}{R_E+h} + \frac{\sin 2\psi_{nw}}{R_N+h} & 0 \\
\frac{\sin 2\psi_{nw}}{R_N+h} - \frac{\sin 2\psi_{nw}}{R_E+h} & \frac{\cos 2\psi_{nw}}{R_N+h} - \frac{\cos 2\psi_{nw}}{R_E+h} & 0 \\
0 & 0 & 0
\end{bmatrix}\delta\psi_{nw}
$$

$$
+ \begin{bmatrix}
-\frac{\cos\psi_{nw}\sin\psi_{nw}}{(R_E+h)^2} + \frac{\cos\psi_{nw}\sin\psi_{nw}}{(R_N+h)^2} & -\frac{\cos^2\psi_{nw}}{(R_E+h)^2} - \frac{\sin^2\psi_{nw}}{(R_N+h)^2} & 0 \\
\frac{\cos^2\psi_{nw}}{(R_N+h)^2} + \frac{\sin^2\psi_{nw}}{(R_E+h)^2} & \frac{-\cos\psi_{nw}\sin\psi_{nw}}{(R_N+h)^2} + \frac{\cos\psi_{nw}\sin\psi_{nw}}{(R_E+h)^2} & 0 \\
0 & 0 & 0
\end{bmatrix}\delta h \ .
$$

Then, forming the product with $\mathbf{v}^w$, we arrive at the expression

$$
\begin{aligned}
\delta\mathbf{W}\,\mathbf{v}^w \approx & \begin{bmatrix} \frac{v_x^w \cos 2\psi_{nw}}{R_E+h} - \frac{v_x^w \cos 2\psi_{nw}}{R_N+h} - \frac{v_y^w \sin 2\psi_{nw}}{R_E+h} + \frac{v_y^w \sin 2\psi_{nw}}{R_N+h} \\ \frac{v_x^w \sin 2\psi_{nw}}{R_N+h} - \frac{v_x^w \sin 2\psi_{nw}}{R_E+h} + \frac{v_y^w \cos 2\psi_{nw}}{R_N+h} - \frac{v_y^w \cos 2\psi_{nw}}{R_E+h} \\ 0 \end{bmatrix} \delta\psi_{nw} \quad + \\
& \begin{bmatrix} -\frac{v_x^w \cos\psi_{nw}\sin\psi_{nw}}{(R_E+h)^2} + \frac{v_x^w \cos\psi_{nw}\sin\psi_{nw}}{(R_N+h)^2} - \frac{v_y^w \cos^2\psi_{nw}}{(R_E+h)^2} - \frac{v_y^w \sin^2\psi_{nw}}{(R_N+h)^2} \\ \frac{v_x^w \cos^2\psi_{nw}}{(R_N+h)^2} + \frac{v_x^w \sin^2\psi_{nw}}{(R_E+h)^2} - \frac{v_y^w \cos\psi_{nw}\sin\psi_{nw}}{(R_N+h)^2} + \frac{v_y^w \cos\psi_{nw}\sin\psi_{nw}}{(R_E+h)^2} \\ 0 \end{bmatrix} \delta h \\
= & \begin{bmatrix} \frac{-v_x^w \cos 2\psi_{nw}+v_y^w \sin 2\psi_{nw}}{R_N+h} + \frac{v_x^w \cos 2\psi_{nw}-v_y^w \sin 2\psi_{nw}}{R_E+h} \\ \frac{v_x^w \sin 2\psi_{nw}+v_y^w \cos 2\psi_{nw}}{R_N+h} - \frac{v_x^w \sin 2\psi_{nw}+v_y^w \cos 2\psi_{nw}}{R_E+h} \\ 0 \end{bmatrix} \delta\psi_{nw} \quad + \\
& \begin{bmatrix} \frac{v_x^w \cos\psi_{nw}\sin\psi_{nw}-v_y^w \sin^2\psi_{nw}}{(R_N+h)^2} - \frac{v_x^w \cos\psi_{nw}\sin\psi_{nw}+v_y^w \cos^2\psi_{nw}}{(R_E+h)^2} \\ \frac{v_x^w \cos^2\psi_{nw}-v_y^w \cos\psi_{nw}\sin\psi_{nw}}{(R_N+h)^2} + \frac{v_x^w \sin^2\psi_{nw}+v_y^w \cos\psi_{nw}\sin\psi_{nw}}{(R_E+h)^2} \\ 0 \end{bmatrix} \delta h \\
= & \begin{bmatrix} 0 & 0 & \frac{-v_x^w \cos 2\psi_{nw}+v_y^w \sin 2\psi_{nw}}{R_N+h} + \frac{v_x^w \cos 2\psi_{nw}-v_y^w \sin 2\psi_{nw}}{R_E+h} \\ 0 & 0 & \frac{v_x^w \sin 2\psi_{nw}+v_y^w \cos 2\psi_{nw}}{R_N+h} - \frac{v_x^w \sin 2\psi_{nw}+v_y^w \cos 2\psi_{nw}}{R_E+h} \\ 0 & 0 & 0 \end{bmatrix} \delta\boldsymbol{\psi}_{ew}^w \quad + \\
& \begin{bmatrix} \frac{v_x^w \cos\psi_{nw}\sin\psi_{nw}-v_y^w \sin^2\psi_{nw}}{(R_N+h)^2} - \frac{v_x^w \cos\psi_{nw}\sin\psi_{nw}+v_y^w \cos^2\psi_{nw}}{(R_E+h)^2} \\ \frac{v_x^w \cos^2\psi_{nw}-v_y^w \cos\psi_{nw}\sin\psi_{nw}}{(R_N+h)^2} + \frac{v_x^w \sin^2\psi_{nw}+v_y^w \cos\psi_{nw}\sin\psi_{nw}}{(R_E+h)^2} \\ 0 \end{bmatrix} \delta h \\
= & \mathbf{W}_2\,\delta\boldsymbol{\psi}_{ew}^w + \mathbf{w}_3\,\delta h\ ,
\end{aligned}
\tag{C.146}
$$

where we have exploited that $\delta\psi_{nw} = \delta\boldsymbol{\psi}_{ew,3}^w$ and it is noted that $\mathbf{W}_2$ is a 3×3 matrix, while $\mathbf{w}_3$ is a 3×1 vector. In the polar regions, the wander angle approaches $\pm 90°$, such that $\sin\psi_{nw} \approx 1$ and $\cos\psi_{nw} \approx 0$. This can cause some significant numerical rounding errors, when evaluating the above matrices. Instead, the following approximations should be used:

$$\begin{aligned}\mathbf{W} &\approx \left(\frac{a}{\sqrt{1-e^2}}+h\right)^{-1}\begin{bmatrix}0 & 1 & 0\\ -1 & 0 & 0\\ 0 & 0 & 0\end{bmatrix}\\ \mathbf{W}_2 &\approx \mathbf{0}_3\\ \mathbf{w}_3 &\approx \left(\frac{a}{\sqrt{1-e^2}}+h\right)^{-2}\begin{bmatrix}-v_y^w\\ v_x^w\\ 0\end{bmatrix},\end{aligned} \tag{C.147}$$

where a is the semi-major axis of the ellipsoid and e is the eccentricity.

To summarize, we have that

$$\delta\dot{\boldsymbol{\psi}}_{ws}^{w} = -\boldsymbol{\Omega}_{iw}^{w}\,\delta\boldsymbol{\psi}_{ws}^{w} - \mathbf{W}\,\delta\mathbf{v}^{w} - \left\{\omega_{ie}\left[\mathbf{C}_{e:,3}^{w}\times\right] + \mathbf{W}_2\right\}\delta\boldsymbol{\psi}_{ew}^{w} - \mathbf{w}_3\,\delta h + \mathbf{C}_s^w\,\delta\boldsymbol{\psi}_{is}^{s}\,. \tag{C.148}$$

Velocity Errors

Applying the perturbation operator to the differential equation governing the velocity in (C.38), we have that

$$\begin{aligned}\frac{\mathrm{d}}{\mathrm{d}t}\delta\mathbf{v}^w &= \delta\mathbf{f}^w - \delta\left(2\boldsymbol{\Omega}_{ie}^{w}+\boldsymbol{\Omega}_{ew}^{w}\right)\mathbf{v}^w - \left(2\boldsymbol{\Omega}_{ie}^{w}+\boldsymbol{\Omega}_{ew}^{w}\right)\delta\mathbf{v}^w + \delta\mathbf{g}^w(\mathbf{p})\\ &= \mathbf{C}_s^w\,\delta\mathbf{f}^s - [\mathbf{f}^w\times]\,\delta\boldsymbol{\psi}_{ws}^{w} - \left(2\delta\boldsymbol{\Omega}_{ie}^{w}+\delta\boldsymbol{\Omega}_{ew}^{w}\right)\mathbf{v}^w - \left(2\boldsymbol{\Omega}_{ie}^{w}+\boldsymbol{\Omega}_{ew}^{w}\right)\delta\mathbf{v}^w\\ &\quad + \delta\mathbf{g}^w + \boldsymbol{\Gamma}^w\,\delta\mathbf{p}^w\\ &= \mathbf{C}_s^w\,\delta\mathbf{f}^s - [\mathbf{f}^w\times]\,\delta\boldsymbol{\psi}_{ws}^{w} + 2\,[\mathbf{v}^w\times]\,\delta\boldsymbol{\omega}_{ie}^{w} + [\mathbf{v}^w\times]\,\delta\boldsymbol{\omega}_{ew}^{w} - \left(2\boldsymbol{\Omega}_{ie}^{w}+\boldsymbol{\Omega}_{ew}^{w}\right)\delta\mathbf{v}^w\\ &\quad + \mathbf{C}_n^w\,\delta\mathbf{g}^n + \boldsymbol{\Gamma}^w\,\delta\mathbf{p}^w\,,\end{aligned} \tag{C.149}$$

where the position changes $\delta\mathbf{p}^w$ are along the forward, starboard and through-the-floor directions of the wander-azimuth frame:

$$\delta\mathbf{p}^w = \begin{bmatrix}\delta\boldsymbol{\psi}_{ew,1}^{w}\\ \delta\boldsymbol{\psi}_{ew,2}^{w}\\ \delta h\end{bmatrix}\,. \tag{C.150}$$

The expressions for $\delta\boldsymbol{\omega}_{ie}^{w}$ and $\delta\boldsymbol{\omega}_{ew}^{w}$ in the above have just been derived in the previous section as

$$\begin{aligned}\delta\boldsymbol{\omega}_{ie}^{w} &= \omega_{ie}\left[\mathbf{C}_{e:,3}^{w}\times\right]\delta\boldsymbol{\psi}_{ew}^{w} \quad \text{and}\\ \delta\boldsymbol{\omega}_{ew}^{w} &= \mathbf{W}_2\,\delta\boldsymbol{\psi}_{ew}^{w} + \mathbf{w}_3\,\delta h + \mathbf{W}\,\delta\mathbf{v}^w\,,\end{aligned} \tag{C.151}$$

such that the above can be written as

$$\begin{aligned}\delta\dot{\mathbf{v}}^w = &-[\mathbf{f}^w\times]\,\delta\boldsymbol{\psi}_{ws}^{w} + \left\{2\left[-\mathbf{C}_e^w\,\boldsymbol{\omega}_{ie}^{e}\times\right] + \left[-\boldsymbol{\omega}_{ew}^{w}\times\right] + [\mathbf{v}^w\times]\,\mathbf{W}\right\}\delta\mathbf{v}^w\\ &+ \left\{2\omega_{ie}\,[\mathbf{v}^w\times]\left[\mathbf{C}_{e:,3}^{w}\times\right] + [\mathbf{v}^w\times]\,\mathbf{W}_2 + \boldsymbol{\Gamma}_2\right\}\delta\boldsymbol{\psi}_{ew}^{w} + \left\{[\mathbf{v}^w\times]\,\mathbf{w}_3 + \boldsymbol{\Gamma}_3\right\}\delta h\\ &+ \mathbf{C}_s^w\,\delta\mathbf{f}^s + \mathbf{C}_n^w\,\delta\mathbf{g}^n\,.\end{aligned} \tag{C.152}$$

Position Errors

The latitude, longitude and wander azimuth errors are contained in the error angles

$$\delta\boldsymbol{\omega}_{ew}^{w} = \mathbf{W}\,\delta\mathbf{v}^{w} + \mathbf{W}_2\,\delta\boldsymbol{\psi}_{ew}^{w} + \mathbf{w}_3\,\delta h\ , \tag{C.153}$$

while the vertical position error is

$$\delta\dot{h} \approx -\delta v_z^w\ . \tag{C.154}$$

State-Space Representation

Finally, putting everything together, we have that

$$\dot{\mathbf{x}}^{w} = \mathbf{F}^{w}\,\mathbf{x}^{w}\ , \tag{C.155}$$

with

$$\mathbf{x}^{w} = \begin{bmatrix}\delta\boldsymbol{\psi}_{ws}^{w} & \delta\mathbf{v}^{w} & \delta\boldsymbol{\psi}_{ew}^{w} & \delta h & \delta\mathbf{f}^{s} & \delta\boldsymbol{\omega}_{is}^{s} & \delta\mathbf{g}^{n}\end{bmatrix}^{\top}\ . \tag{C.156}$$

The system matrix is

$$\mathbf{F}^{w} = \left[\begin{array}{cccc|ccc} [-\boldsymbol{\omega}_{iw}^{w}\times] & -\mathbf{W} & \mathbf{F}_{13}^{w} & -\mathbf{w}_3 & \mathbf{0}_3 & \mathbf{C}_s^w & \mathbf{0_3} \\ [-\mathbf{f}^{w}\times] & \mathbf{F}_{22}^{w} & \mathbf{F}_{23}^{w} & \mathbf{F}_{24}^{w} & \mathbf{C}_s^w & \mathbf{0}_3 & \mathbf{C}_n^w \\ \mathbf{0}_3 & \mathbf{W} & \mathbf{W}_2 & \mathbf{w}_3 & \mathbf{0}_3 & \mathbf{0}_3 & \mathbf{0}_3 \\ \mathbf{0}_{1\times 3} & [0,0,-1] & \mathbf{0}_{1\times 3} & 0 & \mathbf{0}_{1\times 3} & \mathbf{0}_{1\times 3} & \mathbf{0}_{1\times 3} \\ \hline \mathbf{0}_3 & \mathbf{0}_3 & \mathbf{0}_3 & \mathbf{0}_3 & \mathbf{0}_3 & \mathbf{0}_3 & \mathbf{0}_3 \\ \mathbf{0}_3 & \mathbf{0}_3 & \mathbf{0}_3 & \mathbf{0}_3 & \mathbf{0}_3 & \mathbf{0}_3 & \mathbf{0}_3 \\ \mathbf{0}_3 & \mathbf{0}_3 & \mathbf{0}_3 & \mathbf{0}_3 & \mathbf{0}_3 & \mathbf{0}_3 & \mathbf{0}_3 \end{array}\right]\ , \tag{C.157}$$

where

$$\mathbf{F}_{13}^{w} = -\omega_{ie}\left[\mathbf{C}_{e:,3}^{w}\times\right] - \mathbf{W}_2\ , \tag{C.158}$$

$$\mathbf{F}_{22}^{w} = 2\left[-\mathbf{C}_e^w\,\boldsymbol{\omega}_{ie}^{e}\times\right] + \left[-\boldsymbol{\omega}_{ew}^{w}\times\right] + \left[\mathbf{v}^{w}\times\right]\mathbf{W}\ , \tag{C.159}$$

$$\mathbf{F}_{23}^{w} = 2\omega_{ie}\left[\mathbf{v}^{w}\times\right]\left[\mathbf{C}_{e:,3}^{w}\times\right] + \left[\mathbf{v}^{w}\times\right]\mathbf{W}_2 + \begin{bmatrix}\Gamma_{11} & \Gamma_{12} & 0\\ \Gamma_{21} & \Gamma_{22} & 0\\ \Gamma_{31} & \Gamma_{32} & 0\end{bmatrix} \tag{C.160}$$

and

$$\mathbf{F}_{24}^{w} = \left[\mathbf{v}^{w}\times\right]\mathbf{w}_3 + \begin{bmatrix}\Gamma_{13}\\ \Gamma_{23}\\ \Gamma_{33}\end{bmatrix}\ . \tag{C.161}$$

D Stochastic Processes, Error Models and Linear Dynamic Systems

D.1 Random Processes

When we consider a signal representing some physical quantity, usually as a function of time or space, we are in fact considering real variables. Such signals may be deterministic or random and should be described appropriately.

- A signal is said to be **deterministic** if it can be predicted exactly for the time span of interest. Deterministic signals can usually be described using a functional relationship, $x(t)$, such that any value of x can be determined exactly if we specify the numeric value of t.
- A **random** or **stochastic** signal, on the other hand, will have some element of chance associated with it, meaning that it will not be predictable in a deterministic sense. The outcome of the stochastic process, $X(t)$, at time t is simply random.

notice that capital letters refer to stochastic processes, while lower case letters refers to deterministic functions. In order to start analysing a random signal, we can imagine taking samples of the signal at subsequent times t_1, t_2, t_3, etc., noticing that the outcome of each sample will be governed by chance. However, in order to fully explore the behaviour of the signal, it is not sufficient to sample the same signal at different points in time, since such samples would not be independent. A fundamental concept in random signals is therefore the conceptual scenario of an **ensemble of sample realisations**, all obtained under independent, but completely identical circumstances. Obviously, in most cases, an ensemble of sample realisations is not available and we must attempt to describe the signal based on a single realisation of the stochastic process. In the following subsections, we will further explore how random processes can be described under such circumstances, based on some assumptions.

D.1.1 Probabilistic Description of a Random Process

Typically, stochastic signals are described in terms of probability density functions and their joint distributions. If we again consider a single random signal as shown in Figure D.1, we can imagine taking samples at subsequent times t_1, t_2, ..., t_k in order to sample the variables $X(t_1)$, $X(t_2)$, ..., $X(t_k)$. Each of these random variables will be governed by a first-order density distribution $f_{X_1}(x)$, $f_{X_2}(x)$, ..., $f_{X_k}(x)$, which may or may not be identical. These first-order densities supply information on the amplitude distribution of the process.

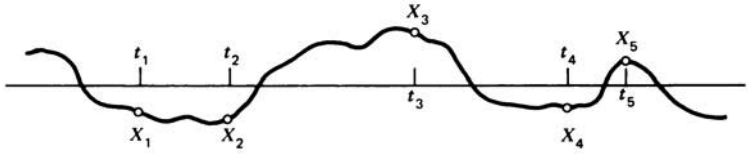

Figure D.1: Sample signal of a typical noise process. Image credit: [5, Fig. 2.5].

Specifying the second-order density distributions, $f_{X_1X_2}(x_1, x_2)$, $f_{X_1X_3}(x_1, x_3)$, etc., is important in order to describe how rapidly the signal changes with time and therefore also

concerns the spectral content of the signal. Similarly, the third, fourth and sub-sequent higher-order density functions will add information to the description of the process. Consequently, in order to completely describe the characteristics of the signal, a kth order density function is required. In practice, the formulation of a complete multivariate density function is generally impossible. Instead, one usually approximates the stochastic process by considering only the first- and second-order joint density functions.

Probability density functions are often described more compactly in terms of moments of the distribution. The first two moments, namely the mean and variance of the distribution, are:

$$\mu_X(t) \equiv \mathrm{E}\left[X(t)\right] = \int_{-\infty}^{\infty} x(t) f_X\left(x(t)\right)\, \mathrm{d}x(t) \quad \text{and} \tag{D.1}$$

$$\sigma_X^2 \equiv \mathrm{E}\left[\left(X(t) - \mu_X(t)\right)^2\right] = \int_{-\infty}^{\infty} \left(x(t) - \mu_X(t)\right)^2 f_X\left(x(t)\right)\, \mathrm{d}x(t)\ , \tag{D.2}$$

where σ_X is also known as the standard deviation. It should be noted that a probability density function is, in general, not completely described based on only the first two moments of the distribution. These two parameters present a very compact and useful way of describing the first-order density distribution. A similarly compact, but generally not complete, concept for describing the second-order density distribution of a stochastic signal is the autocorrelation function, which will be presented in the next section.

D.1.2 Correlation and Covariance Functions

The **autocorrelation** function is an important descriptor of the random process, $X(t)$, since it represents a compact way of describing how the signal evolves with time. More specifically, it contains information on how well the process is correlated with itself at two different times. It may be defined as

$$\begin{aligned} R_X\left(t_1, t_2\right) &\equiv \mathrm{E}\left[X\left(t_1\right) X\left(t_2\right)\right] \\ &= \int_{-\infty}^{\infty}\int_{-\infty}^{\infty} x\left(t_1\right) x\left(t_2\right) f_{X_1 X_2}\left(x\left(t_1\right), x\left(t_2\right)\right)\, \mathrm{d}x\left(t_1\right) \mathrm{d}x\left(t_2\right)\ , \end{aligned} \tag{D.3}$$

where t_1 and t_2 are arbitrary sample times. A related measure is the **auto-covariance** function, defined as

$$\begin{aligned} C_X\left(t_1, t_2\right) &\equiv \mathrm{E}\left[\left(X\left(t_1\right) - \mu_X\left(t_1\right)\right)\left(X\left(t_2\right) - \mu_X\left(t_2\right)\right)\right] \\ &= \int_{-\infty}^{\infty}\int_{-\infty}^{\infty} \left\{x\left(t_1\right) - \mu_X\left(t_2\right)\right\}\left\{x\left(t_2\right) - \mu_X\left(t_2\right)\right\} f_{X_1 X_2}\left(x\left(t_1\right), x\left(t_2\right)\right)\, \mathrm{d}x\left(t_1\right) \mathrm{d}x\left(t_2\right)\ , \end{aligned} \tag{D.4}$$

which reduces to the usual variance measure for $t_1 = t_2$. The autocorrelation and autocovariance functions are simply related as

$$\begin{aligned} C_X\left(t_1, t_2\right) &= \mathrm{E}\left[\left(X\left(t_1\right) - \mu_X\left(t_1\right)\right)\left(X\left(t_2\right) - \mu_X\left(t_2\right)\right)\right] \\ &= \mathrm{E}\left[X\left(t_1\right) X\left(t_2\right)\right] - \mathrm{E}\left[X\left(t_1\right) \mu_X\left(t_2\right)\right] - \mathrm{E}\left[\mu_X\left(t_1\right) X\left(t_2\right)\right] + \mathrm{E}\left[\mu_X\left(t_1\right) \mu_{X_2}\right] \\ &= R_X\left(t_1, t_2\right) - \mu_X\left(t_1\right) \mu_X\left(t_2\right) - \mu_X\left(t_1\right) \mu_X\left(t_2\right) + \mu_X\left(t_1\right) \mu_X\left(t_2\right) \\ &= R_X\left(t_1, t_2\right) - \mu_X\left(t_1\right) \mu_X\left(t_2\right)\ . \end{aligned} \tag{D.5}$$

The reader should notice that the definitions of the autocorrelation and auto-covariance functions are not consistent in the literature. Sometimes the autocorrelation function, as defined here, is referred to as the auto-covariance function.

The idea of autocorrelation may be extended to describe the relation between two different stochastic processes, $X(t)$ and $Y(t)$. This concept is known as the **cross-correlation** function and is defined as

$$\begin{aligned} R_{XY}(\tau) &= \mathrm{E}\left[X(t_1)\, Y(t_2)\right] \\ &= \int_{-\infty}^{\infty}\int_{-\infty}^{\infty} x(t_1)\, y(t_2)\, f_{XY}(x(t_1), y(t_2))\, \mathrm{d}x(t_1)\, \mathrm{d}y(t_2) \ , \end{aligned} \tag{D.6}$$

which is related to a similarly defined cross-covariance matrix as

$$C_{XY}(t_1, t_2) = R_{XY}(t_1, t_2) - \mu_X(t_1)\, \mu_Y(t_2) \ . \tag{D.7}$$

Before continuing, I would like to add a comment to the idea of autocorrelation of a process (or the cross-correlation between two stochastic processes for that matter). A process is said to be uncorrelated in time if

$$R_Z(t_1, t_2) = \mathrm{E}\left[X(t_1)\, X(t_2)\right] = \mathrm{E}\left[X(t_1)\right]\mathrm{E}\left[X(t_2)\right] \quad \text{for} \quad t_1 \neq t_2 \ , \tag{D.8}$$

which is obviously related to the concept of independence. A process which is independent (white) is also uncorrelated. However, since the concept of correlation only concerns the second moment of the process, a process that is uncorrelated is generally not independent. This is because a stochastic process is generally not completely described in terms of the first two moment only and independence is consequently related to all higher-order moments also.

With the concepts of autocorrelation and cross-correlation introduced, we will now continue to present the properties of stationarity and ergodicity of stochastic processes. These properties will certainly not characterise all stochastic processes, but will only be valid for certain processes. If the stochastic process is either stationary or ergodic, this will significantly simplify the description and analysis of the associated process.

D.1.3 Stationarity

A process is said to be (time) stationary if all of its statistics are invariant when subject to a time shift. To phrase this in a more mathematical way, consider a set of time samples, $X(t_1)$, $X(t_2)$, ..., $X(t_k)$, of the random process. We then have that

$$f(X(t_1), X(t_2), ..., X(t_k)) = f(X(t_1 + \tau), X(t_2 + \tau), ..., X(t_k + \tau)) \ , \tag{D.9}$$

which must also hold for any marginal probability distribution of the process. Consequently, any statistical parameters, such a mean and variance, do also not change over time. This kind of stationarity is commonly known as **strict stationarity** in order to distinguish it from **wide-sense stationarity**, which is a less restrictive form of stationarity, that concerns only the first- and second-order probabilities. A process that is wide-sense stationary has some very convenient properties [5, p. 67-68]:

1. The mean of the first-order probability distribution is constant in time, i.e. $\mu_X(t) = \mathrm{E}\left[X(t)\right] = \text{constant}$

2. The variance of the first-order probability distribution is constant in time, i.e. $\sigma_X^2 = \mathrm{E}\left[(X(t) - \mu_X)^2\right] = \text{constant}$

3. The autocorrelation and auto-covariance functions, related to the second-order probability distribution, depends only on the time difference $\tau = t_2 - t_1$. That is, $R_X(\tau) = \mathrm{E}[X(t)X(t+\tau)]$

4. The value $R_X(\tau = 0)$ is the mean-square of the stationary process. If the mean is zero, it is the variance

5. The autocorrelation is an even function, i.e. $R_X(\tau) = R_X(-\tau)$

6. The autocorrelation function attains its maximum value at $\tau = 0$, such that $R_X(|\tau|) \leq R_X(0)$ for all τ. More specifically, this means that the correlation between the two random variables, $X(t)$ and $X(t+\tau)$, can never be greater than the correlation of the variable with itself.

A typical stationary auto-correlation function is shown in figure D.2. It usually decreases, at least for small values of τ, and tends to zero as $\tau \to 0$. That is, unless $X(t)$ contains some periodic element.

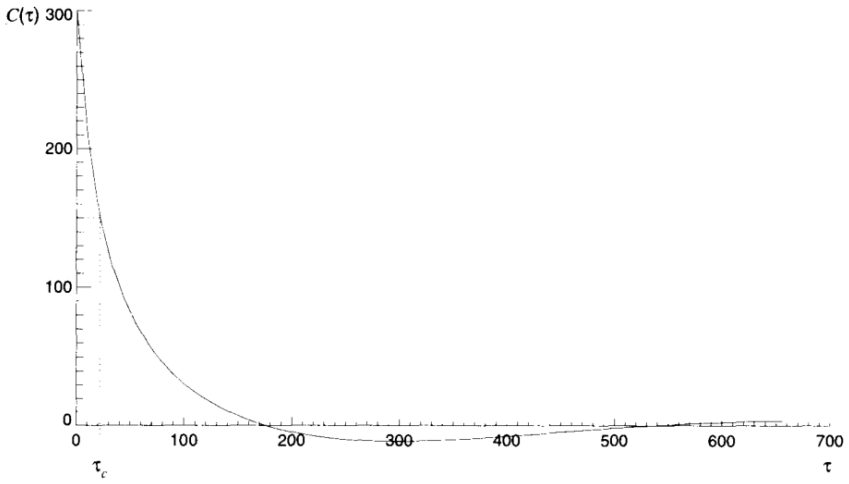

Figure D.2: Typical stationary autocorrelation function. Image credit: [15, Fig. 6.3].

The **correlation time**, τ_c, of the stochastic signal is a measure of the time interval, where the process is considered to be correlated with itself. In practice, such a measure is only approximate and usually defined as being some time interval, where the autocorrelation is a significantly reduced fraction of the variance. Some examples of its definition are [15, Eq. 6.41]:

$$\frac{R_X(\tau_c)}{R_X(0)} = \frac{1}{2} \quad \text{or} \quad \frac{R_X(\tau_c)}{R_X(0)} = e^{-1} \,. \tag{D.10}$$

As we have just seen, these properties related to stationarity of a stochastic process are very convenient and greatly simplifies the treatment of the signal. In general, we concern

ourselves only with the first two orders of the probability density distribution when describing random signals. Consequently, we also generally concern ourselves with wide sense stationarity. In the following, we will look at an important "subclass" of stationarity, which further simplifies the treatment of a relevant stochastic process.

D.1.4 Ergodicity

First of all, the concept of ergodicity is related only to stationary stochastic processes. Such a process is said to be ergodic if its statistical properties can be deduced from a single, sufficiently long, sample of the process. This means that time averaging is equivalent to ensemble averaging and that no additional information is gained by observing an ensemble of signal realisations over a single realisation. Consequently, the mean, variance and higher-order moments associated with the underlying probabilities can be derived using only the temporal average of a single sample. For example, the mean can be estimated from a single realisation, $X_A(t)$, as

$$\mu_X = E\left[X(t)\right] = \lim_{T\to\infty} \frac{1}{T}\int_0^T X_A(t)\,\mathrm{d}t \approx \frac{1}{T}\int_0^T X_A(t)\,\mathrm{d}t\ , \tag{D.11}$$

where the integration from 0 to T is over the entire sample. In theory, the integration interval should be infinitely long, but in practice, the process is realised for only a limited time interval. Therefore, the estimate reduces to an approximate value.

This property is very useful in practice, since we often have only a single realisation of the process. It should, however, be noticed that there is no easy way of telling whether a real signal is ergodic or not. Often one simply assumes ergodicity in order to derive statistical parameters from the signal. For example, assuming ergodicity, the autocorrelation function may be estimated from a single realisation using a time average, rather than an ensemble average, as

$$\begin{aligned} R_X(\tau) &= \lim_{T\to\infty} \frac{1}{T}\int_0^T X_A(t)\,X_A(t+\tau)\ \mathrm{d}t \\ &\approx \frac{1}{T}\int_0^T X_A(t)\,X_A(t+\tau)\ \mathrm{d}t\ , \end{aligned} \tag{D.12}$$

where it is tacitly assumed that the sample realisation is adequately long.

D.1.5 Power Spectral Density

The autocorrelation function is often used as a descriptor of stochastic signals. Qualitatively, it tells us something about how fast the signal changes with time. Therefore, the autocorrelation function contains information about the frequency content of the process. Similar to deterministic signals, Fourier transform theory can be exploited to form a frequency-domain representation of the process known as the Power Spectral Density (PSD) function. For a wide-sense stationary process, the PSD is defined in terms of the autocorrelation function, $R_X(\tau)$, as [5, Eq. 2.7.1]:

$$\boxed{S_X(f) = \mathfrak{F}\left[R_X(\tau)\right] = \int_{-\infty}^{\infty} R_X(\tau)\,e^{-i2\pi f\tau}\,\mathrm{d}\tau\ ,} \tag{D.13}$$

where $\mathfrak{F}[.]$ denotes the Fourier transform and f is the frequency, which has the units of Hz = 1/s. In general, the PSD will therefore contain both real and imaginary components, being even and odd functions with respect to the frequency, f, respectively [17, Sec. 4.3]. The unit of the PSD will be $(\text{quantity})^2$ /Hz

As with deterministic signals, we can apply the inverse Fourier transform in order to retrieve the time-wise signal from its spectral description. The autocorrelation function can therefore be obtained from the PSD as

$$R_X(\tau) = \mathfrak{F}^{-1}[S_X(f)] = \int_{-\infty}^{\infty} S_X(f)\, e^{i2\pi\tau f}\, \mathrm{d}f\ , \tag{D.14}$$

which, for $\tau = 0$, equals the mean square value of the (stationary) random process. This expression also hints as to why $S_X(f)$ is called the power spectral density function. A relatively large value of the PSD, at a particular frequency, suggests that a high degree of correlation occurs at this frequency. Therefore the process has high power at this frequency. If we wanted to obtain the signal power in a finite band, we could integrate over the appropriate band of frequencies as

$$\text{Power in the range } f_1 \le f \le f_2 = \int_{-f_2}^{-f_1} S_X(f)\ \mathrm{d}f + \int_{f_1}^{f_2} S_X(f)\ \mathrm{d}f\ . \tag{D.15}$$

For a deterministic signal, the spectral content is obtained by applying the Fourier transform to the mathematical functional description of the signal. For the stochastic signal, the Fourier transform is applied to the autocorrelation function. The two concepts are therefore clearly related, but the connection is not straightforward. First of all, if the process $X(t)$ is stationary, the signal wanders on ad infinitum and cannot be integrated. Thus, in order to make the integral converge, we must consider only a limited part of the signal, $X_T(t)$, which is truncated to zero outside some timespan, T. Under this assumption, the Fourier transform of a sample realisation will exist. We can then consider the Fourier transform, $\mathfrak{F}[X_T(t)]$, of a sample realisation, $X_T(t)$. This means that, for every realisation, $X_T(t)$, exists a corresponding Fourier transform, $\mathfrak{F}[X_T(t)]$, and for every ensemble of realisations exists a corresponding ensemble of Fourier transforms. These Fourier transforms will therefore have stochastic attributes, which can be estimated in terms of mean, variance and so forth. The expectation of the ensemble of Fourier transforms is related to the PSD as [5, Eq. 2.7.9]:

$$\boxed{\mathrm{E}\left[\frac{1}{T}\left|\mathfrak{F}[X_T(t)]\right|^2\right] \quad \Rightarrow \quad \int_{-\infty}^{\infty} R_X(\tau)\, e^{-i2\pi f\tau}\, \mathrm{d}\tau \quad \text{as} \quad T \to \infty\ ,} \tag{D.16}$$

where the quantity inside the brackets is known as the **periodogram** of the particular sample realisation, $X_T(t)$. The term on the LHS above is therefore the average periodogram, where the average is done over an ensemble of Fourier transforms, while the term of the RHS is the PSD. This relation is very important, since it relates the probabilistic concept of a PSD to the Fourier transform of a signal in the time domain. It therefore provides the tie between probabilistic and spectral descriptors of the process.

This concludes the short introduction to stochastic processes and its probabilistic description. In the applications related to this dissertation, we will attempt to model stochastic signals in terms of their autocorrelation functions. These stochastic processes are most

frequently described in terms of their PSD. However, as we have just seen, the PSD and autocorrelation functions are complementary descriptors and one can be retrieved from the other. In the following, we will have a look at some common random processes, that are relevant for our purposes. That is, for the random signals that we encounter, we will attempt to model them as one of these known processes, although their true nature does not fit this description exactly.

D.2 White Noise

A white noise process, $\mathcal{W}(t)$, is a stationary process that is defined in terms of its PSD and autocorrelation function as

$$S_{\text{wn}}(f) = A \quad \text{and} \quad R_{\text{wn}}(\tau) = A\delta(\tau) \ , \tag{D.17}$$

where A is the spectral amplitude and δ denotes the Dirac delta function. These functions are sketched in Figure D.3. The PSD therefore describes a process with equal power at any frequency, while the autocorrelation function describes a signal that is completely decorrelated with itself, except at $\tau = 0$ where the correlation is infinite. This also means that the variance of the signal is infinite. Qualitatively, this would suggest a signal that jumps around infinitely fast and infinitely far.

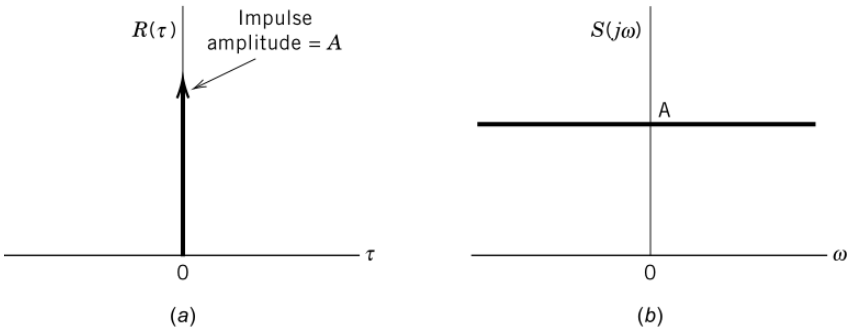

Figure D.3: White noise. (a) Autocorrelation function. (b) Power spectral density function. Image credit: [5, Fig. 2.12]

A true continuous white noise process is only a conceptual process that never truly occurs in the real world. Such a process would require infinite bandwidth and infinite power. Luckily, all physical systems are bandlimited to some extent. **Bandlimited white noise** is characterised by having a constant amplitude over some finite range of frequencies and zero amplitude outside that range. A bandlimited white noise process, where the bandwidth includes the origin, can be described as

$$S_{\text{bwn}}(f) = \begin{cases} A & \text{for} \quad |f| \leq B \\ 0 & \text{for} \quad |f| > B \end{cases} \ , \tag{D.18}$$

where B is the bandwidth (in Hz). The corresponding autocorrelation function is obtained from (D.14), using Eulers formula, as

$$R_{\text{bwn}}(\tau) = 2BA \frac{\sin(2\pi B\tau)}{2\pi B\tau} . \tag{D.19}$$

The PSD and autocorrelation function of bandlimited white noise are sketched in Figure D.4. Figure D.4a shows that the autocorrelation function is zero at the points $\tau = 1/2B$, B, $3/2B$, etc. This suggests that, if we sample the signal at a rate of 2B Hz, i.e. the Nyquist rate, the resulting set of random variables will be uncorrelated.

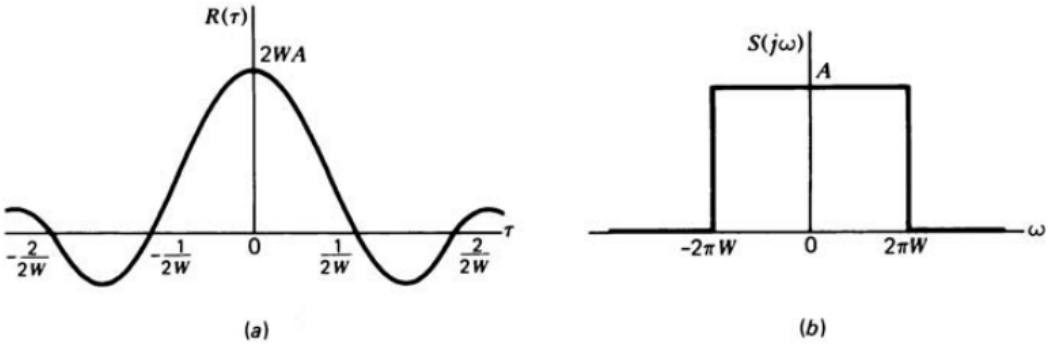

Figure D.4: Bandlimited white noise. (a) Autocorrelation function. (b) Power spectral density function. Image credit: [5, Fig. 2.13]

In the real world, pure bandlimited white noise does also not occur, since the bandwidth will usually not be truncated as nicely, i.e. the PSD will not be box-shaped. However, it is common for noise processes to be approximately white at some limited portion of low frequencies and coloured at high frequencies[4], with some transition zone between the two. In this case, the process may be treated as white when sampled at time scales that greatly exceed the correlation time of the process.

A **white noise sequence**, $W(t_k)$, is the discrete-time equivalent of the white noise process. It is a time-wise sequence of mutually uncorrelated random variables from a zero mean distribution with the property that

$$\text{cov}(w_i, w_j) = \text{E}[w_i w_j] = \begin{cases} \sigma_w^2 & \text{for} \quad i = j \\ 0 & \text{for} \quad i \neq j \end{cases} , \tag{D.20}$$

where w_i and w_j are the samples. The transition from a continuous to a discrete white noise process can be defined in terms of an averaging procedure [15, p. 179]. In this case, the discrete random variable at time t_k is the average of the continuous white noise process over a small interval, $\triangle t$, as

$$W(t_k) = \frac{1}{\triangle t} \int_{t_k - \triangle t}^{t_k} \mathcal{W}(t)\, \text{d}t . \tag{D.21}$$

This leads to the following relation between the spectral amplitude, A, of the continuous white process and the variance, σ_w^2, of the discrete white noise sequence

[4] Noise processes that are not white are referred to as coloured.

$$\begin{aligned}\sigma_w^2 &= \mathrm{E}\left[W\left(t_k\right) W\left(t_k\right)\right] \\ &= \frac{1}{\left(\triangle t\right)^2} \int_{t_k-\triangle t}^{t_k} \int_{t_k-\triangle t}^{t_k} \mathrm{E}\left[\mathcal{W}(t)\mathcal{W}(t')\right] \,\mathrm{d}t\,\mathrm{d}t' \\ &= \frac{1}{\left(\triangle t\right)^2} \int_{t_k-\triangle t}^{t_k} \int_{t_k-\triangle t}^{t_k} A\delta\left(t-t'\right) \,\mathrm{d}t\,\mathrm{d}t' \\ &= \frac{A}{\triangle t} \,.\end{aligned} \tag{D.22}$$

Again, assuming that a bandlimited white noise process is sampled at a rate much less than the bandwidth, the sample sequence may be treated as a white noise sequence. The variance of the discrete white noise process and the PSD of the continuous white noise process is simply related as described above.

If the distribution of each random variable of the white noise process, i.e. each sample, is normally distributed with zero mean, the process is called a **Gaussian white noise** process. In this case, the process can be denoted

$$W_k \sim \mathcal{N}\left(0, A/\triangle t\right) \quad \text{or} \quad \mathcal{W} \sim \mathcal{N}\left(0, A\right) \,, \tag{D.23}$$

where A is the spectral amplitude of the continuous signal and $\triangle t$ is the averaging interval of the discrete-time sequence.

D.3 Stochastic Error Models

This section introduces three stochastic processes that will become useful when attempting to model the errors of an inertial navigation system. They can all be described using linear differential equations. The largest source of error in such a navigation system is the presence of a bias in the output of accelerometers and gyroscopes. Such a bias may be modelled as a random constant. The random walk and Gauss-Markov processes can both be used to model systems driven by white noise, which we assume that our sensor output contains to some extent.

D.3.1 Random Constant

A random constant is a stochastic process that is constant for all times. It can be described using the differential equation with initial condition:

$$\dot{X}(t) = 0 \quad \text{and} \quad X\left(t_0\right) = X_0 \,, \tag{D.24}$$

where the constant X_0 is a random variable. This means that the initialisation of the process is random, while the realisation will continue to have this constant initialisation value for all future times. This behaviour is characteristic for accelerometers and gyroscopes. When the instrument is turned on, its output will be subject to an unknown bias. This bias will be different each time the sensor is turned on. By turning the device on and off repeatedly, one may obtain information about the mean and variance of the bias.

The mean of the process may be assumed zero. This is usually assured through instrument calibration. The autocorrelation function of the process will be constant for all values of τ as

$$\mu_X = 0 \quad \text{and} \quad R_X(\tau) = \sigma_X^2 \ , \tag{D.25}$$

where σ_X^2 is the variance of the random variable. Notice that, given the value of the process at some time, it is known for all times without uncertainty. We should also notice that the process is stationary, but not ergodic, since the temporal average will not equal the ensemble average. From (D.13) we obtain the PSD of the process:

$$S_X(f) = \sigma_X^2 \, \delta(f) \ , \tag{D.26}$$

where the units of the delta function are [s] = [1/Hz]. The autocorrelation and PSD functions are illustrated in Figure D.5.

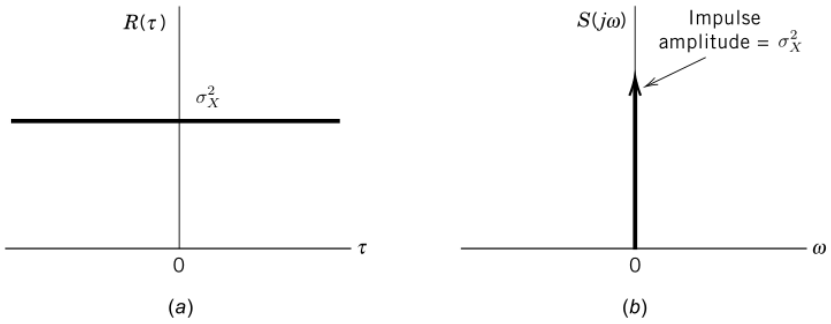

Figure D.5: Random constant. (a) Autocorrelation function. (b) Power spectral density function.

D.3.2 Random Walk

A random walk process is defined as integrated white noise and can be described using the differential equation with initial condition:

$$\dot{X}(t) = \mathcal{W}(t) \quad \Rightarrow \quad X(t) = \int_{t_0}^{t} \mathcal{W}(t') \, \mathrm{d}t' \quad \text{and} \quad X(t_0) = 0 \ . \tag{D.27}$$

In inertial navigation systems one integrates the sensed accelerations and angular rates in order to perform navigation. If the sensor output contains a white noise component, the stochastic process underlying the resulting estimates (velocity and attitude) can be modelled as a random walk process. The expectation value of the process is zero, since

$$\mu_X = \mathrm{E}[X(t)] = \int_{t_0}^{t} \mathrm{E}[\mathcal{W}(t')] \, \mathrm{d}t' = 0 \ , \tag{D.28}$$

and the autocorrelation is

$$\begin{aligned} R_X(t_1,t_2) &= \mathrm{E}\left[X(t_1)\,X(t_2)\right] = \int_{t_0}^{t_2}\int_{t_0}^{t_1} \mathrm{E}\left[\mathcal{W}(t_1')\,\mathcal{W}(t_2')\right]\,\mathrm{d}t_1'\mathrm{d}t_2' \\ &= \int_{t_0}^{t_2}\int_{t_0}^{t_1} A\delta(t_2'-t_1')\,\mathrm{d}t_1'\mathrm{d}t_2' \\ &= \begin{cases} A(t_1-t_0) & \text{for} \quad t_2 \geq t_1 > t_0 \\ A(t_2-t_0) & \text{for} \quad t_1 > t_2 > t_0 \end{cases}, \end{aligned} \tag{D.29}$$

where A is the spectral amplitude of the white noise process. Since the mean of the process is zero, the variance of the process will be

$$\sigma_X^2 = R_X(t,t) = A(t-t_0)\ , \tag{D.30}$$

which grows linearly with time, indicating that the random walk is **not a stationary process** and that a PSD cannot be formed for this process. The process is therefore also not ergodic.

If the underlying white noise process is Gaussian, then the resulting random walk will also be Gaussian. This is because integration is a linear operation and Gaussianity is preserved under linear operations. In this case the process is known as a **Wiener** or **Brownian-motion** process.

D.3.3 Gauss-Markov Process

The introduction of the random constant and random walk processes was motivated by known error characteristics of the system. The Gauss-Markov process on the other hand can be used more generally to model stochastic processes. As shown in Figure D.2, the autocorrelation function for a stationary process is often decreasing exponentially for small values of τ. This is the motivation for the introduction of the **stationary Gauss-Markov process**, which has an exponentially decreasing autocorrelation function of the form

$$R_X(\tau) = \sigma^2 e^{-\beta|\tau|} \quad \text{and} \quad S_X(f) = \frac{2\sigma^2\beta}{4\pi^2 f^2 + \beta^2}\ , \tag{D.31}$$

where σ^2 is the variance and $\beta \geq 0$ is a constant. The exponential autocorrelation function indicates that the samples become increasingly uncorrelated as the separation between them increases. The PSD of the process is flat at low frequencies and then tails off at frequencies comparable to $1/\beta$, which is defined as the correlation time of the process. The autocorrelation and PSD functions are illustrated in Figure D.6, noticing that the plots converge to those of white noise in Figure D.3 as $1/\beta \to 0$ and to those of a random constant in Figure D.5 as $1/\beta \to \infty$. This is a kind of bandlimited process that is a good approximation to many practical systems.

Besides being a good approximation to many physical systems, the Gauss-Markov model is also tractable due to its mathematical simplicity. The differential equation governing the process is of the form

$$\dot{X}(t) + \beta X(t) = \mathcal{W}(t) \quad \Leftrightarrow \quad \dot{X}(t) = -\beta X(t) + \mathcal{W}(t)\ , \tag{D.32}$$

indicating that the future value of $X(t)$ depends only on its present value and a white noise process $\mathcal{W}(t)$. Since this is a first-order differential equation, the process is also known as a **first-order Gauss-Markov process**. The auto-correlation of the white noise process is [15, Eq. 6.70]:

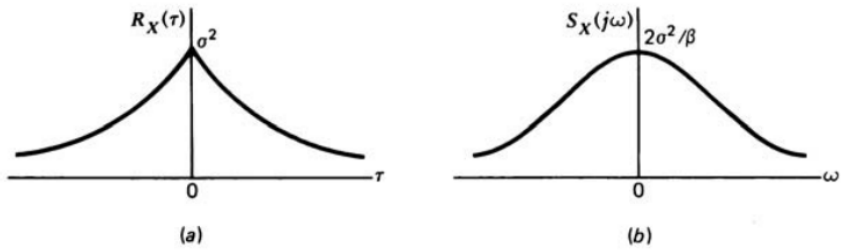

Figure D.6: Gauss-Markov Process. (a) Autocorrelation function. (b) Power spectral density function. Image credit: [5, Fig. 2.15]

$$R_{\text{wn},1}(\tau) = 2\sigma^2\beta\delta(\tau) \,. \tag{D.33}$$

Similarly, a **first-order Gauss-Markov sequence** is the discrete-time sequence, X_k, which depends only on its previous value, X_{k-1}, and a white noise sequence, W_{k-1}, as

$$X_k = e^{-\beta\triangle t}X_{k-1} + W_{k-1} \,, \tag{D.34}$$

where $\triangle t = t_k - t_{k-1}$ is the time between the samples. Since the next value in the sequence depends only on the current value of the sequence, the process may be said to be memoryless, which is the definition of the Markov property. As an extension, any process that depends on the previous n values is known as an nth order Markov process. If the probability density function governing the white noise component, $\mathcal{W}(t)$, is Gaussian, the adjective "Gauss" is added to the name.

A **second-order Gauss-Markov process** can be defined in terms of a second-order differential equation

$$\ddot{X}(t) + 2\beta_2\dot{X}(t) + \beta_2^2 X(t) = \mathcal{W}(t) \,, \tag{D.35}$$

with white noise auto-correlation function [15, Eq. 6.79]:

$$R_{\text{wn},2}(\tau) = 4\sigma^2\beta^3\delta(\tau) \,. \tag{D.36}$$

This may be expressed conveniently in vector form as

$$\frac{\mathrm{d}}{\mathrm{d}t}\begin{bmatrix} X(t) \\ \dot{X}(t) \end{bmatrix} = \begin{bmatrix} 0 & 1 \\ -\beta_2^2 & -2\beta_2 \end{bmatrix}\begin{bmatrix} X(t) \\ \dot{X}(t) \end{bmatrix} + \begin{bmatrix} 0 \\ \mathcal{W}(t) \end{bmatrix} \,. \tag{D.37}$$

In a similar form, the **third-order Gauss-Markov process** is defined in [16]:

$$\frac{\mathrm{d}}{\mathrm{d}t}\begin{bmatrix} X(t) \\ \dot{X}(t) \\ \ddot{X}(t) \end{bmatrix} = \begin{bmatrix} 0 & 1 & 0 \\ 0 & 0 & 1 \\ -\beta_3^3 & -3\beta_3^2 & -3\beta_3 \end{bmatrix}\begin{bmatrix} X(t) \\ \dot{X}(t) \\ \ddot{X}(t) \end{bmatrix} + \begin{bmatrix} 0 \\ 0 \\ \mathcal{W}(t) \end{bmatrix} \,. \tag{D.38}$$

with white noise auto-correlation function [15, Eq. 6.81]:

$$R_{\text{wn},3}(\tau) = \frac{16}{3}\sigma^2\beta^5\delta(\tau) \,. \tag{D.39}$$

In Table D.1, the form of the autocorrelation and PSD functions are listed for any order of the Gauss-Markov process and in Figure D.7, the autocorrelation and PSD functions are illustrated for first-, second- and third-order processes.

Order	PSD $S_X(f)$	Auto-Correlation $R_X(\tau)$
1	$\frac{2\beta_1\sigma^2}{(2\pi f)^2+\beta_1^2}$	$\sigma^2 e^{-\beta_1\lvert\tau\rvert}$
2	$\frac{4\beta_2^3\sigma^2}{\left[(2\pi f)^2+\beta_2^2\right]^2}$	$\sigma^2 e^{-\beta_2\lvert\tau\rvert}\left(1+\beta_2\lvert\tau\rvert\right)$
3	$\frac{16\beta_3^5\sigma^2}{3\left[(2\pi f)^2+\beta_3^2\right]^3}$	$\sigma^2 e^{-\beta_3\lvert\tau\rvert}\left(1+\beta_3\lvert\tau\rvert+\frac{1}{3}\beta_3^2\lvert\tau\rvert^2\right)$
n	$\frac{(2\beta_n)^{2n-1}\lvert\Gamma(n)\rvert^2}{(2n-2)![(2\pi f)^2+\beta_n^2]^n}$	$\sigma^2 e^{-\beta_n\lvert\tau\rvert}\sum_{k=0}^{n-1}\frac{\Gamma(n)(2\beta_n\lvert\tau\rvert)^{n-k-1}}{(2n-2)!k!\Gamma(n-k)}$
$n\to\infty$	$4\pi^2\sigma^2\delta(f)$	σ^2

Table D.1: Characteristics of the stationary Gauss-Markov process from [9, Tab. 2.2-1]. $\Gamma(n)$ denotes the Gamma function

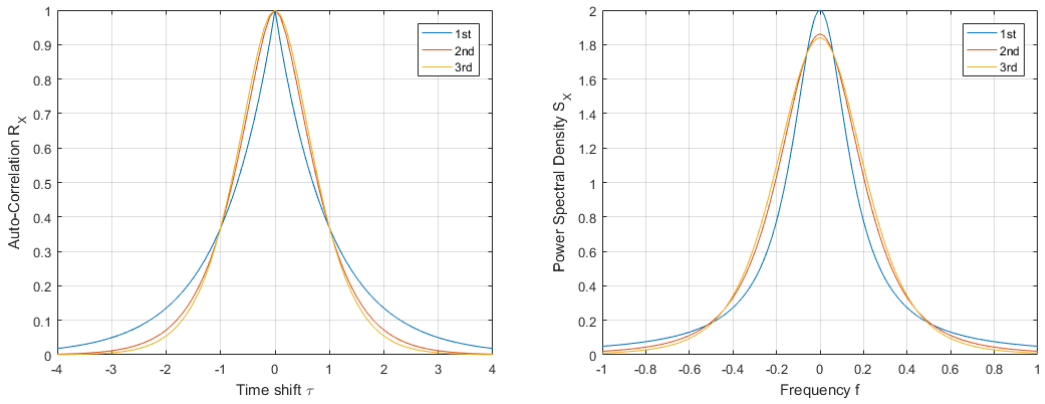

Figure D.7: Auto-correlation and power spectral density functions for the first, second and third order Gauss-Markov processes. The variance is $\sigma^2 = 1$ and the correlation parameter for the first order case is $\beta_1 = 1$. The second and third order correlation parameter is adjusted such that $R_X(\tau = 1) = \sigma^2 e^{-\beta_1}$. (Left): auto-correlation; (Right): power spectral density

D.4 Linear Dynamic System Models

Suppose we are confronted with a physical system that can be subjected to both controllable deterministic input and uncontrollable stochastic input. Moreover, suppose that the dynamics of such a system can be described "adequately" in the form of a linear differential equation which we can express using **state-space notation** as [17, Eq. 2-38]:

$$\dot{\mathbf{x}}(t) = \mathbf{F}(t)\,\mathbf{x}(t) + \mathbf{B}(t)\,\mathbf{u}(t) + \mathbf{G}(t)\,\mathbf{w}_s(t)\,, \tag{D.40}$$

where

- $\mathbf{x}(t)$ is an n-dimensional state vector containing the set of n variables that are used to describe the system. In inertial navigation, these variables are typically position, velocity, attitude and sensor biases
- $\mathbf{F}(t)$ is an $n \times n$ system matrix describing the dynamics of the situation and typically represents the "physics" of the situation. In inertial navigation it is formed using the navigation equations or the error dynamics equations
- $\mathbf{u}(t)$ is an r-dimensional vector representing deterministic input to the system
- $\mathbf{B}(t)$ is an $n \times r$ input matrix, relating the input forces to the state variables
- $\mathbf{w}_s(t)$ is a k-dimensional vector representing stochastic input to the system Here we restrict ourselves to Gaussian white noise
- $\mathbf{G}(t)$ is an $n \times k$ system noise distribution matrix relating white noise to the state variables of the system

From this physical system, we want to extract certain outputs and characterise them in terms of their mean and covariance values at all times. This can be expressed as [17, Eq. 2-39]:

$$\mathbf{z}(t) = \mathbf{H}(t)\,\mathbf{x}(t) + \mathbf{w}_m(t)\ , \tag{D.41}$$

where

- $\mathbf{z}(t)$ is an m-dimensional measurement vector
- $\mathbf{H}(t)$ is an $m \times n$ measurement matrix relating the state variables to the system output or observables
- $\mathbf{w}_m(t)$ is an m-dimensional measurement noise vector

such that each system observable is assumed to be a linear combination of state variables, corrupted by white Gaussian noise.

Since we are dealing with stochastic processes, the state vector, $\mathbf{x}(t)$, and measurement vector, $\mathbf{z}(t)$, will represent probability distributions. These distributions will be characterised by their first- and second-order moments, i.e. the mean values, $\hat{\mathbf{x}}(t)$ and $\hat{\mathbf{z}}(t)$, and the associated error covariance matrix, $\mathbf{P}(t)$, and measurement noise covariance matrix, $\mathbf{R}(t)$, respectively. These are defined as

$$\mathbf{Q}(t) = \mathrm{E}\left[\mathbf{w}_s(t)\,\mathbf{w}_s^\top(t)\right] \qquad \textbf{(system noise covariance matrix)}$$

$$\mathbf{R}(t) = \mathrm{E}\left[\mathbf{w}_m(t)\,\mathbf{w}_m^\top(t)\right] \qquad \textbf{(measurement noise covariance matrix)}$$

$$\mathbf{P}(t) = \mathrm{E}\left[\left\{\mathbf{x}(t) - \hat{\mathbf{x}}(t)\right\}\left\{\mathbf{x}(t) - \hat{\mathbf{x}}(t)\right\}^\top\right] = \mathrm{E}\left[\delta\mathbf{x}(t)\,\delta\mathbf{x}^\top(t)\right] \quad \textbf{(error covariance matrix)}$$

where the system noise covariance matrix, $\mathbf{Q}(t)$, was also introduced. The error covariance related to the state vector is therefore defined in terms of the **state vector residual**, $\delta\mathbf{x}(t)$, which is the difference between the true state vector, $\mathbf{x}(t)$, and the Kalman filter estimates thereof, $\hat{\mathbf{x}}(t)$. Since we will assume that these distributions are Gaussian, the first two

moments fully describe the probability distribution and no higher order moments are needed. The system noise, measurement noise and state vector residuals are moreover assumed to be non-correlated:

$$\mathrm{E}\left[\mathbf{w}_s(t)\,\mathbf{w}_m^\top(t)\right] = \mathrm{E}\left[\mathbf{w}_m(t)\,\mathbf{w}_s^\top(t)\right] = \mathbf{0} \tag{D.42}$$

$$\mathrm{E}\left[\mathbf{w}_s(t)\,\delta\mathbf{x}^\top(t)\right] = \mathrm{E}\left[\delta\mathbf{x}(t)\,\mathbf{w}_s^\top(t)\right] = \mathbf{0} \tag{D.43}$$

$$\mathrm{E}\left[\mathbf{w}_m(t)\,\delta\mathbf{x}^\top(t)\right] = \mathrm{E}\left[\delta\mathbf{x}(t)\,\mathbf{w}_m^\top(t)\right] = \mathbf{0} \tag{D.44}$$

and assuming that the noise sources are white, the system and measurement noise vectors will be uncorrelated in time:

$$\begin{aligned}\mathrm{E}\left[\mathbf{w}_s(t)\,\mathbf{w}_s^\top(t')\right] &= \mathbf{Q}(t)\,\delta\left(t-t'\right)\\ \mathrm{E}\left[\mathbf{w}_m(t)\,\mathbf{w}_m^\top(t')\right] &= \mathbf{R}(t)\,\delta\left(t-t'\right)\ ,\end{aligned} \tag{D.45}$$

where δ is the Dirac delta function. Since the noise sources are assumed white, a comparison with (D.17) implies that $\mathbf{Q}(t)$ and $\mathbf{R}(t)$ are diagonal matrices comprising the amplitude of the power spectral density components. They are therefore known as **spectral density matrices** that can be converted to covariance matrices through multiplication by the Dirac delta function.

The equations (D.40) and (D.41) represent the basic continuous-time description of a linear dynamic system and the associated measurements. For the applications in this dissertation, we can omit the deterministic driving terms in the system model. Moreover, we are interested in data samples rather than continuous output. The **system and measurement models** may therefore be modified for our purposes [10, Eqs. 3.26,3.51]:

$$\boxed{\dot{\mathbf{x}}(t) = \mathbf{F}(t)\,\mathbf{x}(t) + \mathbf{G}(t)\,\mathbf{w}_s(t)\ ,} \tag{D.46a}$$

$$\boxed{\mathbf{z}(t_k) = \mathbf{H}(t_k)\,\mathbf{x}(t_k) + \mathbf{w}_m(t_k)\ ,} \tag{D.46b}$$

where the state vector, $\mathbf{x}(t)$, and measurement vector, $\mathbf{z}(t_k)$, are characterised in terms of both mean values and error covariance. The dynamic processes underlying the system model will be continuous in time, while the measurement model has a discrete-time nature, t_k, related to the sampling times.

D.4.1 Sampled Continuous-Time Systems

In order to obtain samples from the linear system, we need to solve the differential equation (D.46a) at discrete instances in time. From (B.35) the solution can be written on the form[5]

$$\mathbf{x}\left(t_k\right) = \mathbf{\Phi}\left(t_k, t_0\right)\,\mathbf{x}\left(t_0\right) + \int_{t_0}^{t_k} \mathbf{\Phi}\left(t_k, t'\right)\,\mathbf{G}\left(t'\right)\mathbf{w}_s\left(t'\right)\,\mathrm{d}t'\ , \tag{D.47}$$

where $\mathbf{\Phi}\left(t_k, t_0\right)$ is known as the state transition matrix and is governed by the matrix differential equation

$$\frac{\mathrm{d}}{\mathrm{d}t}\mathbf{\Phi}\left(t_k, t_0\right) + \mathbf{F}(t)\,\mathbf{\Phi}\left(t_k, t_0\right) = \mathbf{0} \quad \text{with} \quad \mathbf{\Phi}\left(t_k, t_k\right) = \mathbf{I}\ , \tag{D.48}$$

[5] A proper derivation of this expression, taking into account the stochastic nature of the second term, can be found in [17, Sec. 4.4-4.8]

and where t_0 is the time at which we know the initial or current value of $\mathbf{x}$. This may seem like we have just substituted one differential equation for another. However, in the case that $\mathbf{F}(t) = \mathbf{F}$ is a constant matrix, the transition matrix may be expressed in the form (B.27)

$$\mathbf{\Phi}\left(t_k, t_0\right) = e^{\mathbf{F}(t_k - t_0)} = \mathbf{I} + \sum_{n=1}^{\infty} \frac{\mathbf{F}^n \left(t_k - t_0\right)^n}{n!} \ , \tag{D.49}$$

where the solution must be written as a truncated series, since $e^{\mathbf{F}(t_k - t_0)}$ cannot be evaluated on closed form. Thus, assuming that $\mathbf{F}(t)$ is constant during each update interval, $\delta t = t_k - t_{k-1}$, the state vector may be propagated recursively as

$$\begin{aligned} \mathbf{x}\left(t_k\right) &= \mathbf{\Phi}\left(t_k, t_{k-1}\right) \mathbf{x}\left(t_{k-1}\right) + \int_{t_{k-1}}^{t_k} \mathbf{\Phi}\left(t_k, t'\right) \mathbf{G}\left(t'\right) \mathbf{w}_s\left(t'\right) \mathrm{d}t' \\ &= \mathbf{\Phi}\left(t_k, t_{k-1}\right) \mathbf{x}\left(t_{k-1}\right) + \mathbf{w}_d\left(t_{k-1}\right) \ , \end{aligned} \tag{D.50}$$

between each time sample, t_k, or possibly at even smaller time increments in order to achieve better precision. This expression is closely related to the **discrete-time system model**

$$\mathbf{x}_k = \mathbf{\Phi}_{k-1} \mathbf{x}_{k-1} + \mathbf{\Gamma}_{k-1} \mathbf{w}_{s,k-1} \ , \tag{D.51}$$

where

$$\begin{aligned} \mathbf{\Phi}_{k-1} &\equiv \mathbf{\Phi}\left(t_k, t_{k-1}\right) = e^{\mathbf{F}(t_k - t_{k-1})} \quad \text{and} \\ \mathbf{\Gamma}_{k-1} \mathbf{w}_{s,k-1} &\equiv \mathbf{w}_d\left(t_{k-1}\right) = \int_{t_{k-1}}^{t_k} \mathbf{\Phi}\left(t_k, t'\right) \mathbf{G}\left(t'\right) \mathbf{w}_s\left(t'\right) \mathrm{d}t' \ , \end{aligned} \tag{D.52}$$

noticing that $\mathbf{\Gamma}_{k-1} \mathbf{w}_{s,k-1}$ is a vector of stochastic processes and that only the matrix-vector product is defined, not the individual terms, $\mathbf{\Gamma}_{k-1}$ and $\mathbf{w}_{s,k-1}$.

Now, having derived such a discrete-time model from the continuous-time model, we are interested in the propagation of the first two moments of the stochastic process, namely the mean and the covariance of the process, over the update interval, $\delta t = t_k - t_{k-1}$. These two will be treated separately in the following.

The State Vector

The mean value of the stochastic process, $\hat{\mathbf{x}}$, represents the estimate of the state vector and is defined as

$$\begin{aligned} \hat{\mathbf{x}}\left(t_k\right) &\equiv \mathrm{E}\left[\mathbf{x}\left(t_k\right)\right] = \mathrm{E}\left[\mathbf{\Phi}\left(t_k, t_{k-1}\right) \mathbf{x}\left(t_{k-1}\right) + \mathbf{w}_d\left(t_{k-1}\right)\right] \\ &= \mathbf{\Phi}\left(t_k, t_{k-1}\right) \mathrm{E}\left[\mathbf{x}\left(t_{k-1}\right)\right] + \mathrm{E}\left[\mathbf{w}_d\left(t_{k-1}\right)\right] \\ &= \mathbf{\Phi}\left(t_k, t_{k-1}\right) \hat{\mathbf{x}}\left(t_{k-1}\right) \ , \end{aligned} \tag{D.53}$$

where it was assumed that the expectation operator, $\mathrm{E}[.]$, commutes with the transition matrix, $\mathbf{\Phi}\left(t_k, t_{k-1}\right)$, since it is a known function and that

$$\begin{aligned} \mathrm{E}\left[\mathbf{w}_d\left(t_k\right)\right] &= \mathrm{E}\left[\int_{t_{k-1}}^{t_k} \mathbf{\Phi}\left(t_k, t'\right) \mathbf{G}\left(t'\right) \mathbf{w}_s\left(t'\right) \mathrm{d}t'\right] \\ &= \int_{t_{k-1}}^{t_k} \mathbf{\Phi}\left(t_k, t'\right) \mathbf{G}\left(t'\right) \mathrm{E}\left[\mathbf{w}_s\left(t'\right)\right] \mathrm{d}t' \\ &= \mathbf{0} \ , \end{aligned} \tag{D.54}$$

since the mean of a Gaussian white noise process is zero.

The Error Covariance Matrix
The covariance of the stochastic process, $\mathbf{P}$, corresponds to the error covariance matrix associated with the state vector and is defined as

$$\begin{aligned}
\mathbf{P}\left(t_k\right) &\equiv \mathrm{E}\left[\delta\mathbf{x}(t_k)\delta\mathbf{x}^\top(t_k)\right] \\
&= \mathrm{E}\left[\left\{\mathbf{\Phi}\left(t_k,t_{k-1}\right)\delta\mathbf{x}(t_{k-1})+\mathbf{w}_d\left(t_{k-1}\right)\right\}\left\{\mathbf{\Phi}\left(t_k,t_{k-1}\right)\delta\mathbf{x}(t_{k-1})+\mathbf{w}_d\left(t_{k-1}\right)\right\}^\top\right] \\
&= \mathrm{E}\left[\left\{\mathbf{\Phi}\left(t_k,t_{k-1}\right)\delta\mathbf{x}(t_{k-1})+\mathbf{w}_d\left(t_{k-1}\right)\right\}\left\{\delta\mathbf{x}^\top(t_{k-1})\mathbf{\Phi}^\top\left(t_k,t_{k-1}\right)+\mathbf{w}_d^\top\left(t_{k-1}\right)\right\}\right] \\
&= \mathrm{E}\Big[\mathbf{\Phi}\left(t_k,t_{k-1}\right)\delta\mathbf{x}(t_{k-1})\delta\mathbf{x}^\top(t_{k-1})\mathbf{\Phi}^\top\left(t_k,t_{k-1}\right)+\mathbf{\Phi}\left(t_k,t_{k-1}\right)\delta\mathbf{x}(t_{k-1})\mathbf{w}_d^\top\left(t_{k-1}\right) \\
&\qquad +\mathbf{w}_d\left(t_{k-1}\right)\delta\mathbf{x}^\top(t_{k-1})\mathbf{\Phi}^\top\left(t_k,t_{k-1}\right)+\mathbf{w}_d\left(t_{k-1}\right)\mathbf{w}_d^\top\left(t_{k-1}\right)\Big] \\
&= \mathbf{\Phi}\left(t_k,t_{k-1}\right)\mathrm{E}\left[\delta\mathbf{x}(t_{k-1})\delta\mathbf{x}^\top(t_{k-1})\right]\mathbf{\Phi}^\top\left(t_k,t_{k-1}\right) \\
&\qquad +\mathbf{\Phi}\left(t_k,t_{k-1}\right)\mathrm{E}\left[\delta\mathbf{x}(t_{k-1})\mathbf{w}_d^\top\left(t_{k-1}\right)\right] \\
&\qquad +\mathrm{E}\left[\mathbf{w}_d\left(t_{k-1}\right)\delta\mathbf{x}^\top(t_{k-1})\right]\mathbf{\Phi}^\top\left(t_k,t_{k-1}\right)+\mathrm{E}\left[\mathbf{w}_d\left(t_{k-1}\right)\mathbf{w}_d^\top\left(t_{k-1}\right)\right] \\
&= \mathbf{\Phi}\left(t_k,t_{k-1}\right)\mathbf{P}\left(t_{k-1}\right)\mathbf{\Phi}^\top\left(t_k,t_{k-1}\right)+\mathbf{Q}_k\ ,
\end{aligned} \tag{D.55}$$

where the non-correlation properties of (D.42) were exploited and the system noise covariance matrix is defined as

$$\begin{aligned}
\mathbf{Q}_k &\equiv \mathrm{E}\left[\mathbf{w}_d\left(t_{k-1}\right)\mathbf{w}_d^\top\left(t_{k-1}\right)\right] \\
&= \mathrm{E}\left[\left\{\int_{t_{k-1}}^{t_k}\mathbf{\Phi}\left(t_k,t'\right)\,\mathbf{G}\left(t'\right)\mathbf{w}_s\left(t'\right)\,\mathrm{d}t'\right\}\left\{\int_{t_{k-1}}^{t_k}\mathbf{\Phi}\left(t_k,t''\right)\,\mathbf{G}\left(t''\right)\mathbf{w}_s\left(t''\right)\,\mathrm{d}t''\right\}^\top\right] \\
&= \int_{t_{k-1}}^{t_k}\int_{t_{k-1}}^{t_k}\mathbf{\Phi}\left(t_k,t'\right)\,\mathbf{G}\left(t'\right)\,\mathrm{E}\left[\mathbf{w}_s\left(t'\right)\,\mathbf{w}_s^\top\left(t''\right)\right]\mathbf{G}^\top\left(t''\right)\mathbf{\Phi}^\top\left(t_k,t''\right)\,\mathrm{d}t'\mathrm{d}t'' \\
&= \int_{t_{k-1}}^{t_k}\int_{t_{k-1}}^{t_k}\mathbf{\Phi}\left(t_k,t'\right)\,\mathbf{G}\left(t'\right)\,\mathbf{Q}(t')\delta\left(t'-t''\right)\,\mathbf{G}^\top\left(t''\right)\mathbf{\Phi}^\top\left(t_k,t''\right)\,\mathrm{d}t'\mathrm{d}t'' \\
&= \int_{t_{k-1}}^{t_k}\mathbf{\Phi}\left(t_k,t'\right)\,\mathbf{G}\left(t'\right)\,\mathbf{Q}(t')\,\mathbf{G}^\top\left(t'\right)\mathbf{\Phi}^\top\left(t_k,t'\right)\,\mathrm{d}t'\ .
\end{aligned} \tag{D.56}$$

This expression may again be related to a discrete-time system model as

$$\mathbf{\Gamma}_{k-1}\,\mathbf{Q}_{k-1}\,\mathbf{\Gamma}_{k-1}^\top \equiv \mathbf{Q}_k = \int_{t_{k-1}}^{t_k}\mathbf{\Phi}\left(t_k,t'\right)\,\mathbf{G}\left(t'\right)\,\mathbf{Q}(t')\,\mathbf{G}^\top\left(t'\right)\mathbf{\Phi}^\top\left(t_k,t'\right)\,\mathrm{d}t'\ , \tag{D.57}$$

where

$$\mathbf{\Gamma}_{k-1}\,\mathbf{Q}_{k-1}\,\mathbf{\Gamma}_{k-1}^\top = \mathrm{E}\left[\left(\mathbf{\Gamma}_{k-1}\,\mathbf{w}_{s,k-1}\right)\left(\mathbf{\Gamma}_{k-1}\,\mathbf{w}_{s,k-1}\right)^\top\right]\ , \tag{D.58}$$

is the error covariance matrix of the corresponding random sequence. It should be noticed that the nature of the two matrices, $\mathbf{Q}(t)$ and $\mathbf{Q}_k$, are different. As already mentioned $\mathbf{Q}(t)$ is a spectral density matrix, whereas $\mathbf{Q}_k$ is a covariance matrix. From (D.17) we know that a spectral density matrix can be converted to a covariance matrix through multiplication with the Dirac delta function, which has units of 1/time [9, Sec. 3.6].

D.4.2 The Discrete-Time System Model

Our starting point for describing a linear dynamic system was the continuous-time model in (D.46), sampled at discrete points in time as

$$\begin{aligned} \dot{\mathbf{x}}(t) &= \mathbf{F}(t)\,\mathbf{x}(t) + \mathbf{G}(t)\,\mathbf{w}_s(t)\ , \\ \mathbf{z}(t_k) &= \mathbf{H}(t_k)\,\mathbf{x}(t_k) + \mathbf{w}_m(t_k)\ . \end{aligned} \tag{D.59}$$

In the previous section, we developed the **corresponding discrete-time model** as

$$\boxed{\mathbf{x}_{k+1} = \boldsymbol{\Phi}_k\,\mathbf{x}_k + \boldsymbol{\Gamma}_k\,\mathbf{w}_{s,k}\ ,} \tag{D.60a}$$

$$\boxed{\mathbf{z}_k = \mathbf{H}_k\,\mathbf{x}_k + \mathbf{w}_{m,k}\ ,} \tag{D.60b}$$

which could be used to propagate the state vector, $\mathbf{x}_k$, and associated error covariance matrix, $\mathbf{P}_k$, forward in time recursively as

$$\mathbf{x}_{k+1} = \boldsymbol{\Phi}_k\,\mathbf{x}_k \quad \text{and} \quad \mathbf{P}_{k+1} = \boldsymbol{\Phi}_k\,\mathbf{P}_k\,\boldsymbol{\Phi}_k^\top + \boldsymbol{\Gamma}_k\,\mathbf{Q}_k\,\boldsymbol{\Gamma}_k^\top\ . \tag{D.61}$$

Assuming that the system matrix, $\mathbf{F}(t)$, is constant during the propagation interval, $\delta t = t_{k+1} - t_k$, the transition matrix, $\boldsymbol{\Phi}_k$, can be computed from the system matrix using the series expansion

$$\boldsymbol{\Phi}_k \equiv \boldsymbol{\Phi}\left(t_{k+1}, t_k\right) = e^{\mathbf{F}_k \delta t} = \mathbf{I} + \sum_{n=1}^{\infty} \frac{(\mathbf{F}_k \delta t)^n}{n!}\ , \tag{D.62}$$

which must be truncated at some degree, depending on the desired accuracy. The system noise in the continuous-time and discrete-time models were related as

$$\boldsymbol{\Gamma}_k\,\mathbf{Q}_k\,\boldsymbol{\Gamma}_k^\top \equiv \int_{t_k}^{t_{k+1}} e^{\mathbf{F}_k\left(t_{k+1}-t'\right)}\,\mathbf{G}_k\,\mathbf{W}_{s,k}\,\mathbf{G}_k^\top e^{\mathbf{F}_k^\top\left(t_{k+1}-t'\right)}\,\mathrm{d}t'\ , \tag{D.63}$$

where the system noise distribution matrix, $\mathbf{G}\,(t)$, is assumed constant over the propagation interval and $\mathbf{W}_{s,k}$ is the spectral density matrix. The system noise contribution can therefore be computed by evaluating the above integral. The above expression is dependent on the actual system model and must therefore be evaluated on a case-by-case basis.

For systems of large dimensionality it becomes cumbersome to form explicit expressions for $\boldsymbol{\Phi}$ and $\boldsymbol{\Gamma}_k\,\mathbf{Q}_k\,\boldsymbol{\Gamma}_k^\top$. An efficient approach for solving large scale system was formulated by [20]. This **method of van Load** is outlined in [5, Sec. 3.9]:

1. Form the $2n \times 2n$ matrix

$$\mathbf{A}_k = \left[\begin{array}{c|c} -\mathbf{F}_k & \mathbf{G}_k\,\mathbf{W}_{s,k}\,\mathbf{G}_k^\top \\ \hline \mathbf{0} & \mathbf{F}^\top \end{array}\right] \delta t\ , \tag{D.64}$$

   where n is the dimension of $\mathbf{x}$ and δt is the propagation interval

2. Form the matrix exponential (can be done using MATLAB or other software)

$$\mathbf{B}_k = \operatorname{expm}\left(\mathbf{A}_k\right) = \left[\begin{array}{c|c} e^{-\mathbf{F}_k \delta t} & e^{-\mathbf{F}_k \delta t}\boldsymbol{\Gamma}_k\,\mathbf{Q}_k\,\boldsymbol{\Gamma}_k^\top \\ \hline \mathbf{0} & e^{\mathbf{F}_k^\top \delta t} \end{array}\right] = \left[\begin{array}{c|c} \boldsymbol{\Phi}_k^{-1} & \boldsymbol{\Phi}_k^{-1}\boldsymbol{\Gamma}_k\,\mathbf{Q}_k\,\boldsymbol{\Gamma}_k^\top \\ \hline \mathbf{0} & \boldsymbol{\Phi}_k^\top \end{array}\right] \tag{D.65}$$

3. Obtain the transition matrix, $\mathbf{\Phi}_k$, by transposing the lower-right partition of $\mathbf{B}_k$
4. Obtain the system noise covariance matrix, $\mathbf{\Gamma}_k \, \mathbf{Q}_k \, \mathbf{\Gamma}_k^\top$, by applying the transition matrix, $\mathbf{\Phi}_k$, to the upper-right partition of $\mathbf{B}_k$

This numerical approach to the evaluation of $\mathbf{\Phi}$ and $\mathbf{\Gamma}_k \, \mathbf{Q}_k \, \mathbf{\Gamma}_k^\top$ is quite useful when experimenting with various system and stochastic models.

Another option that is only valid for small propagation intervals ($\delta t \leq 0.2$ seconds) is to completely neglect the transition matrix over the propagation interval and approximate the system noise covariance matrix as [10, Eq. 14.82]

$$\mathbf{\Gamma}_k \, \mathbf{Q}_k \, \mathbf{\Gamma}_k^\top \approx \mathbf{G}_k \, \mathbf{W}_{s,k} \, \mathbf{G}_k^\top \, \delta t \; , \tag{D.66}$$

which represents the limit as $\delta t \to 0$, omitting terms order δt^2 and is known as the impulse approximation [9, Sec. 3.7].

D.4.3 Shaping Filters and State Augmentation

In the applications related to the Kalman filter, we are limiting ourselves to the use of white Gaussian noise, which may not be adequate to describe the underlying stochastic processes. However, using a linear time-invariant system, also known as a **shaping filter**, other stochastic processes such as random constants, random walks and Gauss-Markov processes can be generated using white Gaussian noise as the driving source. First, suppose that our system and measurement models are

$$\dot{\mathbf{x}}(t) = \mathbf{F}(t) \, \mathbf{x}(t) + \mathbf{G}(t) \, \mathbf{n}(t) \; , \tag{D.67a}$$
$$\mathbf{z}(t_i) = \mathbf{H}(t_i) \, \mathbf{x}(t_i) + \mathbf{w}_m(t_i) \; , \tag{D.67b}$$

where $\mathbf{n}(t)$ is a time-correlated, non-white stochastic process. Then, suppose that the noise, $\mathbf{n}(t)$, can be generated using a linear shaping filter as [17, Eq. 4.148]:

$$\dot{\mathbf{x}}_f(t) = \mathbf{F}_f(t) \, \mathbf{x}_f(t) + \mathbf{G}_f(t) \, \mathbf{w}(t) \; , \tag{D.68a}$$
$$\mathbf{n}(t) = \mathbf{H}_f(t) \, \mathbf{x}_f(t) \; . \tag{D.68b}$$

We can then define an **augmented state vector**, $\mathbf{x}_a(t)$, representing the state variables in an augmented system model:

$$\begin{aligned} \dot{\mathbf{x}}_a(t) &= \mathbf{F}_a(t) \, \mathbf{x}_a(t) + \mathbf{G}_a(t) \, \mathbf{w}(t) \\ \left[\begin{array}{c} \dot{\mathbf{x}}(t) \\ \hline \dot{\mathbf{x}}_f(t) \end{array} \right] &= \left[\begin{array}{c|c} \mathbf{F}(t) & \mathbf{G}(t) \, \mathbf{H}_f(t) \\ \hline \mathbf{0} & \mathbf{F}_f(t) \end{array} \right] \left[\begin{array}{c} \mathbf{x}(t) \\ \hline \mathbf{x}_f(t) \end{array} \right] + \left[\begin{array}{c} \mathbf{0} \\ \hline \mathbf{G}_f(t) \end{array} \right] \mathbf{w}(t) \; , \end{aligned} \tag{D.69}$$

and the associated augmented measurement model

$$\begin{aligned} \dot{\mathbf{z}}(t) &= \mathbf{H}_a(t) \, \mathbf{x}_a(t) + \mathbf{w}_m(t) \\ \mathbf{z}(t) &= \left[\begin{array}{c|c} \mathbf{H}(t) & \mathbf{0} \end{array} \right] \left[\begin{array}{c} \mathbf{x}(t) \\ \hline \mathbf{x}_f(t) \end{array} \right] + \mathbf{w}_m(t) \; , \end{aligned} \tag{D.70}$$

which then represents an augmented linear dynamic system model, driven only by white Gaussian noise.

In the following, some relevant examples will be briefly introduced. The stochastic processes were already introduced in Section D.3. We start by assuming that the state variables are the position, $\mathbf{p}$, velocity, $\mathbf{v}$ and attitude, $\boldsymbol{\psi}$, of a vehicle, such that the state vector and associated system model becomes

$$\mathbf{x}(t) = \begin{bmatrix} \mathbf{p}(t) \\ \mathbf{v}(t) \\ \boldsymbol{\psi}(t) \end{bmatrix} \quad \text{and} \quad \dot{\mathbf{x}}(t) = \mathbf{F}(t)\,\mathbf{x}(t) + \mathbf{G}(t)\,\mathbf{n}(t)\ , \tag{D.71}$$

and that we want to take samples of velocity and position, such that the measurement vector and model becomes

$$\mathbf{z}(t_i) = \begin{bmatrix} \mathbf{p}(t_i) \\ \mathbf{v}(t_i) \end{bmatrix} \quad \text{and} \quad \mathbf{z}(t_i) = \begin{bmatrix} \mathbf{I}_3 & \mathbf{0}_3 & \mathbf{0}_3 \\ \mathbf{0}_3 & \mathbf{I}_3 & \mathbf{0}_3 \end{bmatrix} \mathbf{x}(t_i) + \mathbf{w}_m(t_i)\ . \tag{D.72}$$

Random Walk

The accelerometer and gyro observations are typically corrupted by noise. Assuming this noise is white and Gaussian, the velocity and attitude errors will be subject to integrated white noise, i.e. random walk. This model is also known as Brownian motion and is governed by the differential equation (D.27):

$$\dot{x}_f(t) = w(t) \quad \text{and} \quad x_f\,(t_0) = 0\ , \tag{D.73}$$

where $w(t)$ is a zero-mean, white Gaussian process. This is achieved by adding a driving noise term to the augmented system model as

$$\begin{bmatrix} \dot{\mathbf{p}}(t) \\ \dot{\mathbf{v}}(t) \\ \dot{\boldsymbol{\psi}}(t) \end{bmatrix} = \mathbf{F}(t) \begin{bmatrix} \mathbf{p}(t) \\ \mathbf{v}(t) \\ \boldsymbol{\psi}(t) \end{bmatrix} + \begin{bmatrix} \mathbf{0}_3 & \mathbf{0}_3 \\ \mathbf{I}_3 & \mathbf{0}_3 \\ \mathbf{0}_3 & \mathbf{I}_3 \end{bmatrix} \begin{bmatrix} \mathbf{w}_a(t) \\ \mathbf{w}_g(t) \end{bmatrix}\ , \tag{D.74}$$

where $\mathbf{w}_a(t)$ and $\mathbf{w}_g(t)$ are 3-component vectors representing the stochastic driving terms for each of the six sensors. This does not require any augmentation of the system, i.e. any additional state variables. One could also introduce noise on the position, but this is currently omitted.

The stochastic properties of the random walk process is usually defined in terms of the PSD of the associated white noise process, rather than the associated variance or standard deviation. Manufacturers often specify the root of the PSD, such that the units for the gyroscope random walk is $\mathrm{rad}/s/\sqrt{\mathrm{Hz}}$ (or similarly $^\circ/\sqrt{\mathrm{hr}}$) and for the accelerometer random walk is $m/s^2/\sqrt{\mathrm{Hz}}$ (or similarly $\mathrm{mGal}/\sqrt{\mathrm{Hz}}$). The square of these values can therefore occupy the diagonal elements of the spectral density matrix, $\mathbf{W}_{s,k}$. The manufacturer specifications can however generally only be used as guidelines, as the actual stochastic process must also take into account imperfections in the dynamic system model. From (D.22), the standard deviation of the random noise samples is obtained from the root PSD by dividing by the root of the sampling interval.

Random Constant

As mentioned in Section 6.1, the sensor output will often be characterised by a run-to-run bias, which is different each time the sensor is turned on, but constant during operating time. Such errors can be modelled as a random constant, which is governed by the differential equation (D.24):

$$\dot{x}_f(t) = 0 \quad \text{and} \quad x_f\left(t_0\right) = x_{f,0}\ , \tag{D.75}$$

where $x_{f,0}$ is the initial condition, modelled as a Gaussian random variable with mean and variance. In this case, there is no driving noise term in the equation, meaning that the noise components are zero and the augmented system model becomes:

$$\left[\begin{array}{c} \dot{\mathbf{p}}(t) \\ \dot{\mathbf{v}}(t) \\ \dot{\boldsymbol{\psi}}(t) \\ \hline \dot{\mathbf{b}}_a \\ \dot{\mathbf{b}}_g \end{array}\right] = \left[\begin{array}{c|cc} & \mathbf{0}_3 & \mathbf{0}_3 \\ \mathbf{F}(t) & \mathbf{C} & \mathbf{0}_3 \\ & \mathbf{0}_3 & \mathbf{C} \\ \hline \mathbf{0}_{6\times 9} & \multicolumn{2}{c}{\mathbf{0}_6} \end{array}\right] \left[\begin{array}{c} \mathbf{p}(t) \\ \mathbf{v}(t) \\ \boldsymbol{\psi}(t) \\ \hline \mathbf{b}_a \\ \mathbf{b}_g \end{array}\right] + \left[\begin{array}{cc} \mathbf{0}_3 & \mathbf{0}_3 \\ \mathbf{I}_3 & \mathbf{0}_3 \\ \mathbf{0}_3 & \mathbf{I}_3 \\ \hline \mathbf{0}_3 & \mathbf{0}_3 \\ \mathbf{0}_3 & \mathbf{0}_3 \end{array}\right] \left[\begin{array}{c} \mathbf{w}_a(t) \\ \mathbf{w}_g(t) \end{array}\right] , \tag{D.76}$$

where $\mathbf{C}$ represents the transformation matrix from the sensor frame to the relevant reference frame, e.g. b-frame to n-frame. Manufacturers often specify the statistics of this run-to-run bias in terms of bias repeatability or instability which is in units of rad/s or °/hr for the gyroscope and m/s^2 or mGal for the accelerometer. These numbers refer to the standard deviation of the process and are used to form the initial error covariance matrix, $\mathbf{P}_0$. The run-to-run bias estimate is therefore only utilised in the initialisation process, since no system noise is added to the model. The associated augmented measurement model is

$$\begin{bmatrix} \mathbf{p}(t_i) \\ \mathbf{v}(t_i) \end{bmatrix} = \left[\begin{array}{ccc|c} \mathbf{I}_3 & \mathbf{0}_3 & \mathbf{0}_3 & \mathbf{0}_6 \\ \mathbf{0}_3 & \mathbf{I}_3 & \mathbf{0}_3 & \end{array}\right] \mathbf{x}(t_i) + \mathbf{w}_m(t_i)\ . \tag{D.77}$$

The random constant assumes that the bias magnitude does not change in time. As a result, an optimal filter will estimate its magnitude using initial data, but will essentially disregard all measurements that come later [17, Sec. 4.11]. A more appropriate model is perhaps to allow the bias to vary slowly in time. This variation may also be modelled as a random walk by adding a driving noise term to the augmented system model as

$$\left[\begin{array}{c} \dot{\mathbf{p}}(t) \\ \dot{\mathbf{v}}(t) \\ \dot{\boldsymbol{\psi}}(t) \\ \hline \dot{\mathbf{b}}_a(t) \\ \dot{\mathbf{b}}_g(t) \end{array}\right] = \left[\begin{array}{c|cc} & \mathbf{0}_3 & \mathbf{0}_3 \\ \mathbf{F}(t) & \mathbf{C} & \mathbf{0}_3 \\ & \mathbf{0}_3 & \mathbf{C} \\ \hline \mathbf{0}_{6\times 9} & \multicolumn{2}{c}{\mathbf{0}_6} \end{array}\right] \left[\begin{array}{c} \mathbf{p}(t) \\ \mathbf{v}(t) \\ \boldsymbol{\psi}(t) \\ \hline \mathbf{b}_a(t) \\ \mathbf{b}_g(t) \end{array}\right] + \left[\begin{array}{cccc} \mathbf{0}_3 & \mathbf{0}_3 & \mathbf{0}_3 & \mathbf{0}_3 \\ \mathbf{I}_3 & \mathbf{0}_3 & \mathbf{0}_3 & \mathbf{0}_3 \\ \mathbf{0}_3 & \mathbf{I}_3 & \mathbf{0}_3 & \mathbf{0}_3 \\ \hline \mathbf{0}_3 & \mathbf{0}_3 & \mathbf{I}_3 & \mathbf{0}_3 \\ \mathbf{0}_3 & \mathbf{0}_3 & \mathbf{0}_3 & \mathbf{I}_3 \end{array}\right] \left[\begin{array}{c} \mathbf{w}_a(t) \\ \mathbf{w}_g(t) \\ \hline \mathbf{w}_{a,\text{bias}}(t) \\ \mathbf{w}_{g,\text{bias}}(t) \end{array}\right] . \tag{D.78}$$

The statistic properties of the bias variation can also be specified in terms of the root PSD of the associated white noise process. For the gyroscope, this is in units of rad/$s^2/\sqrt{\text{Hz}}$ (or similarly °/hr/$\sqrt{s}$) and for the accelerometer the units are $m/s^3/\sqrt{\text{Hz}}$ (or similarly mGal/$\sqrt{s}$). The root PSD of the bias variation is rarely specified by the manufacturer, since the bias variation is not truly a random walk process. Instead, the in-run bias instability is often specified, which indicates the accuracy to which the bias can be estimated. This

is typically expressed as a standard deviation in units of rad/s for the gyroscope and m/s^2 for the accelerometer.

First-Order Gauss-Markov Model

The temporal variation of sensor biases may also be modelled as an exponentially time-correlated random process, also known as a Gauss-Markov process. The first-order Gauss-Markov model is governed by the differential equation (D.32):

$$\dot{x}_f(t) = -\beta x_f(t) + w(t) \,, \tag{D.79}$$

where $\beta = 1/T$ is the correlation time and $w(t)$ is (again) a zero-mean white Gaussian process. The state vector may be augmented by separating the bias states into static and dynamic components as

$$\dot{\mathbf{b}}_a(t) = \dot{\mathbf{b}}_{a,s} + \dot{\mathbf{b}}_{a,d}(t) \quad \text{and} \quad \dot{\mathbf{b}}_g(t) = \dot{\mathbf{b}}_{g,s} + \dot{\mathbf{b}}_{g,d}(t) \tag{D.80}$$

leading to the augmented system model

$$\begin{aligned}
\begin{bmatrix} \dot{\mathbf{p}}(t) \\ \dot{\mathbf{v}}(t) \\ \dot{\boldsymbol{\psi}}(t) \\ \hline \dot{\mathbf{b}}_{a,s} \\ \dot{\mathbf{b}}_{a,d}(t) \\ \dot{\mathbf{b}}_{g,s} \\ \dot{\mathbf{b}}_{g,d}(t) \end{bmatrix} &= \left[\begin{array}{c|cccc} & \mathbf{0}_3 & \mathbf{0}_3 & \mathbf{0}_3 & \mathbf{0}_3 \\ \mathbf{F}(t) & \mathbf{C} & \mathbf{C} & \mathbf{0}_3 & \mathbf{0}_3 \\ & \mathbf{0}_3 & \mathbf{0}_3 & \mathbf{C} & \mathbf{C} \\ \hline & \mathbf{0}_3 & \mathbf{0}_3 & \mathbf{0}_3 & \mathbf{0}_3 \\ \mathbf{0}_{12\times 9} & \mathbf{0}_3 & -\boldsymbol{\beta}_a & \mathbf{0}_3 & \mathbf{0}_3 \\ & \mathbf{0}_3 & \mathbf{0}_3 & \mathbf{0}_3 & \mathbf{0}_3 \\ & \mathbf{0}_3 & \mathbf{0}_3 & \mathbf{0}_3 & -\boldsymbol{\beta}_g \end{array}\right] \begin{bmatrix} \mathbf{p}(t) \\ \mathbf{v}(t) \\ \boldsymbol{\psi}(t) \\ \hline \mathbf{b}_{a,s} \\ \mathbf{b}_{a,d}(t) \\ \mathbf{b}_{g,s} \\ \mathbf{b}_{g,d}(t) \end{bmatrix} \\
&+ \left[\begin{array}{cccc} \mathbf{0}_3 & \mathbf{0}_3 & \mathbf{0}_3 & \mathbf{0}_3 \\ \mathbf{I}_3 & \mathbf{0}_3 & \mathbf{0}_3 & \mathbf{0}_3 \\ \mathbf{0}_3 & \mathbf{I}_3 & \mathbf{0}_3 & \mathbf{0}_3 \\ \hline \mathbf{0}_3 & \mathbf{0}_3 & \mathbf{0}_3 & \mathbf{0}_3 \\ \mathbf{0}_3 & \mathbf{0}_3 & \mathbf{I}_3 & \mathbf{0}_3 \\ \mathbf{0}_3 & \mathbf{0}_3 & \mathbf{0}_3 & \mathbf{0}_3 \\ \mathbf{0}_3 & \mathbf{0}_3 & \mathbf{0}_3 & \mathbf{I}_3 \end{array}\right] \begin{bmatrix} \mathbf{w}_a(t) \\ \mathbf{w}_g(t) \\ \hline \mathbf{w}_{a,\text{bias}}(t) \\ \mathbf{w}_{g,\text{bias}}(t) \end{bmatrix} \,,
\end{aligned} \tag{D.81}$$

where $\boldsymbol{\beta}_a$ and $\boldsymbol{\beta}_g$ are a diagonal matrices

$$\boldsymbol{\beta}_a = \begin{bmatrix} \beta_{a,x} & 0 & 0 \\ 0 & \beta_{a,y} & 0 \\ 0 & 0 & \beta_{a,z} \end{bmatrix} \quad \text{and} \quad \boldsymbol{\beta}_g = \begin{bmatrix} \beta_{g,x} & 0 & 0 \\ 0 & \beta_{g,y} & 0 \\ 0 & 0 & \beta_{g,z} \end{bmatrix} \,, \tag{D.82}$$

with diagonal elements representing the correlation time along each of the three sensor axes. The PSD amplitude of the associated white noise process is from (D.17) and (D.33):

$$S_{wn,1} = 2\sigma^2\beta \,, \tag{D.83}$$

where $\beta = 1/T$ is the correlation time with units of $1/s$ and σ is the standard deviation in units of rad/s for the gyro and m/s^2 for the accelerometer. The units of the root PSD are therefore $^\circ/\text{hr}/\sqrt{s}$ and $\text{mGal}/\sqrt{s}$, as for the random walk processes.

Higher-Order Gauss-Markov Models

When performing inertial navigation, the accelerometers will also sense a component of gravitational force. Since this acceleration does not originate from the movement of the vehicle, the sensed acceleration must first be corrected for this gravitational component before integrating for velocity. This is usually done using a gravitational model, which is of course not perfect. Therefore, we can add a state variable, $\delta\mathbf{g}$, accounting for the error in the gravity model. The stochastic behaviour of this error term could for example be approximated using an exponentially time-correlated model as a **second order Gauss-Markov** model, governed by the differential equation (D.35):

$$\ddot{x}(t) = -2\beta_2\dot{x}(t) - \beta_2^2 x(t) + w(t)\ , \tag{D.84}$$

where $\beta = 1/T$ is the correlation time and $w(t)$ is (again) a zero-mean white Gaussian process. This leads to the augmented system model

$$\begin{aligned}
\left[\begin{array}{c} \dot{\mathbf{p}}(t) \\ \dot{\mathbf{v}}(t) \\ \dot{\boldsymbol{\psi}}(t) \\ \hline \dot{\mathbf{b}}_a(t) \\ \dot{\mathbf{b}}_g(t) \\ \frac{\mathrm{d}}{\mathrm{d}t}\delta\mathbf{g}(t) \\ \frac{\mathrm{d}}{\mathrm{d}t}\delta\dot{\mathbf{g}}(t) \end{array}\right] &= \left[\begin{array}{ccc|cccc} & & & \mathbf{0}_3 & \mathbf{0}_3 & \mathbf{0}_3 & \mathbf{0}_3 \\ & \mathbf{F}(t) & & \mathbf{C} & \mathbf{0}_3 & \mathbf{I}_3 & \mathbf{0}_3 \\ & & & \mathbf{0}_3 & \mathbf{C} & \mathbf{0}_3 & \mathbf{0}_3 \\ \hline & & & \mathbf{0}_3 & \mathbf{0}_3 & \mathbf{0}_3 & \mathbf{0}_3 \\ & \mathbf{0}_{12\times 9} & & \mathbf{0}_3 & \mathbf{0}_3 & \mathbf{0}_3 & \mathbf{0}_3 \\ & & & \mathbf{0}_3 & \mathbf{0}_3 & \mathbf{0}_3 & \mathbf{I}_3 \\ & & & \mathbf{0}_3 & \mathbf{0}_3 & -\boldsymbol{\beta}_2^2 & -2\boldsymbol{\beta}_2 \end{array}\right] \left[\begin{array}{c} \mathbf{p}(t) \\ \mathbf{v}(t) \\ \boldsymbol{\psi}(t) \\ \hline \mathbf{b}_a(t) \\ \mathbf{b}_g(t) \\ \delta\mathbf{g}(t) \\ \delta\dot{\mathbf{g}}(t) \end{array}\right] \\
&+ \left[\begin{array}{ccccc} \mathbf{0}_3 & \mathbf{0}_3 & \mathbf{0}_3 & \mathbf{0}_3 & \mathbf{0}_3 \\ \mathbf{I}_3 & \mathbf{0}_3 & \mathbf{0}_3 & \mathbf{0}_3 & \mathbf{0}_3 \\ \mathbf{0}_3 & \mathbf{I}_3 & \mathbf{0}_3 & \mathbf{0}_3 & \mathbf{0}_3 \\ \hline \mathbf{0}_3 & \mathbf{0}_3 & \mathbf{I}_3 & \mathbf{0}_3 & \mathbf{0}_3 \\ \mathbf{0}_3 & \mathbf{0}_3 & \mathbf{0}_3 & \mathbf{I}_3 & \mathbf{0}_3 \\ \mathbf{0}_3 & \mathbf{0}_3 & \mathbf{0}_3 & \mathbf{0}_3 & \mathbf{0}_3 \\ \mathbf{0}_3 & \mathbf{0}_3 & \mathbf{0}_3 & \mathbf{0}_3 & \mathbf{I}_3 \end{array}\right] \left[\begin{array}{c} \mathbf{w}_a(t) \\ \mathbf{w}_g(t) \\ \hline \mathbf{w}_{a,\mathrm{bias}}(t) \\ \mathbf{w}_{g,\mathrm{bias}}(t) \\ \mathbf{w}_{\delta g_2}(t) \end{array}\right]\ ,
\end{aligned} \tag{D.85}$$

where the bias variation is again modelled as a random walk process. The PSD amplitude of the associated white noise process is from (D.17) and (D.36):

$$S_{\mathrm{wn},2} = 4\sigma^2\beta_2^3\ , \tag{D.86}$$

where σ is the standard deviation in units if m/s^2 and $\beta_2 = 1/T$ is the correlation time. As the gravity signal varies with position rather than time, the along-track correlation length β_2', in units of $1/m$, is typically used instead of correlation time, β_2. Although the correlation length is in general direction dependent, it is usually only divided into horizontal and vertical components, from which the correlation time may be derived as

$$\beta_{2,N} = |v_{\mathrm{hor}}|\,\beta_{2,\mathrm{hor}}'\ , \quad \beta_{2,E} = |v_{\mathrm{hor}}|\,\beta_{2,\mathrm{hor}}' \quad \text{and} \quad \beta_{2,D} = |v_{\mathrm{hor}}|\,\beta_{2,\mathrm{ver}}'\ , \tag{D.87}$$

where $|v_{\mathrm{hor}}| = \sqrt{v_N^2 + v_E^2}$ is the ground speed. Similarly, the PSD of the associated white noise processes may be derived as

$$\begin{aligned} S_{\text{wn},2,N} &= 4\sigma_{\text{hor}}^2 \left(\beta'_{2,\text{hor}}\right)^3 |v_{\text{hor}}|^3 , \\ S_{\text{wn},2,E} &= 4\sigma_{\text{hor}}^2 \left(\beta'_{2,\text{hor}}\right)^3 |v_{\text{hor}}|^3 \quad \text{and} \\ S_{\text{wn},2,D} &= 4\sigma_{\text{ver}}^2 \left(\beta'_{2,\text{ver}}\right)^3 |v_{\text{hor}}|^3 , \end{aligned} \tag{D.88}$$

where σ_{hor} and σ_{ver} are the standard deviations associated with the horizontal and vertical stochastic processes. The units associated with the root PSD are therefore $\text{mGal}/\sqrt{s^3}/\sqrt{\text{Hz}} = \text{mGal}/s$. The diagonal matrices in (D.85) contain the correlation times as

$$\boldsymbol{\beta}_2 = \begin{bmatrix} \beta_{2,N} & 0 & 0 \\ 0 & \beta_{2,E} & 0 \\ 0 & 0 & \beta_{2,D} \end{bmatrix} \quad \text{and} \quad \boldsymbol{\beta}_2^2 = \begin{bmatrix} \beta_{2,N}^2 & 0 & 0 \\ 0 & \beta_{2,E}^2 & 0 \\ 0 & 0 & \beta_{2,D}^2 \end{bmatrix} . \tag{D.89}$$

If we want to additionally extract the gravity error from the system, we have the measurement model

$$\left[\begin{array}{c} \mathbf{p}(t_i) \\ \mathbf{v}(t_i) \\ \hline \delta\mathbf{g}(t_i) \end{array}\right] = \left[\begin{array}{ccc|c} \mathbf{I}_3 & \mathbf{0}_3 & \mathbf{0}_3 & \multirow{2}{*}{$\mathbf{0}_{6\times 12}$} \\ \mathbf{0}_3 & \mathbf{I}_3 & \mathbf{0}_3 & \\ \hline \mathbf{0}_3 & \mathbf{0}_3 & \mathbf{0}_3 & \mathbf{0}_3 \; \mathbf{0}_3 \; \mathbf{I}_3 \; \mathbf{0}_3 \end{array}\right] \mathbf{x}(t_i) + \mathbf{w}_m(t_i) . \tag{D.90}$$

In a similar way, the gravity error may be modelled as a **third order Gauss-Markov model** with the augmented system

$$\begin{aligned} \left[\begin{array}{c} \dot{\mathbf{p}}(t) \\ \dot{\mathbf{v}}(t) \\ \dot{\boldsymbol{\psi}}(t) \\ \hline \dot{\mathbf{b}}_a(t) \\ \dot{\mathbf{b}}_g(t) \\ \frac{\mathrm{d}}{\mathrm{d}t}\delta\mathbf{g}(t) \\ \frac{\mathrm{d}}{\mathrm{d}t}\delta\dot{\mathbf{g}}(t) \\ \frac{\mathrm{d}}{\mathrm{d}t}\delta\ddot{\mathbf{g}}(t) \end{array}\right] &= \left[\begin{array}{c|ccccc} \multirow{3}{*}{$\mathbf{F}(t)$} & \mathbf{0}_3 & \mathbf{0}_3 & \mathbf{0}_3 & \mathbf{0}_3 & \mathbf{0}_3 \\ & \mathbf{C} & \mathbf{0}_3 & \mathbf{I}_3 & \mathbf{0}_3 & \mathbf{0}_3 \\ & \mathbf{0}_3 & \mathbf{C} & \mathbf{0}_3 & \mathbf{0}_3 & \mathbf{0}_3 \\ \hline \multirow{6}{*}{$\mathbf{0}_{15\times 9}$} & \mathbf{0}_3 & \mathbf{0}_3 & \mathbf{0}_3 & \mathbf{0}_3 & \mathbf{0}_3 \\ & \mathbf{0}_3 & \mathbf{0}_3 & \mathbf{0}_3 & \mathbf{0}_3 & \mathbf{0}_3 \\ & \mathbf{0}_3 & \mathbf{0}_3 & \mathbf{0}_3 & \mathbf{I}_3 & \mathbf{0}_3 \\ & \mathbf{0}_3 & \mathbf{0}_3 & \mathbf{0}_3 & \mathbf{0}_3 & \mathbf{I}_3 \\ & \mathbf{0}_3 & \mathbf{0}_3 & -\boldsymbol{\beta}_3^3 & -3\boldsymbol{\beta}_3^2 & -3\boldsymbol{\beta}_3 \end{array}\right] \left[\begin{array}{c} \mathbf{p}(t) \\ \mathbf{v}(t) \\ \boldsymbol{\psi}(t) \\ \hline \mathbf{b}_a(t) \\ \mathbf{b}_g(t) \\ \delta\mathbf{g}(t) \\ \delta\dot{\mathbf{g}}(t) \\ \delta\ddot{\mathbf{g}} \end{array}\right] \\ &+ \left[\begin{array}{ccccc} \mathbf{0}_3 & \mathbf{0}_3 & \mathbf{0}_3 & \mathbf{0}_3 & \mathbf{0}_3 \\ \mathbf{I}_3 & \mathbf{0}_3 & \mathbf{0}_3 & \mathbf{0}_3 & \mathbf{0}_3 \\ \mathbf{0}_3 & \mathbf{I}_3 & \mathbf{0}_3 & \mathbf{0}_3 & \mathbf{0}_3 \\ \hline \mathbf{0}_3 & \mathbf{0}_3 & \mathbf{I}_3 & \mathbf{0}_3 & \mathbf{0}_3 \\ \mathbf{0}_3 & \mathbf{0}_3 & \mathbf{0}_3 & \mathbf{I}_3 & \mathbf{0}_3 \\ \mathbf{0}_3 & \mathbf{0}_3 & \mathbf{0}_3 & \mathbf{0}_3 & \mathbf{0}_3 \\ \mathbf{0}_3 & \mathbf{0}_3 & \mathbf{0}_3 & \mathbf{0}_3 & \mathbf{0}_3 \\ \mathbf{0}_3 & \mathbf{0}_3 & \mathbf{0}_3 & \mathbf{0}_3 & \mathbf{I}_3 \end{array}\right] \left[\begin{array}{c} \mathbf{w}_a(t) \\ \mathbf{w}_g(t) \\ \hline \mathbf{w}_{a,\text{bias}}(t) \\ \mathbf{w}_{g,\text{bias}}(t) \\ \mathbf{w}_{\delta g_3}(t) \end{array}\right] , \end{aligned} \tag{D.91}$$

where the PSD of the associated white noise process is from (D.17) and (D.39):

$$S_{\text{wn},3} = \frac{16}{3}\sigma^2\beta^5 . \tag{D.92}$$

where σ is again the standard deviation and β the correlation time, with units as before. Assuming that these are again divided into horizontal and vertical components, the correlation time may be derived from (D.87) and the PSD of the associated white noise processes are

$$\begin{aligned} S_{\mathrm{wn},3,N} &= \tfrac{16}{3}\sigma^2_{\mathrm{hor}} \left(\beta'_{2,\mathrm{hor}}\right)^5 |v_{\mathrm{hor}}|^5 \,, \\ S_{\mathrm{wn},3,E} &= \tfrac{16}{3}\sigma^2_{\mathrm{hor}} \left(\beta'_{2,\mathrm{hor}}\right)^5 |v_{\mathrm{hor}}|^5 \quad \text{and} \\ S_{\mathrm{wn},3,D} &= \tfrac{16}{3}\sigma^2_{\mathrm{ver}} \left(\beta'_{2,\mathrm{ver}}\right)^5 |v_{\mathrm{hor}}|^5 \,, \end{aligned} \tag{D.93}$$

with units of the root PSD as $\mathrm{mGal}/\sqrt{s^5}/\sqrt{Hz} = \mathrm{mGal}/s^2$.

D.4.4 Optimal Linear Filtering

We have now developed a linear stochastic model for dynamic systems, assuming that the "state" of the system can be adequately described in terms of a state vector, $\mathbf{x}$, with a finite number of elements. We have also seen how the associated mean and covariance of these state variables can be propagated forward in time recursively, by formulating a corresponding discrete-time model. Finally, we have introduced measurements into the system as

$$\mathbf{z}_k = \mathbf{H}_k \, \mathbf{x}_k + \mathbf{w}_{m,k} \,, \tag{D.94}$$

which relates the observations, $\mathbf{z}_k$, to the state variables, $\mathbf{x}_k$, at some discrete instances in time, t_k. In general, all of the state variables cannot be observed directly and must be estimated indirectly from the available data. This procedure is however complicated since our system model will not be perfect, but partly driven by uncontrollable input and characterised by uncertainty in variable and output interrelations. Moreover, observations will be corrupted to some degree by noise, biases and other uncertainties in the instruments.

We therefore need to develop a framework that combines all of the available data, including any a priori knowledge, and filters all the information in order to arrive at optimal estimates of the state variables. Here optimal refers to a filter that minimises the errors in a statistical sense. In the following, we will pursue the minimum variance criteria, but assuming that the measurement model is linear and that system and measurement noises are white and Gaussian, the results will be the same for any statistical measure that makes sense [9, Sec. 4] and [17, Sec. 5].

Having obtained some observations, $\mathbf{z}_k$, at time, t_k, we want to introduce these observations into our system. Letting $\hat{\mathbf{x}}_k^-$ denote the estimate of the state vector at this time, it can be argued that an improved estimate, $\hat{\mathbf{x}}$, is obtained through a linear combination of the two

$$\hat{\mathbf{x}}_k = \mathbf{K}_k \mathbf{z}_k + \mathbf{L}_k \hat{\mathbf{x}}_k^- \tag{D.95}$$

where the superscript minus refers to the "non-improved", "non-updated" or *a priori* estimate, obtained by recursive means from the estimate at the previous epoch. $\mathbf{K}_k$ and $\mathbf{L}_k$ are weighting matrices. The relative weighting of the two matrices, $\mathbf{K}_k$ and $\mathbf{L}_k$, can be interpreted as a trade-off between the influence of the forward propagated state estimate, $\hat{\mathbf{x}}_k^-$, and the influence of the measurement, $\mathbf{z}_k$. This trade-off should therefore reflect the relative confidence that we have in our previous state estimate, $\hat{\mathbf{x}}_{k-1}$, the system model represented by the transition matrix, $\mathbf{\Phi}_{k-1}$, and the observation, $\mathbf{z}_k$.

The error on the estimate, $\hat{\mathbf{x}}$, is represented by the diagonal elements of the error covariance matrix, $\mathbf{P}$. These are the elements we want to minimise with respect to the weighting matrices, $\mathbf{K}$ and $\mathbf{L}$. First, however, we want to reformulate (D.95) in terms of $\mathbf{K}$ only, such

that we only need to minimise with respect to this term. We start by inserting (D.94) into (D.95) to obtain the expression

$$\hat{\mathbf{x}}_k = \mathbf{K}_k\mathbf{H}_k\mathbf{x}_k + \mathbf{K}_k\mathbf{w}_{m,k} + \mathbf{L}_k\hat{\mathbf{x}}_k^- \tag{D.96}$$

and then noting that the recursive method is an unbiased estimation algorithm [9, Sec. 3.7], the expectation of the state estimates, $\hat{\mathbf{x}}_k$, $\mathbf{x}_k$ and $\hat{\mathbf{x}}_k^-$, at the same time step, are the same. The expectation of the measurement noise is zero. Therefore, taking the expectation of the above expression, we have

$$\begin{aligned} \mathrm{E}\left[\hat{\mathbf{x}}_k\right] &= \mathbf{K}_k\mathbf{H}_k\mathrm{E}\left[\mathbf{x}_k\right] + \mathbf{K}_k\mathrm{E}\left[\mathbf{w}_{m,k}\right] + \mathbf{L}_k\mathrm{E}\left[\hat{\mathbf{x}}_k^-\right] \quad \Leftrightarrow \\ \mathbf{I} &= \mathbf{K}_k\mathbf{H}_k + \mathbf{L}_k \ , \end{aligned} \tag{D.97}$$

where is has been exploited that $\mathbf{K}_k$ and $\mathbf{H}_k$ commutes with the expectation operator. Isolating $\mathbf{L}_k$ and inserting into (D.95) we obtain the expression

$$\boxed{\hat{\mathbf{x}}_k = \hat{\mathbf{x}}_k^- + \mathbf{K}_k\left(\mathbf{z}_k - \mathbf{H}_k\hat{\mathbf{x}}_k^-\right) = \hat{\mathbf{x}}_k^- + \mathbf{K}_k\delta\mathbf{z}_k^- \ ,} \tag{D.98}$$

where

$$\delta\mathbf{z}_k^- = \mathbf{z}_k - \mathbf{H}_k\hat{\mathbf{x}}_k^- \tag{D.99}$$

is the **measurement innovation**. The weighting matrix, $\mathbf{K}_k$, is known as the **Kalman gain matrix**. How this matrix is chosen in a statically optimal way is shown in a moment. First, we shall see how the error covariance matrix is updated.

Error Covariance Matrix

Substituting (D.94) into (D.98) we obtain the following expression for the state vector residual

$$\begin{aligned} \hat{\mathbf{x}}_k &= \mathbf{K}_k\left(\mathbf{H}_k\mathbf{x}_k + \mathbf{w}_{m,k}\right) + \left(\mathbf{I} - \mathbf{K}_k\mathbf{H}_k\right)\hat{\mathbf{x}}_k^- \\ \hat{\mathbf{x}}_k - \mathbf{x}_k &= \mathbf{K}_k\mathbf{H}_k\mathbf{x}_k - \mathbf{x}_k + \left(\mathbf{I} - \mathbf{K}_k\mathbf{H}_k\right)\hat{\mathbf{x}}_k^- + \mathbf{K}_k\mathbf{w}_{m,k} \\ \hat{\mathbf{x}}_k - \mathbf{x}_k &= \left(\mathbf{I} - \mathbf{K}_k\mathbf{H}_k\right)\left(\hat{\mathbf{x}}_k^- - \mathbf{x}_k\right) + \mathbf{K}_k\mathbf{w}_{m,k} \ . \end{aligned} \tag{D.100}$$

The error covariance matrix is therefore

$$\begin{aligned} \mathbf{P}_k &\equiv \mathrm{E}\left[\left(\hat{\mathbf{x}}_k - \mathbf{x}_k\right)\left(\hat{\mathbf{x}}_k - \mathbf{x}_k\right)^\top\right] \\ &= \mathrm{E}\left[\left(\left(\mathbf{I} - \mathbf{K}_k\mathbf{H}_k\right)\left(\hat{\mathbf{x}}_k^- - \mathbf{x}_k\right) + \mathbf{K}_k\mathbf{w}_{m,k}\right)\left(\left(\mathbf{I} - \mathbf{K}_k\mathbf{H}_k\right)\left(\hat{\mathbf{x}}_k^- - \mathbf{x}_k\right) + \mathbf{K}_k\mathbf{w}_{m,k}\right)^\top\right] \\ &= \mathrm{E}\Big[\left(\mathbf{I} - \mathbf{K}_k\mathbf{H}_k\right)\left(\hat{\mathbf{x}}_k^- - \mathbf{x}_k\right)\left(\hat{\mathbf{x}}_k^- - \mathbf{x}_k\right)^\top\left(\mathbf{I} - \mathbf{K}_k\mathbf{H}_k\right)^\top + \mathbf{K}_k\mathbf{w}_{m,k}\mathbf{w}_{m,k}^\top\mathbf{K}_k^\top \\ &\quad + \left(\mathbf{I} - \mathbf{K}_k\mathbf{H}_k\right)\left(\hat{\mathbf{x}}_k^- - \mathbf{x}_k\right)\mathbf{w}_{m,k}^\top\mathbf{K}_k^\top + \mathbf{K}_k\mathbf{w}_{m,k}\left(\hat{\mathbf{x}}_k^- - \mathbf{x}_k\right)^\top\left(\mathbf{I} - \mathbf{K}_k\mathbf{H}_k\right)^\top\Big] \\ &= \left(\mathbf{I} - \mathbf{K}_k\mathbf{H}_k\right)\mathrm{E}\left[\left(\hat{\mathbf{x}}_k^- - \mathbf{x}_k\right)\left(\hat{\mathbf{x}}_k^- - \mathbf{x}_k\right)^\top\right]\left(\mathbf{I} - \mathbf{K}_k\mathbf{H}_k\right)^\top + \mathbf{K}_k\mathrm{E}\left[\mathbf{w}_{m,k}\mathbf{w}_{m,k}^\top\right]\mathbf{K}_k^\top \\ &\quad + \left(\mathbf{I} - \mathbf{K}_k\mathbf{H}_k\right)\mathrm{E}\left[\left(\hat{\mathbf{x}}_k^- - \mathbf{x}_k\right)\mathbf{w}_{m,k}^\top\right]\mathbf{K}_k^\top + \mathbf{K}_k\mathrm{E}\left[\mathbf{w}_{m,k}\left(\hat{\mathbf{x}}_k^- - \mathbf{x}_k\right)^\top\right]\left(\mathbf{I} - \mathbf{K}_k\mathbf{H}_k\right)^\top \ . \end{aligned} \tag{D.101}$$

Now, since the state estimates are uncorrelated with the measurement noise, we have that

$$\boxed{\mathbf{P}_k = \left(\mathbf{I} - \mathbf{K}_k\mathbf{H}_k\right)\mathbf{P}_k^-\left(\mathbf{I} - \mathbf{K}_k\mathbf{H}_k\right)^\top + \mathbf{K}_k\mathbf{R}_k\mathbf{K}_k^\top \ .} \tag{D.102}$$

The Kalman Gain Matrix

The variance of the state estimates are represented by the diagonal elements of, $\mathbf{P}_k$. A minimum variance estimate of $\mathbf{K}_k$ is therefore accomplished as

$$\frac{\partial}{\partial \mathbf{K}_k} \mathrm{Tr}\left[\mathbf{P}_k\right] = 0 \,, \tag{D.103}$$

meaning that we want to adjust $\mathbf{K}_k$ in order to minimise the diagonal terms in $\mathbf{P}_k$. From (D.102) we obtain the following expression

$$\begin{aligned} \mathbf{P}_k &= \left(\mathbf{P}_k^- - \mathbf{K}_k\mathbf{H}_k\mathbf{P}_k^-\right)\left(\mathbf{I} - \mathbf{H}_k^\top\mathbf{K}_k^\top\right) + \mathbf{K}_k\mathbf{R}_k\mathbf{K}_k^\top \\ &= \mathbf{P}_k^- - \mathbf{P}_k^-\mathbf{H}_k^\top\mathbf{K}_k^\top - \mathbf{K}_k\mathbf{H}_k\mathbf{P}_k^- + \mathbf{K}_k\left(\mathbf{H}_k\mathbf{P}_k^-\mathbf{H}_k^\top + \mathbf{R}_k\right)\mathbf{K}_k^\top \,. \end{aligned} \tag{D.104}$$

In order to proceed we need to the following two matrix differentiation formulas [5, Eqs. 4.2.12-13]:

$$\frac{d\mathrm{Tr}\left[\mathbf{AB}\right]}{d\mathbf{A}} = \mathbf{B}^\top \quad \text{and} \quad \frac{d\mathrm{Tr}\left[\mathbf{ACA}^\top\right]}{d\mathbf{A}} = 2\mathbf{AC} \,, \tag{D.105}$$

where $\mathbf{AB}$ and $\mathbf{C}$ must be square matrices. Then inserting (D.104) into (D.103) and applying the above two relations, we have that

$$\begin{aligned} 0 &= \frac{\partial \mathrm{Tr}\left[\mathbf{P}_k\right]}{\partial \mathbf{K}_k} \\ &= \frac{\partial \mathrm{Tr}\left[\mathbf{P}_k^-\right]}{\partial \mathbf{K}_k} - \frac{\partial \mathrm{Tr}\left[\mathbf{P}_k^-\mathbf{H}_k^\top\mathbf{K}_k^\top\right]}{\partial \mathbf{K}_k} - \frac{\partial \mathrm{Tr}\left[\mathbf{K}_k\mathbf{H}_k\mathbf{P}_k^-\right]}{\partial \mathbf{K}_k} \\ &\quad + \frac{\partial \mathrm{Tr}\left[\mathbf{K}_k\left(\mathbf{H}_k\mathbf{P}_k^-\mathbf{H}_k^\top + \mathbf{R}_k\right)\mathbf{K}_k^\top\right]}{\partial \mathbf{K}_k} \\ &= -2\left(\mathbf{H}_k\mathbf{P}_k^-\right)^\top + 2\mathbf{K}_k\left(\mathbf{H}_k\mathbf{P}_k^-\mathbf{H}_k^\top + \mathbf{R}_k\right) \,, \end{aligned} \tag{D.106}$$

which can be re-arranged to arrive at

$$\boxed{\mathbf{K}_k = \mathbf{P}_k^-\,\mathbf{H}_k^\top\left(\mathbf{H}_k\,\mathbf{P}_k^-\,\mathbf{H}_k^\top + \mathbf{R}_k\right)^{-1} \,,} \tag{D.107}$$

which is refered to as the **Kalman gain matrix**.

E Related Software

This appendix describes the implementation of some routines that were developed and used in connection with this dissertation. They are all implemented in MATLAB or as MEX/C-routines readable by MATLAB.

E.1 A Model for the Normal Gravity Field

In order to perform inertial navigation, one needs to take into account the contribution from gravity and remove this effect before integrating the sensed acceleration. This is usually done in terms of a gravitational model, which must be defined. The highest accuracy global gravity models come in the form of a set of spherical harmonic coefficients, which must be used in conjunction with (3.12) as described in Appendix E.2. This approach however requires a large number of coefficients to be stored on the computer and an associated demanding computational task.

Instead, one often use a model for the normal gravity field, presented in section 3.3.2. The resulting gravity field will correspond to a scenario where the Earth is a perfect ellipsoid with constant rotational velocity and total mass as defined by the chosen geodetic reference system. It is independent of the density distribution within the Earth, depending only on the total mass. The difference in magnitude between normal gravity and true gravity is known as the gravity disturbance and the difference in direction as the deflection of the vertical.

What we eventually want in order to determine gravity from airborne surveys, is to use a model for the normal gravity field and then model the gravity disturbance as a stochastic process. This will be more thoroughly described in section REF. This appendix is devoted to the development of a model for the normal gravity field.

The normal gravity field is composed of gravitational acceleration (attraction from mass) and centrifugal acceleration (due to Earth rotation). In section 3.3.2, the formulas for computing the normal gravity vector $(\gamma_u, \gamma_\beta, \gamma_\lambda)$, resolved about the axes of the ellipsoidal-harmonic coordinates, were presented. Eventually, we want to end up with a vector resolved about the north-, east- and down-axes of the n-frame. These axes refer to the directions of the geodetic reference system, i.e. γ_ϕ, γ_λ and $-\gamma_h$, with the vertical direction being normal to the reference ellipsoid. Such a composition is accomplished using the transformations in (3.32), (3.33) and (3.34) followed by a change of sign on the vertical axis:

$$\begin{bmatrix} \gamma_N \\ \gamma_E \\ \gamma_D \end{bmatrix} = \begin{bmatrix} 1 & 0 & 0 \\ 0 & 1 & 0 \\ 0 & 0 & -1 \end{bmatrix} \begin{bmatrix} \gamma_\phi \\ \gamma_\lambda \\ \gamma_h \end{bmatrix} . \tag{E.1}$$

One should however notice that the east-component of normal gravity will always be zero. Usually, we are given geodetic coordinates for the point of interest. Therefore, as outlined in [14], the computational procedure involves the following steps:

1. Compute Cartesian (x, y, z) coordinates from geodetic (ϕ, λ, h) coordinates
2. Compute ellipsoidal (u, β, λ) coordinates from geodetic coordinates
3. Compute normal gravity vector, resolved about the axes of the ellipsoidal-harmonic coordinate frame
4. Transform vector into rectangular frame

5. Transform vector into spherical frame

6. Transform vector into navigation frame

This will result in a computational scheme absent of approximations. The precision will therefore only be limited by numerical precision of the computer. The magnitude of the normal gravity vector varies as a function of altitude and latitude as illustrated in figure E.1.

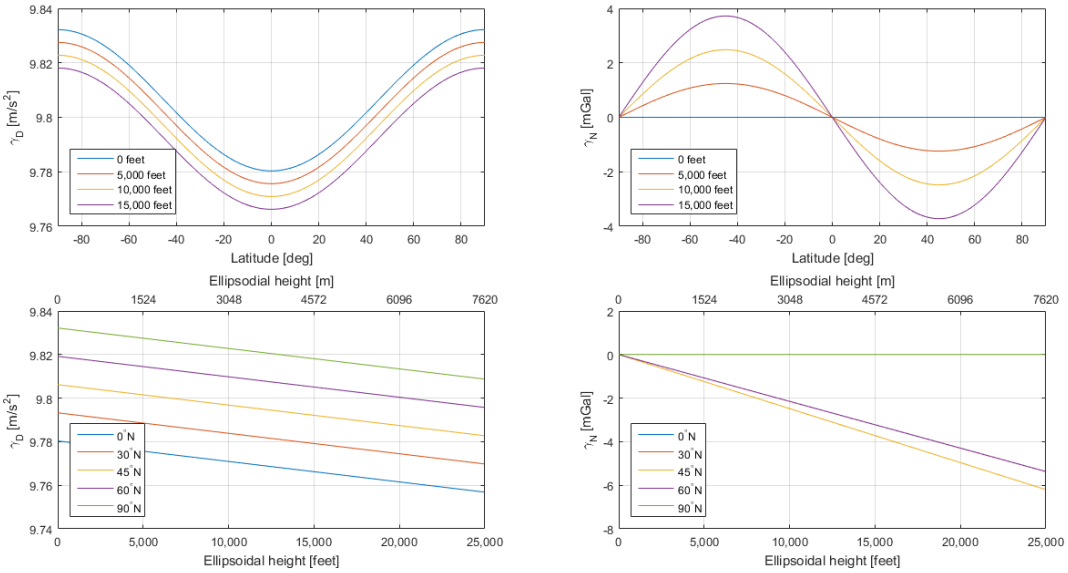

Figure E.1: Vertical and horizontal components of normal gravity computed using a precise method, i.e. a method with no approximations. Notice that ellipsoidal height is declared above the figures.

As with true gravity, the direction of the vertical is not constant but varies with height according to the plumb line. In the n-frame, the vertical direction is defined as the normal to the reference ellipsoid, at the ellipsoidal surface. For this reason the magnitude of the north component is zero at the ellipsoid and increases with height. At altitudes around 10,000 ft ($\sim$3 km) the magnitude of the north component is about 2 mGal.

E.1.1 Approximate Computation of the Normal Gravity Vector

The computational scheme presented above indicates that such an algorithm may be computationally demanding. Therefore, one usually uses an approximate model for the normal gravity vector, $\boldsymbol{\gamma}$. For near-Earth problems, such an approximate model may be based on an upward continuation of the gravity value at the ellipsoid. For the vertical component, a Taylor series expansion is used, while the horizontal component is based on a consideration of the geometry of the field, see e.g. [12], [19].

At the surface of the ellipsoid, the magnitude of the normal gravity vector can be computed using the **formula of Somigliana** [19, Eq. 4.41a]

$$\gamma_0 = \frac{a\,\gamma_e \cos^2\phi + b\,\gamma_p \sin^2\phi}{\sqrt{a^2\cos^2\phi + b^2\sin^2\phi}}\,, \tag{E.2}$$

where γ_e and γ_p are normal gravity at the equator and the pole, respectively, see table 2.3. An alternative form of Somigliana's formula, which is more convenient for numerical computations is [19, Eq. 4.41b]:

$$\gamma_0 = \gamma_e \frac{1 + k\sin^2\phi}{\sqrt{1 - e^2\sin^2\phi}} \quad \text{with} \quad k = \frac{b\,\gamma_p}{a\,\gamma_e} - 1\,. \tag{E.3}$$

We want to express the normal gravity vector in terms of the north, east and down axes of the n-frame. Since the down-direction is defined along the local vertical at the surface of the ellipsoid, we have that

$$\boldsymbol{\gamma} = \begin{bmatrix} 0 \\ 0 \\ \gamma_0 \end{bmatrix} \qquad \text{at the surface of the ellipsoid}\,. \tag{E.4}$$

However, since the equipotential surfaces of the normal gravity field are not parallel. the vector will deviate from perpendicular in the meridian plane, as we move away from the ellipsoid. This means that

$$\boldsymbol{\gamma} = \begin{bmatrix} \gamma_N \\ 0 \\ \gamma_D \end{bmatrix} \qquad \text{above the surface of the ellipsoid}\,. \tag{E.5}$$

Therefore, in order to perform an upward continuation of the vector from the surface of the ellipsoid, we need to consider the gradients along both the down and northward directions. For the vertical component, this can be accomplished in terms of a Taylor series expansion of the normal gravity vector as

$$\gamma_D = \gamma_0 + \frac{1}{1!}\left.\frac{\partial\gamma_D}{\partial h}\right|_{h=0} h + \frac{1}{2!}\left.\frac{\partial^2\gamma_D}{\partial h^2}\right|_{h=0} h^2 + \frac{1}{3!}\left.\frac{\partial^3\gamma_D}{\partial h^3}\right|_{h=0} h^3 + \ldots\,, \tag{E.6}$$

which is truncated at some degree, depending on the desired accuracy. Such a model is presented for example in [19, Eq. 4.63], including terms until second order and with some approximation:

$$\begin{aligned} \gamma_D(\phi, h) &= \gamma_0\left(1 - \frac{2}{a}\left(1 + f + m - 2f\sin^2\phi\right)h + \frac{3}{a^2}h^2\right) \\ &\approx \gamma_0 - \left(3.0877\cdot 10^{-6} - 4.3\cdot 10^{-9}\,\sin^2\phi\right)h + 0.72\cdot 10^{-12}\,h^2\,, \end{aligned} \tag{E.7}$$

where

$$m = \frac{\omega_{ie}^2 a^2 b}{GM}\,. \tag{E.8}$$

The computation of the horizontal component is based on the curvature of the normal plumb line, which we have from [12, Eqs. 2-50,2-51]:

$$\kappa_1 = \frac{1}{\gamma}\frac{\partial \gamma}{\partial x} = \frac{1}{\gamma}\frac{1}{R_N}\frac{\partial \gamma}{\partial \phi} \qquad \text{and} \qquad \kappa_2 = \frac{1}{\gamma}\frac{\partial \gamma}{\partial y} = \frac{1}{\gamma}\frac{1}{R_E \cos\lambda}\frac{\partial \gamma}{\partial \lambda} = 0 \,, \tag{E.9}$$

which are then integrated in order to determine the total change along the plumb line as

$$\gamma_N(\phi, h) = -\int_0^h \gamma\, \kappa_1 \, \mathrm{d}h' = -\int_0^h \frac{1}{R_N}\frac{\partial \gamma}{\partial \phi}\, \mathrm{d}h' \,. \tag{E.10}$$

This approach can be made more or less precise depending on how the expression for γ is formed. In order to perform an upward continuation, the gradient $\partial\gamma/\partial\phi$ is evaluated at the reference ellipsoid and normal gravity is assumed constant, such that

$$\gamma_N(\phi, h) \approx -\frac{1}{R_N}\left.\frac{\partial \gamma}{\partial \phi}\right|_{h=0} \int_0^h \mathrm{d}h' = -\frac{1}{R_N}\left.\frac{\partial \gamma}{\partial \phi}\right|_{h=0} h \,. \tag{E.11}$$

In [19, Eq. 4.53], the expression for γ_0 is then formed using the approximation

$$\gamma_0 = \gamma_e\left(1 + f^\star \sin^2\phi\right) \qquad \text{where} \qquad f^\star = \frac{\gamma_p - \gamma_e}{\gamma_e} \tag{E.12}$$

is known as the gravity flattening. Inserting this into the above, we arrive at the expression [19, Eq. 4.72b]:

$$\gamma_N(\phi, h) = -\gamma_e \frac{f^\star}{R_N} \sin(2\phi)\, h \approx 8.2 \cdot 10^{-9} \sin(2\phi)\, h \,, \tag{E.13}$$

for the northward component of normal gravity. Figure E.2 shows a comparison between this "approximate" model and the "precise" model developed in the previous section. It is evident that the two models differ in accuracy on the order of $10^{-2}\,\mathrm{mGal} = 10^{-7}\,\mathrm{m/s^2}$.

E.1.2 A Higher-Order Model for Normal Gravity

Since the vertical model derived in the previous section was based on a Taylor series expansion on the surface of the reference ellipsoid, one can derive a more precise model by including higher-order terms in the series expansion as described in [21]. For the horizontal component, one can substitute the approximation in (E.12) and instead use the derivative of Somigliana's formula (E.3).

The Vertical Component

The first derivative is the most important, since it contributes the most to the expansion. An expression for this term is given by **Bruns formula** [21, Eq. 16]:

$$\left.\frac{\partial \gamma_D}{\partial h}\right|_{h=0} = -\frac{\gamma_e}{a\left(1 - e^2\right)}\left(2 - e^2 - e^2\sin^2\phi\right)\sqrt{1 - e^2\sin^2\phi} - 2\omega_{ie}^2 \,. \tag{E.14}$$

For the higher order terms we do not need very high accuracy [21, p. 27]. We can therefore restrict ourselves to a second order spherical harmonic expansion of the normal potential using (3.28):

$$\begin{aligned} U(\mathbf{r}) &\approx \frac{GM}{r} - \frac{GM}{r}\left(\frac{a}{r}\right)^2 J_2\, P_2(\sin\phi') + \frac{1}{2}\omega_{ie}^2\, r^2 \sin^2\phi' \\ &= \frac{GM}{r} - \frac{GM}{r}\left(\frac{a}{r}\right)^2 J_2\left(\frac{3}{2}\sin^2\phi' - \frac{1}{2}\right) + \frac{1}{2}\omega_{ie}^2\, r^2\cos^2\phi' \,, \end{aligned} \tag{E.15}$$

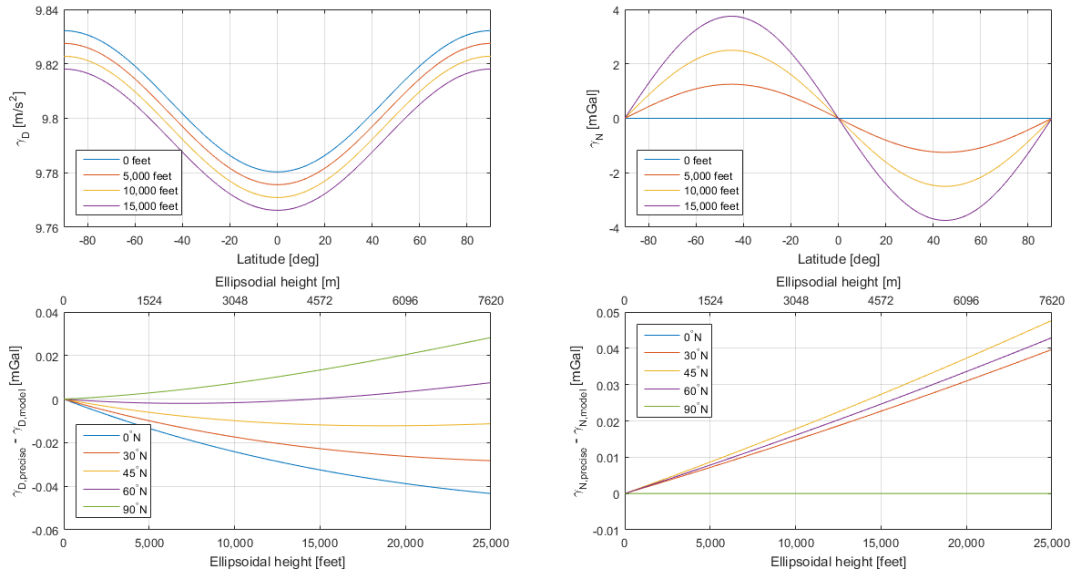

Figure E.2: (Upper row): Vertical and horizontal components of normal gravity computed using the second/first order model developed in [19, sect. 4.2]. (Lower row): Difference between this model and the "precise" model presented in figure E.1.

where all the constants, including the second-degree harmonic J_2, can be found in table 2.3. The second-degree Legendre polynomial is computed using [19, Eq. 3.83a]:

$$P_2\left(\sin\phi'\right) = \frac{3}{2}\sin^2\phi' - \frac{1}{2}\,. \tag{E.16}$$

The higher-order derivatives can then be computed from the potential as

$$\frac{\partial^2\gamma_D}{\partial h^2} \approx -\frac{\partial^3 U\left(\mathbf{r}\right)}{\partial r^3} = \frac{6GM}{r^4} - \frac{60GM}{r^4}\left(\frac{a}{r}\right)^2 J_2\left(\frac{3}{2}\sin^2\phi' - \frac{1}{2}\right) \quad \text{and} \tag{E.17a}$$

$$\frac{\partial^3\gamma_D}{\partial h^3} \approx -\frac{\partial^4 U\left(\mathbf{r}\right)}{\partial 4^3} = -\frac{24GM}{r^5} + \frac{360GM}{r^5}\left(\frac{a}{r}\right)^2 J_2\left(\frac{3}{2}\sin^2\phi' - \frac{1}{2}\right)\,. \tag{E.17b}$$

Assuming that the geocentric and geodetic latitude are the same, i.e. $\phi \approx \phi'$, and that $r \approx a\sqrt{1 - e^2\sin^2\phi}$, we arrive at the expressions [21, Eqs. 22,23]:

$$\left.\frac{\partial^2\gamma_D}{\partial h^2}\right|_{h=0} \approx \frac{6\,GM}{a^4\left(1 - e^2\sin^2\phi\right)^2} - \frac{30\,GM\,J_2\left(3\sin^2\phi - 1\right)}{a^4\left(1 - e^2\sin^2\phi\right)^3} \quad \text{and} \tag{E.18a}$$

$$\left.\frac{\partial^3\gamma_D}{\partial h^3}\right|_{h=0} \approx -\frac{24\,GM}{a^5}\,. \tag{E.18b}$$

for the second and third order gradients at the surface of the Earth. In figure E.3, this model is compared with the vertical component of the "precise" model derived previously. It is

evident that the two models differ in accuracy on the order of 10^{-4} mGal $= 10^{-9}$ m/s^2, when the third order term is included.

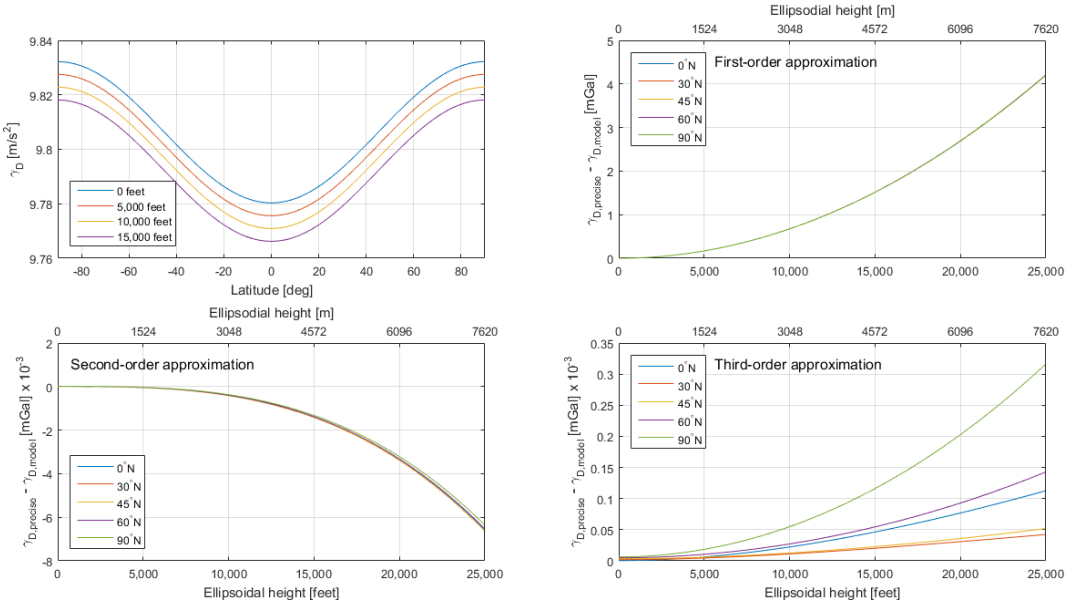

Figure E.3: (Upper right): Vertical component of the third order model. The remaining three figures show the difference with the "precise" model presented in figure E.1. It is evident that the precision increases as more terms are added to the expansion.

The Horizontal Component

For the horizontal component, we will use the formula of Somigliana (E.3) in order to derive an expression for the horizontal gradient of normal gravity:

$$\left.\frac{\partial \gamma_N}{\partial \phi}\right|_{h=0} = -\gamma_e \left[\frac{k}{\sqrt{1-e^2\sin^2\phi}} + \frac{e^2\left(1+k\sin^2\phi\right)}{2\left(1-e^2\sin^2\phi\right)^{3/2}}\right]\sin\left(2\phi\right) \ , \tag{E.19}$$

with

$$k = \frac{b\,\gamma_p}{a\,\gamma_e} - 1 \ . \tag{E.20}$$

Using this expression in (E.11), we have that

$$\gamma_N\left(\phi, h\right) \approx -\frac{\gamma_e}{R_N}\left[\frac{k}{\sqrt{1-e^2\sin^2\phi}} + \frac{e^2\left(1+k\sin^2\phi\right)}{2\left(1-e^2\sin^2\phi\right)^{3/2}}\right]\sin\left(2\phi\right) h \ . \tag{E.21}$$

The difference between this approximate model and the "precise" model presented previously is illustrated in figure E.4. It is evident from the figure that the inconsistency between the two is on the order of 10^{-3} mGal $= 10^{-8}$ m/s^2.

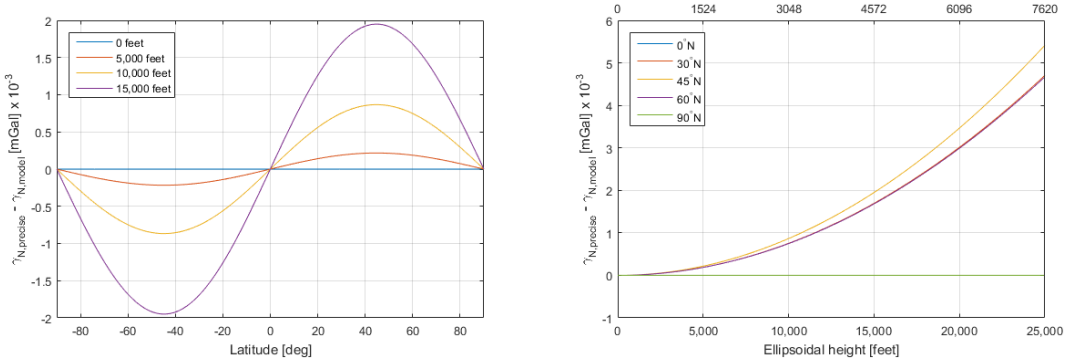

Figure E.4: Difference between the horizontal components of the "precise" model presented in figure E.1 and the "approximate" model presented in this section.

E.2 Evaluation of Spherical Harmonic Models

A common way to represent global models of the Earth's gravitational field is in terms of spherical harmonic coefficients, $C_{n,m}$ and $S_{n,m}$, also known as Stokes coefficients, up to some maximum degree, N, and order, M. The geopotential model is then evaluated at a point $\mathbf{r} = (r, \phi', \lambda)$ in space using (3.12):

$$V\left(r, \phi', \lambda\right) = \frac{GM}{r} \sum_{n=0}^{N} \left(\frac{a}{r}\right)^n \sum_{m=0}^{n} \bar{P}_{n,m}\left(\sin\phi'\right) \left[C_{n,m}\cos m\lambda + S_{n,m}\sin m\lambda\right] \ , \tag{E.22}$$

where (r, ϕ', λ) are spherical and *not* geodetic coordinates. Notice that authors often use colatitude $\theta = 90° - \phi'$ instead of latitude. The constants GM and a refer to the product of gravitational constant times Earth's mass and the Earth radius, respectively. In principle, they are scaling coefficients related to the spherical harmonic coefficients. Usually the value of $C_{0,0}$ is set equal to one, in order to preserve the meaning of these constants. The functions $\bar{P}_{n,m}\left(\sin\phi'\right)$ denote the fully normalised associated Legendre polynomials of degree, n, and order, m.

The first derivatives of (E.22) are [1]:

$$\begin{aligned}
V_r &= \frac{\partial}{\partial r} V \\
&= -\frac{GM}{r^2} \sum_{n=0}^{N} \left(\frac{a}{r}\right)^n (n+1) \sum_{m=0}^{n} \bar{P}_{n,m}\left(\sin\phi'\right) \left[C_{n,m}\cos m\lambda + S_{n,m}\sin m\lambda\right] \\
V_\lambda &= \frac{1}{r\cos\phi'} \frac{\partial}{\partial \lambda} V \\
&= \frac{GM}{r^2\cos\phi'} \sum_{n=0}^{N} \left(\frac{a}{r}\right)^n \sum_{m=0}^{n} m\bar{P}_{n,m}\left(\sin\phi'\right) \left[S_{n,m}\cos m\lambda - C_{n,m}\sin m\lambda\right] \\
V_{\phi'} &= \frac{1}{r} \frac{\partial}{\partial \phi'} V \\
&= \frac{GM}{r} \sum_{n=0}^{N} \left(\frac{a}{r}\right)^n \sum_{m=0}^{n} \frac{\partial \bar{P}_{n,m}\left(\sin\phi'\right)}{\partial \phi'} \left[C_{n,m}\cos m\lambda + S_{n,m}\sin m\lambda\right]
\end{aligned} \tag{E.23}$$

E.2.1 Definition of the Associated Legendre Functions

Legendre polynomials are functions that satisfy Legendre's differential equation

$$\frac{\mathrm{d}}{\mathrm{d}t}\left[\left(1-t^2\right)\frac{\mathrm{d}}{\mathrm{d}t}P_n(t)\right]+n\left(n+1\right)P_n(t)=0\,, \tag{E.24}$$

and the solutions for $n=0,1,2,...$ form a sequence of orthogonal polynomials known as the Legendre polynomials that may be expressed using Rodrigues' formula [12, Eq. 1.59]:

$$P_n(t)=\frac{1}{2^n n!}\frac{\mathrm{d}^n}{\mathrm{d}t^n}\left[\left(t^2-1\right)^n\right]\,. \tag{E.25}$$

These functions are also known as Legendre functions of the first kind. This is because a second set of solutions, known as Legendre functions of the second kind, exist for the Legendre differential equation, see e.g. [12, section 1.8].

The associated Legendre functions (ALFs) are solutions to the general Legendre equation

$$\frac{\mathrm{d}}{\mathrm{d}t}\left[\left(1-t^2\right)\frac{\mathrm{d}}{\mathrm{d}t}P_n(t)\right]+\left[n\left(n+1\right)-\frac{m^2}{1-t^2}\right]P_n(t)=0\,, \tag{E.26}$$

given in [12, Eq. 1.56][6]. The solutions to this equation are related to the Legendre polynomials as [12, Eq. 1.65]:

$$\begin{aligned}P_{n,m}(t)&=\left(1-t^2\right)^{m/2}\frac{\mathrm{d}^m}{\mathrm{d}t^m}P_n(t)\\&=\frac{1}{2^n n!}\left(1-t^2\right)^{m/2}\frac{\mathrm{d}^{n+m}}{\mathrm{d}t^{n+m}}\left[\left(t^2-1\right)^n\right]\end{aligned} \tag{E.27}$$

and has two subscripts, i.e. the ALFs have both degree and order. In our case, we define

$$t:=\sin\phi'=\cos\theta\quad\text{and}\quad u:=\cos\phi'=\sin\theta\,, \tag{E.28}$$

and make the substitution $\left(1-t^2\right)^{m/2}=\cos^m\phi'=u^m$, such that

$$P_{n,m}(t)=u^m\frac{\mathrm{d}^m}{\mathrm{d}t^m}P_n(t)\,. \tag{E.29}$$

One should be aware that there is also another common sign convention for the ALFs, which is generally denoted $P_n^m(t)$ and related to the above polynomials as

$$P_n^m(t)=(-1)^m P_{n,m}(t)=\frac{(-1)^m}{2^n n!}\left(1-t^2\right)^{m/2}\frac{\mathrm{d}^{n+m}}{\mathrm{d}t^{n+m}}\left[\left(t^2-1\right)^n\right]\,, \tag{E.30}$$

where the factor $(-1)^m$ is known as the Condon-Shortly phase.

E.2.2 Computation of the Associated Legendre Functions

Usually, the ALFs are evaluated using recursion formulas, which can take various forms [13]:

- Forward column method (most common),
- Forward row method,

[6] There is a printing error in the book, so this equation is a bit different from the reference

- Reverse column method, and
- Clenshaw summation methods,

using the following values as seed values for the recursion:

$$P_{0,0}(t) = 1 \quad \text{and} \quad P_{1,1}(t) = u \; . \tag{E.31}$$

The recursion process may be visualized using a lower triangular matrix as in Figures E.5 and E.6, where each circle corresponds to a particular ALF of degree, n, and order, m. The recursion then starts by computing the diagonal (sectorial) values and then moves either along the vertical or horizontal in order to compute values of constant degree or order. The implementation that is pursued here is a modified version of the forward row method, illustrated in Figure E.6.

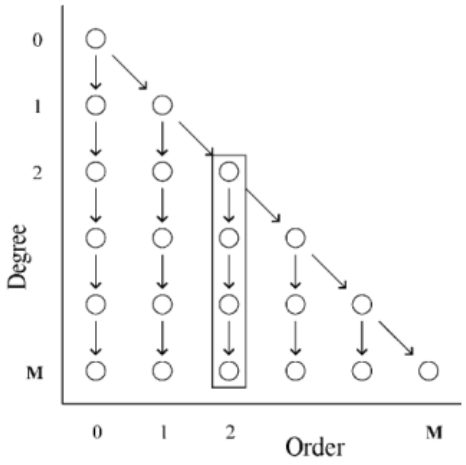

Figure E.5: Schematic illustration of the recursion sequence in the forward column method algorithm. Credit: [13]

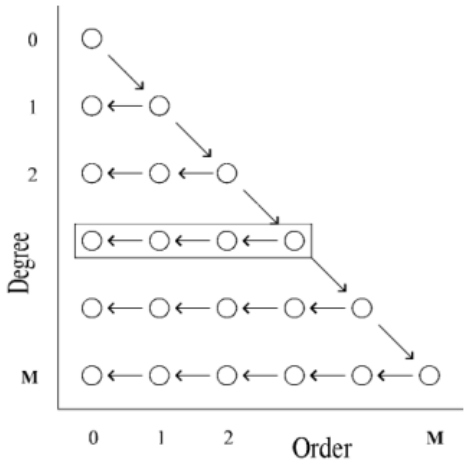

Figure E.6: Schematic illustration of the recursion sequence in the forward row method algorithm. Credit: [13]

Let us first introduce the following short-hand notation for the ALFs

$$P_{n,m} := P_{n,m}(t) \; , \quad t = \sin\phi' \; . \tag{E.32}$$

The basic recurrence relation for **degree and order** is [2, Eq. 1]:

$$P_{n,m} = (2n-1)\, u P_{n-1,m-1} + P_{n-2,m} \; , \tag{E.33}$$

noting that $P_{n,m} = 0$ for any $m > n$, such that the second right-hand term above vanishes for $m = n$ and $m = n-1$. For the **diagonal and first off-diagonal** elements we therefore have the relations

$$P_{n,n} = (2n-1)\; u\, P_{n-1,n-1} \; , \tag{E.34}$$

$$P_{n,n-1} = (2n-1)\; u\, P_{n-1,n-2} \; . \tag{E.35}$$

For **varying order**, we have [2, Eq. 4]:

$$P_{n,m+2} = (2m+1)\,\frac{t}{u}P_{n,m+1} - (n-m)\,(n+m+1)\,P_{n,m}\ , \tag{E.36}$$

and for **varying degree**, we have [2, Eq. 5]::

$$(2n+1)\,tP_{n,m} = (n+m)\,P_{n-1,m} + (n-m+1)\,P_{n+1,m}\ . \tag{E.37}$$

We can therefore use (E.34) to compute the diagonal elements, while (E.36) or (E.37) can be used in the row or column recursive schemes. However, the implementation of these recursive formulas faces severe problems of underflow or overflow in the numerical evaluation. To this end, several techniques have been proposed in order to overcome these difficulties [8]:

- Normalization of the ALFs,
- Higher precision environment in the evaluation (e.g. quadruple precision arithmetic),
- Global scaling factors,
- Separation of the problematic u^m factor and/or
- Extended exponent arithmetic.

In the following I will describe the modifications made to the forward row method in [13], in order to make an implementation stable to degree and order $n = m = 2700$.

Normalisation of the ALFs

The normalization of the ALFs is a standard approach and the normalised polynomials occur in the standard expression for the geopotential, i.e. (E.22). This leads to the fully normalized ALFs [12, Section. 1.10]:

$$\bar{P}_{n,m} := N_{n,m}P_{n,m}\ , \tag{E.38}$$

with

$$N^2_{n,m} = (2-\delta_{0,m})\,(2n+1)\,\frac{(n-m)!}{(n+m)!}\ , \quad \delta_{0,m} = \begin{cases} 1 & \text{for } m = 0 \\ 0 & \text{otherwise} \end{cases}\ . \tag{E.39}$$

The normalisation used in geodesy is such that the spherical harmonics are normalised to unity on the sphere, i.e.

$$\frac{1}{4\pi}\int_0^{\pi}\int_0^{2\pi} (P_{n,m}\cos m\lambda)\,(P_{n',m'}\cos m'\lambda)\,\sin\phi'\,\mathrm{d}\phi'\,\mathrm{d}\lambda = \delta_{l,l'}\delta_{m,m'} \quad \text{and} \tag{E.40}$$

$$\frac{1}{4\pi}\int_0^{\pi}\int_0^{2\pi} (P_{n,m}\sin m\lambda)\,(P_{n',m'}\sin m'\lambda)\,\sin\phi'\,\mathrm{d}\phi'\,\mathrm{d}\lambda = \delta_{l,l'}\delta_{m,m'}\ . \tag{E.41}$$

One should be aware that other normalisations exist and are being used in fields such as e.g. magnetics and quantum mechanics, which also use spherical harmonic functions.

Applying the normalisation factor to (E.34), noting that $m = n$ and $1 < m \leq n$, we obtain the expression

$$\bar{P}_{m,m} = u\sqrt{\frac{2m+1}{2m}}\bar{P}_{m-1,m-1} \,, \tag{E.42}$$

which is initialised using the seed values

$$\bar{P}_{0,0} = 1 \quad \text{and} \quad \bar{P}_{1,1} = \sqrt{3}u \,. \tag{E.43}$$

Similarly, applying the normalisation factor to (E.36), we obtain

$$\bar{P}_{n,m} = \sqrt{\frac{2-\delta_{0,m}}{2}}\left(g_{n,m}\frac{t}{u}\bar{P}_{n,m+1} - h_{n,m}\bar{P}_{n,m+2}\right) \,, \tag{E.44}$$

where

$$g_{n,m} = \frac{2\,(m+1)}{\sqrt{(n-m)\,(n+m+1)}} \quad \text{and} \quad h_{n,m} = \sqrt{\frac{(n+m+2)\,(n-m-1)}{(n-m)\,(n+m+1)}} \,, \tag{E.45}$$

noticing that $h_{n,n-1} = 0$.

Scaling by the u^m Factor

Taking a look at the sectorial values, we can write (E.42) as

$$\bar{P}_{m,m} = u^m\,\Pi_m \,, \quad \forall \quad m \geq 1 \,, \tag{E.46}$$

where $u^m = \cos^m\phi'$ and

$$\Pi_m = \sqrt{3}\prod_{m}^{i=2}\sqrt{\frac{2i+1}{2i}} \,, \quad \forall \quad m \geq 1 \,. \tag{E.47}$$

The Π_m factor is shown in Figure E.7 as a function of order, m, and does not seem to introduce any computational difficulties. In contrast, the factor $u^m = \cos^m\phi'$ becomes increasingly small as $u \to 0$. This introduces a possible overflow or underflow issue in numerical precision as m becomes large or as ϕ' approaches the poles.

For this reason, [13] suggests to scale all the coefficients by the factor u^m and instead compute the coefficients $\bar{P}_{n,m}/u^m$ in order to reduce the magnitude of the computed coefficients. Applying this factor to Eqs. (E.42) and (E.44), we obtain the recursion formulas

$$\left\{\frac{\bar{P}_{m,m}}{u^m}\right\} = \sqrt{\frac{2m+1}{2m}}\left\{\frac{\bar{P}_{m-1,m-1}}{u^{m-1}}\right\} \quad \text{and} \tag{E.48}$$

$$\left\{\frac{\bar{P}_{n,m}}{u^m}\right\} = \sqrt{\frac{2-\delta_{0,m}}{2}}\left(g_{n,m}t\left\{\frac{\bar{P}_{n,m+1}}{u^{m+1}}\right\} - h_{n,m}u^2\left\{\frac{\bar{P}_{n,m+2}}{u^{m+2}}\right\}\right) \,, \tag{E.49}$$

with the seed values

$$\frac{\bar{P}_{0,0}}{u^0} = 1 \quad \text{and} \quad \frac{\bar{P}_{1,1}}{u^1} = \sqrt{3} \,. \tag{E.50}$$

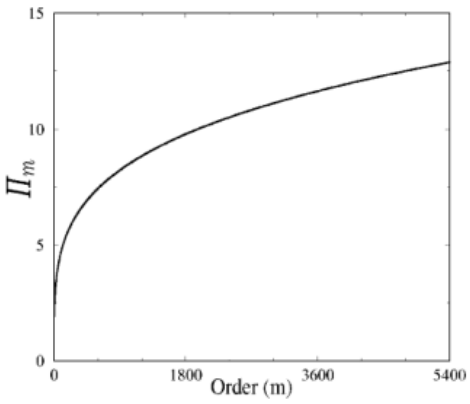

Figure E.7: Variation of Π_m [(E.47)] with order m. Credit: [13]

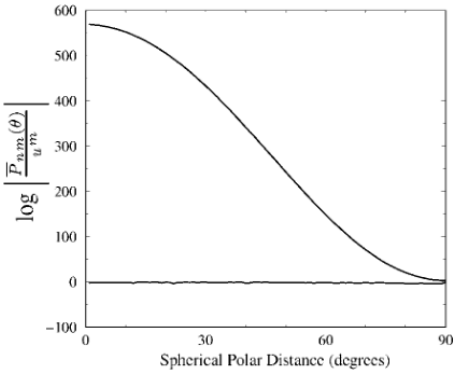

Figure E.8: Logarithm plot of maximum (upper line) and minimum (lower line) values of $|\bar{P}_{n,m}/u^m|, \forall n, m \leq 2700$. Credit: [13]

In order to evaluate (E.22), one would then later have to apply the missing u-factors. This can be done using Horner's scheme [13], i.e. when evaluating the sum, after introducing the spherical harmonic coefficients and the sinusoidal terms. This will be introduced in Section E.2.3.

Global Scaling Factor

The entire range of maximum and minimum values of $|\bar{P}_{n,m}/u^m|$ for maximum order $M = 2700$ is shown in Figure E.8. Taking into account that the range of values possible in IEEE double precision are $[-1.7977; 1.7977] \cdot 10^{308}$, this figure implies that further factorisation is required in order to prevent overflowing in IEEE double precision.

One solution, suggested by [13], is the application of a global scale factor of magnitude 10^{-280}. This is accomplished by modifying the seed values as

$$\frac{\bar{P}_{0,0}}{u^0} = 10^{-280} \quad \text{and} \quad \frac{\bar{P}_{1,1}}{u^1} = \sqrt{3} \cdot 10^{-280}\,, \tag{E.51}$$

which will then propagate linearly into all estimates of $|\bar{P}_{n,m}/u^m|$ when using the recursive formulas in (E.48) and (E.49). Because the propagation is linear, this will lead to scaled values, $V \cdot 10^{-280}$, of the geopotential using (E.22). These values are then multiplied by 10^{280} in order to yield V.

E.2.3 Evaluation of the Gravitational Potential

In the previous section it was described how the factorised and scaled ALFs, $\bar{P}_{n,m}/u^m$, could be computed using a modified version of the forward row recursion formulas, as outlined in [13]. These are needed in the evaluation of (E.22). The coefficients, $C_{n,m}$ and $S_{n,m}$, along with the constants GM and a, represent the spherical harmonic model that we want to evaluate. This allows us to evaluate (E.22) at any point in space $\mathbf{r} = (r, \phi', \lambda)$, noticing

that (r, ϕ', λ) are spherical coordinates. The conversion from geodetic coordinates (ϕ, λ, h) to spherical coordinates is described in standard textbooks such as e.g. [19] and [12].

In the numerical evaluation of the geopotential, it is useful to re-write (E.22) in terms of partial sums, such that

$$X_{C,m} = \sum_{n=\mu}^{N} \left(\frac{a}{r}\right)^n \bar{P}_{n,m} C_{n,m} \quad \text{and} \quad X_{S,m} = \sum_{n=\mu}^{N} \left(\frac{a}{r}\right)^n \bar{P}_{n,m} S_{n,m} \ , \tag{E.52}$$

where $\mu = \min[m, M]$,

$$\Omega = \sum_{m=0}^{M} \Omega_m \quad \text{with} \quad \Omega_m = X_{C,m} \cos m\lambda + X_{S,m} \sin m\lambda \tag{E.53}$$

and

$$V(r, \phi', \lambda) = \frac{GM}{r} \Omega \ , \tag{E.54}$$

which outlines a strategy for the implementation. The two terms, $X_{C,m}$ and $X_{S,m}$, are vectors of length M, containing terms that are independent of longitude. In a grid computation, these vectors therefore only need to be computed once for points of similar latitude, ϕ', and geocentric distance, r.

If instead, we use the factorised and scaled ALFs, the two vectors would be formed as

$$\left\{\frac{X_{C,m}}{u^m}\right\} = \sum_{n=\mu}^{N} \left(\frac{a}{r}\right)^n \left\{\frac{\bar{P}_{n,m}}{u^m}\right\} C_{n,m} \quad \text{and} \quad \left\{\frac{X_{S,m}}{u^m}\right\} = \sum_{n=\mu}^{N} \left(\frac{a}{r}\right)^n \left\{\frac{\bar{P}_{n,m}}{u^m}\right\} S_{n,m} \ , \tag{E.55}$$

whereas the second sum would be formed using Horner's scheme as

$$\Omega = \left[\left\{\left(\cdots\left\{\frac{\Omega_M}{u^M}u + \frac{\Omega_{M-1}}{u^{M-1}}\right\}u + \cdots + \frac{\Omega_3}{u^3}\right)u + \frac{\Omega_2}{u^2}\right\}u + \frac{\Omega_1}{u}\right]u + \Omega_0 \ , \tag{E.56}$$

with

$$\frac{\Omega_m}{u^m} = \left\{\frac{X_{C,m}}{u^m}\right\} \cos m\lambda + \left\{\frac{X_{S,m}}{u^m}\right\} \sin m\lambda \ . \tag{E.57}$$

Finally, the geopotential value is computed as

$$V(r, \phi', \lambda) = \frac{GM}{r} \Omega \cdot 10^{280} \ . \tag{E.58}$$

E.2.4 First Derivatives of the Associated Legendre Functions

If we instead wanted to derive the gravitational vector from a geopoetial model using (E.23), we would moreover need the first derivatives of the ALFs. The basic formulas are [2, Eqs. 6,7]:

$$uP^{(1)}_{n,m} = mtP_{n,m} - uP_{n,m+1} \tag{E.59}$$

and

$$uP^{(1)}_{n,m} = ntP_{n,m} - (n+m)\, P_{n-1,m} \ , \tag{E.60}$$

where

$$P_{n,m}^{(1)} := \frac{\mathrm{d}P_{n,m}\left(\sin\phi'\right)}{\mathrm{d}\phi'} \ . \tag{E.61}$$

After normalisation, factorisation and scaling, (E.59) looks like [13, Eq. 30]

$$\left\{\frac{\bar{P}_{n,m}^{(1)}}{u^m}\right\} = m\frac{t}{u}\left\{\frac{\bar{P}_{n,m}}{u^m}\right\} - e_{n,m}u\left\{\frac{\bar{P}_{n,m+1}}{u^{m+1}}\right\} \quad \forall \quad n \geq m \ , \tag{E.62}$$

with

$$e_{n,m} = \sqrt{\frac{2-\delta_{0,m}}{2}}\sqrt{(n+m+1)\,(n-m)} \ , \tag{E.63}$$

noticing that $e_{m,m} = 0$, such that the last term vanishes for all sectorial (diagonal) terms. The order of magnitude of these terms (before global scaling) is shown in Figure E.9, indicating that the computation of these terms should be stable up to degree and order $n = m = 2700$ (after global scaling).

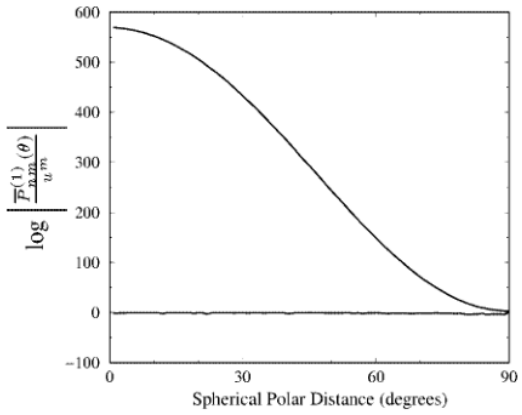

Figure E.9: Logarithm plot of maximum (upper line) and minimum (lower line) values of $|\bar{P}_{n,m}^{(1)}/u^m|$ for all $n, m \leq 2700$. Credit: [13]

However, since $u \to 0$ as we approach the poles, the term t/u introduces a polar singularity. Instead, we will compute the terms

$$\left\{u\frac{\bar{P}_{n,m}^{(1)}}{u^m}\right\} = mt\left\{\frac{\bar{P}_{n,m}}{u^m}\right\} - e_{n,m}u^2\left\{\frac{\bar{P}_{n,m+1}}{u^{m+1}}\right\} \quad \forall \quad n \geq m > 0 \ , \tag{E.64}$$

which, since $0 \leq |u| \leq 1$, should not lead to any additional overflow/underflow issues. The singularity is not an issue for the zonal terms since $m = 0$. For reasons of convenience (next section), the zonal terms will therefore still be evaluated as

$$\begin{aligned} \left\{\frac{\bar{P}^{(1)}_{n,m}}{u^m}\right\} &= m\frac{t}{u}\left\{\frac{\bar{P}_{n,m}}{u^m}\right\} - e_{n,m}u\left\{\frac{\bar{P}_{n,m+1}}{u^{m+1}}\right\} \\ \Rightarrow \quad \left\{\bar{P}^{(1)}_{n,0}\right\} &= -e_{n,0}u\left\{\frac{\bar{P}_{n,1}}{u}\right\} \quad \text{for} \quad m = 0\,. \end{aligned} \tag{E.65}$$

E.2.5 Evaluation of the Gravitational Attraction

In order to compute the gravitational attraction from a geopotential model of spherical harmonic coefficients, we need to evaluate each of the terms in (E.23). As before, it is convenient to define the following partial sums

$$\begin{aligned} \left\{\frac{X^r_{C,m}}{u^m}\right\} &= \sum_{n=\mu}^{N}\left(\frac{a}{r}\right)^n (n+1)\left\{\frac{\bar{P}_{n,m}}{u^m}\right\} C_{n,m} \quad \text{and} \\ \left\{\frac{X^r_{S,m}}{u^m}\right\} &= \sum_{n=\mu}^{N}\left(\frac{a}{r}\right)^n (n+1)\left\{\frac{\bar{P}_{n,m}}{u^m}\right\} S_{n,m} \quad \text{for} \quad n \geq m \geq 0 \end{aligned} \tag{E.66}$$

for the radial component and

$$\begin{aligned} \left\{\frac{X^\lambda_{C,m}}{u^m}\right\} &= \sum_{n=\mu}^{N}\left(\frac{a}{r}\right)^n \left\{\frac{\bar{P}_{n,m}}{u^m}\right\} C_{n,m} \quad \text{and} \\ \left\{\frac{X^\lambda_{S,m}}{u^m}\right\} &= \sum_{n=\mu}^{N}\left(\frac{a}{r}\right)^n \left\{\frac{\bar{P}_{n,m}}{u^m}\right\} S_{n,m} \quad \text{for} \quad n \geq m \geq 0 \end{aligned} \tag{E.67}$$

for the longitudinal component. For the latitudinal component, we define the sums

$$\begin{aligned} \left\{u\frac{X^{\phi'}_{C,m}}{u^m}\right\} &= \sum_{n=\mu}^{N}\left(\frac{a}{r}\right)^n \left\{u\frac{\bar{P}^{(1)}_{n,m}}{u^m}\right\} C_{n,m} \quad \text{and} \\ \left\{u\frac{X^{\phi'}_{S,m}}{u^m}\right\} &= \sum_{n=\mu}^{N}\left(\frac{a}{r}\right)^n \left\{u\frac{\bar{P}^{(1)}_{n,m}}{u^m}\right\} S_{n,m} \quad \text{for} \quad n \geq m > 0 \end{aligned} \tag{E.68}$$

and

$$\left\{X^{\phi'}_{C,0}\right\} = \sum_{n=\mu}^{N}\left(\frac{a}{r}\right)^n \left\{\bar{P}^{(1)}_{n,0}\right\} C_{n,0} \quad \text{and} \quad \left\{X^{\phi'}_{S,0}\right\} = 0 \quad \text{for} \quad m = 0 \tag{E.69}$$

noting that $S_{n,0} = 0$ and $\bar{P}^{(1)}_{n,0}/u^0 = \bar{P}^{(1)}_{n,0}$ for all n. This means that there are two sums for each vector component and six vectors in the numerical evaluation. Then, defining the following quantities

$$\begin{aligned}
\frac{\Omega_{m,r}}{u^m} &= \left\{\frac{X^r_{C,m}}{u^m}\right\}\cos m\lambda + \left\{\frac{X^r_{S,m}}{u^m}\right\}\sin m\lambda \quad \text{for} \quad n \geq m \geq 0 \\
\frac{\Omega_{m,\lambda}}{u^m} &= \left\{\frac{X^\lambda_{S,m}}{u^m}\right\}\cos m\lambda - \left\{\frac{X^\lambda_{C,m}}{u^m}\right\}\sin m\lambda \quad \text{for} \quad n \geq m \geq 0 \\
u\frac{\Omega_{m,\phi'}}{u^m} &= \left\{u\frac{X^{\phi'}_{C,m}}{u^m}\right\}\cos m\lambda + \left\{u\frac{X^{\phi'}_{S,m}}{u^m}\right\}\sin m\lambda \quad \text{for} \quad n \geq m > 0 \\
\Omega_{0,\phi'} &= \left\{X^{\phi'}_{C,0}\right\} \quad \text{for} \quad m = 0\,,
\end{aligned} \tag{E.70}$$

the summation over order, m, is again accomplished using Horner's scheme as

$$\begin{aligned}
\Omega_r &= \left[\left\{\left(\cdots\left\{\frac{\Omega_{M,r}}{u^M}u + \frac{\Omega_{M-1,r}}{u^{M-1}}\right\}u + \cdots + \frac{\Omega_{3,r}}{u^3}\right)u + \frac{\Omega_{2,r}}{u^2}\right\}u + \frac{\Omega_{1,r}}{u}\right]u + \Omega_{0,r} \\
\frac{\Omega_\lambda}{u} &= \left\{\left(\cdots\left\{M\frac{\Omega_{M,\lambda}}{u^M}u + (M-1)\frac{\Omega_{M-1,\lambda}}{u^{M-1}}\right\}u + \cdots + 3\frac{\Omega_{3,\lambda}}{u^3}\right)u + 2\frac{\Omega_{2,\lambda}}{u^2}\right\}u + \frac{\Omega_{1,\lambda}}{u} \\
\Omega_{\phi'} &= \left\{\left(\cdots\left\{u\frac{\Omega_{M,\phi'}}{u^M}u + u\frac{\Omega_{M-1,\phi'}}{u^{M-1}}\right\}u + \cdots + u\frac{\Omega_{3,\phi'}}{u^3}\right)u + u\frac{\Omega_{2,\phi'}}{u^2}\right\}u + u\frac{\Omega_{1,\phi'}}{u} + \Omega_{0,\phi'}\,.
\end{aligned} \tag{E.71}$$

Finally, the components of the gravitational attraction can be evaluated as

$$V_r = -\frac{GM}{r^2}\,\Omega_r\,, \quad V_\lambda = \frac{GM}{r^2}\,\frac{\Omega_\lambda}{u} \quad \text{and} \quad V_{\phi'} = \frac{GM}{r^2}\,\Omega_{\phi'}\,, \tag{E.72}$$

noticing that these are vector components, resolved about the axes:

- r along the radial axis between the center of the Earth and the point of evaluation,
- λ along east direction and
- ϕ' along north direction.

E.2.6 Functionals of the Geopotential

In the following is a brief overview of some of the functionals that can be derived from a geopotential model. For a more complete overview, the reader is referred to [1].

Gravitational Potential

The gravitational potential, $V(\mathbf{r})$, represents the attracting potential from the volume of masses that make up the Earth. The definition of this field is presented in Section 3.1.1, where it is also argued that $V(\mathbf{r})$ is a harmonic function outside the attracting masses. The spherical harmonic coefficients are a direct representation of this potential, which can be evaluated using (E.22):

$$V(r,\phi',\lambda) = \frac{GM}{r}\sum_{n=0}^{N}\left(\frac{a}{r}\right)^n\sum_{m=0}^{n}\bar{P}_{n,m}(\sin\phi')\left[C_{n,m}\cos m\lambda + S_{n,m}\sin m\lambda\right]\,. \tag{E.73}$$

Gravity Potential

On the rotating Earth, additionally to the attraction force, a centrifugal force is present. The centrifugal potential, $\Phi(\mathbf{r})$, is from (3.19):

$$\Phi(\mathbf{r}) = \frac{1}{2}\omega_{ie}^2 r^2 \cos^2\phi' \ , \tag{E.74}$$

and can be added to the gravitational potential, $V(\mathbf{r})$, in order to obtain the gravity potential, $W(\mathbf{r})$ as

$$W(\mathbf{r}) = V(\mathbf{r}) + \Phi(\mathbf{r}) \ . \tag{E.75}$$

Gravitational Attraction

The gravitational attraction, $\bar{\mathbf{g}}(\mathbf{r})$, is a vector field representing the pull from the attracting masses of the Earth. It can be derived from the gravitational potential, $V(\mathbf{r})$, as (3.4):

$$\bar{\mathbf{g}}(\mathbf{r}) = -\nabla V(\mathbf{r}) \ , \tag{E.76}$$

which is written out in (E.23).

Gravity

The gravity vector, $\mathbf{g}(\mathbf{r})$, represents the combined pull from attracting forces, $\bar{\mathbf{g}}(\mathbf{r})$, and the centrifugal force, $\mathbf{f}_c(\mathbf{r})$, which are given by the components

$$\mathbf{f}_c(\mathbf{r}) = \begin{bmatrix} f_{r,c} \\ f_{\lambda,c} \\ f_{\phi,c} \end{bmatrix} = \begin{bmatrix} \frac{\partial\Phi(\mathbf{r})}{\partial r} \\ \frac{1}{r\cos\phi'}\frac{\partial\Phi(\mathbf{r})}{\partial\lambda} \\ \frac{1}{r}\frac{\partial\Phi(\mathbf{r})}{\partial\phi'} \end{bmatrix} = \begin{bmatrix} \omega_{ie}^2 r \cos^2\phi' \\ 0 \\ -\omega_{ie}^2 r \cos\phi' \sin\phi' \end{bmatrix} \ . \tag{E.77}$$

The gravity vector thus represents the combined effect

$$\mathbf{g}(\mathbf{r}) = \bar{\mathbf{g}}(\mathbf{r}) + \mathbf{f}_c(\mathbf{r}) \ , \tag{E.78}$$

whereas the term gravity usually refers to the magnitude of this vector, i.e.

$$g = |\mathbf{g}(\mathbf{r})| \ . \tag{E.79}$$

Gravity Disturbance

The gravity disturbance vector, $\delta\mathbf{g}(\mathbf{r})$, is the difference between the gravity vector, $\mathbf{g}(\mathbf{r})$, and the normal gravity vector, $\boldsymbol{\gamma}(\mathbf{r})$, introduced in Section 3.3.2. This quantity is thus defined as (3.35)

$$\delta\mathbf{g}(\mathbf{r}) = \mathbf{g}(\mathbf{r}) - \boldsymbol{\gamma}(\mathbf{r}) \ , \tag{E.80}$$

whereas the gravity disturbance as a scalar quantity is defined as the difference in magnitude as (3.36)

$$\delta g(\mathbf{r}) = \|\mathbf{g}(\mathbf{r})\| - \|\boldsymbol{\gamma}(\mathbf{r})\| \ . \tag{E.81}$$

The normal gravity vector, $\boldsymbol{\gamma}(\mathbf{r})$, may also be evaluated in terms of spherical harmonic coefficients. The expansion of the normal potential contains only coefficients of order $m = 0$ (rotational symmetry) and degree $n =$ even (equatorial symmetry) [1, Sec. 4.1]. The coefficients are known as geometric coefficients are are for WGS84:

$C_{2,0}$	-0.484166774985E-03
$C_{4,0}$	0.790303733511E-06
$C_{6,0}$	-0.168724961151E-08
$C_{8,0}$	0.346052468394E-11
$C_{10,0}$	-0.265002225747E-14

Additionally, one should notice that the constants GM and a of the normal gravity model and geopotential model are generally not the same.

E.2.7 Comparison with Other Algorithms

The ICGEM website (icgem.gfz-potsdam.de) provides an online calculation service for the evaluation of geopotential models and functionals thereof. The following is a comparison of results between the algorithm implemented here and the results from this online calculation service. Figures (E.10) and (E.11) illustrates the gravitational potential and gravity, respectively.

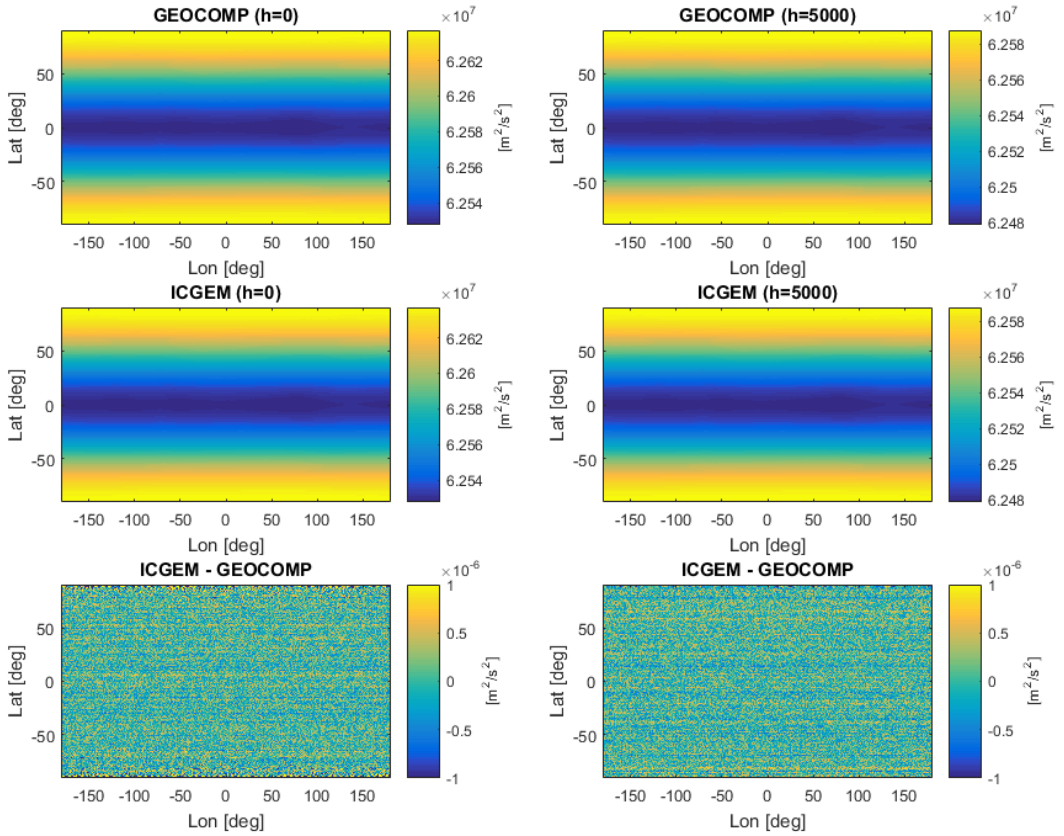

Figure E.10: Comparison of gravitational potential computed using ICGEM online calculation service (ICGEM) and the algorithm outlined here (GEOCOMP). The potential is computed at two different ellipsoidal heights, i.e. $h = 0$ m and $h = 5000$ m

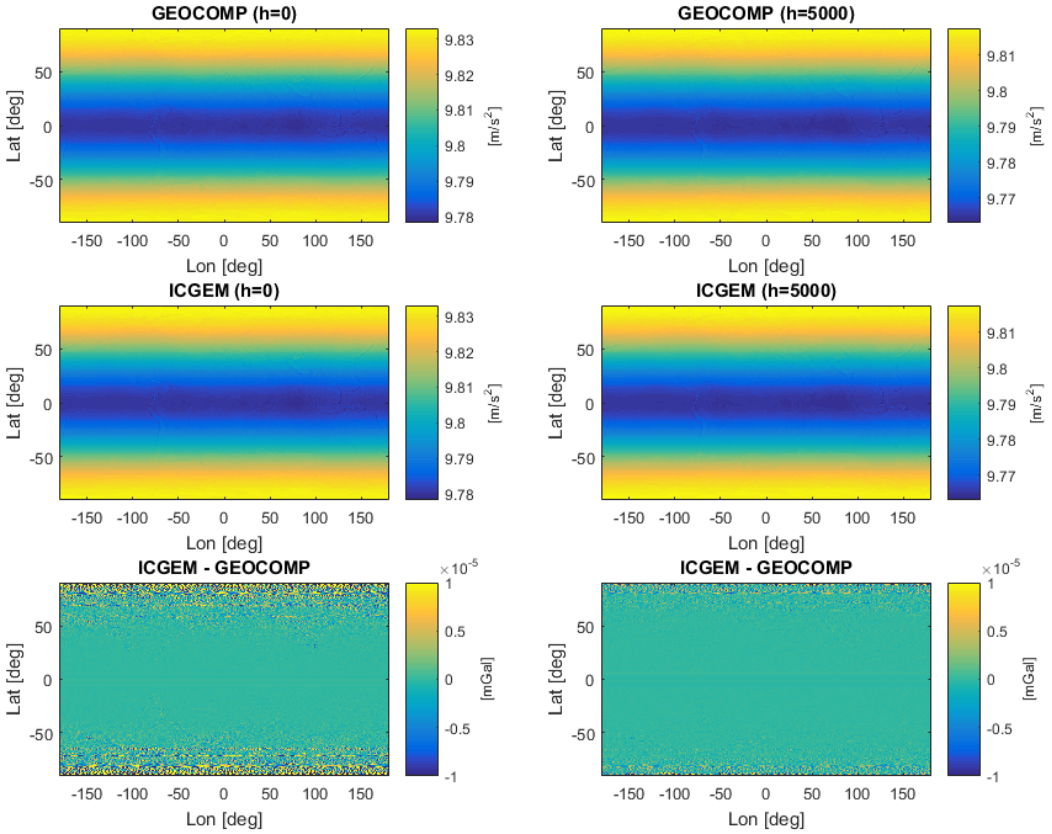

Figure E.11: Comparison of gravity computed using ICGEM online calculation service (ICGEM) and the algorithm outlined here (GEOCOMP). The gravity is computed at two different ellipsoidal heights, i.e. $h = 0$ m and $h = 5000$ m

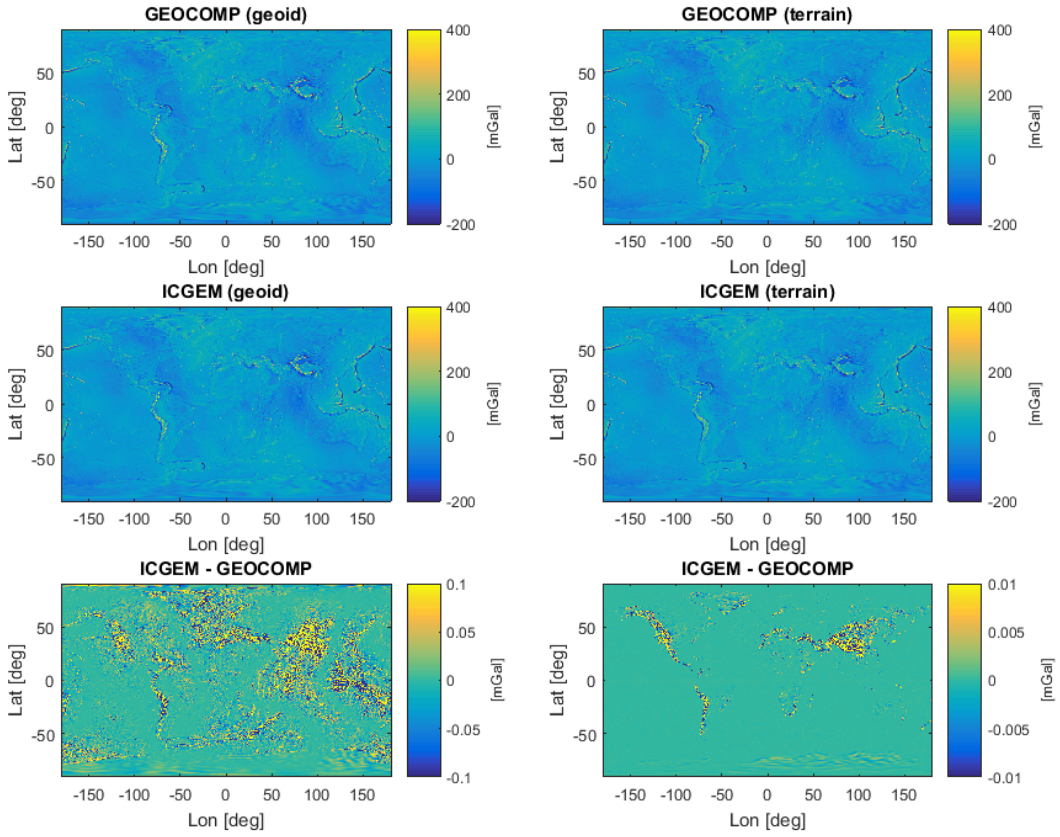

Figure E.12: Comparison of gravity disturbance computed using ICGEM online calculation service (ICGEM) and the algorithm outlined here (GEOCOMP) on the geoid (left) and on the terrain (right). It should be noted that differences in the are as large as 0.2 mGal in the Himalayas mountain region when computed on the terrain

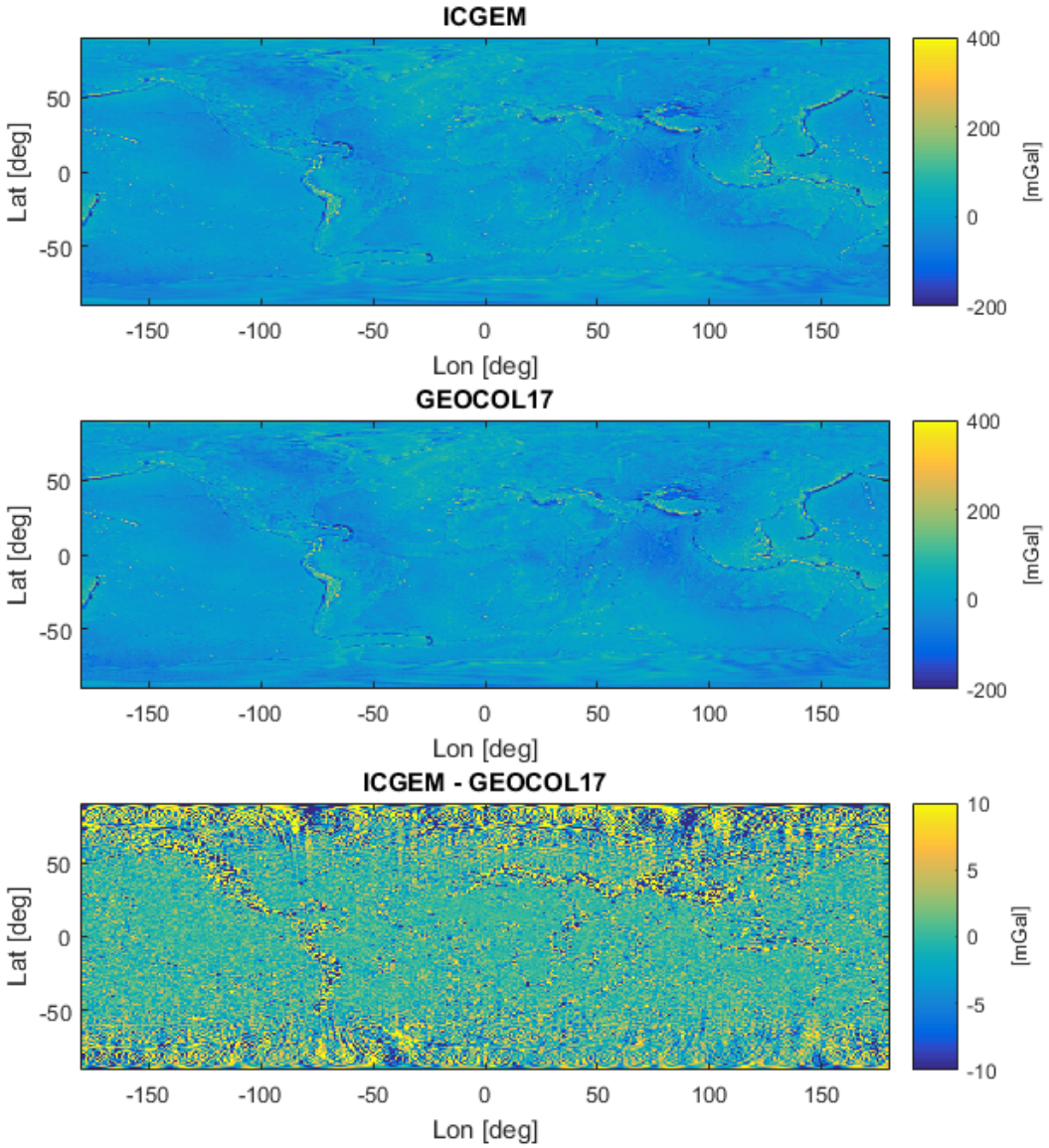

Figure E.13: Comparison of gravity disturbance computed using ICGEM online calculation service (ICGEM) and the GEOCOL17 program from the GRAVSOFT suite, evaluated on the terrain. It should be noted that differences are larger than 50 mGal in mountain regions and in the polar areas

F Articles

F.1 New Geoid of Greenland: A Case Study of Terrain and Ice Effects, GOCE and Use of Local Sea Level Data

New Geoid of Greenland: A Case Study of Terrain and Ice Effects, GOCE and Use of Local Sea Level Data

Rene Forsberg and Tim Jensen

Abstract

Making an accurate geoid model of Greenland has always been a challenge due to the ice sheet and glaciers, and the rough topography and deep fjords in the ice free parts. Terrestrial gravity coverage has for the same reasons been relatively sparse, with an older airborne survey of the interior being the only gravity field data over the interior, and terrain and ice thickness models being insufficient both in terms of resolution and accuracy. This data situation has in the later years changed substantially, first of all due to GOCE, but also new airborne gravity and ice thickness data from the NASA IceBridge mission, and new terrain models from ASTER, SPOT-5 and digital photogrammetry.

In the paper we use all available data to make a new geoid of Greenland and surrounding ocean regions, using remove-restore techniques for ice and topography, spherical FFT techniques and downward continuation by least squares collocation. The impact of GOCE and the new terrestrial data yielded a much improved geoid, as evidenced by comparison to GPS measurements along fjords, which serves as a proxy for GPS leveling data, and comparisons to new GPS leveling data in Iceland. The comparisons show significant improvements over EGM08 and older geoid models, and also highlight the problems of global sea level models, especially in sea ice covered regions, and the definition of a new consistent vertical datum of Greenland.

Keywords

Geoid • Gravity • Greenland

1 Introduction

Greenland presents a major challenge for geoid determination, due to sparse gravity data, rugged topography, deep fjords, ice sheets and glaciers, and the absence of GPS leveling. Current gravimetric geoids date back to year 2000 (for the "official" GPS-fitted version), to intermediate North Atlantic Geoid models (Forsberg et al. 2004), and to EGM2008 (Pavlis et al. 2012), which incorporated all available gravity field information up to that point in time. All geoid models have up to now, however, had many local errors, especially due to lack of good digital elevation model data in the ice free part, due to lack of data over deep fjords, and due to lack of ice sheet thickness in marginal regions.

Several new data sets have aided in improving this situation in recent years, especially new high-resolution digital DEM data, gravity and radar and ice thickness data from NASA IceBridge airborne campaigns, and GOCE satellite data. Combined with the need for a new vertical datum for the towns and ice free regions of Greenland, for precise GPS surveying in support of infrastructure such as hydropower and mining development, the computation of a new geoid

R. Forsberg (✉) • T. Jensen
National Space Institute, Technical University of Denmark, Elektrovej 327, DK2800 Lyngby, Denmark
e-mail: rf@space.dtu.dk

International Association of Geodesy Symposia,
DOI 10.1007/1345_2015_50,

model is therefore timely. This also accentuates the need for a new vertical datum, since all towns and settlements have local height systems based on historical tide gauge data of varying quality, with no leveling connections between towns. Combined with large climate-induced land uplift values in many regions, this make the definition of a consistent height system between towns and settlements quite a challenge.

In this paper we will therefore outline a new geoid determination, incorporating all available new gravity, DEM, ice thickness and satellite data, and compare to existing GPS and tide gauge height information in towns, and – in the absence of leveling – compare the new geoid to fjord GPS-tide gauge profiles and Iceland leveling, demonstrating major improvements.

2 Geoid Determination Method

The methodology for the new Greenland gravimetric geoid is based on remove-restore techniques. The anomalous gravity potential T is split into three parts

$$T = T_{EGM} + T_{RTM} + T_{res} \tag{1}$$

where T_{EGM} is the contribution of a combined GOCE/EGM2008 spherical harmonic expansion, T_{RTM} the terrain effect, and T_{res} the residual field

$$T_{EGM} = \frac{GM}{r}\sum_{n=2}^{N}\left(\frac{R}{r}\right)^{n} \times \sum_{m=0}^{n}\left(C'_{nm}\cos m\lambda + S_{nm}\sin m\lambda\right) P_{nm}(\sin\varphi) \tag{2}$$

where GM is the mass of the earth times the gravitational constant, and R the earth radius. The spherical harmonic coefficients of the anomalous gravity field C'_{nm} and S_{nm} are taken from EGM2008 up to a maximal degree 360 after subtraction of the normal field coefficients, but with coefficients of the ESA GOCE Release 4 "direct" model (Pail et al. 2011) substituted in the harmonic degree band 80–200 (with a gradual linear blending of EGM08 and GOCE R4 in the bands 80–90 and 180–200). This approximate approach has been used to improve the mid-wavelength bands of EGM2008 with GOCE data. The EGM2008 model has not been used to the full degree, since better high-resolution data is now available in Greenland than was available for EGM2008.

The reference field and the geoid determination will be done rigorously as a quasigeoid computation, i.e. referring to the geoid to the surface of the terrain by

$$\zeta = \frac{T(\varphi, \lambda, H)}{\gamma_0} \tag{3}$$

where ζ is the height anomaly (quasigeoid) and γ_0 normal gravity. For the same reason the reference field T_{EGM} is computed as a spatial "sandwich grid" at 3 separate elevations of 0, 3 and 8 km, and then interpolated to the actual height of a gravity observation point or a quasi-geoid computation point (some IceBridge transit flight legs were at a flight elevation of 10 km).

Terrain reductions are done by the RTM method using space-domain prism integration (Forsberg 1984), based on a reference DEM formed from the detailed DEM by a low-pass filtering at a corresponding resolution to the used reference field. To handle the terrain and ice together in the RTM method, equivalent rock topography was used over the ice covered regions, i.e.

$$h^{EQ} = h^{DEM} - \frac{2.67}{0.92}t^{ice} \tag{4}$$

where t^{ice} is the thickness of the ice, h^{DEM} the surface elevation, and h^{EQ} the equivalent rock topography, assuming a rock density of 2.67 g/cm^3 (2,670 kg/m^3) and ice 0.92 kg/m^3. The use of rock-equivalent topography for terrain reductions, rather than the full 3-D mass field, is justified by the flat nature of the interior of the ice sheet (i.e., ice effects can with good approximation be treated as a Bouguer plate effect; the terrain effect from a Bouguer plate is independent of actual heights, only total mass per area).

The DEM used for Greenland was based on IceSat data, augmented in the ice-free and marginal ice zone parts by ASTER and SPOT5 stereo photogrammetry (Howat et al. 2014), edited and converted to an orthometric height DEM, and supplemented with DEM data from national mapping projects in northern Greenland, Iceland and Arctic Canada regions. Ice thickness data in Greenland were taken from the compilation of radio echo sounding by Bamber et al. (2013), and rock-equivalent heights subsequently computed within regions classified as ice by national mapping masks. Due to lack of radar echo sounding data in some margin areas and outlying ice caps, significant errors in the terrain reductions are expected there. For Iceland radar ice thickness data were provided by the University of Iceland for the three main ice caps. The composite rock-equivalent DEM was computed at 15″ resolution, and shown in Fig. 1.

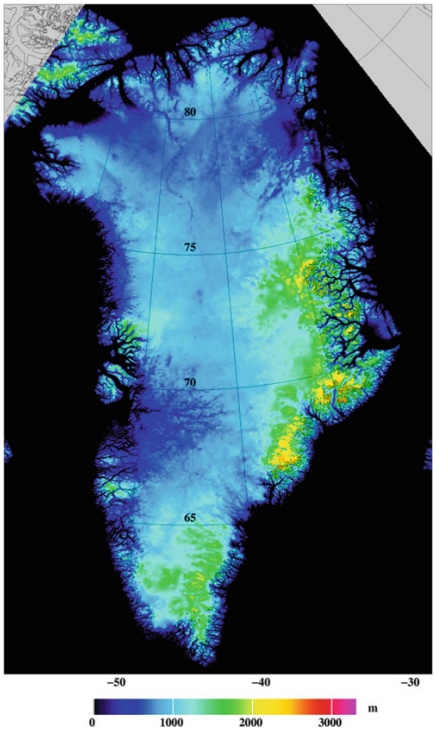

Fig. 1 Rock-equivalent topography DEM of Greenland, highlighting coastal mountains. (the actual height of the ice sheet is more than 3,000 m in the center of Greenland)

After reduction of data for reference model and RTM, airborne and surface gravimetry data is downward continued and gridded at the surface of the rock-equivalent terrain by least-squares collocation using the planar logarithmic covariance function (Forsberg 1987), used in a block scheme of 1° resolution blocks with 50% overlap to neighboring blocks. The conversion from gravity to geoid is subsequently done using bandwise spherical Fourier techniques, for details of the methods see Forsberg and Sideris (1993). In the method the Stokes integral is evaluated by a series of convolutions, each accurate around a certain reference latitude φ

$$\begin{aligned}\zeta_{res} &= S_{ref}(\Delta\varphi, \Delta\lambda) * [\Delta g_{res}(\varphi, \lambda) \sin\varphi] \\ &= F^{-1}[F(S_{ref})\, F(\Delta g_{res} \sin\varphi)]\end{aligned} \tag{5}$$

where F[·] is the two-dimensional Fourier transform, S_{ref} the Stokes function at the reference latitude and Δg_{res} the residual gravity anomaly.

To prevent the inherently highly accurate GRACE/GOCE gravity field information in the EGM model to be "overruled" by the influence from terrestrial gravity data, *modified* Stokes functions are used. The modified Wong-Gore formulation used here is of form

$$S_{mod}(\psi) = S(\psi) - \sum_{n=2}^{N_2} \alpha(n) \frac{2n+1}{n-1} P_n \cos(\psi) \tag{6}$$

where the "GRACE-transition" coefficient $\alpha(n)$ increase linearly from 0 to 1 between degrees N_1 and N_2

$$\alpha(n) = \begin{cases} 1 & for \quad 2 \le n \le N_1 \\ \frac{N_2 - n}{N_2 - N_1} & for\ N_1 \le n \le N_2 \\ 0 & for \quad N_2 \le n \end{cases}, n = 2, \ldots, N \tag{7}$$

The estimation of N_1 and N_2 can only be done empirically, but values in the range 180–200 would be expected, based on the error characteristics of GRACE and GOCE; these values have therefore been used here.

After the spherical Fourier transformation from gravity to quasigeoid, and restoring of the terrain and EGM-effects on the geoid, the classical geoid N is obtained by

$$\zeta - N \approx -\frac{\Delta g_B}{\gamma_0} H \tag{8}$$

where Δg_B is the Bouguer anomaly, readily computed from the reduced anomalies by restoring of the reference field and the Bouguer effect of the smooth reference DEM. It should be noted that the formula (8) is *exact* if Helmert-type normal density orthometric heights are used; for details see Heiskanen and Moritz (1967).

3 Gravity Data and Gravimetric Geoid

The new Greenland gravimetric geoid was computed in the geographic region 58–85°N, 78–7°W, at a $1.2' \times 3'$ grid (about 2 km resolution). The gravity data used originate from a large variety of national and international land, marine and airborne surveys, including the Greenland-wide first airborne survey of the US Naval Research Laboratory 1991–1992 (Brozena 1991), DTU Space airborne surveys of coastal and Arctic Ocean regions 1998–2009, and NASA IceBridge gravity data 2010–2012 (Cochran and Bell 2010).

All data in the database were quality checked and transformed to a common, geoid-based gravity reference system, and subsequently reduced for EGM and RTM terrain effects.

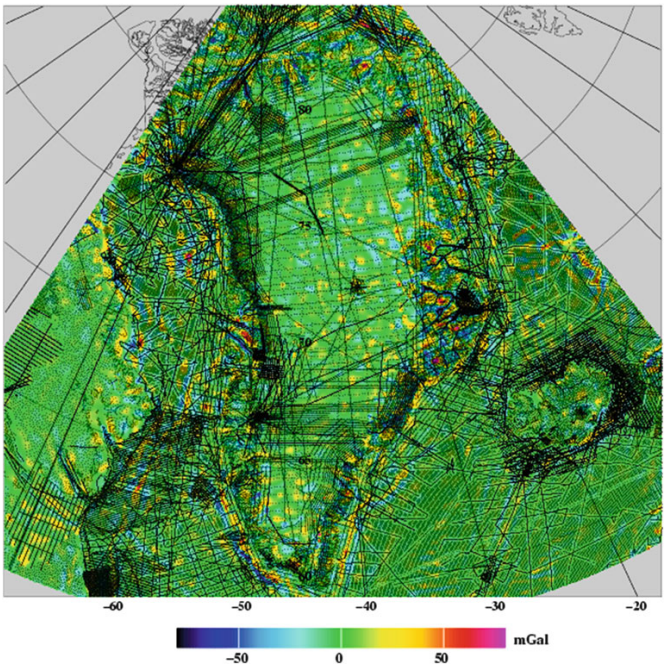

Fig. 2 Gravity data coverage overlaid on EGM-and RTM-reduced gravity grid

Table 1 Statistics of gravity data reductions for selected, thinned data sets (mGal)

		Original data		Reduced data	
Data	No. of points	Mean	Std.dev.	Mean	Std.dev.
Land gravity	8,503	−16.8	44.8	−4.6	16.0
IceBridge airborne	56,921	10.5	44.3	−1.7	12.9
NRL airborne	32,010	16.4	38.0	0.1	11.5
DTU airborne	64,265	9.8	38.1	0.3	16.1

Figure 2 shows a plot of all used gravity data, overlaid on the gridded, reduced and downward continued data set, taking into account the varying standard deviations of the various data. For marine areas with no marine gravity data, DTU10 satellite altimetry gravity was used as fill-in. Especially the IceBridge data, with low-level flights along the ice margins, major outlet glaciers and fjords, have made a major difference relative to the data used in EGM2008. Table 1 shows the statistics for the data reductions of some main data sets.

It is seen from Table 1 that all airborne data sets, after reductions, give a consistent near-zero bias, and small standard deviation. For the land data, the bias likely express the uneven distribution of the land gravity points, mostly done by helicopter on mountains and nunataks, and fjord/local ice cap effects. The r.m.s. statistics of data have been used as a guide to the determination of the covariance function used for the downward continuation.

After the Fourier transformation, the restoral of terrain and EGM effects, and the conversion from quasigeoid to geoid, a final gravimetric geoid is obtained (Fig. 3).

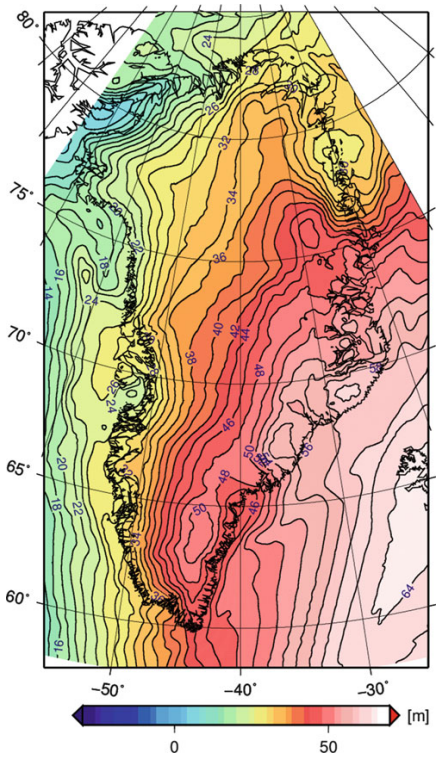

Fig. 3 New gravimetric geoid of Greenland from surface, airborne and satellite gravity

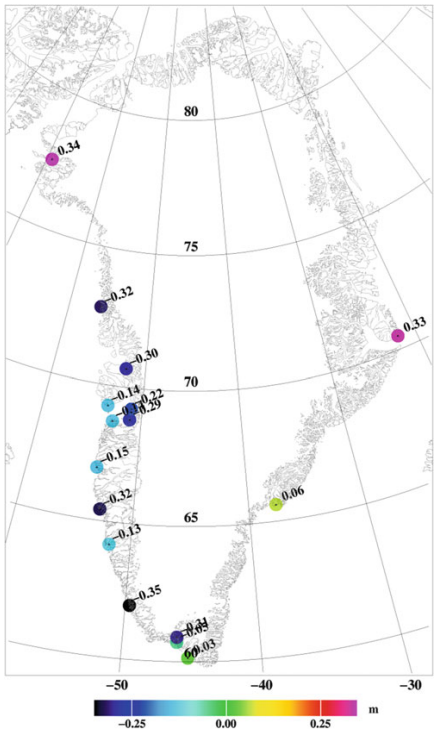

Fig. 4 Differences (m) between GPS/leveling (Asiaq) and the new geoid is the Greenland towns

4 Evaluation of the New Geoid

Validating the new geoid is difficult, as no GPS leveling exists between settlements. The Greenland height system is based on local tide gauge measurements in the towns, of varying duration from few days to years, and all dating back to the 1960s or earlier. Figure 4 shows the offsets of the new geoid in the main towns, based on precise first order GPS measurements (REFGR), and the local tide gauge heights from the Greenland Survey (ASIAQ). With land uplift values up to several mm/year, and spatially changing mean sea level, is it quite natural that the geoid would not fit; basically the present vertical datum of Greenland is a historical mean sea level system, and not geoid-based.

Since the new geoid of Greenland also covers Iceland, and Iceland recently has done a releveling of whole country, the fit of the geoid to Iceland GPS leveling can give an independent check of accuracy. Iceland shares with Greenland the mountainous terrain and several large ice caps, but has a relatively good gravity coverage, and a coherent leveling network, cf. Fig. 5. Table 2 shows the fit of the geoid to Iceland GPS, showing a major improvement over EGM2008.

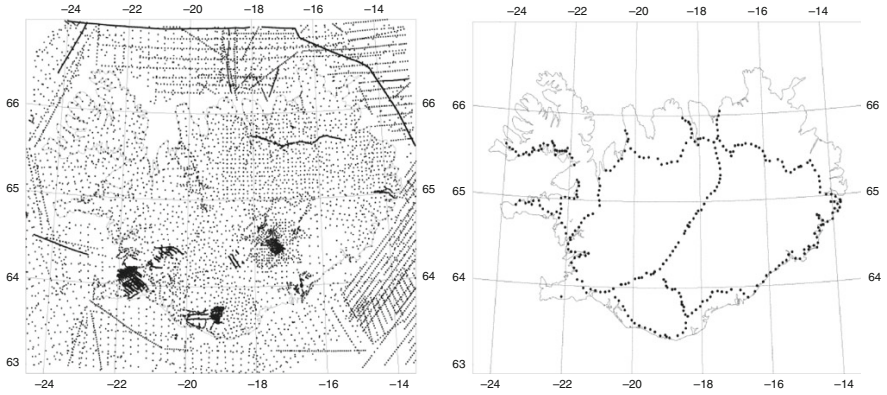

Fig. 5 Gravity coverage of Iceland (*left*), and recently observed GPS and leveling data (*right*)

Table 2 Comparison between GPS-leveling data and geoids in Iceland (unit: m)

Comparison (311 GPS points)	Mean	Std.dev.
Original GPS-leveling data	65.54	0.794
Difference GPS minus new geoid	−0.10	0.037
Difference GPS/lev minus EGM08	−0.12	0.113

To get an estimate of geoid accuracy in Greenland, profiles with GPS observations of sea level have been done along a number of long fjords. The long fjords in Greenland have relatively small dynamic topography, and detailed oceanographic observations of the Godthåbsfjord region has confirmed changes in mean dynamic topography at the level of 5 cm and less (Mortensen, Greenland Climate Research Centre, pers.comm.). Therefore the fjords, except for the tides, can be treated as an approximation to an equipotential surface. Because wind conditions along Greenland fjords are often calm, it is relatively simple to determine instantaneous heights of the fjord relative to a GPS antenna to an accuracy level of few cm by local leveling.

By making *relative* tidal measurements, with temporary tide gauges positioned temporarily along the fjords, and combined with GPS observations, a "quasi" GPS/leveling data set can be observed in a matter of few days. This has been done along several fjords in Greenland, at typical profile lengths of 100–150 km, either in winter where fjords are frozen (and kinematic GPS "tide gauges" can be put directly on the sea ice, cf. Fig. 6 for an example), or in summer with slightly less accurate local GPS observations of apparent sea level heights along the coasts. Table 3 shows the results of the geoid comparisons along a number of fjords, confirming a geoid accuracy of 10 cm or better.

5 Conclusions

A new geoid of Greenland has been computed, based on multiple sources of land, marine and airborne gravity data, GOCE and EGM2008/GRACE data, and new high-resolution DEM and ice thickness data. The inclusion of GOCE, new DEM, and new airborne gravity data from IceBridge, has given a much more accurate geoid than earlier geoid models, confirmed also by new hydropower surveys (Asiaq, pers.comm.). With the use of GOCE/GRACE reference model data, and modified Stokes kernels preventing local data from changing the long-wavelength satellite information, the geoid accuracy at long wavelength should be similar to GOCE, i.e. at the cm-level for wavelengths longer than some 400–500 km. Local accuracy depends on the gravity data coverage and the errors coming from unknown fjord depths or local ice cap thickness. Results from Iceland and fjord profiles point to errors in the 5–10 cm range.

Given the uncertainty in the existing vertical datum, it is clear that a new geoid-based height system of Greenland would be superior for GPS use, with higher intrinsic accuracy, similar to the recently adopted new vertical reference system of Canada. Discussions are therefore currently ongoing with Greenland and Danish authorities for the possible adoption of a new height system.

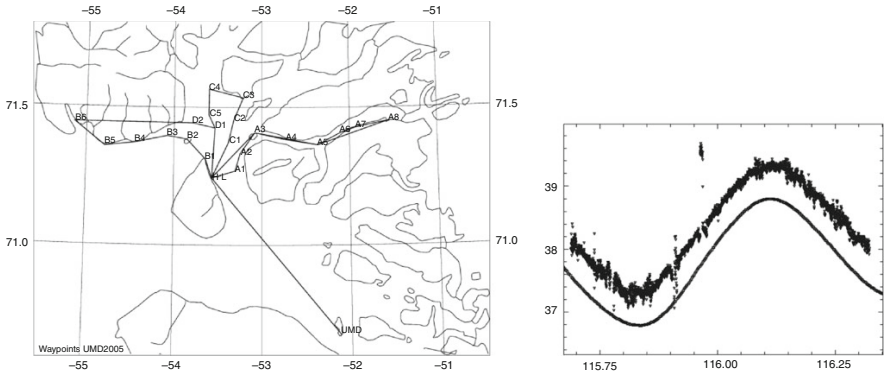

Fig. 6 Example of a 160 km long winter fjord profile in central W Greenland (Uummannaq area). *Left*: GPS points on ice, *right*: example of a GPS (*upper curve*) and local tide gauge observation (*lower curve*) of sea level at the reference point (x-axis: time in Julian days, y-axis height in m)

Table 3 Comparison of the Greenland geoid along selected fjord profiles (unit: m)

Comparison fjord	Mean	Std.dev.	EGM08 st.dev.
Svartenhuk-Kangerlussuaq (NW Greenland)	−0.24	0.073	0.302
Ameralik (Nuuk; SW Greenland)	−0.08	0.117	0.158
Tasermiut (South Greenland)	0.05	0.127	0.137
Ammassalik Fjord (Tasiilaq, East Grenland)	−0.14	0.089	0.139

Acknowledgements Gravity data for the new Greenland geoid have been contributed by NASA IceBridge, Iceland Geodetic Survey, Geodetic Survey Division, Canada, and numerous government and commercial surveys in Greenland. GPS and leveling data in Iceland were provided by Gudmundur Valsson, Iceland Geodetic Survey.

References

Bamber J, Griggs JA, Hurkmans RTWL, Dowdeswell JA, Gogineni SP, Howat I, Mouginot J, Paden J, Palmer S, Rignot E, Steinhage D (2013) A new bed elevation dataset for Greenland. Cryosphere 7:499–510. doi:10.5194/tc-7-499-2013

Brozena J (1991) The greenland aerogeophysics experiment: airborne gravity, topographic and magnetic mapping of an entire continent. In: Colombo (ed) From Mars to Greenland: charting gravity with space and airborne instruments. IAG Symposium Series 110. Springer Verlag, pp 203–214

Cochran JR, Bell RE (2010) IceBridge Sander AIRGrav L1B geolocated free air gravity anomalies 2010-12. Boulder. National Snow and Ice Data Center, Colorado USA

Forsberg R (1984) A study of terrain reductions, density anomalies and geophysical inversion methods in gravity field modelling. Reports of the Department of Geodetic Science and Surveying, No. 355, The Ohio State University, Columbus, Ohio

Forsberg R (1987) A new covariance model for inertial gravimetry and gradiometry. J Geophys Res 92(B2):1305–1310

Forsberg R, Sideris MG (1993) Geoid computations by the multi-band spherical FFT approach. Manuscript Geod 18:82–90

Forsberg R, Olesen A, Vest A, Solheim D, Hipkin R, Omang O, Knudsen P (2004) Gravity field improvements in the north atlantic region. Proceedings GOCE Workshop, ESA-ESRIN

Heiskanen W, Moritz H (1967) Physical geodesy. W.H. Freeman and Co, San Francisco

Howat IM, Negrete A, Smith BE (2014) The Greenland Ice mapping project (GIMP) land classification and surface elevation datasets. Cryosphere 8:1509–1518. doi:10.5194/tc-8-1509-2014

Pail R, Bruinsma SL, Migliaccio F, Förste C, Goiginger H, Schuh WD, Höck E, Reguzzoni M, Brockmann JM, Abrikosov O, Veicherts M, Fecher T, Mayrhofer R, Krasbutter I, Sanso F, Tscherning CC (2011) First GOCE gravity field models derived by three different approaches. J Geod 85(11):819–843. doi:10.1007/s00190-011-0467-x

Pavlis NK, Holmes SA, Kenyon S, Factor JK (2012) The development and evaluation of the earth gravitational model 2008 (EGM2008). J Geophys Res. doi:10.1029/2011JB008916

F.2 Strapdown Airborne Gravimetry Using a Combination of Commercial Software and Stable-Platform Gravity Estimates

Strapdown Airborne Gravimetry Using a Combination of Commercial Software and Stable-Platform Gravity Estimates

Tim E. Jensen, J. Emil Nielsen, Arne V. Olesen, and Rene Forsberg

Abstract

For the past two decades, airborne gravimetry using a Strapdown Inertial Measurement Unit (SIMU) has been producing gravity estimates comparable to the traditional stable-platform single-axis gravimeters. The challenge has been to control the long term drift of the IMU sensors, propagating into the long-wavelengths of the gravity estimates. This has made the stable-platform approach the preferred method for geodetic applications. In the summer of 2016, during a large airborne survey in Malaysia, a SIMU system was flown alongside a traditional LaCoste&Romberg (LCR) gravimeter. The SIMU observations were combined with GNSS observations using the commercial software product "Inertial Explorer" from NovAtel's Waypoint software suite, and it is shown how gravity estimates can be derived from these results. A statistical analysis of the crossover differences yields an RMS error of 2.5 mGal, which is comparable to the results obtained from the LCR gravimeter. The properties of the SIMU and LCR systems are compared and a merging of the two is performed. A statistical analysis of the crossover differences of the merged product yields an RMS error of 1.3 mGal. These results indicate that the properties of the two units are complementary and that a combination of the two can result in improved gravity estimates.

Keywords

Airborne gravimetry • Inertial Explorer • Strapdown IMU

1 Introduction

Airborne gravimetry provides a fast and efficient way of covering large areas that are remote or otherwise inaccessible. Moreover, this technique is capable of providing seamless coverage in near-coastal areas, were shallow water makes it difficult for marine gravimetry and satellite altimetry derived models are generally not reliable (Andersen et al. 2015).

The advantages of airborne gravimetry were recognized early on (Thompson 1959). However, the technique did not become fully operational until the Global Positioning System (GPS) became available in the late eighties. The Geodynamics Department at the National Space Institute of Denmark (DTU Space) has carried out large airborne surveys since the early nineties (Brozena 1992), back then known as the Danish National Survey and Cadastre (KMS), using a LaCoste&Romberg (LCR) spring-type gravimeter (Valliant 1992). The concept was to mount a single-axis accelerometer on a stabilized platform, that to some extent isolates the movements of the gravimeter from the movements of the aircraft. This allows only for scalar gravimetry which, in contrast to vector gravimetry, estimates only the magnitude of the gravity acceleration.

The use of Inertial Measurement Units (IMUs) for airborne gravimetry has been attempted since the early nineties (Schwarz et al. 1992; Jekeli 1994; Wei and Schwarz 1998). The obvious advantages being smaller size, ease of operation and lower prize, compared to traditional air gravimeters.

T.E. Jensen (✉) • J.E. Nielsen • A.V. Olesen • R. Forsberg
Department of Geodynamics, DTU Space, Elektrovej 327, 2800 Kgs. Lyngby, Denmark
e-mail: timj@space.dtu.dk

International Association of Geodesy Symposia,
DOI 10.1007/1345_2017_9, © Springer International Publishing AG 2017

Since the IMU contains three perpendicular accelerometers, it has the potential to do vector gravimetry and estimate the deflection of the vertical. Glennie et al. (2000) reported accuracies similar to the LCR system, with the IMU outperforming the LCR gravimeter in the short-wavelength components. The biggest challenge, when using the IMU for gravimetry, is the separation of gravity variation from long term drift in the sensors, leaking into the long-wavelengths of the gravity estimates (Glennie and Schwarz 1999; Jekeli and Kwon 1999; Glennie et al. 2000). However, the majority of the drift has been associated with temperature variation and temperature calibrations have been seen to significantly improve the results (Huang et al. 2012; Becker et al. 2015b; Becker 2016).

Since 2013, DTU Space has been flying an iMAR RQH IMU alongside the LCR system on a number of campaigns. This was done in collaboration with the Technical University of Darmstadt, who owns the unit. The IMU has been physically bolted to the floor of the aircraft, which is commonly known as strapdown mode. This approach will therefore be referred to as Strapdown IMU (SIMU) airborne gravimetry, or simply strapdown gravimetry. In April 2016, DTU Space purchased a similar iMAR RQH unit. The unit was flown alongside the LCR system on a large campaign in Malaysia during the summer of 2016.

Using the observations from this Malaysia campaign, this paper aims to show that gravity estimates can be produced using the commercial software product "Inertial Explorer", from NovAtel's Waypoint software suite. Although this method can be used to derive the full gravity vector, only the vertical component is considered here. It will also be shown that a combination with estimates from the LCR system yields results superior to the individual estimates.

2 Basic Principles

A gravimeter is basically an accelerometer, measuring specific force, $\mathbf{f}$. This is a combination of gravitational acceleration, $\mathbf{g}$, and kinematic acceleration, $\ddot{\mathbf{r}}$, where dots refer to time derivatives. In order to derive gravity from the observations, one must therefore separate the two effects as

$$\mathbf{g} = \ddot{\mathbf{r}} - \mathbf{f} \,, \tag{1}$$

where the kinematic component, $\ddot{\mathbf{r}}$, must be observed using some alternative sensor. Commonly, the Global Navigation Satellite System (GNSS) is used to estimate position, which is then double-differentiated in order to yield acceleration. This *direct approach* has been the most common method in airborne gravimetry (Jekeli 2001). However, one can also follow a more *indirect approach* by double-integrating the sensed accelerations as

$$\mathbf{r} = \iint (\mathbf{f} + \mathbf{g}) \, \mathrm{d}t \,, \tag{2}$$

and then derive gravity from a comparison of position estimates. This approach is commonly used in integrated IMU/GNSS navigation systems, where the entire theoretical framework is already well-developed. In this approach, one typically models the gravity variation as a stochastic process, which is based on the assumption of random variation with respect to spatial coordinates. Further assumptions such as stationarity, ergodicity and isotropy are typically also used, all of which can of course be questioned. Stochastic interpretations of the gravity field is however not unknown in the field of geodesy and is frequently used in e.g. least-squares collocation. See Jekeli (2001) for a more thorough discussion on the subject.

NovAtel's Inertial Explorer software uses the second approach for combining GNSS and IMU observations using a Kalman filter framework. The intended application is navigation, in which the two types of observations are often combined due to their complementary properties. The GNSS observations have a low short-term precision, compared to IMU observations, but a long term stability. The IMU observations are accurate on short time scales, but because errors are integrated, the long term stability is poor. In airborne gravimetry, however, this argument is no longer valid, since it is the difference between the two signals that is of interest.

In this framework, we therefore have to think of the IMU as a navigation system. The basic principle is that angular rates, measured by the gyroscopes, are integrated for attitude. The accelerations, measured by the accelerometers, are integrated once to yield velocity and twice to yield position. In this way, the IMU works as an Inertial Navigation System (INS), supplying estimates of attitude, velocity and position. These are then combined with GNSS estimates using a Kalman filter framework.

2.1 The Kalman Filter

The Kalman filter is a useful framework for combing estimates in a statistically optimal way. It is an *optimal recursive data processing algorithm*, rather than a filter (Maybeck 1979). Basically, the algorithm consists of two phases:

1. A measurement update phase
2. A system propagation phase

In order to get a more intuitive impression of how the algorithm works, consider the following one-dimensional example. In the **measurement update phase**, we have two observations, x and z, of the position, both associated with some standard deviation, σ_x and σ_z. The underlying assumption is that the associated probability density functions are

Gaussian. These two observations can be combined into one optimal estimate using the principle of least squares as

$$\mu = \frac{\sigma_z^2}{\sigma_x^2+\sigma_z^2}x + \frac{\sigma_x^2}{\sigma_x^2+\sigma_z^2}z = x + \frac{\sigma_x^2}{\sigma_x^2+\sigma_z^2}(z-x) \\ = x + K\delta z \tag{3}$$

and

$$\sigma^2 = \frac{1}{1/\sigma_x^2+1/\sigma_z^2} = \sigma_x^2 + K\sigma_x^2 \,, \tag{4}$$

where $K = \sigma_x^2/\left(\sigma_x^2+\sigma_z^2\right)$ is known as the Kalman gain and $\delta z = z - x$ as the measurement innovation. With an assumption of Gaussian error distribution, this estimate is optimal according to any statistical measure (Maybeck 1979). The new estimate will therefore represent some linear combination of the two observations, with the weight distributed according to the confidence in each observation. The weighting factor is the Kalman gain.

In the **system propagation phase**, the current estimate, μ, is propagated forward in time by integrating the IMU observations. This is done until the next GNSS observation, at which point the two observations are again combined. The GNSS estimate comes with some associated uncertainty from the GNSS processing software used. The confidence in the IMU estimate is propagated forward in time from the previous estimate. In order to do this, one must define the following two properties:

- A *system model* consisting of a set of dynamics equations, basically describing the physics of the situation
- A *stochastic model* defining how gyroscope and accelerometer errors propagate onto the estimates. This model includes random noise, bias variation, scale factors etc., but also any vehicle dynamics not included in the system model as for example aircraft vibration

This one-dimensional example outlines the basic principles and recursive nature of the Kalman filter framework, on which the Inertial Explorer software is based. The system model is already included in the software and cannot be altered by the user. The user has the option to define her own stochastic model, corresponding to the error characteristics of her own IMU. The software does however have a number of pre-defined stochastic models, associated with both NovAtel's own products and a number of third party IMUs.

2.2 Inseparability of Accelerometer Bias and Gravity Variation

Extending the number of dimensions from one to three, there are nine basic navigation parameters to be estimated, along with a number of additional parameters determined by the user. In this case there are six additional parameters, giving a total of 15 parameters (five three-dimensional vectors) as

$$\mathbf{x} = \{\boldsymbol{\psi}, \mathbf{v}, \mathbf{p}, \mathbf{b}_\omega, \mathbf{b}_a\} \,, \tag{5}$$

where $\boldsymbol{\psi}$ denotes the attitude in terms of three Euler angles, $\mathbf{v}$ is the velocity and $\mathbf{p}$ the position. The two vectors, $\mathbf{b}_\omega$ and $\mathbf{b}_a$, represent estimates of gyroscope and accelerometer bias, respectively. The vector $\mathbf{x}$ is known as the state vector. The IMU provides estimates of attitude, velocity and position, while the GNSS system provides estimates of position and velocity. In order to obtain estimates of all 15 state parameters, the Kalman filter must exploit the covariance matrix which is built through the forward propagation phase, using the system dynamics equations defined within the Inertial Explorer software. In general, however, the observability and estimability, of the states depend on the type of observations and vehicle dynamics (Becker et al. 2015a).

Typically, to estimate gravity using this indirect Kalman filter approach, additional states are added to the state vector in order to model gravity as a stochastic process (Deurloo 2011; Becker 2016). This is not possible within the Inertial Explorer Software. However, when the aircraft manoeuvring is limited to horizontal non-accelerated flight, as is typically the case for long-range airborne gravity campaigns, the accelerometer bias variation and gravity variation become inseparable (Glennie and Schwarz 1999; Jekeli and Kwon 1999; Deurloo 2011; Becker 2016). In this static configuration, where both accelerometer bias and gravity varies with time, the system cannot separate the two sources of variability. Gravity will therefore be absorbed by the accelerometer bias estimates and consequently be a combination of actual bias variation and gravity variation.

This inseparability is usually the largest challenge in strapdown gravimetry. However, it can also be exploited to derive gravity estimates using a commercial software product, as will be shown in the following. Since Inertial Explorer already corrects for part of the gravitational signal using a model for the normal gravity field. The component of gravity that remains in the accelerometer bias estimates is the gravity disturbance.

3 Data

The dataset consists of 25 flights (129 h/27,257 km), flown in the South China Sea, Malaysia, during summer 2016. These flights were broken into 91 flight lines (68 h/21,288 km) as illustrated in Fig. 1. The entire survey was carried out using a BeechCraft King Air 200 aircraft.

The scientific instruments on board the flight were several GNSS receivers, linked to a GNSS antenna, along with

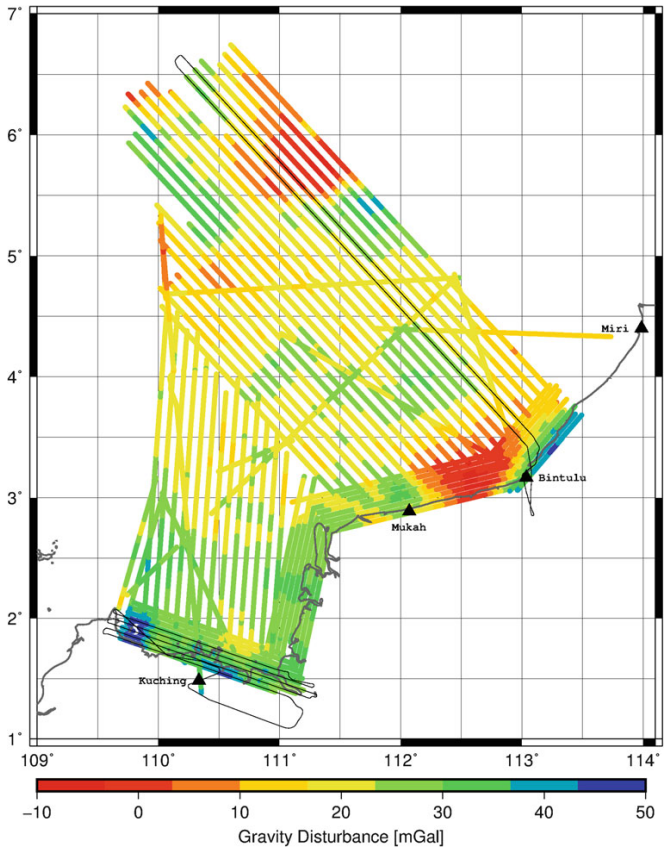

Fig. 1 Estimated gravity disturbance (combined IMU/LCR product) for the entire survey, consisting of 91 flight lines. The average speed was 88 m/s (std. dev. = 0.3, min. = 87, max. = 89) and the average altitude was 1966 m (std. dev. = 14, min. = 1885, max. = 1989), with only two low altitude outliers representing short line segment in the airport return phase. For two flights, the flight track is drawn in *black*. The results from these two flights are shown in Fig. 2

Table 1 Specification of the gyroscope and accelerometer components in the iMAR RQH unit owned by DTU Space

	Gyroscopes	Accelerometers
Bias instability[a]	$<0.002°/h$	$<10\,\mu g$
Random walk	$<0.0011°/\sqrt{h}$	$<8\,\mu g/Hz$
Scale factor	<5 ppm	<100 ppm

[a]Const. temperature

a LaCoste&Romberg single-axis gravimeter mounted on a stabilised platform (LCR system) and the iMAR RQH-unit mounted in strapdown mode (Table 1). For most of the flights, there was an on-ground reference GPS system at the airport.

4 Processing Methodology

The GNSS observations were processed using the Waypoint software. Where observations from a reference station were available, a differential solution was preferred. Otherwise a Precise Point Positioning (PPP) solution was produced. The processing was done using the final satellite ephemerid products.

Gravity disturbance was estimated from the LCR system according to the direct approach introduced earlier. In order to estimate the kinematic component, positions derived from GNSS were double-differenced and the Eötvös effect was accounted for. Besides removing the kinematic contribution,

the LCR accelerations were subjected to a platform tilt correction and a subsequent two-pass Butterworth filter of 150 s filter length (Olesen and Forsberg 2007). For a more thorough description of the LCR processing, see Olesen (2002).

The IMU logs the observed specific force and angular rates with an associated time stamp and temperature. The IMU unit contains an internal GNSS receiver, which synchronizes the observations with GPS time. The first step in the processing was to inspect the time stamps, since these were found to have some artefacts that needed to be corrected. The second step was to apply a simple warm-up temperature calibration to the vertical accelerometer only, which is observing the majority of the gravity signal (Becker et al. 2015b).

The IMU and GNSS data from all 25 flights were then processed in a loosely coupled mode using Inertial Explorer. Loosely coupled means that estimated GNSS observations are processed separately and introduced as positions and velocities (Groves 2013). The Inertial Explorer software has a pre-defined stochastic model associated with the error characteristics of the iMAR RQH unit. This model was used in the processing. The software will automatically process the data both forwards and backwards in time, apply a Rauch-Tung-Striebel (RTS) smoother (Brown and Hwang 2012) and combine the two results.

The products of further interest are the estimated attitudes and accelerometer biases. The accelerometer bias estimates are naturally along the three body-axes of the IMU, i.e. the front, starboard and down directions. The attitude solution allows us to transform any quantity between the body-frame and the local-level frame formed by the north, east and plumb-line directions, see e.g. Groves (2013).

4.1 Separating Gravity from Bias Variation

To arrive at gravity estimates, the gravity variation must be separated from the actual bias variation. In lack of better knowledge, it will be assumed that the bias variation is linear with respect to time. The gravity anomaly varies with position, which is constant in the beginning and end of the flight, since the aircraft is standing still.

At the beginning and end of the flight it is possible to separate the bias and gravity signals using tie values, i.e. external gravity measurements at these physical locations (Torge 1989). The measured tie value is along the local plumb-line direction and can be projected onto the three body-axes using the attitude solution.

Having projected the tie values onto each of the three body axes, a linear trend was estimated for each flight. Some statistics from these trends are presented in Table 2. These trends are assumed to represent accelerometer bias variation and are removed from the bias estimates in order to derive gravity. The gravity estimates are then transformed into the local-level frame and subjected to a two-pass Butterworth filter with a length of 150 s. The choice of filter length is based on a visual comparison with both LCR estimates, Earth Gravitational Model 2008 (EGM08) estimates, parallel flight tracks and cross-over points. For the further analysis, only the plumb-line component is considered.

Table 2 Statistics of the accelerometer bias drift estimates

Axis	Mean	Std	Min	Max	
x	15.2	74.0	−144.9	186.9	μGal/h
y	−6.6	213.2	−534.8	326.4	μGal/h
z	−3.8	14.3	−35.2	19.8	μGal/h

Finally, each flight was split into flight lines by manually discarding parts of the flight that contained a large degree of manoeuvring.

4.2 Merging IMU and LCR Estimates

A simple merging of the IMU and LCR estimates was performed. Since LCR estimates have proven themselves very reliable in the long-wavelength components (Valliant 1992), the objective was to prioritise the short-wavelength components from the IMU estimates and the long-wavelength components from the LCR estimates.

This simple merging was done based on a linear least squares fit of a straight line in the time domain. For each line produced by the IMU/Inertial Explorer processing, LCR estimates on that same line were identified based on time stamps. A straight line was then fitted to both time series, using only estimates with common time stamps. The linear model of the IMU estimates was then removed and replaced by the linear model estimated from the LCR estimates.

Three of the lines did not have any time stamps in common with the LCR estimates and were excluded in the analysis. For two of the lines, we found that not enough time stamps were in common for a linear fit. Instead a bias was estimated and used for the correction.

5 Results

Gravity disturbance estimates from both IMU and LCR systems were produced, together with a merged product. A statistical analysis, based on the line cross-over differences was performed and is summarized in Table 3. The merged IMU/LCR estimates are shown for all 91 flight lines in Fig. 1.

In Fig. 2, the IMU and LCR estimates are shown for two entire flights, together with gravity disturbance computed from EGM08. The top figure represents a flight over the

Table 3 Cross-over statistics from the gravity disturbance estimates

	iMAR	LCR	Merged	
No. of crossings	257	113	252	
Mean	0.59	−0.13	−0.08	mGal
Min	−10.28	−8.01	−4.38	mGal
Max	8.97	6.74	5.93	mGal
RMS	3.55	3.17	1.86	mGal
RMS error	2.51	2.24	1.32	mGal

No cross-over adjustment was applied

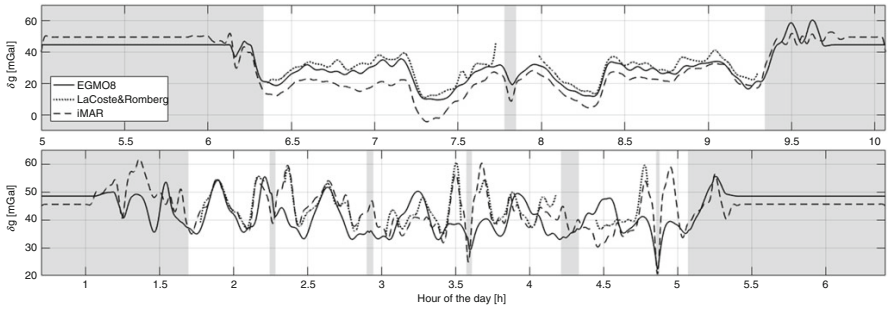

Fig. 2 Estimated gravity disturbances from both the IMU and LCR systems together with EGM08 up to degree 2190 and order 2159. The entire flight is shown above, but only the flight lines (*white areas*) are used in the statistical analysis. (*Top*) These two lines are mostly over the ocean and are shown in the north-eastern part of Fig. 1; (*Bottom*) These five lines were flown in the coastal area north of Kuching, see Fig. 1

ocean north of Bintulu and the bottom figure represents a flight in the coastal area north of Kuching, see Fig. 1.

6 Discussion

In Fig. 2, both IMU and LCR estimates are shown together with EGM08. The top figure represents a flight over the ocean north of Bintulu. Since satellite altimetry derived gravity is part of EGM08, we assume that EGM08 is quite reliable for this flight. The IMU estimates show both a bias and trend with respect to the LCR and EGM08 estimates, indicating that the long-wavelength components of the signal are not reliable. Except for this bias and trend, the variations in the three signals do seem to agree quite well, indicating that the short-wavelength components of the estimates are more reliable. In contrast, the LCR estimates appear to control the long-wavelength components well, while its high sensitivity to turbulence and manoeuvring become apparent at some occasions. This figure illustrates quite well the complementary properties of the IMU and LCR systems.

The bottom figure represents a flight in the coastal area north of Kuching. Here it is seen that the IMU and LCR estimates agree quite well, while EGM08 shows large deviations. This example represents a coastal area that altimetry-derived gravity, marine gravimetry and terrestrial methods can not cover and EGM08 therefore contains limited information. As mentioned in the introduction, airborne gravimetry is the only feasible method of covering these areas. Since most of the world's coastlines remain un-surveyed, although the majority of the population lives in coastal areas, this example clearly shows why airborne gravimetry is still needed in a time of satellite models.

Based on the statistical analysis in Table 3, the IMU and LCR gravity estimates are of similar quality. A comparison of the number of crossing points, on which the statistical analysis is based, indicates how large a portion of the LCR data that is usually discarded due to turbulence, manoeuvring and dynamic conditions in general.

These indications imply that the properties of the two systems are different. The IMU estimates appear to be more resilient to aircraft dynamics, resulting in more reliable results under such circumstances and more control over the short-wavelengths of the gravity estimates. On the other hand, the LCR gravimeter appears to have an excellent bias stability, making it superior in the long-wavelengths. These complementary properties motives a combined product, which leads to improved gravity estimates, based on the statistical analysis.

7 Conclusions

Using the commercial software product "Inertial Explorer", the IMU and GNSS observations were combined in order to form a navigation solution. This led to the gravity variation being absorbed by the accelerometer bias estimates. A simple approach was introduced to separate gravity from accelerometer bias. This separation was identified as the major challenge in strapdown gravimetry and was seen to influence the long-wavelength components of the gravity estimates.

A comparison of the IMU and LCR properties was performed. It was seen that the LCR system is very sensitive to dynamic conditions, which influence the short-wavelength components of the signal. The long-wavelength components are however very reliable. These features nicely complement the properties of the SIMU system, which can be exploited in order to arrive at improved gravity estimates.

Comparing the airborne estimates with EGM08, a good agreement was found in areas of open ocean. Large differences in the 10–20 mGal range was observed in coastal areas.

Acknowledgements The airborne survey in the South China Sea was done as part of the Marine Geodetic Infrastructure in Malaysian Waters (MAGIC) project on behalf of Info-Geomatik Sdn. Bhd. and the Department of Survey and Mapping Malaysia (JUPEM).

References

Andersen O, Knudsen P, Stenseng L (2015) The DTU13 MSS (mean sea surface) and MDT (mean dynamic topography) from 20 years of satellite altimetry. Springer, Berlin, Heidelberg, pp 1–10. doi:10.1007/1345_2015_182, http://dx.doi.org/10.1007/1345_2015_182

Becker D (2016) Advanced calibration methods for strapdown airborne gravimetry. PhD thesis, Technische Universität Darmstadt, Darmstadt. http://tuprints.ulb.tu-darmstadt.de/5691/

Becker D, Becker M, Leinen S, Zhao Y (2015a) Estimability in strapdown airborne vector gravimetry. Springer, Berlin, Heidelberg, pp 1–5. doi:10.1007/1345_2015_209, http://dx.doi.org/10.1007/1345_2015_209

Becker D, Nielsen JE, Ayres-Sampaio D, Forsberg R, Becker M, Bastos L (2015b) Drift reduction in strapdown airborne gravimetry using a simple thermal correction. J Geodesy 89(11):1133–1144. doi:10.1007/s00190-015-0839-8, http://dx.doi.org/10.1007/s00190-015-0839-8

Brown RG, Hwang PYC (2012) Introduction to random signals and applied Kalman filtering: with MATLAB exercises, 4th edn. Wiley, New York

Brozena JM (1992) The greenland aerogeophysics project: airborne gravity, topographic and magnetic mapping of an entire continent. Springer, New York, NY, pp 203–214. doi:10.1007/978-1-4613-9255-2_19, http://dx.doi.org/10.1007/978-1-4613-9255-2_19

Deurloo R (2011) Development of a Kalman filter integrated system and measurement models for a low-cost strapdown airborne gravimetry system. PhD thesis, Department of Geosciences, Environment and Planning, Faculty of Sciences, University of Porto

Glennie C, Schwarz KP (1999) A comparison and analysis of airborne gravimetry results from two strapdown inertial/dgps systems. J Geodesy 73(6):311–321. doi:10.1007/s001900050248, http://dx.doi.org/10.1007/s001900050248

Glennie CL, Schwarz KP, Bruton AM, Forsberg R, Olesen AV, Keller K (2000) A comparison of stable platform and strapdown airborne gravity. J Geodesy 74(5):383–389. doi:10.1007/s001900000082, http://dx.doi.org/10.1007/s001900000082

Groves PD (2013) Principles of GNSS, inertial, and multisensor integrated navigation systems, 2nd edn. Artech House Remote Sensing Library, Boston

Huang Y, Olesen AV, Wu M, Zhang K (2012) Sga-wz: a new strapdown airborne gravimeter. Sensors 12(7):9336–9348. doi:10.3390/s120709336, http://www.mdpi.com/1424-8220/12/7/9336

Jekeli C (1994) Airborne vector gravimetry using precise, position-aided inertial measurement units. Bull géodésique 69(1):1–11. doi:10.1007/BF00807986, http://dx.doi.org/10.1007/BF00807986

Jekeli C (2001) Inertial navigation systems with geodetic applications. Walter De Gruyter, Berlin

Jekeli C, Kwon JH (1999) Results of airborne vector (3-d) gravimetry. Geophys Res Lett 26(23):3533–3536. doi:10.1029/1999GL010830, http://dx.doi.org/10.1029/1999GL010830

Maybeck PS (1979) Stochastic models, estimation and control, vol 1. Academic, New York

Olesen AV (2002) Improved airborne scalar gravimetry for regional gravity field mapping and geoid determination. PhD thesis, Faculty of Science, University of Copenhagen

Olesen A, Forsberg R (2007) Airborne scalar gravimetry for regional gravity field mapping and geoid determination. In: Proceedings, Gravity Field of the Earth – 1st Meeting of the International Gravity Field Service, vol. 73, issue 18, 28th August–1st September, 2006. Harita Dergisi, Istanbul, pp 277–282.

Schwarz KP, Colombo O, Hein G, Knickmeyer ET (1992) Requirements for airborne vector gravimetry. Springer, New York, NY, pp 273–283. doi:10.1007/978-1-4613-9255-2_25, http://dx.doi.org/10.1007/978-1-4613-9255-2_25

Thompson LGD (1959) Airborne gravity meter test. J Geophys Res 64(4):488–488. doi:10.1029/JZ064i004p00488, http://dx.doi.org/10.1029/JZ064i004p00488

Torge W (1989) Gravimetry. De Gruyter, Berlin

Valliant HD (1992) The LaCoste and Romberg air/sea gravimeter: an overview. In: CRC handbook of geophysical exploration at sea. Hydrocarbons, 2nd edn. CRC Press, Boca Raton, FL, pp 141–176

Wei M, Schwarz KP (1998) Flight test results from a strapdown airborne gravity system. J Geodesy 72(6):323–332. http://dx.doi.org/10.1007/s001900050171

F.3 Helicopter Test of a Strapdown Airborne Gravimetry System

MDPI

Article

Helicopter Test of a Strapdown Airborne Gravimetry System

Tim E. Jensen [1] and Rene Forsberg [1]

[1] National Space Institute, Technical University of Denmark, Kgs. Lyngby, Denmark
* Correspondence: timj@space.dtu.dk

Academic Editor: name
Version August 14, 2018 submitted to Sensors

Abstract: Airborne gravimetry from a helicopter has been a feasible tool since the 1990s, with gravimeters mounted on a gyro-stabilised platform. In contrasts to fixed-wing aircrafts, the helicopter allows for a higher spatial resolution, since it can move slower and closer to the ground. In August 2016, a strapdown gravimetry test was carried out over the Jakobshavn Glacier in Greenland. To our knowledge, this was the first time that a strapdown system was used in a helicopter. The strapdown configuration is appealing because it is easily installed and requires no operation during flight. While providing additional information over the thickest part of the glacier, the survey was designed to assess repeatability both within the survey and with respect to profiles flown previously using a gyro-stabilised gravimeter. The systems ability to fly at an altitude following the terrain, i.e. draped flying, was also tested. The accuracy of the gravity profiles was estimated to 2 mGal and a method for inferring the spatial resolution was investigated, yielding a half-wavelength spatial resolution of 4.5 km at normal cruise speed.

Keywords: airborne gravimetry; strapdown inertial measurement unit; helicopter test; Kalman filter

1. Introduction

The first airborne gravimetry flight test was carried out in 1958 by mounting a LaCoste shipboard gravimeter on board an Air Force KC-135 fixed-wing aircraft [1]. The observed gravity values were averaged over 5 minute intervals, yielding an accuracy of about 10 mGal, which waw adequate for geodetic purposes at the time. However, since this accuracy did not meet the requirements of the exploration industry, the idea of using a helicopter platform emerged. The helicopter would be able to fly closer to the ground and move at a slower speed, allowing for a higher spatial resolution of the gravity measurements. After an unsuccessful test in 1963, the U.S. Naval Oceanographic Office made the first successful helicopter test in 1965 using an Air Force CH3E helicopter, equipped with the latest LaCoste&Romberg platform stabilised gravimeter [2].

Initially, most development of airborne gravimetry was driven by government mapping agencies and military branches of the U.S. government. These efforts were aimed at surveying large-scale regions and involved fixed-wing aircrafts [3,4]. From 1970, the exploration industry joined the effort, leading to the introduction of a helicopter-borne gravity system by Carson Services in 1977 and other companies in the 1990s [5]. Most airborne systems consist of a single-axis accelerometer on a gyro-stabilised platform that attempts to null the horizontal accelerations through a mechanical feedback loop. The AIRGrav system from Sander Geophysics (SGL) differs from these systems in that it uses three inertial-grade accelerometers on a fully gyro-stabilised platform, that does not attempt to compensate for the horizontal accelerations. The advantages of this approach are: lower accelerometer noise, higher resolution and less sensitivity to turbulence [6]. The claimed resolution of the AIRGrav system is 0.2 mGal at 2.2 km (fixed-wing) and 0.2 mGal at 0.7 km (helicopter). Although

helicopter-mounted gravimetry is mostly aimed at exploration, it is also carried out for research purposes such as studying tectonically active regions [7,8] and mapping bathymetry below ice shelves [9]. In particular, the use of helicopter-based gravimetry operated from a ship at sea may play an important role in studying ice shelves and marine-terminating glaciers in remote areas otherwise inaccessible.

The AIRGrav system development was to some degree inspired by pioneering work on the use of Inertial Measurement Units (IMU) for airborne gravimetry at the University of Calgary in the 1990s [10]. Since the gyroscopes of the IMU measures angular rates, the rotational motion can be accounted for computationally, instead of having a control loop feeding a mechanical platform. As a result, the platform can be completely neglected and the IMU installed in a strapdown configuration, i.e. by physically attaching the unit to the vehicle. This approach is appealing, because it is easily installed and does not require any operation during the flight. The first test of a Strapdown Airborne Gravimetry (SAG) system was carried out in 1995 using a fixed-wing aircraft. The reported accuracy was 2-3 mGal at 5-7 km (half wavelength) resolution after applying 90-120 s (full wavelength) filtering [11]. The higher dynamic range of the IMU made the gravity system more resilient to turbulence and less filtering was required to obtain an accuracy similar to the traditional single-sensor stabilised-platform systems [12]. However, the instability of the accelerometers propagates into the gravity estimates and corrupts the long wavelength information, which is vital for geodetic applications. The majority of the sensor instability has been shown to originate from temperature variation and to a large extent accounted for using laboratory calibration methods [13]. In collaboration with the Technical University of Darmstadt, the National Space Institute of Denmark (DTU Space) has flown a SAG system on a number of campaigns showing significant improvement after applying temperature calibrations [14]. A large component of the difference in accelerometer stability between the IMU and traditional systems may therefore be due to temperature stabilisation.

In order to test the feasibility of using a strapdown IMU in a helicopter environment, a flight test was carried out in August 2016 over the Jakobshavn Glacier in Greenland. This location was chosen because it has previously been surveyed using the SGL AIRGrav system within NASA's Operation IceBridge (OIB). Since the fast-flowing ice stream is more than 1 km thick [15], the relatively fast-moving fixed-wing aircraft flown by OIB is not expected to capture the full resolution of the gravity signal in this area. The slower-moving helicopter platform may therefore add information to the gravity signal over the glacier, while the OIB flight lines provide a reference for the helicopter estimates. It should be noted that Jakobshavn Glacier was surveyed by a helicopter in 2012 using the SGL AIRGrav system [16]. This data was however unavailable to the authors for this study.

2. Instrumentation, Survey Overview and Data

In August 2016, a SAG system was mounted inside a Eurocopter AS350 helicopter at Ilulissat airport (JAV), Greenland. The SAG system consists of an iMAR iNAT IMU unit (iNAT), two JAVAD DELTA GNSS receivers and two NovAtel ANT-532-C dual frequency GNSS antennas along with some batteries and cables. The installation was done using straps and tape and took less than an hour, see Figure 1.

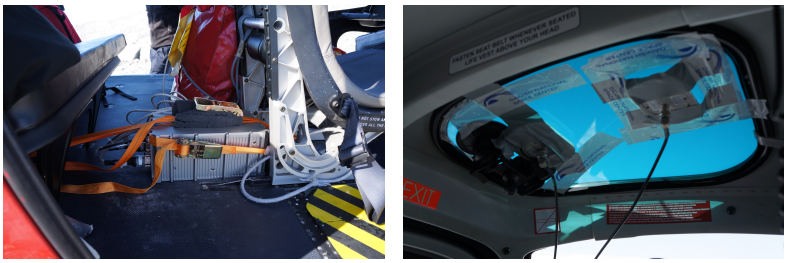

Figure 1. Photographs from the installation: (**left**) The IMU is physically strapped to the floor of the helicopter. (**right**) The GNSS antenna is taped to the inside of the windscreen.

The entire survey amounts to approximately 400 km (3.5 hours), see Figure 2, and was designed to repeat flight lines both from OIB and within the survey itself. The profile between JAV and Kangia North GPS station (KAGA) was repeated three times, but not flown at the same altitude for operational reasons. The three profiles between the waypoints P1-P2, P3-P4 and P5-P6 correspond to flight lines from OIB. Two of these lines were flown in draped mode and one at constant altitude. From Figure 2a-c it is evident that the fixed-wing aircraft from OIB was equipped with an autopilot, whereas the helicopter was not. Finally, a line from P7 to KAGA that crosses over the three OIB lines was additionally flown. This resulted in seven flight lines of approximately 300 km (1.5 hours). The average ground speed for these seven profiles was 52 m/s (standard deviation of 6 m/s).

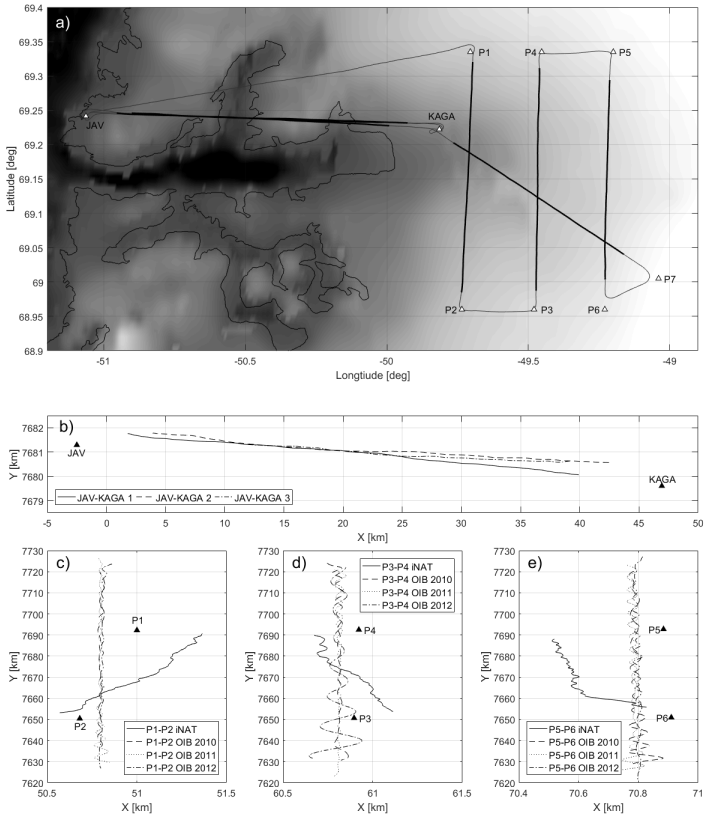

Figure 2. Survey overview: (**a**) Ground track of the entire survey (gray) along with line profiles (black). Coordinates are with respect to WGS84. (**b**) Ground track of the three repeat lines between JAV and KAGA. (**c**) Ground track of the profiles between P1 and P2. (**d**) Ground track of the profiles between P3 and P4. (**e**) Ground track of the profiles between P5 and P6. Rectangular coordinates are with respect to UTM zone 22. Notice the difference in scale between X and Y axes.

2.1. The IMU Data

The iNAT unit outputs accelerations and angular rates at 300 Hz with associated time and temperature stamps. It contains an internal GNSS receiver that provides time stamps in GPS time. A simple warm-up temperature calibration was applied to the vertical Z-axis accelerometer only [17]. This led to a reduction in the accelerometer drift, see Table 1.

Table 1. Accelerometer drift over the entire flight

	X-axis	Y-axis	Z-axis	
Total drift				
- without calibration	1.730	-1.192	-8.422	mGal
- with calibration	1.419	-0.820	3.496	mGal
Drift rate				
- without calibration	391.8	-269.8	-1907	μGal/h
- with calibration	321.3	-185.7	791.8	μGal/h

2.2. The GNSS Data

The GNSS receivers logs both GPS and GLONASS observations at 1 Hz. Using NovAtel's Waypoint software suite, a Precise Point Positioning (PPP) solution was produced using the final GPS and GLONASS ephemerides from the International GNSS Service (IGS). The GNSS observations were thus processed independently from the IMU observations, in order to arrive at position and velocity estimates, with associated error covariance matrices.

Using data from the nearby KAGA GPS station, a differential GNSS solution was also produced. The differential solution did however not lead to any improvement compared to the PPP solution. One possible explanation is that the KAGA receiver only logs GPS observations, leading to a reduction in the number of satellites used for the solution.

2.3. AIRGrav Gravity Estimates from Operation IceBridge

Gravity estimates from OIB are available with 70 s, 100 s and 140 s full wavelength filters applied to the Eötvös corrected gravity disturbance estimates (see acknowledgements). The three lines flown in this survey, were covered by OIB in the years 2010, 2011 and 2012. A visual comparison of the three profiles for each line indicated that the 100 s filter led to reasonable agreement between the gravity estimates. The internal mean and standard deviation (STD) of the difference in OIB gravity estimates for each line and year are shown in Table 2. From this table it is clear that the stated 0.2 mGal accuracy of the AIRGrav system is not reached over the Jakobshavn Glacier. This may be due to the high speed of the aircraft not accounting for the full resolution of the gravity signal in this area. The average ground speed for these nine profiles was 134 m/s (standard deviation of 9 m/s), meaning that the spatial resolution is approximately 6.7 km (half wavelength). The nine OIB lines were flown in draped mode at a similar altitude for each line (the maximum difference is 300 m and the standard deviation is 80 m).

Table 2. Mean and standard deviation of the difference in gravity estimates (100 s full wavelength filtering) along the three OIB lines.

		2010 - 2011	2010 - 2012	2011 - 2012	
P1-P2	Mean	1.03	1.04	-0.13	mGal
	STD	2.66	2.93	1.65	mGal
P3-P4	Mean	0.65	0.44	-0.20	mGal
	STD	1.84	1.82	1.43	mGal
P5-P6	Mean	-0.17	-1.06	-0.95	mGal
	STD	2.70	3.19	3.74	mGal

3. Processing Methodology

Observations form IMU and GNSS are often combined in order to improve the navigation solution. Although the main objective is not improving the navigation solution, the tools for IMU/GNSS integration are well-developed and can be exploited here. In the first two of the following five sub-sections, the concepts of inertial navigation and IMU/GNSS integration will be briefly introduced.

In the third sub-section, we describe how this framework can be exploited to arrive at gravity estimates, the fourth sub-section introduces external gravity observations, i.e. tie values, and the final sub-section outlines how smoothing is performed.

In this context, it is important to introduce some reference frames that are relevant for our purposes, see Table 3. Since the IMU is rigidly attached to the helicopter, the observations are naturally resolved about the body frame (b-frame) of the helicopter. Being inertial sensors, the accelerometers and gyroscopes measure with respect to inertial space, which is represented by an inertial reference frame (i-frame). The Earth-Centred-Earth-Fixed frame (e-frame) is relevant because coordinates and velocity are defined with respect to this frame. Finally, the attitude of the vehicle is usually specified with respect to the navigation frame (n-frame), which is moreover closely related to the gravity field.

Table 3. Overview of relevant reference frames

Frame	Origin	Z-axis	X-axis	Y-axis
i	Earth centre of mass	Earth rotational axis	Equatorial plane, vernal equinox	Completes right-handed system
e	Earth centre of mass	Earth rotational axis	Equatorial plane, Greenwich meridian	Completes right-handed system
n	Instrument location	Down along ellipsoidal normal	North	East
b	Instrument location	Through-the-floor (down)	Forward	Starboard (right)

3.1. Inertial Navigation

Initialisation of the position is done using the GNSS solution, while the attitude is initialised through levelling and gyrocompassing [18, Ch. 5.6.2]. After initialisation, inertial navigation is performed by sequentially adding small increments derived by integrating the IMU observations of specific force, $\mathbf{f}^b$, and angular rate, $\boldsymbol{\omega}_{ib}^b$. Before integration, the observations are transformed from the b-frame into the n-frame and corrected for the effect of gravity along with any fictitious forces arising from the choice of reference frame. This process is expressed mathematically in terms of a coupled set of differential equations [19, Ch. 4.3.4]:

$$\begin{aligned}
\dot{\phi} &= v_N / \left(R_N + h\right) \\
\dot{\lambda} &= v_E / \left(R_E + h\right) / \cos\phi \\
\dot{h} &= -v_D \\
\dot{\mathbf{v}}^n &= \mathbf{C}_b^n \, \mathbf{f}^b - \left(2\boldsymbol{\Omega}_{ie}^n + \boldsymbol{\Omega}_{en}^n\right) \mathbf{v}^n + \mathbf{g}^n \\
\dot{\mathbf{C}}_b^n &= \mathbf{C}_b^n \, \boldsymbol{\Omega}_{nb}^b \, ,
\end{aligned} \tag{1}$$

where (ϕ, λ, h) are geodetic coordinates, $\mathbf{v}^n$ the Earth-referenced velocity resolved about the n-frame axes and $\mathbf{C}_b^n$ is the rotation matrix from the b-frame to the n-frame. The parameters R_E and R_N are the radii of curvature of the prime vertical and meridian, respectively. The term $\boldsymbol{\Omega}_{ie}^n$ is the rotation of the Earth with respect to inertial space and $\boldsymbol{\Omega}_{en}^n$ is the transport-rate, i.e. the rotational motion required to keep the reference frame aligned with the north, east and vertical axes as the vehicle travels across the surface of the Earth. Both these rotational rates are resolved about the n-frame axes and expressed in skew-symmetric form. For a more complete introduction, the reader is referred to standard textbooks, e.g. [18–20]. Finally, the rotational rate, $\boldsymbol{\Omega}_{nb}^b$, is related to the observed angular rate as

$$\boldsymbol{\omega}_{nb}^b = \boldsymbol{\omega}_{ne}^b + \boldsymbol{\omega}_{ei}^b + \boldsymbol{\omega}_{ib}^b = \boldsymbol{\omega}_{ib}^b - \mathbf{C}_n^b \left(\boldsymbol{\omega}_{en}^n + \mathbf{C}_e^n \, \boldsymbol{\omega}_{ie}^e\right) \, . \tag{2}$$

The gravity vector, $\mathbf{g}^n$, is approximated using a model of normal gravity [21, Ch. 2.8], which can be computed as described in [22, Ch. 4]. The implementation of Eq. (1) is discussed in [18, Ch. 5]. The combined system of IMU and inertial navigation processor is denoted an Inertial Navigation

System (INS). The attitude in terms of three Euler angles, $\boldsymbol{\psi}_{nb} = (\alpha_{nb}, \beta_{nb}, \gamma_{nb})$, can be derived from the transformation matrix, $\mathbf{C}_b^n$, as [18, Eq. 2.25]:

$$\alpha_{nb} = \arctan_2\left(\mathbf{C}^n_{b3,2}, \mathbf{C}^n_{b3,3}\right) , \quad \beta_{nb} = -\arcsin\left(\mathbf{C}^n_{b3,1}\right) \quad \text{and} \quad \gamma_{nb} = \arctan_2\left(\mathbf{C}^n_{b2,1}, \mathbf{C}^n_{b1,1}\right) . \tag{3}$$

3.2. IMU/GNSS Integration

The GNSS position estimates are only used to initialise the position for inertial navigation, meaning that the INS and GNSS navigation solutions are independent. The GNSS system provides estimates of position and velocity, while the INS provides estimates of position, velocity and attitude. These two estimates are combined in a cascaded (loosely coupled) approach using an Empirical Kalman Filter (EKF). The Kalman filter framework revolves around a linear dynamic system model [23, Eq. 4-102]:

$$\dot{\mathbf{x}} = \mathbf{F}(t)\,\mathbf{x}(t) + \mathbf{G}(t)\,\mathbf{w}_s(t) , \tag{4}$$

where $\mathbf{x}(t)$ is known as the state vector and contains all the variables describing the system, i.e. position, velocity, attitude and sensor biases, $\mathbf{F}(t)$ is the system matrix describing the dynamics of the system, i.e. the navigation equations, $\mathbf{w}_s(t)$ is a vector representing stochastic input to the system and $\mathbf{G}(t)$ is a system noise distribution matrix, relating the stochastic driving terms to the state variables. The stochastic components imply that the state variables also have a stochastic nature and are defined in terms of probability density functions (PDFs). However, assuming that the associated PDFs are Gaussian, these distributions are completely defined in terms of their first two moments, i.e. the mean and covariance.

The system matrix, $\mathbf{F}(t)$, is formed using the navigation equations (1), while the system noise vector, $\mathbf{w}_s(t)$, represents sensor errors such as random noise and bias variation. Since the system model is linear, the navigation equations are linearised about the trajectory generated by the INS. This kind of linearisation is what characterises the EKF. Inertial navigation is then performed in a recursive manner by generating a navigation solution from current time, t_k, until the time where the next GNSS estimates are available, t_{k+1}. The associated error covariance estimates are accordingly propagated as

$$\mathbf{P}_{k+1} = \boldsymbol{\Phi}_k\,\mathbf{P}_k\,\boldsymbol{\Phi}_k^\top + \boldsymbol{\Gamma}_k\,\mathbf{Q}_k\,\boldsymbol{\Gamma}_k^\top , \tag{5}$$

where the transition matrix, $\boldsymbol{\Phi}_k$, and system noise, $\boldsymbol{\Gamma}_k\,\mathbf{Q}_k\,\boldsymbol{\Gamma}_k^\top$, can be formed from Eq. (4) using the method of Van Loan [24,25]. The transition matrix, $\boldsymbol{\Phi}_k$, is formed using the system matrix, $\mathbf{F}(t)$, such that it eventually defines the correlation between the navigation parameters through the error covariance matrix. In this way, the stochastic driving terms do also not influence the navigation estimates themselves, but only the error covariance matrix. These stochastic processes are defined by the user and will eventually determine the weighting of information between INS and GNSS navigation estimates. Here, random noise on the accelerometer and gyro observations are modelled as white noise processes, while the bias variation is modelled as Brownian motion, i.e. random walk processes. These processes are defined in terms of Power Spectral Density (PSD) of the associated white noise processes and are tuned by the user to give the best navigation solution. The values used for processing this data are shown in Table 4.

Table 4. Stochastic models and amplitude of the associated power spectral densities

	Error model	PSD amplitude	
Accelerometer noise	White noise	0.05	$\mathrm{mm/s}/\sqrt{\mathrm{s}}$
Gyroscope noise	White noise	0.2	$\mathrm{arcsec}/\sqrt{\mathrm{s}}$
Accelerometer bias variation	Random walk	0.01	$\mathrm{mGal}/\sqrt{\mathrm{s}}$
Gyroscope bias variation	Random walk	$3.0 \cdot 10^{-5}$	$^\circ/\mathrm{h}/\sqrt{\mathrm{s}}$

Any observations, $\mathbf{z}(t_k)$, at discrete time instances, t_k, are included into the Kalman filter using a linear measurement model [23, Eq. 4-136]:

$$\mathbf{z}(t_k) = \mathbf{H}(t_k)\,\mathbf{x}(t_k) + \mathbf{w}_m(t_k)\,, \tag{6}$$

where $\mathbf{H}(t_k)$ is the measurement matrix relating those observations to the system variables and $\mathbf{w}_m(t_k)$ is a measurement noise vector. The observations are thus assumed to be a linear combination of state variables, corrupted by noise. The formation of such a measurement model for GNSS position and velocity observations is discussed in [18, Ch. 14.3]. From the GNSS and INS estimates, $\hat{\mathbf{p}}_{k,\mathrm{GNSS}} = (\phi_{k,\mathrm{GNSS}}, \lambda_{k,\mathrm{GNSS}}, h_{k,\mathrm{GNSS}})$, $\hat{\mathbf{v}}^n_{k,\mathrm{GNSS}}$, $\hat{\mathbf{p}}_{k,\mathrm{INS}}$ and $\hat{\mathbf{v}}^n_{k,\mathrm{INS}}$, the measurement innovation is formed:

$$\delta\mathbf{z}_k \approx \begin{bmatrix} \hat{\mathbf{p}}_{k,\mathrm{GNSS}} - \hat{\mathbf{p}}_{k,\mathrm{INS}} \\ \hat{\mathbf{v}}^n_{k,\mathrm{GNSS}} - \hat{\mathbf{v}}^n_{k,\mathrm{INS}} \end{bmatrix}\,, \tag{7}$$

which is used to update the Kalman filter estimates as [18, Eqs. 3.24&3.61]:

$$\hat{\mathbf{x}}_k = \hat{\mathbf{x}}_k^- + \mathbf{K}_k\,\delta\mathbf{z}_k \quad \text{and} \quad \mathbf{P}_k = \mathbf{P}_k^- - \mathbf{K}_k\left(\mathbf{H}_k\,\mathbf{P}_k^-\right)\,, \tag{8}$$

where the superscript minus denotes values before the measurement update and $\mathbf{K}_k$ is a weighting factor determining the influence of the new information. This factor is also known as the Kalman gain and is derived by minimising the trace of the updated error covariance matrix, $\mathbf{P}_k$, i.e. minimising squared errors.

The processing is thus performed using a semi-cascaded approach. First, the GNSS observations are processed into position and velocity estimates for the entire survey. Having initialised the INS solution, inertial navigation is performed until the next GNSS estimates are available. The INS solution is used to form a linear system model (4), which allows the propagation of the error covariance matrix forward in time, alongside the INS estimates. The stochastic error terms accounting for sensor errors will also influence this forward propagation. The INS and GNSS estimates are combined, using a least squares approach based on the associated error covariance, in order to yield statistically optimal estimates of the state variables. These optimal estimates are then used to correct the INS estimates, which are again propagated forward in time. This is illustrated in Figure 3.

The Kalman filter therefore has a cyclic nature, alternating between forward propagations and measurement updates. Since correlation between different state variables is built through the forward propagation phase, the Kalman filter also provides estimates of other states than those directly observed. In this way, the GNSS observations are not only used to correct the navigation solution, but also to continually calibrate the IMU, since estimates of sensor errors will be available.

Finally, in order to minimise linearisation errors and processing time, an error-state implementation was used in contrast to a total-state implementation. This means that the system model can be expressed as

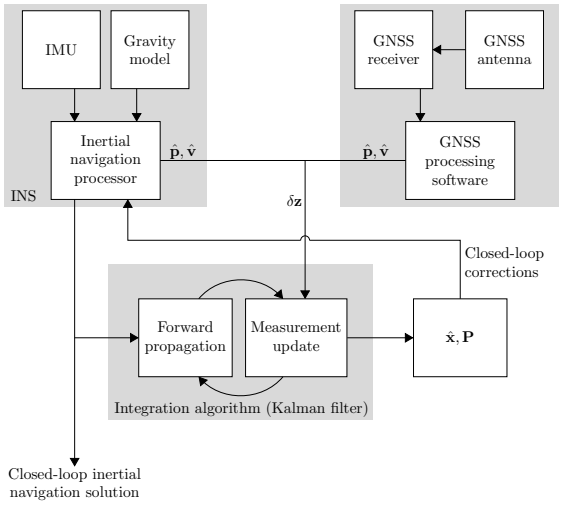

Figure 3. Overview of processing and data integration architecture

$$\begin{bmatrix} \delta\dot{\mathbf{p}}(t) \\ \delta\dot{\mathbf{v}}^n(t) \\ \hline \delta\dot{\boldsymbol{\psi}}_{nb}(t) \\ \dot{\mathbf{b}}_a(t) \\ \dot{\mathbf{b}}_g(t) \end{bmatrix} = \left[\begin{array}{c|cc} \mathbf{F}_{\mathrm{INS}}(t) & \mathbf{0}_3 & \mathbf{0}_3 \\ & \mathbf{C}_b^n & \mathbf{0}_3 \\ & \mathbf{0}_3 & \mathbf{C}_b^n \\ \hline \mathbf{0}_{6\times 9} & \multicolumn{2}{c}{\mathbf{0}_6} \end{array}\right] \begin{bmatrix} \delta\mathbf{p}(t) \\ \delta\mathbf{v}^n(t) \\ \hline \delta\boldsymbol{\psi}_{nb}(t) \\ \mathbf{b}_a(t) \\ \mathbf{b}_g(t) \end{bmatrix} + \left[\begin{array}{cccc} \mathbf{0}_3 & \mathbf{0}_3 & \mathbf{0}_3 & \mathbf{0}_3 \\ \mathbf{I}_3 & \mathbf{0}_3 & \mathbf{0}_3 & \mathbf{0}_3 \\ \mathbf{0}_3 & \mathbf{I}_3 & \mathbf{0}_3 & \mathbf{0}_3 \\ \mathbf{0}_3 & \mathbf{0}_3 & \mathbf{I}_3 & \mathbf{0}_3 \\ \mathbf{0}_3 & \mathbf{0}_3 & \mathbf{0}_3 & \mathbf{I}_3 \end{array}\right] \begin{bmatrix} \mathbf{w}_a(t) \\ \mathbf{w}_g(t) \\ \hline \mathbf{w}_{a,\mathrm{bias}}(t) \\ \mathbf{w}_{g,\mathrm{bias}}(t) \end{bmatrix}, \tag{9}$$

where δ denotes errors, $\mathbf{b}_a$ are accelerometer biases and $\mathbf{b}_g$ are gyroscope biases. The stochastic terms $\mathbf{w}_a(t)$, $\mathbf{w}_g(t)$, $\mathbf{w}_{a,\mathrm{bias}}(t)$ and $\mathbf{w}_{g,\mathrm{bias}}(t)$ are white noise processes defined in terms of their PSD. The form of the matrix, $\mathbf{F}_{\mathrm{INS}}(t)$, is derived from the navigation equations by first applying a perturbation operator and then linearising with respect to the state variables [19, Ch. 5.4].

3.3. Modelling Gravity as a Stochastic Process

Since the gravity model used for inertial navigation is not perfect, the gravity error (or disturbance) can be modelled as a stochastic process [19, Ch. 6.6]. A third-order exponentially time-correlated (Gauss-Markov) model is characterised by the autocorrelation function [26, Table 2.2-1]:

$$R(\tau) = \sigma^2 e^{-\beta|\tau|}\left(1 + \beta|\tau| + \tfrac{1}{3}\beta^2|\tau|^2\right), \tag{10}$$

where σ is the standard deviation and β is a correlation parameter related to the correlation time as $T = 2.903/\beta$. Since the Kalman filtering framework only allows the stochastic driving terms to be zero-mean white noise processes, the system model must be augmented as [27]:

$$\left[\begin{array}{c} \dot{\mathbf{p}}(t) \\ \dot{\mathbf{v}}^n(t) \\ \dot{\boldsymbol{\psi}}_{nb}(t) \\ \hline \dot{\mathbf{b}}_a(t) \\ \dot{\mathbf{b}}_g(t) \\ \frac{\mathrm{d}}{\mathrm{d}t}\delta\mathbf{g}(t) \\ \frac{\mathrm{d}}{\mathrm{d}t}\delta\dot{\mathbf{g}}(t) \\ \frac{\mathrm{d}}{\mathrm{d}t}\delta\ddot{\mathbf{g}}(t) \end{array}\right] = \left[\begin{array}{c|ccccc} & \mathbf{0}_3 & \mathbf{0}_3 & \mathbf{0}_3 & \mathbf{0}_3 & \mathbf{0}_3 \\ \mathbf{F}_{\mathrm{INS}}(t) & \mathbf{C}_b^n & \mathbf{0}_3 & \mathbf{I}_3 & \mathbf{0}_3 & \mathbf{0}_3 \\ & \mathbf{0}_3 & \mathbf{C}_b^n & \mathbf{0}_3 & \mathbf{0}_3 & \mathbf{0}_3 \\ \hline & \mathbf{0}_3 & \mathbf{0}_3 & \mathbf{0}_3 & \mathbf{0}_3 & \mathbf{0}_3 \\ & \mathbf{0}_3 & \mathbf{0}_3 & \mathbf{0}_3 & \mathbf{0}_3 & \mathbf{0}_3 \\ \mathbf{0}_{15\times 9} & \mathbf{0}_3 & \mathbf{0}_3 & \mathbf{0}_3 & \mathbf{I}_3 & \mathbf{0}_3 \\ & \mathbf{0}_3 & \mathbf{0}_3 & \mathbf{0}_3 & \mathbf{0}_3 & \mathbf{I}_3 \\ & \mathbf{0}_3 & \mathbf{0}_3 & -\beta^3\mathbf{I}_3 & -3\beta^2\mathbf{I}_3 & -3\beta\mathbf{I}_3 \end{array}\right] \left[\begin{array}{c} \mathbf{p}(t) \\ \mathbf{v}^n(t) \\ \boldsymbol{\psi}_{nb}(t) \\ \hline \mathbf{b}_a(t) \\ \mathbf{b}_g(t) \\ \delta\mathbf{g}(t) \\ \delta\dot{\mathbf{g}}(t) \\ \delta\ddot{\mathbf{g}} \end{array}\right] + \left[\begin{array}{ccccc} \mathbf{0}_3 & \mathbf{0}_3 & \mathbf{0}_3 & \mathbf{0}_3 & \mathbf{0}_3 \\ \mathbf{I}_3 & \mathbf{0}_3 & \mathbf{0}_3 & \mathbf{0}_3 & \mathbf{0}_3 \\ \mathbf{0}_3 & \mathbf{I}_3 & \mathbf{0}_3 & \mathbf{0}_3 & \mathbf{0}_3 \\ \hline \mathbf{0}_3 & \mathbf{0}_3 & \mathbf{I}_3 & \mathbf{0}_3 & \mathbf{0}_3 \\ \mathbf{0}_3 & \mathbf{0}_3 & \mathbf{0}_3 & \mathbf{I}_3 & \mathbf{0}_3 \\ \mathbf{0}_3 & \mathbf{0}_3 & \mathbf{0}_3 & \mathbf{0}_3 & \mathbf{0}_3 \\ \mathbf{0}_3 & \mathbf{0}_3 & \mathbf{0}_3 & \mathbf{0}_3 & \mathbf{0}_3 \\ \mathbf{0}_3 & \mathbf{0}_3 & \mathbf{0}_3 & \mathbf{0}_3 & \mathbf{I}_3 \end{array}\right] \left[\begin{array}{c} \mathbf{w}_a(t) \\ \mathbf{w}_g(t) \\ \hline \mathbf{w}_{a,\mathrm{bias}}(t) \\ \mathbf{w}_{g,\mathrm{bias}}(t) \\ \mathbf{w}_{\mathrm{GM3}}(t) \end{array}\right], \tag{11}$$

where the additional terms serve to "shape" the white noise into a Gauss-Markov process. The PSD amplitude of the associated white noise process, $\mathbf{w}_{\mathrm{GM3}}(t)$, is related to the uncertainty and correlation parameters of the Gauss-Markov process as

$$S_{\mathrm{GM3}} = \frac{16}{3}\,\sigma^2\,\beta^5 = \frac{16}{3}\,\sigma^2\,\left(|v_{\mathrm{hor}}|\,\beta'\right)^5 \ . \tag{12}$$

where the along-track correlation, $\beta = |v_{\mathrm{hor}}|\,\beta'$, is specified in terms of distance instead of time and $v_{\mathrm{hor}}^2 = v_N^2 + v_E^2$ is the ground speed. This is because the gravity signal varies with position rather than time.

3.4. Introducing External Gravity Observations

External gravity observations can be introduced into the Kalman filter framework similar to position and velocity estimates, using a measurement model. For this flight test we introduced observations from an A10 gravity meter at both JAV and KAGA stations. Although these observations represent only the magnitude of the gravity vector, the tie values are introduced as vector estimates

$$\mathbf{z}_{\delta g} = \begin{bmatrix} 0 & 0 & \delta g \end{bmatrix}^\top \quad \text{with} \quad \mathbf{R}_{\delta g} \equiv \begin{bmatrix} 0.03 & 0 & 0 \\ 0 & 0.03 & 0 \\ 0 & 0 & 0.03 \end{bmatrix}, \tag{13}$$

where $\mathbf{R}_{\delta g}$ is the associated error covariance matrix in units of mGal. The A10 measurement is corrected for the gravity model at the measurement location, meaning that the gravity disturbance is formed.

3.5. Smoothing

Instead of applying a regular filter, the Kalman filter estimates are smoothed by processing the data both forward and backward in time. The two solutions are then combined as

$$\hat{\mathbf{x}}_k = \mathbf{P}_k \left(\mathbf{P}_{f,k}^{-1}\,\hat{\mathbf{x}}_{f,k} + \mathbf{P}_{b,k}^{-1}\,\hat{\mathbf{x}}_{b,k}\right) \quad \text{and} \quad \mathbf{P}_k = \left(\mathbf{P}_{f,k}^{-1} + \mathbf{P}_{b,k}^{-1}\right)^{-1}, \tag{14}$$

where f denotes the forward solution and b the backward solution. This is accomplished in a processor-efficient way using the Rauch-Tung-Striebel (RTS) smoother [26, Ch. 5].

4. Results

Inertial navigation was performed using an implementation of Eq. (1) and combined with GNSS velocity and position estimates using a Kalman filtering framework as described above. This resulted in an integrated IMU/GNSS solution, which was subsequently smoothed using an implementation of the RTS smoother. The gravity disturbance was modelled as a third-order Gauss-Markov process with initial parameters of σ = 100 mGal and β = 2.903/20km. From the resulting gravity disturbance estimates, the autocorrelation function was estimated for each of the seven profiles, see Figure 4. A least squares fit of the Gauss-Markov autocorrelation function in Eq. (10) yielded parameters of σ = 57.84 mGal and $1/\beta$ = 5.647 km, implying a correlation length of around 16 km, which was used for a second processing iteration.

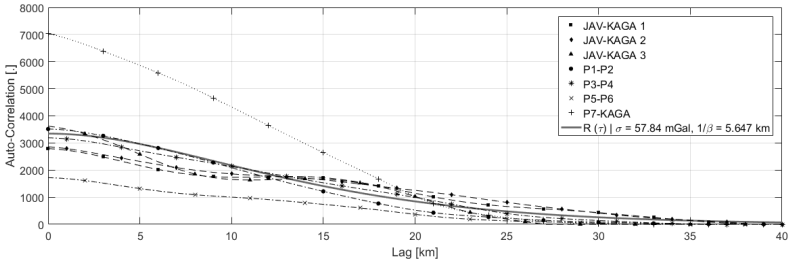

Figure 4. Estimated autocorrelation functions for the seven profiles along with the (least squares) best fitting third-order Gauss-Markov autocorrelation function. The parameters σ = 57.84 mGal and $1/\beta$ = 5.647 km.

4.1. Repeated Lines

Gravity disturbance estimates for the three flights along the JAV-KAGA profile are shown in Figure 5, along with flight altitude and topography from the SRTM30 data product. The gravity variation clearly varies with topography, noticing that the areas around 15-25 km and 35 km are covered by ice.

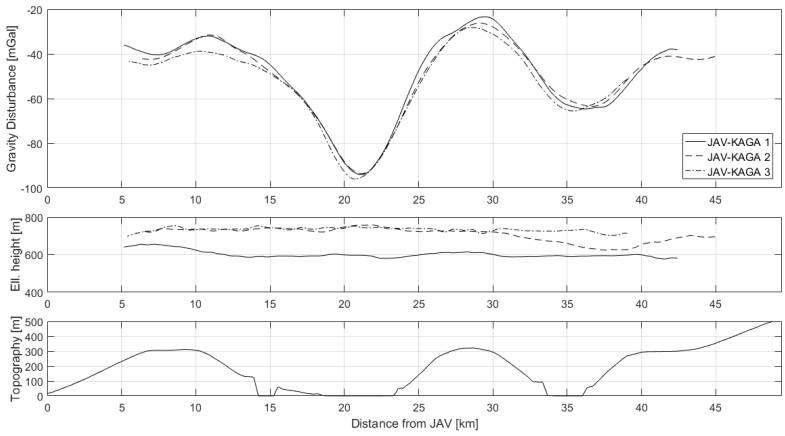

Figure 5. Profiles for the three repeated lines between JAV and KAGA. The gravity disturbance was modelled using a third-order Gauss-Markov model with uncertainty, σ = 57.84 mGal, and correlation, $1/\beta$ = 5.647 km: (**top**) Gravity disturbance estimates. (**middle**) Ellipsoidal height. (**bottom**) Topography from SRTM30 with respect to WGS84 ellipsoid.

The mean and standard deviation of the differences between the three profiles are shown in Table 5. Since the long wavelength information is assumed to be corrupted by sensor error variation, the profiles are corrected for a bias and linear trend, before the differences are formed.

Table 5. Mean and standard deviation of the difference in gravity estimates for the three repeated lines along the JAV-KAGA profile. The difference was formed from the profiles directly and by first removing a bias and linear trend from each profile.

		No Correction	Bias + Trend	
Line 1-2	Mean	-0.83	0	mGal
	STD	2.00	1.95	mGal
Line 1-3	Mean	-3.25	0	mGal
	STD	2.73	2.38	mGal
Line 2-3	Mean	-3.31	0	mGal
	STD	2.28	2.15	mGal

4.2. Comparison with AIRGrav Profiles

Gravity disturbance estimates along the three profiles, P1-P2, P3-P4 and P5-P6, are shown in Figures 6-8, along with the AIRGrav gravity profiles from OIB. From the height profiles it is evident that the lines P1-P2 and P3-P4 were flown in draped mode (following the topography). The first line closely follows the terrain, whereas the second line is more smooth. The third line, P5-P6, was flown at constant altitude. The OIB lines were also flown in draped mode. Since the gravity signal attenuates with distance from source, the elevation will influence the spatial resolution of the gravity profile. However, aircraft dynamics will influence the observed signal and may therefore also have an impact on the recovered gravity signal.

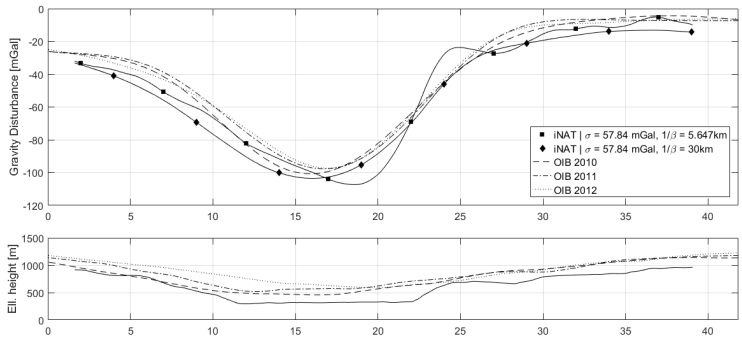

Figure 6. Gravity disturbance estimates for the profile between P1 and P2 for two different Gauss-Markov correlation lengths: (**top**) Gravity disturbance profile. (**bottom**) Height profile.

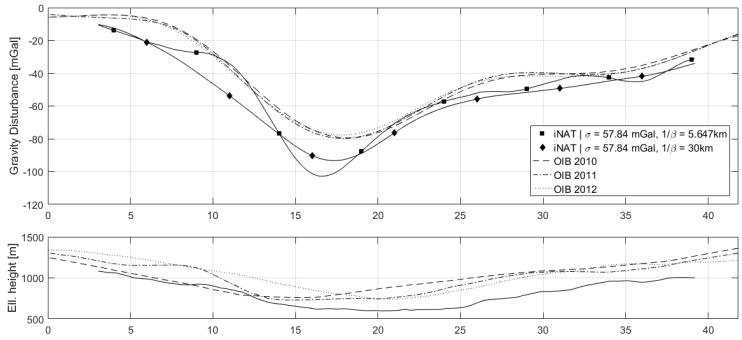

Figure 7. Gravity disturbance estimates for the profile between P3 and P4 for two different Gauss-Markov correlation lengths: (**top**) Gravity disturbance profile. (**bottom**) Height profile.

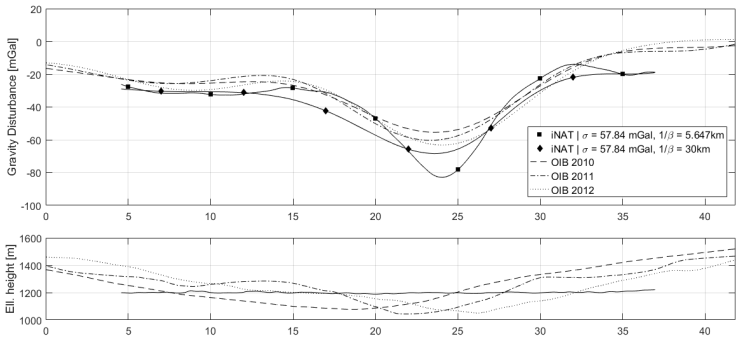

Figure 8. Gravity disturbance estimates for the profile between P5 and P6 for two different Gauss-Markov correlation lengths: (**top**) Gravity disturbance profile. (**bottom**) Height profile.

The AIRGrav instrument was carried by a fixed-wing aircraft flying at approximately 134 m/s, whereas the iNAT instrument was flown in a helicopter at approximately 52 m/s. Therefore, the iNAT gravity profiles have a higher spatial resolution than the OIB profiles. This is also evident from the figures, indicating that the glacier gravity anomaly is more sharp than indicated by the OIB profiles. Since the correlation length of the Gauss-Markov stochastic process will influence the resolution of the gravity profile, it was increasing in order to arrive at gravity profiles with a resolution similar to that of the OIB estimates. The optimal similarity in terms of Root-Mean-Square (RMS) difference occurs around $1/\beta = 30$ km. The resulting profiles are also shown in the above figures and the statistics of the differences are shown in Table 6.

Table 6. Mean and standard deviation of the difference in gravity estimates along the three profiles. The gravity estimates were smoothed by increasing the correlation parameter to $1/\beta = 30$ km.

		No Correction			**Bias + Trend**			
		2010	**2011**	**2011**	**2010**	**2011**	**2012**	
P1-P2	Mean	7.10	8.86	8.46	0	0	0	mGal
	STD	3.79	4.90	4.20	3.59	4.20	3.70	mGal
P3-P4	Mean	10.8	10.4	10.5	0	0	0	mGal
	STD	4.96	4.42	4.19	3.84	3.51	2.83	mGal
P5-P6	Mean	8.46	8.04	6.07	0	0	0	mGal
	STD	3.40	2.96	5.28	3.16	2.91	5.22	mGal

4.3. Cross-Over Evaluation

The gravity profile along the P7-KAGA line is shown in Figure 9 together with the gravity estimates from the crossing lines. This line was flown at constant altitude over the glacier before increasing in altitude to reach the KAGA site. The cross over differences are listed in Table 7.

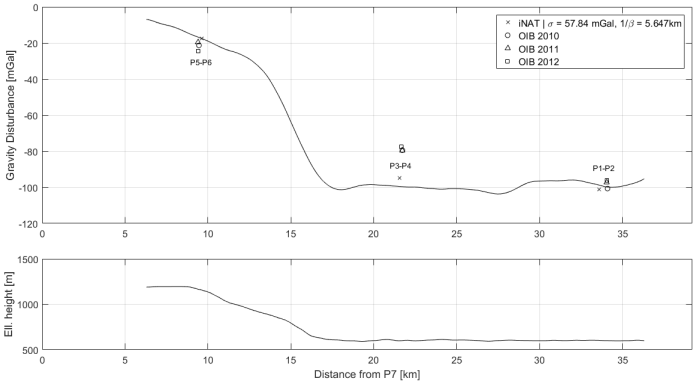

Figure 9. Profile along the P7-KAGA line which crosses over the three OIB lines: (**top**) Gravity disturbance profile values from crossing lines. (**bottom**) Height profile.

Table 7. Difference in gravity disturbance at the intersection points between the P7-KAGA line and the three OIB lines.

	iNAT	**OIB 2010**	**OIB 2011**	**OIB 2011**	
P1-P2	2.36	0.85	2.56	3.61	mGal
P3-P4	4.83	20.2	20.0	22.2	mGal
P5-P6	0.07	4.42	2.98	7.78	mGal

5. Discussion

The statistics from the repeated lines in Table 5 suggests that the gravity estimates are biased with respect to one another. As argued in the introduction, the temperature variation is suspected to corrupt the long wavelength information in the gravity estimates. The first two profiles are least biased and are flown consecutively at the beginning of the survey. The third profile, which has a larger bias, was flown at the end of the survey, where the sensor errors have had time to evolve. With the mean value removed, the agreement between the profiles are 2.00-2.73 mGal and by additionally removing a linear trend, the agreement improves to 1.95-2.38 mGal. The convention for comparing airborne gravity estimates is in terms of the Root-Mean-Square-Error (RMSE), which is related to the standard deviation as

$$\sigma = \sqrt{\frac{\sum (x - \bar{x})^2}{N-1}}\,, \quad RMS = \sqrt{\frac{\sum x^2}{N}} \quad \text{and} \quad RMSE = RMS/\sqrt{2}\,, \tag{15}$$

meaning that the accuracy is better than 2 mGal. The cross over differences from Table 7 do also fit within this confidence level.

Since the RTS smoother does not have an associated filter length, it is not straightforward to associate the profiles with a spatial resolution. This is however an important issue, if the results are to be compared with other studies. In Figures 6-8 it was shown how the correlation length of the Gauss-Markov process could be varied to effectively control the degree of smoothing applied to the gravity profile. However, since the standard deviation of the process will also influence the

degree of smoothing, the connection between correlation length and equivalent filter length is also not straightforward. Moreover, the parameters of the stochastic model will influence the Kalman filter estimates themselves and not only the RTS smoothed estimates, further complicating the issue.

In order to estimate the equivalent filter length and thus the spatial resolution of the gravity estimates, a set of alternative gravity estimates, independent of any stochastic model, was derived from the data. From Eq. (1) the specific force, $\mathbf{f}^b$, observed by the IMU is related to gravity as

$$\mathbf{g}^n = \dot{\mathbf{v}}^n - \left(\mathbf{C}_b^n \, \mathbf{f}^b - (2\boldsymbol{\Omega}_{ie}^n + \boldsymbol{\Omega}_{en}^n) \, \mathbf{v}^n \right) , \tag{16}$$

where the term inside the parenthesis can be formed using the RTS smoothed Kalman filter estimates. The observed specific force is corrected for bias variation, resolved about the n-frame axes and corrected for the velocity dependent fictitious forces. The term, $\dot{\mathbf{v}}^n$ can be derived from the GNSS position solution using a 2nd order central difference approach. Gravity estimates are derived by differencing these two components and applying a two-pass Butterworth filter. By tuning the filter length to match the Kalman filter gravity estimates, an estimate of the equivalent filter length is available. This was done on a line-to-line basis. Then, using the average ground speed along each line, the filter length was converted to a (half-wavelength) spatial resolution. The average spatial resolution for the seven lines is 3.2 km with a standard deviation of 1.1 km. The power spectrum for the entire survey is shown in Figure 10.

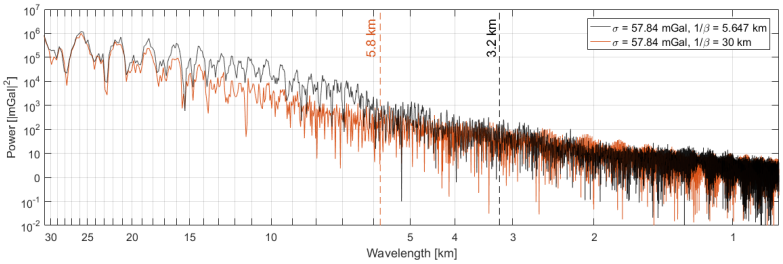

Figure 10. Power spectrum of the estimated gravity disturbance across the entire flight. The spectrum is also shown for the over-smoothed estimates and the estimated spatial resolutions are indicated by vertical lines.

Due to the significant variation in estimated spatial resolution, a conservative estimate is 4.5 km, where the power spectrum reaches the 10^2 magnitude level. Also shown in the figure is the power spectrum for the over-smoothed solution, i.e. with $1/\beta = 30$ km, containing less power in the 6-20 km wavelength interval. Using the same approach as before, the spatial resolution was estimated to 5.8 km with a standard deviation of 1.1 km. Since these estimates were tuned to mimic the AIRGrav OIB profiles, the expected spatial resolution is 6.7 km, which is within the confidence bounds. Some inconsistency may also originate from the filter, since the shape of the filter applied in the AIRGrav processing is unknown to the authors.

This approach does however not seem to form a consistent connection between spatial resolution in terms of a filter and in terms of a stochastic model. As this connection is important in order to compare results, further investigations are encouraged.

6. Conclusions

It has been shown that strapdown airborne gravimetry is feasible from a helicopter platform. The strapdown system is attractive since it is easily installed and does not require any operation during the

flight. Moreover, no signs of degradation was seen during draped flying. With mean values removed, the accuracy was estimated to better than 2 mGal at a half-wavelength spatial resolution of 4.5 km.

It was also found that the fixed-wing OIB profiles across the Jakobshavn Glacier underestimated the peak gravity anomaly by up to 20 mGal as a consequence of the faster aircraft speed.

Author Contributions: Conceptualization, Tim Jensen and Rene Forsberg; Data curation, Tim Jensen and Rene Forsberg; Formal analysis, Tim Jensen; Funding acquisition, Rene Forsberg; Investigation, Tim Jensen; Methodology, Tim Jensen; Project administration, Rene Forsberg; Software, Tim Jensen; Supervision, Rene Forsberg; Visualization, Tim Jensen; Writing – original draft, Tim Jensen.

Acknowledgments: The data from Operation IceBridge is made available by NASA at https://icebridge.gsfc.nasa.gov and the data from KAGA GPS station made available by UNAVCO at https://unavco.org. Funding for the test was provided by DTU Space as part of work for maintaining the Greenland gravity network on behalf of the Danish Mapping Agency (SDFE)

References

1. Thompson, L.G.D.; LaCoste, L.J.B. Aerial gravity measurements. *Journal of Geophysical Research* **1960**, *65(1)*, pp. 305-322, DOI 10.1029/JZ065i001p00305.
2. Gumert, W.R. An historical review of airborne gravity. *The Leading Edge* **1998**, *17(1)*, pp. 113-116, DOI 10.1190/1.1437808.
3. Brozena, J.M. The Greenland Aerogeophysics Project: Airborne gravity, topographic and magnetic mapping of an entire continent. In *From Mars to Greenland: Charting Gravity with Space and Airborne Instruments*, International Association of Geodesy Symposia, vol 110; Colombo, O.; Springer: Berlin-Verlag, 1992; pp. 203-214, DOI 10.1007/978-1-4613-9255-2_19.
4. Forsberg, R., Olesen, A.V. Airborne Gravity Field Determination. In *Sciences of Geodesy - I: Advances and Future Directions*; Xu, G.; Springer Berlin Heidelberg, 2010; pp. 93-104, DOI 10.1007/978-3-642-11741-1_3.
5. Fairhead, J.D.; Odegard, M.E. Advances in gravity survey resolution. *The Leading Edge* **2002**, *21(1)*, pp. 36-37, DOI 10.1190/1.1445845.
6. Sander, S.; Argyle, M.; Elieff, S.; Ferguson, S.; Lavoie, V. and Sander, L. The AIRGrav airborne gravity system. *Recorder* **2005**, *30(8)*.
7. Götze, H-.J.; Meyer, U.; Choi, S. Helicopter Gravity Survey in the Dead Sea Area. *EOS Transactions American Geophysical Union* **2010**, *91(12)*, pp. 109-110, DOI 10.1029/2010EO120002.
8. Segawa, J.; Joseph E., J.; Nakayama, E.; Kumar K., V.; Kusumoto, S.; Ito, T.; Sekizaki, S.; Ishihara, T.; Komazawa, M. Application of Gravimetry by Helicopter to Identify Marine Active Faults and Improve Accuracy of Geoid at Coastal Zones. In *A Window on the Future of Geodesy*, International Association of Geodesy Symposia, vol 128; Sansó, F.; Springer: Berlin, Heidelberg, 2005; pp. 229-235, ISBN 978-3-540-27432-2.
9. Greenbaum, J.; Richter, T.; Young, D.; Blankenship, D. UTIG airborne gravity operations in Antarctica from 2008 to 2016 and future directions. Presented at *2016 Airborne Gravimetry for Geodesy Summer School*; Hosted by the National Geodetic Survey, Silver Spring, Maryland, USA, May 23-27, 2016; URL https://ngs.noaa.gov/GRAV-D/2016SummerSchool/presentations/day-1/10Greenbaum_NGS_UTIG_v2.pdf.
10. Schwarz, K.P.; Li., Z. An introduction to airborne gravimetry and its boundary value problems. In *Geodetic Boundary Value Problems in View of the One Centimeter Geoid*, Lecture Notes in Earth Sciences, vol 65; Sansó, F., Rummel, R.; Springer: Berlin, Heidelberg, 1997; pp. 312-358, ISBN 978-3-540-68353-7.
11. Wei, M.; Schwarz, K.P. Flight test results from a strapdown airborne gravity system. *Journal of Geodesy* **1998**, *72(6)*, pp. 323–332, DOI 10.1007/s001900050171.
12. Glennie, C.; Schwarz, K.P.; Bruton, A.; Forsberg, R.; Olesen, A.V.; Keller, K. A comparison of stable platform and strapdown airborne gravity. *Journal of Geodesy* **2000**, *74(5)*, pp. 383–389, DOI 10.1007/s001900000082.
13. Becker, D. Advanced Calibration Methods for Strapdown Airborne Gravimetry. *PhD Thesis*; Technische Universität Darmstadt, 2016; URL http://tuprints.ulb.tu-darmstadt.de/5691/.
14. Becker, D.; Becker, M.; Olesen, A.V.; Nielsen, J.E.; Forsberg, R. Latest results in strapdown airborne gravimetry using an iMAR RQH unit. In *Proceedings of the 4th IAG Symposium on Terrestrial Gravimetry: Static and Mobile Measurements (TG-SMM 2016)*; State Research Center of the Russian Federation, 2016; pp. 19-25, ISBN 9785919950332.

15. Arnold, E.; Rodiguez-Morales, F.; Paden, J.; Leuschen, C.; Keshmiri, S.; Yan, S.; Ewing, M.; Hale, R.; Mahmood, A.; Blevins, A.; Mishra, A.; Karidi, T.; Miller, B.; Sonntag, J. HF/VHF Radar Sounding of Ice from Manned and Unmanned Airborne Platforms. *Geosciences* **2018**, *8(5)*, 182, DOI 10.3390/geosciences8050182.
16. An, L.; Rignot, E.; Ellief, S.; Morlighem, M.; Millan, R.; Mouginot, J.; Holland, D.M.; Paden, J. Bed elevation of Jakobshavn Isbræ, West Greenland, from high-resolution airborne gravity and other data. *Geophysical Research Letters* **2017**, *44*, 3728-3736, DOI 10.1002/2017GL073245.
17. Becker, D.; Nielsen, J.E.; Ayres-Sampaio, D.; Forsberg, R.; Becker, M.; Bastos, L. Drift reduction in strapdown airborne gravimetry using a simple thermal correction. *Journal of Geodesy* **2015**, *89(11)*, pp. 1133-1144, DOI 10.1007/s00190-015-0839-8.
18. Groves, P.D. *Principles of GNSS, Inertial, and Multisensor Integrated Navigation Systems*, 2nd ed.; Artech House: Boston, London, 2013; ISBN 978-1-60807-005-3.
19. Jekeli, C. *Inertial Navigation Systems with Geodetic Applications*; Walter de Gruyter: Berlin, New York, 2001; ISBN 3-11-015903-l.
20. Titterton, D.H.; Weston, J.L. *Strapdown Inertial Navigation*, 2nd ed.; Institution of Electrical Engineers: Stevenage, United Kingdom, 2004; ISBN 0 86341 358 7.
21. Hofmann-Wellenhof, B.; Moritz, H. *Phyiscal Geodesy*, 2nd ed.; SpringerWienNewYork, 2006; ISBN 978-3-211-33544-4.
22. National Imagery and Mapping Agency. *Department of Defense World Geodetic System 1984, Its Definition and Relationships with Local Geodetic Systems*, 3rd ed.; NIMA Technical Report TR8350.2, 1997; URL http://earth-info.nga.mil/GandG/publications/tr8350.2/tr8350_2.html.
23. Maybeck, P.S. *Stochastic models, estimation and control*, vol. 1; Mathematics in Science and Engineering, vol. 141; Bellman, R., 1979; ISBN 0-12-480701-1.
24. Van Loan, C.F. Computing Integrals Involving the Matrix Exponential. *IEEE Transactions on Automatic Control* **1978**, *23(3)*, pp. 395-404, DOI 10.1109/TAC.1978.1101743.
25. Brown, R.G.; Hwang, P.Y.C. *Introduction to Random Signals and Applied Kalman Filtering*, 4th Ed.; John Wiley and Sons Inc.: Hoboken, USA, 2012; ISBN 978-0-470-60969-9.
26. Gelb, A. *Applied Optimal Estimation*; The M.I.T Press: Cambridge, Massachusetts and London, England, 2013; ISBN 0-262-20027-9.
27. Kwon, J.H.; Jekeli, C. A new approach for airborne vector gravimetry using GPS/INS. *Journal of Geodesy* **2001**, *74(10)*, pp. 690–700, DOI 10.1007/s001900000130.

References

[1] Franz Barthelmes. *Definition of Functionals of the Geopotential and their calculation from spherical harmonic modeles*. Tech. rep. Helmholtz-Zentrum Potsdam, 2013. DOI: 10.2312/GFZ.b103-0902-26.

[2] W Bosch. "On the computation of derivatives of Legendre functions". In: *Physics and Chemistry of the Earth, Part A: Solid Earth and Geodesy* 25.9-11 (2000), pp. 655–659. ISSN: 14641895. DOI: 10.1016/S1464-1895(00)00101-0.

[3] William E Boyce and Richard C DiPrima. *Elementary Differential Equations and Boundary Value Problems*. 8th. John Wiley and Sons, Inc, 2005, p. 806. ISBN: 978-0-471-43338-5. DOI: 10.2307/2320609.

[4] Kenneth R. Britting. *Inertial Navigation Systems Analysis*. 1971, p. 267. ISBN: 978-1608070787.

[5] Robert Grover Brown and Patric Y. C. Hwang. *Random Signals and Applied Kalman Filtering*. John Wiley & Sons, Inc., 2012. ISBN: 978-0-470-60969-9.

[6] João R. Cardoso and F. Silva Leite. "Exponentials of skew-symmetric matrices and logarithms of orthogonal matrices". In: *Journal of Computational and Applied Mathematics* 233.11 (2010), pp. 2867–2875. ISSN: 03770427. DOI: 10.1016/j.cam.2009.11.032. URL: http://dx.doi.org/10.1016/j.cam.2009.11.032.

[7] Kenth Engø. "On the BCH-formula in so(3)". In: *Bit Numerical Mathematics* 41.3 (2001), pp. 629–632. ISSN: 00063835. DOI: 10.1023/A:1021979515229. URL: http://link.springer.com/10.1023/A:1021979515229.

[8] Toshio Fukushima. "Numerical computation of spherical harmonics of arbitrary degree and order by extending exponent of floating point numbers: III integral". In: *Computers and Geosciences* 63.X (2012), pp. 17–21. ISSN: 00983004. DOI: 10.1016/j.cageo.2013.10.010.

[9] Arthur Gelb et al. *Applied optimal estimation*. Ed. by Arthur Gelb. The M.I.T Press, 1974. ISBN: 0262200279.

[10] Paul D. Groves. *Principles of GNSS, Inertial, and Multisensor Integrated Navigation Systems*. 2nd. Artech House Remote Sensing Library, 2013. ISBN: 978-1608070053.

[11] Michael T. Heath. *Scientific Computing: An Introductory Survey*. 2nd. McGraw-Hill Higher Education, 2002. ISBN: 978-0-07-239910-3.

[12] Bernhard Hofmann-Wellenhof and Helmut Moritz. *Physical Geodesy*. 2nd, corrected. SpringerWienNewYork, 2006. ISBN: 3-211-33544-7.

[13] S. A. Holmes and W. E. Featherstone. "A unified approach to the Clenshaw summation and the recursive computation of very high degree and order normalised associated Legendre functions". In: *Journal of Geodesy* 76.5 (2002), pp. 279–299. ISSN: 09497714. DOI: 10.1007/s00190-002-0216-2.

[14] David Y Hsu. "An Accurate and Efficient Approximation to the Normal Gravity". In: *Position Location and Navigation Symposium, IEEE 1998*. 1998, pp. 38–44. DOI: 10.1109/PLANS.1998.669866.

[15] Christopher Jekeli. *Inertial Navigation Systems with Geodetic Applications*. 2001, pp. 51–54. ISBN: 3110159031. DOI: 10.1515/9783110800234.

[16] J. H. Kwon and C. Jekeli. "A new approach for airborne vector gravimetry using GPS/INS". In: *Journal of Geodesy* 74.10 (2001), pp. 690–700. ISSN: 09497714. DOI: 10.1007/s001900000130.

[17] P S Maybeck. *Stochastic models, estimation, and control*. Vol. 1. 1. 1979. ISBN: 0124807011. URL: http://www.cs.unc.edu/{~}welch/media/pdf/maybeck{_}ch1.pdf.

[18] Kkf Kenneth Franklin Riley, Michael Paul Hobson, and Stephen John Bence. *Mathematical Methods for Physics and Engineering*. 2006, p. 1333. ISBN: 1139450999.

[19] Wolfgang Torge. *Geodesy*. Walter de Gruyter, 2001, p. 432. ISBN: 3-11-017072-8. DOI: 10.1515/9783110879957.

[20] Charles F. Van Loan. "Computing Integrals Involving the Matrix Exponential". In: *IEEE Transactions on Automatic Control* 23.3 (1978), pp. 395–404. ISSN: 15582523. DOI: 10.1109/TAC.1978.1101743.

[21] H. G. Wenzel. "On the Definition and Numerical Computation of Free Air Graity Anomalies". In: *Bulletin d'Information - Bureau Gravimetrique International* 64 (1989), pp. 23–40.

Glossary and Index

List of Acronyms

ALF	Associated Legendre Function
CIRS	Conventional Inertial Reference System
CTRS	Conventional Terrestrial Reference System
DCM	Direction Cosines Matrix
ECEF	Earth-Centred, Earth-Fixed
ECI	Earth-Centred Inertial
EGM96	Earth Gravitational Model 1996
GNSS	Global Navigation Satellite System
GPS	Global Positioning System
GPST	GPS Time
GRS80	Geodetic Reference System 1980
ICRF	International Celestial Reference Frame
ICRS	International Celestial Reference System
IERS	International Earth Rotation Service
ICKF	Indirect Centralised Kalman Filter
IGS	International GNSS Service
iMAR	Gesellschaft für Inertiale Meß-, Automatiserungs- und Regelsysteme
IMU	Inertial Measurement Unit
iNAT	The iMAR iNAT-RQH-0001 IMU owned by DTU Space
INS	Inertial Navigation System
ITRF	International Terrestrial Reference Frame
ITRS	International Terrestrial Reference System
IVP	Initial Value Problem
JD	Julian Date
LHS	Left Hand Side
MJD	Modified Julian Date
ODE	Ordinary Differential Equation
OIB	Operation IceBridge
PPS	Pulse-Per-Second
PSD	Power Spectral Density
RHS	Right Hand Side
RLG	Ring Laser Gyroscope
RQH	The iMAR-RQH-1003 IMU owned by TU Darmstadt

SAG	Strapdown Airborne Gravimetry
SI	Système International d'unités
TAI	International Atomic Time
UAV	Unmanned Arial Vehicle
UTC	Coordinated Universal Time
WGS84	World Geodetic System 1984

List of Symbols

Reference Frames

a	Arbitrary reference frame
b	Body frame
e	Terrestrial or Earth-Centred-Earth-Fixed reference frame
i	Inertial or Earth-Centred Inertial reference frame
n	Navigation or North-East-Down frame
s	Sensor frame
t	Arbitrary reference frame
w	Wander-Azimuth frame

Scalars

a	Semi-major axis
b	Semi-minor axis
e	First eccentricity
E	Linear eccentricity
f	Flattening
g_0	Standard gravity, $g_0 = 9.80655\ \mathrm{m/s^{-2}}$
h	Height above ellipsoid (geodetic height)
t	Time
t_k	Time at current epoch
t_{k+1}	Time at next epoch
v_N	North-component of velocity
v_E	East-component of velocity
v_D	Down-component of velocity
G	Gravitational constant
GM	Gravitational constant times Earth mass
H	Height above sea level (orthometric height)
N	Geoidal height (geoid height with respect to ellipsoid)
M	Earth's mass
P	Point in space
Q	Point on reference ellipsoid
r	Geocentric distance to point
R	Radius of the Earth
R_E	Radius of curvature of the prime vertical (east)
R_N	Radius of curvature of meridian (north)
U	Normal gravity potential

V	Gravitational potential
W	Gravity potential
x	First component of Cartesian position
y	Second component of Cartesian position
z	Third component of Cartesian position
α	Roll angle or Euler angle
β	Pitch angle or Euler angle
β	Reduced latitude
γ	Yaw angle or Euler angle
δt	Navigation equations update interval / measurement interval
θ	Arbitrary angle
θ	Co-latitude
κ	Curvature
λ	Geodetic longitude
ρ	Density
ϱ	Radius of curvature
τ	Kalman filter update interval
ϕ	Geodetic latitude
ϕ'	Geocentric latitude
Φ	Potential from centrifugal force
ψ_{nw}	Wander angle
ω_{ie}	Angular rate of Earth rotation with respect to inertial space
ω_x	Angular rate about x-axis
ω_y	Angular rate about y-axis
ω_z	Angular rate about z-axis

Vectors

$\mathbf{a}$	Acceleration
$\mathbf{b}$	Bias errors
$\mathbf{e}_x$	Unit vector along x-direction
$\mathbf{e}_y$	Unit vector along y-direction
$\mathbf{e}_z$	Unit vector along z-direction
$\mathbf{f}$	Specific force vector
$\mathbf{g}$	Gravity vector (gravitation plus centrifugal force)
$\bar{\mathbf{g}}$	Gravitation vector (gravitational attraction from mass)
$\mathbf{l}$	Lever arm
$\mathbf{n}$	Surface normal
$\mathbf{p}$	Geodetic position vector
$\mathbf{q}$	Quaternion attitude

$\mathbf{r}$	Cartesian position vector
$\mathbf{v}$	Arbitrary vector
$\mathbf{v}$	Velocity vector
$\mathbf{w}$	Vector of white noise
$\mathbf{w}_m$	Measurement noise vector
$\mathbf{w}_s$	System noise vector
$\mathbf{x}$	State vector
$\mathbf{z}$	Measurement vector
$\delta\mathbf{g}$	Gravity disturbance vector
$\delta\mathbf{z}$	Measurement innovation
$\boldsymbol{\gamma}$	Normal gravity vector
$\boldsymbol{\psi}$	Ordered triple of roll, pitch and yaw or Euler angles $[\alpha \ \ \beta \ \ \gamma]^\top$
$\boldsymbol{\omega}$	Angular rate of rotation
$\boldsymbol{\omega}_{at}$	Angular rate of a-frame with respect to t-frame. These frames are arbitrary. The order of the subscripts is **not** arbitrary, see appendix REF!!.

Matrices

$\mathbf{C}_t^a$	Transformation matrix from t to a frame. These frames are arbitrary
$\mathbf{C}$	Covariance matrix
$\mathbf{F}$	System model
$\mathbf{H}$	Measurement model
$\mathbf{I}$	Identity matrix
$\mathbf{K}$	Kalman gain matrix
$\mathbf{M}$	Scale-factor and cross-coupling errors
$\mathbf{P}$	Error covariance matrix
$\mathbf{Q}$	System noise covariance matrix
$\mathbf{R}$	Measurement noise covariance matrix
$\mathbf{R}_x(\theta)$	Rotation matrix that rotates a vector by the angle θ around the x-axis
$\mathbf{R}_y(\theta)$	Rotation matrix that rotates a vector by the angle θ around the y-axis
$\mathbf{R}_z(\theta)$	Rotation matrix that rotates a vector by the angle θ around the z-axis
$\boldsymbol{\Phi}$	Transition matrix
$\boldsymbol{\Psi}$	Skew symmetric matrix for incremental rotation (small angles)
$\boldsymbol{\Omega}$	Skew symmetric form of the angular velocity $\boldsymbol{\omega}$
$\boldsymbol{\Omega}_{at}$	Skew symmetric form of the angular velocity $\boldsymbol{\omega}_{at}$

Other Symbols

$\dot{\mathbf{v}}$	Time-derivative of $\mathbf{v}$
$\hat{\mathbf{v}}$	Estimate of $\mathbf{v}$
$[\boldsymbol{\psi}\times]$	Skew symmetric form of $\boldsymbol{\psi}$, i.e. $[\boldsymbol{\psi}\times] \equiv \boldsymbol{\Omega}$

$[\boldsymbol{\psi}\wedge]$	4×4 skew symmetric form of $\boldsymbol{\psi}$. This form is also denoted as $[\boldsymbol{\psi}\wedge] \equiv \mathbf{A}$
$\mathcal{O}(.)$	Refers to the order of whatever quantity is put inside the brackets
$(-)$	Refers to the beginning of the navigation processing cycle
$(+)$	Refers to the end of the navigation processing cycle

List of Figures

List of Tables

Index